

This PDF was created from the British Library's microfilm copy of the original thesis. As such the images are greyscale and no colour was captured.

Due to the scanning process, an area greater than the page area is recorded and extraneous details can be captured.

This is the best available copy

D

D74933'87

Attention is drawn to the fact that the copyright of this thesis rests with its author.

This copy of the thesis has been supplied on condition that anyone who consults it is understood to recognise that its copyright rests with its author and that no quotation from the thesis and no information derived from it may be published without the author's prior written consent.

III

534



D 2033/87

JARVIS K.E.

TARGET A.

NOT FOR H/C

Plates,
Color Plates
Double Sides.
-- leaflet
in back cover

534

CITY OF LONDON
POLY (CNAA)

**The petrogenesis and geochemistry of the dioritic
complexes south of Balmoral forest, Angus.**

by

Kym E. Jarvis

Submitted to the Council for National Academic Awards
in partial fulfilment of the requirements for the degree
of Doctor of Philosophy.
City of London Polytechnic, May 1987

**MAPS/CHARTS
RELATING TO THIS THESIS
HAVE NOT BEEN FILMED**

**PLEASE APPLY DIRECT
TO ISSUING UNIVERSITY**

A

The petrogenesis and geochemistry of the dioritic complexes South of Balmoral Forest, Angus.

Kym Jarvis

The Glen Doll and Juan Jorge Complexes are two contrasting late Caledonian calc-alkaline plutons intruded into Middle Dalradian metasediments at the northern end of Glen Clova, in the Angus District of Tayside, Scotland. The Glen Doll Complex (12km²) constitutes a wide range of rock types from olivine gabbro, through diorite, to adamellite. The bulk (>80%) of the succession consists of heterogeneous hornblende- and pyroxene-bearing diorites. Partially assimilated rafted metasedimentary xenoliths, are common in the intermediate rock types. The basic rocks are cumulates which display wall-parallel layering. Mineralogical variation displays a transition from pyroxene-dominated anhydrous assemblages to amphibole-dominated hydrous assemblages. The diorites by contrast display floor-parallel layering and typically contain cumulate magnetite and ilmenite. Petrographic and mineralogical data suggests that convective fractionation played an important role in the evolution of the cumulate rocks. Bulk rock major and trace element chemistry is consistent with crystal accumulation in the diorites and basic rocks. Certain trace-element patterns (e.g. Zn), however, indicate assimilation of now-eroded Middle Dalradian metasediments containing strata-bound zinc mineralisation. Strontium isotope data indicates that the basic rocks are crystallised from a mantle derived magma. The intermediate rocks and adamellites display a wide range of initial strontium-isotope ratios from 0.70632 to 0.71137. These ratios are consistent with a mantle-derived magma subsequently modified by assimilation of continental crust. In contrast to Glen Doll, the Juan Jorge Complex (6km²) is composed of homogeneous quartz-mica diorite and granite, displaying only gradual and subtle changes in mineralogy. Empirical major-element modelling and Rayleigh-fractionation models confirm that magmatic processes in the Glen Doll Complex were dominated by crystal accumulation and country-rock assimilation, while the Juan Jorge Complex was formed essentially by fractional crystallisation of a single parent magma.

This thesis is dedicated to Sam and Violet-Elizabeth.

Acknowledgements

This thesis would not have been completed without the help, guidance and continuing support of my husband Ian. Supervision from Alistair Baxter and Ian Platten is gratefully acknowledged. Thanks are due to Theresa Gluyas and Rosie G. Gent for their moral support, and to Paula Haslock and Ian Slipper for assistance with computing matters. Chris Turner provided valuable comparative data for the Glen Tilt Complex. The Department of Geology, City of London Polytechnic provided analytical facilities and gave partial financial assistance.

Additional analytical facilities were kindly made available by the following institutions: Kings College London (ICP-AES), University of Edinburgh (Electron Microprobe) and British Geological Survey London (strontium isotope analysis). Help by Nick Walsh, Simon Chenery (Kings College, London), Peter Hill (Edinburgh) and Bob Pankhurst (BGS, London) is gratefully acknowledged.

Hospitality was provided by Ann and Bill Edwards during the many visits to Glen Clova. Last, but not least, thanks to Lily May and Len for support during the final stages of this thesis.

Access to the field area was granted by the Nature Conservancy Council, the Forestry Commission and Clova Estates.

Contents

	Acknowledgements.....		
Chapter 1 Introduction			
1.1	Geographical setting.....		25
1.2	Geological history.....		29
1.2.1	Structural context.....		30
1.2.2	Metamorphic geology.....		37
1.2.3	Post intrusion events.....		40
Chapter 2 Previous research			
2.1	Introduction.....		41
2.2	Magmatic processes.....		41
2.2.1	Fractional crystallisation.....		42
2.2.2	Partial melting.....		42
2.2.3	Magma mixing.....		43
2.2.4	Contamination.....		44
2.2.5	Metasomatism.....		45
2.3	Caledonian igneous rocks of the British Isles.		47
2.3.1	Scottish calc-alkaline complexes.....		47
2.3.2	Irish calc-alkaline complexes.....		50
2.3.3	Recent geochemical research.....		50
2.4	The Glen Doll and Juan Jorge Complexes.....		53
Chapter 3 Field relationships			
3.1	Introduction.....		55
3.2	Glen Doll Complex.....		58
3.2.1	Diorites.....		58
3.2.2	Basic rocks.....		69
3.2.3	Adamellites.....		75
3.2.4	Xenoliths.....		79
3.3	Juan Jorge Complex.....		83
3.3.1	Diorite.....		83
3.3.2	Granite.....		87
3.3.3	Xenoliths.....		88
3.4	Features common to both complexes.....		90
3.4.1	Dykes - intermediate and acid.....		90
3.4.2	Faulting.....		95
3.5	Bridge Outcrops.....		97
Chapter 4 Petrography			
4.1	Introduction.....		101
4.2	Glen Doll Complex.....		101
4.2.1	Diorite.....		104
4.2.2	Monzonite.....		115
4.2.3	Adamellite.....		119
4.2.4	Basic rocks.....		121
4.3	Juan Jorge Complex.....		136
4.3.1	Diorite.....		136
4.3.2	Granite.....		138
4.4	Bridge Outcrops.....		139
4.5	Xenoliths and dykes from the Glen Doll and Juan Jorge Complexes.....		142
Chapter 5 Mineral Chemistry			
5.1	Introduction.....		149
5.2	Amphiboles.....		149

5.2.1	Amphiboles from the diorites and monzonites...	153
5.2.3	Amphiboles in the gabbroic rocks.....	156
5.2.4	Amphiboles from the appinitic rocks.....	157
5.2.5	Factors affecting amphibole chemistry.....	175
5.2.6	Relationship between amphibole composition and bulk rock chemistry.....	179
5.2.7	Summary of amphibole chemistry.....	181
5.3	Pyroxenes.....	182
5.3.1	Orthopyroxenes.....	184
5.3.2	Clinopyroxenes.....	185
5.4	Olivine.....	191
5.5	Mica.....	194
5.5.1	Phlogopite.....	194
5.5.2	Biotite.....	195
5.6	Plagioclase.....	196
5.6.1	Compositional variation.....	198
5.6.2	Zoning in plagioclase.....	202
5.7	Oxide minerals.....	204
5.7.1	Oxides from rafted metasedimentary xenoliths Glen Doll Complex.....	207
5.8	Sphene and apatite.....	207
5.8.1	Sphene.....	208
5.8.2	Apatite.....	208
5.8.3	Discussion of apatite and sphene chemistry....	209

Chapter 6 Geochemistry

6.1	Introduction.....	211
6.2	Major element chemistry.....	218
6.2.1	Silicon and aluminium.....	243
6.2.2	Titanium, iron and manganese.....	244
6.2.3	Calcium.....	245
6.2.4	Sodium and potassium.....	246
6.2.5	Phosphorus.....	246
6.2.6	Olivine gabbros.....	247
6.2.7	Discussion of the major element chemistry....	248
6.3	Trace element chemistry.....	251
6.3.1	Barium.....	251
6.3.2	Strontium.....	253
6.3.3	Vanadium and scandium.....	254
6.3.4	Nickel and chromium.....	255
6.3.5	Rubidium.....	257
6.3.6	Lithium.....	258
6.3.7	Copper and zinc.....	259
6.3.8	Zirconium.....	261
6.3.9	Discussion.....	263
6.4	Geochemistry of the microdiorite dykes and microdiorite xenoliths.....	264
6.5	Geochemistry of the appinites.....	264
6.6	Rare earth element geochemistry.....	265
6.6.1	Basic rocks.....	268
6.6.2	Diorites.....	270
6.6.3	Monzonites.....	272
6.6.4	Adamellites.....	272
6.6.5	Juan Jorge Complex.....	274
6.6.6	Discussion of the REE data.....	274

Chapter 7 Isotope geochemistry

7.1	Introduction.....	278
7.2	Strontium isotopes.....	278
7.2.1	Age of the Glen Doll and Juan Jorge Complexes.	282
7.7.2	Initial strontium isotope ratios.....	283
7.2.2.1	Diorites and basic rocks.....	283
7.2.2.2	Glen Doll adamellites.....	289
7.2.2.3	Juan Jorge and Lochnagar samples.....	291
7.3	Suggested further work on strontium isotope systematics.....	291
7.4	Summary.....	292
7.5	A comparison of data with other late Caledonian complexes.....	293

Chapter 8 Petrogenesis

8.1	Introduction.....	297
8.2	Parental liquids and starting compositions....	303
8.2.1	Glen Doll Complex.....	303
8.2.2	Juan Jorge Complex.....	309
8.3	Other liquid compositions.....	311
8.4	Isotope modelling.....	313
8.5	Modelling.....	315
8.5.1	Glen Doll Complex.....	315
8.5.1.1	Trace element modelling for the olivine gabbros, gabbros and diorites.....	316
8.5.1.2	Major element modelling of the diorites and gabbroic rocks.....	328
8.5.1.3	Semi-quantitative trace element modelling of the adamellites.....	344
8.5.1.4	Strontium isotope modelling of the Glen Doll Complex.....	350
8.5.2	Juan Jorge Complex.....	355
8.5.2.1	Trace element modelling.....	355
8.5.2.2	Major element modelling.....	360
8.6	Conclusions.....	362
8.6.1	Glen Doll Complex.....	362
8.6.1.1	Intermediate and basic rocks.....	362
8.6.1.2	Adamellites.....	365
8.6.2	Juan Jorge Complex.....	366

Chapter 9 Conclusions

9.1	Introduction.....	368
9.2	Glen Doll Complex.....	369
9.2.1	The cumulate rocks.....	369
9.2.2	Contamination.....	373
9.2.3	History of the rafted xenoliths.....	374
9.2.4	Relative importance of cumulate processes and contamination.....	374
9.2.5	Adamellites.....	374
9.3	Juan Jorge Complex.....	375
9.4	Dykes.....	377
9.5	Development of future work.....	377
9.6	Comparison of the study areas with other Scottish late Caledonian calc-alkaline plutonic complexes.....	378
9.7	Summary.....	380

References.....	381
Appendix A Sample localities and rock types.....	403
Appendix B Electron microprobe analyses.....	407
Key to tables B.1 to B.9 inclusive.....	407
Table B.1 Amphiboles.....	408
Table B.2 Amphibole nomenclature.....	418
Table B.3 Biotites.....	422
Table B.4 Olivines.....	428
Table B.5 Pyroxenes.....	429
Table B.6 Plagioclase.....	433
Table B.7 Apatite.....	442
Table B.8 Sphene.....	445
Table B.9 Oxides.....	451
Appendix C Whole rock geochemical analyses.....	
Table C.1 Glen Doll Complex.....	455
Table C.2 Juan Jorge Complex.....	474
Table C.3 Rare-earth elements, Glen Doll Complex.....	477
Table C.4 Rare-earth elements, Juan Jorge Complex.....	482
Appendix D Analytical techniques.....	
D.1 Bulk rock major and trace element analysis...	483
D.1.1 Preparation of solutions for trace element determination using an open acid digestion...	484
D.1.2 Preparation of solutions for major analysis using a lithium metaborate fusion.....	485
D.1.3 Determination of phosphorus by colorimetry...	486
D.1.3.1 Preparation of standards.....	486
D.1.3.2 Preparation of reagent.....	487
D.2 Rare-earth element analysis.....	487
D.3 Strontium isotope analysis.....	489
D.3.1 Ion-exchange procedure.....	489
D.4 Electron microprobe analysis.....	490

Enclosures

Fig. 3.1 Geology of the Glen Doll and Juan Jorge Complexes

Jarvis, I and Jarvis, K.E. 1985
 Rare-earth element geochemistry of standard sediments: a
 study using inductively coupled plasma spectrometry.
Chem. Geol. 53, 335-344.

Chapter 1 Figures

- Figure 1.1 General geology of the Eastern Highlands.
- Figure 1.2 Geology of the area around Glen Doll and Juan Jorge.
- Figure 1.3 Reconstruction of the Southern Uplands-Grampian Highlands area during Ordovician and Silurian times.
- Figure 1.4 Generalised map of the Scottish Caledonides showing the major divisions of the Dalradian and some Late Caledonian intrusive complexes.
- Figure 1.5 Suggested stratigraphical and structural relationships in the area around Glen Doll and Juan Jorge.

Chapter 2 Figures

- Figure 2.1 A map showing the distribution of the major late Caledonian complexes in Scotland (after Halliday et al., 1985).
- Figure 2.2 A map showing the locations of the major late Caledonian intrusions in Ireland (after Kennan, 1979)
- Figure 2.3 A sketch map to show the position of the Glen Doll and Juan Jorge Complexes to the south of the Lochnagar Granite, and the distribution of the northern and eastern diorites.

Chapter 3 Figures

- Figure 3.1 Geological map of the Glen Doll and Juan Jorge Complexes.
- Figure 3.2 Distribution of the monzonitic rocks of the Glen Doll Complex.
- Figure 3.3 Distribution of the coarse-grained dioritic facies of the Glen Doll Complex.
- Figure 3.4 A view looking NE showing the variable orientation of the igneous fabric in the hornblende diorite around a coarse-grained zone.
- Figure 3.5 Distribution of the pyroxene diorites in the Glen Doll Complex.
- Figure 3.6 Distribution of the basic rocks in the Glen Doll Complex.
- Figure 3.7 A lithological log along Kilbo Burn.
- Figure 3.8 Distribution of the xenoliths in the Glen Doll Complex.
- Figure 3.9 Distribution of areas of high concentrations of dykes, Glen Doll Complex.
- Figure 3.10 A rose diagram to show the orientation of the dykes in the Glen Doll Complex.
- Figure 3.11 Plan view of the rocks exposed at the Bridge Outcrops.

Chapter 4 Figures

- Figure 4.1 A lithological log along the Kilbo Burn, Glen Doll Complex.
- Figure 4.2 A drawing of a thin section of a pool of quartz at the Bridge Outcrop.

Chapter 5 Figures

- Figure 5.1 Titanium plotted against Al(IV) in amphiboles from the Glen Doll and Juan Jorge Complexes.
- Figure 5.2 A plot of Al(IV) against Al(VI) in amphiboles from the Glen Doll and Juan Jorge Complexes.
- Figure 5.3 A plot of Na+K against Al(IV) in amphiboles from the Glen Doll and Juan Jorge Complexes.
- Figure 5.4 Amphibole and whole-rock magnesium/iron ratios (wt. %) for the Glen Doll and Juan Jorge Complexes.
- Figure 5.5 A plot of titanium content of amphibole against titanium content of the whole rock for the Glen Doll and Juan Jorge Complexes.
- Figure 5.6 Pyroxenes and olivines plotted into the Wo-En-Fs triangle.
- Figure 5.7 A plot of titanium against Al(IV) in pyroxenes from the Glen Doll Complex.
- Figure 5.8 Diagram to show the compositions of clinopyroxenes from the Glen Doll Complex.
- Figure 5.9 Pyroxenes, olivines and amphiboles plotted into the Ca-Mg-Fe triangle for the Glen Doll and Juan Jorge Complexes (atomic %).
- Figure 5.10 Geochemical variation of orthopyroxenes and olivines, from the Glen Doll Complex (atomic %).
- Figure 5.11 Biotite compositions plotted into the Mg-(Na+K)-(Fe+Ti+Mn) triangle (atomic %).
- Figure 5.12 Plagioclase compositions plotted into the system Or-Ab-An.

Figure 5.13 Anorthite content of plagioclase feldspar plotted against whole-rock MgO for the Glen Doll and Juan Jorge Complexes.

Chapter 6 Figures

- Figure 6.1 AFM diagram for the Glen Doll and Juan Jorge Complexes (wt %).
- Figure 6.2 AFM diagram for the appinites, microdiorite dykes and microdiorite xenoliths from the Glen Doll Complex (wt %).
- Figure 6.3 Bivariate plot of SiO₂ and Al₂O₃ with MgO
- Figure 6.4 Bivariate plot of TiO₂ and FeO with MgO
- Figure 6.5 Bivariate plot of MnO and CaO with MgO
- Figure 6.6 Bivariate plot of Na₂O and K₂O with MgO
- Figure 6.7 Bivariate plot of P₂O₅ and CaO (incl. olivine gabbros) with MgO.
- Figure 6.8 Bivariate plot of FeO and MnO (incl. olivine gabbros) with MgO.
- Figure 6.9 Bivariate plot of TiO₂ with FeO and MnO with FeO.
- Figure 6.10 Bivariate plot of Ba and Sr with MgO.
- Figure 6.11 Bivariate plot of V and Sc with MgO.
- Figure 6.12 Bivariate plot of Ni and Cr with MgO.
- Figure 6.13 Bivariate plot of Rb and Li with MgO.
- Figure 6.14 Bivariate plot of Cu and Zn with MgO.
- Figure 6.15 Bivariate plot of Zr with MgO.
- Figure 6.16 Bivariate plot of Cr and Ni (incl. olivine gabbros) with MgO.

- Figure 6.17 Bivariate plot of Y and La with MgO.
- Figure 6.18 Bivariate plot of Sr and V with MgO.
- Figure 6.19 Bivariate plot of V with FeO and Sc with V.
- Figure 6.20 Bivariate plot of Sr/CaO and K₂O/Rb with MgO.
- Figure 6.21 Bivariate plot of La with P₂O₅ and La with TiO₂.
- Figure 6.22 Chondrite-normalised REE patterns for gabbros from the Glen Doll Complex.
- Figure 6.23 Chondrite-normalised REE patterns of diorites from the Glen Doll Complex.
- Figure 6.24 Chondrite-normalised REE patterns of monzonites and adamellites from the Glen Doll Complex.
- Figure 6.25 Summary diagram of the chondrite-normalised REE patterns of the Glen Doll Complex showing compositional ranges and comparative patterns from the Juan Jorge Complex.
- Figure 6.26 Chondrite-normalised REE patterns for xenoliths from the Glen Doll Complex and the Dalradian country rocks
- Figure 6.27 Chondrite-normalised REE patterns for andesitic lavas from the Lorne Plateau and the Sidlaw Hills.

Chapter 7 Figures

- Figure 7.1 Pseudoisochron for the adamellites of the Glen Doll Complex.
- Figure 7.2 Initial strontium-isotope ratios plotted against Rb/Sr for the Glen Doll and Juan Jorge Complexes
- Figure 7.3 Initial strontium-isotope ratios plotted against K/Rb for the Glen Doll and Juan Jorge Complexes.
- Figure 7.4 Initial strontium-isotope ratios plotted against strontium for the Glen Doll and Juan Jorge Complexes.
- Figure 7.5 Initial strontium-isotope ratios plotted against zinc for the Glen Doll adamellites.

Chapter 8 Figures

- Figure 8.1 Geochemistry of the Lorne and Sidlaw Hills lavas with fields for the plutonic rocks from the Glen Doll Complex.
- Figure 8.2 Incompatible-element mantle-normalised diagram for two basaltic andesites from the Lorne Plateau.
- Figure 8.3 Bivariate plot of Rb-Ba for basic and intermediate rocks from the Glen Doll Complex with modelling vectors.
- Figure 8.4 Bivariate plot of Cr-Ni for basic and intermediate rocks from the Glen Doll Complex with modelling vectors.
- Figure 8.5 Bivariate plot of Y-Ba for basic and intermediate rocks from the Glen Doll Complex with modelling vectors.
- Figure 8.6 Bivariate plot of Ce-Yb for basic and intermediate rocks from the Glen Doll Complex with modelling vectors.
- Figure 8.7 Modelling pathways for the Glen Doll Complex.
- Figure 8.8 Bivariate plot of Rb-Ba for the Glen Doll adamellites
- Figure 8.9 Bivariate plot of Sc-Sr for the Glen Doll adamellites
- Figure 8.10 Bivariate plot of Sr-Ba for the Glen Doll adamellites
- Figure 8.11 Bivariate plot of Ce-Yb for the Glen Doll adamellites
- Figure 8.12 A diagram to show the effect of assimilation of potential crustal contaminants.
- Figure 8.13 Bivariate plot of Ba-Rb for the Juan Jorge Complex
- Figure 8.14 Bivariate plot of Cr-Ni for the Juan Jorge Complex
- Figure 8.15 Bivariate plot of Ba-La for the Juan Jorge Complex

Figure 8.16 Bivariate plot of Ce-Yb for the Juan Jorge Complex

Figure 8.17 Incompatible-element mantle-normalised diagram for the basic rocks of the Glen Doll Complex.

Figure 8.18 Incompatible-element mantle-normalised diagram for the dioritic rocks of the Glen Doll Complex.

Chapter 4 Tables

Table 4.1 Summary of the modal mineralogy of the Glen Doll and Juan Jorge Complexes.

Chapter 5 Tables

Table 5.1 A table to show the number of microprobe analyses for each sample from the Glen Doll and Juan Jorge Complexes.

Table 5.2 Classification of calcic amphiboles (after Leake, 1978).

Table 5.3 Representative amphibole microprobe analyses from the Glen Doll and Juan Jorge Complexes.

Table 5.4 Representative pyroxene microprobe analyses from the Glen Doll Complex.

Table 5.5 Representative olivine microprobe analyses from the Glen Doll Complex.

- Table 5.6 Representative biotite and phlogopite microprobe analyses from the Glen Doll and Juan Jorge Complexes.
- Table 5.7 Representative plagioclase microprobe analyses from the Glen Doll and Juan Jorge Complexes.
- Table 5.8 Representative oxide microprobe analyses from the Glen Doll and Juan Jorge Complexes.
- Table 5.9 Representative sphene microprobe analyses from the Glen Doll and Juan Jorge Complexes.
- Table 5.10 Representative apatite microprobe analyses from the Glen Doll and Juan Jorge Complexes.

Chapter 6 Tables

- Table 6.1 Representative analyses of basic rocks and appinites from the Glen Doll Complex.
- Table 6.2 Representative analyses of the dioritic rocks from the Glen Doll Complex.
- Table 6.3 Representative analyses of monzonites and adamellites from the Glen Doll Complex.
- Table 6.4 Representative rock analyses from the Juan Jorge Complex and the Bridge Outcrops.
- Table 6.5 Representative analyses of intermediate and acid dykes from the Glen Doll Complex.
- Table 6.5A Representative analyses of microdiorite xenoliths from the Glen Doll and Juan Jorge Complexes.
- Table 6.6 Average chemical composition of some igneous rocks.
- Table 6.7 Average trace element abundances from a range of Caledonian plutonic rocks.
- Table 6.8 Ranges of selected trace elements for the Glen Doll Complex.

Chapter 7 Tables

Table 7.1 Strontium isotope data for the Glen Doll and Juan Jorge Complexes.

Chapter 8 Tables

- Table 8.1 Partition coefficients used in trace-element modelling.
- Table 8.2 Parental compositions used to model the evolution of the Glen Doll and Juan Jorge Complexes.
- Table 8.3 Average values for potential source materials.
- Table 8.4 Modelled data for pathway A-B (22-11% MgO) from olivine gabbro to gabbro.
- Table 8.5 Modelled data for pathway B-B1 (11-8% MgO) for the high magnesian gabbros.
- Table 8.6 Modelled data for pathway B1-C (8-6% MgO) for the low magnesian gabbros.
- Table 8.7 Modelled data for pathway D-F from a low to high titanium diorite.
- Table 8.8 Modelled data for pathway E-G from a low to high titanium-phosphorus diorite.
- Table 8.9 Modelled data for pathway H-I from a low titanium, uncontaminated diorite to a high titanium contaminated diorite.
- Table 8.10 A model for the production of a rafted xenolith from the Dalradian country rocks by partial melting.
- Table 8.11 Modelled data for the Juan Jorge Complex.

Chapter 1 Plates

- Plate 1.1 General view looking NW towards Craig Mellon. The lower slopes are extensively forested and craggy outcrops occur on the high valley sides (30007400).
- Plate 1.2 View looking SE along the glaciated valley of Glen Clova. The South Esk River meanders across a wide alluvium-covered flood plain (27777685).
- Plate 1.3 View looking north across a peat-covered plateau (580m) to the peak of Lochnagar (29297808).
- Plate 1.4 View of the southeastern part of the Glen Doll Complex looking across Glen Clova towards Red Craig. The zig-zag path provides access to an area only recently planted with coniferous trees and still affording good exposure of the hornblende diorite (27957665).
- Plate 1.5 A view looking SW from Moulzie, the diorites form steep bluffs along the high valley sides. The pink scree is formed from aplite blocks (28457795).
- Plate 1.6 View of the quarry at Braedownie (foreground) where diorite is extracted for local repair work (29177596).

Chapter 3 Plates

- Plate 3.1 General view looking west along Glen Doll across the Caenlochan National Nature Reserve and White Water River (28977612).
- Plate 3.2 View from Braedownie to Winter Corrie (below helicopter) looking west (28857572).
- Plate 3.3 Typical outcrop of well exposed hornblende diorite (28637624).
- Plate 3.4 View of a coarse grained hornblende diorite grading into a medium grained diorite over a distance of 3m. Coarse grained zones are particularly common in the White Water River (27847604).
- Plate 3.5 Plan view of a medium-grained hornblende diorite grading into a coarse-grained diorite. Note the biotite crystals weathering out (27847604).
- Plate 3.6 Plan view of a coarse grained patch of diorite containing skeletal amphibole with plagioclase cores (27847604).
- Plate 3.7 Appinitic pod enclosed within a hornblende bearing pegmatite which is seen veining the host gabbro (28707835).
- Plate 3.8 View of sharp contacts between gabbro (upper part of plate), appinite (centre) and pegmatite (lower) in Moulzie Burn (28707835).
- Plate 3.9 View of adamellite back veined diorite at Capel Road (29047844).
- Plate 3.10 View of an atypical angular rafted metasedimentary xenolith (lower centre) in a medium grained hornblende

- diorite (28917615).
- Plate 3.11 A group of fine-grained mafic xenoliths thought to be the remnants of fine-grained metasediments (29557555).
- Plate 3.12 Fine-grained xenolith composed of plagioclase, cpx and quartz showing a sharp contact with the host hornblende diorite in White Water River (27967603).
- Plate 3.13 Abundant xenoliths of both gneiss, fine-grained metasediment and microdiorite along the margin of the Juan Jorge diorite (26227923).
- Plate 3.14 Angular xenolith of gneiss in the Juan Juan diorite (26227923).
- Plate 3.15 View of the igneous fabric defined by the alignment of tabular plagioclase feldspar in the Juan Jorge diorite 25227984).
- Plate 3.16 Fine-grained metasedimentary xenoliths in the Juan Jorge granite (26677919).
- Plate 3.17 A typical view of an aplite dyke from White Water River 27937604).
- Plate 3.18 View of a rare curved white porphyry dyke from The Rives (27467739).
- Plate 3.19 View of a fault controlled valley below The Rives. Remnants of a quartz, feldspar porphyry dyke crop out on the lower slopes of the valley sides (27507737).
- Plate 3.20 A QFP dyke intruded into the Dalradian metasediments. The dyke is seen to follow the gneissose banding (27937517).
- Plate 3.21 View of the cross-cutting relationships seen between two sets of QFP dykes. The double dyke trends N-S and

the single dyke NE-SW (27847604).

Plate 3.22 A typical example of a microdiorite dyke intruding a medium-grained hornblende diorite. A chilled margin occurs on both sides of the dyke (27967603).

Plate 3.23 View along the fault-controlled valley of Moulzie Burn which cuts down from the high plateau through the northern gabbros (28727840).

Plate 3.24 Outcrop of coarse-grained porphyritic granite at the Bridge. The granite has a fine-grained chill against the banded gneiss country rock. Angular xenoliths of microdiorite display dark chilled margins (27757919).

Plate 3.25 Coarse-grained granite containing angular blocks of banded and unbanded gneiss, and microdiorite. All xenoliths are randomly orientated (27747893).

Chapter 4 Plates

- Plate 4.1 A typical hornblende diorite showing tabular plagioclase, biotite and green secondary, subsolidus amphibole (ppl).
- Plate 4.2 Same view as plate 4.1 but in XPL. Plagioclase feldspars display multiple twins. Secondary amphibole has a fibrous habit (xpl).
- Plate 4.3 View of a hornblende diorite showing a basal section of hornblende partially enclosing a tabular plagioclase crystal and a rounded orthopyroxene. The opx is preserved by the later surrounding amphibole (ppl).
- Plate 4.4 As above, a basal section of a hornblende crystal enclosing a subhedral crystal of opx (xpl).
- Plate 4.5 Single crystal of secondary actinolitic amphibole replacing clinopyroxene. The fibrous, colourless core contains exolved magnetite crystals. Around the core is a green rim composed of primary amphibole. Small apatite crystals are poikilitically enclosed within this rim (ppl).
- Plate 4.6 View of hornblende diorite showing the occurrence of prehnite. Abundant apatite is seen poikilitically enclosed by a basal section of amphibole (ppl).
- Plate 4.7 View of a hornblende diorite showing the close association of anhedral and rounded magnetite with biotite (xpl).
- Plate 4.8 Typical view of a hornblende diorite showing anhedral sphene in close association with amphibole and biotite. Magnetite crystals are seen poikilitically enclosing

apatite rods (ppl).

Plate 4.9 The centre of the slide shows a single crystal of bronzite with a corroded margin jacketed by primary amphibole. The orthopyroxene displays a subophitic texture with plagioclase (ppl).

Plate 4.10 As 4.9 but in crossed polars, clearly showing a margin of primary amphibole around an orthopyroxene crystal. The enclosed plagioclase shows a displacement, possibly along a shear plane (xpl).

Plate 4.11 Typical view of a quartz monzonite containing abundant biotite poikilitically enclosing magnetite and apatite (ppl).

Plate 4.12 Highly sericitised plagioclase crystal in a quartz monzonite. Biotite is interstitial to plagioclase (ppl).

Plate 4.13 Orthoclase in adamellite displaying a perthitic texture (xpl).

Plate 4.14 Olivine gabbro showing a large opx crystal and uneven growth boundary with plagioclase. Olivine primocrysts vary in size from 0.5-2.0mm and are poikilitically enclosed by plagioclase (xpl).

Plate 4.15 Olivine gabbro showing a plagioclase megacryst poikilitically enclosing small rounded olivine crystals. The olivines may occur in aggregates and typically form a cumulate framework (xpl).

Plate 4.16 General view of a low magnesia gabbro showing opx, cpx and primary brown amphibole poikilitically enclosing cpx and plagioclase. The dark crystal in the centre is biotite (xpl).

- Plate 4.17 View of a gabbro from Kilbo Burn showing a large poikilitic amphibole enclosing small, tabular plagioclase crystals. Locally large plagioclase primocrysts are developed. The plagioclase is randomly orientated and does not define a lamination (ppl).
- Plate 4.18 As above but showing clearly a large brown poikilitic amphibole enclosing plagioclase, opx and cpx (xpl).
- Plate 4.19 Single crystal of brown amphibole poikilitically enclosing plagioclase oikocrysts (xpl).
- Plate 4.20 Rafted xenolith containing characteristic aggregates of hercynitic spinel (ppl).
- Plate 4.21 Aggregate of spinel in quartz monzonite (xpl).
- Plate 4.22 General view of a microdiorite xenolith containing plagioclase phenocrysts (xpl).
- Plate 4.23 Porphyritic microdiorite dyke containing phenocrysts of secondary amphibole which are thought to be replacement products after pyroxene (xpl).

CHAPTER 1

Introduction

1.1 Geographical Setting

The two areas of study for this project are the Late Caledonian Glen Doll and Juan Jorge dioritic complexes. They are located at the north-western end of Glen Clova, Angus, and lie 60km north-west of Dundee (Fig. 1.1). The complexes together occupy an area of 35km². Exposure of the bed rocks is variable, with good continuous exposure in river bed sections and upper valley sides but very poor exposure on lower valley sides and on the high flat plateau (Plate 1.1). In order to make a detailed study of the geological relationships, the area was mapped at a scale of 1:10,000 using base maps published in 1972 (Ordnance Survey NO 27). All grid references quoted in this thesis fall within the Ordnance Survey grid square NO.

The area has been extensively glaciated, thus the main valley of Glen Clova is a modified U-shaped valley with little exposure on the low valley sides, which are covered with till (Plate 1.2). The River South Esk meanders across a wide flood plain and alluvium covers the valley floor. The Glen Doll Complex is trisected by the South Esk and White Water rivers which converge at the southern margin of the complex, and flow south-east through Glen Clova (Fig. 1.2). The valleys through which the White Water and South Esk flow, are steep-sided and flat-bottomed with a maximum vertical relief of 580m. The valleys are filled with alluvium and lateral moraines cover the bedrock in the lower valley slopes.

Above 580m there is an extensive peat-covered plateau (Plate

Plate 1.1
General view looking NW towards Craig Mellon. The lower slopes
are extensively forested and craggy outcrops occur on the high
valley sides.

(300074000)



Plate 1.2
View looking SE along the glaciated valley of Glen Clova. The
South Esk River meanders across a wide alluvium covered flood
plain.

(27777400)



Plate 1.1
General view looking NW towards Craig Mellon. The lower slopes are extensively forested and craggy outcrops occur on the high valley sides.

(300074000)



Plate 1.2
View looking SE along the glaciated valley of Glen Clova. The South Esk River meanders across a wide alluvium covered flood plain.

(27777400)



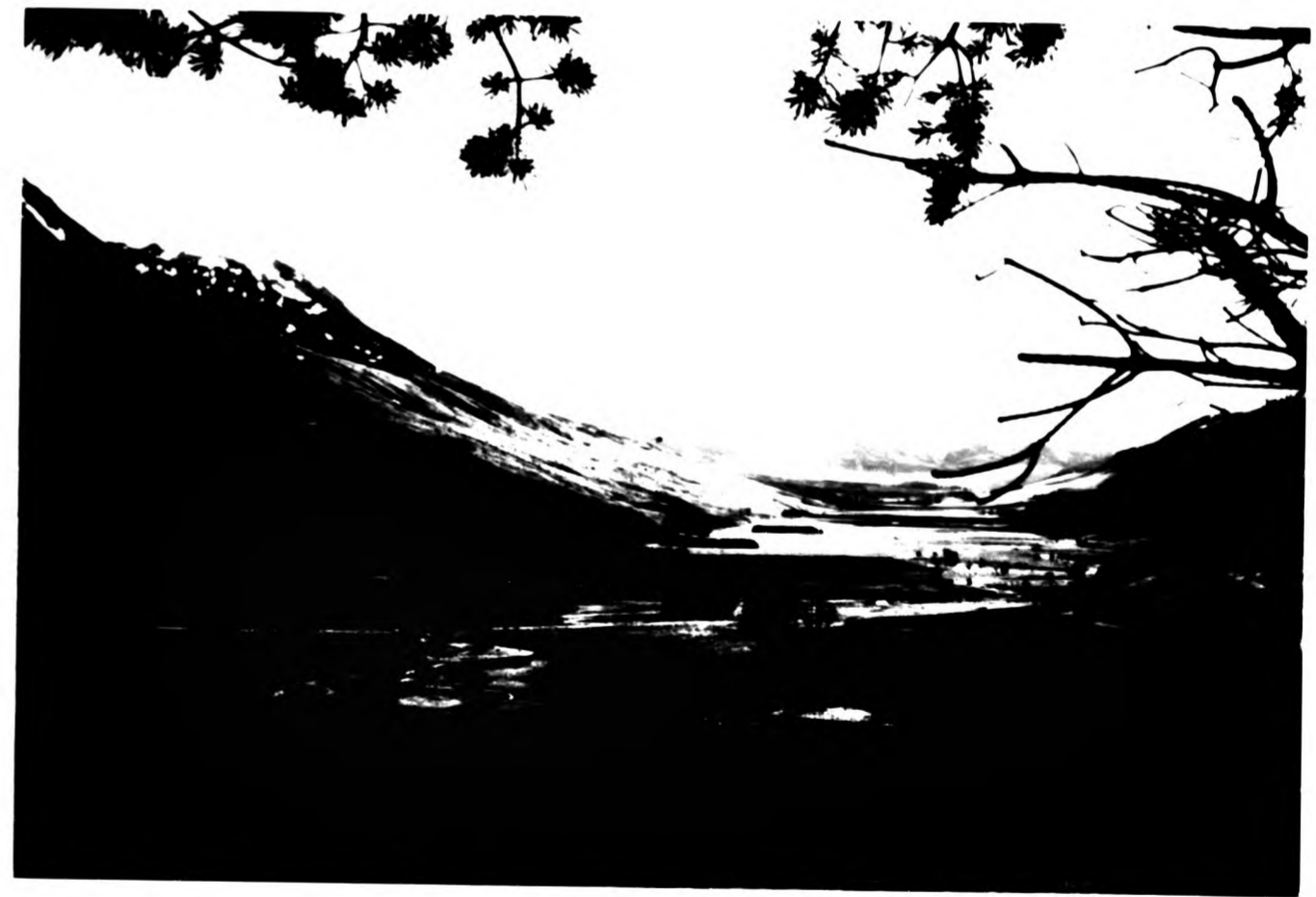
Plate 1.1
General view looking NW towards Craig Mellon. The lower slopes
are extensively forested and craggy outcrops occur on the high
valley sides.

(300074000)



Plate 1.2
View looking SE along the glaciated valley of Glen Clova. The
South Esk River meanders across a wide alluvium covered flood
plain.

(27777400)



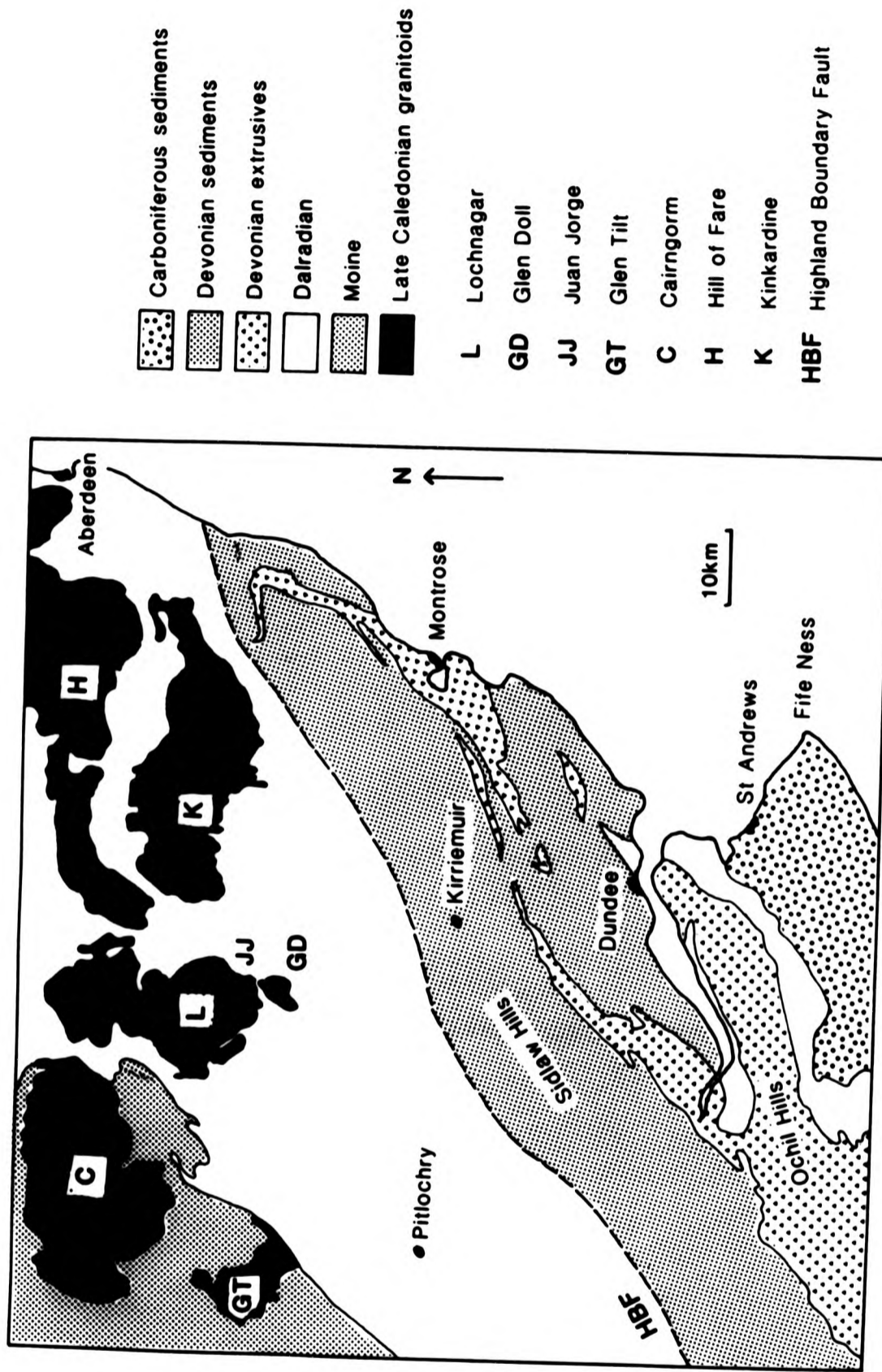


Fig. 1.1 General geology of the eastern Highlands (after Geological Survey Ten Mile Map Third Edition, 1979)

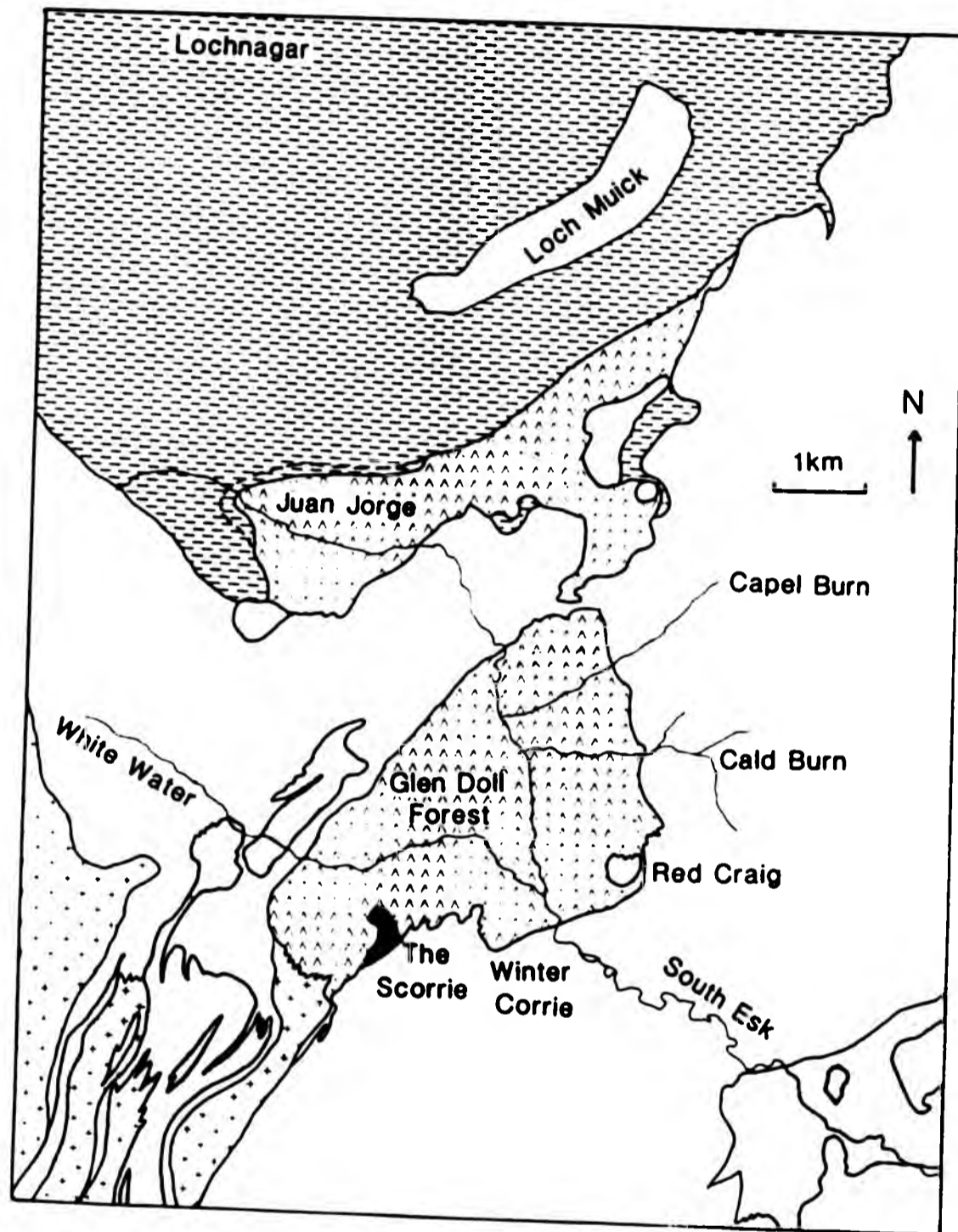








Fig. 1.2 Geology of the area around Glen Doll and Juan Jorge
(from BGS sheet 65)

- | | | | |
|---|-----------------------------------|---|--------------------------|
|  | Granite (late Caledonian) |  | Olivine gabbro |
|  | Granite gneiss (early Caledonian) |  | Epidiorite |
|  | Diorite |  | Dalradian meta-sediments |

1.3), stretching across Juan Jorge and north beyond Lochnagar (Figure 1.2). Small streams cutting down to the valley floor from the high plateau provide excellent vertical sections through the complex.

The valley base and sides up to 550m have been planted by the Forestry Commission with a variety of coniferous trees forming a dense impenetrable cover in some places. The south-eastern part of Glen Doll Complex (Plate 1.4) has only recently been planted so the good exposure there is still accessible. Due to the local climate, the growth of the trees is slow and although those to the west were planted in 1955, they are still relatively immature. Glen Doll has been leased to the Nature Conservancy Council who administer the Caenlochan National Nature Reserve. Forestry commission roads and fire breaks provide access to the forested areas and to additional exposures in drift covered areas. The diorites (the dominant rock type) form steep bluffs along the high valley sides in both Glen Doll and Juan Jorge (Plate 1.5).

A small quarry at Braedownie (28847572) in the south east of the Glen Doll complex has been used to extract the diorites for local roadstone and building repair (Plate 1.6).

1.2 Geological History

This section includes the structural development of Scotland during the Caledonian Orogeny and the regional metamorphism in the area north of the Highland Boundary Fault (HBF). The latter part of the section (1.2.1) concentrates on the thermal metamorphism caused by the emplacement of the Glen Doll and Juan Jorge Complexes, and the post-intrusion faulting in the local area.

Plate 1.3
View looking north across a peat covered plateau (580m) to
the peak of Lochnagar.

(29297808)

Plate 1.4
View of the southeastern part of the Glen Doll Complex looking
across Glen Clova towards Red Craig. The zig-zag path provides
access to an area only recently planted with coniferous trees
and still affording good exposure of the hornblende diorite.

(27957665)



Plate 1.3
View looking north across a peat covered plateau (580m) to
the peak of Lochnagar.

(29297808)

Plate 1.4
View of the southeastern part of the Glen Doll Complex looking
across Glen Clova towards Red Craig. The zig-zag path provides
access to an area only recently planted with coniferous trees
and still affording good exposure of the hornblende diorite.

(27957665)



Plate 1.3
View looking north across a peat covered plateau (580m) to
the peak of Lochnagar.

(29297808)

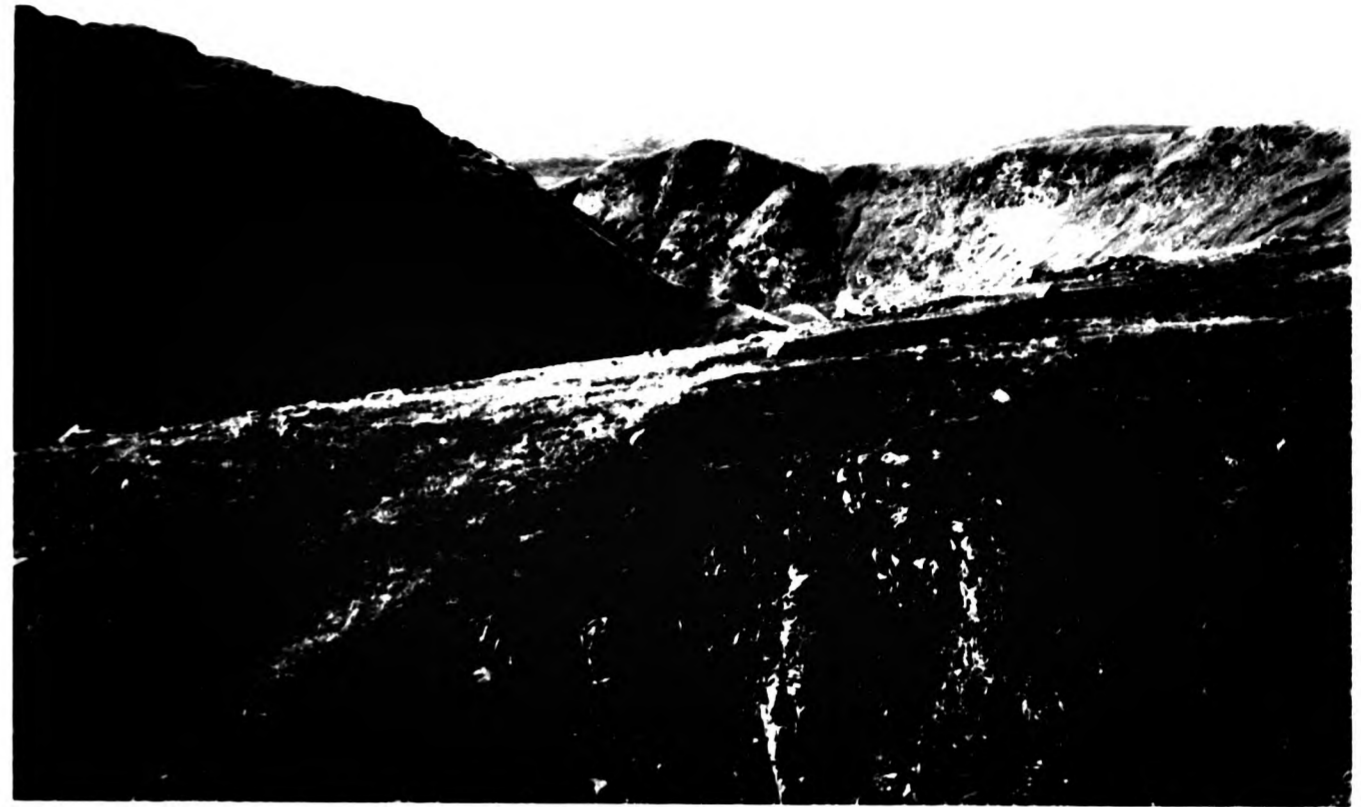


Plate 1.4
View of the southeastern part of the Glen Doll Complex looking
across Glen Clova towards Red Craig. The zig-zag path provides
access to an area only recently planted with coniferous trees
and still affording good exposure of the hornblende diorite.

(27957665)



1.2.1 Structural Context

The British Caledonides comprise one of the primary segments of the North Atlantic Caledonian Orogenic Belt. The magmatic activity in Britain largely post-dates the polyphase deformation and metamorphism of the Grampian Orogeny which ceased to be active by ~450Ma.

The region of Caledonian magmatism in Britain extends from the Archean Lewisian foreland of NW Scotland to the Upper Palaeozoic Variscan fold belt of SW England, and is divided into three structural-stratigraphic provinces. North-west of the Great Glen Fault (GGF) is a highly deformed basement of Lewisian Archean granulites and gneisses with a thick unconformable cover of Moinian sediments. Between the GGF and the HBF zone lie the Orthotectonic Caledonides (Harmon et al., 1984), a structurally complex metamorphic fold belt of Proterozoic to early Palaeozoic supracrustal rocks (Dalradian). Southeast of the Southern Uplands Fault (SUF) is a region of largely non-metamorphic, weakly deformed pelitic rocks, the Paratectonic Caledonides, deposited during early Palaeozoic geosynclinal sedimentation.

The sub-surface structure of Scotland has been inferred from geophysical studies (Bamford et al., 1977), which show a distinct difference in the nature of the underlying continental crust in the Para and Ortho-Caledonides. The latter have a three layered crustal structure. The lower layer, 6-15km thick, is presumed to be granulite facies meta-igneous rock gradational from gabbro to eclogite in composition (Hall and Simmons, 1979). The middle layer, 6-12km thick, has the seismic character of intermediate composition

Plate 1.5

View looking SW from Moulzie, the diorites form steep bluffs along the high valley sides. The pink scree is formed from aplite blocks.

(28457795)



Plate 1.6

View of the quarry at Braedownie (foreground) where diorite is extracted for local repair work.

(29177596)



Plate 1.5

View looking SW from Moulzie, the diorites form steep bluffs along the high valley sides. The pink scree is formed from aplite blocks.

(28457795)

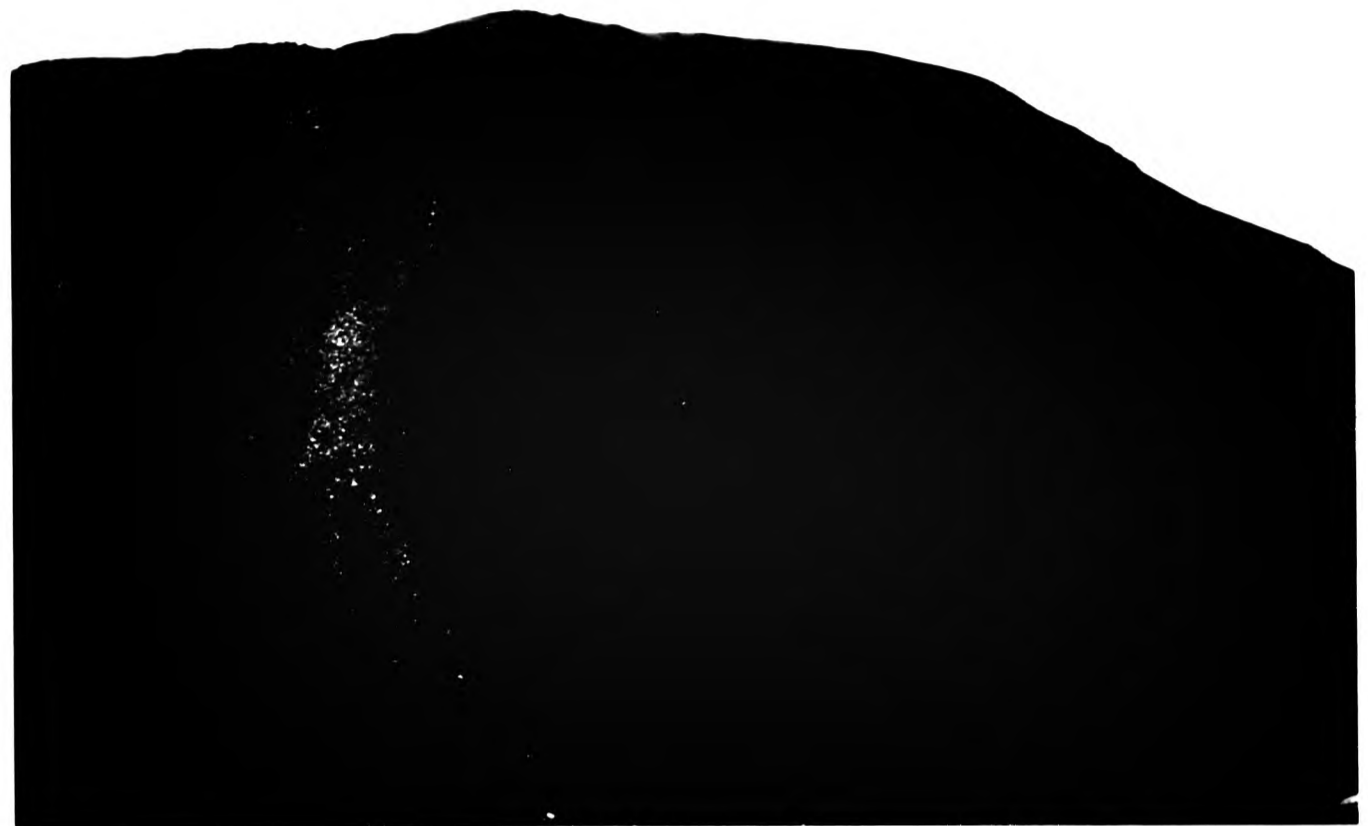


Plate 1.6

View of the quarry at Braedownie (foreground) where diorite is extracted for local repair work.

(29177596)



Plate 1.5

View looking SW from Moulzie, the diorites form steep bluffs along the high valley sides. The pink scree is formed from aplite blocks.

(28457795)



Plate 1.6

View of the quarry at Braedownie (foreground) where diorite is extracted for local repair work.

(29177596)



granulite (Hall and Al-Haddad, 1976) and is considered to be pre-Caledonian basement. The upper crust, 14-25km thick (Harris et al., 1978; Bamford et al., 1977) is thought to consist of Moine and Dalradian metasediments, and younger (New Caledonian) granitoid intrusions. By comparison, the Para-Caledonides have a layer of Lower Palaeozoic geosynclinal sediments, derived from uplifted areas of Ortho-Caledonides, which overlie pre-Caledonian basement.

The Caledonian rocks of the Scottish highlands have been considered for some time to result from an Alpine-type orogeny, dating from the early Ordovician, undergoing uplift during the Ordovician and later times. More recently, the recognition of the Southern Uplands Zone as an accretionary prism with imbricate thrusts developed in series towards the south (McKerrow et al., 1977), is consistent with ideas put forward by several authors suggesting that oceanic crust was being subducted to the north (Johnson et al., 1979; Van Breeman and Bluck, 1981). The current views of the regional setting of Scotland during the late Caledonian have been summarised by Watson (1984): the Caledonian cycle ended in a collision orogeny between the European and North Atlantic plates; during the early stages of this event the plates were separated by the Iapetus Ocean which opened during the Cambrian and closed towards the end of the Silurian.

Contrasting views have been put forward on the tectonic setting in Scotland and northern England throughout the period of Caledonian activity. It is generally assumed that the Caledonian granitoids are strongly related to a destructive plate margin. However there is debate about the position of this margin and particularly about the number and positions of any subduction zones.

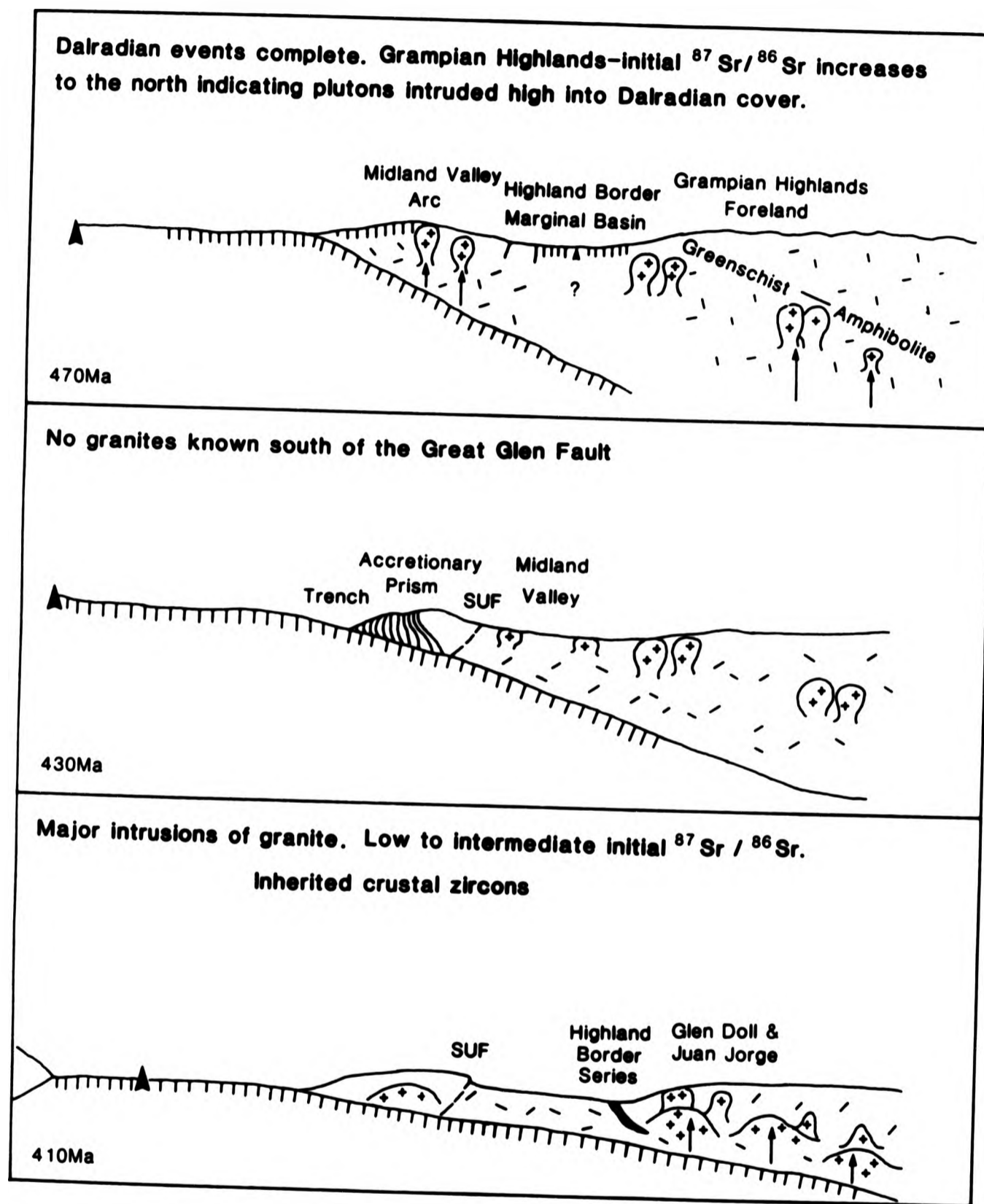


Fig. 1.3 Reconstruction of the Southern Uplands–Grampian Highlands area during the Ordovician and Silurian times. (After VanBreeman & Bluck, 1981)

Phillips et al. (1976) presented a plate tectonic model involving the evolution of a subduction zone with time. Subsequent positions of non-parallel subduction zones were presented with the final position (during the late Ordovician) south of the Southern Uplands zone. This proposed line of subduction trends ENE-WSW with Iapetus oceanic crust being subducted to the NNW.

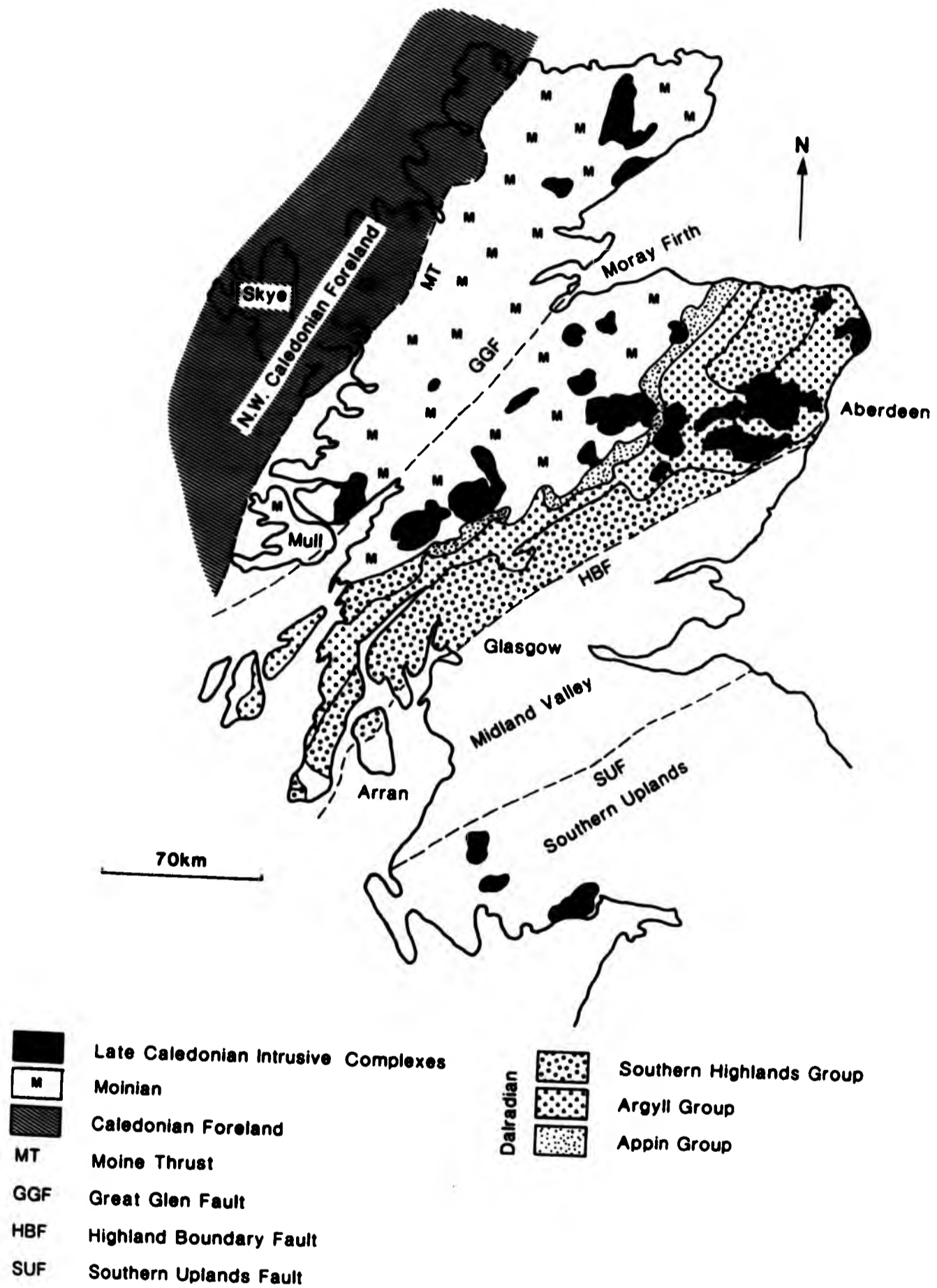
A recent model put forward by Van Breeman and Bluck (1981) incorporates recently acquired geochemical data in order to further constrain the model. A model for the evolution of the area from Girvan to Inverness is proposed from 470-410ma. The model proposes an initial steep northerly facing subduction zone at 470ma, giving rise to the Midland Valley intrusives in the south and progressively deeper-seated intrusions further north (Fig. 1.3). By 410ma, the angle of subduction shallows, and the northerly granitoids emplaced at this time e.g. Lochnagar, show evidence of longer crustal residence times and typically contain inherited zircons. If the plate tectonic models put forward for the evolution of the Caledonian are correct, then a majority of the late Caledonian granites or 'Newer Granites' (Read, 1961) in Scotland and Ireland were emplaced above subducting oceanic crust.

The connection between modern subduction zones, where oceanic crust is being subducted under continental crust, and the production of both volcanic and plutonic rocks has been investigated by many authors, for example Eichelberger (1978).

The geochemistry of many late Caledonian intrusions often reflects their complex origins. Some of the intrusions are considered to be essentially mantle-derived but with a continental

Fig. 1.4

Generalised map of the Scottish Caledonides showing the major divisions of the Dalradian and some of the late Caledonian intrusive complexes
(after Johnson et al., 1979)



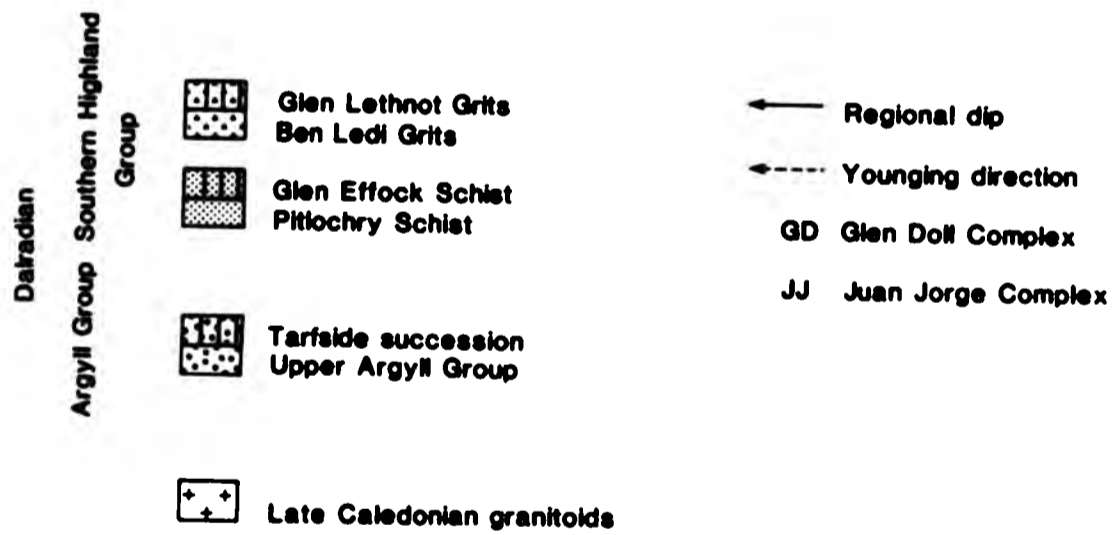
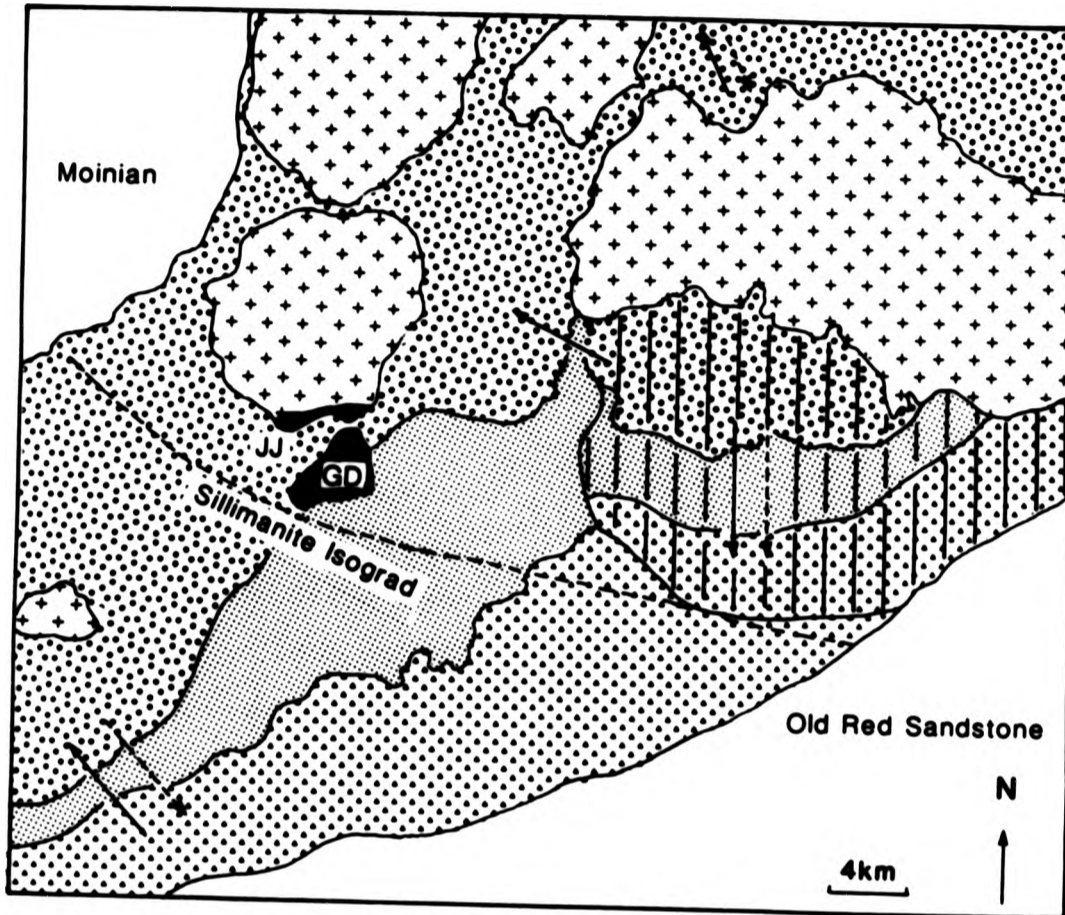
crustal component (Halliday et al., 1979; Thirlwall, 1982). The volcanic rocks of Old Red Sandstone (ORS) age, including those of the Lorne Plateau (Thirlwall, 1982) and the Sidlaw Hills (Gandy, 1975), are closely associated geochemically with the Late Caledonian plutonic complexes. Rb/Sr isotope data however suggests that they postdate the emplacement of the majority of the intrusive complexes. The andesitic lavas display some primitive characteristics with high chromium, nickel and magnesium levels (Thirlwall, 1982), and are considered to represent near primary magmas derived from the upper mantle.

1.2.2 Metamorphic Geology

The Glen Doll and Juan Jorge Complexes are intruded into a series of shallowly-dipping Middle Dalradian metasediments at the north-western end of Glen Clova (Figure 1.2). Here Barrow (1893) first described regional zoning of metamorphic minerals in pelitic gneisses and schists (He erroneously related the zoning to the thermal effects of the early Caledonian intrusions).

The metasediments fall within the Argyll Group and the Southern Highland Group both part of the Dalradian Supergroup (Figure 1.4). The metasediments may be correlated with the Loch Tay Limestone, Pitlochry Schists and Green Beds (Harte, 1979) (Fig. 1.5) whose type sections lie to the west. The Glen Doll Complex, at least to the south and south-west, intrudes migmatites assigned to the Ben Lui Schists (correlated with the Tarfside succession) and carbonate rich rocks at Corrie Sharroch may correlate with the Loch Tay Limestone (Argyll Group) (Durig, 1981). The area lies within the 'flat belt' of the Tay Nappe and the sequence is considered to be inverted (Shackleton, 1957) (Fig. 1.5).

Fig. 1.5
Suggested stratigraphical and structural relations of the Dalradian in the
area around the Glen Doll and Juan Jorge Complexes (after Harte, 1979)



Upper names of each pair refer to stratigraphical units in the Tarfside Nappe, lower names refer to the Tay Nappe (stratigraphy after Harte, 1979)

The Glen Doll and Juan Jorge Complexes are intruded into sillimanite zone assemblages, with the sillimanite isograd lying 1km south of the complexes (Harte, 1979). This zone represents the highest grade of a sequence of metamorphic assemblages (e.g. Chinner, 1965) characterised by chlorite (lowest grade), biotite, garnet, staurolite, kyanite and sillimanite (highest grade) (Fig. 1.5). The Dalradian in the area around Glen Doll and Juan Jorge is composed of predominantly psammitic schists with pelitic layers, semi-pelites, haematite-bearing gneisses and Green Beds. These are intruded by older (presumed early Caledonian) para-amphibolite and epidiorite and by granite gneiss associated with early Caledonian deformation (Chinner, 1960; Schumacher, 1985).

Bradbury (1979), demonstrated the coeval nature of the peak of Barrovian metamorphism and migmatitisation at 514ma in the area immediately north of the HBF. Subsequently at ~400ma, during a period of uplift, the cooled regionally metamorphosed rocks were intruded by the plutonic complexes (Bradbury, 1979).

The metasediments have therefore undergone several phases of regional metamorphism prior to local thermal metamorphism during the emplacement of the late Caledonian complexes. Neither the Glen Doll nor the Juan Jorge Complex has been affected by any metamorphic event.

From mineralogical studies in the regionally metamorphosed pelitic rocks around the Glen Doll Complex, Durig (1981) has estimated a regional lithostatic pressure at 500Ma of 6-8Kbar and a temperature of 650-690°C prior to the intrusion of the igneous rocks. The mineral assemblage from the pyroxene hornfels facies of

the Glen Doll Complex gives a lithostatic pressure of 1-2Kbar and a temperature of 500-800°C at the time of intrusion of the complex (i.e.~400ma). The difference in pressure between initial (regional) metamorphism at 500ma and the thermal event at 400ma is ~6.5Kbar (22.75km). This figure suggests a rate of uplift prior to emplacement of the igneous complex of 0.23mm/year (Durig, 1981).

1.2.3 Post Intrusion Events

Post 400ma, there is evidence of sedimentation and volcanic activity during lower ORS time in Scotland. To the southeast of Glen Clova in the Sidlaw Hills are extensive andesite and basalt lavas extruded onto Lower ORS sediments (Gandy, 1975). The sequence consists of interbedded lavas, sandstones and conglomerates indicating a period of uplift and erosion prior to the eruption of the lava sequence. A similar sequence in the Ochill Hills to the south, contains volcanic vents (Gandy, 1975). To the north of Glen Clova, Middle ORS outliers occur around Tomintoul and Lumsden indicating that the metasediments of Dalradian age were eroded down to close to their present level prior to deposition of the Middle ORS.

Post-intrusion faulting has been limited in the immediate area. The Glen Doll fault, described by Barrow et al. (1912) is cut by the complex and shows no evidence of later propagation. Small fractures and normal faults are seen throughout the complexes and are discussed in Chapter 3. On a regional scale, Middle ORS sediments around Inverness are cut by the GGF.

CHAPTER 2

Previous Research

2.1 Introduction

This chapter will concentrate on the previous research undertaken both locally in the area around Glen Doll and Juan Jorge and more widely on research on many of the late Caledonian calc-alkaline igneous complexes in Scotland and Ireland. An introduction is also given concerning the major processes which give rise to acid-intermediate-basic associations, many of which are appropriate to the origin of the late Caledonian "granitoids".

2.2 Magmatic Processes

Extensive studies have been undertaken on many 'Granitoid' complexes, the relationship between basic, intermediate and acid rocks, the tectonic setting of calc-alkaline complexes and the petrogenetic processes which have operated on them. The most commonly described petrogenetic processes which can give rise to the association of basic, intermediate and acid rocks in varying tectonic settings throughout the world are discussed below. These processes which, are not mutually exclusive, are:-

2.2.1 Fractional crystallisation

2.2.2 Partial melting

2.2.3 Magma mixing

2.2.4 Contamination

2.2.5 Metasomatism

2.2.1 Fractional Crystallisation

It was first suggested by Bowen (1912) that fractional crystallisation of a basic magma could produce both intermediate and acid rock types. More recently detailed geochemical studies have shown that, fractional crystallisation is an important process in the evolution of many igneous complexes (e.g. Best, 1963; Pearce and Norry, 1979; Walsh and Clarke, 1982). For example, experimental work on synthetic systems (Osborne, 1962) has shown fractional crystallisation of an olivine basalt can produce andesite liquids, provided that O_2 is added to the system. Other work has shown that fractional crystallisation may be coupled to other magmatic processes such as contamination and magma mixing (Briqueu and Lancelot, 1979; Wiebe and Wild, 1983) to produce gabbro, diorite and granite assemblages.

2.2.2 Partial Melting

Partial melting of crustal material as a mechanism for generating intermediate magma compositions, has not been favoured by many authors. However a recent geochemical study by Scott and Vogel (1980) suggests that partial melting of two sources could give rise to gabbro, diorite and granitic rocks in the Tichka Massif of Morocco. Their model involves the partial melting of garnet-bearing mantle to produce the gabbroic rocks and partial melting of lower crust to produce the granitic rocks. Mixing of these two end members could give rise to the intermediate rock compositions.

In their classic work on the genesis of the calc-alkaline

igneous suite. Green and Ringwood (1968), discuss some popular theories for the petrogenesis of the calc-alkaline suite. Extensive experimental studies support three possible models which could give rise to the range of lithologies observed in the suite. The model favoured by the authors takes place in two stages. The first is the initial partial melting of a pyrolite mantle to produce undersaturated basaltic magma. The magma is required to remain dry and eventually transform to eclogite after some crystal fractionation has occurred. The second stage requires the partial melting of eclogite to give rise to basaltic andesite or andesite (plutonic diorite or quartz diorite) under dry conditions and dacite or rhyodacite (plutonic granodiorite or adamellite) under wet conditions.

Arth and Hanson (1972) applied Green and Ringwoods model to the late Precambrian Vermilion Complex (plutonic-volcanic) in Ontario, and showed that the range of rock types present, essentially quartz diorite compositions, could be produced by partial melting of eclogite or amphibolite at mantle depths.

2.2.3 Magma mixing

Magma mixing, as a process for generating magmas of intermediate composition from basic and acid end members, has been proposed by many authors e.g Vogel, 1982; Eichelberger, 1978; McDonald and Katsura, 1965; Anderson, 1976; Reid et al., 1983. Vogel (1982) demonstrated, using linear regression modelling of major element data, that mixing of a silicic magma and primitive mafic magma coupled with moderate fractional crystallisation could readily produce the intermediate rocks seen in the Tertiary net veined complex of

Ardnamurchan. Other studies suggest the local formation of intermediate plutonic rocks by hybridisation of granodiorite and gabbro (e.g. Hutchison, 1964). In a classic study from the Scottish Caledonides, Deer (1935, 1937, 1938) proposes magma mixing as a mode of formation of the dioritic compositions in the Glen Tilt and Carsphairn Complexes. With particular reference to the calc-alkaline suite, Eichelberger (1978) proposed mixing of upper mantle and lower crustal melts as a mechanism for the production of andesitic magmas at many subduction zones.

2.2.4 Contamination

Some of the early work on the Scottish late Caledonian igneous complexes was directed towards those which had undergone contamination with crustally derived material e.g. Garabal Hill Complex (Nockolds, 1940). The complexes typically contain abundant metasedimentary xenoliths, the partial melting of which provide an opportunity for contamination of the magma. The Bibette Head granite, Alderney, is an additional example of an igneous complex containing fine grained basic xenoliths which are thought to have interacted with the magma which encloses them (Nockolds, 1932). A theoretical study of high level contamination of acid magmas by basic material was published by Nockolds (1933). His study divided contamination processes into two types, chemical contamination by reaction of the xenolith with its host, and mechanical contamination by disaggregation of a xenolith. Nockolds concluded that the former could lead to the production of "normal" rock types. In addition, he suggested that contamination is intimately associated with the volatile content of a magma.

More recently a number of studies have considered the possibility of large scale contamination of mantle derived liquids by continental crust as a means of generating intermediate (dioritic and andesitic) magma compositions (Halliday et al., 1980; Harmon and Halliday, 1980; Stephens and Halliday, 1984; Halliday et al., 1985). Extensive studies of Sm/Nd , Rb/Sr , U/Pb and O^{18} systems have been used to distinguish mantle derived, mantle -crust contaminated and crustally derived magmas. Initial $^{87}\text{Sr}/^{86}\text{Sr}$ ratios for example, vary from 0.7255 in the Dalradian to 0.7030 in MORB type mantle (Harmon et al., 1984) and thus the resulting magma formed from the two sources displays an intermediate ratio controlled by the degree of contamination.

Contamination may therefore account, in part, for the reason why no simple evolutionary magmatic process can easily explain the association of some basic-intermediate and granite complexes and why the two rock types are frequently assigned to independent sources (Scott and Vogel, 1980).

As suggested by many authors, the plutonic association of gabbro-diorite-granite and their extrusive equivalents, may originate through a combination of petrogenetic processes involving early partial melting followed by fractional crystallisation and contamination.

2.2.5 Metasomatism

Metasomatism has been proposed by some authors as a process whereby intermediate (dioritic) rocks can be produced. A study by Key (1974) and Bishop and French (1982) suggests that metasomatism

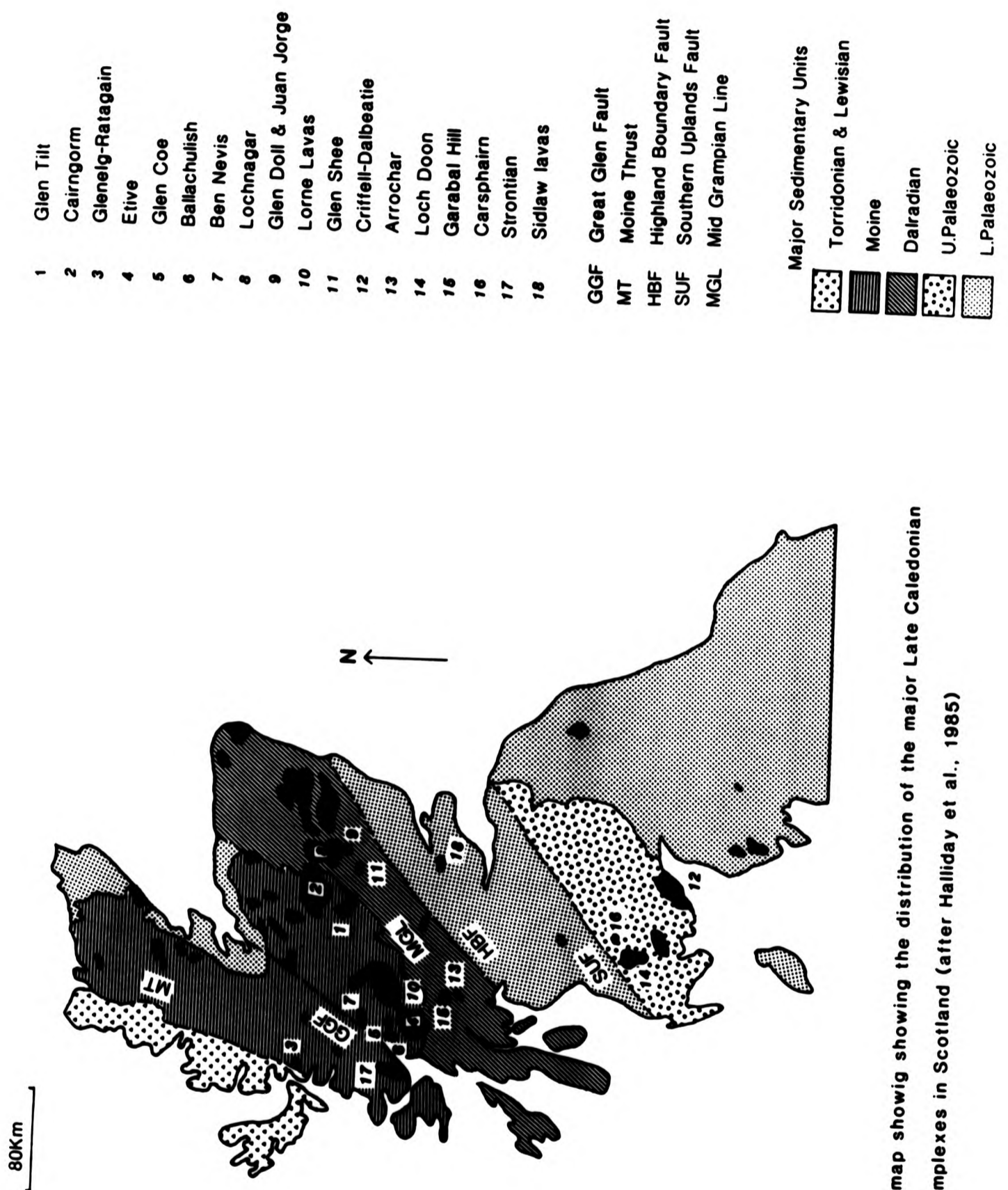


Fig. 2.1 A map showing the distribution of the major Late Caledonian complexes in Scotland (after Halliday et al., 1985)

of pre-existing layered gabbros in the Chouet igneous complex in northern Guernsey, has led to the formation of the layered diorites there. However, other studies of the same area, suggest that the layered diorites are primary igneous features (Brown et al., 1980; Topley et al., 1982).

2.3 Caledonian igneous rocks of the British Isles

Many studies have been made of the late Caledonian intrusive and extrusive complexes and more recently a wealth of data has been published on isotope systematics. Interpretation of the isotope data has largely concentrated on the evidence they provide for the nature of the deep crust and upper mantle below the complexes at the time of emplacement.

2.3.1 Scottish Calc-alkaline complexes

The early work in Scotland was broadly descriptive and included data from complexes both north and south of the "Mid Grampian line" (Fig. 2.1). This line is considered to divide Caledonian complexes with differing chemical characteristics and corresponds to the Moine-Dalradian boundary (Halliday et al., 1985).

Those complexes to the north include:- Glen Tilt (Deer, 1938a, 1938b, 1950, 1953), Cairngorm (Harry, 1965), Glen Banvie (Holgate, 1951), Glen Elg-Ratagain (Nicholls, 1950), Ballachulish (Bowes, 1962), Glen Coe (Bailey, 1960), Etive (Anderson, 1937; Clayburn et al., 1983; Nockolds, 1933), Ben Nevis (Anderson, 1935; Haslam, 1968, 1970), Lochnagar (Oldershaw, 1958, 1974) and the Lorne lavas (Groome and Hall, 1974; Thirlwall, 1979).

Those to the south include:- Glen Shee (Williamson, 1933), Criffell (Philips, 1956), Arrochar (Anderson, 1935), Loch Doon (Gardiner and Reynolds, 1932; Brown et al., 1979; Tindle and Pearce, 1981,1983), Garabal Hill (Dakyns and Teall, 1892; Wyllie and Scott, 1913; Nockolds, 1940; Summerhayes, 1966), Carsphairn (Deer, 1935,1937,1937b), Cairnmore of Fleet (Gardiner and Reynolds, 1937) and the Sidlaw lavas (Gandy, 1975).

The early work, , concentrated on the detailed field and petrographic description of the complexes. This work showed the main differences between some of the most important complexes. Many, such as Etive and Ben Nevis (Anderson, 1937; Haslam, 1968) were shown to be dominantly composed of intermediate to acid compositions (tonalite, quartz mica diorite and granite). Others like Glen Doll showed a range of compositions from ultra-mafic, through basic, to intermediate and acid compositions, for example Garabal Hill which contains pyroxenite, gabbro, quartz diorite and granodiorite (Nockolds, 1940). Diorites were shown to be common at Glen Tilt (Deer, 1938), Ballachulish (Bowes, 1962) and Arrochar (Anderson, 1935). Nockolds (1940) proposed that the range of rock types preserved at Garabal Hill could be produced by fractional crystallisation of a pyroxene mica diorite liquid coupled with contamination by "earlier igneous or sedimentary matter". A major study by Deer (1950,1953) led him to propose hybridisation of intermediate and acid magma as the model for formation of granite-diorite rocks in Glen Tilt.

Haslam (1968,1970) undertook an extensive geochemical study of Ben Nevis and showed that, on the basis of mineral chemistry data, many of the amphiboles from the quartz diorites are secondary

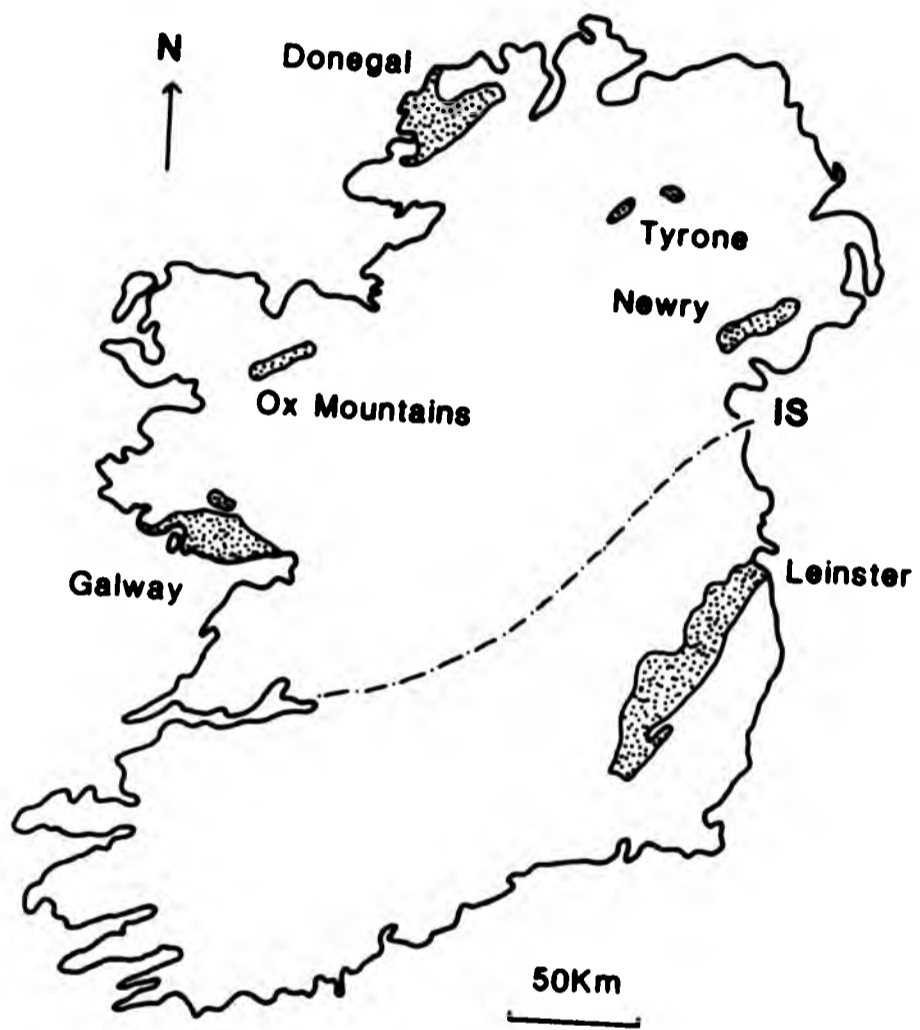


Fig. 2.2 Sketch map to show the locations of the major late Caledonian granite intrusions in Ireland (after Kennan, 1979). IS is the suggested position of the Iapetus Suture (Phillips, 1978).

features after primary pyroxene. A similar relationship was noted earlier in the Garabal Hill Complex by Nockolds (1940).

2.3.2 Irish Calc-alkaline complexes

At a similar time to Haslam's work in Scotland, classic study was undertaken in Ireland on the Donegal Granites (summarised by Pitcher and Berger, 1972). The work included the cluster of dioritic intrusions around the Ardara Pluton (Akaad, 1956a, 1956b; Hall, 1966, 1967; French, 1966, 1976). Other complexes studied include Leinster (Brindley, 1970) which is associated with dioritic rocks, Connemara (Bradshaw et al., 1969) and Rosses (Pitcher, 1953; Hall, 1966, 1967). A review of Irish Caledonian magmatism was made by Leake (1978) who proposed that the emplacement of granitic intrusions in Ireland was related to known major tectonic lineaments (Fig. 2.2).

The Donegal granites (Pitcher and Berger, 1972), a group of eight plutons, were intruded over 20Ma. They form a particularly interesting group in that they display a range of synchronous intrusive mechanisms including active stoping, wall rock reaction, passive stoping, permissive emplacement and forceful diapiric emplacement. The complexes are dominantly granitic, but associated with the Ardara pluton are numerous appinitic bodies (French, 1966) similar to those described from western Scotland (Bowes and McArthur, 1976; Wright and Bowes, 1979).

2.3.3 Recent Geochemical Research

More recently isotope data have been used both to date many of the complexes and for provenance studies. Some of the complexes

have been dated using Rb/ Sr data. These include the Lochnagar granite (Halliday, 1980) dated at 415ma and the Garabal Hill diorite-granite complex (Summerhayes, 1966) dated at 392ma, amongst many others. Most recently, extensive isotope studies using Rb-Sr, Nd-Sm and U-Pb have been employed (Halliday et al., 1979; Hamilton et al., 1980; Halliday, 1984) to aid interpretation of the regional geochemistry. These studies have concentrated mainly on the more granitic complexes in Scotland.

A systematic variation in the trace element and isotope geochemistry of the complexes occurs from south to north across the "Mid Grampian Line". Thirwall (1982), has shown that the abundance of Sr, Ba, K, P and the light rare-earth elements (LREE) increases to the north-west, conversely ϵ_{Nd} is variable and ϵ_{Sr} decreases to the north-west. According to Thirwall, the variation in chemistry cannot be attributed to a change in the degree of partial melting but is probably controlled by heterogeneities in the mantle.

Some of the complexes for example Ben Nevis, Strontian (Hamilton et al., 1980) and Etive (Frost and O'Nions, 1985) are considered on isotopic evidence to be essentially the products of fractional crystallisation of liquids which may have originated from the upper mantle, but which have subsequently undergone some degree of contamination within the lower crust (Hamilton et al., 1980; Harmon and Halliday, 1980; Halliday, 1984).

Several studies have been made of ORS lava sequences (Gandy, 1975; Groome and Hall, 1974; Thirwall, 1979). Some of the sequences studied are geochemically primitive (high Cr, Ni and low Fe/Mg), and may therefore represent mantle-derived liquids

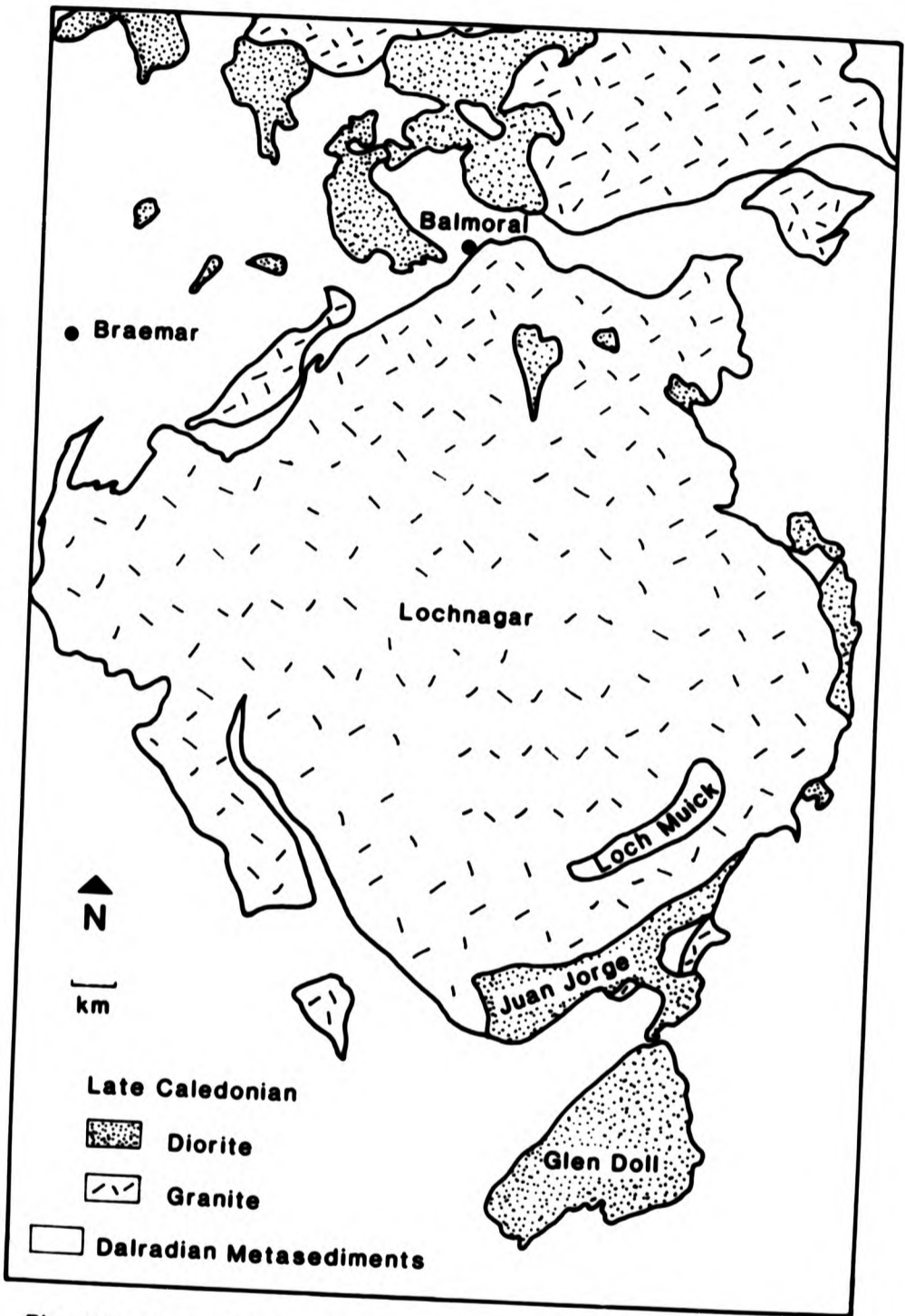


Fig. 2.3 Sketch map showing the diorites associated with the Lochnagar Granite

(Thirlwall, 1982). The range of lavas observed, including basalt and andesite, are chemically closely related to their plutonic equivalents, seen in some of the intrusive complexes (see Chapter 7).

2.4 The Glen Doll and Juan Jorge Complexes

Previous published work in the area around Glen Doll and Juan Jorge is limited in extent. The first studies were made by Barrow and Cunningham-Craig (1912), and are described in the regional memoir which accompanied the 1" Geological Survey sheet published in 1904 (Fig. 1.2). The authors describe the variable exposure in Glen Doll and notes that the major rock type is a rather basic diorite. The authors mention also a very basic facies referred to (incorrectly) as picrite, and a description is given of a granitic margin to the complex. A brief note was made on the Juan Jorge Diorite to the north of Glen Doll (Fig. 2.3). Juan Jorge is referred to as "singularly uniform in composition" (Barrow and Cunningham-Craig, 1912)

The complexes were not investigated further until 1958 when Oldershaw (1958, 1974) made a petrographic and field study of the Lochnagar granites and the surrounding diorites. His detailed mapping of Juan Jorge revealed a range of rock types consisting of an essentially homogeneous hornblende diorite showing a sharp contact with a pink porphyritic granite to the east, and the Lochnagar granite to the north and west. The Juan Jorge complex predates the intrusion of the Lochnagar granite to the north, which has been dated by Rb/Sr techniques at 415ma (Halliday et al., 1980). On the basis of field evidence the Glen Doll Complex is thought to be similar in age. Oldershaw did not study the Glen Doll Complex.

Even with the wealth of information available on the petrogenesis of gabbro-diorite-granite complexes, many questions still remain unanswered. Modern work in Scotland has concentrated on the acid members of the suite i.e. the rocks which represent only one end of an evolutionary sequence. However, basic and intermediate compositions dominate many calc-alkaline volcanic complexes and it is clear that a detailed study of the plutonic equivalents of these facies is needed in order to produce a viable model of evolution for the suite particularly in the context of the late Caledonian complexes.

The Glen Doll and Juan Jorge Complexes were chosen for study for several reasons. The level of exposure with deep glaciated valleys cutting through the complexes is good and in general the rocks are fresh and unaffected by later hydrothermal processes. They are also unaffected by any significant metamorphic event, so that original textures and mineralogy are well preserved. Access to both areas is good.

The range of rock types is extensive and includes olivine gabbro, gabbro, pyroxene diorites, hornblende diorites, monzonite, quartz mica diorite, adamellite and granite.

The complexes are closely associated with the Lochnagar granite, one of the passively emplaced 'Newer' granites (Read, 1961) of late Caledonian age, thus providing control on the time of emplacement of the complexes. Geochemical, isotope and mineral chemistry data should provide petrogenetic constraints applicable to the interpretation of other late Caledonian complexes.

CHAPTER 3

Field Relationships

3.1 Introduction

The Juan Jorge and Glen Doll Complexes were mapped at a scale of 1:10,000 (Fig. 3.1) with more detailed studies undertaken in particularly well exposed areas. The nature of the contact and the range of rock types encountered was found to be more complex and extensive than shown on the BGS 1" to 1 mile map, sheet 65.

The division of the different rock types was initially based on hand specimen identification. This division has been modified after a study of thin sections, which allowed the confident identification of cpx in hand specimen, in the diorites. In the Juan Jorge Complex, field observations made first hand were used in conjunction with field data from Oldershaw (1958) and Hardy (1985), to construct a 1:10,000 scale map.

Samples (1kg) were collected using a geological hammer, for geochemical analysis and detailed petrographic examination from both complexes. The heterogenous diorites in Glen Doll were sampled along traverses where possible, or from available outcrop to give a comprehensive cover of the area. Juan Jorge was sampled less densely due to the apparently homogenous nature of the rock types.

The Glen Doll Complex is dominated by heterogenous, xenolithic hornblende and pyroxene diorites which together form 80% of the complex, with local areas of olivine gabbro in the SW and of gabbro in the NE. A discontinuous ring of adamellite occurs around the

Plate 3.1
General view looking west along Glen Doll across the Caenlochan
Nature Reserve and the White Water River.
(28977612)

Plate 3.2
View from Braedownie to Winter Corrie (below helicopter)
looking west.
(28857572)



Plate 3.1
General view looking west along Glen Doll across the Caenlochan
Nature Reserve and the White Water River.
(28977612)



Plate 3.2
View from Braedownie to Winter Corrie (below helicopter)
looking west.
(28857572)



Plate 3.1
General view looking west along Glen Doll across the Caenlochan
Nature Reserve and the White Water River.
(28977612)



Plate 3.2
View from Braedownie to Winter Corrie (below helicopter)
looking west.
(28857572)



margin of the complex. Plate 3.1 shows a general view of Glen Doll.

The Juan Jorge Complex, conversely, is dominated by an homogeneous quartz-mica diorite, which is generally xenolith free but locally contains abundant xenoliths, particularly close to its southern contact with a pink porphyritic granite. A second small granite, the Gourock granite (Oldershaw, 1958), crops out in the NE. The contacts to the north and west against the Lochnagar granite are sharp and the margins of the diorite are thermally metamorphosed by the emplacement of the later granite.

The margins of the Glen Doll Complex are near vertical in the south, north and east, and this can be clearly seen, for example, just south of Red Craig (29507580) and to the south of Winter Corrie (27707680). Plate 3.2 shows a general view of Winter Corrie. Work by Durig (1981) shows that along the south-west margin of the complex, the metamorphic aureole is wider (>50m) than elsewhere. Although it is not exposed in this area, the contact is inferred to follow the topographic contours. The above evidence suggests that in the southwest, the contact is locally sub-horizontal.

Both complexes are cut by a series of late intermediate and acid dykes. To the north of the Glen Doll Complex and south of the Juan Jorge Complex are the Bridge outcrops. The igneous rocks here are intruded into the Dalradian metasediments, but their relationship with the two complexes is unclear. The field and lithological relationships for each complex are discussed below.

3.2 Glen Doll Complex

3.2.1 Diorites

3.2.2 Basic rocks

3.2.3 Adamellite

3.2.4 Xenoliths

3.3 Juan Jorge Complex

3.3.1 Diorite

3.3.2 Granite

3.3.3 Xenoliths

3.4 Features common to both complexes

3.4.1 Dykes - intermediate and acid

3.4.2 Faulting

3.5 Bridge Outcrops

3.2 Glen Doll Complex

3.2.1 Diorites

The dioritic rocks are the dominant lithology in the area, comprising 80% of the complex. They are generally medium grained although both coarse and fine grained types occur. The diorites have been subdivided here on the basis of their mineralogy into both hornblende and pyroxene-bearing facies but gradation from one type to the other is extensive. Hornblende diorites comprise 90% of the dioritic rocks of the complex (Plate 3.3).

The hornblende diorites contain variable amounts of brown and

Plate 3.3
Typical outcrop of well exposed hornblende diorite.
(Flowers 20cm high)
(28637624)



Plate 3.4
View of a coarse grained hornblende diorite grading into a
medium grained diorite over a distance of 3m. Coarse grained
zones are particularly common in the White Water river.
(Hammer shaft 60cm)
(27847604)



Plate 3.3
Typical outcrop of well exposed hornblende diorite.
(Flowers 20cm high)
(28637624)



Plate 3.4
View of a coarse grained hornblende diorite grading into a
medium grained diorite over a distance of 3m. Coarse grained
zones are particularly common in the White Water river.
(Hammer shaft 60cm)
(27847604)



Plate 3.3
Typical outcrop of well exposed hornblende diorite.
(Flowers 20cm high)
(29637624)



Plate 3.4
View of a coarse grained hornblende diorite grading into a
medium grained diorite over a distance of 3m. Coarse grained
zones are particularly common in the White Water river.
(Hammer shaft 60cm)
(27847604)



green amphibole which are either subhedral or tabular in habit. Green amphibole is dominant over brown varieties. While no discrete pyroxene crystals occur, many of the green amphiboles have remnant opx or cpx cores.

The pyroxene diorites are characterised by isolated discrete crystals of opx and cpx. However between the hornblende diorites and pyroxene diorites, a complete gradation in mineralogy is observed. Both types contain variable amounts of plagioclase feldspar, biotite, magnetite ± sphene ± quartz.

3.2.1.1 Hornblende Diorites

The hornblende diorites are both heterogenous and variable in mineralogy across the complex. The diorites contain small discontinuous layers of quartz monzonite in the SE and grade into monzonite towards the contact in the south. The diorites may enclose appinitic patches and may pass into pyroxene diorite e.g. south of The Rives (27707729). In the SE they tend to contain substantial amounts of biotite and green and brown amphibole. The diorites grade both laterally and vertically into quartz monzonite by the gradual addition of quartz, K-feldspar and biotite, with a corresponding decrease in plagioclase and amphibole. There are no sharp contacts between the diorites and monzonites. The monzonites contain little amphibole, biotite being the dominant mafic phase. Laterally, the layers may be traced for up to 200m and vertically for only a few metres suggesting they have the form of subhorizontal sheets. The trend of the outcrops of monzonite are N-S i.e. parallel to the eastern contact of the diorite against the country rocks. This trend is also parallel to the strike of the igneous



Fig. 3.2 Distribution of monzonitic rocks



Fig. 3.3 Distribution of coarse grained facies of hornblende diorite

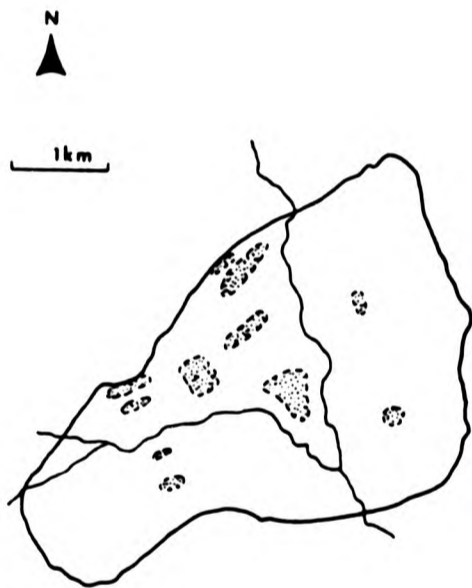


Fig. 3.5 Distribution of pyroxene diorites.
Shaded areas contain small zones and do not represent single masses



Fig. 3.6 Distribution of basic rocks (stippled) and appinites (black)

Diagrams to show the distribution of the lithologies within the Glen Doll Complex.

lamination seen locally in the diorite (see below). Figure 3.2 shows the distribution of the monzonitic rocks across the complex.

As the external contact is approached the diorite containing the monzonitic layers has an abrupt boundary with the marginal adamellite which separates the diorite from the country rocks around much of the complex. About 5m from the adamellite boundary the hornblende diorite becomes more leucocratic with an increase in the proportion of plagioclase and quartz. There is no apparent decrease in grain size, suggesting that either no diorite chill formed or that it was subsequently stopped off. There is no evidence in this area of veining of either the diorite by the adamellite or vice-versa.

To the south and west of Red Craig (29507580), the sequence of diorite and monzonite is replaced by a xenolithic fine-grained diorite. The contact between these two facies is not exposed. The fine-grained diorite contains abundant angular xenoliths (sometimes composing 60% of the rock) of biotite gneiss. The abundance of xenoliths decreases to the northwest. The banding in the gneiss displays a random orientation with respect to that in the country rocks where the banding is sub-horizontal. The xenoliths are variable in length and width from 0.2x0.1m to 3.0mx2.0m. They have sharp margins against the diorite and show no sign of partial melting or of assimilation.

Along the western margin of the fine-grained xenolithic diorite is a layer (50m thick) of meladiorite containing large (<5mm diameter) crystals of amphibole. The colour index of this is greater than that of the fine-grained diorite and is similar to the

basic rocks in the northeast part of the complex. The layer is traceable along a NNE-SSW trend for ~200m where it displays a sharp contact with a septum of gneiss. The orientation of the banding in the gneiss is horizontal and similar to that in the country rocks to the east.

Along the southern margin of the fine-grained diorite is a medium grained adamellite packed with gneiss xenoliths similar to those described above. The contact between the adamellite and the fine-grained diorite is gradational.

Evidence as to the nature and orientation of the contact is clearly seen around the Scorrie (27857525). In this area the adamellite forms a zone 50m wide between the country rock and the diorites. The inner and outer contacts are vertical. The rock type on the inner side of the adamellite is a quartz monzonite, the same as that seen to the east. This monzonite grades into hornblende diorite over a distance of 30m. The monzonites contain some green amphibole, but with more abundant biotite and a few oxides (typically magnetite). Over a distance of 30m the amphiboles become larger (4mm length), some brown but dominantly green. Biotite decreases in abundance with this change and magnetite is very common.

One interesting feature of the hornblende diorites is that they occasionally develop coarse grained facies (Figure 3.3) and this is particularly well seen in the bed of the White Water River (26857590) where they occur in two forms. The first, a coarse grained facies occurring as diffuse zones while the second is as discrete elliptical pods (in plan view).

Plate 3.5
Plan view of a medium-grained hornblende diorite grading into a coarse grained diorite. Note the biotite crystals weathering out. (Lens cap 5cm)
(27847604)

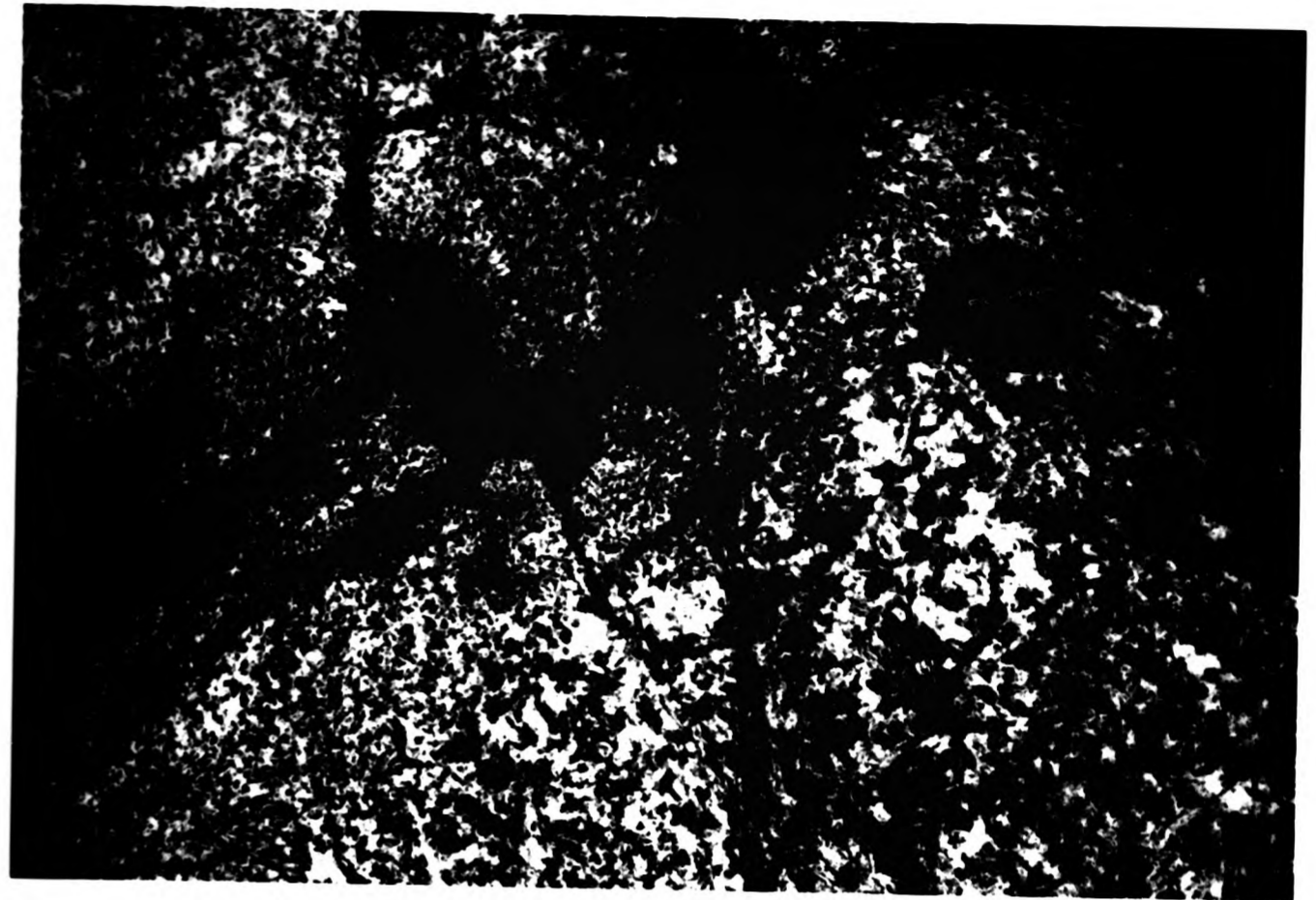


Plate 3.6
Plan view of a coarse grained patch of diorite containing skeletal amphibole crystals with plagioclase cores. (Lens cap 5cm)
(27847604)



Plate 3.5
Plan view of a medium-grained hornblende diorite grading into a coarse grained diorite. Note the biotite crystals weathering out. (Lens cap 5cm)

(27847604)

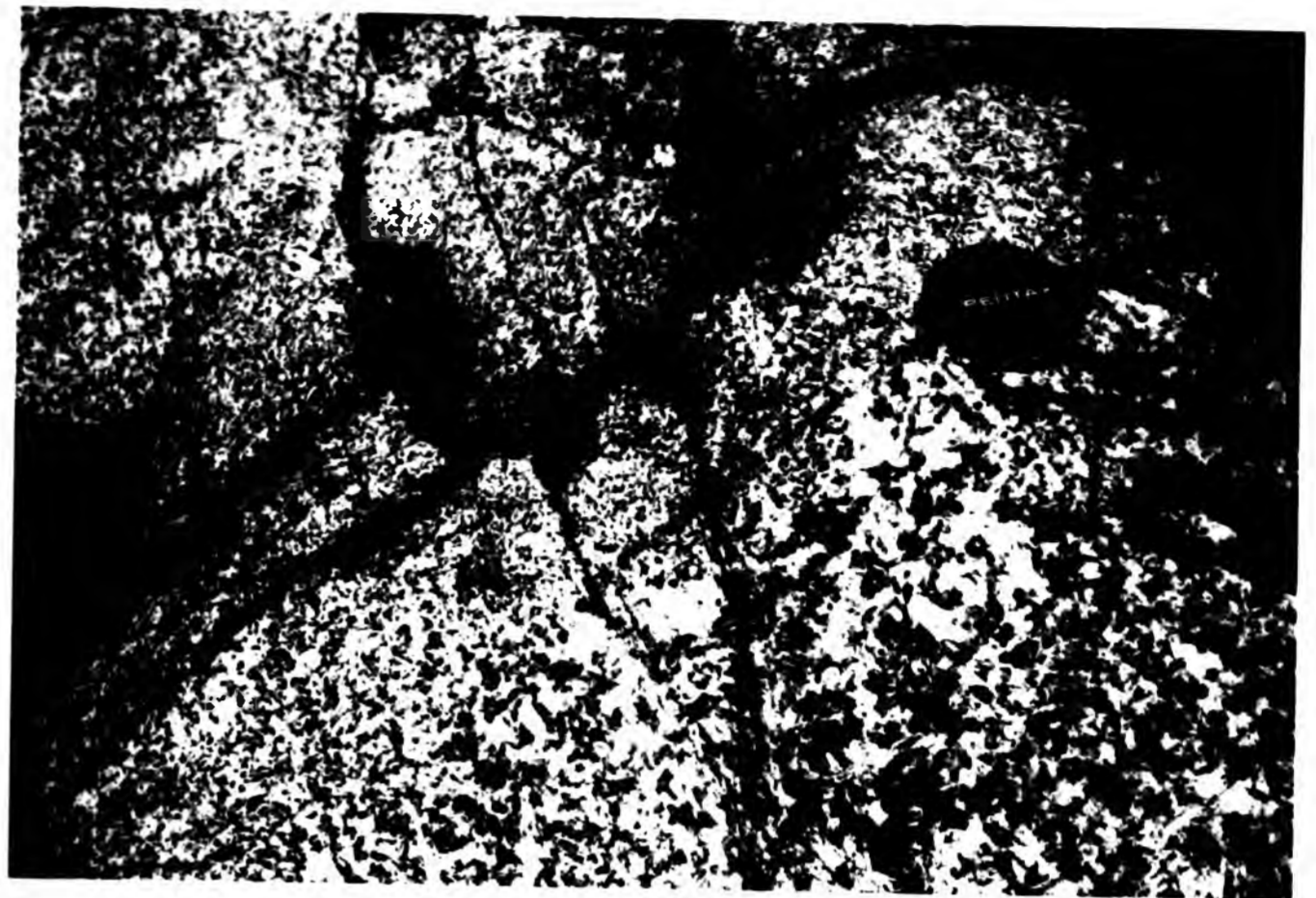


Plate 3.6
Plan view of a coarse grained patch of diorite containing skeletal amphibole crystals with plagioclase cores. (Lens cap 5cm)

(27847604)



Plate 3.5
Plan view of a medium-grained hornblende diorite grading into a coarse grained diorite. Note the biotite crystals weathering out. (Lens cap 5cm)

(27847604)

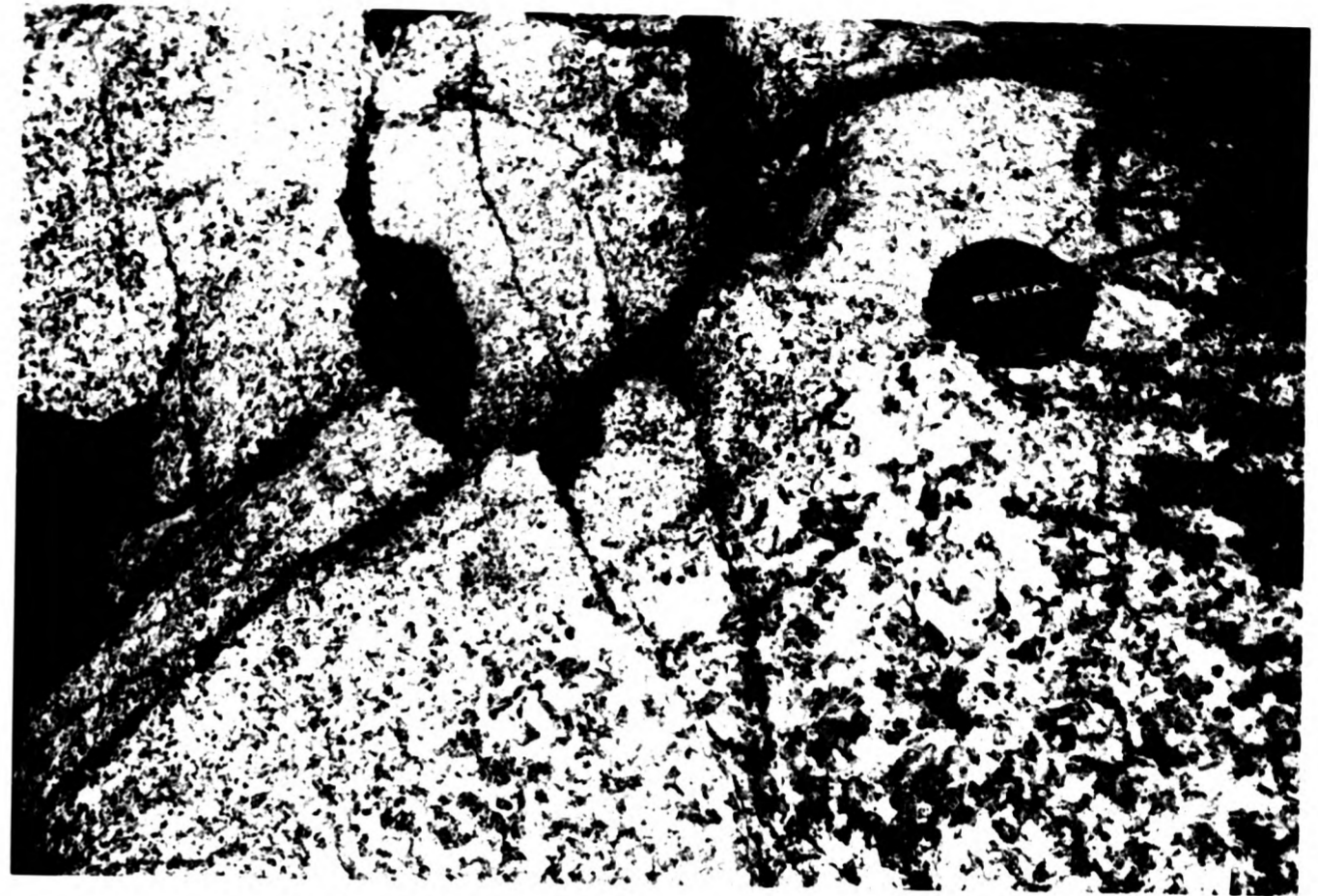


Plate 3.6
Plan view of a coarse grained patch of diorite containing skeletal amphibole crystals with plagioclase cores.

(27847604)



(i) Diffuse zones

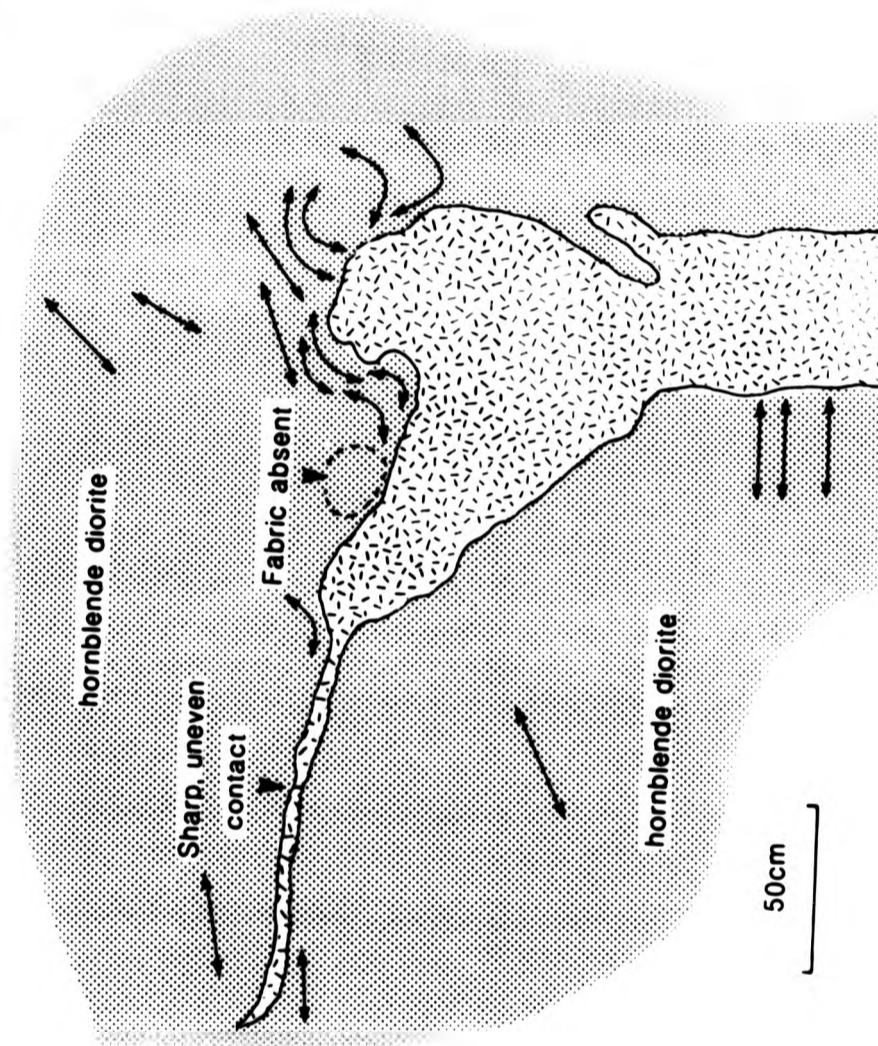
The diffuse zones range in diameter from 0.5m to 4m (Plate 3.4). In plan they are equidimensional structures, composed of large euhedral hornblende up to 1cm in length with plagioclase feldspar, biotite flakes and interstitial quartz. The contact between this coarse grained facies and the normal diorite and gradational and the zones seem to simply represent a change in grain size (Plate 3.5).

(ii) Discrete elliptical pods

The two dimensional form of the pods is of an elongate ellipsoid (Plate 3.6). They are usually small, 0.5m long, and display a similar mineralogy to the larger diffuse zones. The euhedral brown hornblendes (<10cm long) are however often skeletal, with cores filled with plagioclase feldspar. The contact with the medium hornblende diorite is relatively sharp and uneven.

Although the three dimensional form of these patches is not displayed in the river White Water, it is clearly seen in an outcrop in the southeastern part of the complex (28707622). The base of the outcrop exposes a parallel sided body of coarse grained diorite apparently intruded into a medium grained hornblende diorite (Figure 3.4). This intrusion truncates the igneous fabric in the host diorite (see below). In the upper part of the exposure a diffuse area of coarse grained diorite is seen containing abundant large (10cm long) skeletal hornblende with plagioclase at the core. The orientation of these hornblendes is random. Vugs are common and frequently contain quartz crystals displaying perfect termina-

Fig. 3.4 View looking NE from 2731 7624 showing the variable orientation of the igneous fabric around a coarse grained zone in the hornblende diorite, Glen Doll Complex.



tions. Narrow horizontal apophyses of the coarse grained facies is seen trending north. The hornblende crystals in this zone are orientated with their long axis in a horizontal plane.

3.2.1.2 Origin of the coarse facies

Similar textural features in dioritic rocks have been described by Pitcher and Berger (1972) from Donegal and by Bishop (1964) from Jersey. Amphibole displaying a skeletal habit similar to that described above are considered by them, to be indicative of growth in a volatile rich environment. The occurrence of vugs supports this view. The coarse grained zones described from the Glen Doll Complex may have formed due to a combination of processes. These could include (a) an upward streaming of volatiles from lower in the complex, perhaps derived from metasedimentary xenoliths undergoing assimilation, followed by (b) the movement of interstitial melt from the adjacent diorite into the volatile-rich areas.

The diorites and monzonites in the south of the complex display particularly well the development of a strong planar igneous fabric picked out by tabular plagioclase. This feature tends to be emphasised on highly weathered surfaces. Towards the contacts the lamination strikes parallel or subparallel to the contact and dips towards it. The dip is generally low but highly variable (2-24°) but tends to increase close to the contact. Towards the central part of the complex (north of Braedownie 28647605) dips and strikes are highly variable and show no coherent orientation. The igneous fabric is seen less clearly in other parts of the complex and is absent from much of the diorite. A comparable fabric was described from Glen Banvie Complex (Holgate, 1951) and interpreted

as a flow structure.

A detailed examination of the fabric in two parts of the complex (28707622 and 26857590) shows that the variability may in some cases be related to the coarse grained zones described above. Figure 3.4 shows a lower 'dyke like' section of coarse grained diorite which truncates the igneous fabric in the hornblende diorite. The fabric around the more diffuse area above, varies in orientation from horizontal to vertical and is sometimes curved. The igneous fabric is frequently absent.

The variation in the orientation of the fabric is interpreted as being caused by a collapse of the plagioclase framework in the diorite, due to the expulsion of interstitial liquid.

3.2.1.3 Pyroxene Diorites

The pyroxene diorites occur throughout the complex as isolated outcrops (e.g. Fee Burn (26267569), Rough Burn (27787660), White Water (26857590) and an area covering 500m² east of Glen Doll Youth Hostel (28107645)(Figure 3.5)). They occur at variable topographic heights, from 300m around the youth hostel, to 700m close to the contact above the Rives (27357750), and are more common in the western than eastern part of the complex. The larger outcrops are shown on Figure 3.1 and their distribution, including those too small to be mapped at 1:10,000 scale are shown on Figure 3.5. The contact between the pyroxene diorites and hornblende diorites is not seen. It is locally covered by drift on the lower ground, and on the steep valley sides the critical exposure is absent. However, the igneous fabric which penetrates some of the diorites (see below) is continuous in orientation from the hornblende to

pyroxene diorites suggesting that the pyroxene diorites are merely a local facies in the diorite complex.

Samples collected from across the complex, reveal that the change from hornblende to pyroxene diorite is probably gradational since a complete range in mineralogy is observed. Some pyroxene diorites occur which contain a basic plagioclase with only local patches of amphibole. The pyroxene in these, includes both opx and cpx, is fresh and subhedral, and forms the main mafic component of the rock. The change in mineralogy is gradational, from examples which have some isolated pyroxene which is jacketed or partly replaced by amphibole, to varieties with virtually no free pyroxene. The lithological boundary between pyroxene and hornblende diorites has been drawn between those diorites which contain free pyroxene and those which contain pyroxene which is always jacketed by, or replaced by, amphibole.

3.2.2 Basic rocks

Two areas of basic rocks crop out in the Glen Doll Complex. The first of these is in the northeast part of the complex, in Moulzie Burn (Figure 3.6) and the second in the south west in Kilbo Burn. Both consist of gabbro, associated in Kilbo Burn with olivine gabbro.

3.2.2.1 North-eastern gabbro

The dominant rock type is a medium to coarse grained gabbro which contains clino and ortho-pyroxene, hornblende and occasionally biotite. The hornblende (<1cm in length) is characteristic of

the gabbro and may poikilitically enclose both orthopyroxene and plagioclase. The gabbro is frequently finer grained than the diorite and contains a greater proportion of mafic minerals. Intermittant textural change occurs from medium to fine grained gabbro but the poikilitic habit of the hornblende persists through this. A gradual change between medium and fine grained gabbro is observed on a traverse up stream through Moulzie Burn. The changes occur over a distance of ~50m. The layers defined by the local differences in mineralogy and grain size are considered to strike across the burn (NW-SE) and are therefore approximately parallel to the northeastern contact. The contact between the gabbro and the marginal adamellite is not exposed.

A weak igneous lamination, again defined by tabular plagioclase, is sometimes present in the coarser varieties. It is variable in orientation and dips from 16-28°. This variation in strike is not apparently related to the orientation of the layering or the attitude of the contacts.

The contact of the gabbros with the hornblende diorites to the south is not well exposed but detailed mapping suggests that it is steeply dipping. However, as the contact is approached both rock types become progressively more fractured and shattered. The fractures are open and do not show any mineralisation. The zone of shattering is broadly linear, displaying two separate trends (Figure 3.1). The contact is therefore assumed to be faulted. The fault trace is not seen cutting the marginal adamellite. However the adamellite is exposed in its expected position on either side of the inferred fault and it has therefore not been displaced to any great extent by a strike slip fault. The type of fault present

Plate 3.7
Appinitic pod enclosed within a hornblende bearing pegmatite
which is seen veining the host gabbro. (Lens cap 5cm)
(28707835)

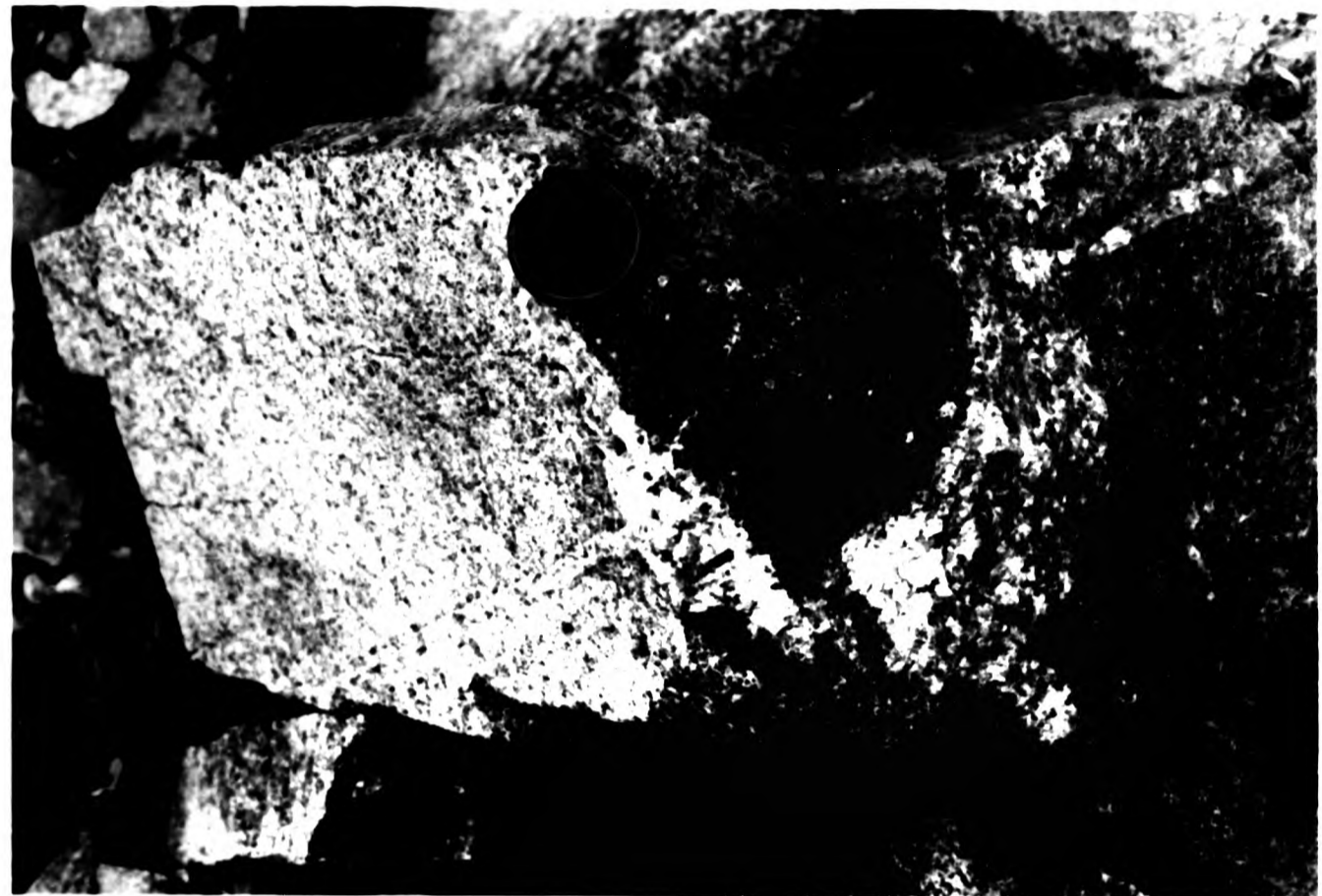


Plate 3.8
View of sharp contacts between gabbro (upper), appinite
(centre) and pegmatite (lower) in Moulzie Burn. (Hammer shaft 30cm)
(28707835)

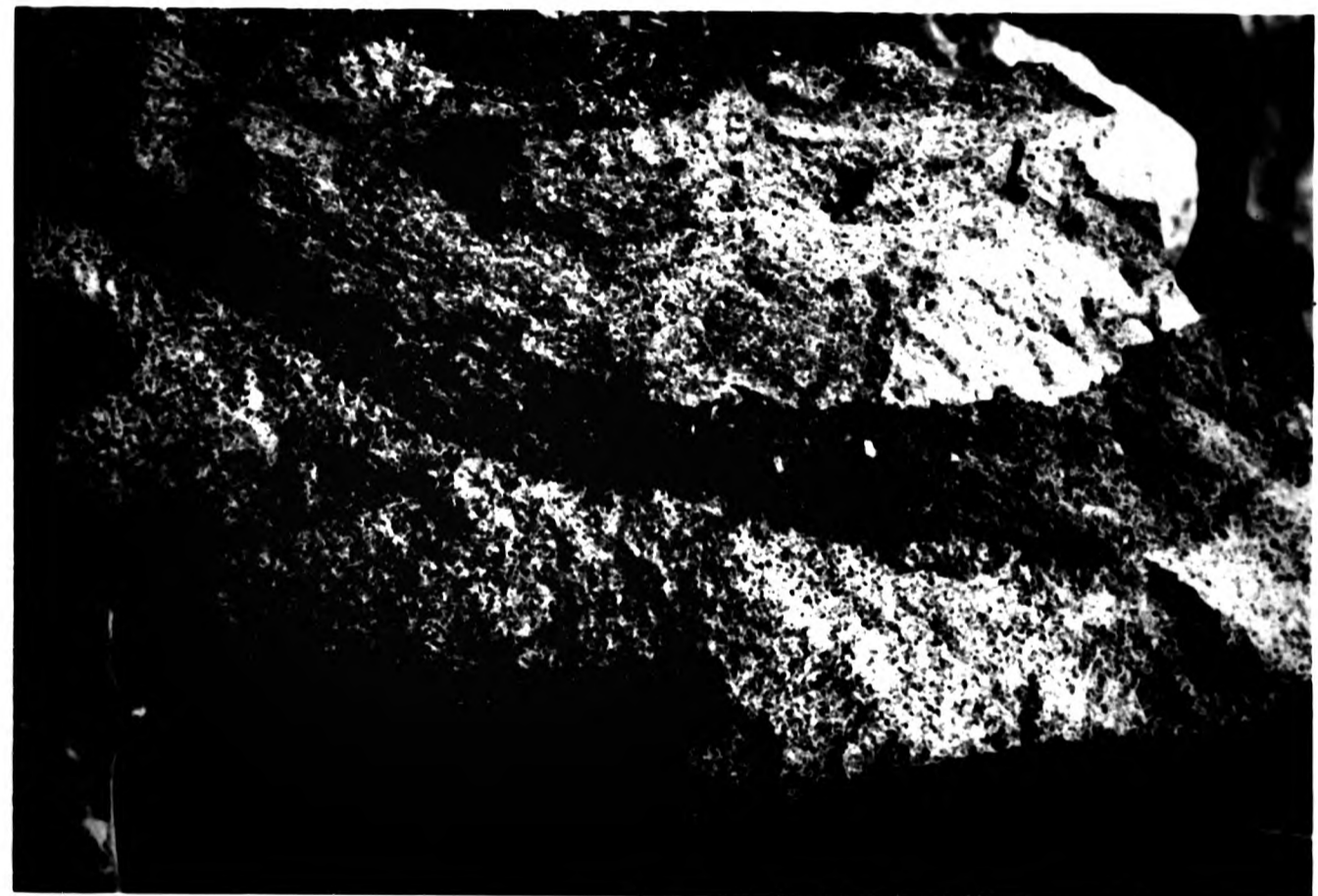


Plate 3.7
Appinitic pod enclosed within a hornblende bearing pegmatite
which is seen veining the host gabbro. (Lens cap 5cm)
(28707835)



Plate 3.8
View of sharp contacts between gabbro (upper), appinite
(centre) and pegmatite (lower) in Moulzie Burn. (Hammer shaft 30cm)
(28707835)

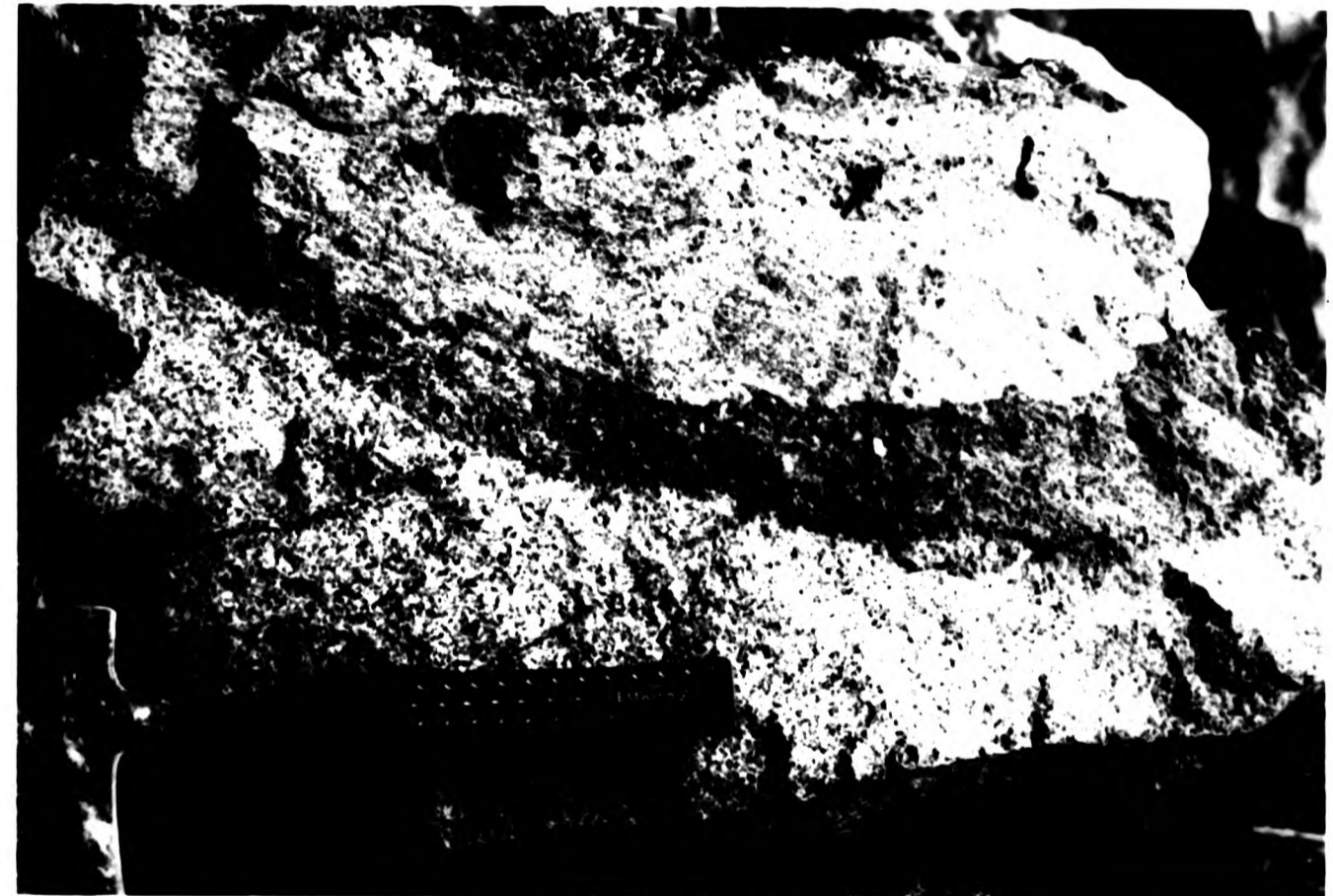
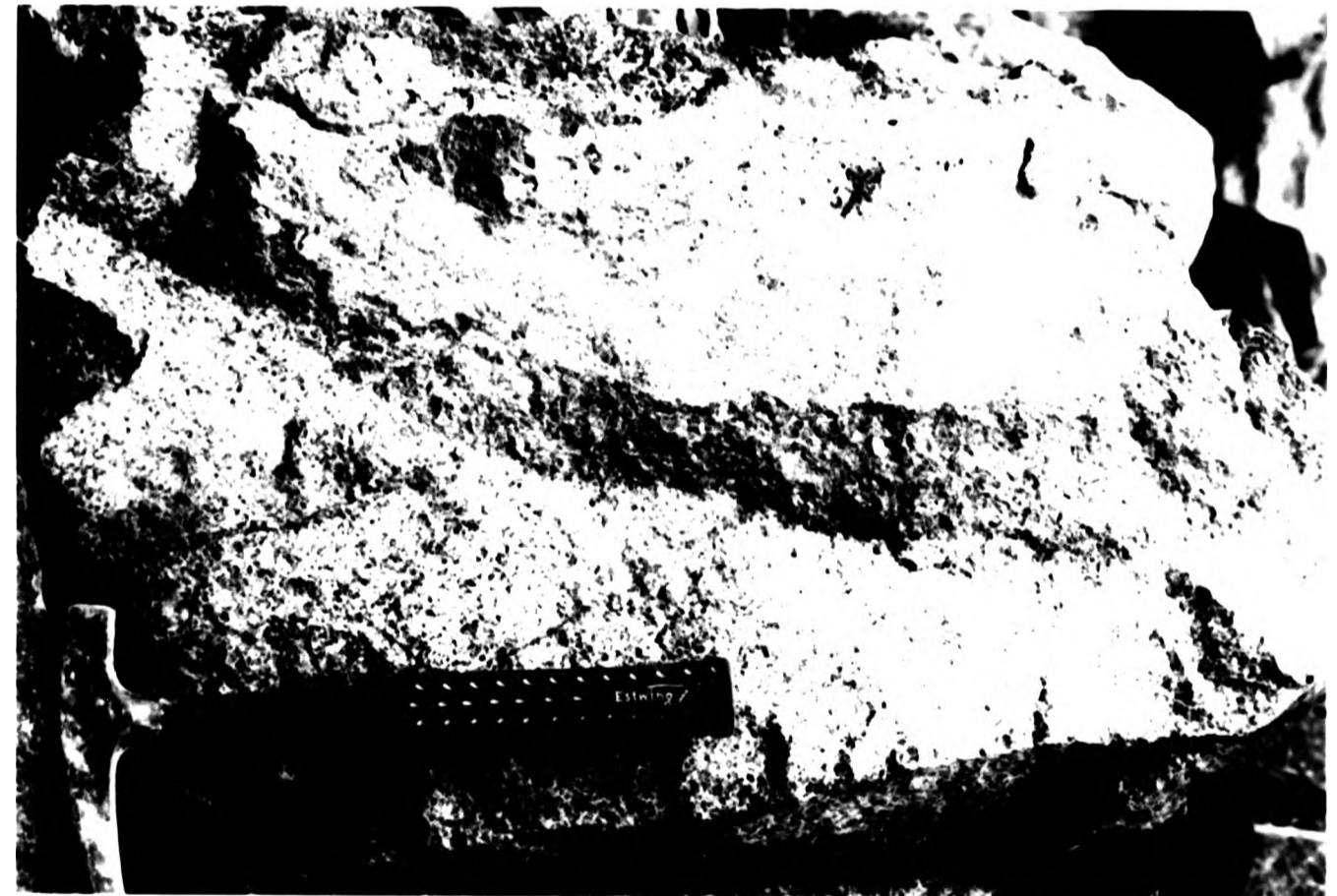


Plate 3.7
Appinitic pod enclosed within a hornblende bearing pegmatite
which is seen veining the host gabbro. (Lens cap 5cm)
(28707835)



Plate 3.8
View of sharp contacts between gabbro (upper), appinite
(centre) and pegmatite (lower) in Moulzie Burn. (Hammer shaft 30cm)
(28707835)



here is therefore assumed to be a dip slip fault. The age relations of the gabbros to the diorites is not clear. The general orientation of the gabbroic layers and their mineralogy, suggest that they may have been deposited parallel to the walls of the intrusion prior to the crystallisation of the diorites. Geochemical and petrographic data are used in Chapter 8 to establish how far, if at all, the two are genetically related.

Within the gabbros there are limited exposures of an appinitic hornblende meladiorite, significantly more mafic than the dominant hornblende diorite of the complex. These zones of appinite are highly weathered and poorly exposed (Figure 3.6). Outcrops are ~4m long and their contacts with the gabbro are not seen. Abundant loose boulders, however, reveal details of the relationship of this facies to the host gabbro. The appinite is often associated with a coarse grained diorite pegmatite composed of quartz, plagioclase feldspar, biotite and hornblende and the contact between the two is sharp. The pegmatite is frequently seen veining the gabbro (Plate 3.7). Alternating layers of pegmatite (3-8cm thick) and appinite (<16cm thick) often occur, with sharp contacts between the two (Plate 3.8). The appinite is also seen in direct contact with the gabbro where a sharp but uneven contact is noted. Lobes of appinite occasionally protrude into the gabbro. The appinite is therefore considered to be intrusive into the gabbro. The pegmatite facies associated with it, may be a reaction product formed by the interaction of magma with volatile rich fluids rising through the magma. It seems unlikely that the appinite post dates the gabbro, but the presence of lobes of appinite in the gabbro suggests that at the time of emplacement the two rock types were still plastic.

The above evidence suggests that a close relationship exists between the appinites and the coarse grained facies of the hornblende diorites in the south-west.

3.2.2.2 South-western gabbro

These facies outcrop extensively in Kilbo Burn (26857540) in the southwestern part of the complex. The unit as a whole was mapped by Barrow and Cunningham-Craig (1912) as 'picrite'. A detailed examination of the rocks has shown this description to be incorrect and the rock types have been named according to the scheme of Streckeisen (1975) as olivine gabbro, gabbro and norite. The distribution of the gabbros here is not dissimilar to those in the north east. The form of the gabbro is poorly defined since there is good exposure only in the stream bed of Kilbo Burn. Exposure in forested areas around the burn is very sparse. The rocks display a vertical layering parallel to the contact with the country rocks. This layering strikes out into the dioritic rocks exposed to the east but the contact between the two rock types is not exposed. The marginal adamellite is not exposed here. The layering, involving gabbro and norite, is rhythmic in nature, and is defined by textural and mineralogical change. The bulk of the characteristics of the layered sequence are shown in a lithological log along Kilbo Burn (Figure 3.7). The sequence is composed of a series of cumulate rocks forming layers between 10 and 100m thick. There is a repetition of some of the rock types through the sequence (see below).

The layer nearest to the contact (~20m), is an olivine gabbro (unit 1a) of medium grain size containing interstitial amphibole.

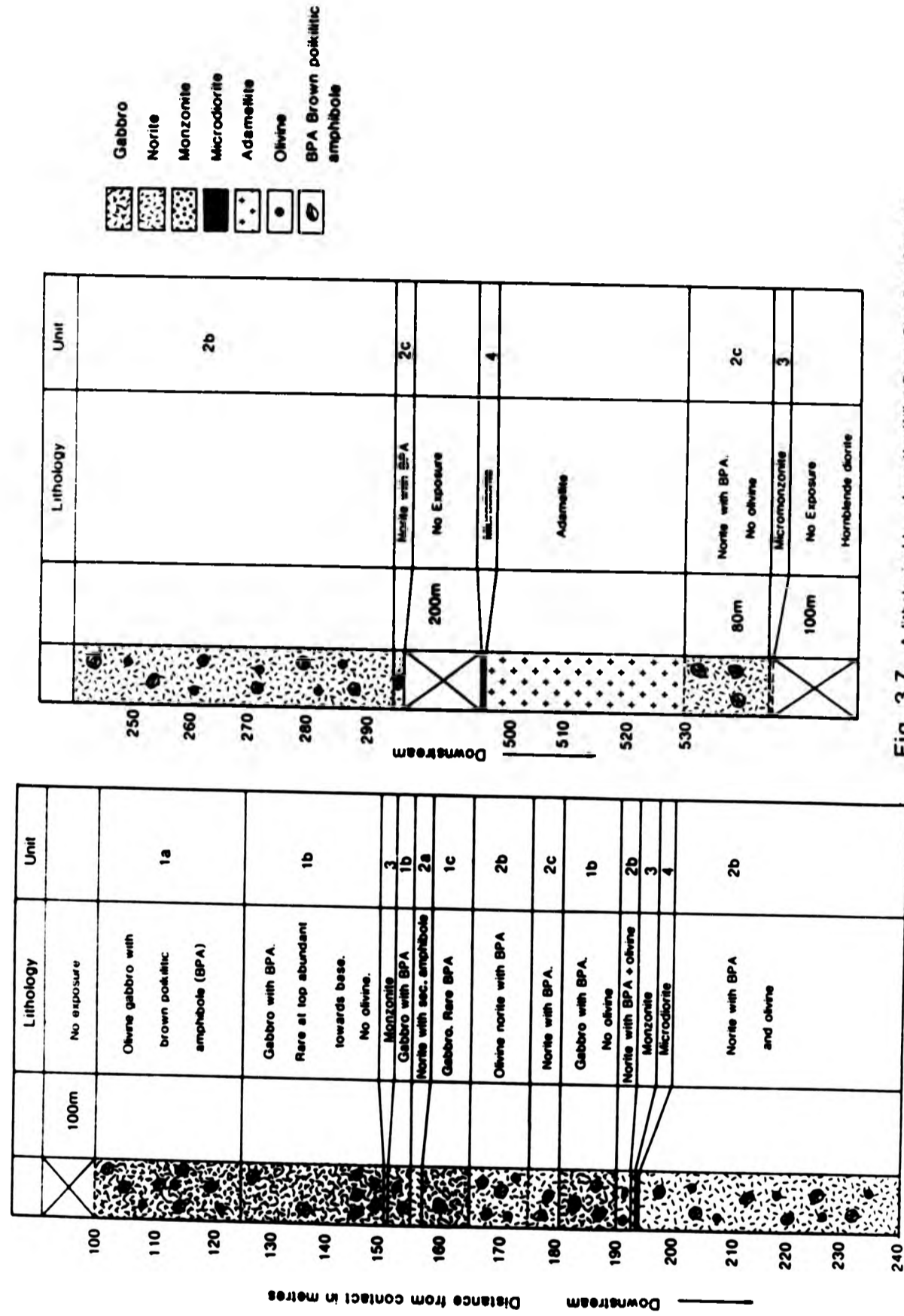


Fig. 3.7 A lithological log along the Kilbo Burn, Glen Doll Complex

The second layer is olivine-free and locally contains very large (1cm) poikilitic amphibole crystals enclosing tabular plagioclase (unit 1b). This unit continues for 75m and the abundance of amphibole and biotite increases. This unit is again repeated after a narrow layer (35cm) of quartz monzonite (unit 3). The contact between the layers is vertical.

Unit 2a has opx dominant over cpx and is a norite. Unit 1b is a gabbro traceable for only 3m into unexposed ground, but is assumed to continue for 20m downstream where unit 2b is exposed. Unit 2b is an olivine norite which gives way to an olivine-free norite over 20m (unit 2c). The succession continues downstream with alternating olivine-bearing and olivine-free facies and occasional layers of quartz monzonite.

The field data has been interpreted as indicating the presence of a series of cumulate gabbros and norites occurring in the form of wall parallel layered rocks, similar to that described from the Skargaard intrusion (Wager and Brown, 1968). The quartz monzonite layers, which display the same orientation as the basic rocks, are interpreted as having been intruded between the pre-existing basic layers along zones of weakness. Several later micro diorite dykes have also intruded along the same orientation.

3.2.3 Adamellite

This is a medium grained, homogenous, xenolithic rock composed of orthoclase, plagioclase, biotite and quartz. The marginal adamellite is present at all exposed external contacts except between the septum of gneiss at Red Craig and the country rocks,

Plate 3.9
View of adamellite back veining the hornblende diorite at
Capel Road. (Hammer shaft 30cm)
(29047844)

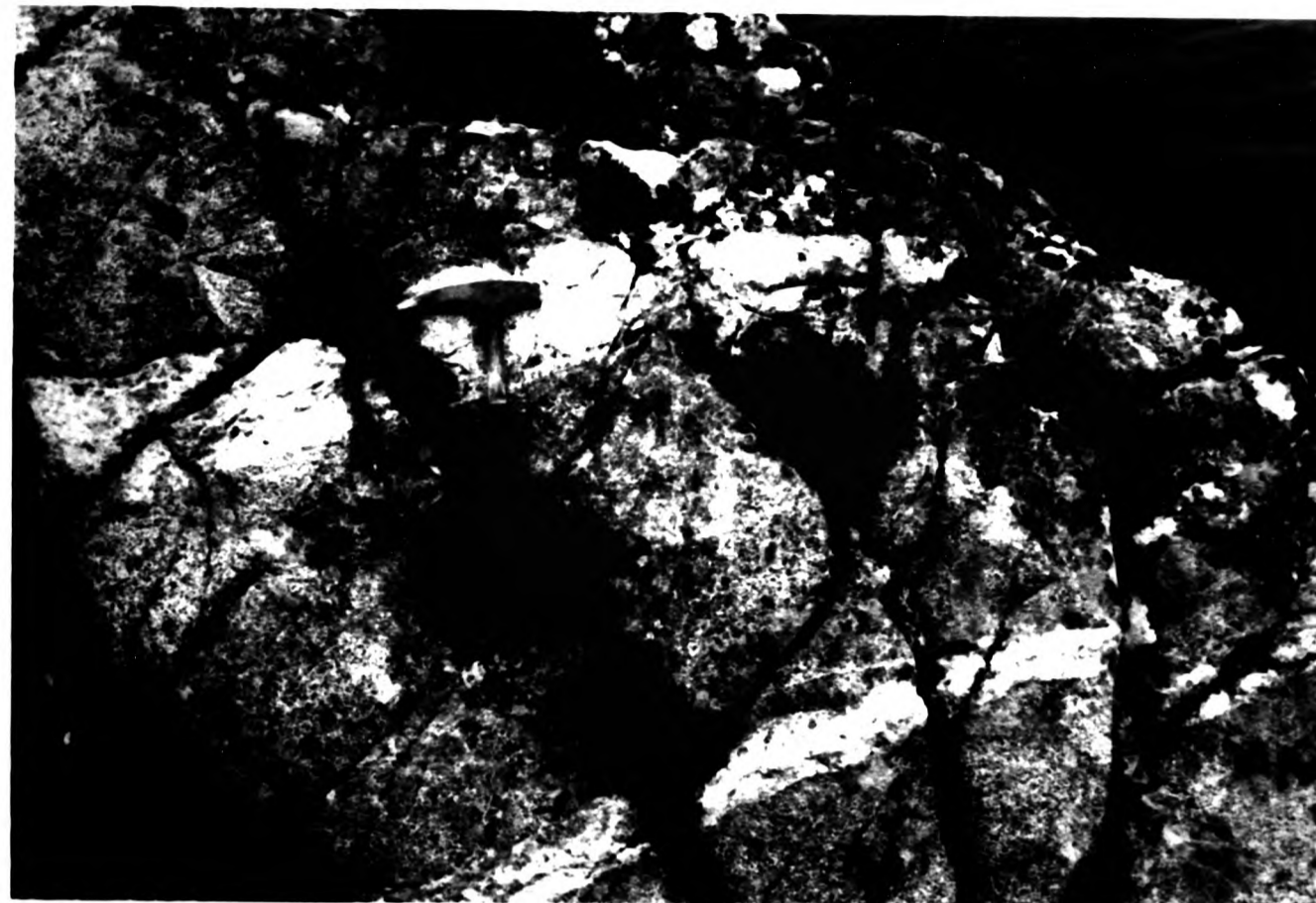


Plate 3.10
View of an atypical angular rafted xenolith (lower centre)
in hornblende diorite host. (Hammer shaft 60cm)
(28917615)



Plate 3.9
View of adamellite back veining the hornblende diorite at
Capel Road. (Hammer shaft 30cm)
(29047844)



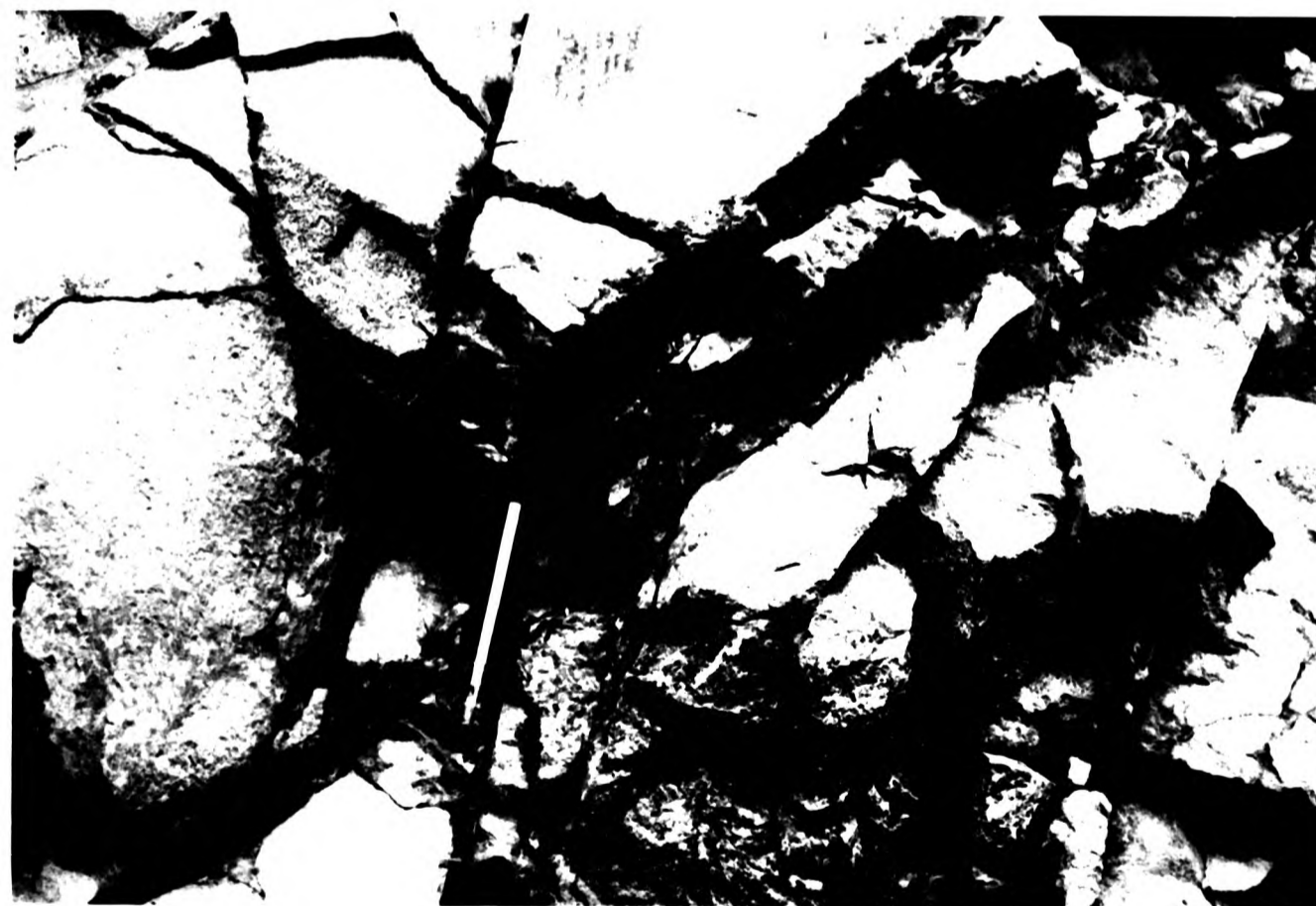
Plate 3.10
View of an atypical angular rafted xenolith (lower centre)
in hornblende diorite host. (Hammer shaft 60cm)
(28917615)



Plate 3.9
View of adamellite back veining the hornblende diorite at
Capel Road. (Hammer shaft 30cm)
(29047844)



Plate 3.10
View of an atypical angular rafted xenolith (lower centre)
in hornblende diorite host. (Hammer shaft 60cm)
(28917615)



where a fine-grained diorite is present, and is assumed to be continuous around most of the complex. The width of this marginal facies is variable from 20m in the NE, 50m in the SE but <300m in the SW where it forms an embayment into the hornblende diorite (Figure 3.1). In Kilbo Burn the adamellite is 350m wide and is intruded into the layered basic sequence. The contacts with the basic rocks are not exposed.

The inner and outer contacts of the adamellite are vertical and the general three dimensional form is of a vertical cylinder. The contact with the country rocks is sharp but locally inter-fingered as displayed at Winter Corrie (27707680). At this locality the adamellite has invaded open fractures in the country rocks and veining may persist for several metres into the latter. In the NE at Capel Road (29257837) the adamellite is clearly seen back veining fractures in the hornblende diorite indicating that it post dates this facies (Plate 3.9).

There is no chill developed in the adamellite either internally against the hornblende diorite, or at its external contact with the country rock. Equally the diorite does not chill against the adamellite. The adamellite along the southeastern margin however, does contain patches of a finer grained, more biotite rich adamellite which may represent chilled material now incorporated as autoliths in the adamellite. The lack of a chilled facies may indicate that at the time of emplacement, the temperature of the country rocks was elevated. The aureole mineralogy, investigated by Durig (1981), indicates an outer aureole temperature of <200°C and pressures of 1.5-2kb and an inner aureole temperature of ~600°C.

Diagrams to the distribution of the xenoliths and dykes within the
Glen Doll Complex.

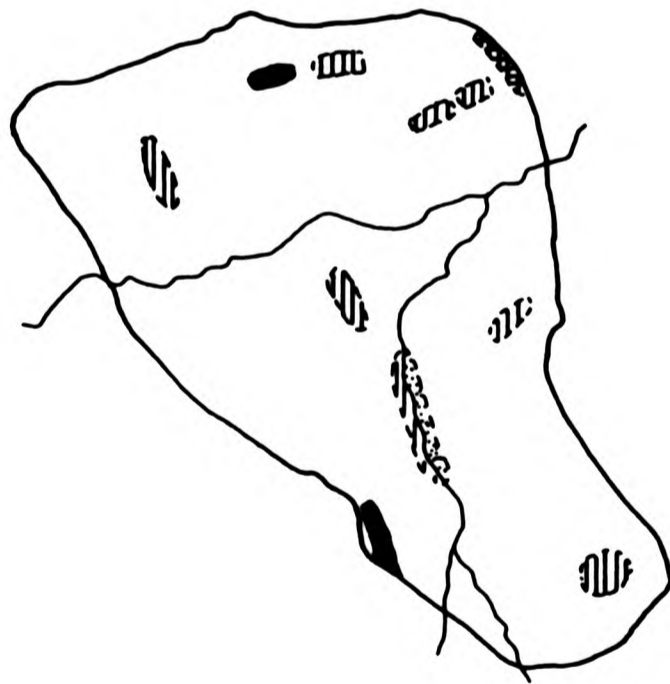


Fig. 3.8 Distribution of xenoliths in dioritic and granitic rocks

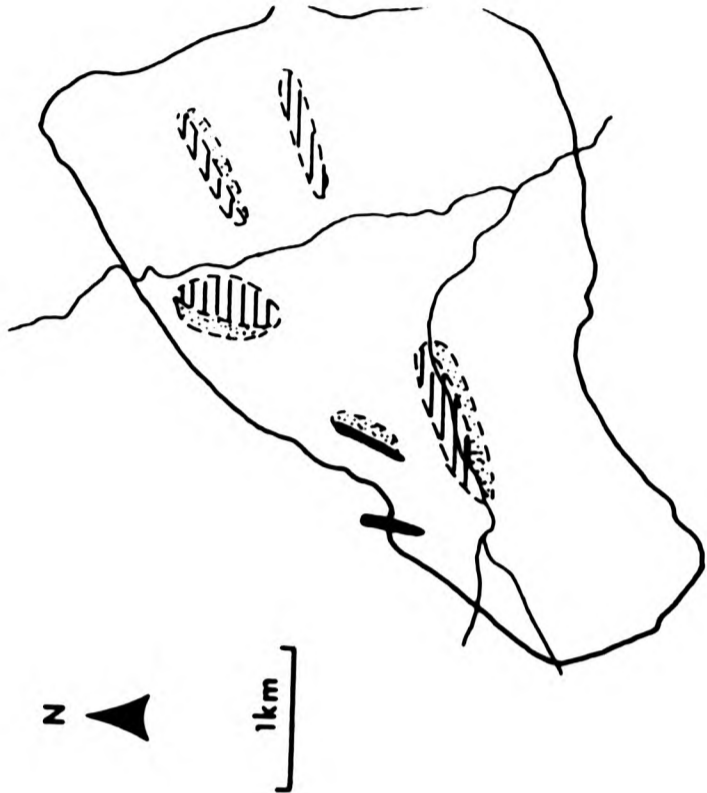


Fig. 3.9 Distribution of areas with high concentration of dykes



3.2.4 Xenoliths

Five types of xenoliths occur within the complex and their distribution may be related to particular intrusive facies (Figure 3.8). The five types are:-

3.2.4.1 Rafted metasediments

3.2.4.2 Fine-grained metasediments

3.2.4.3 Gneiss

3.2.4.4 Epi-diorite

3.2.4.5 Microdiorite

3.2.4.1 Rafted metasediments

This xenolith type is distributed throughout the dioritic rocks of the complex but does not occur in either the marginal adamellite or in the gabbros. The shape of the xenoliths is variable but many are elongated and tabular or raft-like. Many are however angular (Plate 3.10). They are commonly 3-4m across, but exceptionally 100m across as seen at Red Craig (28257583). These xenoliths compose <1% of the complex. They are composed of coarse grained quartzo-feldspathic layers with fine-grained mafic patches or layers between them, often containing abundant biotite. The layers may be invaded by the medium grained hornblende diorite. The internal stratification is parallel to the upper and lower margins of the xenolith. The internal layering is also frequently orientated parallel to the igneous lamination described in the diorites. Their contacts with the host diorite are sharp and

Plate 3.11
A group of fine-grained mafic xenoliths thought to be the remnants
of fine-grained metasediments. (Lens cap 5cm)
(29557555)



Plate 3.12
Fine-grained xenolith composed of plagioclase, clinopyroxene and
quartz showing a sharp contact with the host hornblende diorite
in White Water River. (Hammer shaft 60cm)
(27967603)

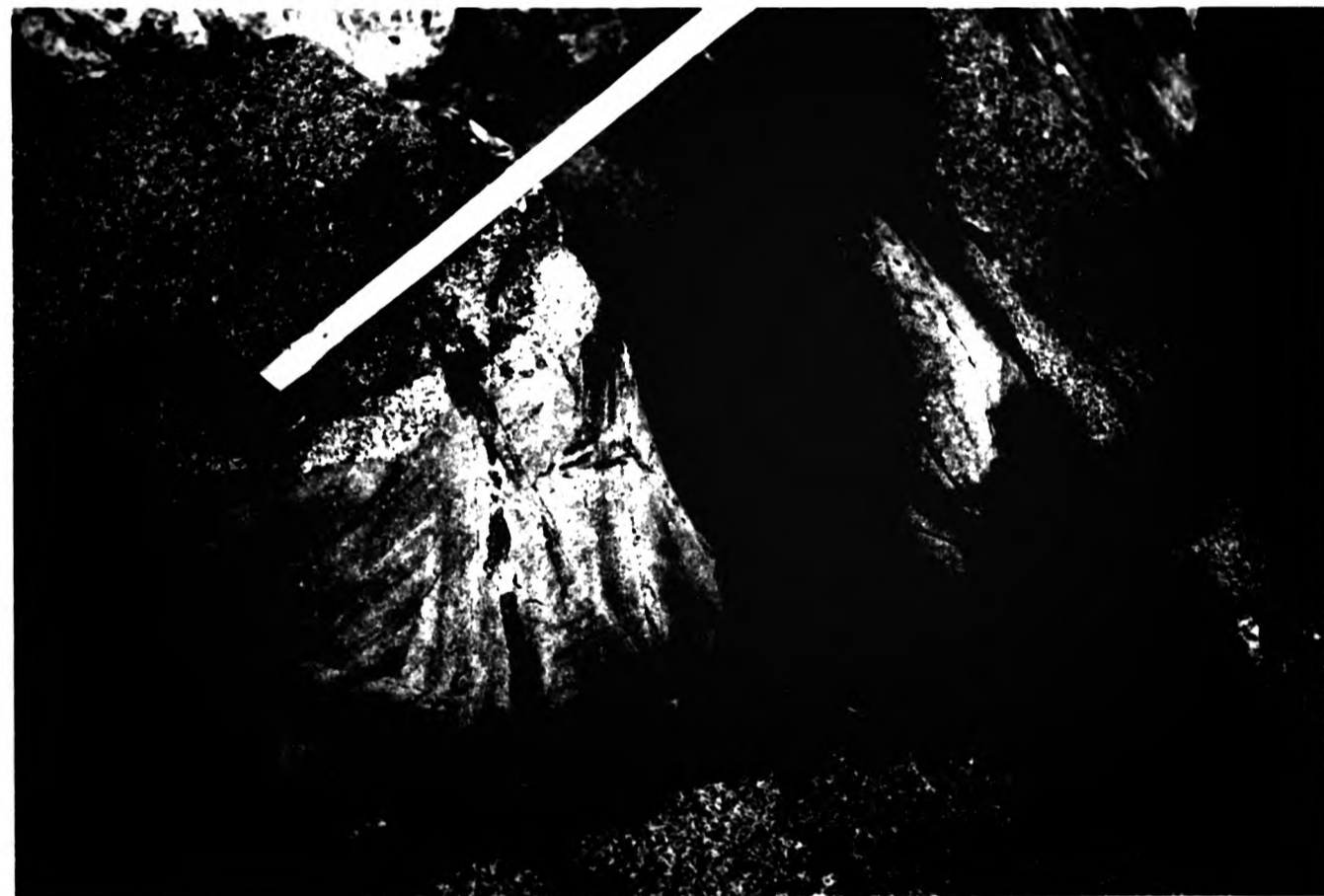


Plate 3.11

A group of fine-grained mafic xenoliths thought to be the remnants of fine-grained metasediments. (Lens cap 5cm)

(29557555)



Plate 3.12

Fine-grained xenolith composed of plagioclase, clinopyroxene and quartz showing a sharp contact with the host hornblende diorite in White Water River. (Hammer shaft 60cm)

(27967603)



Plate 3.11
A group of fine-grained mafic xenoliths thought to be the remnants
of fine-grained metasediments. (Lens cap 5cm)
(29557555)

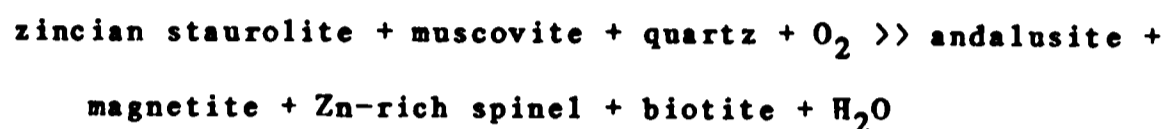


Plate 3.12
Fine-grained xenolith composed of plagioclase, clinopyroxene and
quartz showing a sharp contact with the host hornblende diorite
in White Water River. (Hammer shaft 60cm)
(27967603)



uneven. They tend also to be highly weathered, rotted and are therefore friable.

One characteristic feature of these rafts is that they contain rounded aggregates (<0.5cm) of green hercynitic spinel. A similar mineralogical feature is seen in the inner part of the metamorphic aureole around Glen Doll, where they are considered by Schumacher (1985) to have formed by the reaction:-



Textural, mineralogical and geochemical evidence presented in later chapters suggests that the rafted xenoliths have been derived from Dalradian metasediments, though not necessarily from the level exposed today, and that they have undergone prograde metamorphism leading to partial melting with diorite liquid invading the original gneissose (see Chapter 6 and 8).

3.2.4.2 Fine-grained metasediments

These xenoliths are elongate mafic structures. They are commonly <15cm in length and form elongate discs or stringers. They occur only in the marginal adamellite where they may compose <5% of the rock. Commonly occurring in clusters, individual members of such groups are mutually parallel (Plate 3.11) but random orientation between groups is seen. Each cluster is typically 20cm across. The margins of the xenoliths are sharp. They have a granoblastic texture and are composed of plagioclase, quartz, orthoclase, green amphibole and chlorite.

The form of these disc-like xenoliths is similar to those described by Oldershaw (1958) from Lochnagar and Juan Jorge where they occur in the coarse grained granite facies. They display parallel orientation and are also parallel to the intrusive contacts. They are considered to delineate a flow structure in the granite (Oldershaw, 1958). Oldershaw, however, considers the lithology forming these xenoliths to be locally derived as they display a texture similar to that seen in fold closures in the local Dalradian metasediments. Didier (1973) described this type of xenolith as schlieren, and proposed two hypotheses for their origin. The first is that they are formed by magmatic differentiation and the second that they are the remains of broken-up enclaves. The latter mode of origin seems likely for the origin of these xenoliths in the Glen Doll Complex since their mineralogy and texture is comparable with some of the local metasediments.

3.2.4.3 Gneiss

Xenoliths of gneiss which appear to be locally derived, from the Dalradian gneiss into which the Complex is intruded, are restricted to the southeastern part of the complex around Red Craig. They occur in both the fine-grained diorite facies and in the adamellite. They are frequently tabular and range in size from 20cm by 10cm to 3m by 2m. Exceptionally they reach 20m by 10m in size. Their orientation, with respect to the internal layering, is random and they have not undergone any degree of assimilation.

3.2.4.4 Epidiorite

This third xenolith type is restricted to the Glen Doll dioritic facies and occurs in outcrops west of Rough Burn (25147660),

northeast of Rough Burn (27557702) and elsewhere. They are elongate, tabular and 0.2-2m long. They are composed of a fine grained matrix of granular cpx, plagioclase, quartz, magnetite and large amphibole porphyroblasts. The amphiboles form distinctive bands which display a variable orientation. These layers of amphibole are discontinuous and a single layer may only be traced for 15cm. They are probably picking out a foliation present in the original rock.

This third xenolith type is considered to represent material derived locally from the many epi-diorite bodies some of which outcrop due west of the Glen Doll Complex. These epi-diorites are thought to represent early Caledonian basic igneous rocks (Harte, 1979).

3.2.4.5 Microdiorite

These fine-grained xenoliths are angular, <60cm across and have a sharp contact with the hornblende diorite in which they occur (Plate 3.12). They are clearly exposed in the bed of White Water (26157590) where they are found in association with the coarse grained facies of the diorite. These xenoliths are composed of equigranular cpx, opx, plagioclase and quartz.

3.3 Juan Jorge Complex

3.3.1 Diorites

The character of the dioritic facies in the Juan Jorge Complex is substantially different to that described from Glen Doll. It is

Plate 3.13
Abundant xenoliths of both gneiss, fine-grained metasediments and
microdiorite along the margin of the Juan Jorge diorite.
(Hammer shaft 60cm)
(26227923)



Plate 3.14
Angular xenolith of gneiss in the Juan Jorge diorite.
(Hammer shaft 60cm)
(26227923)



Plate 3.13
Abundant xenoliths of both gneiss, fine-grained metasediments and
microdiorite along the margin of the Juan Jorge diorite.
(Hammer shaft 60cm)
(26227923)



Plate 3.14
Angular xenolith of gneiss in the Juan Jorge diorite.
(Hammer shaft 60cm)
(26227923)



Plate 3.13
Abundant xenoliths of both gneiss, fine-grained metasediments and
microdiorite along the margin of the Juan Jorge diorite.
(Hammer shaft 60cm)
(26227923)



Plate 3.14
Angular xenolith of gneiss in the Juan Jorge diorite.
(Hammer shaft 60cm)
(26227923)



dominantly composed of a medium to coarse grained leucocratic quartz-mica diorite. Some of the minor variation in the nature of this diorite seems to be entirely due to the thermal effects of the emplacement of the Lochnagar granite to the north and west (see below).

The quartz mica diorite is usually fresh and unaltered and is composed quartz, biotite, hornblende and magnetite. This facies is homogenous and there are no changes in grain size. Subtle changes in mineralogy are observed over nearly 1km traverse along the South Esk. Along this traverse, the diorites display a slight decrease in the abundance of mafic phases towards the contact with the Lochnagar granite and modal biotite becomes dominant over amphibole. Within 200m of the contact, the diorite becomes pinker and the feldspars may be altered. Here, the diorites may also contain scattered orthoclase porphyroblasts. The steep bluffs at Juan Jorge itself (26507950) and Mounie Craig (27007968), about 170m above the valley floor, are composed of the same heterogenous quartz-mica diorite as in the valley floor to the southwest, indicating that the changes in mineralogy may be essentially associated with the closeness of the contact.

Along the southwestern margin of the diorite is a zone 100m wide which contains abundant xenoliths of both gneiss, fine grained metasedimentary material and micro diorite (see below)(Plate 3.13). The abundance of the two types of xenolith is locally variable, gneiss being the more common type. The abundance is not related to proximity to the contact with the Juan Jorge granite. Since both xenolith types are frequently equant there is no apparent orientation displayed (Plate 3.14).

Plate 3.15
View of the igneous fabric defined by the alignment of tabular
plagioclase feldspar in the Juan Jorge diorite. (Hammer shaft 30cm)
(25227984)



Plate 3.16
Fine-grained metasedimentary xenoliths in the Juan Jorge granite.
(Hammer shaft 60cm)
(26677919)



Plate 3.15
View of the igneous fabric defined by the alignment of tabular
plagioclase feldspar in the Juan Jorge diorite. (Hammer shaft 30cm)
(25227984)

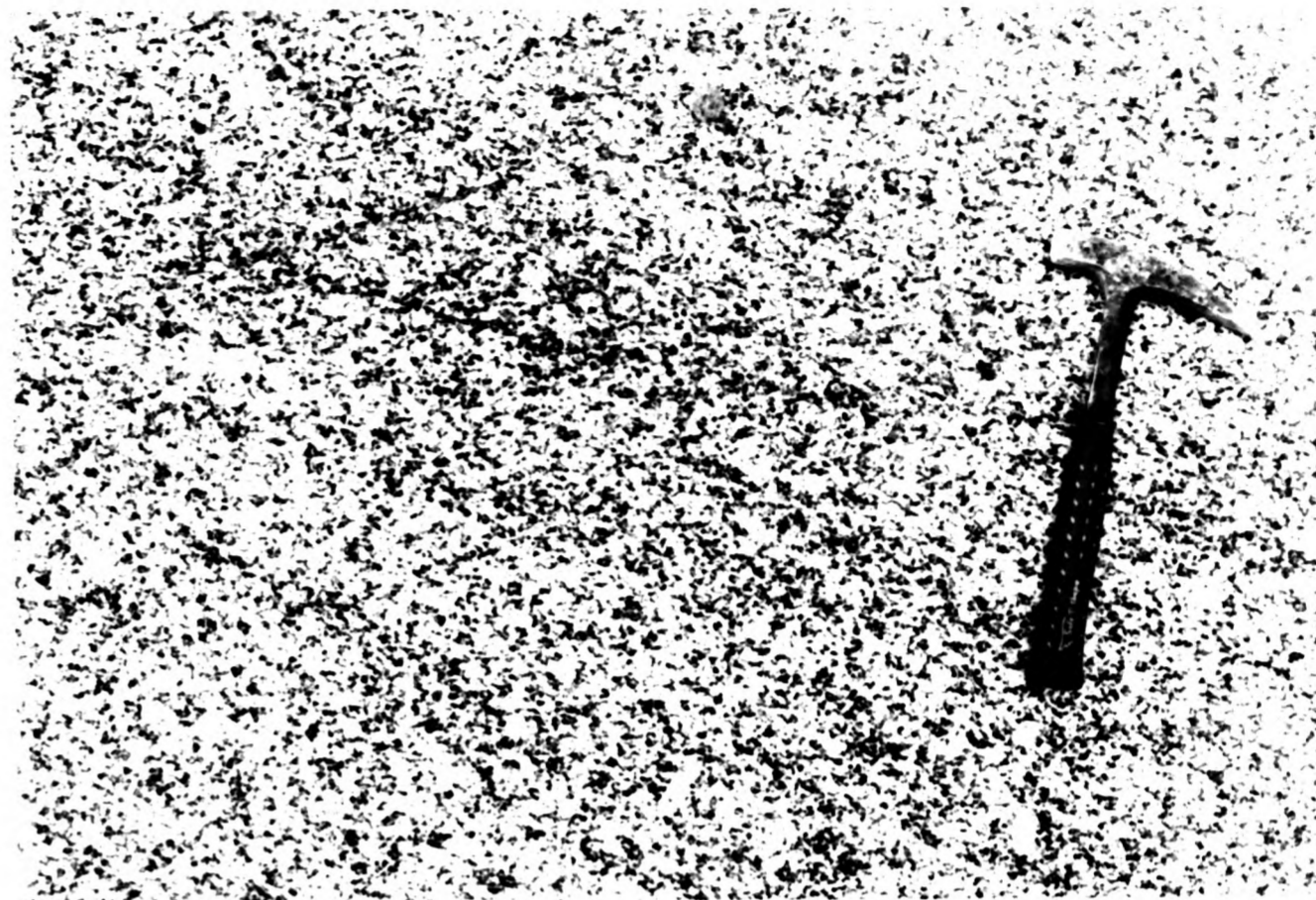


Plate 3.16
Fine-grained metasedimentary xenoliths in the Juan Jorge granite.
(Hammer shaft 60cm)
(26677919)



Plate 3.15
View of the igneous fabric defined by the alignment of tabular
plagioclase feldspar in the Juan Jorge diorite. (Hammer shaft 30cm)
(25227984)



Plate 3.16
Fine-grained metasedimentary xenoliths in the Juan Jorge granite.
(Hammer shaft 60cm)
(26677919)



An igneous lamination, similar to that described from the Glen Doll diorites, is recorded in much of the Juan Jorge diorite. It is defined by the alignment of tabular plagioclase (Plate 3.15). The orientation is variable but tends to be vertical (striking W-E) in the central part of the complex. In the east the fabric strikes N-S, sub-parallel to the external contact and dips at 40° away from the contact. In the west the fabric trends W-E, is vertical and is cut by the intrusion of the later Lochnagar Granite.

3.3.2 Granite

Two areas of granite were mapped, the Juan Jorge granite and the Gourock Granite (Oldershaw, 1958). The two are composed of the same rock type, a coarse grained pink (frequently porphyritic) granite. The abundance of orthoclase phenocrysts increases away from the contacts with both the diorite and the country rocks. Neither granite is foliated and they are typically homogenous.

Close to the contact (within 100m) of the Juan Jorge granite with the country rocks, the granite contains abundant elliptical xenoliths of a fine grained grey metasedimentary rock. Many are elongate with dimensions typically 60 by 25cm (Plate 3.16). Their margins are sharp but uneven and the xenoliths may display a preferential alignment, striking at 60° i.e. parallel to the external contact with the country rocks. The fine-grained xenoliths persist towards the central part of the granite where they are generally smaller, less abundant and show no preferential alignment. To the west of the Juan Jorge granite, is the leucocratic Juan Jorge diorite. The contact between the two is not exposed, but in the bed of the river South Esk (26347918), a septum of country rock gneiss

remains between the two intrusive facies. The granite displays no chill against the gneiss and 3m into the septum, the gneiss is mobilised and the internal banding is highly contorted. The western contact of the septum displays the diorite-gneiss contact. The contact is sharp and the diorite unchilled at this point.

3.3.3 Xenoliths

Three types of xenolith occur in the Juan Jorge Complex:-

3.3.3.1 Gneiss

3.3.3.2 Fine-grained grey metasediments

3.3.3.3 Microdiorite

3.3.3.1 Gneiss

This xenolith type most commonly occurs in the diorite and less frequently in the granite. Their distribution has been described earlier (Section 3.3.2). The xenoliths are angular and frequently rectangular in plan view. Their contacts with the host are sharp and there is no evidence of either partial melting or assimilation. Their composition is of a biotite gneiss and they are thought therefore to be derived locally.

3.3.3.2 Fine-grained grey metasediments

These xenoliths are fine-grained and grey in colour and occur most commonly in the Juan Jorge granite and less frequently in the granitic rocks. In the granite they show a preferential alignment parallel to the outer contact of granite with the country rocks. They are usually small, typically 20 by 10cm and have rounded, sharp outlines in plan view (Plate 3.16). They are considered by

Plate 3.17
A typical view of an aplite dyke from White Water River.
(Hammer shaft 60cm)
(27937604)



Plate 3.18
View of a rare curved white porphyry dyke from The Rives.
(Hammer shaft 60cm)
(27467739)

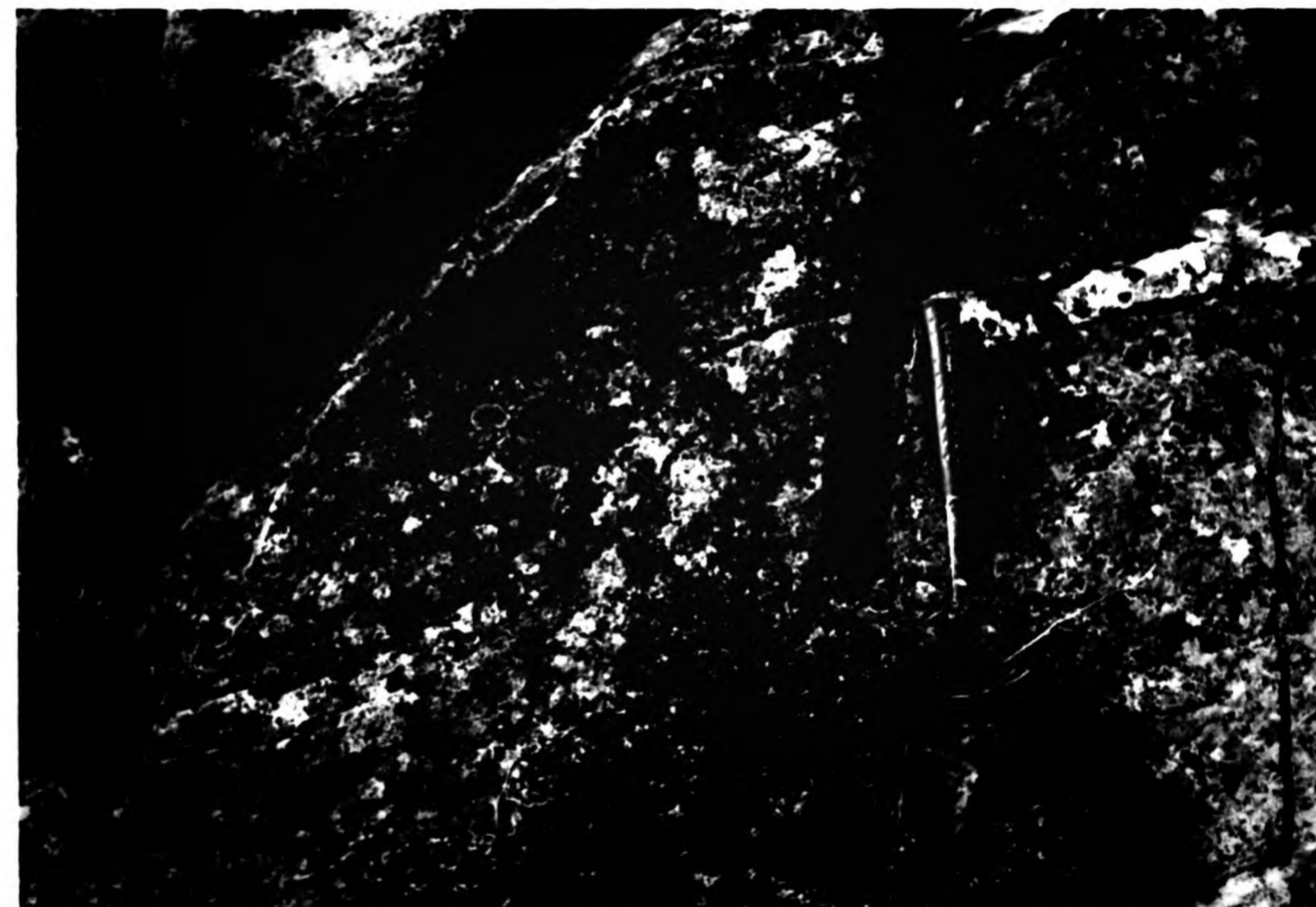


Plate 3.17
A typical view of an aplite dyke from White Water River.
(Hammer shaft 60cm)
(27937604)



Plate 3.18
View of a rare curved white porphyry dyke from The Rives.
(Hammer shaft 60cm)
(27467739)

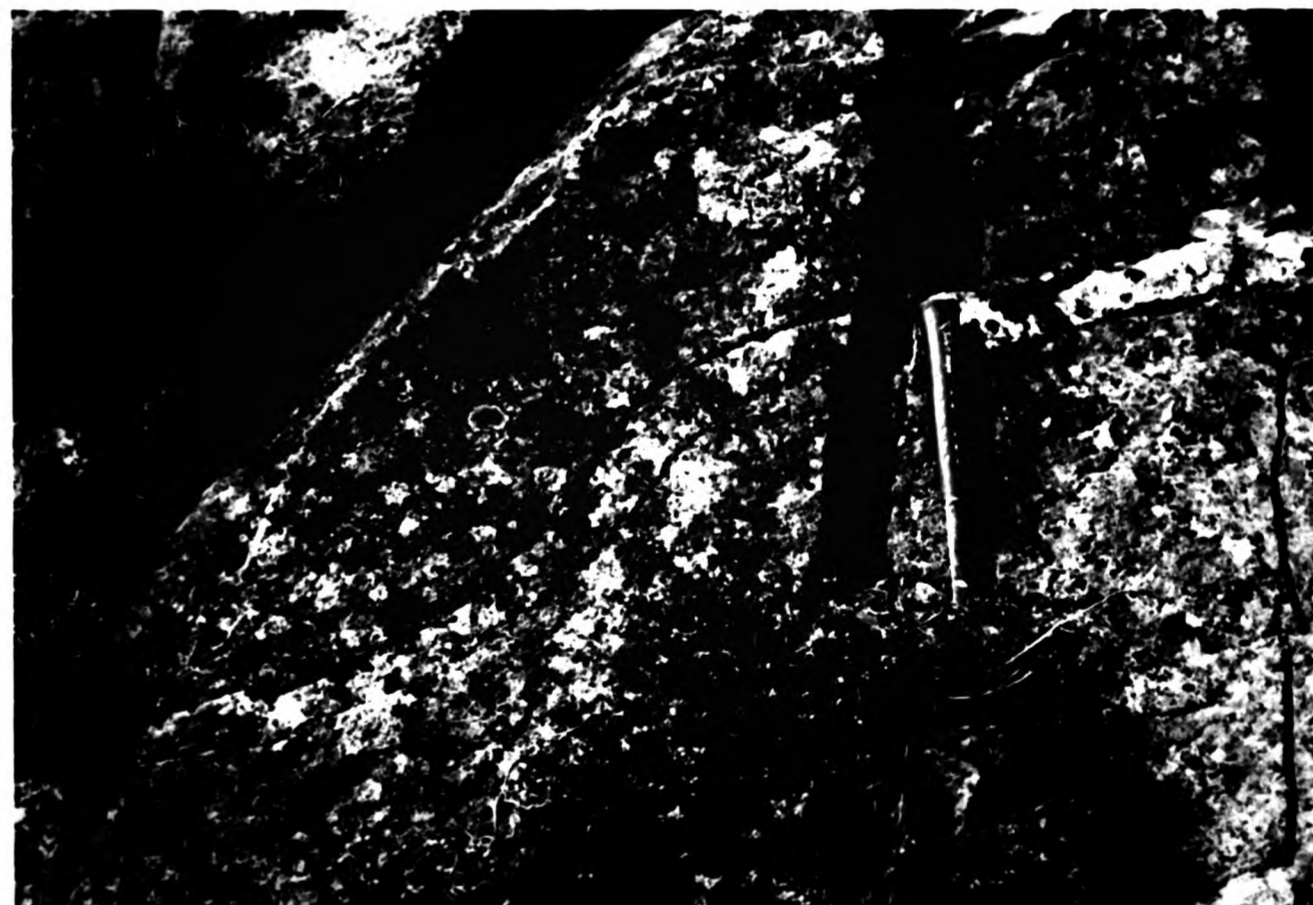


Plate 3.17
A typical view of an aplite dyke from White Water River.
(Hammer shaft 60cm)
(27937604)



Plate 3.18
View of a rare curved white porphyry dyke from The Rives.
(Hammer shaft 60cm)
(27467739)



Oldershaw (1958) to be derived locally from fold closures in the metasedimentary rocks on the basis of texture and mineralogy,

3.3.3.3 Microdiorite

These xenoliths are similar in general appearance to type ii above, but are distinguished by an igneous texture. They are less common than the other xenolithic types and are restricted to the granitic facies. They are typically small (<20cm long) and are occasionally aligned parallel to the fine-grained metasedimentary xenoliths.

3.4 Features common to both complexes

Both complexes are cut by acid and intermediate dykes and have suffered later faulting.

3.4.1 Dykes

A series of both acid and intermediate dykes cut across the area of study (Figure 3.9). Both dyke types cut all of the intrusive rocks in addition to the country rock.

3.4.1.1 Acid Dykes

These include aplite and quartz-feldspar porphyries (QFP). The aplites have a characteristic sugary texture, are pink and are always very fresh (Plate 3.17). The QFP dykes have a medium to fine grained matrix with phenocrysts of plagioclase, K-feldspar and quartz. They are all pink on fresh surfaces or weathered with a brown crust. A single exception is one white dyke which outcrops

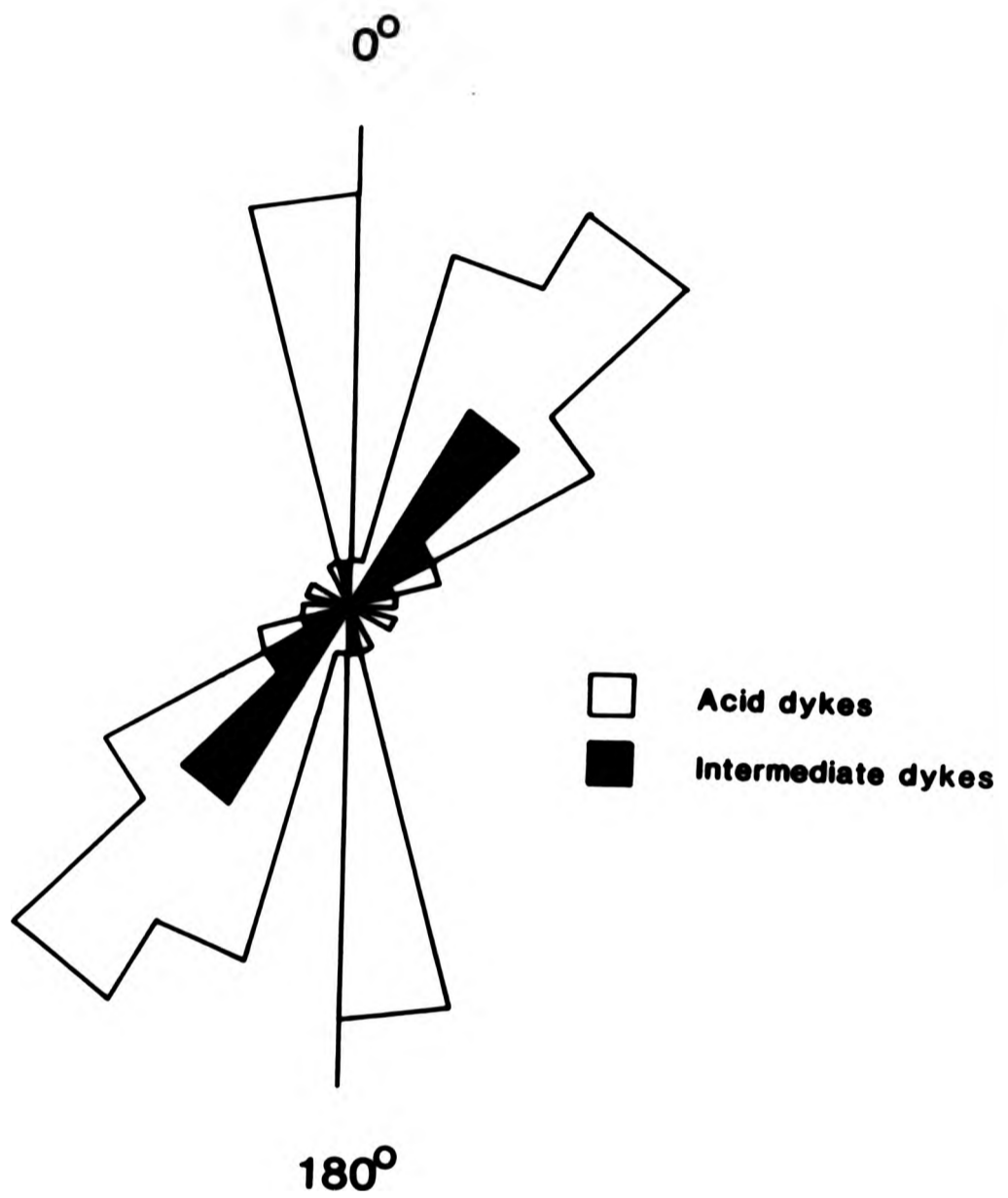


Fig. 3.10 A rose diagram showing the orientation of the acid and intermediate dykes from the Glen Doll Complex

Plate 3.19
View of a fault controlled valley below the Rives. Remnants of a quartz, feldspar porphyry dyke crop out on the lower slopes of the valley sides.
(Person 1.6m)
(27507737)

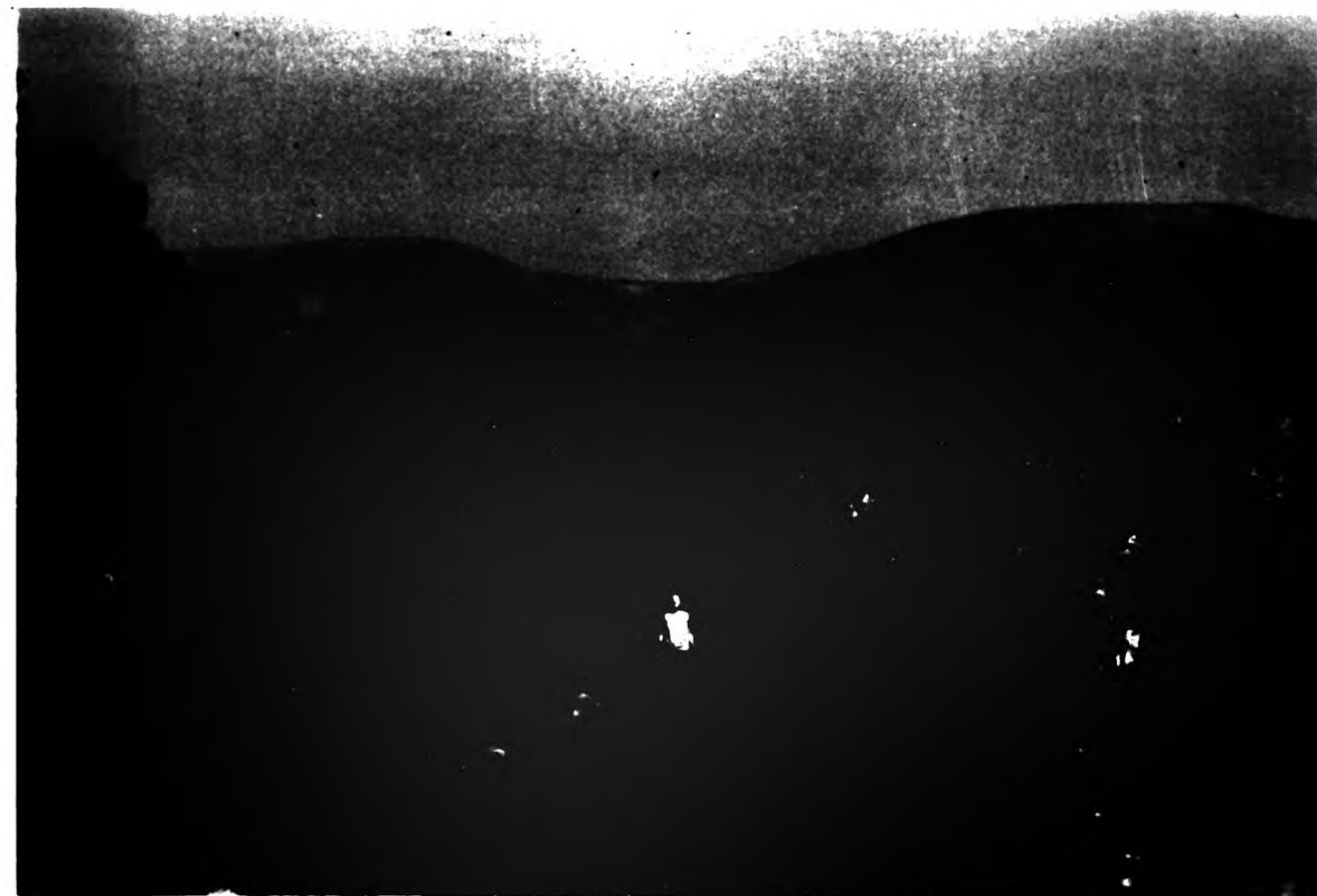


Plate 3.20
Quartz, feldspar porphyry dyke intruded into the Dalradian metasediments. The dyke is seen to follow the gneissose banding.
(27937517)



Plate 3.19
View of a fault controlled valley below the Rives. Remnants of
a quartz, feldspar porphyry dyke crop out on the lower slopes
of the valley sides.
(Person 1.6m)
(27507737)

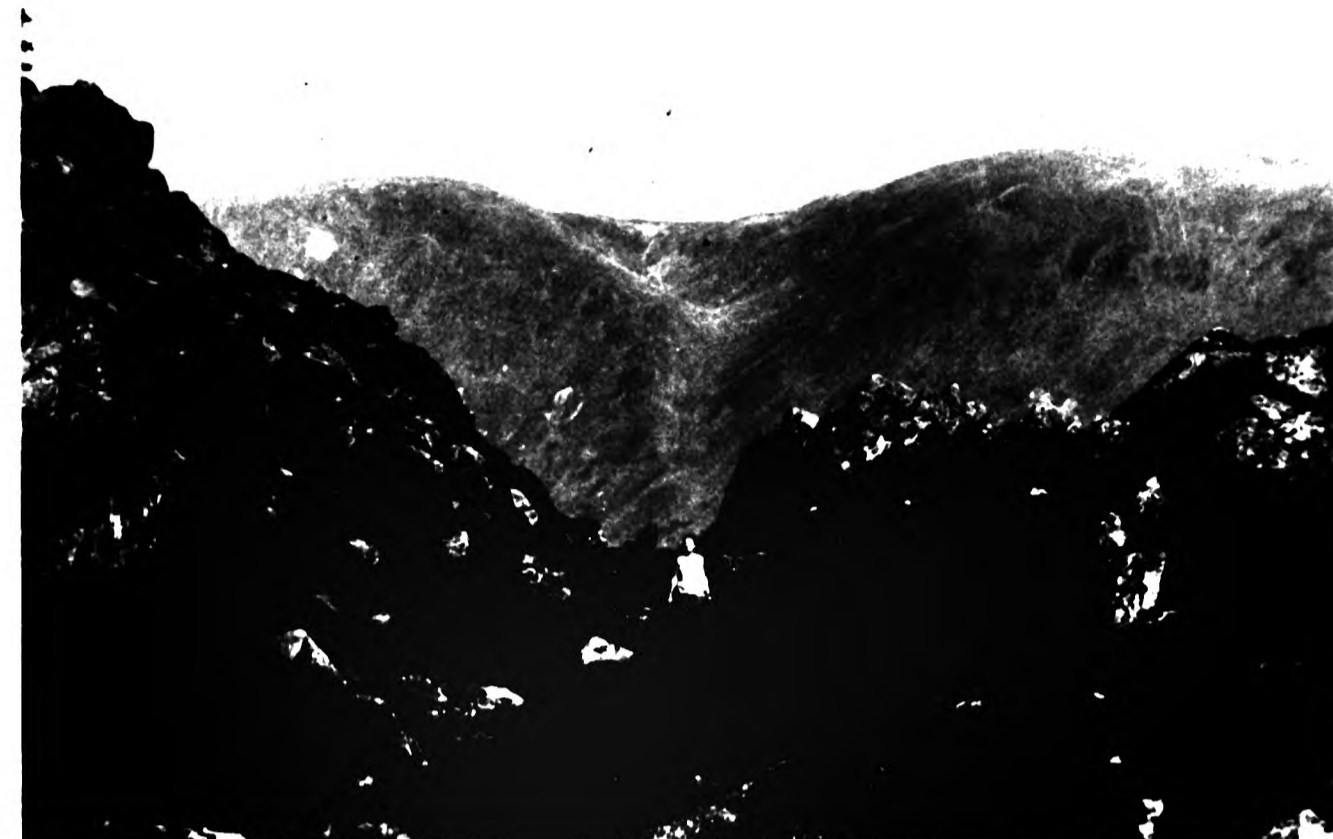


Plate 3.20
Quartz, feldspar porphyry dyke intruded into the Dalradian
metasediments. The dyke is seen to follow the gneissose banding.
(27937517)



Plate 3.19
View of a fault controlled valley below the Rives. Remnants of
a quartz, feldspar porphyry dyke crop out on the lower slopes
of the valley sides.
(Person 1.6m)
(27507737)



Plate 3.20
Quartz, feldspar porphyry dyke intruded into the Dalradian
metasediments. The dyke is seen to follow the gneissose banding.
(27937517)



southeast of the Rives (27707729) (Plate 3.18).

The aplite dykes are also pink with a brown weathering crust. Both dyke types are vertical and their strike has been plotted on a rose diagram to display the range of orientations. The average strike is 020°-030° (Figure 3.10). Their width is variable from 0.1m-6m though more usually <1m. They may be traced for a maximum of 100m (28607688). They compose <1% of the complex.

The orientation of many of the dykes is apparently fault controlled and they are seen to follow the trend of pre-existing faults or fractures (Plate 3.19). Those dykes which are intruded into the Dalradian country rocks close to the contacts of the complex follow the gneissose banding (Plate 3.20).

One example of a cross cutting relationship between two QFP dykes is recorded from White Water (27157602) where a NE-SW dyke cuts a N-S one (Plate 3.21). Also in this area is an example of a strike-slip fault cutting a NE-SW trending dyke. The acid dykes have developed narrow chills (<2cm) and post date the emplacement of all the intrusive rocks of the complexes except for possibly the intermediate dykes (see below).

3.4.1.2 Intermediate dykes

Intermediate dykes occur through both complexes, are fine grained and may be porphyritic, with phenocrysts of plagioclase feldspar and remnant pyroxene. They are less abundant than the acid dykes, only 12 being identified, but are also emplaced vertically, often following pre-existing fault or fracture trends.

Plate 3.21
View of the cross cutting relationship seen between two sets of quartz, feldspar porphyry dykes. The double dyke trends N-S and the single dyke NE-SW. (Hammer shaft 60cm)
(27847604)



Plate 3.22
Typical example of a microdiorite dyke intruding a medium grained hornblende diorite. A chilled margin occurs on both sides of the dyke. (Lens cap 5cm)
(27967603)



Plate 3.21
View of the cross cutting relationship seen between two sets of
quartz, feldspar porphyry dykes. The double dyke trends N-S
and the single dyke NE-SW. (Hammer shaft 60cm)
(27847604)

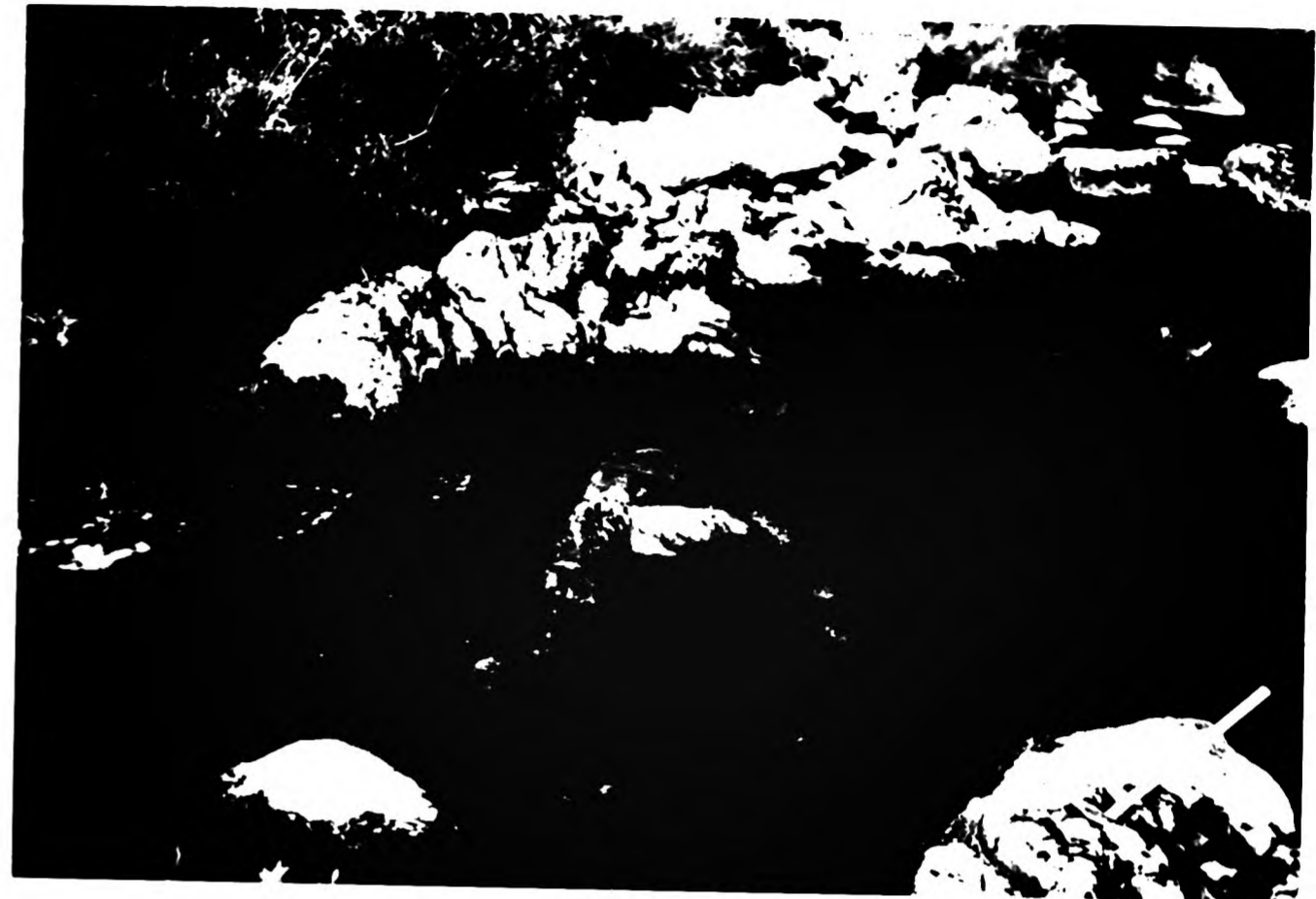


Plate 3.22
Typical example of a microdiorite dyke intruding a medium grained
hornblende diorite. A chilled margin occurs on both sides of
the dyke. (Lens cap 5cm)
(27967603)



Plate 3.21
View of the cross cutting relationship seen between two sets of
quartz, feldspar porphyry dykes. The double dyke trends N-S
and the single dyke NE-SW. (Hammer shaft 60cm)

(27947604)



Plate 3.22
Typical example of a microdiorite dyke intruding a medium grained
hornblende diorite. A chilled margin occurs on both sides of
the dyke. (Lens cap 5cm)

(27967603)



Their orientations have been plotted on a rose diagram and generally strike 020°-030°, in common with the acid dykes (Figure 3.10). Their width ranges from <0.5m-5m and they may be traceable for <30m (Plate 3.22). A fine grained chill <2cm wide exists on most examples where the contact is seen.

Three examples of composite dykes are seen. These dykes have broad acid interiors and narrow microdiorite margins. The core is composed of a medium to coarse grained granodiorite which becomes finer grained towards the contact with the microdiorite. Xenoliths of a fine grained intermediate rock occur within the acid centre. The microdiorite occurs on both sides of the dykes and is ~50cm thick. Within <10cm of the contact with the interior it becomes porphyritic with phenocrysts of plagioclase. The microdiorite is chilled against the host rock which it intrudes. The total width of the dykes is 5-7m.

At the Bridge outcrops, there is clear evidence that locally the intrusion of acid and intermediate magma is broadly synchronous. Other evidence suggests that some intermediate dykes were emplaced relatively early in the history of the complexes. Two gneiss xenoliths from the southeast of the Glen Doll Complex and one from the Juan Jorge diorite, contain unfoliated microdiorite dykes which have clearly been intruded prior to incorporation by the magmas.

3.4.2 Faulting

The Glen Doll Complex is intruded at the site of a pre existing fault trending SW-NE to the southwest of the complex. The

Plate 3.23
View along the fault controlled valley of Moulzie Burn which cuts
down from the high plateau through the northern gabbros.
(28727840)

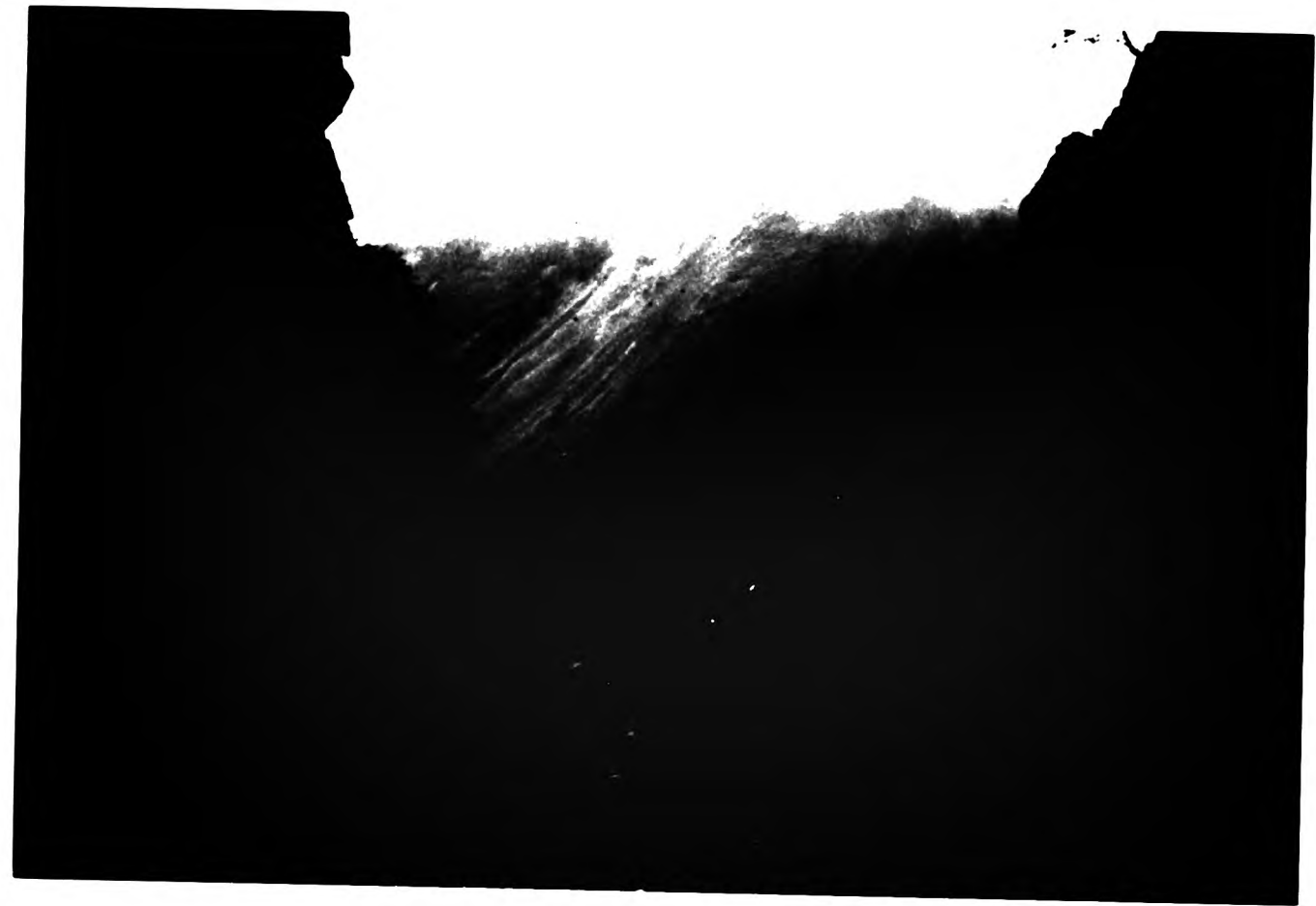


Plate 3.24
Outcrop of coarse grained porphyritic granite at the Bridge. The
granite has a fine grained chill against the banded country
rock gneisses. Angular xenoliths of microdiorite display dark
chilled margins. (Book length 15cm)
(27757919)



Plate 3.23

View along the fault controlled valley of Moulzie Burn which cuts down from the high plateau through the northern gabbros.
(28727840)

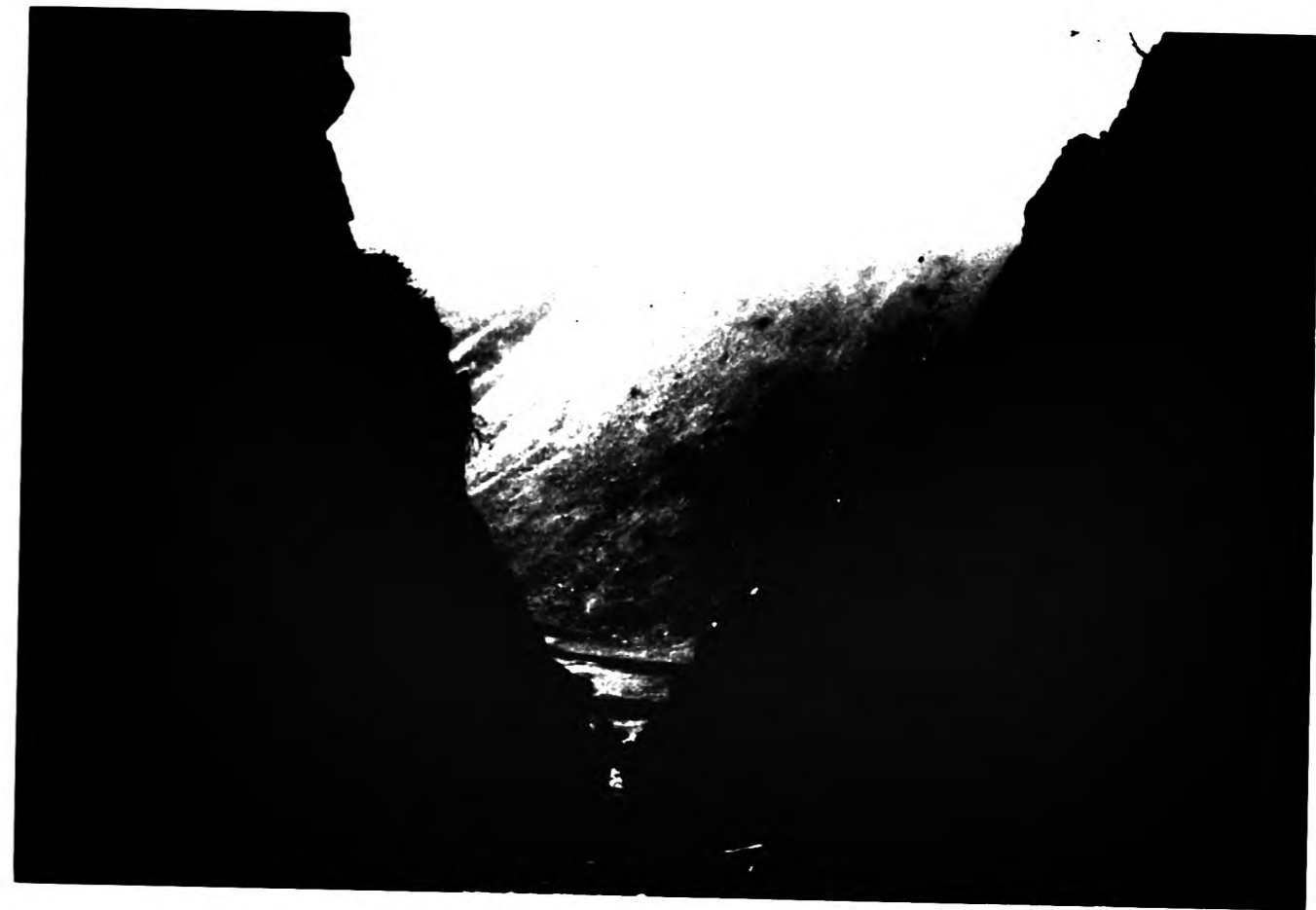


Plate 3.24

Outcrop of coarse grained porphyritic granite at the Bridge. The granite has a fine grained chill against the banded country rock gneisses. Angular xenoliths of microdiorite display dark chilled margins. (Book length 15cm)
(27757919)



Plate 3.23

View along the fault controlled valley of Moulzie Burn which cuts down from the high plateau through the northern gabbros.
(28727840)



Plate 3.24

Outcrop of coarse grained porphyritic granite at the Bridge. The granite has a fine grained chill against the banded country rock gneisses. Angular xenoliths of microdiorite display dark chilled margins. (Book length 15cm)
(27757919)



fault is described by Barrow et al. (1912) who considers that it is traceable to the NE of Glen Doll. Several small faults are seen to cut the hornblende and pyroxene diorites. They generally trend NE-SW though some trend NW-SE or N-S. Some of the small valleys which cut down from the high plateaux may be fault controlled (Plate 3.23). In the zones of faulting, the host diorite may display crushing or fracturing but the direction and magnitude of movement is not seen. The faulting may destroy details of the original contacts between facies, for example between the NE gabbro and the hornblende diorite.

3.5 Bridge outcrops

This group of rocks outcrop between the Glen Doll and Juan Jorge Complexes and are in direct contact with the Dalradian country rocks. Their relationship to the main complexes is not clear. Figure 3.11 shows a plan view of the Bridge outcrops which consist of granite and hornblende diorite.

West of the bridge are two granite dykes intruded into the country rocks. The most westerly is 1.5m wide and is composed of a coarse grained porphyritic granite, carrying phenocrysts of feldspar, displaying no chill. The contact with the country rock gneiss dips at 60° to the west and strikes northeast-southwest.

The second dyke also has a sharp contact with the country rocks and displays a similar orientation to the first. It contains no xenoliths but has a narrow chilled margin (Plate 3.24). The width of the dyke is 10m. To the east of this dyke is an outcrop of coarse grained granite, cropping out parallel to the

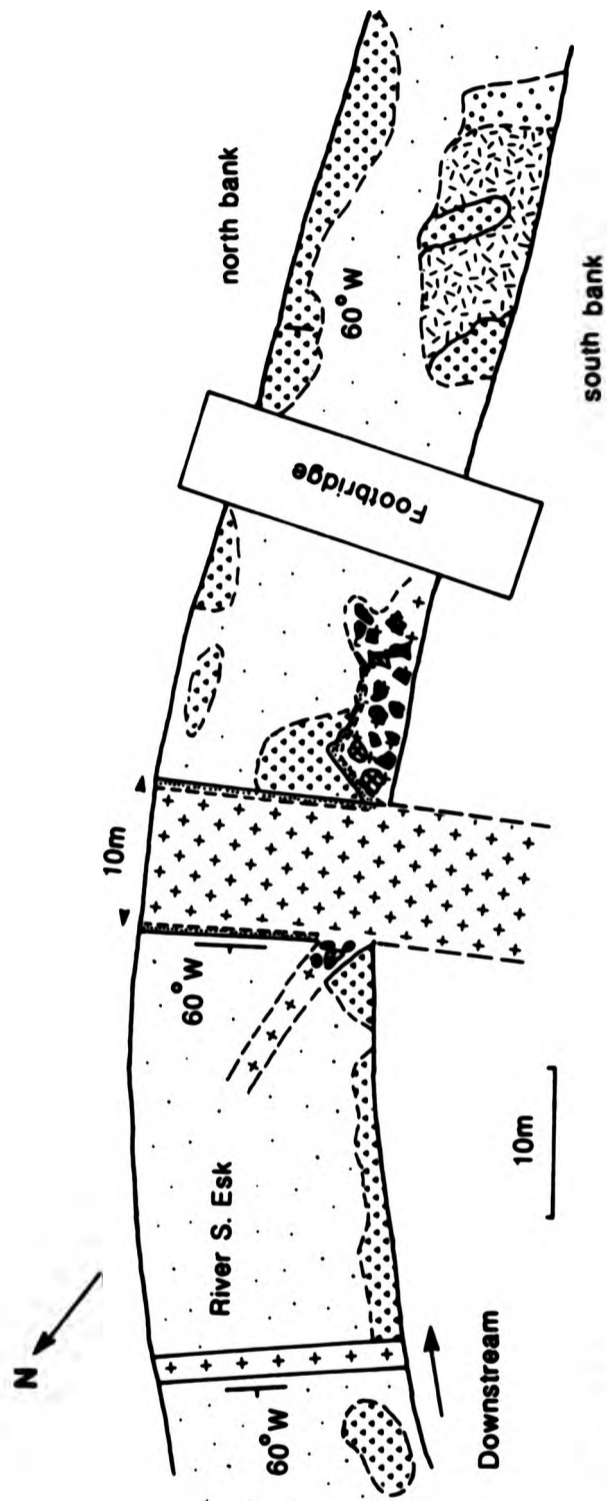


Fig. 3.11

Sketch plan of the rocks exposed at the Bridge Section

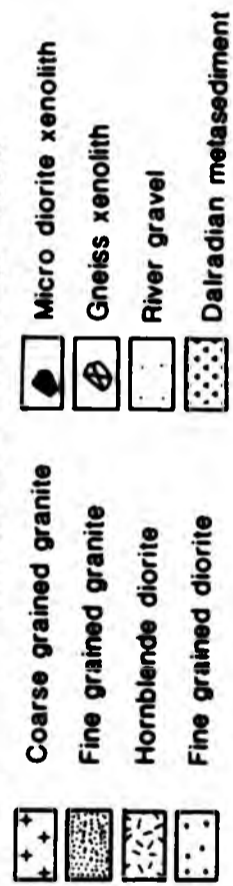


Plate 3.25
Coarse grained granite containing angular blocks of banded and
unbanded gneiss and microdiorite. All xenoliths are randomly
orientatated. (Hammer shaft 30cm)
(27747893)



Plate 3.25
Coarse grained granite containing angular blocks of banded and
unbanded gneiss and microdiorite. All xenoliths are randomly
orientated. (Hammer shaft 30cm)
(27747893)



Plate 3.25
Coarse grained granite containing angular blocks of banded and
unbanded gneiss and microdiorite. All xenoliths are randomly
orientated. (Hammer shaft 30cm)
(27747893)



river bank, containing numerous blocks composed of fine grained microdiorite, foliated micro-diorite, and angular blocks of banded and unbanded country rock gneiss. The blocks are randomly orientated (Plate 3.25). The microdiorite blocks are typically angular and have a very fine grained chill facies (0.5cm wide) around their margins. This evidence, combined with the abundance, shape and distribution of the xenoliths, suggests that the emplacement of the granite was forceful causing brecciation of the gneiss and microdiorite. However the diorite is considered to have been at an elevated temperature at the time of incorporation since the blocks display chilled margins. The acid and intermediate magmas, at least locally, are considered to be contemporaneous.

To the east of the bridge is an outcrop of a medium grained hornblende diorite which grades over a distance of 50cm to the south into a fine grained diorite, presumed to be a chill facies against the country rocks.

CHAPTER 4

Petrography

4.1 Introduction

The petrography of the range of rock types which occur in the Glen Doll and Juan Jorge Complexes is presented below. The chapter will be divided thus:-

4.2 Glen Doll Complex

4.2.1 Diorite

4.2.2 Monzonite

4.2.3 Adamellite

4.2.4 Basic Rocks

4.3 Juan Jorge Complex

4.3.1 Diorite

4.3.2 Granite

4.4 Xenoliths and dykes from the Glen Doll and Juan Jorge Complexes

4.5 Bridge outcrops

4.2 Glen Doll Complex

The range of rock types present in the Glen Doll Complex is extensive and includes basic, intermediate and acid rocks. A summary of the modal mineralogy is given in Table 4.1. The description of each rock type is given in order of abundance. The

Table 4.1 Ranges of modal mineralogy (%) for the lithologies within the Glen Doll Complex

	Olivine Gabbro	Gabbro
Plagioclase	18-20	50-60
Amphibole (primary)	5-25	15-20
Amphibole (secondary)	-	1-5
Cpx	18-22	10-20
Opx	18-20	5-14
Olivine	10-35	-
Biotite	-	1-5
Accessories	<1	<1

	Pyroxene diorite	Hornblende diorite
Plagioclase	50-55	50-55
Amphibole (primary)	2-8	5-10
Amphibole (secondary)	8-17	5-25
Cpx	4-5	-
Opx	2-3	-
Biotite	5-9	5-10
Quartz	1-4	1-4
Accessories	1-3	1-4

	Monzonite	Adamellite
Plagioclase	28-31	28-31
K-feldspar	20-25	18-22
Biotite	8-26	5-8
Amphibole (primary)	5-7	-
Quartz	11-20	35-40
Accessories	1-3	<1

Plate 4.1
A typical hornblende diorite showing tabular plagioclase,
biotite and green secondary, subsolidus amphibole.
(PPL) Field of view 2.2x1.4cm



Plate 4.2
Same view as plate 4.1 but in XPL. Plagioclase feldspars
display multiple twins. Secondary amphibole has a fibrous
habit (left). Field of view 2.2x1.4cm



Plate 4.1
A typical hornblende diorite showing tabular plagioclase,
biotite and green secondary, subsolidus amphibole.
(PPL) Field of view 2.2x1.4cm

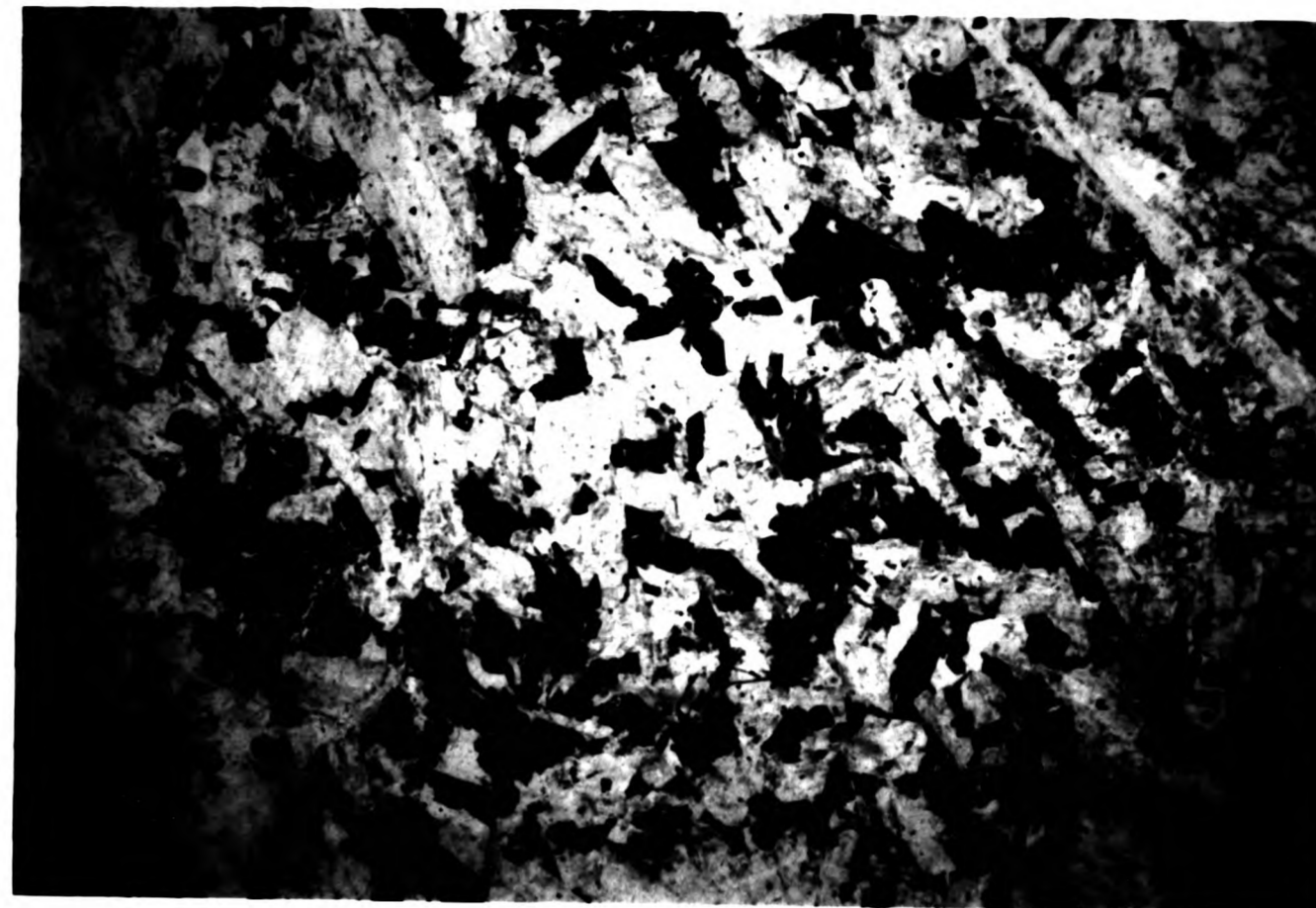


Plate 4.2
Same view as plate 4.1 but in XPL. Plagioclase feldspars
display multiple twins. Secondary amphibole has a fibrous
habit (left). Field of view 2.2x1.4cm

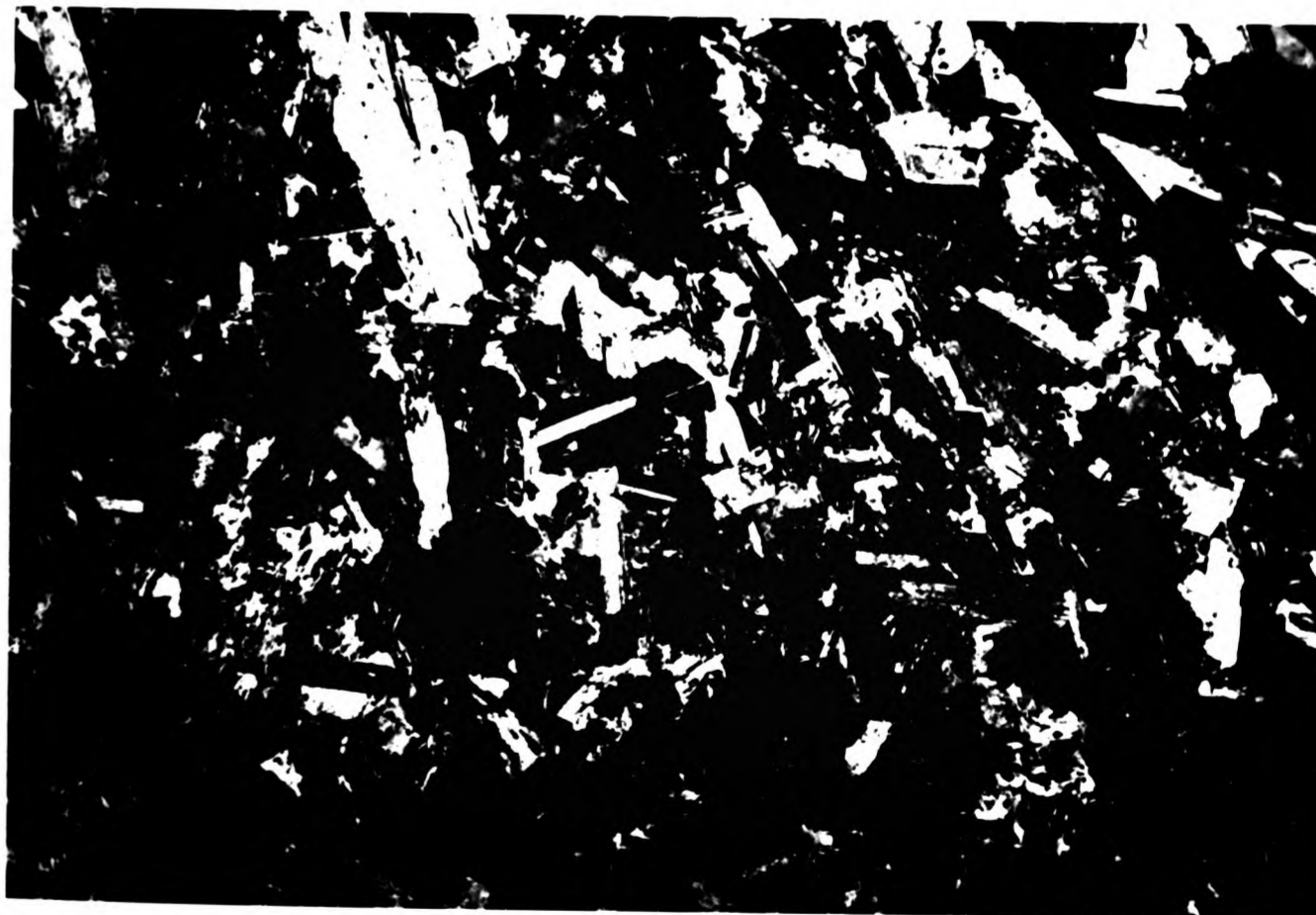


Plate 4.1
A typical hornblende diorite showing tabular plagioclase,
biotite and green secondary, subsolidus amphibole.
(PPL) Field of view 2.2x1.4cm

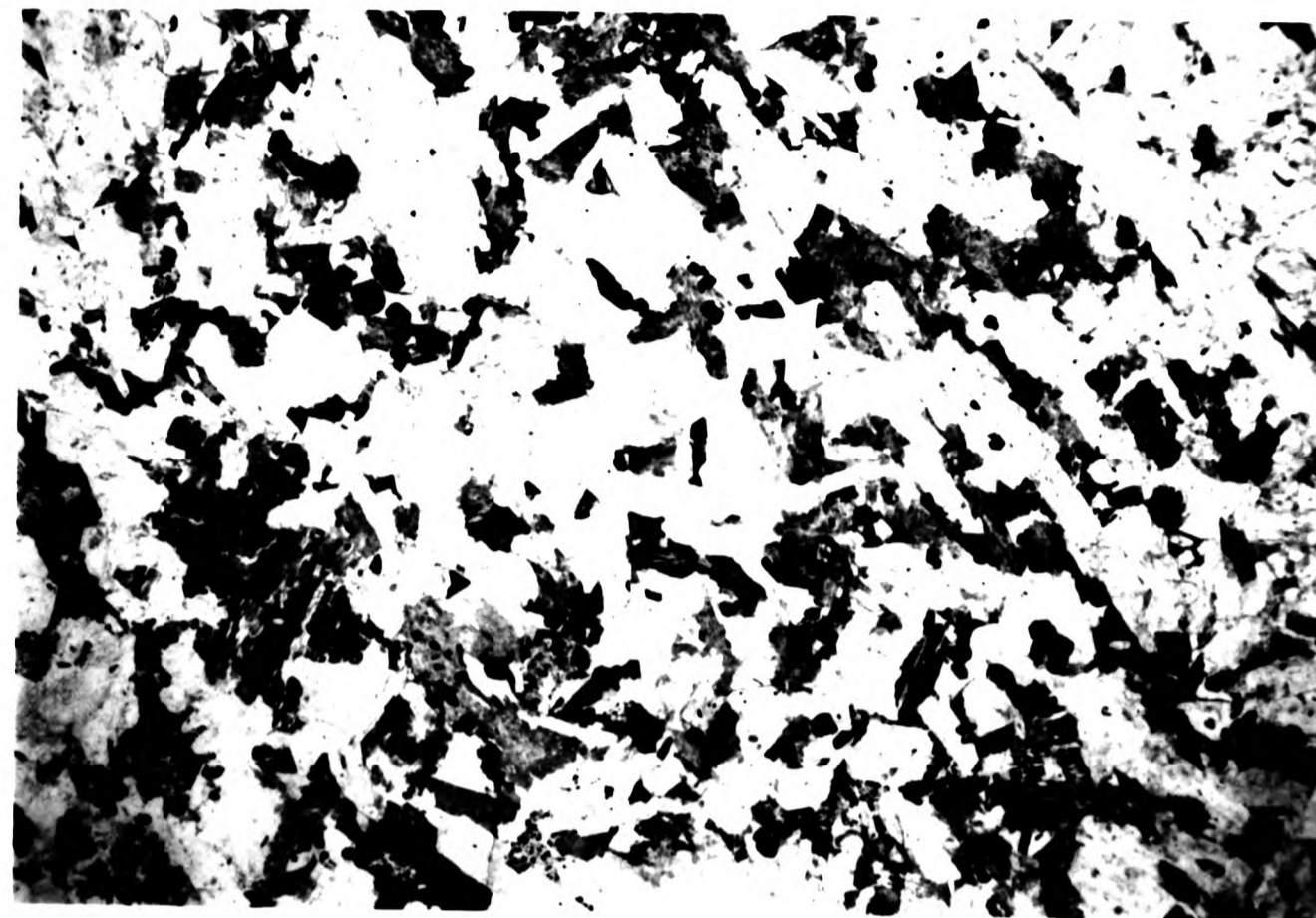
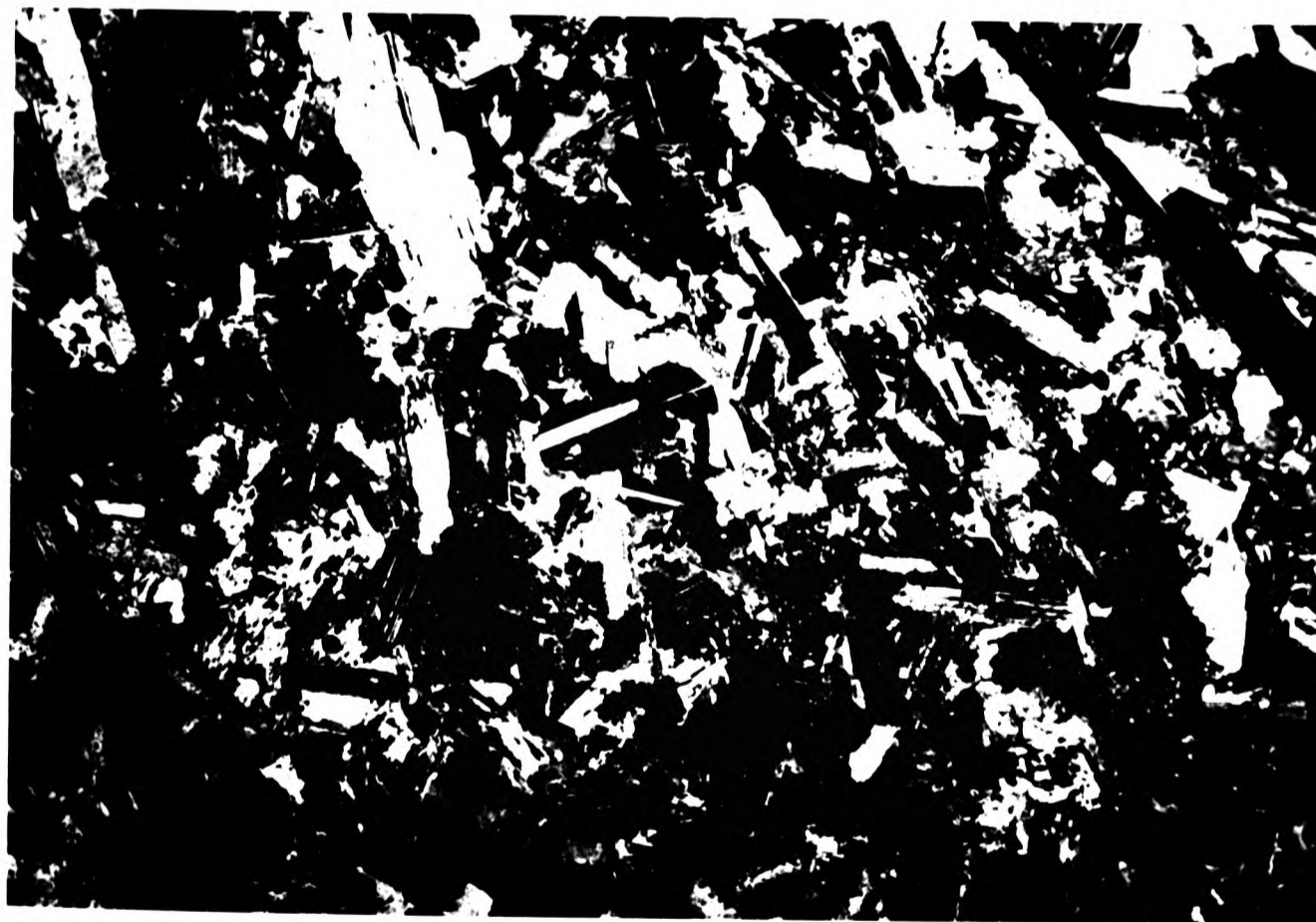


Plate 4.2
Same view as plate 4.1 but in XPL. Plagioclase feldspars
display multiple twins. Secondary amphibole has a fibrous
habit (left). Field of view 2.2x1.4cm



diorites and monzonites contain spinel aggregates derived from metasedimentary xenoliths, a mineral feature which is described in section 4.4. Both hornblende and pyroxene diorites are recognised on the basis that their pyroxene if present is always jacketed or partly replaced by hornblende while in the latter it forms complete euhedral or subhedral crystals.

4.2.1 Diorites

4.2.1.1 Hornblende diorites

This group is typically medium grained, though coarse grained varieties also occur. The mineralogy consists of plagioclase + amphibole + biotite + magnetite ± sphene, apatite, orthoclase and quartz (Plate 4.1 and 4.2; Table 4.1). Some sections contain remnant pyroxene crystals and this will be discussed below. Some samples are very fresh while others are highly altered.

Plagioclase

The tabular crystals of plagioclase are variable in length from <1mm to 4mm. They are often fresh but may be highly sericitised. Normal zoning is common, and more rarely sector zoning occurs (Mackenzie et al., 1982). Many plagioclase crystals have broad more calcic cores of labradorite (An₅₃) with narrow rims of andesine (An₃₅). The dominant composition of unzoned crystals is of andesine (An₃₅). The unzoned crystals are usually the smaller and they may represent later crystals whose size has been physically restricted by the growth of amphibole. The crystals may abut against each other and form a framework. The interstitial areas may be small and filled with late-stage quartz, while larger areas contain mafic phases and accessory minerals. Plagioclase is the

most abundant mineral phase and composes 40-60% of the mode.

The plagioclase crystals define the igneous lamination described in chapter 3, although under high magnification in thin section the parallel alignment of the tabular crystals is not clear. A low magnification plate, however, displays well the alignment of the plagioclase crystals (Plates 4.1 and 4.2).

Amphibole

Amphibole is the dominant mafic phase in about 90% of the samples, the remaining 10% having biotite in greater abundance. Total amphibole in the hornblende diorites comprises 6-25% of the mode, with a decrease in abundance accompanied by an increase in modal biotite. The amphibole occurs in three forms, with more than one form commonly occurring in any one section.

- (a) Primary green/brown euhedral crystals
- (b) Primary interstitial green/brown anhedral crystals
- (c) Green or colourless fibrous crystals of secondary origin

(a) Primary euhedral amphibole

Crystals are typically large (<4mm), equant and display a broad brown euhedral cores with a narrow green rim. The change in colour is abrupt from core to rim. Crystals are typically poikilitic and enclose small (<1mm) unzoned plagioclase and anhedral oxides, suggesting that the crystallisation of amphibole postdates the initial crystallisation of these phases (Plate 4.3). This

Plate 4.3
View of a hornblende diorite showing a basal section of
hornblende partially enclosing a tabular plagioclase crystal
and a rounded orthopyroxene. The opx is preserved by the
later surrounding amphibole. (PPL) Field of view 3mm



Plate 4.4
As above, a basal section of a hornblende crystal enclosing a
subhedral crystal of orthopyroxene (centre).
XPL Field of view 3mm



Plate 4.3
View of a hornblende diorite showing a basal section of
hornblende partially enclosing a tabular plagioclase crystal
and a rounded orthopyroxene. The opx is preserved by the
later surrounding amphibole. (PPL) Field of view 3mm

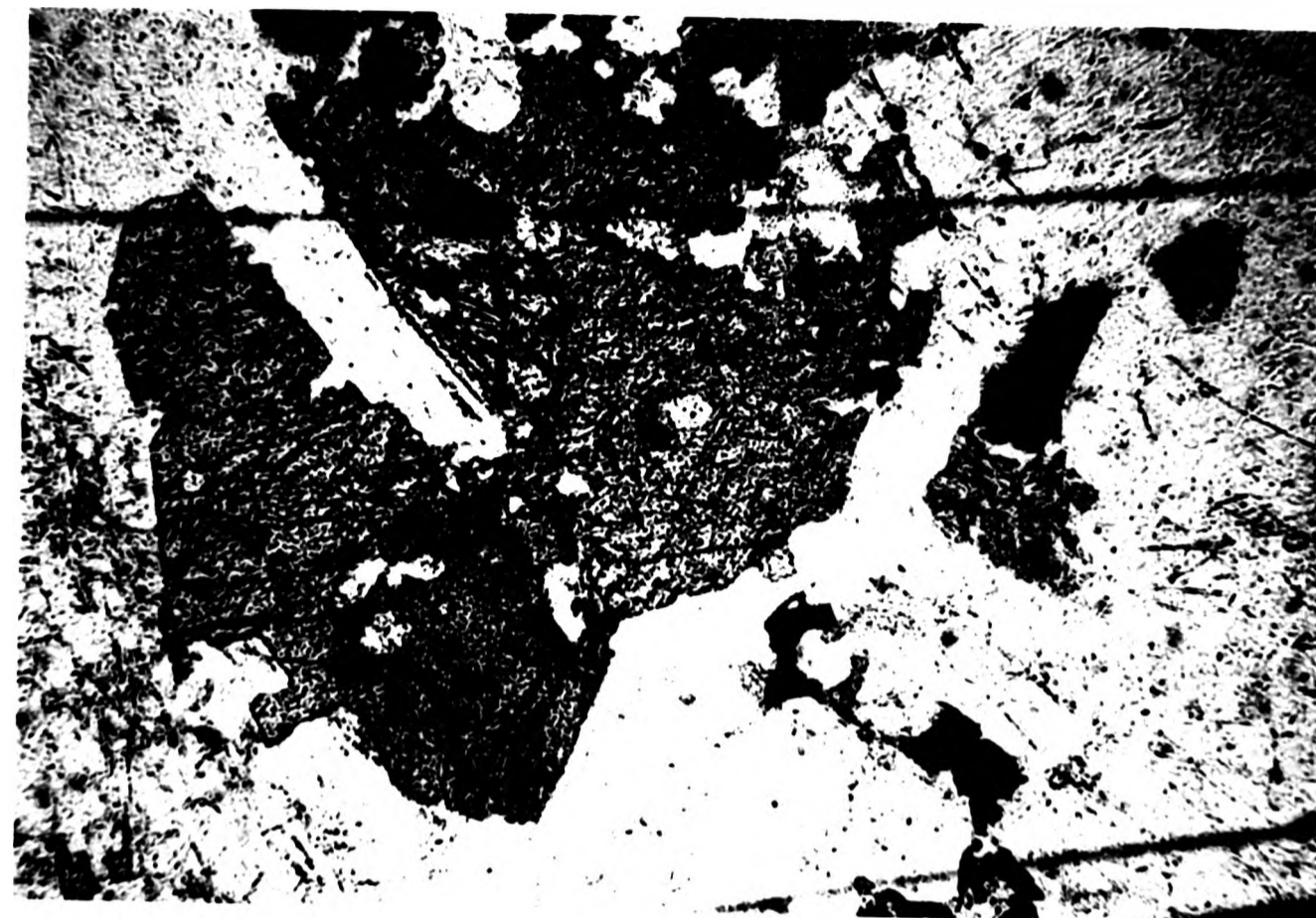


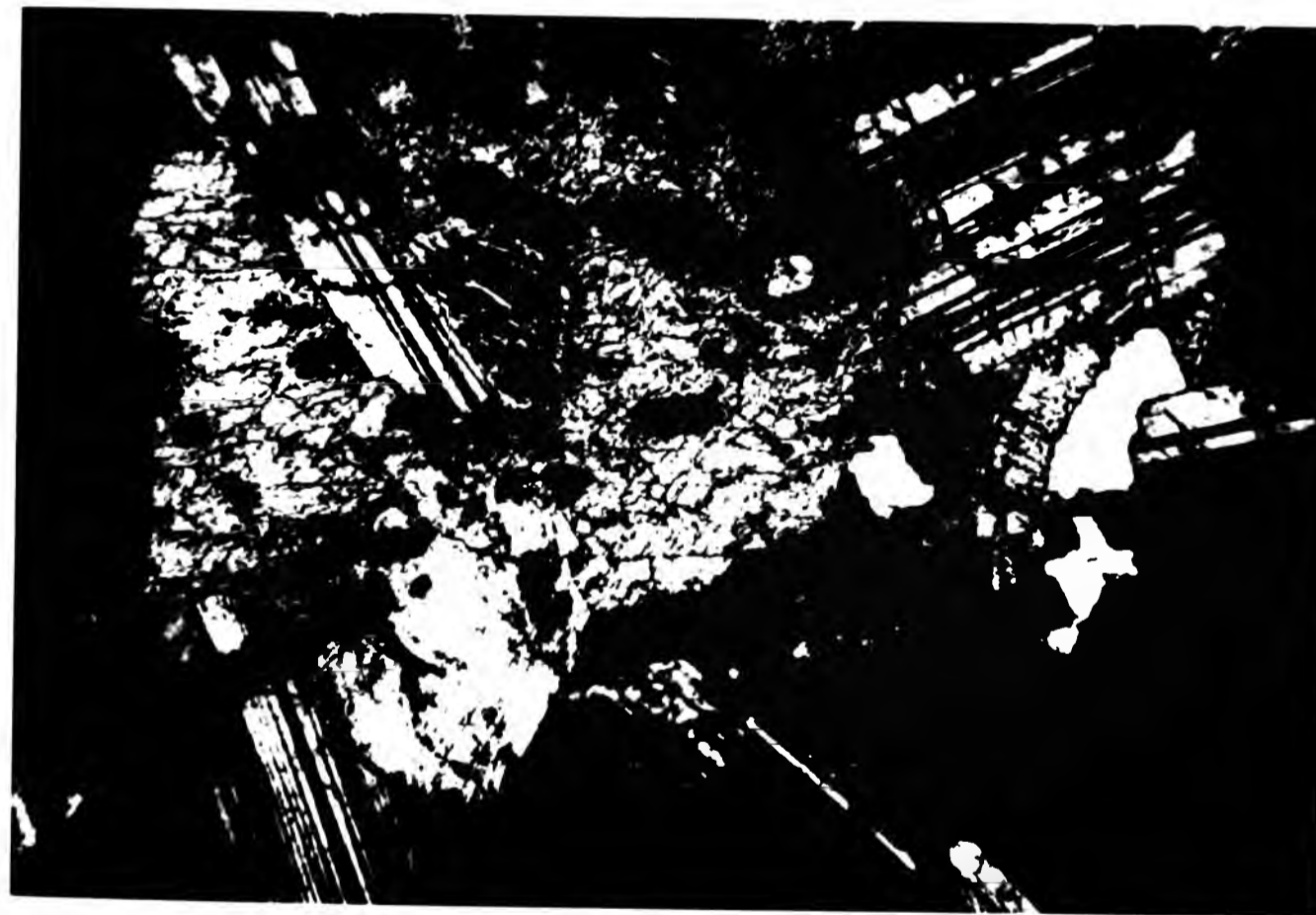
Plate 4.4
As above, a basal section of a hornblende crystal enclosing a
subhedral crystal of orthopyroxene (centre).
XPL Field of view 3mm



Plate 4.3
View of a hornblende diorite showing a basal section of
hornblende partially enclosing a tabular plagioclase crystal
and a rounded orthopyroxene. The opx is preserved by the
later surrounding amphibole. (PPL) Field of view 3mm



Plate 4.4
As above, a basal section of a hornblende crystal enclosing a
subhedral crystal of orthopyroxene (centre).
XPL Field of view 3mm



hornblendic amphibole is less common than the other types and composes <20% of the amphibole present.

(b) Primary interstitial amphibole

This second textural type of amphibole is dominantly brown, or zoned with rounded brown cores and green rims. The amphibole occurs as anhedral interstitial crystals between tabular plagioclase and are usually small (<1mm). Occasionally, poikilitic crystals occur enclosing tiny magnetite crystals. These interstitial crystals compose <10% of the amphibole present.

(c) Secondary amphibole

This textural form of amphibole is the dominant type in the dioritic rocks. It occurs as prisms or anhedral crystals, generally <2mm long, with colourless or green cores and occasional green rims. Occasionally, remnant ortho- or clino- pyroxene is present in the core of the crystals, indicating that the crystals were originally pyroxene and are now partially replaced by secondary actinolitic amphibole. The texture of the amphibole is fibrous, with abundant small exsolved crystals of magnetite in the core region (Plate 4.5). This feature is typical of crystals formed by recrystallisation of primary pyroxene and has been discussed in terms of the crystallisation of intermediate magmas from Ben Nevis (Haslam, 1968). Vegnar (1975) described similar textures from a suite of recrystallised gabbros from Czechoslovakia, where they are clearly secondary features resulting from the recrystallisation of primary pyroxene.

Pyroxene

Plate 4.5

Single crystal of secondary actinolitic amphibole replacing clinopyroxene. The fibrous, colourless core contains exolved magnetite crystals. Around the core is a green rim composed of primary amphibole. Small apatite crystals are poikilitically enclosed within this rim. (PPL) Field of view 3mm

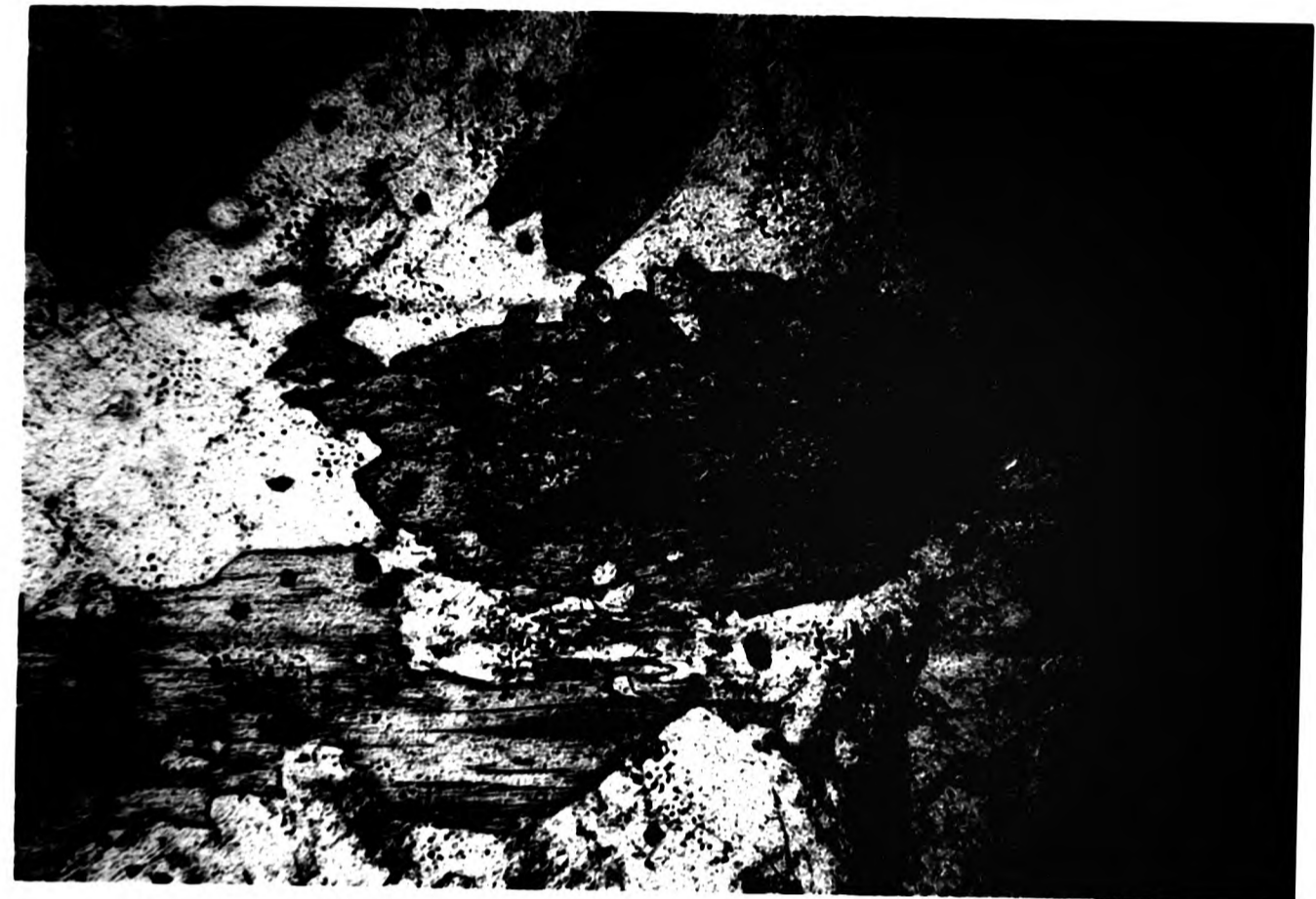


Plate 4.6

View of hornblende diorite showing the occurrence of prehnite (centre right). Abundant apatite is seen poikilitically enclosed by a basal section of amphibole (top centre). (PPL) Field of view 3mm



Plate 4.5

Single crystal of secondary actinolitic amphibole replacing clinopyroxene. The fibrous, colourless core contains exolved magnetite crystals. Around the core is a green rim composed of primary amphibole. Small apatite crystals are poikilitically enclosed within this rim. (PPL) Field of view 3mm



Plate 4.6

View of hornblende diorite showing the occurrence of prehnite (centre right). Abundant apatite is seen poikilitically enclosed by a basal section of amphibole (top centre). (PPL) Field of view 3mm



Plate 4.5

Single crystal of secondary actinolitic amphibole replacing clinopyroxene. The fibrous, colourless core contains exolved magnetite crystals. Around the core is a green rim composed of primary amphibole. Small apatite crystals are poikilitically enclosed within this rim. (PPL) Field of view 3mm

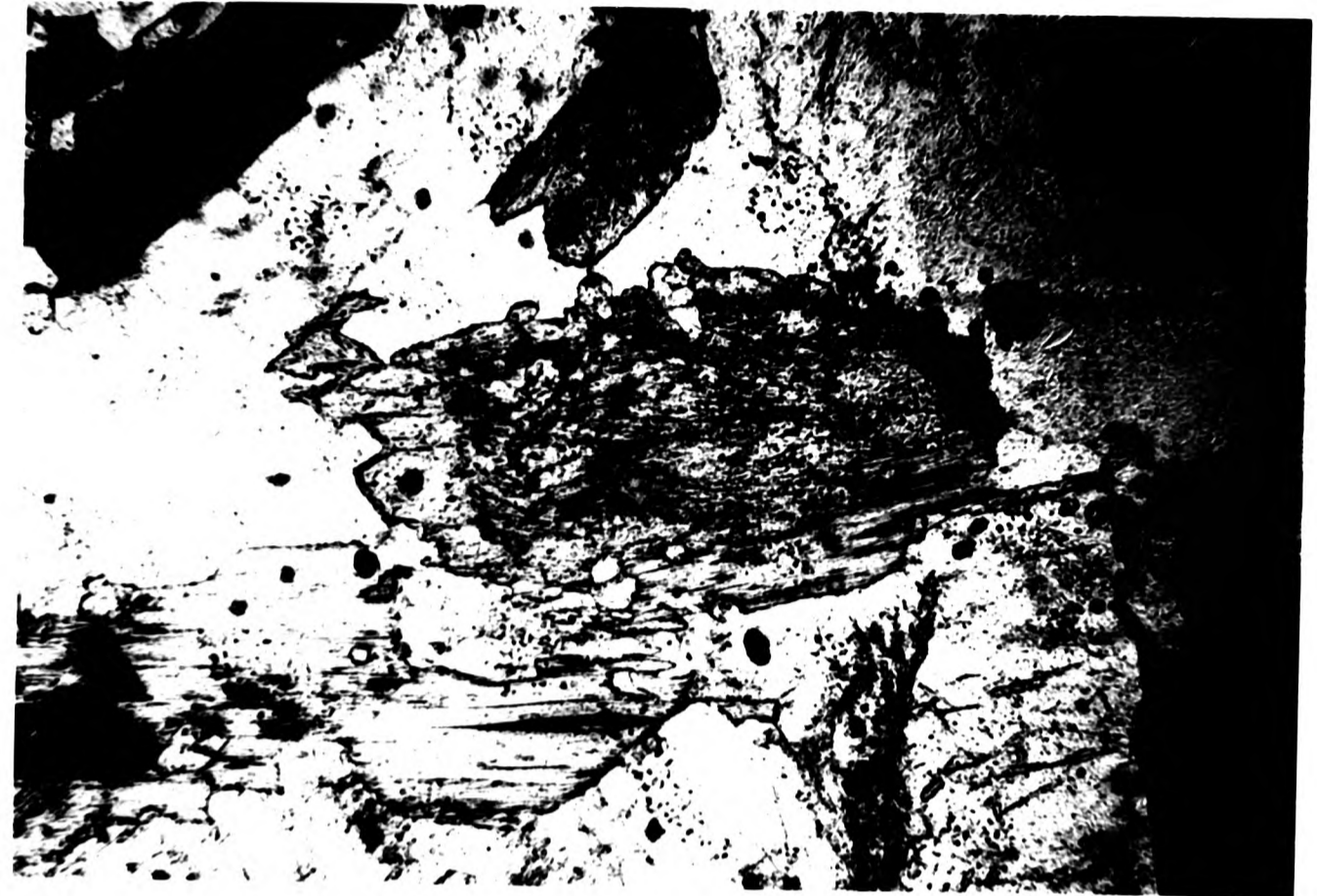


Plate 4.6

View of hornblende diorite showing the occurrence of prehnite (centre right). Abundant apatite is seen poikilitically enclosed by a basal section of amphibole (top centre). (PPL) Field of view 3mm



The pyroxene always occurs as remnant anhedral or subhedral crystals forming the core region to primary or secondary amphibole. Both opx - hypersthene, and cpx - augite, occur, the latter being more common. Plate 4.4 shows a typical occurrence of opx as an anhedral crystal enclosed by primary amphibole.

Biotite

Biotite is seen to a greater or lesser extent in all sections. Some sections contain large (3mm long) euhedral plates while others have only small (0.1mm) interstitial crystals (between hornblende and plagioclase) which are often altered to chlorite. The former commonly poikilitically enclose prisms of apatite and rounded magnetite spinel chadocrysts. Biotite is commonly seen moulding around crystals of plagioclase. Biotite composes from 5-10% of the mode.

Accessory minerals

Magnetite crystals are typically anhedral, varying from <0.5mm to 2mm in diameter. This phase occurs as interstitial crystals to plagioclase, hornblende and biotite or as crystals poikilitically enclosed by biotite and primary hornblendic amphibole. They may themselves poikilitically enclose prisms of apatite. Much of the magnetite is seen intergrown with, or jacketed by, biotite (Plate 4.6 and 4.7). A similar feature is described by Noyes et al. (1983) in granodiorite from Central Sierra Nevada, California where secondary alteration of biotite produces chlorite, sphene and magnetite. A similar alteration relationship is displayed by magnetite with anhedral sphene in the Glen Doll Complex.

Plate 4.7
View of a hornblende diorite showing the close association of
anhedral and rounded magnetite with biotite (bottom centre).
(XPL) Field of view 3mm



Plate 4.8
Typical view of a hornblende diorite showing anhedral sphene
in close association with amphibole and biotite. Magnetite
crystals are seen poikilitically enclosing apatite rods.
(PPL) Field of view 3mm

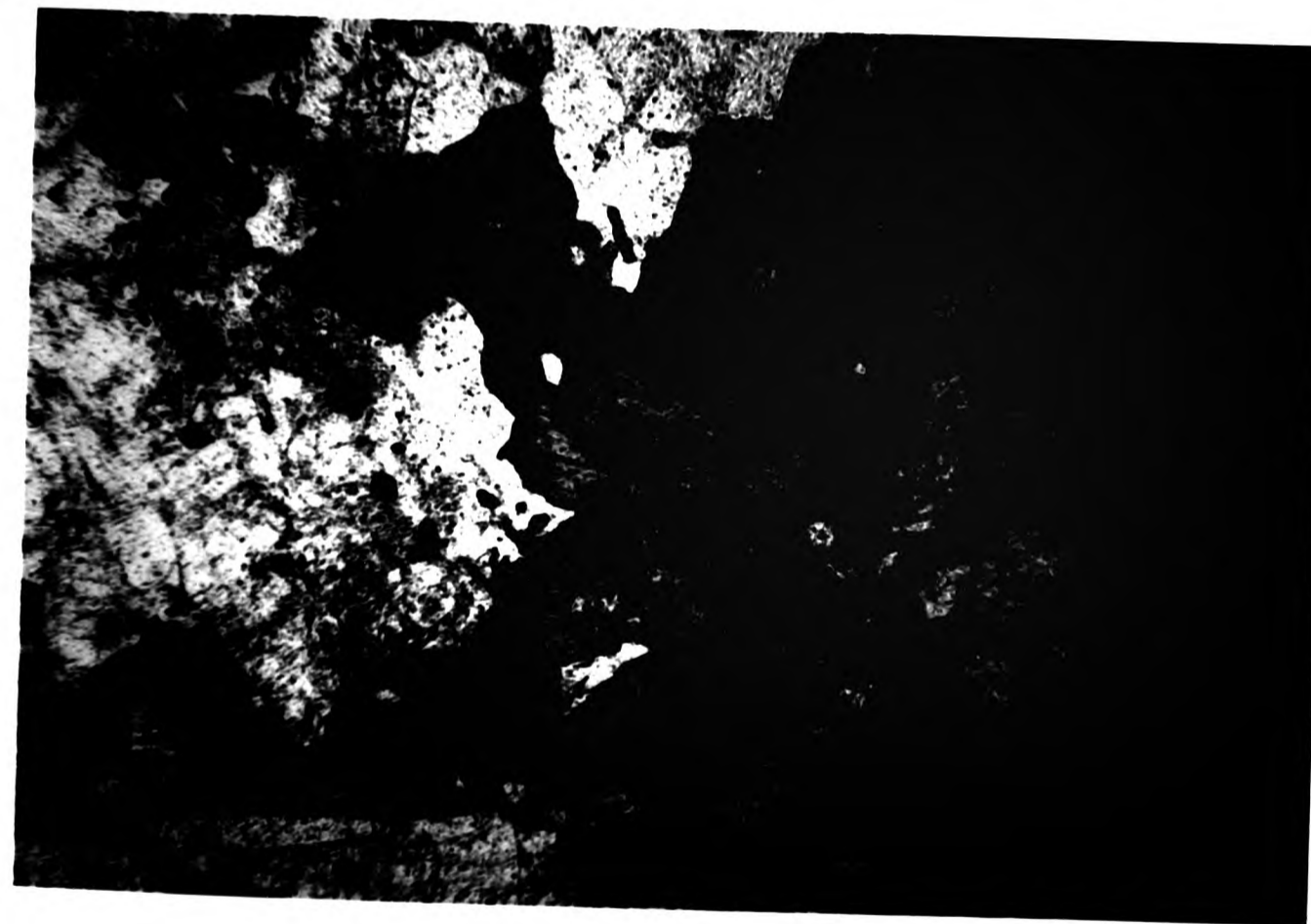


Plate 4.7
View of a hornblende diorite showing the close association of
anhedral and rounded magnetite with biotite (bottom centre).
(XPL) Field of view 3mm



Plate 4.8
Typical view of a hornblende diorite showing anhedral sphene
in close association with amphibole and biotite. Magnetite
crystals are seen poikilitically enclosing apatite rods.
(PPL) Field of view 3mm

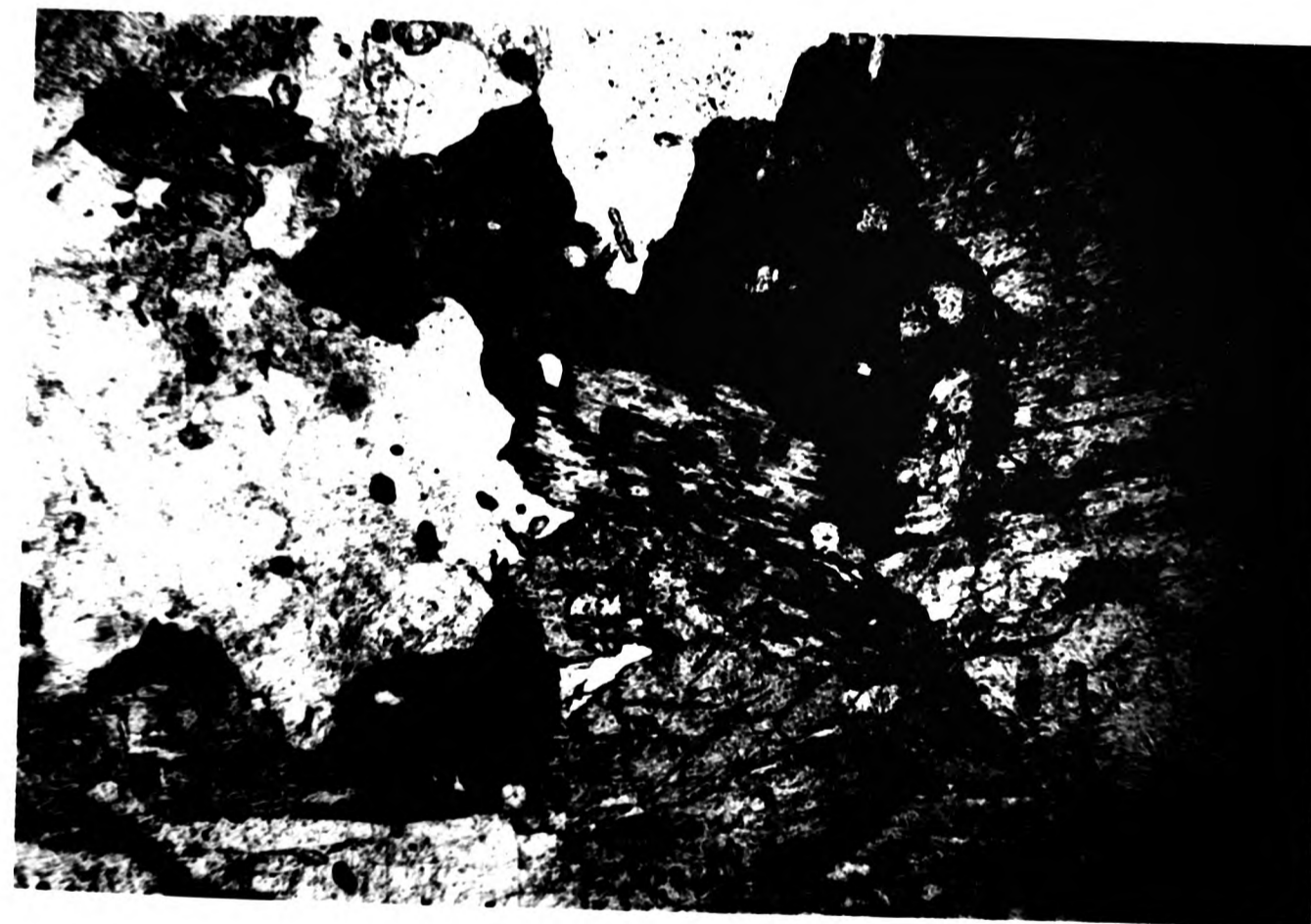
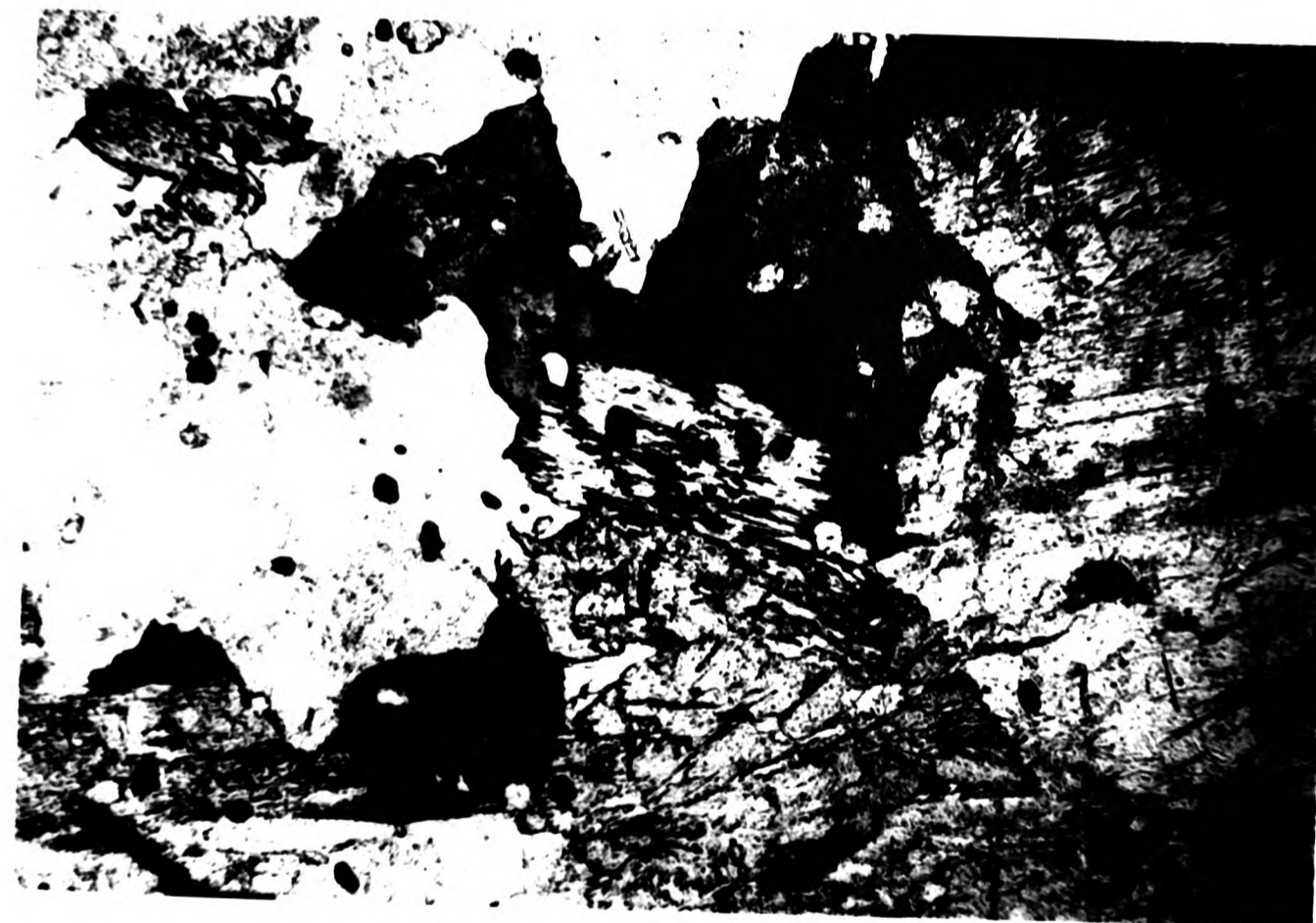


Plate 4.7
View of a hornblende diorite showing the close association of
anhedral and rounded magnetite with biotite (bottom centre).
(XPL) Field of view 3mm



Plate 4.8
Typical view of a hornblende diorite showing anhedral sphene
in close association with amphibole and biotite. Magnetite
crystals are seen poikilitically enclosing apatite rods.
(PPL) Field of view 3mm



A second occurrence of magnetite is as very small ($<0.1\text{mm}$) exsolved crystals in the fibrous cores of secondary actinolitic amphibole (Plate 4.5). These are thought to have formed as a breakdown product of primary pyroxene on conversion to amphibole.

The abundance of magnetite is very variable throughout the diorites, from $<1-5\%$ (excluding magnetite in amphibole) and this variation is clearly reflected in the bulk rock chemistry in terms of both iron and manganese content (see Chapter 6).

Sphene occurs as anhedral interstitial crystals or intergrown with magnetite, probably resulting from secondary breakdown of biotite. The association between magnetite and sphene is clear, with a positive modal correlation (Plate 4.8). The sphene crystals range in width from $<0.1-1\text{mm}$ across and form up to $<1\%$ of the mode.

Apatite is present in all of the diorites but is variable in both abundance and size. The crystals are euhedral, occurring interstitially or as chadocrysts poikilitically enclosed by magnetite, and hornblende but not by pyroxene or plagioclase (Plates 4.3, 4.4, 4.5, 4.6). They are usually small ($<0.1\text{mm}$) but occasionally reach 1mm in length.

Quartz occurs as interstitial fillings with a varying modal percentage from $<1-9\%$. Crystals are clouded, possibly with fluid inclusions (MacKenzie et al., 1982). The quartz crystals occasionally display undulose extinction which is evidence of post crystallisation strain. Small amounts of interstitial orthoclase occurs in some sections. Haematite and skeletal ilmenite occur rarely in some sections. Prehnite occurs, displaying a charac-

teristic bow-tie structure and is commonly seen intergrown with biotite (Plates 4.6 and 4.7).

4.2.1.2 Pyroxene diorites

The overall mineralogy of this rock type is very similar to the hornblende diorites. The range and modal abundance of minerals is similar except for the occurrence of primary pyroxene. Both opx and cpx are present in the pyroxene diorites. The opx is a pink to green pleochroic bronzite, occurring as large (<2mm long) tabular crystals, which commonly have corroded margins and are jacketed by amphibole (Plates 4.9 and 4.10). They typically form discrete crystals but can also form the core area of large crystals of either brown/green or green amphibole. The margins of the opx crystals are uneven and the crystals are traversed by fractures filled with yellow iddingsite. Those enclosed by brown amphibole have a margin of white fibrous amphibole (cummingtonite) around them which must have grown prior to the growth of the brown amphibole (Haslam, 1968). Exsolution lamellae are not present in the opx crystals. Occasionally a sub-ophitic texture is observed involving bronzite and unzoned tabular plagioclase (typically 0.5mm long), indicating the earlier growth of plagioclase relative to opx (Plate 4.8 and 4.9).

The cpx-augite, more commonly occurs as small (<0.5mm) discrete subhedral crystals or as larger (<1mm) anhedral crystals undergoing alteration to a white or green fibrous amphibole. All degrees of alteration are present from moderately well preserved euhedral cpx with areas of amphibole along the crystal margins, through to crystals with only remnants of cpx in large crystals

Plate 4.9

The centre of the slide shows a single crystal of bronzite with a corroded margin jacketed by primary amphibole. The orthopyroxene displays a subophitic texture with plagioclase. (PPL) Field of view 3mm



Plate 4.10

As 4.9 but in crossed polars, clearly showing a margin of primary amphibole around an orthopyroxene crystal. The enclosed plagioclase shows a displacement, possibly along a shear plane. (XPL) Field of view 3mm



Plate 4.9

The centre of the slide shows a single crystal of bronzite with a corroded margin jacketed by primary amphibole. The orthopyroxene displays a subophitic texture with plagioclase. (PPL) Field of view 3mm



Plate 4.10

As 4.9 but in crossed polars, clearly showing a margin of primary amphibole around an orthopyroxene crystal. The enclosed plagioclase shows a displacement, possibly along a shear plane. (XPL) Field of view 3mm



Plate 4.9

The centre of the slide shows a single crystal of bronzite with a corroded margin jacketed by primary amphibole. The orthopyroxene displays a subophitic texture with plagioclase. (PPL) Field of view 3mm



Plate 4.10

As 4.9 but in crossed polars, clearly showing a margin of primary amphibole around an orthopyroxene crystal. The enclosed plagioclase shows a displacement, possibly along a shear plane. (XPL) Field of view 3mm



(<2mm) of white/green secondary actinolitic amphibole. Ophitic texture are absent.

Summary of the crystallisation history of the hornblende and pyroxene diorites

The observed textural data suggests the early crystallisation in both types of diorite of unzoned plagioclase and pyroxene. These minerals are followed in the hornblende diorites by the crystallisation of zoned plagioclase and primary brown amphibole. In the pyroxene diorites however, ophitic textures are seen indicating the continued crystallisation of opx. Primary hornblende then crystallised accompanied by zoned plagioclase rims and cpx. Apatite is present in both rock types by the onset of crystallisation of primary hornblende and biotite. The interstitial minerals, including green amphibole, sphene, quartz and K-feldspar are the last minerals to crystallise in both rock types.

Discussion of the petrographic features of the dioritic rocks

Field data (Chapter 3) suggests that a close relationship exists between the hornblende and pyroxene diorites. Both rock types contain early crystallising plagioclase, opx and cpx which are interpreted as cumulus crystals. The pyroxene diorites contain intercumulus opx (ophitic) while the hornblende diorites contain abundant poikilitic hornblende. The intercumulus crystallisation of the two rocks initially follows two paths, one dominated by crystallisation under wet conditions, while the other crystallises under dry conditions. Both rock types than show the late alteration of pyroxene to secondary actinolitic amphibole.

Alteration of primary pyroxene to amphibole occurs commonly in intermediate rock types and has been frequently described, for example by Haslam (1968). At Ben Nevis, cpx alters directly to green hornblende, where replacement takes place both externally (by reaction with the magma) and internally (by solid state diffusion). Opx is normally first replaced by cummingtonite, which is then gradually converted to green hornblende. This alteration process is considered by Haslam (1968) to be a late magmatic process.

The variation in modal mineralogy, in both the hornblende and pyroxene diorites, is reflected in the heterogenous nature of the diorites. They contain a variable proportion of amphibole in a range of textural forms. The abundance of magnetite is particularly variable and can not be correlated for example, with topographic height in the complex. This variable abundance may however be correlated with the proximity of the sample to partially assimilated metasedimentary xenoliths.

A variation in temperature, at the time of crystallisation, could account for some of the textural features displayed by the amphiboles. However a variation in the modal proportions of magnetite, could be a result of heterogeneity in the magma. Chinner (1960), demonstrated how the metamorphic terraine in Glen Clova contains zones of variable oxygen fugacity. Partial assimilation of locally derived metasedimentary material may therefore allow the introduction of variable amounts of water and oxygen into the magmatic environment. This would allow the development of local variations in the magma.

4.2.2 Monzonite

This group of rocks are of medium grain size and display a uniform mineralogy. They do not contain pyroxene and amphibole is sparse, biotite being the dominant mafic phase (Plate 4.11).

Biotite

Biotite occurs as euhedral to subhedral flakes, often forming aggregates up to 1mm in diameter. Cleavages are frequently deformed giving the crystals a characteristic wavy texture. The subhedral crystals are usually interstitial to the tabular plagioclase, although some are seen moulding around them. Some large euhedral flakes of biotite occur which poikilitically enclose tabular apatite and rounded magnetite (<0.1mm). Biotite composes 20-26% of the mode.

Amphibole

This phase typically composes 1.5-3% of the rock and occurs as small (<1mm) tabular crystals of green secondary actinolitic amphibole, sometimes containing white fibrous cores. These crystals may be seen intermittently intergrown with biotite. The textures displayed by the amphibole in these rocks are similar to that in the diorites, indicating the close relationship between the two. The lack of any primary amphibole may indicate that the original rock was pyroxene-bearing but now contains only secondary actinolite.

Feldspar

Tabular crystals of plagioclase ranging in length from <1-4mm display normal zoning, often with broad cores (An₄₅) and narrow rims (An₂₅). Unzoned varieties are common (An₂₅) and have a simi-

Plate 4.11
Typical view of a quartz monzonite containing abundant biotite
poikilistically enclosing magnetite and apatite. (PPL) Field
of view 3mm

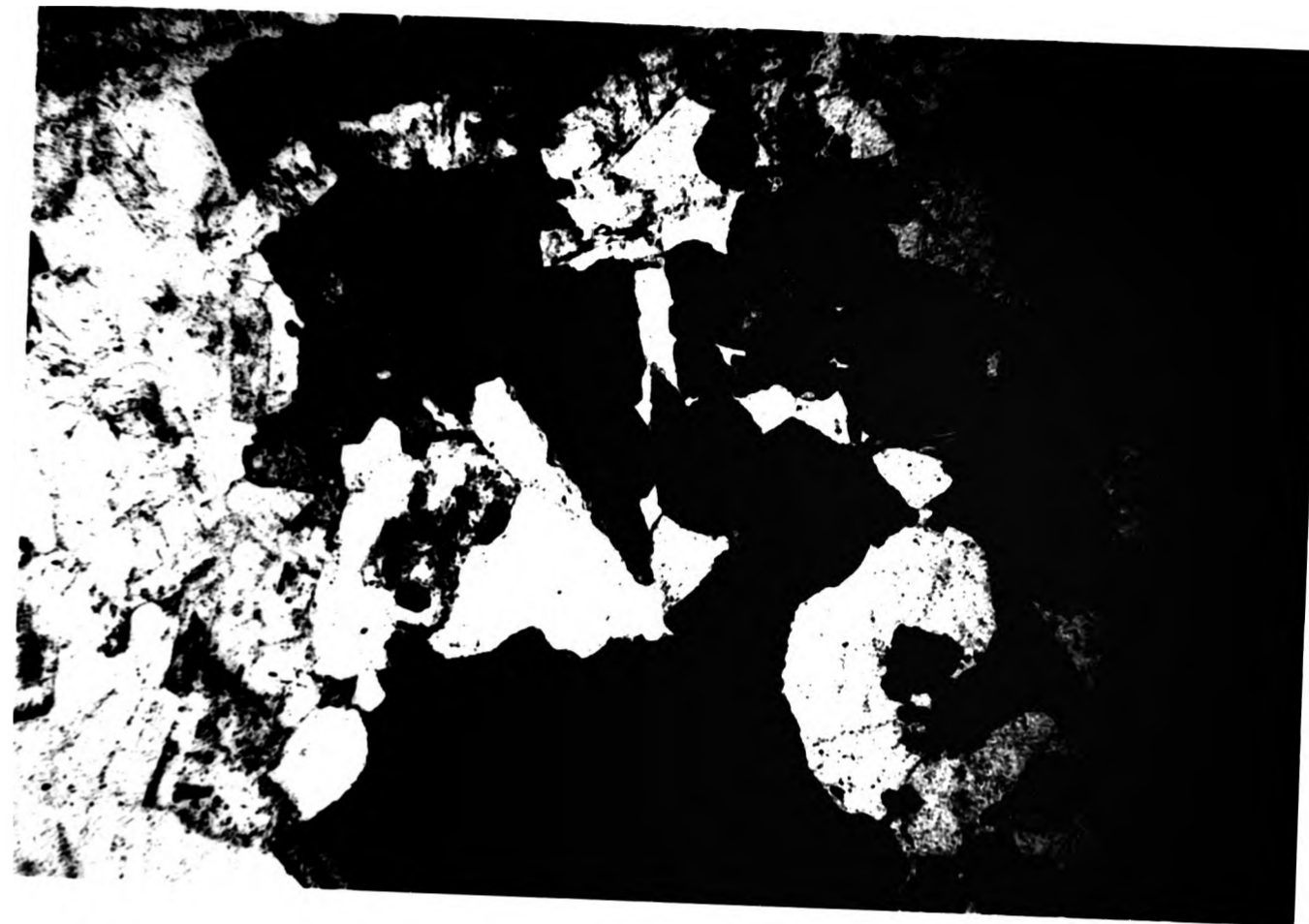


Plate 4.12
Highly sericitised plagioclase crystal in a quartz monzonite.
Biotite is interstitial to plagioclase. (PPL) Field of
view 3mm



Plate 4.11
Typical view of a quartz monzonite containing abundant biotite
poikilitically enclosing magnetite and apatite. (PPL) Field
of view 3mm

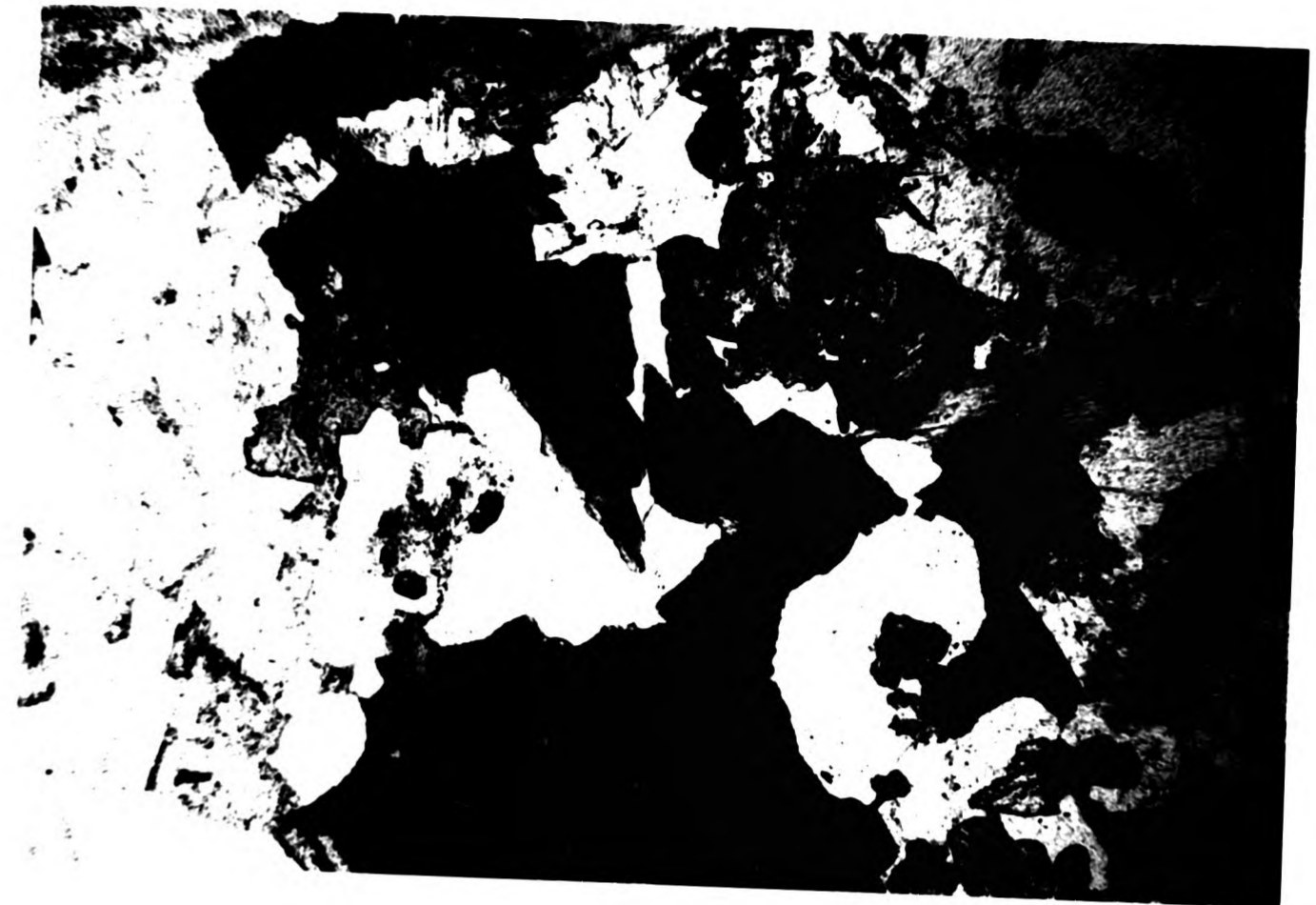


Plate 4.12
Highly sericitised plagioclase crystal in a quartz monzonite.
Biotite is interstitial to plagioclase. (PPL) Field of
view 3mm



Plate 4.11
Typical view of a quartz monzonite containing abundant biotite
poikilitically enclosing magnetite and apatite. (PPL) Field
of view 3mm



Plate 4.12
Highly sericitised plagioclase crystal in a quartz monzonite.
Biotite is interstitial to plagioclase. (PPL) Field of
view 3mm



lar composition to the rims of zoned crystals. Extensive sericitisation is often present (Plate 4.11). Plagioclase composes up to 30% of the mode. Subhedral orthoclase (~25% of the mode) crystals ranging from 2 to 4mm in length occur, which in common with the plagioclase are rarely fresh (Plate 4.12). Perthitic textures are sometimes seen.

Quartz

This mineral, although relatively abundant, forming 11-14% of the mode, occurs as an interstitial phase either in patches (0.2-2mm diameter) or as small anhedral crystals. Quartz commonly shows evidence of strain.

Accessory phases

Magnetite occurs as small anhedral or rounded crystals usually 0.1-2mm across. They commonly occur as inclusions in poikilitic biotite flakes. Magnetite composes <2% of the mode.

The other accessory phase present is euhedral apatite. The crystals occur poikilitically enclosed by plagioclase, biotite, magnetite and amphibole and therefore crystallised prior to these phases. Apatite is a very common accessory phase.

Discussion of the monzonitic rocks

The monzonites occur as layers in the hornblende diorites in the SE of the complex. They are considered to represent zones within the magma body where a large proportion of residual liquid has become trapped (possibly by filter pressing of the diorites above and below) producing a more evolved rock containing primary

biotite, plagioclase, secondary amphibole with interstitial magnetite and apatite and an increased abundance of quartz, orthoclase and biotite relative to the diorites. .

4.2.3 Adamellite

This rock type is typically of medium grain size, sometimes granular and may contain large patches of interstitial quartz. Their mineralogy is less diverse than the diorites and they contain plagioclase, orthoclase, quartz, biotite \pm chlorite and magnetite. Well formed quartz crystals occur in drusy cavities (Chapter 3). The colour index is variable, darker patches occurring in fine grained facies.

Feldspar

Plagioclase occurs as squat rectangular crystals (3mm long), rather than the tabular variety which occur in the diorites. Many crystals show strong oscillatory zoning, but unzoned crystals (An_{30}) occur. Many of the crystal cores are highly sericitised while the rims remain fresh perhaps indicating that the latter are more calcic. Plagioclase composes 30% of the mode.

Orthoclase typically occurs as large anhedral crystals forming up to 20% of the mode. Perthitic textures are common (Plate 4.13).

Quartz

Displaying variable grain size from <0.1-1mm in diameter, the crystals may occur as aggregates or anhedral patches <3mm wide. Some crystals display a concertal texture (Mackenzie et al., 1982)

Plate 4.13
Orthoclase in adamellite displaying a perthitic texture.
(XPL) Field of view 3mm

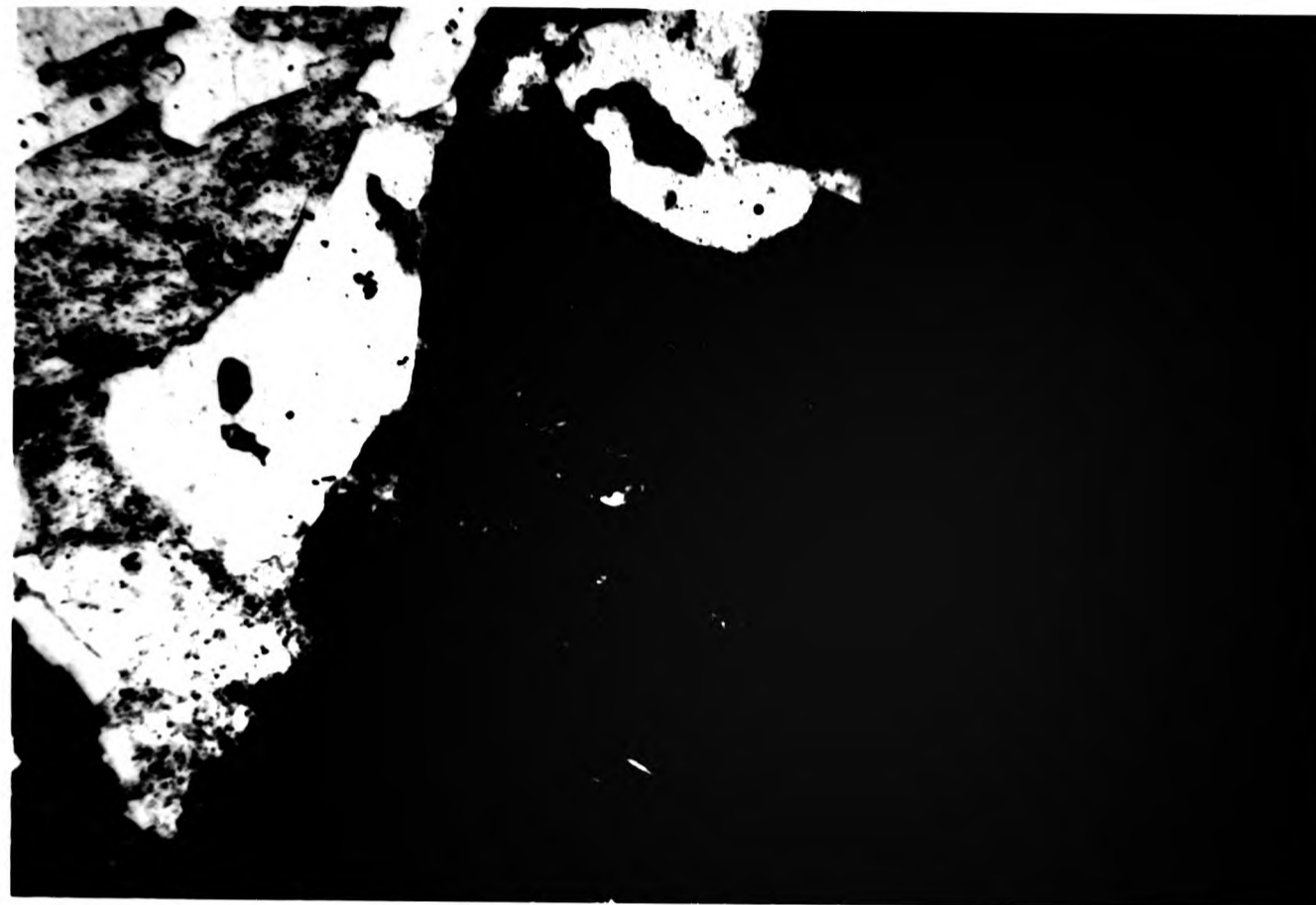


Plate 4.14
Olivine gabbro showing a large orthopyroxene crystal (centre)
and uneven growth boundary with plagioclase (lower centre).
Olivine primocrysts (bottom and right) vary in size from
0.5-2.0mm and are poikilitically enclosed by plagioclase.
(XPL) Field of view 3mm



Plate 4.13
Orthoclase in adamellite displaying a perthitic texture.
(XPL) Field of view 3mm

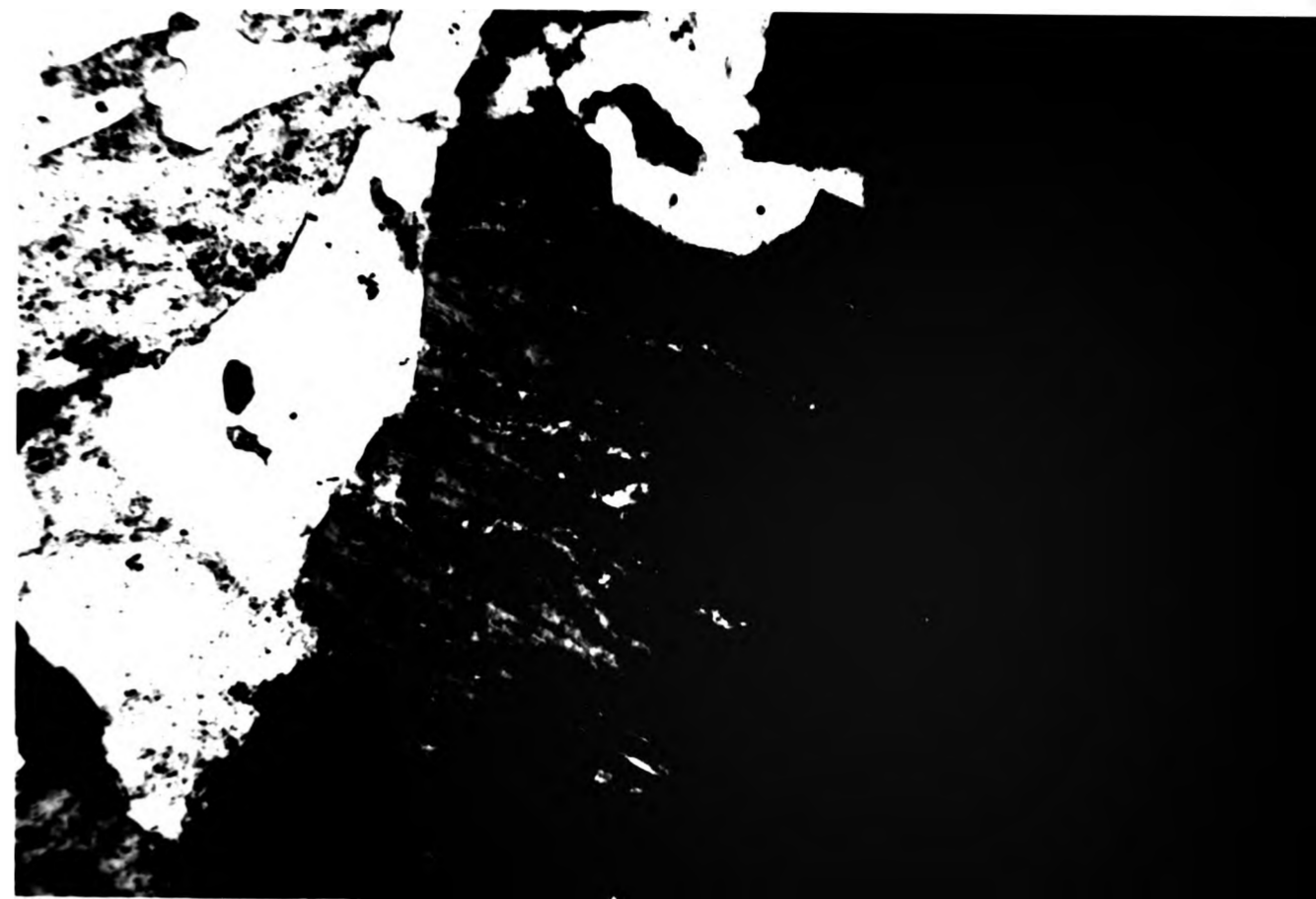


Plate 4.14
Olivine gabbro showing a large orthopyroxene crystal (centre)
and uneven growth boundary with plagioclase (lower centre).
Olivine primocrysts (bottom and right) vary in size from
0.5-2.0mm and are poikilitically enclosed by plagioclase.
(XPL) Field of view 3mm

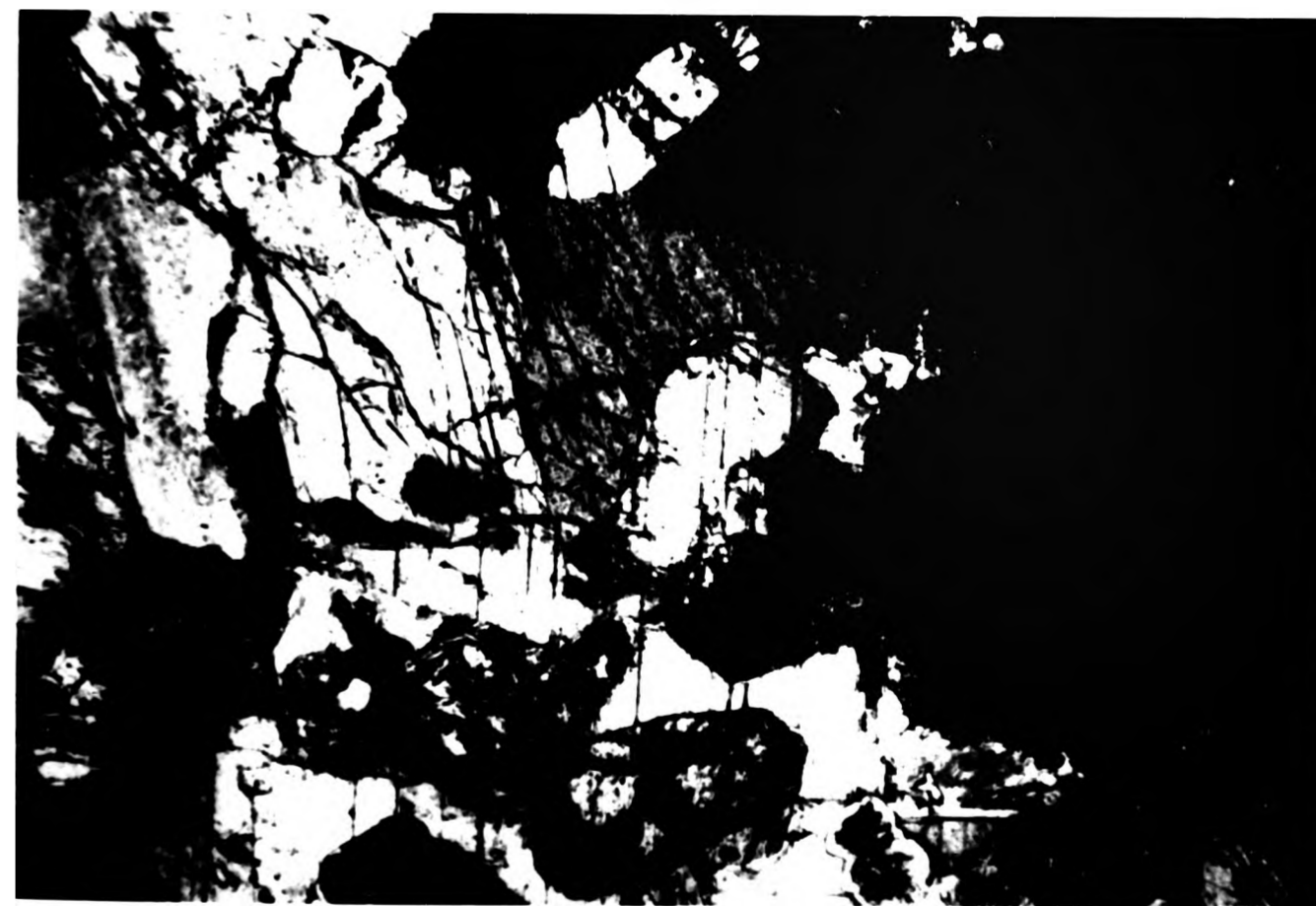


Plate 4.13
Orthoclase in adamellite displaying a perthitic texture.
(XPL) Field of view 3mm

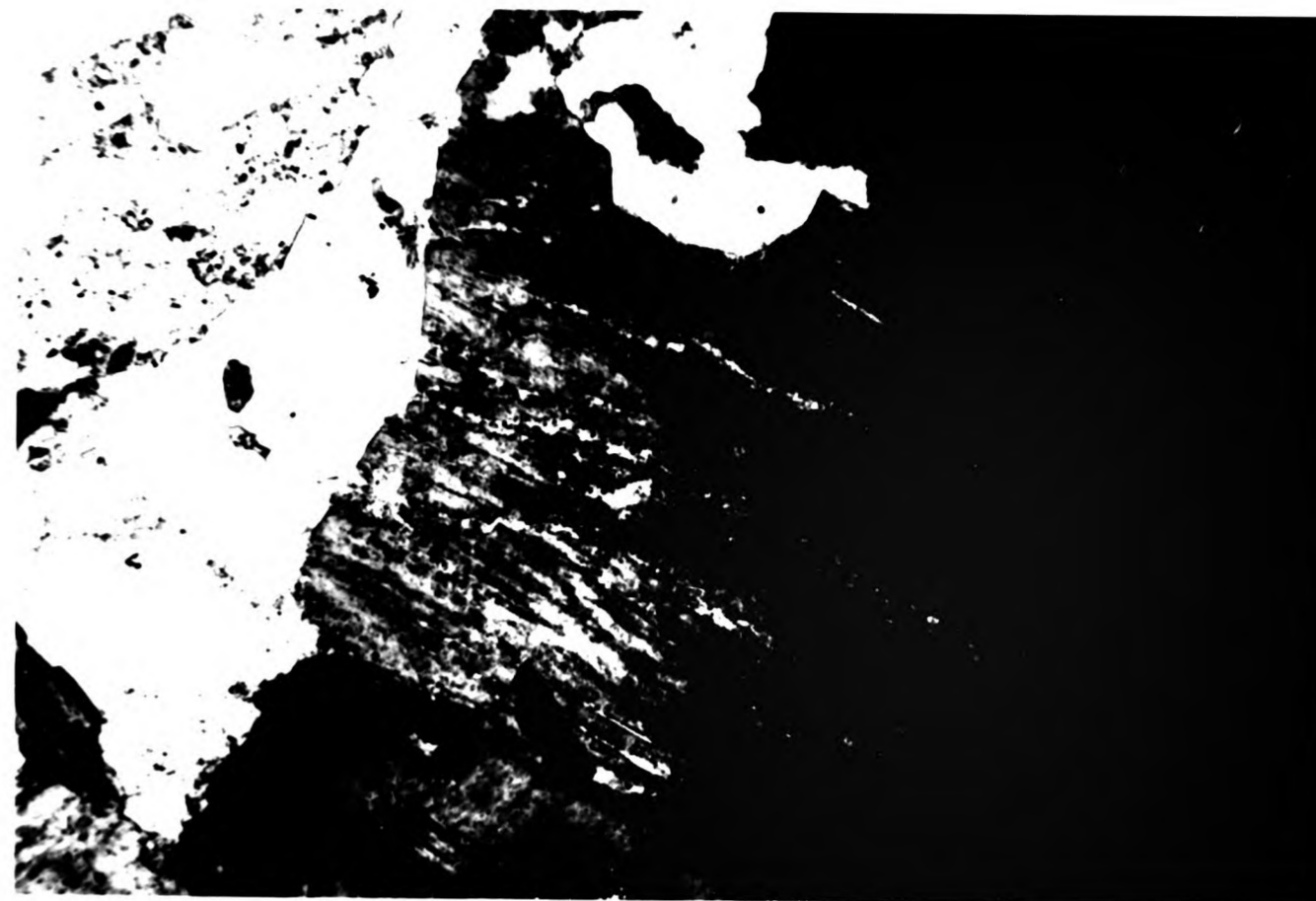
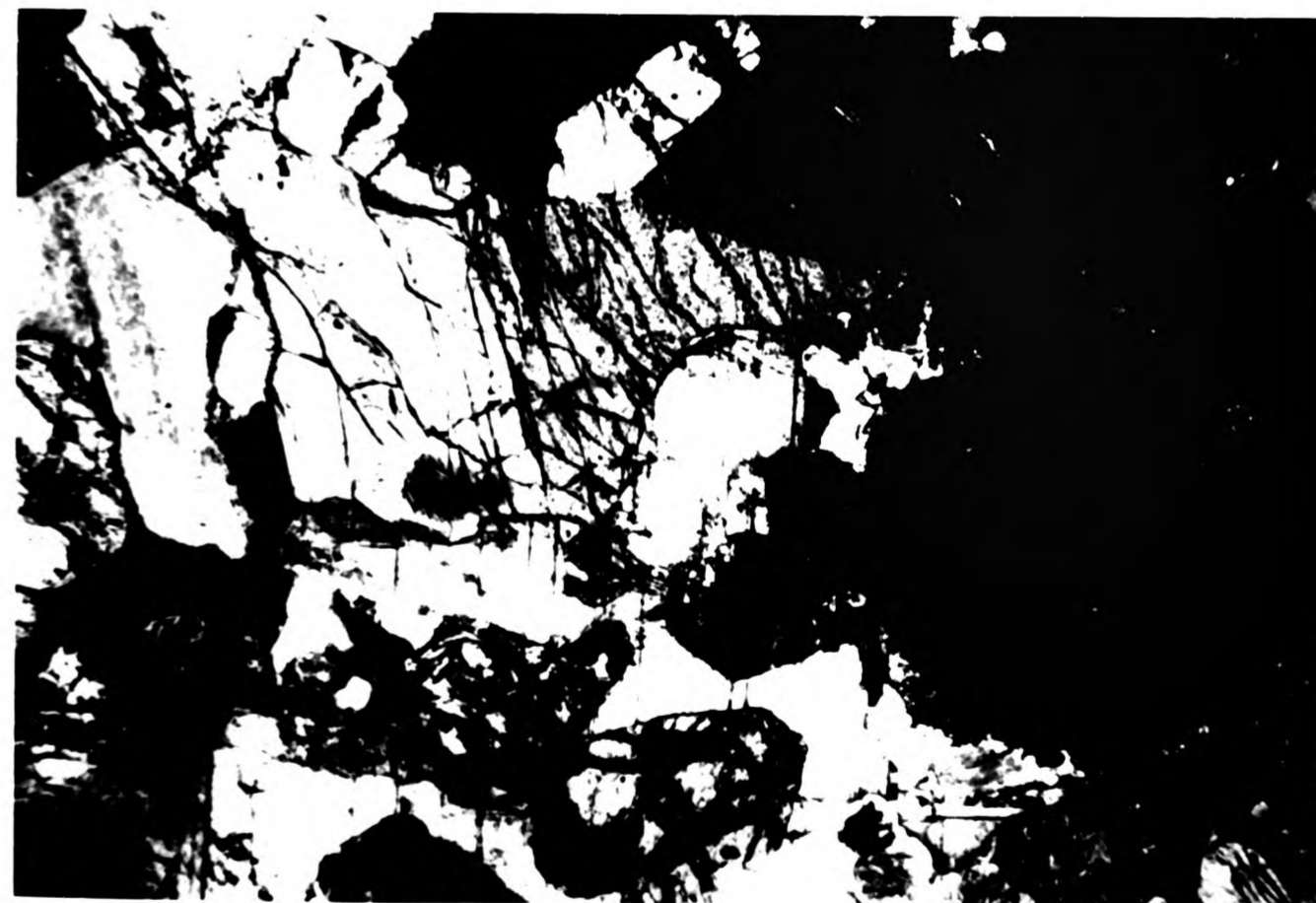


Plate 4.14
Olivine gabbro showing a large orthopyroxene crystal (centre)
and uneven growth boundary with plagioclase (lower centre).
Olivine primocrysts (bottom and right) vary in size from
0.5-2.0mm and are poikilitically enclosed by plagioclase.
(XPL) Field of view 3mm



with intergrown boundaries of quartz with quartz or of quartz with feldspar. Crystals of quartz may be angular or sub-rounded with no overgrowths. Quartz composes 40% of the mode.

Biotite

This mineral is the main mafic phase composing <8% of the mode. It occurs as small (<0.5mm) interstitial flakes altering to chlorite or as 2mm flakes which frequently alter to chlorite along their length. These may poikilitically enclose small (<0.1mm) orthoclase crystals. The smaller flakes commonly contain acicular black rutile.

Accessory phases

These minerals form 2% of the mode and include anhedral magnetite (<0.3mm diameter), which is often skeletal and poikilitically encloses apatite and haematite. Rutile occurs as needles in biotite, apatite as euhedral crystals and rarely, zircon.

4.2.4 Basic rocks

The occurrence of the basic rocks is restricted to the NE and SW parts of the complex and details of their distribution are given in Chapter 3. Gabbro is restricted to the northeastern part of the complex, and in the southwest the rocks include gabbro, olivine gabbro and norites and olivine norite. A description of the major variation in mineralogy is given below, followed by a detailed description of the changes in mineralogy seen through the almost continuous sequence exposed in the SW of the complex in Kilbo Burn. The series of gabbros, norites and diorites exposed here is considered to represent wall parallel layering producing a range of

ortho- and meso-cumulates. Plagioclase typically occurs as tabular crystals which display a cumulate texture but display no preferred orientation.

Olivine gabbro

This is a medium grain size rock composed of cpx, opx and olivine with subordinate plagioclase and small amounts of an oxide phase. Opx-bronzite, crystals are 1-2mm in length, subhedral and highly fractured (Plate 4.14). Cpx is dominant over opx in abundance and the crystals of augite, ranging in length from 2-3mm, are subhedral. Both opx and cpx may be poikilitically enclosed by tabular plagioclase. Olivine (Fe_{80}) occurs as subhedral or rounded highly fractured crystals which are variable in diameter from 0.5-4mm. The fractures are commonly filled with yellow-brown iddingsite. The olivine crystals occasionally form aggregates composed of 6-8 crystals of varying size. Tabular plagioclase crystals of labradorite (An_{55-60}) composition are subordinate to the mafic phases and occur as unzoned fresh crystals. The former may poikilitically enclose olivine, opx and cpx (Plate 4.15). Large phlogopite crystals, 3mm across, occur as anhedral poikilitic crystals enclosing olivine, opx, cpx and biotite. The margins of the phlogopite crystals are embayed and uneven. The observed textures suggest that the cumulus minerals present are olivine, cpx and opx while the intercumulus phases initially include unzoned plagioclase and opx, followed by phlogopite.

Gabbro

The gabbroic rocks display a progressive variation in modal mineralogy reflecting their wide compositional range (6-11% MgO).

Plate 4.15
Olivine gabbro showing a plagioclase megacryst poikilitically enclosing small rounded olivine crystals. The olivines may occur in aggregates and typically form a cumulate framework. (XPL) Field of view 3mm

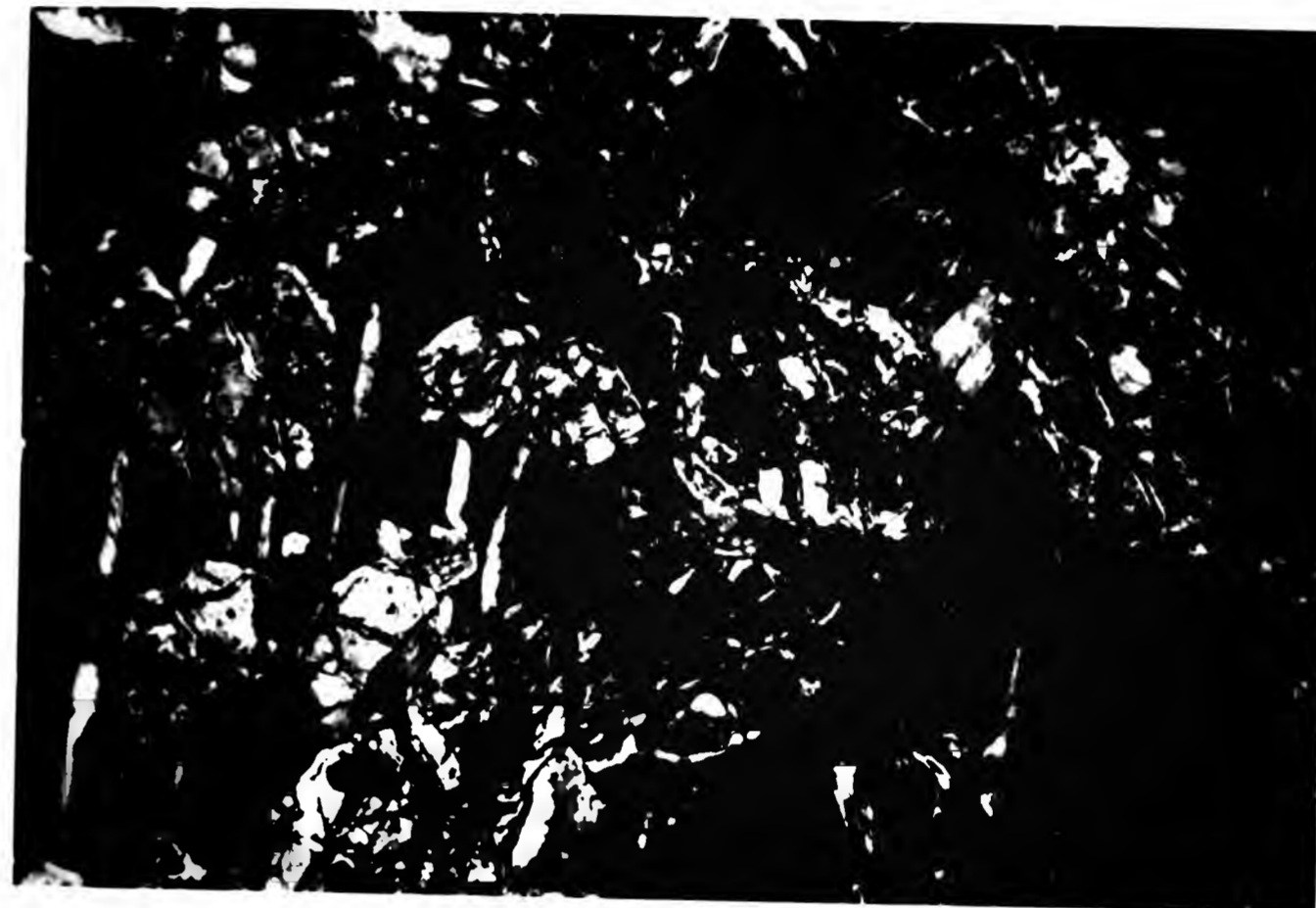


Plate 4.16
General view of a low magnesia gabbro showing orthopyroxene (top right), clinopyroxene (lower part of slide) and primary brown amphibole poikilitically enclosing clinopyroxene and plagioclase (left). The dark crystal in the centre is biotite. (XPL) Field of view 3mm

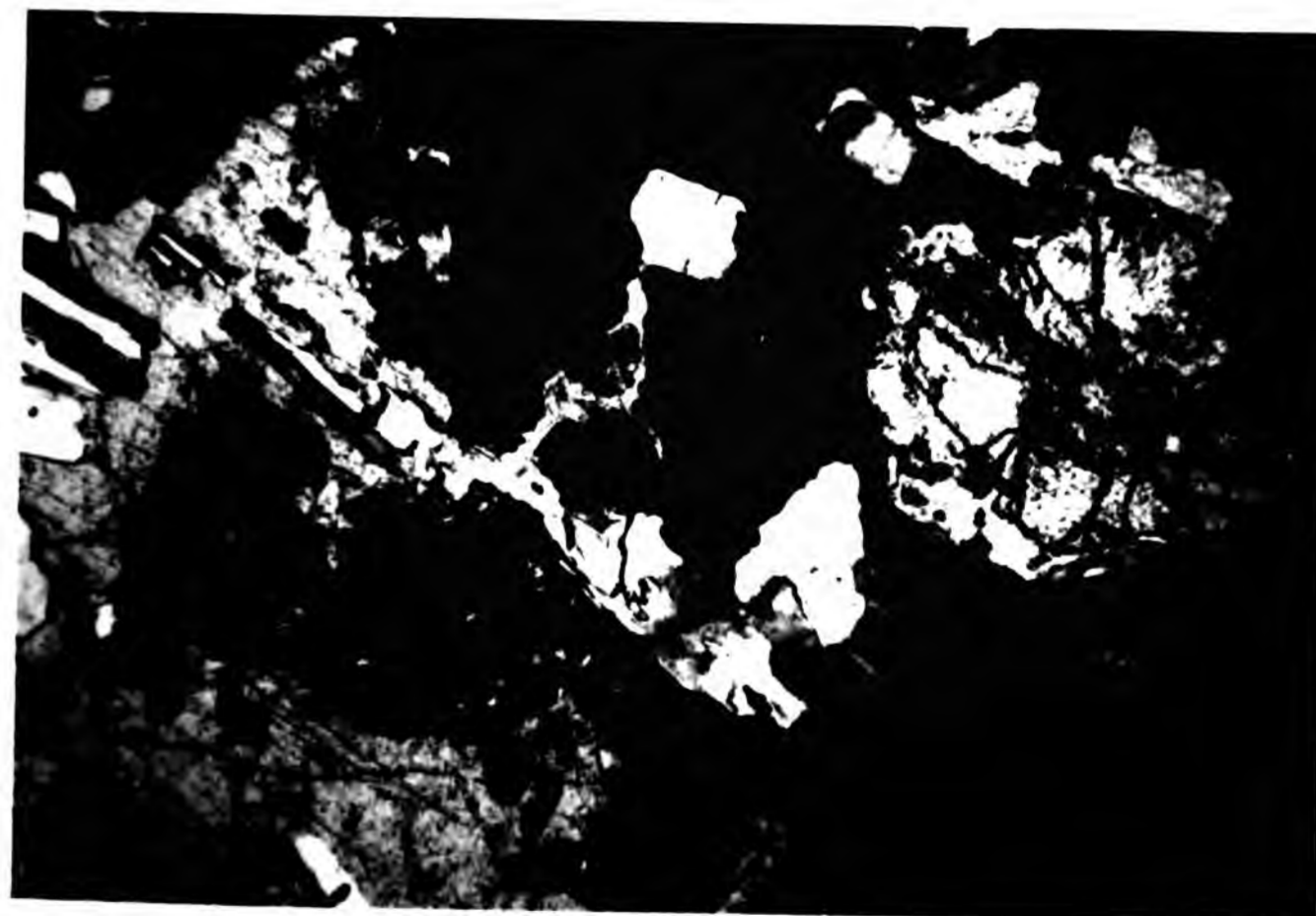


Plate 4.15
Olivine gabbro showing a plagioclase megacryst poikilitically enclosing small rounded olivine crystals. The olivines may occur in aggregates and typically form a cumulate framework. (XPL) Field of view 3mm



Plate 4.16
General view of a low magnesia gabbro showing orthopyroxene (top right), clinopyroxene (lower part of slide) and primary brown amphibole poikilitically enclosing clinopyroxene and plagioclase (left). The dark crystal in the centre is biotite. (XPL) Field of view 3mm

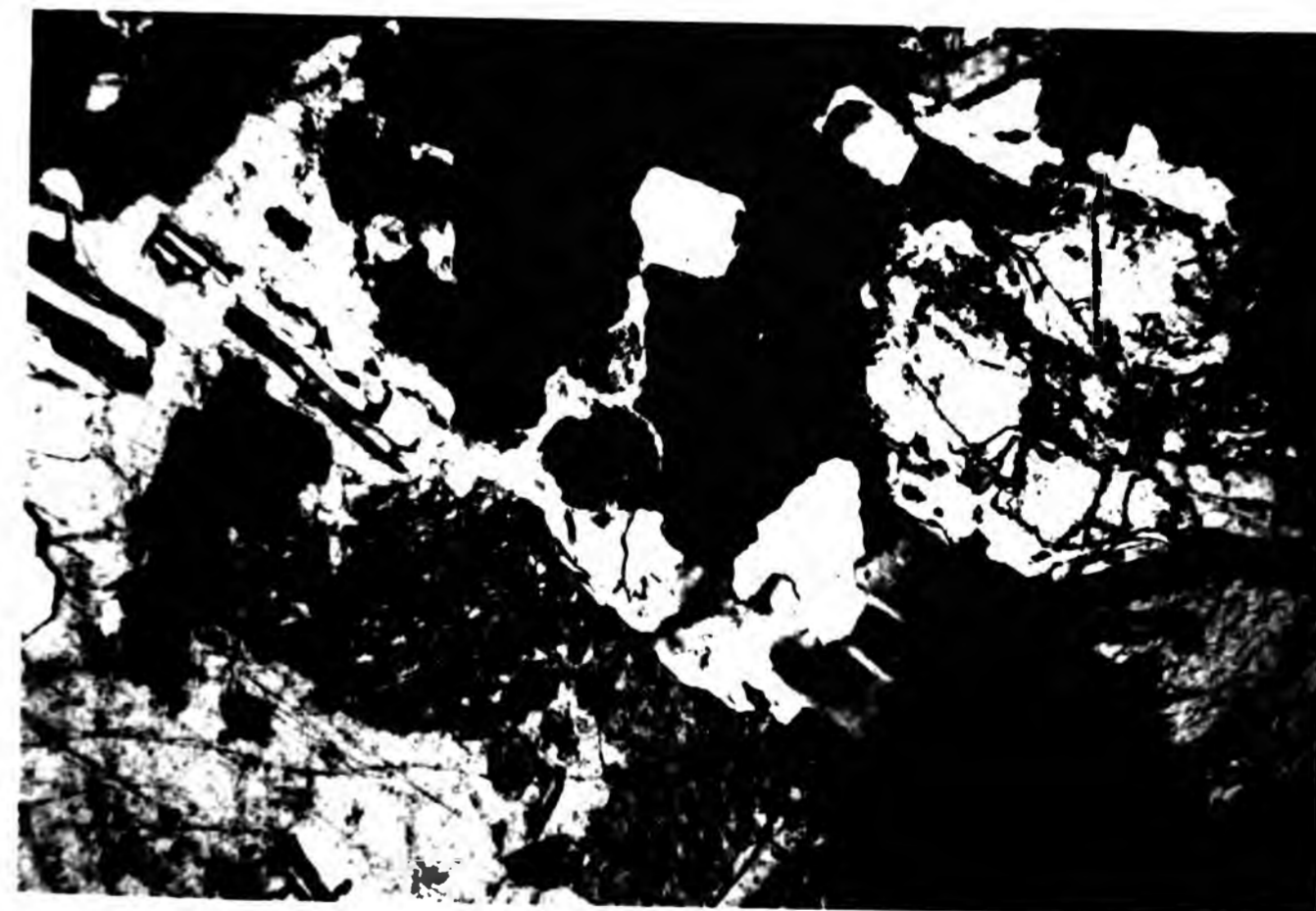
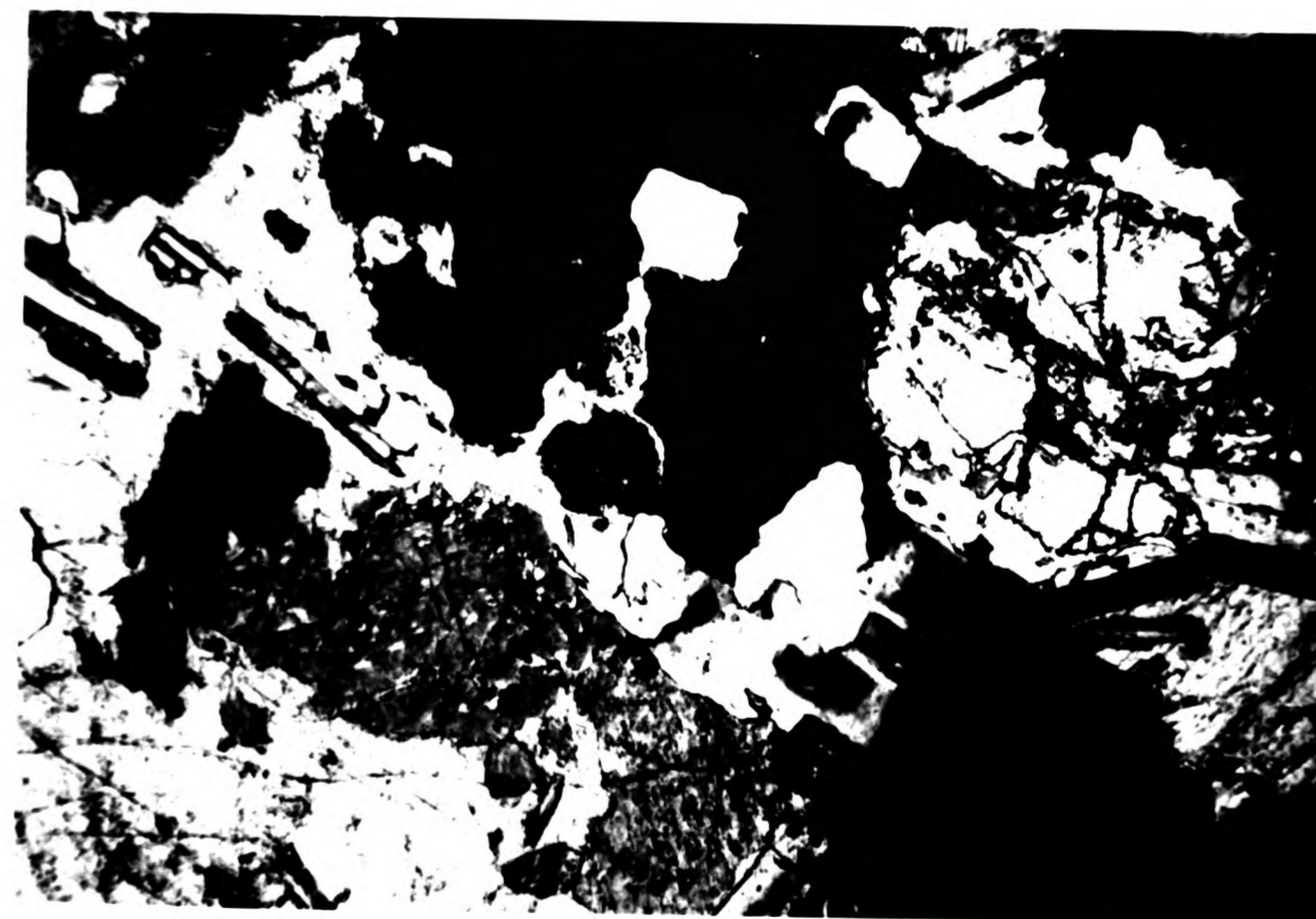


Plate 4.15
Olivine gabbro showing a plagioclase megacryst poikilitically enclosing small rounded olivine crystals. The olivines may occur in aggregates and typically form a cumulate framework. (XPL) Field of view 3mm



Plate 4.16
General view of a low magnesia gabbro showing orthopyroxene (top right), clinopyroxene (lower part of slide) and primary brown amphibole poikilitically enclosing clinopyroxene and plagioclase (left). The dark crystal in the centre is biotite. (XPL) Field of view 3mm



This increase in magnesia is reflected in the gradual change in mineralogy from sections containing abundant opx and cpx, to those with little pyroxene and abundant amphibole.

The lower magnesia types have ca. 60% plagioclase feldspar, occurring as variably fresh to sericitised 1-2mm euhedral crystals ranging from An_{52-55} , with occasional stubby subhedral crystals. Some sections show normal zoning while others are unzoned. A low magnesia gabbro is shown in Plate 4.16.

Brown amphibole commonly occurs as subhedral oikocrysts of hornblende 4-6mm in length, poikilitically enclosing plagioclase crystals (Plate 4.16 and 4.19) and anhedral cpx. Amphibole composes 15-20% of the mode. Plagioclase chadocrysts are labradoritic in composition (An_{54}) and typically display a cumulate texture. Some interstitial green amphibole is present.

Augite is the second most common mafic phase. Crystals are subhedral, elongate and usually <2mm long. Augite crystals commonly display broad jackets of green actinolitic amphibole. Augite forms 10-14% of the mode.

Bronzite may occur as euhedral crystals which are highly fractured and sometimes jacketed by actinolitic hornblende. Some bronzite also occurs as subhedral chadocrysts within large hornblende crystals. A few opx grains poikilitically enclose small (<0.1mm) plagioclase crystals indicating that although most plagioclase grew prior to opx, some of the former crystallised prior to the pyroxene. Opx typically composes 8% of the mode.

Biotite is a subordinate phase in these rock types forming 0-4% of the mode. Crystals are always small (<0.5mm) and often altered to chlorite. Intergrowths between secondary amphibole and biotite are sometimes seen.

Magnetite forms only 1% of the mode, crystals being anhedral and embayed. The magnetite occurs intimately intergrown with biotite. Apatite crystals are extremely rare and occur only as interstitial minerals.

The more MgO rich gabbros show a progressive increase in the abundance of pyroxene and plagioclase, accompanied by a decrease in biotite and hornblende. The crystal form of the plagioclase is similar to that described from the less magnesian samples and compositions vary from An₅₅₋₆₅. Tabular crystals are variable in length, commonly 0.5-1.0mm, more rarely up to 2mm long. No zoning is seen and crystals are usually fresh, showing little alteration. Large crystals may poikilitically enclose opx. Plagioclase composes 60-70% of the mode. Alkali feldspar, in common with the low magnesia varieties, is absent.

Augite composes 20% of the mode, forming subhedral, often rounded crystals from 0.5-1.5mm in length. They commonly occur as aggregates forming an area several millimetres in size. Augite may also occur as interstitial material between plagioclase crystals. There is no evidence of alteration to amphibole. Pleochroic opx-bronzite, forms 8-14% of the mode. It typically occurs in groups of anhedral or subrounded crystals with interstitial iddingsite.

Biotite is absent but phlogopite commonly forms large (4mm

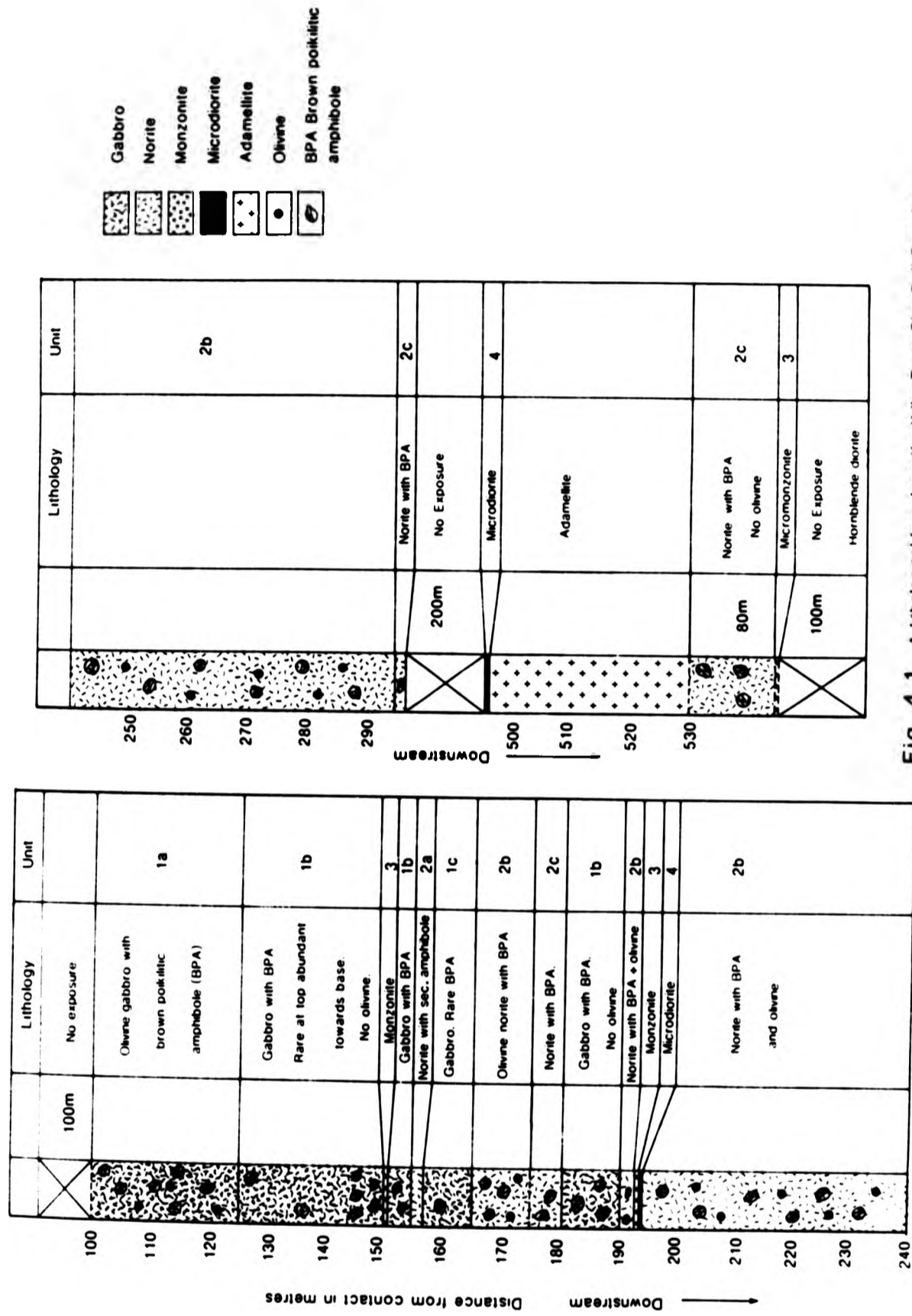


Fig. 4.1 A lithological log along the Kilbo Burn, Glen Doll Complex

long) poikilitic crystals enclosing plagioclase feldspar. Magnetite and apatite are very rare and occur in a similar form to that in the less mafic gabbro.

The textural information suggests the early crystallisation of plagioclase and cpx primocrysts in both the low and high MgO gabbros. These minerals are followed in the high MgO samples by the crystallisation of opx and plagioclase with late stage intercumulus phlogopite and rare magnetite and apatite. After the initial stages of primocryst formation in the low MgO gabbros, opx followed by brown amphibole crystallised. The final interstitial minerals to crystallise are biotite, magnetite and apatite.

Traverse along Kilbo Burn

The relationship between the basic rocks is best studied in the relatively continuous exposure in Kilbo Burn. A traverse across the layered unit in this burn is given in Figure 3.7. The textures described are equally applicable to the series of basic rocks from the NE part of the complex. The rock units have been numbered in the order in which they occur away from the contact with the Dalradian country rocks. The section may be divided into two main rock types which are repeated down stream and inwards from the contact (Figure 4.1). The rock types are gabbro and norite, each of which may contain olivine and primary amphibole. The contacts between the layers are not exposed away from the stream bed but the rapid change from one rock type to another, both on horizontal and vertical sections, suggests that the contacts are steeply dipping (see Chapter 3). Figure 4.1 shows the distribution of the rock units which are described below. Intruded between some

Plate 4.17

View of a gabbro from Kilbo Burn showing a large poikilitic amphibole enclosing small tabular plagioclase crystals (left). Locally large plagioclase primocrysts are developed. The plagioclase is randomly orientated and does not define a lamination. (PPL) Field of view 2.2x1.4cm

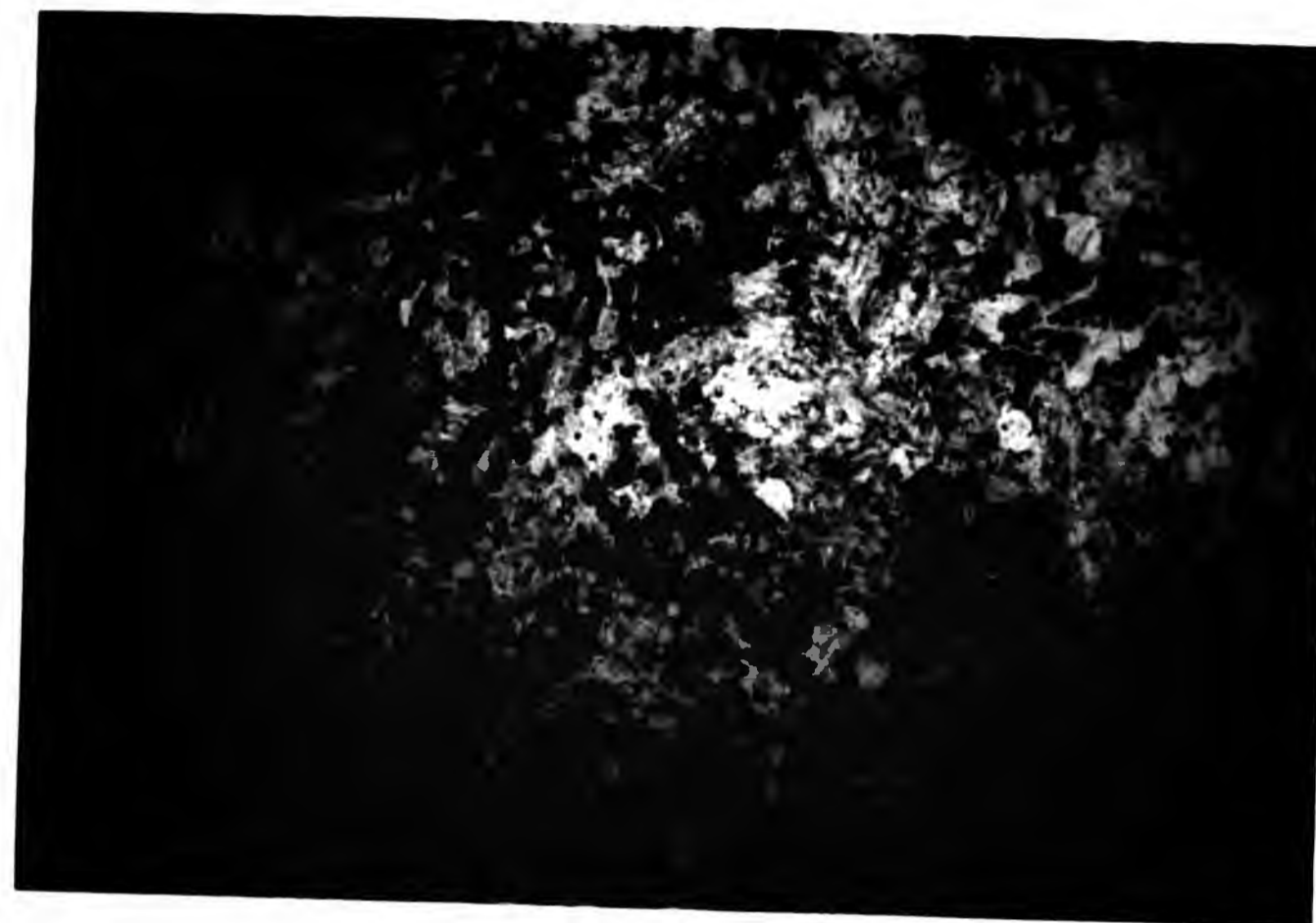


Plate 4.18

As above but showing clearly a large brown poikilitic amphibole enclosing plagioclase, ortho-pyroxene and clinopyroxene (left). (XPL) Field of view 2.2x1.4cm



Plate 4.17

View of a gabbro from Kilbo Burn showing a large poikilitic amphibole enclosing small tabular plagioclase crystals (left). Locally large plagioclase primocrysts are developed. The plagioclase is randomly orientated and does not define a lamination. (PPL) Field of view 2.2x1.4cm

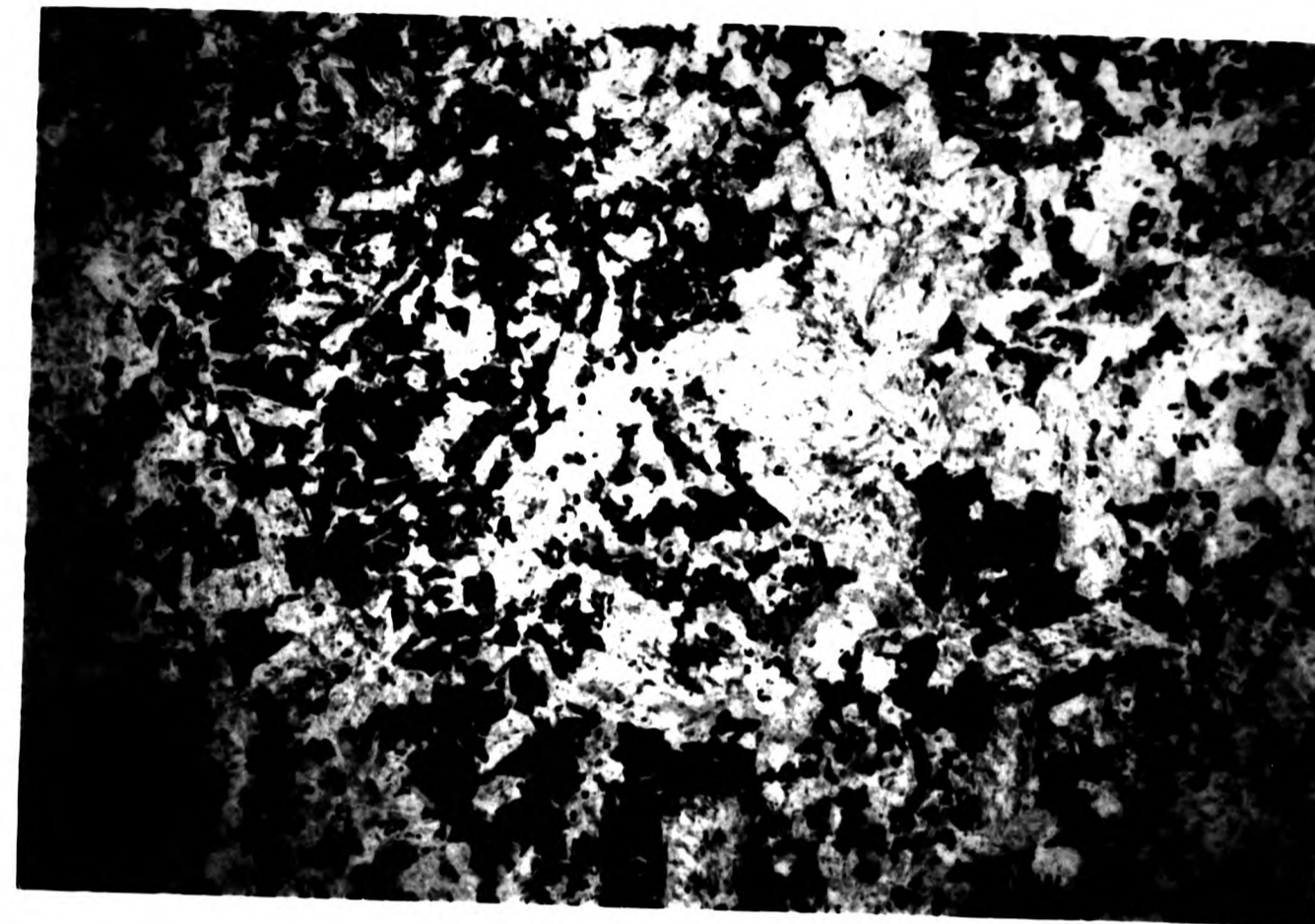


Plate 4.18

As above but showing clearly a large brown poikilitic amphibole enclosing plagioclase, ortho-pyroxene and clinopyroxene (left). (XPL) Field of view 2.2x1.4cm

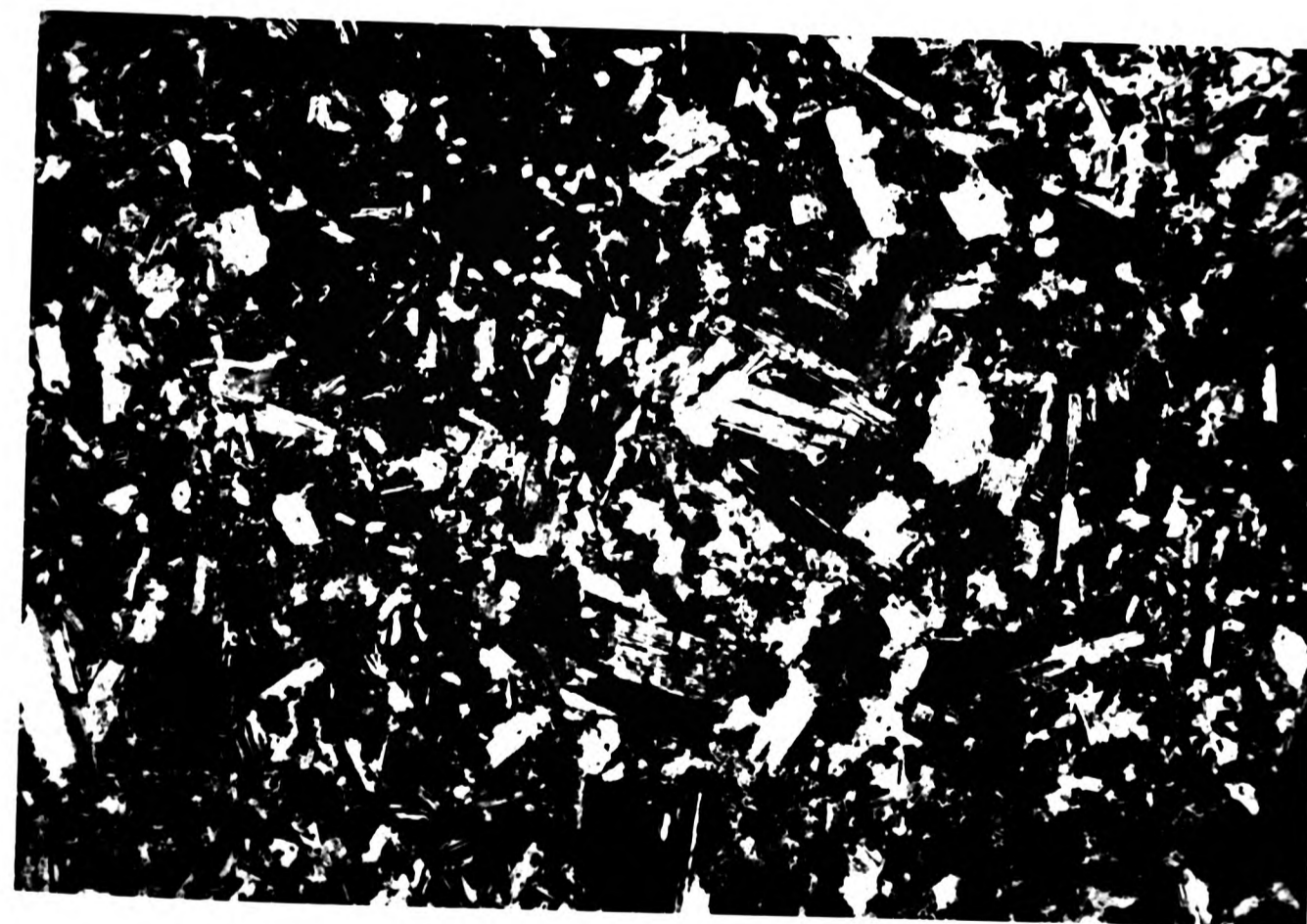


Plate 4.17

View of a gabbro from Kilbo Burn showing a large poikilitic amphibole enclosing small tabular plagioclase crystals (left). Locally large plagioclase primocrysts are developed. The plagioclase is randomly orientated and does not define a lamination. (PPL) Field of view 2.2x1.4cm

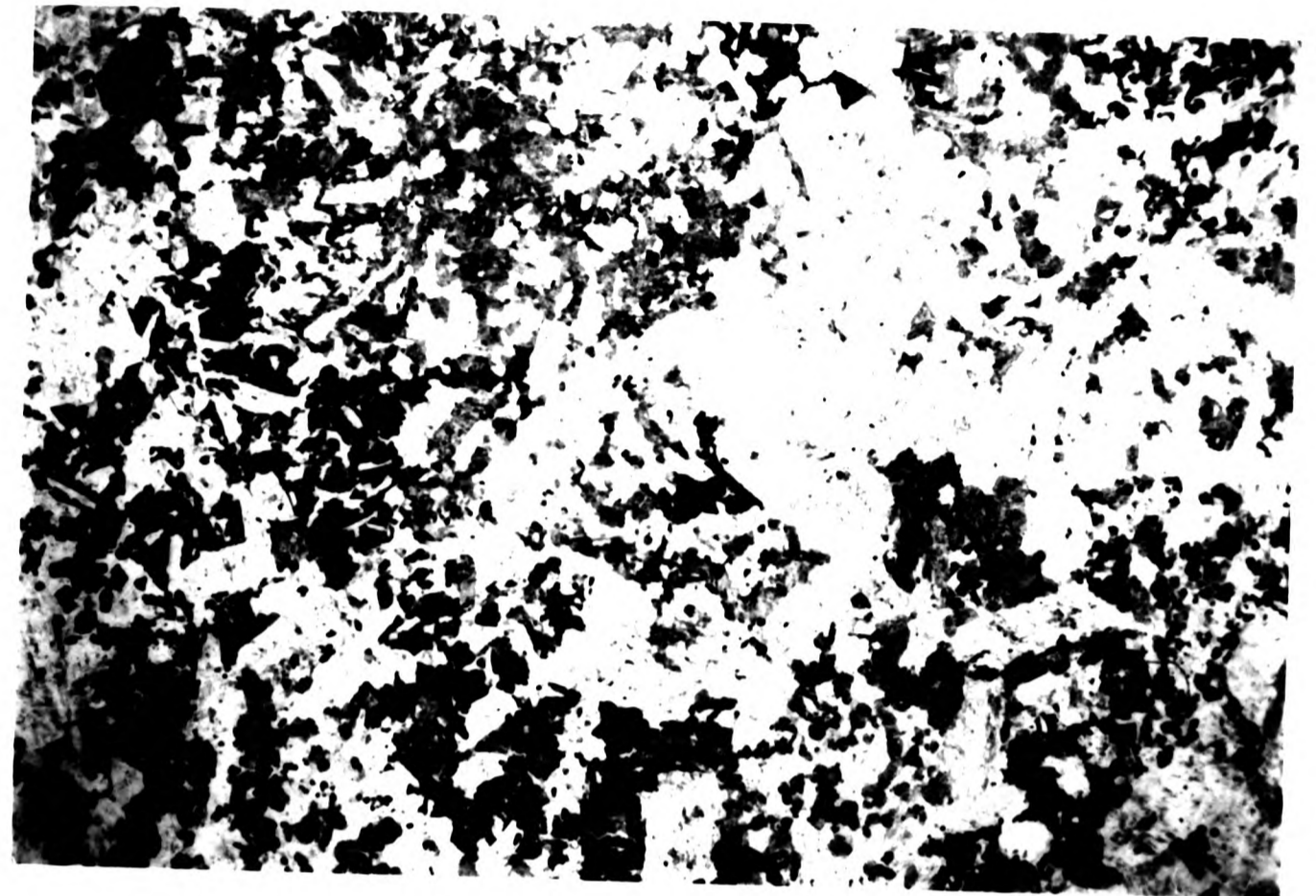
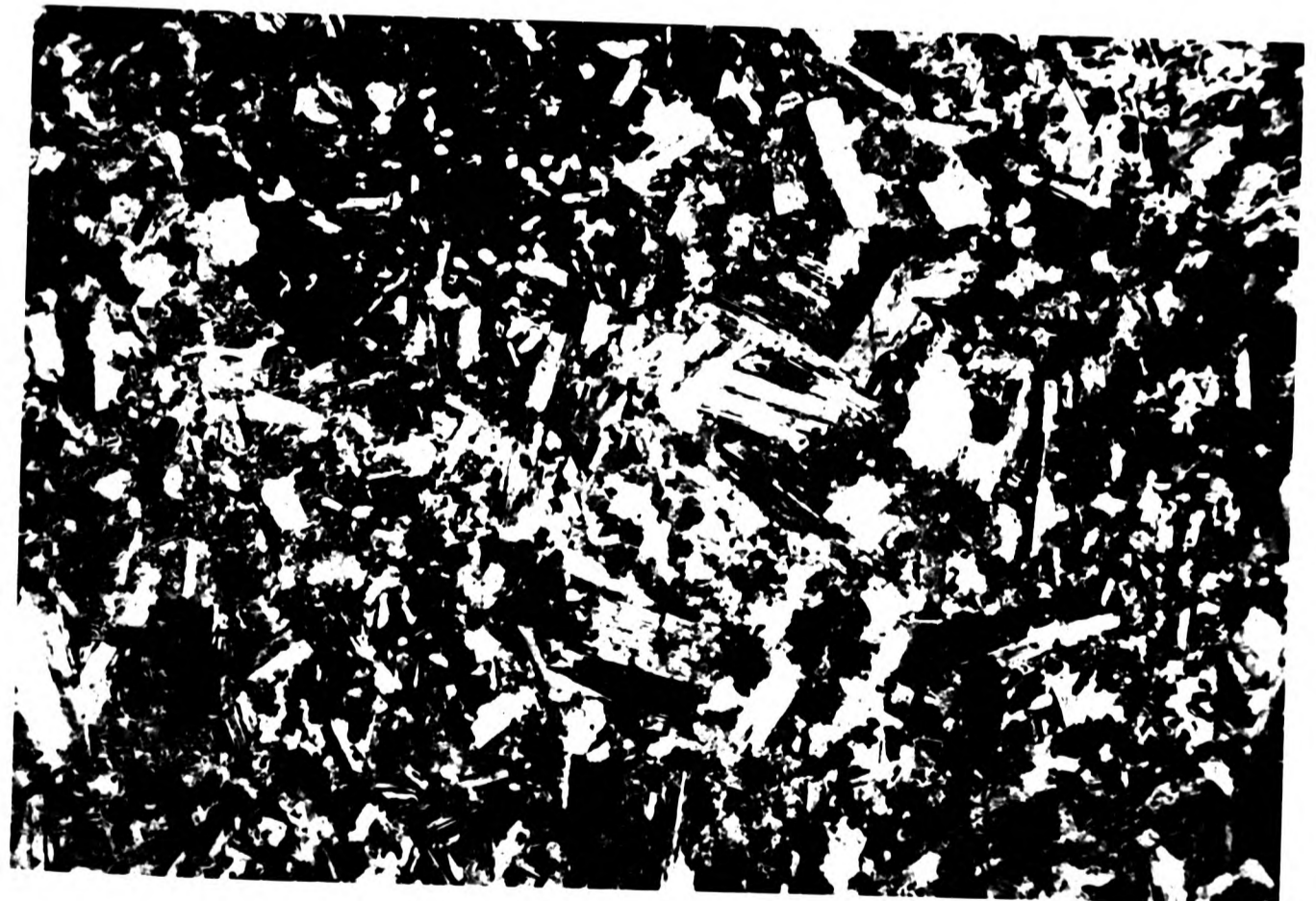


Plate 4.18

As above but showing clearly a large brown poikilitic amphibole enclosing plagioclase, ortho-pyroxene and clinopyroxene (left). (XPL) Field of view 2.2x1.4cm



of the basic rock layers are later monzonite and adamellite layers and microdiorite dykes. The modal mineralogy for the rock types described is given in Table 4.1.

UNIT 1a: Olivine gabbro with poikilitic amphibole.

This rock type occurs only once in the sequence displayed in the burn. The abundance of olivine decreases away from the assumed position of the contact with the country rocks, from 35-10 modal percent. Conversely, amphibole increases in abundance (from 25-5%) and always occurs as large 4mm poikilitic crystals enclosing cpx, opx, plagioclase (An_{55-60}) and olivine. These minerals typically compose cpx 20%, opx 20% and plagioclase 20% of the mode. The textures displayed are of an orthocumulate. The interstitial plagioclase is always fresh and unaltered.

UNIT 1b: Gabbro with poikilitic amphibole

Apart from the absence of olivine, this unit displays similar textures and mineralogy to unit 1a. Plagioclase (An_{54}) is more abundant (60%) than in unit 1a and the texture is of a plagioclase mesocumulate. Brown poikilitic amphiboles (Plate 4.17) are less abundant at the upper margin than the lower margin, and progressively increase through the unit. Similarly plagioclase crystals decrease in abundance towards the lower margin where they form 40% of the rock (Table 4.1). The plagioclase is interstitial, and the texture is of a pyroxene orthocumulate. This unit is repeated twice down sequence (Figure 3.7).

UNIT 1c: Gabbro with poikilitic amphibole and secondary amphibole.

This unit may be distinguished from units 1a and 1b by the presence of secondary fibrous white amphibole which is starting to replace cpx. Brown poikilitic amphiboles are smaller than those described from units 1a and 1b and are skeletal in habit. Brown amphibole comprises 20% of the mode. The overall texture is of a pyroxene orthocumulate, plagioclase being interstitial and composing only 30% of the mode with cpx (20%) and opx (20%). Opx crystals are tabular and fractured and may be jacketed by white fibrous amphibole. The brown poikilitic amphibole may enclose opx, cpx and plagioclase (Plate 4.19) but not the secondary actinolitic amphibole. Actinolitic amphibole comprises ~10% of the mode.

UNIT 2a: Norite with secondary amphibole

This rock unit is composed of a norite and therefore contains more modal opx than cpx. Plagioclase forms 60% of the rock occurring as large zoned relatively fresh tabular crystals. Opx-bronzite is tabular often fractured and may be corroded along the margins. Small crystals may be poikilitically enclosed by plagioclase (An₅₀). Cpx-augite occurs as mottled subhedral crystals forming crystal aggregates. The amphibole occurs as secondary actinolite forming large fibrous patches replacing cpx. This unit is not repeated through the sequence. The texture is of a plagioclase orthocumulate.

UNIT 2b: Olivine norite

The rock type forming this unit is classified as an olivine norite. It contains large brown poikilitic amphibole in common with the gabbros (units 1a, 1b and 1c). This unit is repeated three times in the section (Figure 4.1). The primary mineralogy is

Plate 4.19
Single crystal of brown amphibole poikilitically enclosing
plagioclase oikocrysts. (XPL) Field of view 3mm



Plate 4.20
Rafted xenolith containing characteristic aggregates of
hercynitic spinel. (PPL) Field of view 3mm

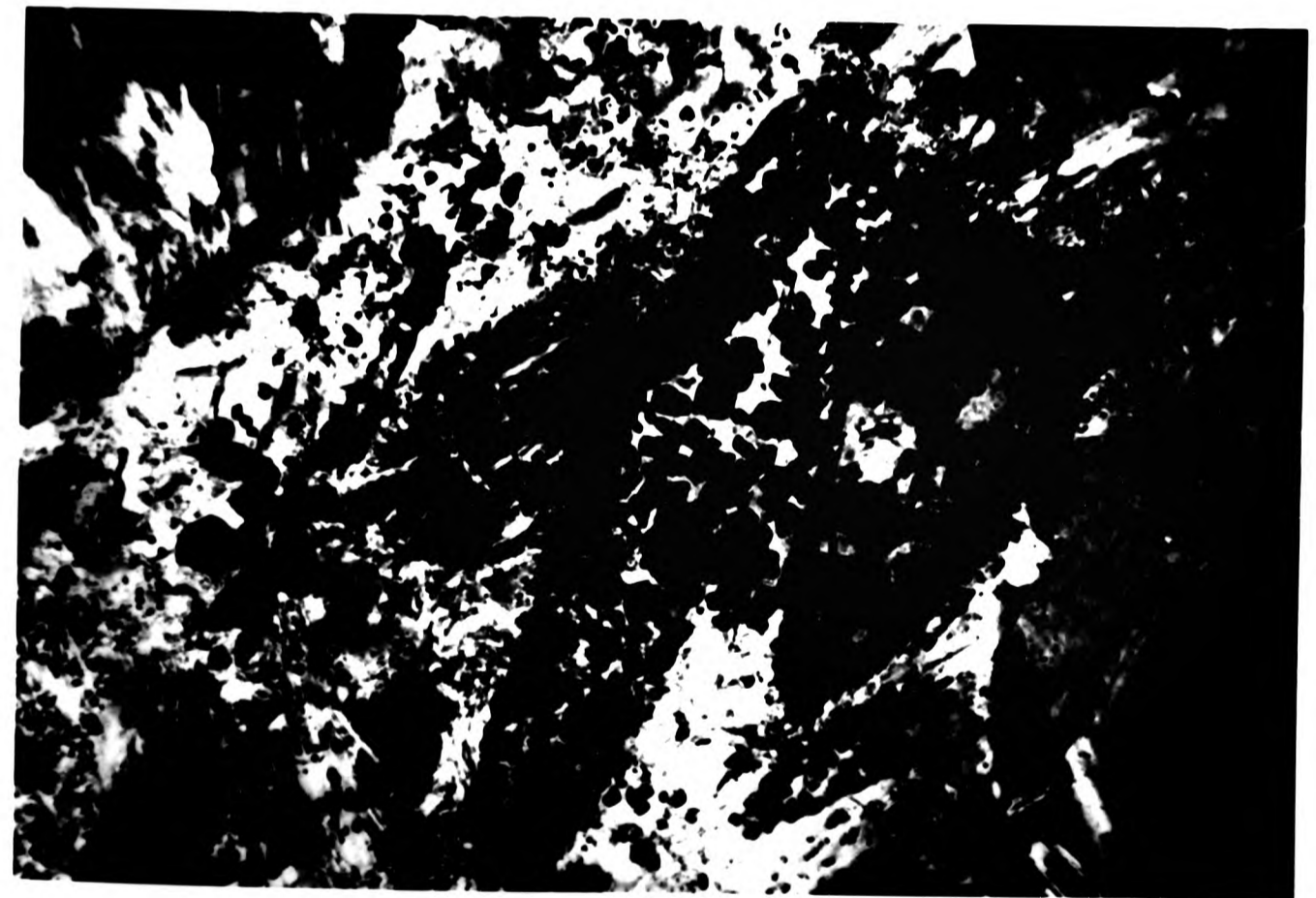


Plate 4.19
Single crystal of brown amphibole poikilitically enclosing
plagioclase oikocrysts. (XPL) Field of view 3mm



Plate 4.20
Rafted xenolith containing characteristic aggregates of
hercynitic spinel. (PPL) Field of view 3mm

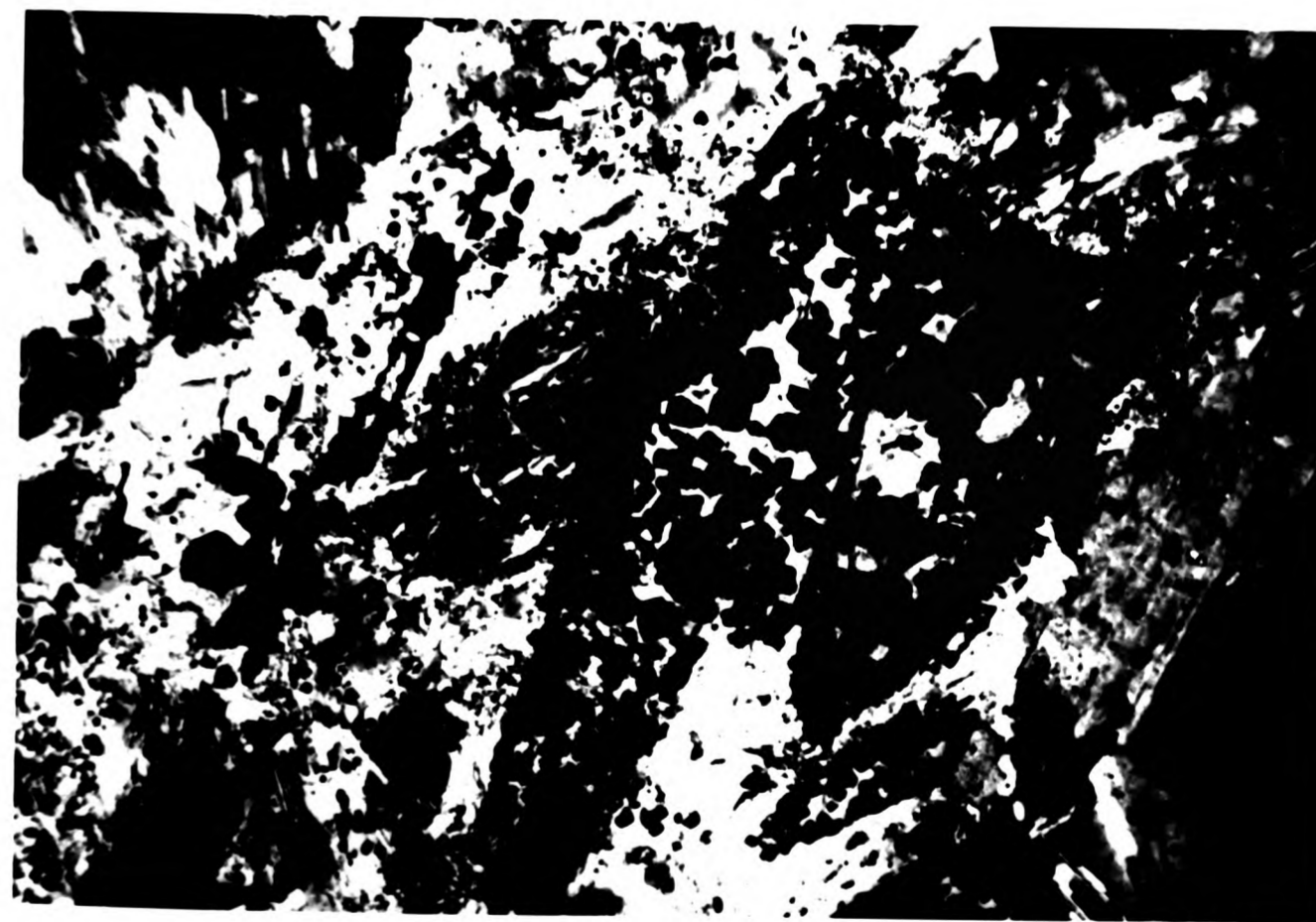


Plate 4.19
Single crystal of brown amphibole poikilitically enclosing
plagioclase oikocrysts. (XPL) Field of view 3mm

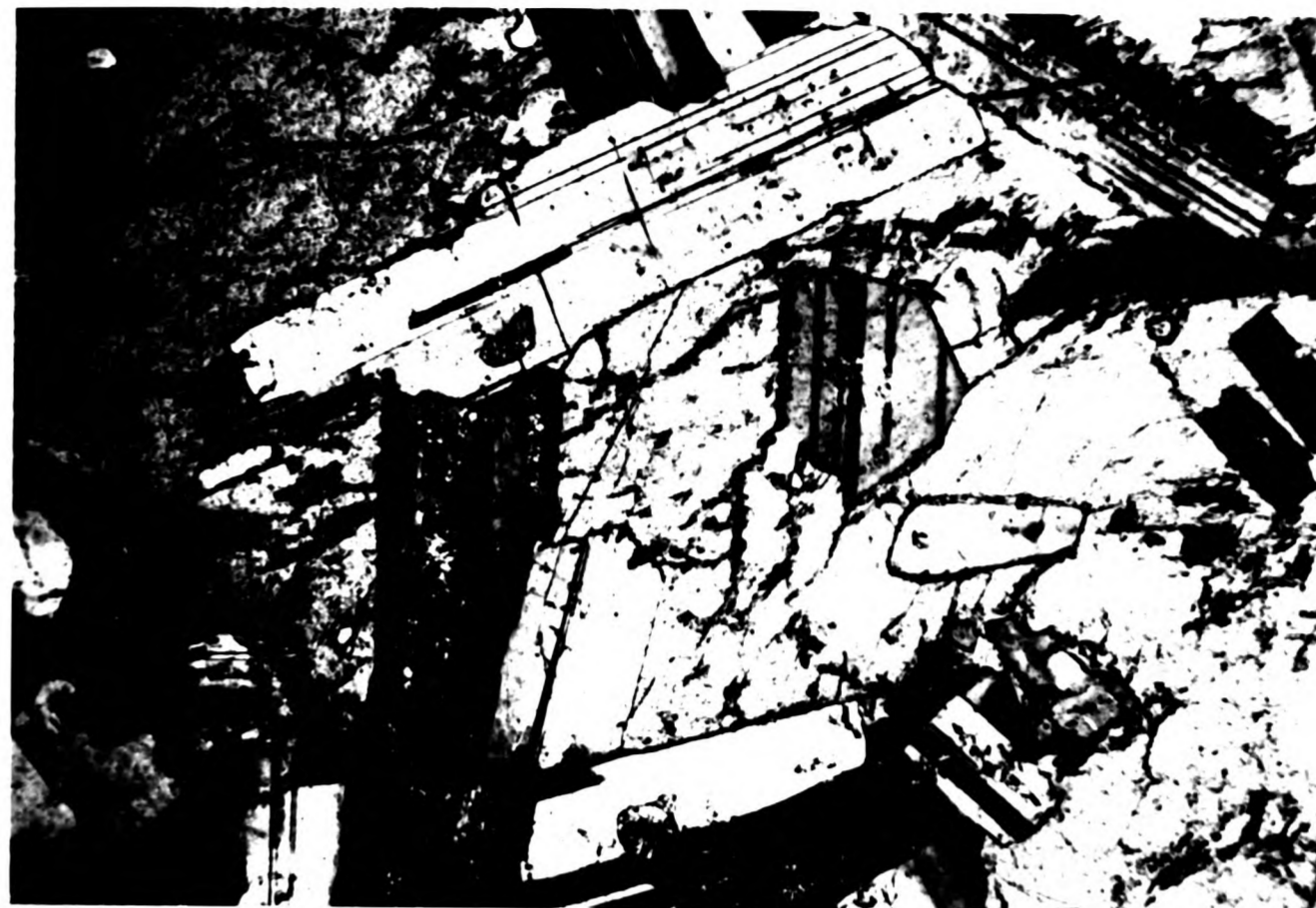
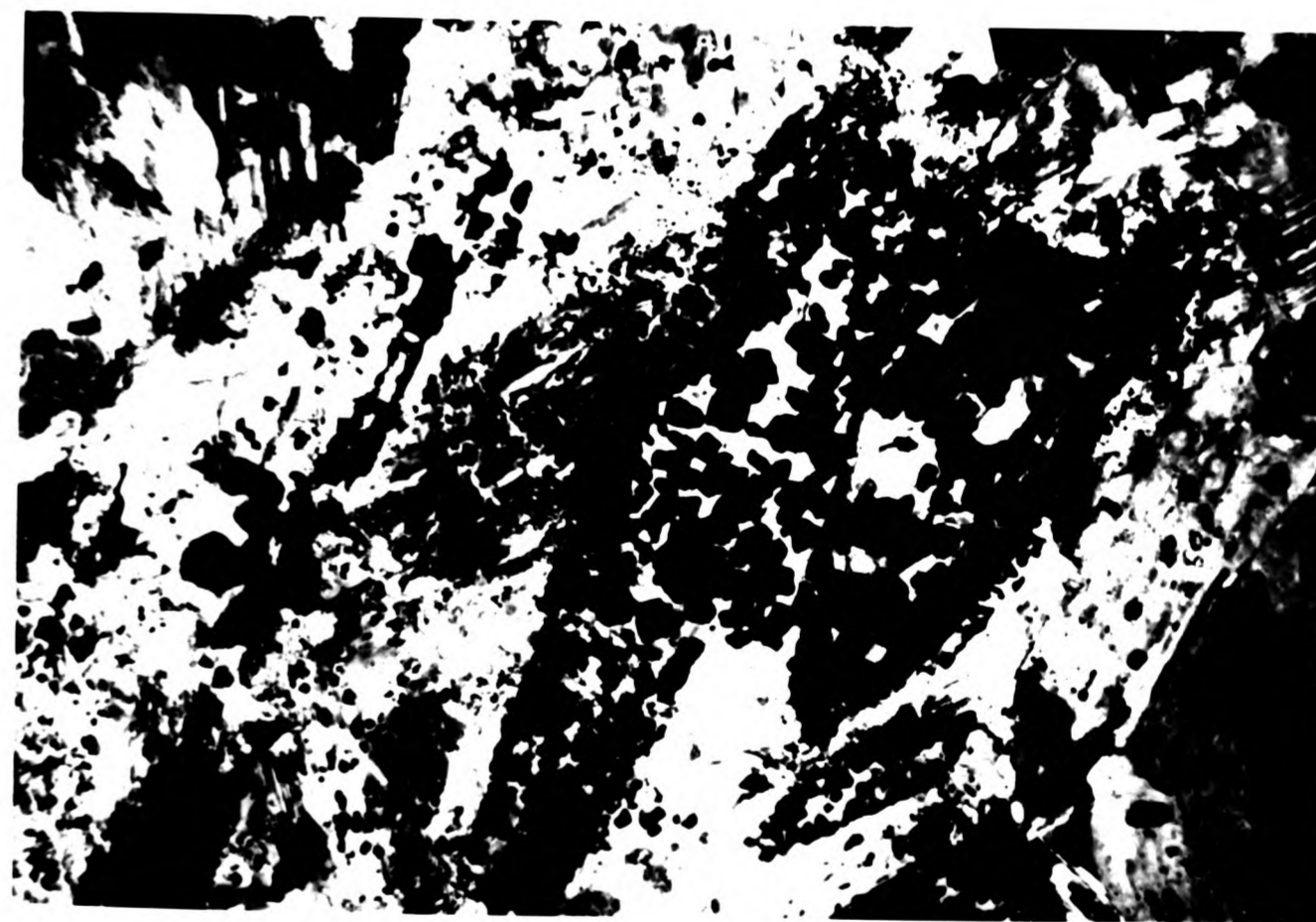


Plate 4.20
Rafted xenolith containing characteristic aggregates of
hercynitic spinel. (PPL) Field of view 3mm



similar to that described in the norite (unit 2a) but in addition the rock contains olivine and primary amphibole.

Olivine is the dominant mafic phase forming 30% of the mode. It typically occurs as small, rounded and highly fractured crystals. The olivine crystals are seen floating in a matrix of opx, amphibole and biotite. The amphibole occurs as large brown poikilitic crystals, forming 20% of the rock, enclosing olivine and pyroxene crystals. Bronzite can occur as large (1.5-2mm long) crystals and typically forms 10% of the rock compared with augite which occurs as small subhedral crystals and forms less than 5%. Plagioclase (An₅₅) is always interstitial and forms only 15% of the mode, the final 20% being biotite. The overall texture is of an olivine orthocumulate.

UNIT 2c: Norite with poikilitic amphibole

The final unit to be considered is a norite containing poikilitic brown amphibole. The textures displayed are variable, from a medium to coarse grained plagioclase orthocumulate (with 55% plagioclase, An₅₄) to a fine to medium grained pyroxene orthocumulate with 45% total pyroxene. Alteration of cpx to green fibrous amphibole is a common feature. Unit 2c is repeated three times through the sequence displayed in Kilbo Burn.

Discussion of the the Kilbo Burn traverse

The sequence displays a range of rock types which are usually of medium grain size. The change from olivine bearing to olivine free facies is abrupt. The alternation of norite and gabbro simply reflects the change in modal abundance of cpx and opx rather than a

textural variation from one rock type to another. A common feature is the large brown poikilitic amphiboles which have crystallised after the olivine, opx and cpx (Plate 4.17 and 4.18). Some sections from both rock types contain abundant secondary green or white fibrous amphibole replacing cpx.

The textures displayed by this series of rock units, indicate that olivine is a primocryst phase in the olivine bearing norite and gabbro. The composition of the olivine is $\sim\text{Fo}_{80}$ in both rock types. This indicates that the magma was only intermittently in the olivine stability field. The return of olivine in the olivine norite (unit 2b) may indicate re-charging of the magma locally. Plagioclase can occur as an early crystallising phase, although some crystals occur which clearly postdate the crystallisation of opx. Plagioclase crystals are typically unzoned although some samples, for example in unit 1b, show normal zoning with broad cores of An_{71} and margins of An_{36} . Normally zoned plagioclase crystals would be expected to crystallise due to falling temperature in the magma. However, unzoned cumulus crystals would not form under these conditions. Tait et al. (1984), propose compositional convection of intercumulus melt in order to form unzoned plagioclase crystals. Convection is propagated by a change in the density of the melt due to the local removal of heavy components. This process allows for the replenishment of intercumulus liquid and thus the lack of zoning which occurs. Crystals showing normal zoning may represent a progressively later stage in which convective fractionation (Sparks et al., 1984) is unable to proceed as trapped intercumulus liquid becomes cut off from the main magma chamber.

Bronzite commonly occurs throughout the series of rocks as

large highly fractured tabular crystals. Their size may indicate a prolonged period of growth. They occur as chadocrysts in poikilitic brown amphibole and therefore predate this phase. Cpx commonly occurs as small rounded crystals often altering extensively to green and white fibrous actinolitic amphibole. Initial crystallisation and accumulation of olivine and opx is frequently followed by cpx. The alteration of cpx and the occurrence of jackets of amphibole on opx crystals indicate the increasing instability of pyroxene accompanied by an increasing stability of an hydrous assemblage. The incoming of primary brown amphibole, poikilitically enclosing all the earlier phases, is indicative of falling temperature and the changing Mg/Mg+Fe ratio of the interstitial liquid. It may also indicate the increasingly hydrous nature of the magma.

The orientation of the layering parallel to the vertical contact is similar to the marginal facies described from other layered intrusions e.g. Skaergaard (Wager and Brown, 1968). The Marginal Border Series of the Skaergaard displays a fine-grained gabbro along the contact with the country rocks. Unfortunately the actual contact is not exposed in the Kilbo Burn, there being 100m of grass before the hornfels rocks are exposed. The most marginal facies is a medium grained olivine gabbro.

Early work by Wager and Brown (1968) suggested that bottom layering in the Skaergaard, formed by convection and crystal settling, however more recent work (McBirney and Noyes, 1979; McBirney, 1979) has shown that the features of layering seen in the Skaergaard are inconsistent with crystal settling. To account for the formation of bottom and wall parallel layering, they propose

in-situ crystallisation involving thermal and chemical diffusion. Crystal settling is an inappropriate mechanism to suggest for the formation of the wall-parallel layering displayed in the gabbroic rocks in the Glen Doll Complex. In-situ crystallisation and convective fractionation could produce the observed textures, such as unzoned plagioclase crystals, and would allow the layering to be formed without the necessity to invoke a mechanism such as large scale convection, for which there is no evidence.

Monzonite and adamellite layers and microdiorite dykes in Kilbo Burn

Figure 3.7 shows the occurrence of three monzonite layers, a thick unit of adamellite and two microdiorite dykes intruded into the sequence of basic rocks. Details of the field relationships are given in Chapter 3. Cutting through unit 1b and 2b, are quartz monzonite layers. They display the same orientation as the basic layers and their contacts are sharp but unchilled. They display the same mineralogy as the monzonite layers described from the south-eastern part of the complex (Section 4.2.2).

A thick (30m) layer of adamellite cuts unit 2c. It is mineralogically and texturally similar to the adamellite margin which persists around much of the complex. Field evidence from elsewhere in the complex (Chapter 3) coupled with geochemical data, suggests that the adamellite post dates the crystallisation of the basic rocks.

The two microdiorite dykes are fine-grained and porphyritic with phenocrysts of plagioclase and secondary amphibole (after

pyroxene). It is thought that they are part of the swarm of micro-diorite dykes which occur throughout the complex and therefore post-date the crystallisation of all the intrusive units.

4.3 Juan Jorge Complex

The range of rock types displayed in this complex is limited to a leucocratic diorite and a pink granite. The rock types are described in order of abundance.

4.3.1 Diorites

The dominant rock type is a coarse grained, homogeneous quartz diorite. The diorite shows minor variations in modal mineralogy. The mineral phases present are biotite, green amphibole, quartz, plagioclase and orthoclase. The dioritic rocks display no evidence of former primary pyroxene.

Amphibole

The modal abundance of amphibole is related to the proximity of the diorite to the Lochnagar granite. The abundance increases away from the contact of the diorite with the outer Lochnagar granite. Crystals are green, typically subhedral, and contain fine grained oxide along their cleavages. They are frequently simply twinned. They commonly occur associated in aggregates with biotite and anhedral or skeletal magnetite. The amphibole is always unzoned. Their length varies from <0.5-4mm. Diorites closest to the diorite/Lochnagar granite contact contain less than 1% amphibole and the abundance grades to a maximum of 15% close to the contact with the pink porphyritic Juan Jorge granite (Figure 3.1).

Biotite

The modal abundance of biotite varies inversely with that of amphibole. Subhedral flakes are often large (<2mm) and may poikil- itically enclose apatite, plagioclase and anhedral magnetite. Crystals are fresh and undeformed. The cleavages are frequently picked out by an oxide phase which has grown along them. Biotite composes 10-20% of the mode.

Feldspar

Plagioclase composes 40-60% of the mode. Tabular euhedral-subhedral crystals are frequently >5mm long though more usually 3-4mm long. The smaller crystals are unzoned (An₄₀) while the large tabular crystals show limited normal (core An₃₃ - rim An₂₅) or patchy sector type zoning. Sections are variably fresh, with alteration being confined to the more calcic cores.

Orthoclase occurs as large <2mm anhedral crystals, commonly highly altered. It composes <2% of the mode. Perthitic textures are common.

Quartz

This mineral always occurs as an interstitial phase, frequently clouded with trails of an opaque mineral. Quartz crystals vary in size from <0.5mm to 3mm in diameter.

Accessory minerals

These include apatite, sphene and magnetite. Magnetite occurs

as rounded or subhedral crystals or may occur as grains along the cleavages of biotite. Sphene occurs in two forms. Some sections contain euhedral lozenge shaped crystals (2mm long) which may be embayed but retain their original crystal shape. They are a uniform pinkish brown colour and are unzoned. Within the same rock sample, sphene may also occur as anhedral interstitial crystals. The two forms represent two generations of growth, a feature described by Noyes et al., (1983) from the Red Lake Pluton, Sierra Nevada. The euhedral crystals of sphene are thought to have crystallised relatively early in the crystallisation history of the rock, while the interstitial crystals are later.

4.3.2 Granite

This rock type occurs in the SE part of the complex -the Juan Jorge granite and in the N-W -the Gourock granite. The granite is typically coarse grained and is composed of orthoclase, quartz, biotite/chlorite and occasional oxide minerals.

Orthoclase

Crystals are commonly <1-4mm long and may be tabular or subhedral. Some occur as pink phenocrysts 4mm long in a medium grained groundmass of orthoclase, quartz and chlorite. The phenocrysts are frequently altered and fresh crystals are rare. Perthitic textures are frequently seen and together with orthoclase, composes 60% of the mode. Plagioclase is not present in this rock type.

Quartz

This mineral is very variable in grain size, from <0.5mm granular crystals to 3mm angular ones. Crystals are commonly clouded and transversed by fine dust trails of magnetite. Quartz composes 35% of the mode.

Biotite

Brown biotite is seen most commonly partially altered to green chlorite. The crystals of biotite, whether composite (biotite-chlorite) or single crystals, are always small, <0.3mm long, anhedral with ragged margins and are interstitial to orthoclase and quartz.

Accessory minerals

Magnetite occurs as anhedral interstitial crystals and composes <0.5% of the mode. Apatite is extremely rare and sphene is absent.

4.5 Bridge Outcrops



Between the Glen Doll and Juan Jorge Complexes is an area of diorite and granite outcrops described in detail in Chapter 3. Its relationship to the other two complexes is unclear but the diorites show characteristics of mineralogy and texture in common with both the Glen Doll hornblende diorite and with the Juan Jorge quartz mica diorites.

The dominant rock type here is a medium grained hornblende diorite which grades towards the contact with the Dalradian country rocks, into a fine grained chilled facies. The former is composed



2mm


Fig. 4.2 Pool of poikilitic quartz enclosing primary amphibole, tabular plagioclase, biotite and apatite needles in a fine-grained diorite at the Bridge

-  Amphibole
-  Apatite
-  Biotite
-  Plagioclase
-  Quartz



2mm

Fig. 4.2 Pool of poikilitic quartz enclosing primary amphibole, tabular plagioclase, biotite and apatite needles in a fine-grained diorite at the Bridge

-  Amphibole
-  Apatite
-  Biotite
-  Plagioclase
-  Quartz

of euhedral to subhedral green or green/brown amphibole. The amphibole crystals are frequently simply twinned and may show a patchy zoning with small brown patches scattered throughout the green crystal. The crystals range in length from <0.1-1mm, and frequently occur in aggregates formed of randomly orientated crystals. Plagioclase (An₃₅) crystals are of a similar size range to the amphibole. They are usually unzoned although normally zoned varieties occur. Amphibole comprises 25% of the mode and plagioclase 60%. Anhedral biotite flakes may be associated with the amphibole aggregates, crystals ranging in size from <0.2-2mm long. Accessory phases are apatite, interstitial anhedral sphene associated with amphibole and biotite and very rare magnetite. Skeletal crystals of sphene are also present. Calcite is commonly seen infilling interstices.

The medium grained diorite grades into a fine grained chill facies. This fine grained diorite contains amphibole, plagioclase, quartz, biotite, orthoclase, sphene and apatite. The amphibole comprises green or green/brown, euhedral and anhedral crystals often occurring as aggregates with biotite and magnetite. Some of the small tabular crystals are zoned with brown cores and green rims. The texture and colour of the amphibole suggests that it is primary and the typical actinolitic amphibole replacing pyroxene present in the diorites in Glen Doll, is absent here. The mafic aggregates occur in a matrix of small (<0.5mm) tabular plagioclase (An₃₇) crystals or totally enclosed in pools of quartz or K-Feldspar 5mm in diameter (Figure 4.2).

At the same locality, but not seen in contact with the diorites, are three pink porphyritic granites with fine grained chills.

These granites are composed of a fine grained granular groundmass of quartz and alkali feldspar, which contains phenocrysts of orthoclase and quartz. These either occur as individual crystals or as large (8mm diameter) crystal aggregates. Orthoclase is frequently altered, particularly in the core region and quartz crystals are clouded with inclusions. Biotite flakes are 1mm in length and occasionally have magnetite crystals around their margins. Interstitial sphene and apatite also occur. Towards the contact of the granites with the country rocks, a chill facies is developed, composed of <0.1mm long quartz and orthoclase with sparse phenocrysts of orthoclase and quartz. Biotite crystals and oxide minerals are rare.

4.4 Xenoliths and dykes from the Glen Doll and Juan Jorge Complexes.

Xenoliths

Four types of xenoliths have been described from the complexes:-

- (a) Rafted metasediments
- (b) Fine-grained metasediments
- (c) Epidiorite
- (d) Microdiorite

(a) Rafted metasediments

This xenolith group displays a varied mineralogy since on a

Plate 4.21
Aggregate of spinel in quartz monzonite. (XPL) Field of view 3mm

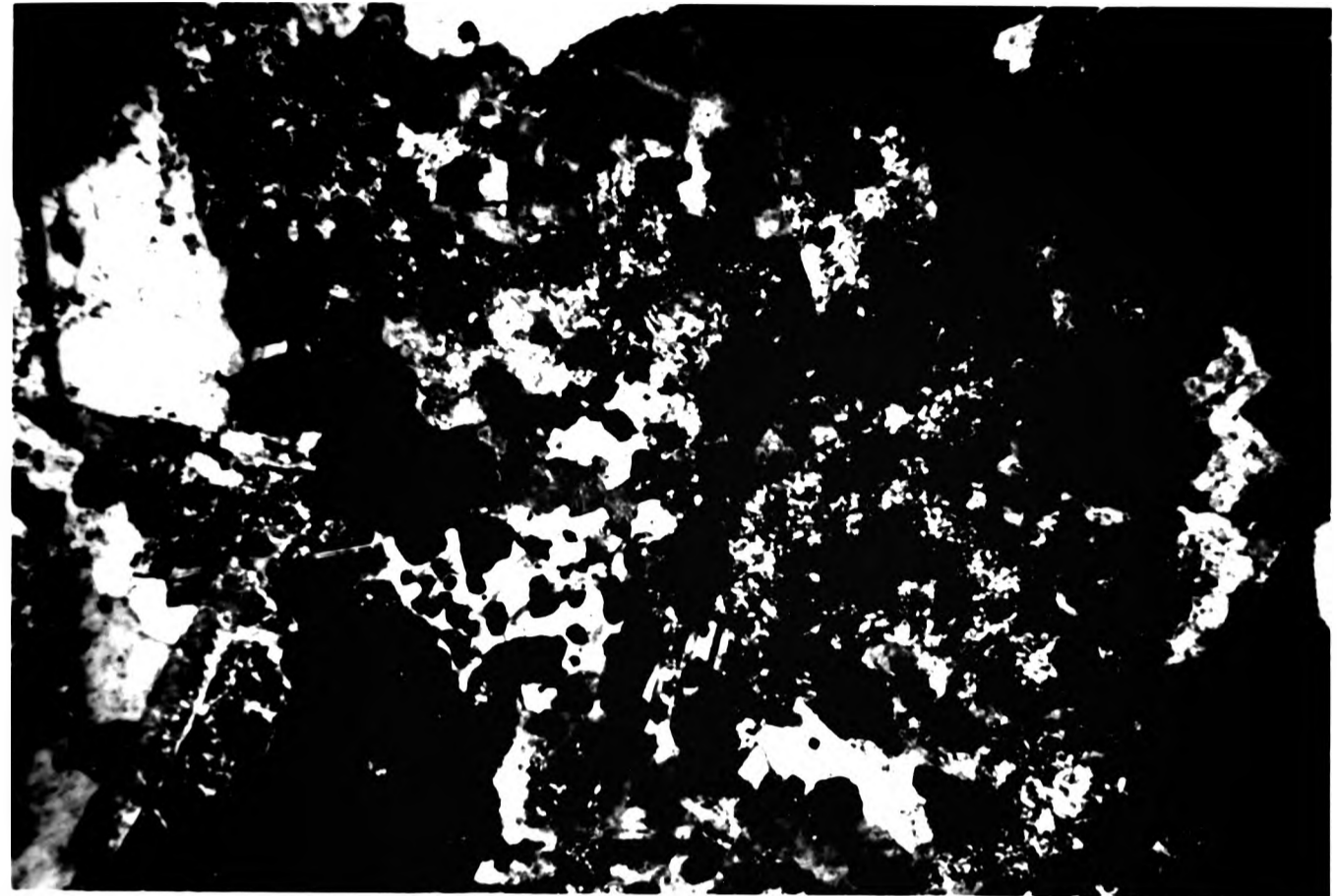


Plate 4.22
General view of a microdiorite xenolith containing plagioclase phenocrysts. (XPL) Field of view 2.2x1.4cm

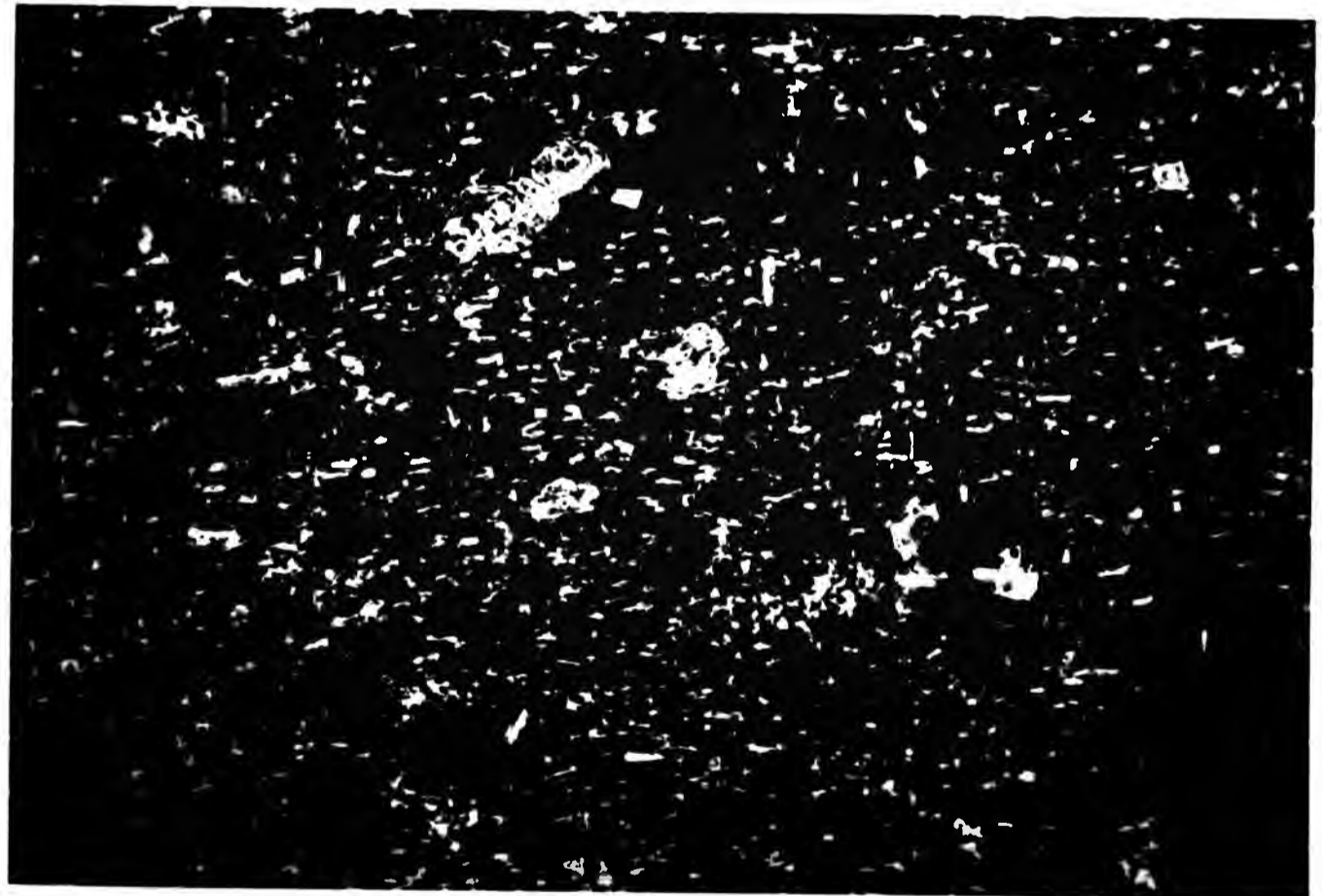


Plate 4.21
Aggregate of spinel in quartz monzonite. (XPL) Field of view 3mm

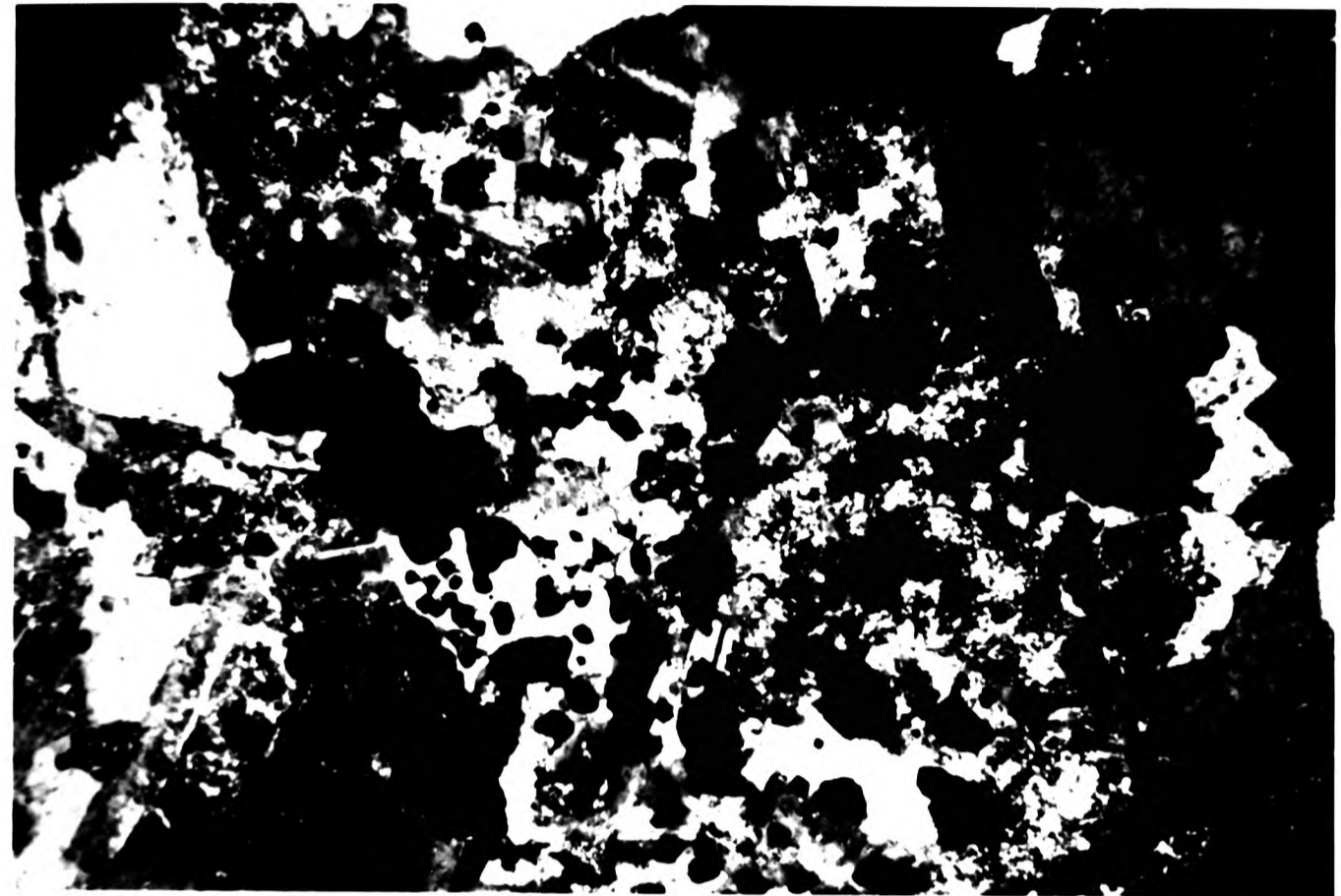


Plate 4.22
General view of a microdiorite xenolith containing plagioclase phenocrysts. (XPL) Field of view 2.2x1.4cm

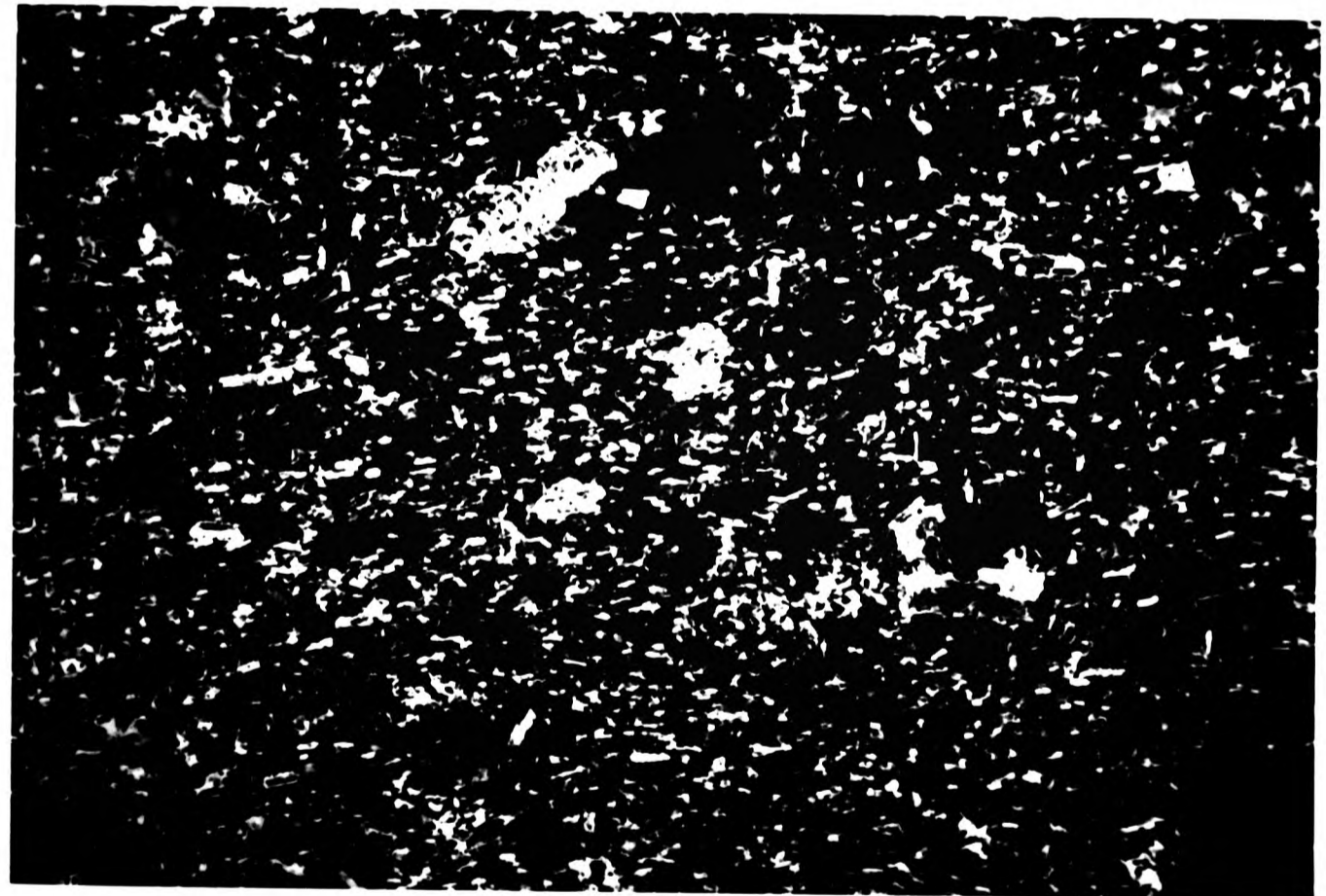


Plate 4.21
Aggregate of spinel in quartz monzonite. (XPL) Field of view 3mm

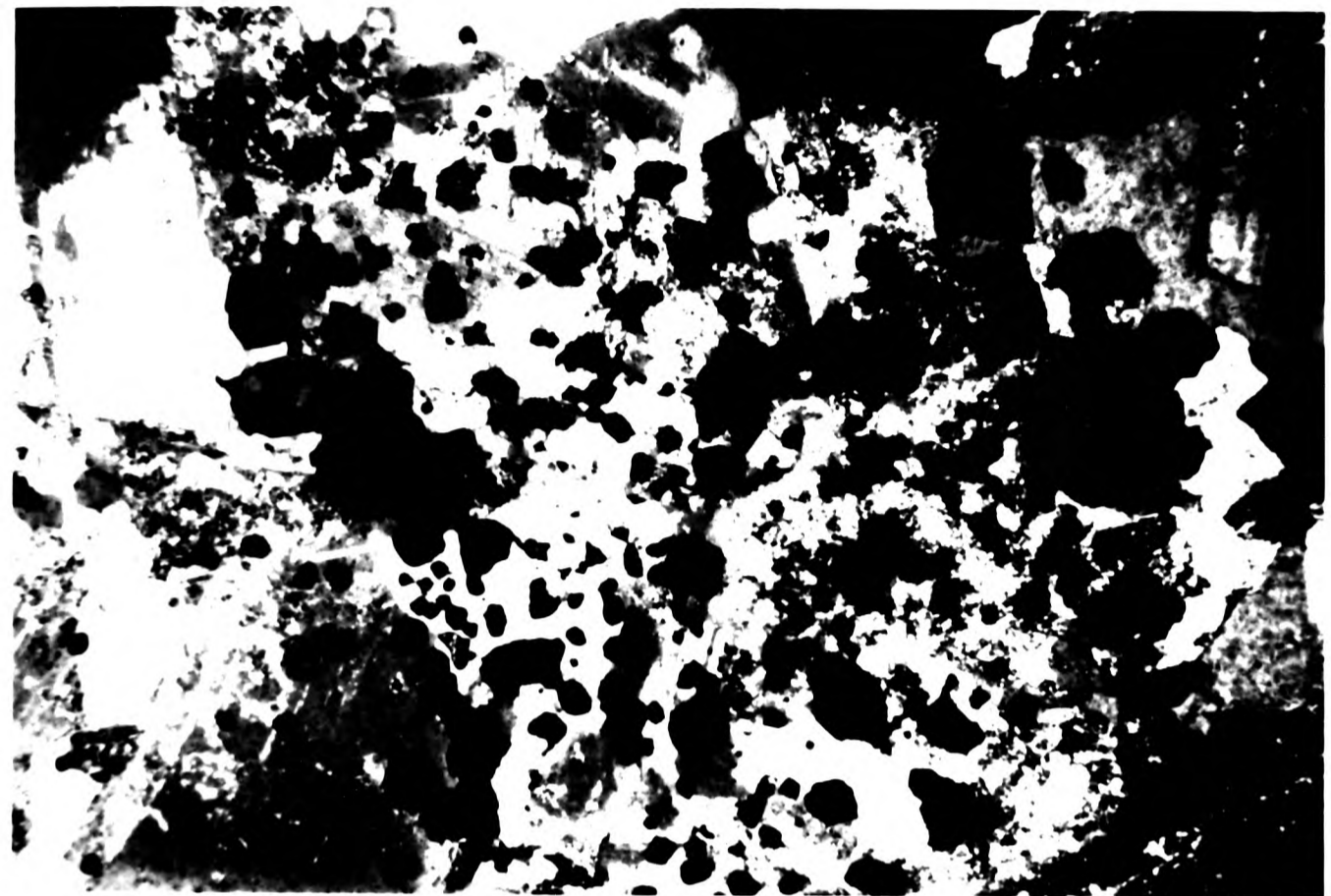
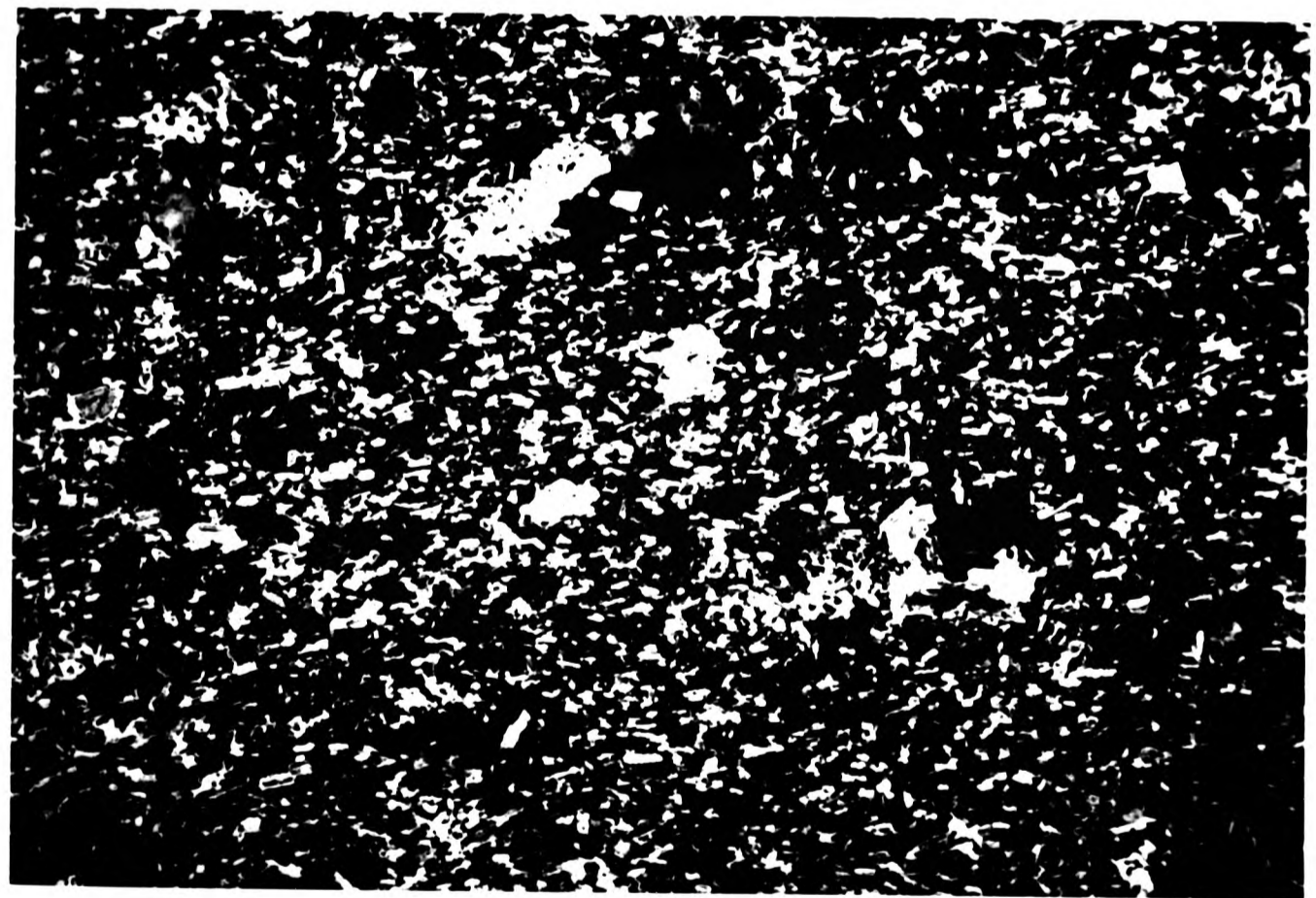


Plate 4.22
General view of a microdiorite xenolith containing plagioclase phenocrysts. (XPL) Field of view 2.2x1.4cm



thin section scale, they are composed of zones of igneous dioritic material "interwoven" with remnants of metasedimentary semi-pelitic material. The layers of metasediment are typically 0.5-1cm thick and are laterally discontinuous. The dioritic material between the semi-pelitic layers is commonly 1cm thick. One feature common to all of this group, is the presence of aggregates of hercynitic spinel (Plate 4.20).

The metasedimentary zones are composed of spinel aggregates, biotite and muscovite with layers entirely composed of quartz and plagioclase feldspar. The diorite associated with them is coarse grained and typically contains large zircons (1mm diameter), sphene (1mm diameter) associated with magnetite, apatite crystals 1-2mm long and 4mm long flakes of biotite. The secondary green amphibole replacing pyroxene has white fibrous cores and is sometimes jacketed by biotite.

The aggregates of hercynitic spinel are green and may occur within the metasedimentary zones or as isolated patches 1-4mm across, in a diorite matrix i.e. being all that remains of a rafted xenolith. These aggregates also occur throughout the Glen Doll diorites and quartz monzonites (Plate 4.21), but are not recorded in the basic rocks nor the adamellite. Rafted xenoliths are not seen in the Juan Jorge Complex. Aggregates of hercynite are considered to be evidence of high level contamination with locally derived metasediment (Pattison and Harte, 1985).

(b) Fine-grained metasediments

This xenolith type occurs only within the adamellite of the Glen Doll Complex but commonly in both the granite and diorite of

Juan Jorge. They are composed of a fine-grained matrix of orthoclase, magnetite and quartz with minor amounts of muscovite. Some examples contain layers rich in small (<0.1mm) flakes of biotite, layers being only 1mm thick. Other examples display a granoblastic texture composed of equigranular diopsidic pyroxene, plagioclase, biotite and quartz. The different mineralogy presumably reflects differences in original composition of the metasediment from which these xenoliths are derived. The origin of these xenoliths is discussed in Chapter 3.

(c) Epidiorite

This xenolith type is restricted to outcrops in the dioritic rocks in the Glen Doll Complex. The texture is of an interlaminated rock (0.5-1mm scale) with alternating layers containing plagioclase and quartz and layers rich in amphibole, diopside or magnetite. The overall texture is of a granular recrystallised rock containing porphyroblasts of brown/green amphibole. The porphyroblasts are 4-5mm in diameter and enclose quartz, plagioclase and muscovite. Remnant subhedral opx (<0.1mm long) crystals occur in some layers and are intimately associated with anhedral magnetite crystals.

(d) Microdiorite

The fourth xenolith type occur extensively in the diorite of the Glen Doll Complex particularly in the White Water river and south of Red Craig, and in the diorites and granites in the Juan Jorge Complex (Chapter 3). They are fine-grained and composed of plagioclase (An₃₁), amphibole, biotite and quartz and are classified as micro diorite (Plate 4.22). Some of these xenoliths in the

Juan Jorge granite contain quartz xenocrysts, a mineralogical feature often seen in rocks formed by magma mixing.

DYKES

Acid

The aplites are fine grained with a characteristic sugary texture. They are composed of equigranular quartz, orthoclase and rarely muscovite. Some may contain phenocrysts of subhedral quartz 0.5mm in diameter.

The quartz-feldspar porphyries have a variable grain size, typically with a fine grained ground mass composed of quartz and orthoclase, with phenocrysts (<4mm diameter) of altered orthoclase and clouded quartz. Yellow iron oxide is seen deposited along crystal boundaries. Biotite also occurs in the groundmass and is commonly altered to chlorite. Some sections display a granophyric texture between large areas of quartz and alkali feldspar. Much of the alkali feldspar is perthitic.

Microdiorite

This rock type is typically fine grained and composed of plagioclase (An₃₂), amphibole, magnetite and biotite in the groundmass with phenocrysts (<1% of the mode) of quartz, plagioclase and secondary amphibole replacing pyroxene.

The groundmass is typically composed of tabular unzoned plagioclase (An₃₅) displaying a random orientation and prismatic pale green amphibole. Plagioclase comprises 50% and amphibole 40% of the mode. Biotite is rarely present and occurs as subhedral

Plate 4.23
Porphyritic microdioritic dyke containing phenocrysts of secondary
amphibole which are thought to be replacement products after
pyroxene. (PPL) Field of view 3mm

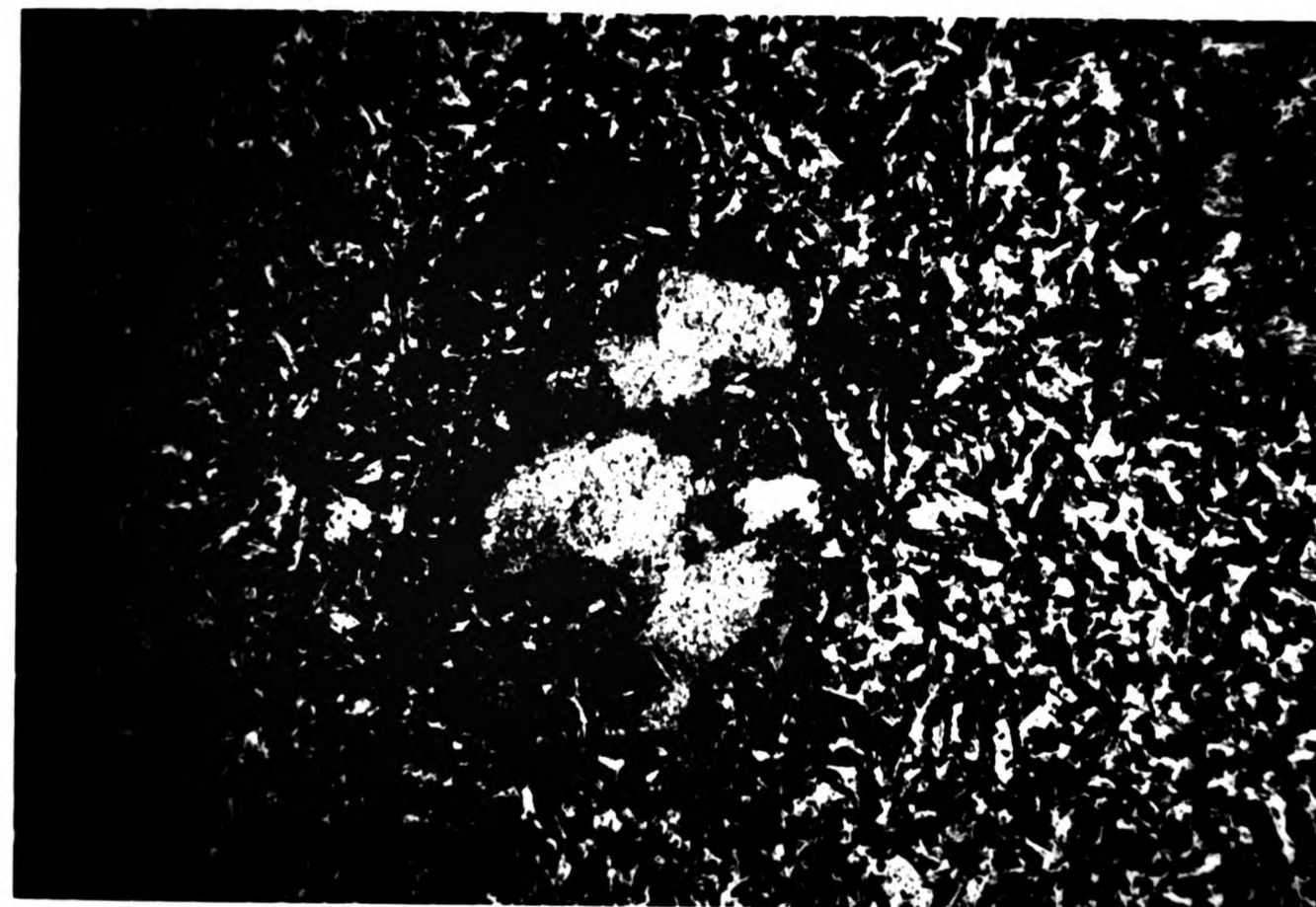


Plate 4.23
Porphyritic microdioritic dyke containing phenocrysts of secondary
amphibole which are thought to be replacement products after
pyroxene. (PPL) Field of view 3mm

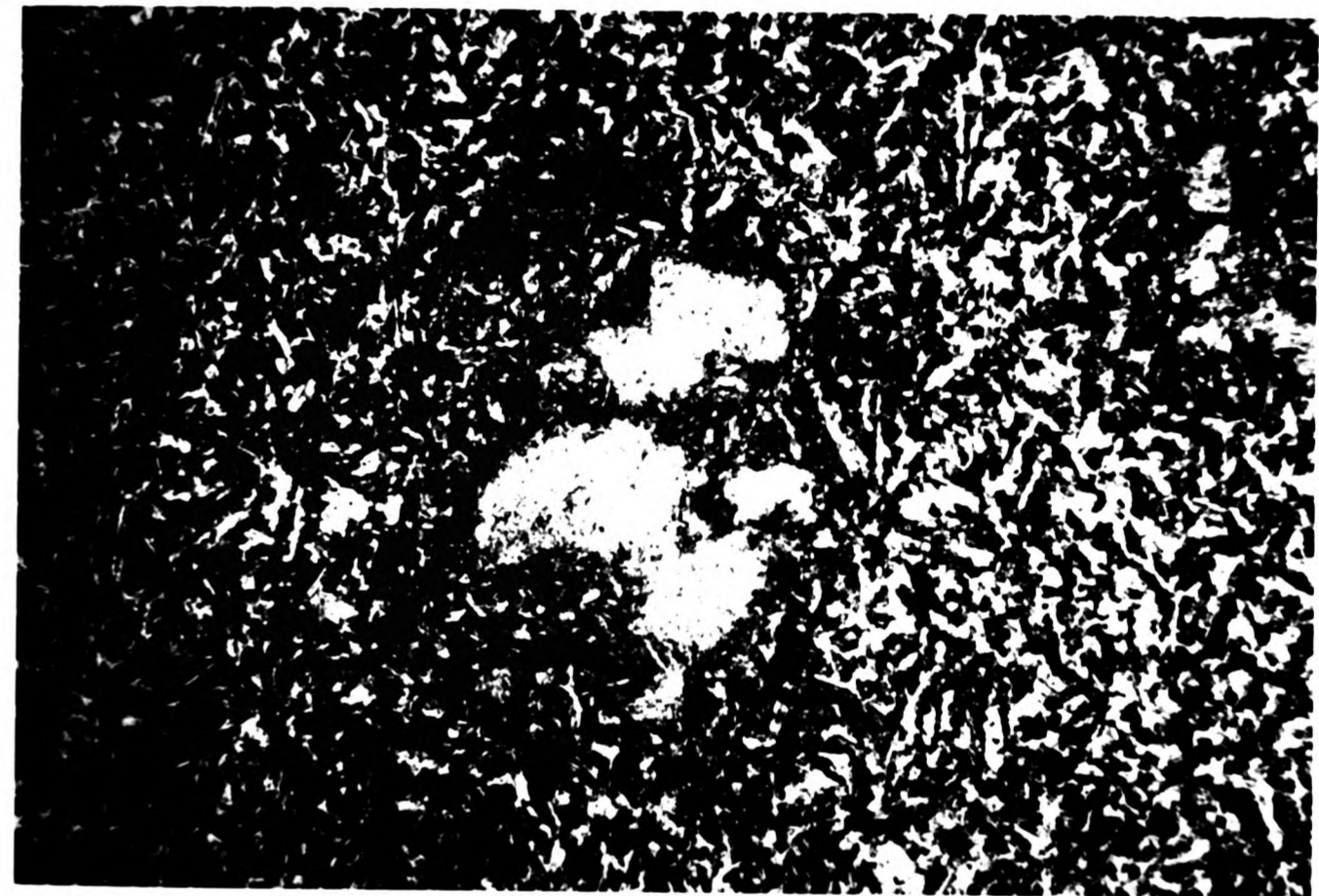
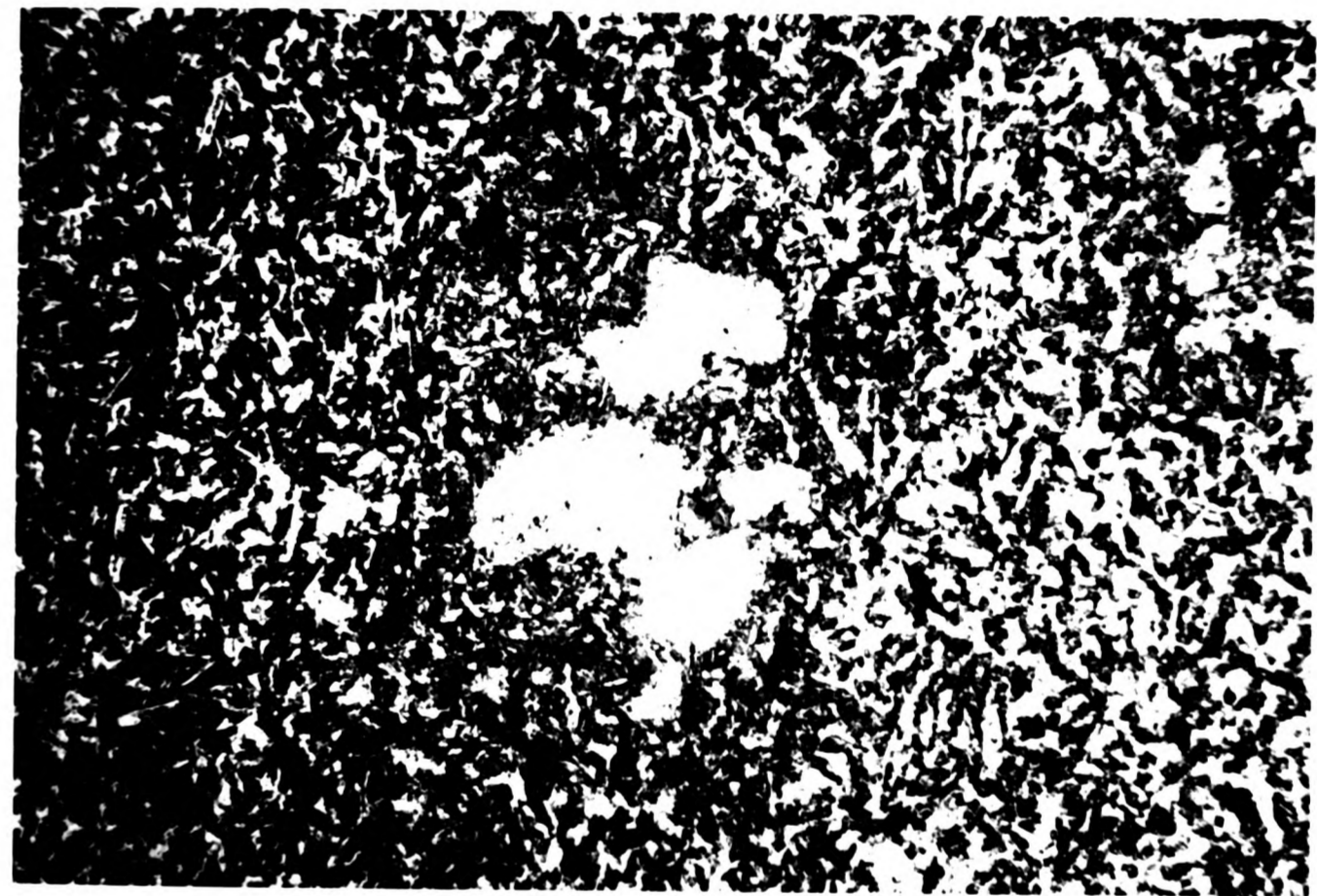


Plate 4.23
Porphyritic microdioritic dyke containing phenocrysts of secondary
amphibole which are thought to be replacement products after
pyroxene. (PPL) Field of view 3mm



flakes. Magnetite occurs as anhedral interstitial crystals.

The crystals of anhedral quartz are usually small (<0.5mm diameter) and have embayed margins perhaps indicating that they are xenocrysts. Plagioclase crystals are larger (1mm long) unzoned and fresh. The amphibole pseudomorphs are typically 2mm long. They are considered to be replacement features after primary amphibole or pyroxene (Plate 4.23).

CHAPTER 5
MINERAL CHEMISTRY

5.1 Introduction

The preceding chapter presented the petrography of the range of rock types seen in the Glen Doll and Juan Jorge Complexes, and at the Bridge outcrops. To characterise the chemical mineralogy and to provide additional information, which can subsequently be used in petrogenetic modelling, the mineral chemistry of the lithologies for each complex has been determined using a wavelength dispersive electron microprobe. The full analytical procedure is outlined in appendix D. A clear understanding of the mineral chemistry is required to fully relate the petrographic data with the bulk rock chemistry.

The silicate phases which have been analysed include olivine, orthopyroxene, clinopyroxene, amphibole, plagioclase and biotite. The accessory phases analysed include apatite, sphene and iron oxides. In total over 400 analyses have been determined from twenty one rocks. The number of analyses from each sample for each mineral phase are given in Table 5.1. Representative analyses are given in each of the following sections. The corresponding bulk rock chemistry for each sample is given in appendix C.

5.2 Amphiboles

The petrographic data (Chapter 4) suggests that both primary magmatic and secondary subsolidus amphiboles occur in the Glen Doll Complex. Textural evidence suggests that the secondary amphibole is a replacement product after pyroxene. A detailed study of the mineral chemistry will provide further evidence to support this

Table 5.1 A table to show the number of microprobe analyses for each sample analysed from the Glen Doll and Juan Jorge Complexes

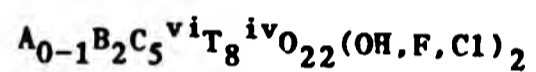
Sample	Rock type	Mineral phase								
		Am	Pl	Bi	Opx	Cpx	Ol	Ap	Ox	Sp
GC21	Monzonite	2	5	6	-	-	-	4	-	-
GC41	Diorite	8	7	-	-	-	-	1	-	1
GC44	Diorite	2	6	4	-	-	-	-	2	-
GC108	Diorite	5	4	3	1	-	-	5	-	6
GC132	Diorite	4	4	1	-	-	-	-	8	2
GC251	Diorite	6	5	5	-	-	-	-	5	4
GC177	Diorite	4	4	-	1	-	-	1	-	4
GC179	Px diorite	11	4	4	-	1	-	-	-	3
GC88	Ol gabbro	4	2	3	5	-	4	-	-	-
GC91	Ol gabbro	7	4	8	6	-	4	-	-	-
GC82	Gabbro	6	7	-	2	2	-	-	-	-
GC161	Gabbro	6	7	2	9	6	-	-	-	-
GC79	Gabbro	2	2	-	7	5	-	-	-	-
GC36	Adamellite	-	7	5	-	-	-	-	-	-
GC26	Xenolith	-	-	-	-	-	-	-	-	6
JJ3	Diorite	2	2	4	-	-	-	-	7	2
JJ4	Diorite	5	5	3	-	-	-	3	11	3
JJ7	Diorite	5	4	3	-	-	-	3	-	3
JJ8	Diorite	6	5	2	-	-	-	4	-	2
JJ17	Granite	-	1	7	-	-	-	5	-	7
JJ19	Xenolith	-	-	-	-	-	-	-	13	3

Note: - = phase not analysed or not present

view and will allow a detailed mineralogical history of the two complexes to be drawn.

5.2.1 Classification of the amphiboles

Traditional optical techniques for determining the composition of amphiboles are restricted by the complex substitutions which occur in the amphibole lattice. The widely adopted nomenclature first proposed by Leake (1978) is used here, with the amphibole formula calculated to 23 oxygens. The allocation of the cations to each site in the formula has been made as shown below. There are eight tetrahedral sites in the formula. The standard amphibole formula is:-



The position used for the allocation of cations follows that recommended by Leake (1978):-

Sum T to 8 using Si, Al then Cr^{3+} , Fe^{3+} and Ti^{4+}

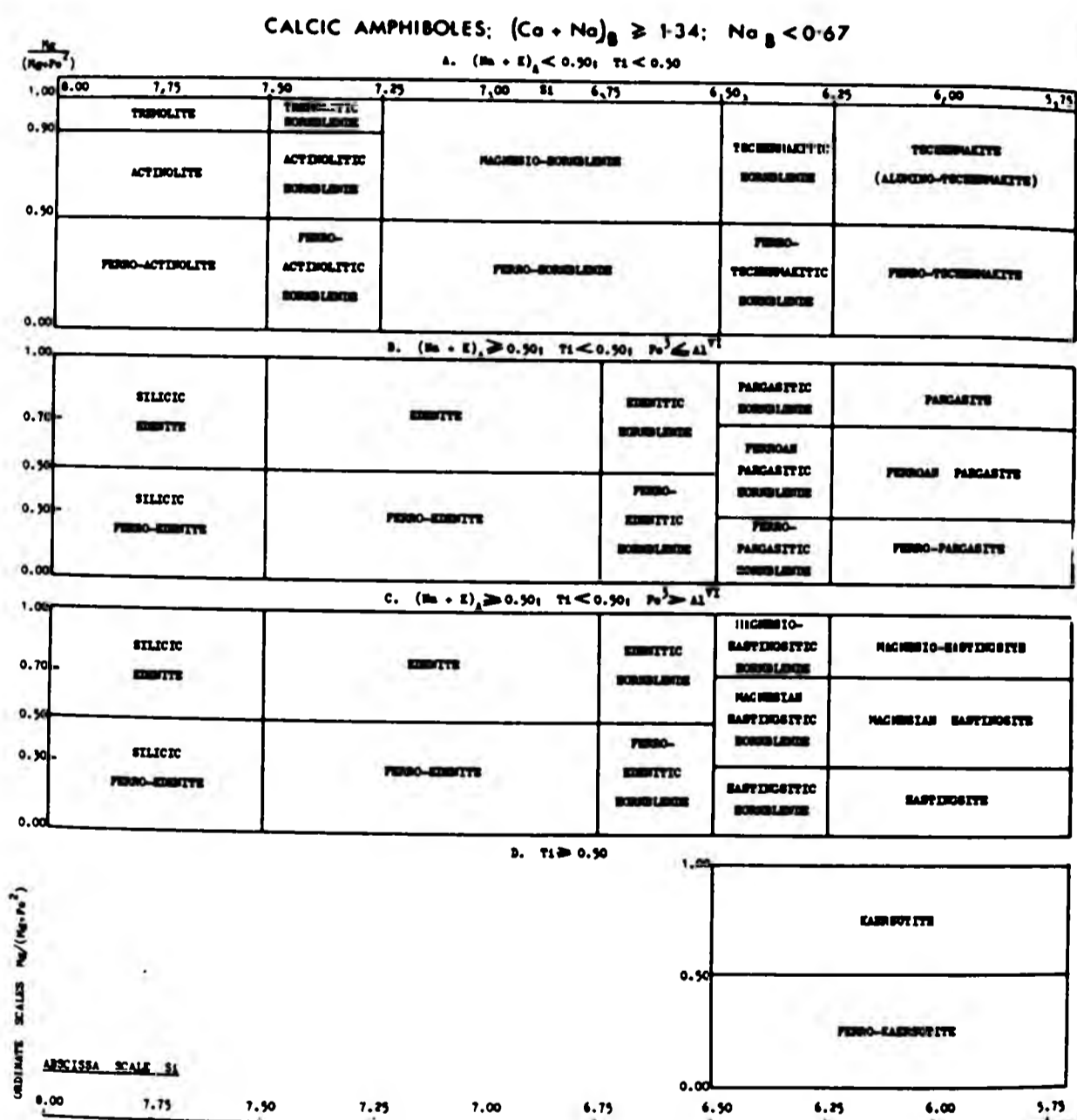
Sum C to 5 using excess Al, Cr, Ti, Fe^{3+} , Mg and Fe^{2+}

Sum B to 2 using excess Fe^{2+} , Mn, Mg, Ca and Na

Sum A to 0-1 using excess Na and K

In the absence of direct measurement techniques for Fe^{2+} or Fe^{3+} , total iron is expressed here as FeO. In the analysed samples iron is not required to fill the T site since there is always an excess of aluminum. All of the iron is allocated to the C site and therefore none is carried over to the B site. Chromium is similarly allocated to the C site.

Table 5.2
 Classification of the calcic amphiboles
 (from Leake, 1978)



Four principal amphibole groups are proposed by Leake (1978) based on the number of cations of (Ca+Na) and Na in the B site (Table 5.2). Of the analysed amphiboles, all fall within the group designated as calcic amphiboles since they have $(Ca+Na)_B$ greater than 1.34 and Na_B less than 0.67. The calcic amphiboles are subdivided on the basis of the atomic ratio $Mg/Mg+Fe^{2+}$, the atomic proportion of silicon and the number of atoms of (Na+K) in the A site and of Ti in the C site (Table 5.2). Many of the analysed samples fall within the top group shown in Table 5.2 although pargasitic and edenitic compositions are recorded. A complete table of analyses for all samples is given in appendix B.

5.2.2 Amphiboles from the diorites and monzonites

Four groups of calcic amphiboles may be recognised in these lithologies on the basis of texture and chemistry:-

- (a) Primary brown (magmatic) amphibole
- (b) Primary green (magmatic) amphibole
- (c) Secondary green or white (subsolidus) amphibole
- (d) Edenitic amphibole

Representatives of more than one group typically coexist in any single rock specimen.

(a) Primary brown (magmatic) amphibole

This type of amphibole occurs in the dioritic rocks from both the Glen Doll and Juan Jorge Complexes. A table of representative analyses is given in Table 5.3. The composition of the brown amphiboles is typically that of ferroan pargasite, pargasitic horn-

blende or magnesio-hornblende. The pargasitic amphiboles contain a relatively high proportion of Al_{iv} (typically 1.51) compared to Al_{vi} (typically 0.23) and more than 0.5 atoms of $(Na+K)_A$ per formula unit (Table 5.2). The $Mg/Mg+Fe^{2+}$ atomic ratio ranges from 0.61-0.66. The magnesio-hornblendes are similarly brown and can occur in the same sample as the pargasitic amphiboles. They contain less Al_{vi} (average of 0.17) and $(Na+K)_A$ than the pargasites but have a similar $Mg/Mg+Fe^{2+}$ atomic ratio of 0.62. Both types of amphibole are frequently zoned, with higher titanium levels in the cores than rims. Analyses 179/AM (Table 5.3) show an example of such zoning, the core containing 1.78% TiO_2 and the rim 1.58% TiO_2 . A corresponding decrease in alumina is observed from 7.01% (core) to 6.45% Al_2O_3 (rim). The pattern reflects the progressive substitution of Al_{vi} for Ti^{4+} in the C site.

(b) Primary green (magmatic) amphibole

This type of amphibole occurs commonly in the Juan Jorge diorites and more rarely in the Glen Doll diorites. The amphiboles are classified as magnesio hornblende and an example from the Juan Jorge diorite is given in Table 5.2. They have an $Mg/Mg+Fe^{2+}$ atomic ratio of 0.5-0.9 and show moderate substitution of Al_{iv} for Si_T^{4+} (average 7.00). The analysed crystals are commonly zoned with higher levels of titanium and iron (e.g 1.76% TiO_2 and 14.37% FeO) in core regions than in the rims (1.01% TiO_2 and 13.6% FeO). This change in chemistry is not reflected by any corresponding change in colour. Titanium and iron commonly substitute for magnesium in the C site, and the decrease in TiO_2 and FeO is accompanied by an increase in MgO from 13.14-13.99% MgO . Sodium varies from 0.8-1.45%, with levels decreasing towards the rims of the crystals.

Potassium shows little variation and is typically around 0.5% K_2O .

(c) Secondary green and white (subsolidus) amphibole

These occur commonly in the Glen Doll diorites and monzonite and rarely in the Juan Jorge diorites. The amphiboles are of fibrous habit and are either green or white. They frequently occur rimmed by magmatic magnesio-hornblende. Their composition is of an actinolitic hornblende or actinolite and some representative analyses are given in Table 5.3. Both of the examples chosen have actinolitic cores with magnesio hornblende rims.

From Table 5.2 one can see that actinolitic amphiboles show little substitution of Al_{iv} for Si and that the $Mg/Mg+Fe^{2+}$ ratio ranges from 0.5-0.9. The analysed samples are frequently zoned with higher titanium levels in the crystal cores than rims (0.82-0.4% TiO_2 for example) although many crystals are unzoned. The characteristic chemical feature of the actinolitic amphiboles studied are that they have low Al_2O_3 , TiO_2 and Na_2O and high SiO_2 and MgO relative to magmatic compositions (Table 5.3). This variation reflects the substitution of magnesium for titanium and aluminium in the C site. The ratio of Al_{vi} to Al_{iv} is greater in the secondary sub-solidus amphiboles than in the primary magmatic varieties.

A study by Haslam (1968) of amphiboles from the Ben Nevis Complex, suggests that secondary amphiboles formed by replacement of pyroxene, contain low total alumina compared with those formed by replacement of primary amphibole. The data from Glen Doll and Juan Jorge is comparable to that from Ben Nevis and provides additional

evidence of a primary mineralogy containing pyroxene.

d) Edenitic amphibole

These compositions typically occur as rims to magnesio-hornblende crystals. They are defined as edenitic since they contain 0.5 atoms of $(\text{Na}+\text{K})_{\text{A}}$, less than 0.5 Ti and an Mg/Mg+Fe ratio of 0.5-1. The substitution of Al_{IV} for Si is restricted to 1.25-1.5 atoms per formula unit.

The edenitic amphiboles are green or green/brown in colour and in this sense they optically resemble the primary magnesio-hornblendes. Table 5.3 shows an example of a magnesio-hornblende core rimmed by edenitic hornblende. A characteristic feature of the edenitic hornblende is the high total alumina (~9% Al_2O_3) and low silica (~43% SiO_2) resulting from the extensive substitution of Al_{IV} for Si_{T} . Titanium and sodium levels are also high, compared with magnesio-hornblende, (2.75% TiO_2 and 1.87% Na_2O) representing the substitution of Ti for Mg_{C} and Na for Ca_{B} . The edenitic amphiboles are of a similar composition to those described from the Glen Tilt Complex (Deer, 1950) from the appinitic facies. The analysed amphiboles contain characteristically high aluminium (~11% Al_2O_3) and low silica (42% SiO_2). These analyses were undertaken using mineral separates and consequently represent the bulk crystal chemistry, therefore zoning is not recorded.

5.2.3 Amphiboles in the gabbroic rocks

The gabbros contain a range of amphibole compositions. Primary green and brown amphiboles are common and secondary amphi-

bole also occurs. Edenitic amphiboles are not recorded in the gabbroic rocks. Brown or brownish-green pargasite and pargasitic hornblende are common. Table 5.3 shows typical analyses for this amphibole type from both an olivine gabbro and gabbro. The pargasitic amphiboles frequently have higher titanium cores (e.g. 3.56% TiO_2) than rims (2.42% TiO_2). Conversely alumina increases from core to rim (e.g. 10.54–13.16% Al_2O_3). The sodium contents of the pargasites are higher in the gabbroic rocks than in the diorites. Sodium also tends to be higher in the olivine gabbro pargasite than in the gabbro pargasite. Both brownish-green pargasites contain less titanium (typically 1.15% TiO_2) than the brown varieties (typically 4.30% TiO_2). The brownish-green and brown pargasites occur together in the same rock. Substitution of iron for magnesium can be extensive and examples of ferroan pargasite are recorded which contain 11.4% FeO and 13.30% MgO (Table 5.3). Exceptionally the atomic proportion of titanium may reach 0.5 (substituting for Al_{vi}) and these amphiboles are classified as kaersutite (Tables 5.2 and 5.3). Less commonly, amphibole of magnesio-hornblende composition occurs. These crystals are occasionally rimmed by actinolitic hornblende.

5.2.4 Amphiboles from the andinitic rocks

The petrographic description of this facies in Chapter 4, notes the occurrence of strongly zoned euhedral amphibole crystals with brown cores and green rims. The cores are composed of tschermakitic or edenitic hornblende and the rims of actinolite or actinolitic hornblende. Some representative analyses are given in Table 5.3. Tschermakitic hornblende is characterised by the substitution of Al for of Fe^{2+} and Fe^{3+} for Mg (Deer et al., 1967).

Fig. 5.1 Titanium plotted against Al(IV) in amphiboles from the Glen Doll and Juan Jorge Complexes

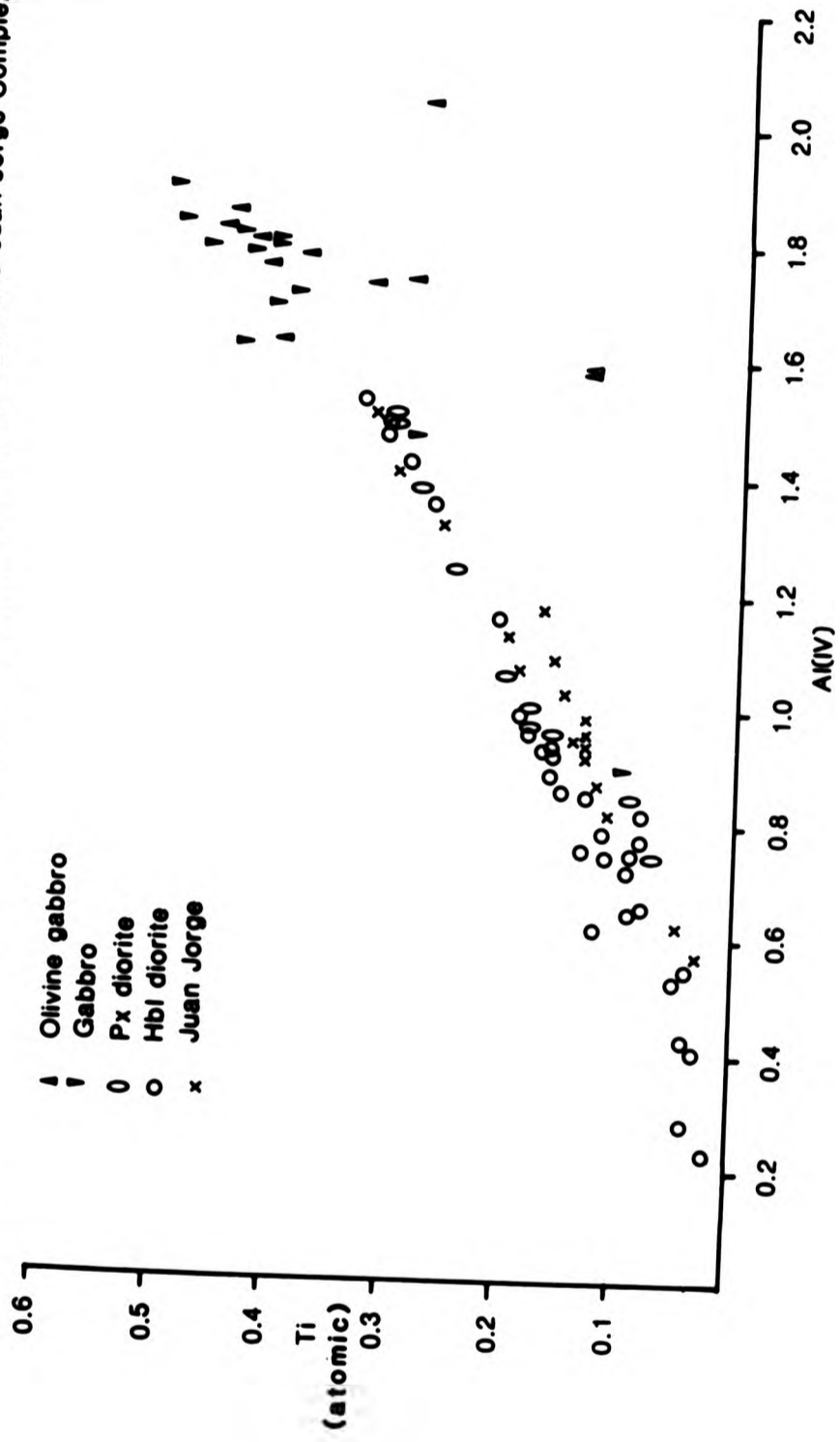


Table 5.3a Representative analyses of secondary and edenitic amphiboles.

	Diorites		Monzonites		Pyroxene diorites		
	251 AM 5C	251 AM 5R	21 AM 121C	21 AM 121R	179 AM 11C	179 AM 11M	179 AM 11R
SiO ₂	50.98	48.77	51.95	50.33	47.75	43.69	43.28
TiO ₂	0.36	0.73	0.38	0.85	1.47	2.79	2.75
Al ₂ O ₃	3.94	5.88	3.25	4.79	6.52	9.64	9.78
*FeO	12.62	13.76	13.76	14.07	12.99	13.54	13.64
MgO	15.30	14.20	15.24	14.78	14.41	13.03	12.71
MnO	0.26	0.19	0.56	0.59	0.24	0.19	0.21
CaO	12.51	12.09	11.08	10.73	11.58	11.32	11.22
Na ₂ O	0.49	0.80	0.66	1.00	1.22	1.85	1.87
K ₂ O	0.22	0.46	0.22	0.29	0.57	0.90	0.92
TOTAL	96.69	96.91	97.09	97.43	96.88	96.97	96.37
Si	7.465	7.193	7.584	7.357	7.050	6.524	6.509
Al(IV)	0.535	0.807	0.416	0.643	0.950	1.476	1.491
Al(VI)	0.145	0.216	0.143	0.182	0.185	0.221	0.243
Ti	0.040	0.081	0.042	0.094	0.163	0.313	0.311
*Fe ²⁺	1.546	1.698	1.680	1.721	1.604	1.691	1.715
Mn	0.032	0.024	0.069	0.074	0.030	0.024	0.027
Mg	3.339	3.122	3.317	3.221	3.174	2.900	2.849
Ca	1.963	1.911	1.733	1.681	1.832	1.811	1.808
Na	0.139	0.229	0.187	0.284	0.349	0.536	0.545
K	0.041	0.087	0.042	0.055	0.107	0.172	0.177

Table 5.3 Representative amphibole analyses from the gabbroic rocks.

	Olivine gabbros			Gabbros				
	91 AM 86C	91 AM 86R	82 AM 42C	82 AM 42R	82 AM 43C	82 AM 43R	161 AM 44C	161 AM 44R
SiO ₂	43.21	38.75	41.36	40.67	48.25	50.00	41.62	41.98
TiO ₂	3.56	2.42	4.33	4.41	0.89	0.70	4.18	3.69
Al ₂ O ₃	10.54	13.16	11.36	11.62	6.16	5.45	11.56	11.75
*FeO	8.26	11.87	10.92	11.44	10.72	10.58	9.88	10.02
MgO	16.04	15.95	13.71	13.39	16.57	16.93	14.32	14.42
MnO	0.13	0.48	0.16	0.20	0.19	0.19	0.15	0.15
CaO	10.52	7.95	11.62	11.40	11.47	11.67	11.05	11.58
Na ₂ O	2.84	2.30	2.00	1.89	0.94	0.82	1.84	2.21
K ₂ O	0.49	0.31	0.88	0.87	0.52	0.42	0.60	0.80
TOTAL	95.59	93.18	96.33	95.89	95.71	96.75	95.54	96.84
Si	6.385	5.964	6.179	6.122	7.110	7.256	6.220	6.208
Al(IV)	1.615	2.036	1.821	1.878	0.890	0.744	1.780	1.792
Al(VI)	0.221	0.352	0.181	0.184	0.181	0.189	0.256	0.257
Ti	0.396	0.280	0.487	0.500	0.099	0.077	0.470	0.411
*Fe ²⁺	1.022	1.528	1.365	1.441	1.321	1.284	1.235	1.240
Mn	0.016	0.063	0.020	0.025	0.024	0.024	0.019	0.019
Mg	3.533	3.659	3.052	3.005	3.640	3.661	3.190	3.179
Ca	1.667	1.311	1.859	1.839	1.812	1.815	1.770	1.835
Na	0.813	0.687	0.578	0.553	0.269	0.231	0.533	0.634
K	0.093	0.061	0.168	0.167	0.098	0.078	0.114	0.151

Table 5.3c Representative analyses of amphiboles from appinitic rocks.

	30 AM 3C	30 AM 3R	30 AM 9C	30 AM 9R
SiO ₂	42.24	51.66	44.00	51.97
TiO ₂	3.79	0.48	2.53	0.30
Al ₂ O ₃	10.72	3.84	9.95	3.36
*FeO	11.07	10.04	10.68	9.15
MgO	14.13	17.63	15.04	18.38
MnO	0.14	0.27	0.16	0.27
CaO	11.14	11.36	11.17	11.22
Na ₂ O	2.48	0.89	2.10	0.84
K ₂ O	0.57	0.20	0.56	0.20
TOTAL	96.27	96.37	96.18	95.67
Si	6.298	7.478	6.518	7.539
Al(IV)	1.702	0.522	1.482	0.461
Al(VI)	0.182	0.134	0.256	0.114
Ti	0.425	0.053	0.283	0.033
*Fe ²⁺	1.380	1.216	1.323	1.110
Mn	0.018	0.034	0.020	0.033
Mg	3.141	3.803	3.322	3.973
Ca	1.780	1.762	1.774	1.744
Na	0.718	0.251	0.603	0.236
K	0.109	0.038	0.107	0.038

Table 5.4 Representative analyses of pyroxenes from the Glen Doll Complex.

	Olivine gabbros				Gabbros				Diorite			
	88 PX 101C	88 PX 101R	79 PX 38C	79 PX 38R	161 PX 72C	161 PX 72R	108 PX 56C	108 PX 56C				
SiO ₂	54.96	55.84	53.53	53.43	53.81	52.86	52.65	52.65				
TiO ₂	0.21	0.06	0.37	0.37	0.36	0.20	0.30	0.30				
Al ₂ O ₃	1.31	1.05	1.54	1.46	1.37	0.77	1.18	1.18				
*FeO	11.88	11.67	14.82	15.33	13.93	15.70	18.72	18.72				
MgO	30.16	30.34	27.68	27.29	28.12	26.37	24.20	24.20				
MnO	0.21	0.20	0.34	0.36	0.37	0.40	0.52	0.52				
CaO	1.00	0.91	0.98	1.19	1.37	0.95	1.11	1.11				
Na ₂ O	BD	BD	0.03	0.02	0.03	0.03	0.02	0.02				
Cr ₂ O ₃	0.06	BD	0.05	0.03	0.03	0.04	BD	BD				
TOTAL	99.78	100.17	99.32	99.45	99.39	97.30	98.69	98.69				
Si	1.955	1.972	1.942	1.942	1.945	1.967	1.960	1.960				
Al(IV)	0.045	0.028	0.058	0.058	0.055	0.033	0.040	0.040				
Al(VI)	0.010	0.016	0.008	0.004	0.003	0.001	0.011	0.011				
Ti	0.006	0.002	0.010	0.010	0.058	0.006	0.008	0.008				
Cr	0.002	-	0.001	0.001	0.001	0.001	-	-				
*Fe ²⁺	0.354	0.345	0.450	0.466	0.421	0.489	0.583	0.583				
Mn	0.007	0.007	0.011	0.011	0.112	0.013	0.016	0.016				
Mg	1.599	1.603	1.496	1.478	1.515	1.463	1.342	1.342				
Ca	0.038	0.035	0.038	0.046	0.053	0.038	0.044	0.044				
Na	-	-	0.002	0.001	0.002	0.002	0.002	0.002				
Wo	1.90	1.76	1.90	2.30	2.66	1.88	2.23	2.23				
En	80.00	80.55	75.03	73.85	75.73	73.08	67.61	67.61				
Fs	18.10	17.69	23.07	23.84	21.62	24.05	30.16	30.16				

Table 5.5 Representative olivine analyses from the Glen Doll Complex.

Element (%)	Sample				
	Olivine gabbros				
	88 OL 101C	88 OL 102C	88 OL 104C	91 OL 108C	91 OL 109C
SiO ₂	38.61	38.15	38.62	38.66	39.28
Al ₂ O ₃	0.06	0.03	0.02	0.01	0.02
*FeO	18.65	19.98	19.25	18.06	17.21
MgO	41.33	41.07	41.60	42.24	42.77
MnO	0.34	0.29	0.25	0.27	0.25
CaO	BD	0.02	BD	BD	BD
NiO	BD	0.05	0.04	0.18	0.20
TOTAL	98.99	99.58	99.78	99.43	99.71
Si	0.998	0.988	0.993	0.993	1.001
Al	0.002	0.001	0.001	-	0.001
Ni	-	0.001	0.001	0.004	0.005
*Fe ²⁺	0.404	0.433	0.414	0.388	0.367
Mn	0.008	0.007	0.006	0.006	0.006
Mg	1.592	1.585	1.594	1.617	1.624
Ca	-	0.001	-	-	-
Wo	-	-	-	-	-
En	79.44	78.23	79.15	80.41	81.32
Fs	20.56	21.77	20.85	19.59	18.68
Fo	69	67	68	70	71

Table 5.6 Representative biotite analyses from the Glen Doll and Juan Jorge Complexes.

	Olivine gabbros			Gabbro			Pyroxene diorite			Diorites		
	88 BI 97C	88 BI 97R	38.48	161 BI 56C	179 BI 35C	179 BI 36R	44 BI 36C	44 BI 36R	251 BI 8C	251 BI 8R	44 BI 36R	44 BI 36R
SiO ₂	37.61	38.48	36.96	36.96	35.48	36.81	35.07	36.44	36.61	36.24	36.44	36.61
TiO ₂	0.76	0.84	5.25	5.25	5.17	5.06	3.67	4.66	4.69	4.38	4.66	4.69
Al ₂ O ₃	14.72	15.01	14.68	14.68	14.05	14.02	13.38	13.61	14.20	14.07	13.61	14.20
*FeO	7.34	7.16	11.90	11.90	18.40	18.75	18.82	16.03	18.14	18.36	16.03	18.14
MgO	22.56	22.17	16.27	16.27	11.61	12.21	12.96	13.81	11.95	11.79	13.81	11.95
MnO	0.02	0.05	0.11	0.11	0.15	0.13	0.16	0.17	0.18	0.17	0.17	0.18
CaO	0.01	0.01	BD	BD	BD	BD	0.06	0.03	BD	BD	0.03	BD
Na ₂ O	1.34	1.27	0.12	0.12	0.15	0.13	0.07	0.07	0.16	0.17	0.07	0.16
K ₂ O	7.69	8.04	9.23	9.23	9.25	9.38	7.87	9.09	9.29	9.35	9.09	9.29
F	BD	0.03	0.25	0.25	BD	BD	BD	0.01	BD	BD	0.01	BD
TOTAL	92.04	93.05	94.93	94.93	94.26	96.57	92.05	93.93	95.21	94.52	93.93	95.21
Si	5.830	5.893	5.722	5.722	5.480	5.555	5.776	5.821	5.570	5.570	5.821	5.570
Al(IV)	2.170	2.107	2.278	2.278	2.520	2.445	2.224	2.179	2.430	2.430	2.179	2.430
Al(VI)	0.521	0.603	0.400	0.400	0.038	0.048	0.374	0.387	0.116	0.117	0.387	0.116
Ti	0.089	0.097	0.611	0.611	0.600	0.574	0.455	0.561	0.537	0.506	0.561	0.537
Fe ²⁺	0.952	0.918	1.541	1.541	2.377	2.316	2.592	2.141	2.309	2.360	2.141	2.309
Mn	0.003	0.007	0.015	0.015	0.020	0.017	0.022	0.024	0.023	0.022	0.024	0.023
Mg	5.212	5.060	3.755	3.755	2.672	2.746	3.181	3.288	2.709	2.700	3.288	2.709
Ca	0.002	0.001	-	-	-	-	0.011	0.006	-	-	0.006	-
Na	0.402	0.378	0.035	0.035	0.044	0.037	0.024	0.023	0.048	0.049	0.023	0.048
K	1.521	1.571	1.823	1.823	1.821	1.806	1.653	1.852	1.803	1.843	1.852	1.803

Table 5.6 (cont.)

	Monzonite		Adamellite	
	21 BI 120C	21 BI 120R	36 BI 25C	36 BI 25R
SiO ₂	36.66	37.30	36.34	36.90
TiO ₂	4.20	4.39	4.91	4.73
Al ₂ O ₃	13.41	13.26	13.00	12.90
*FeO	19.38	19.13	15.94	15.42
MgO	12.10	12.37	14.00	14.40
MnO	0.18	0.17	0.29	0.28
CaO	BD	BD	0.03	0.03
Na ₂ O	0.10	0.12	0.07	0.08
K ₂ O	9.19	9.39	9.26	9.10
F	0.14	0.06	0.14	0.08
TOTAL	95.47	96.18	93.98	93.91
Si	5.862	5.904	5.825	5.886
Al(IV)	2.138	2.096	2.175	2.114
Al(VI)	0.389	0.378	0.282	0.310
Ti	0.505	0.523	0.593	0.568
Fe ²⁺	2.592	2.533	2.137	2.057
Mn	0.025	0.023	0.04	0.038
Mg	2.908	2.918	3.344	3.424
Ca	-	-	0.005	0.005
Na	0.030	0.038	0.023	0.024
K	1.876	1.896	1.895	1.852

Table 5.6 (cont.)

	Granites (Juan Jorge Complex)		Diorites (Juan Jorge Complex)			
	JJ17 BI 52C	JJ17 BI 52R	JJ3 BI 29C	JJ3 BI 29R	JJ4 BI 61C	JJ4 BI 61R
SiO ₂	36.30	37.22	36.71	37.01	35.07	36.82
TiO ₂	4.45	4.02	4.14	3.88	3.96	3.98
Al ₂ O ₃	13.62	13.49	14.02	14.03	13.74	14.23
*FeO	17.71	17.40	17.18	17.57	16.99	16.74
MgO	12.58	13.24	13.05	12.98	13.52	13.69
MnO	0.50	0.47	0.28	0.35	0.31	0.30
CaO	BD	BD	BD	BD	BD	BD
Na ₂ O	0.12	0.07	0.10	0.08	0.09	0.09
K ₂ O	9.22	9.44	9.13	8.95	8.87	8.88
F	BD	BD	BD	BD	BD	BD
TOTAL	94.50	95.35	94.61	94.84	92.54	94.72
Si	5.570	5.643	5.592	5.623	5.481	5.579
Al(IV)	2.430	2.358	2.408	2.377	2.519	2.421
Al(VI)	0.0329	0.053	0.110	0.136	0.012	0.120
Ti	0.514	0.458	0.474	0.443	0.466	0.453
Fe ²⁺	2.274	2.206	2.188	2.233	2.221	2.121
Mn	0.064	0.060	0.036	0.045	0.041	0.039
Mg	2.878	2.992	2.964	2.940	3.150	3.092
Ca	-	-	-	-	-	-
Na	0.035	0.020	0.03	0.024	0.026	0.028
K	1.806	1.826	1.774	1.734	1.768	1.716

Table 5.7 Representative plagioclase analyses from the Glen Doll and Juan Jorge Complexes.

	Olivine gabbros			Gabbros			Diorites		
	88 PL 198C	88 PL 198R	82 PL 47C	82 PL 47R	44 PL 34C	44 PL 34R	44 PL 34M	108 PL 58C	108 PL 58R
SiO ₂	54.40	53.35	47.90	53.53	54.63	53.34	54.58	52.18	59.40
TiO ₂	0.01	0.05	0.05	0.02	0.05	0.08	0.08	BD	BD
Al ₂ O ₃	27.01	28.89	31.98	28.61	27.58	27.51	27.57	29.42	25.29
*FeO	1.01	0.20	0.38	0.30	0.29	0.30	0.30	0.37	0.25
MgO	1.50	0.03	0.03	0.03	0.02	0.02	0.03	0.02	0.02
CaO	9.36	11.71	15.65	11.16	9.85	9.89	9.97	11.74	6.64
Na ₂ O	5.59	4.95	2.46	5.00	5.84	5.83	5.86	4.08	6.01
K ₂ O	0.04	0.07	0.07	0.19	0.26	0.26	0.25	0.22	0.37
TOTAL	98.92	99.22	98.51	98.84	98.52	98.22	98.65	98.02	97.97
Ab	51.8	43.2	22.0	44.3	51	50.8	50.8	38.1	60.6
Or	0.3	0.4	0.4	1.2	1.5	1.5	1.4	1.4	2.5
An	47.9	56.4	77.6	54.5	47.5	47.7	47.8	60.6	37.0

Table 5.7 (cont.)

	Monzonite			Adamellite	
	21 PL 78C	21 PL 78R	21 PL 78M	36 PL 29C	36 PL 29R
SiO ₂	60.06	57.87	60.14	57.85	61.91
TiO ₂	BD	0.02	0.01	0.04	0.01
Al ₂ O ₃	24.07	25.70	24.11	25.86	22.99
*FeO	0.23	0.19	0.13	0.40	0.12
MgO	BD	0.02	0.02	0.02	0.01
CaO	5.59	6.91	5.51	7.76	4.29
Na ₂ O	8.06	7.24	8.33	6.97	8.89
K ₂ O	0.47	0.35	0.29	0.33	0.24
TOTAL	98.48	98.30	98.53	99.22	98.45
Ab	70.3	64.1	72.0	60.7	77.9
Or	2.7	2.1	1.7	1.9	1.3
An	27.0	33.8	26.3	37.4	20.8

Table 5.7 (cont.)

	Diorites (Juan Jorge Complex)						Granite		
	JJ8 PL 33R	JJ7 PL 26C	JJ7 PL 26R	JJ8 PL 32C	JJ8 PL 33C	JJ17 PL 43C			
SiO ₂	57.70	59.28	60.34	57.61	56.89	63.92			
TiO ₂	BD	BD	BD	BD	BD	BD			
Al ₂ O ₃	24.93	25.66	24.70	26.63	26.92	23.49			
*FeO	0.26	0.22	0.26	0.23	0.23	0.23			
MgO	0.03	BD	0.01	0.02	0.02	0.23			
CaO	6.44	6.78	5.35	7.98	8.44	BD			
Na ₂ O	5.88	4.88	4.99	4.84	5.34	3.41			
K ₂ O	0.33	0.21	0.23	0.31	0.30	5.39			
TOTAL	95.48	97.02	95.89	97.63	98.15	96.82			
Ab	60.6	55.7	61.6	51.2	52.3	71.7			
Or	2.3	1.6	1.9	2.2	2.0	3.3			
An	37.1	42.7	36.5	46.7	45.7	25.0			

Table 5.8 Representative oxide analyses from the Glen Doll and Juan Jorge Complexes.

	Pyroxene diorite		Diorites	
	179 OX 11C	132 OX 32C	132 OX 33C	108 OX 66C
SiO ₂	0.05	BD	0.03	1.25
TiO ₂	0.22	48.77	0.09	0.09
Al ₂ O ₃	0.22	0.03	0.23	0.07
*FeO	-	47.63	-	-
*Fe ₂ O ₃	99.98	-	99.36	99.09
MgO	0.05	0.14	BD	0.21
MnO	0.04	1.53	0.01	0.10
Cr ₂ O ₃	0.03	0.03	0.05	0.03
TOTAL	100.59	98.13	99.77	100.84

	Rafted xenolith			Diorites (Juan Jorge Complex)	
	26 OX 68C	26 OX 68R	26 OX 70C	JJ4 OX 69C	JJ8 OX 77C
SiO ₂	BD	1.31	BD	0.07	0.04
TiO ₂	BD	0.04	BD	0.10	0.07
Al ₂ O ₃	59.08	58.68	59.13	0.26	0.11
*FeO	27.93	25.28	28.22	-	-
*Fe ₂ O ₃	-	-	-	98.08	99.17
MgO	11.92	12.21	11.76	0.05	0.03
MnO	0.33	0.30	0.28	0.09	0.06
Cr ₂ O ₃	BD	BD	BD	0.76	0.33
TOTAL	99.26	97.83	99.39	99.41	99.81

Table 5.9 Representative sphene analyses from the Glen Doll and Juan Jorge Complexes.

	Diorites				Diorites (Juan Jorge Complex)			
	132 SH 85C	132 SH 85R	251 SH 37C	251 SH 38C	JJ4 SH 77C	JJ4 SH 77R	JJ3 SH 78C	JJ3 SH 78R
SiO ₂	29.86	29.69	30.01	29.80	29.04	29.24	29.50	30.05
TiO ₂	39.47	39.28	38.72	38.31	37.70	37.30	36.60	37.46
Al ₂ O ₃	0.63	0.56	0.73	1.07	0.89	1.13	1.17	1.15
*FeO	0.68	0.69	0.68	1.05	1.18	1.37	1.66	1.26
MgO	BD	BD	BD	BD	BD	BD	BD	BD
MnO	0.05	0.03	0.05	0.07	0.10	0.12	0.09	0.13
CaO	28.73	28.60	28.38	28.83	27.16	27.80	26.83	27.65
Na ₂ O	BD	BD	BD	BD	BD	BD	BD	BD
K ₂ O	BD	BD	BD	BD	BD	BD	BD	BD
La ₂ O ₃	BD	BD	BD	0.01	0.37	0.21	0.45	0.30
Ce ₂ O ₃	0.19	0.21	0.19	0.20	1.25	0.60	1.62	0.74
TOTAL	99.61	99.06	98.75	99.34	97.69	97.76	97.92	98.74

Table 5.9 (cont.)

(Juan Jorge Complex)
 Microdiorite xenolith Granite (Juan Jorge Complex)

	JJ19 SH 83R	JJ19 SH 83C	JJ17 SH 87C	JJ17 SH 87R
SiO ₂	29.46	29.64	29.58	29.29
TiO ₂	37.70	36.45	37.06	36.90
Al ₂ O ₃	1.04	1.25	1.04	1.23
*FeO	1.17	1.92	1.39	1.81
MgO	BD	BD	BD	BD
MnO	0.13	0.15	0.13	0.17
CaO	27.32	27.46	27.06	27.48
Na ₂ O	BD	BD	BD	BD
K ₂ O	BD	BD	BD	BD
La ₂ O ₃	0.40	0.27	0.48	0.37
Ce ₂ O ₃	1.21	0.88	1.41	0.97
TOTAL	98.43	98.02	98.14	98.22

Table 5.10 Representative apatite analyses from the Juan Jorge and Glen Doll Complexes.

	Diorites		Monzonite		Diorites (Juan Jorge Complex) Granite					
	108 AP 10C	177 AP 12C	21 AP 81C	21 AP 116C	JJ4 AP 22C	JJ7 AP 17C	JJ17 AP 1C	JJ17 AP 2C		
SiO ₂	0.21	0.30	ND	ND	0.19	0.27	1.70	0.27		
*FeO	0.15	0.16	0.05	0.03	0.05	0.13	0.07	0.04		
MgO	0.03	0.08	0.03	0.01	BD	BD	BD	BD		
CaO	46.91	46.23	53.24	53.44	55.94	55.20	52.87	55.46		
Na ₂ O	0.09	0.04	BD	BD	0.03	0.07	0.18	0.06		
P ₂ O ₅	41.73	40.97	39.88	39.48	42.60	42.28	39.57	42.36		
La ₂ O ₃	0.14	0.20	ND	ND	0.23	0.22	1.21	0.22		
Ce ₂ O ₃	0.21	0.29	ND	ND	0.23	0.31	1.58	0.26		
Nd ₂ O ₃	0.13	0.13	ND	ND	0.05	0.15	0.43	0.07		
Cl	ND	ND	0.33	0.31	ND	ND	ND	ND		
F	4.07	3.92	2.11	2.58	5.92	4.80	6.43	5.59		
TOTAL	93.66	92.30	95.65	95.91	105.23	103.42	104.05	104.35		

The analysed example (Table 5.3) from the Glen Doll Complex has characteristically high iron (11.07% FeO) and low magnesium (14.13% MgO). The tschermakitic cores are sometimes rimmed by actinolitic hornblende which has a high silica content (51.66% SiO₂) and therefore a low Al_{iv} content (0.522 atoms per formula unit).

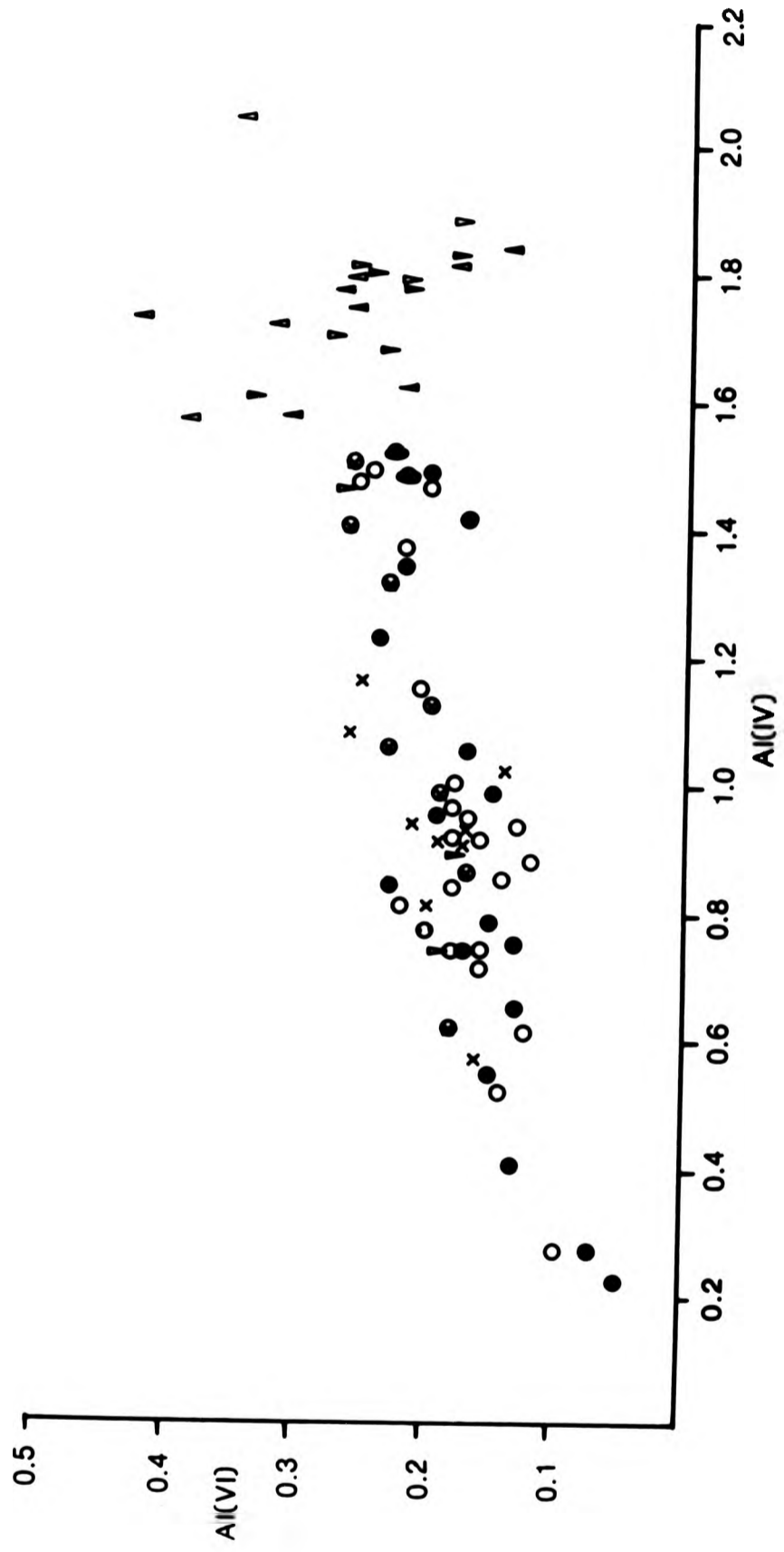
5.2.5 Factors affecting amphibole chemistry

The extensive substitution of cations in the amphibole lattice is considered to be controlled by a number of physical and chemical parameters. Henderson (1966) and Binns (1965) have both demonstrated that the colour of calcic amphiboles is controlled by their titanium content. High titanium is correlated with a brown colour and low titanium with a green colour. The analysed samples from the Glen Doll and Juan Jorge Complexes show a close correlation between titanium content and colour, a feature also observed in primary amphiboles from the Glenelg-Ratagain Complex (Nicholls, 1950).

It is generally considered that temperature is an important factor in controlling the titanium and aluminium content of amphiboles (e.g. Leake, 1965; Holloway and Burnham, 1972; Green and Ringwood, 1968;). Higher temperatures favour the entry of Ti and Al_{iv} in the amphibole structure. A plot of Ti_{amph} vs Al_{iv} amph shows a positive correlation of these elements for all rocks except a few olivine gabbros (Figure 5.1). The amphiboles from the diorites from both complexes display an overlap of compositions and lie on the same linear trend of increasing Ti with increasing Al_{iv}. The Juan Jorge amphiboles lie on the higher Ti and Al_{iv} part of the trend, while the secondary actinolitic amphiboles from the Glen

Fig. 5.2 A plot of Al(VI) against Al(IV) in amphiboles from the
Glen Doll and Juan Jorge Complexes.
Amphibole cores and rims are distinguished

Core Rim
▲ ▲ Olivine gabbro
▼ ▼ Gabbro
● 0 Px diorite
○ ○ Hbl diorite
x x Juan Jorge

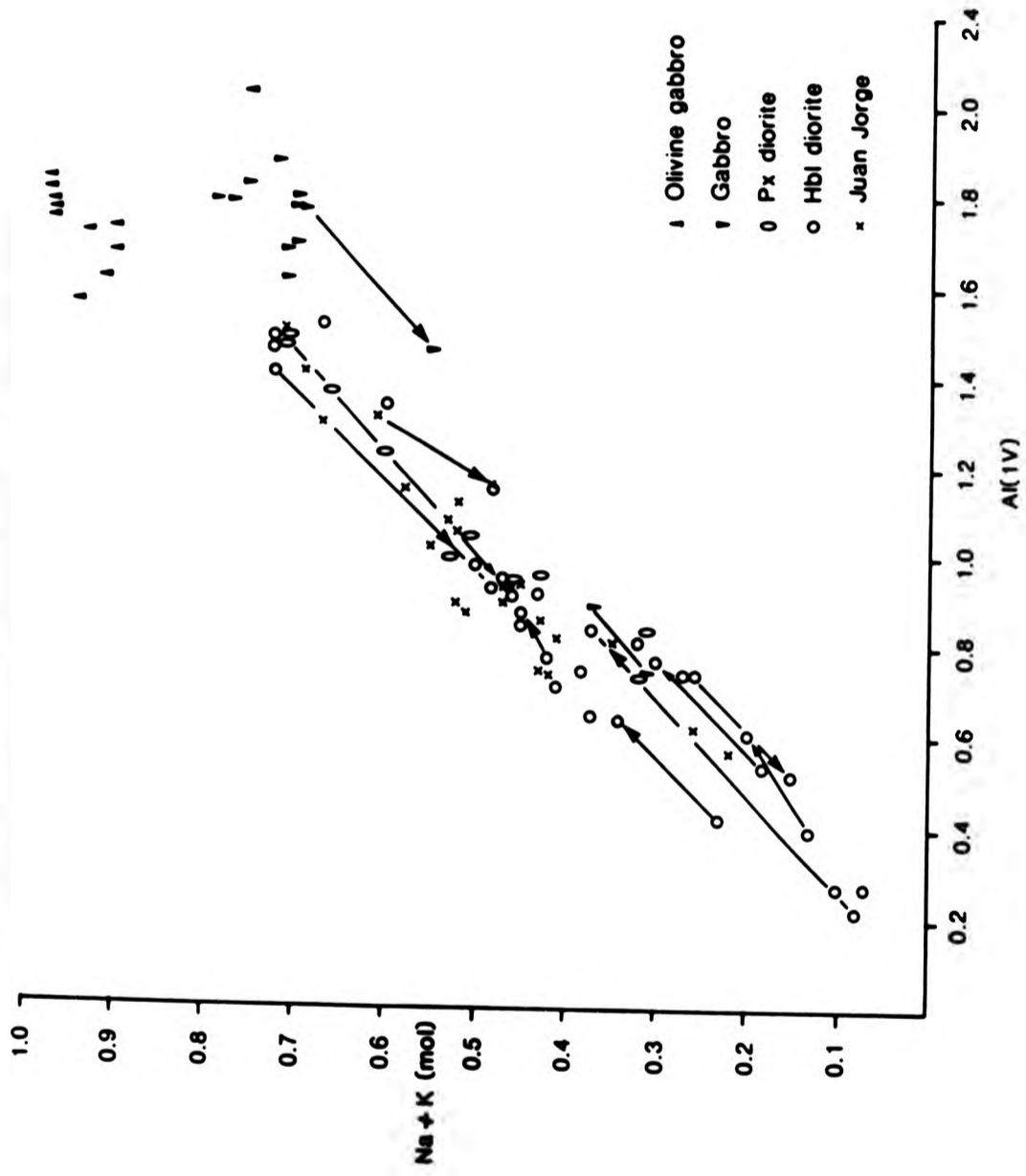


Doll Complex lie on the lower Ti and Al_{iv} end. The paragenetic compositions from the gabbros contain the highest levels of Ti and Al_{iv} . The scatter of data seen in the olivine gabbros may reflect the crystallisation of amphibole from intercumulus fluids, relatively poor in TiO_2 . The olivine gabbros also contain relatively sodic plagioclase, hence the intercumulus liquid may have crystallised under much lower temperatures than the cumulate minerals.

A summary of amphibole data from igneous and metamorphic rocks by Leake (1971), suggests that high temperatures and low pressures favour high Al_{vi} contents. A plot of Al_{iv} vs Al_{vi} for the analysed samples (Figure 5.2) shows a general increase in Al_{iv} with Al_{vi} . The amphiboles from the gabbroic rocks fall on the high Al_{iv} - Al_{vi} end of a broad trend defined by the amphiboles from the dioritic rocks.

The substitution of Al_{iv} for Si_T in amphiboles, is commonly accompanied by substitution in the B site of 2+ cations e.g. Mg and Ca by Na and K. Figure 5.3 shows a positive correlation between (Na+K) and Al_{iv} . The amphiboles at the higher end of the trend are high temperature paragenites from the gabbroic rocks. Intermediate compositions (Na+K 0.4-0.6) are primary brown and green amphiboles, typically magnesio hornblende, from the dioritic rocks. The compositions which plot with the lowest (Na+K) and Al_{iv} values, are secondary actinolitic amphiboles replacing pyroxene. The zoning in the primary compositions is from high (Na+K)- Al_{iv} cores to low (Na+K)- Al_{iv} rims. The sense of zoning in the actinolitic amphiboles is reversed. The composition of primary magmatic amphibole is controlled by the temperature and composition of the magma from which the amphiboles are crystallising, the core there-

Fig. 5.3 A plot of Na+K against Al(IV) in amphiboles from the Glen Doll and Juan Jorge Complexes. Arrows point from core to rim



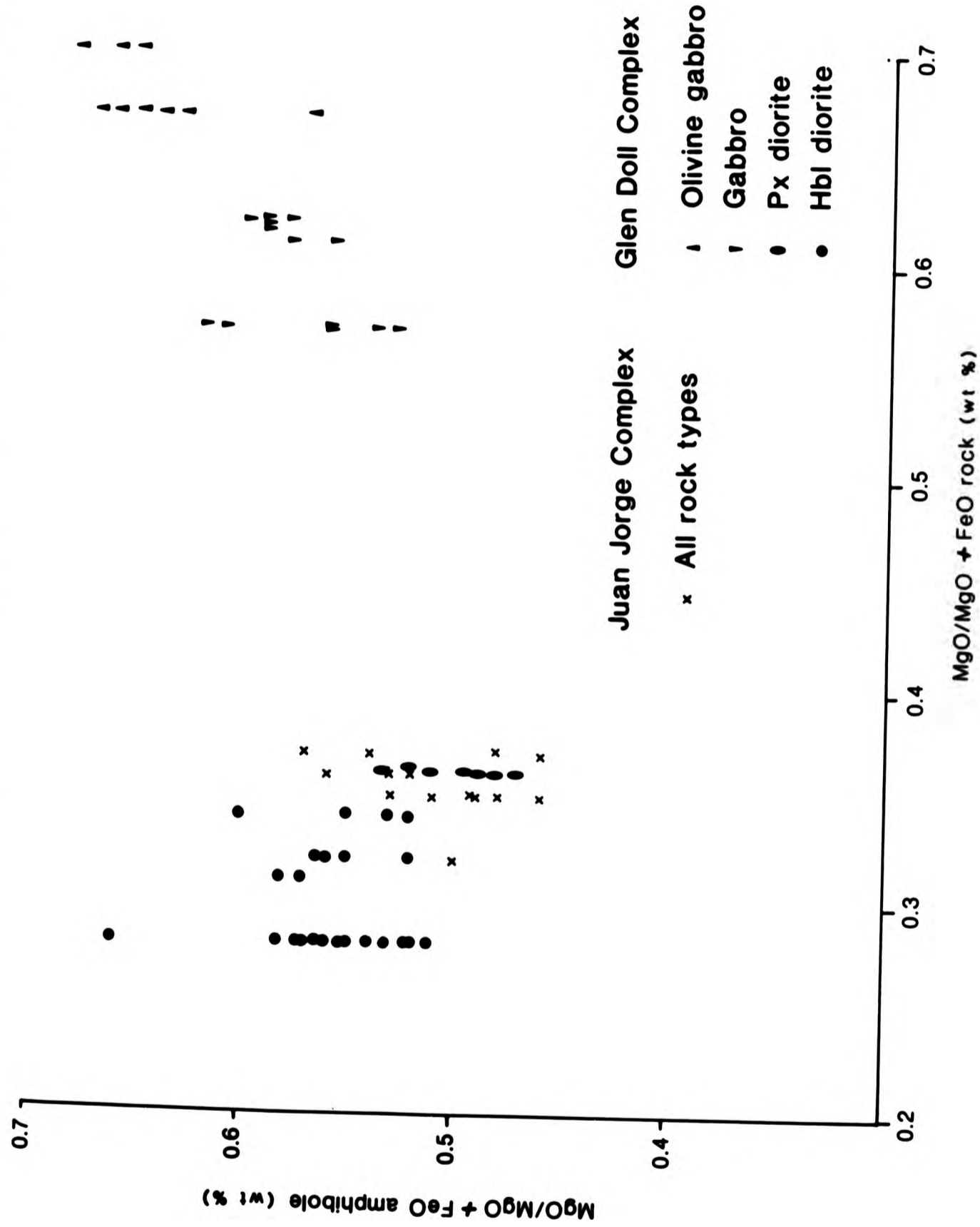
fore contains a higher $(\text{Na}+\text{K})\text{-Al}_{\text{vi}}$ content than the rim. By comparison, the secondary subsolidus amphiboles are formed in two stages. The first with the initial crystallisation of pyroxene with a jacket of primary, relatively high temperature, amphibole. The second is the low temperature breakdown of the core, probably caused by the diffusion of OH^- from the surrounding magma through the primary amphibole jacket. The composition of clinopyroxene essentially mimics that of an 'anhydrous' actinolitic amphibole.

5.2.6 Relationship between amphibole composition and bulk rock chemistry

A useful parameter with which to examine the evolution of genetically related amphibole compositions is their $\text{MgO}/\text{MgO}+\text{FeO}$ ratio (weight percent). During the fractional crystallisation of a basic magma, this ratio generally decreases in the magma with increased crystallisation. Some authors (e.g. Czamanske et al., 1981) have correlated the $\text{MgO}/\text{MgO}+\text{FeO}$ (wt%) ratios of a series of amphiboles with the bulk rock composition of the magma. Other authors (e.g. Green and Ringwood, 1968; Holloway and Burnham, 1972) have suggested that the overriding factors affecting the substitution of the cations, and therefore the composition of the amphibole, are the physical conditions of crystallisation of the magma rather than the bulk rock composition.

Figure 5.4 displays the $\text{MgO}/\text{MgO}+\text{FeO}_{(\text{rock})}$ ratio vs the $\text{MgO}/\text{MgO}+\text{FeO}_{(\text{amphibole})}$ calculated using weight percent of the oxides. The gabbroic rocks lie on a linear trend of decreasing $\text{MgO}/\text{MgO}+\text{FeO}_{(\text{amph})}$ with decreasing $\text{MgO}/\text{MgO}+\text{FeO}_{(\text{rock})}$ and display almost exactly a 1:1 ratio. This observation is most readily

Fig. 5.4 Amphibole and whole-rock magnesium-iron ratios plotted for the Glen Doll and Juan Jorge Complexes.



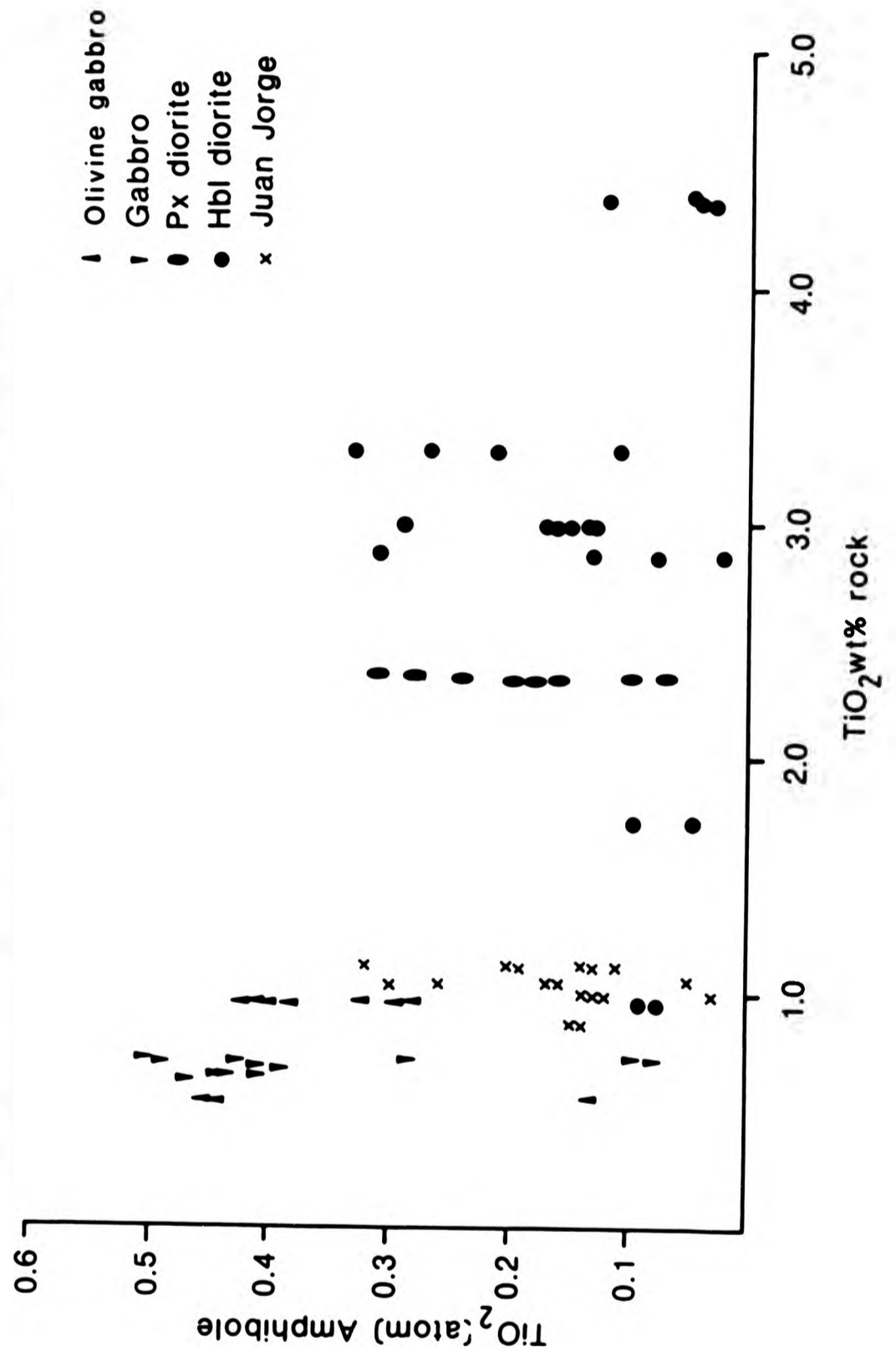
explained by the fact that many of the gabbroic rocks are pyroxene and amphibole cumulates. The $MgO/MgO+FeO$ ratio in the bulk rock therefore reflects the $MgO/MgO+FeO$ ratio in the ferromagnesium minerals. A comparison with amphibole data from the diorites reveals a sharp contrast. An overlap of compositions is seen between complexes and between the pyroxene and hornblende diorites. Those amphiboles which have a ratio of <0.5 are primary brown or green varieties, those with a ratio $0.5-0.54$ are magnesio hornblende and those with a ratio of $0.54-0.6$ are actinolitic amphiboles. Thus the highest ratio is seen in the secondary amphiboles. The $MgO/MgO+FeO$ atomic ratio is the same (0.69) for the secondary subsolidus actinolitic amphibole as for the orthopyroxene from the pyroxene diorite. This probably reflects the ratio in the original pyroxene which has been replaced.

Some authors (e.g. Leake, 1965) have suggested that the titanium content of amphiboles is controlled by the bulk rock titanium content. Figure 5.5 demonstrates the relationship between Ti_{amph} and Ti_{rock} . There is no observed correlation between the two parameters. This may reflect the contemporaneous crystallisation of other titanium bearing minerals such as sphene and/or ilmenite both of which commonly occur in the dioritic rocks.

5.2.7 Summary of amphibole chemistry

The amphiboles from the gabbroic rocks systematically contain higher Ti, Fe and Al_{iv} than those from the dioritic rocks. The higher titanium amphiboles from all rock types are brown and there is a positive correlation between titanium content and colour. The lowest levels of Ti, Fe and Al_{iv} occur in the actinolitic amphi-

Fig. 5.5
 A plot of titanium content of amphiboles against titanium content of the whole rock for the Glen Doll and Juan Jorge Complexes



boles which are considered to be replacement products after pyroxene, particularly since they contain low total alumina. The positive correlation between $MgO/MgO+FeO_{rock}$ and $MgO/MgO+FeO_{amph}$ in the gabbros supports the view that they are primary magmatic amphiboles. The rather variable $MgO/MgO+FeO$ ratio in the dioritic rocks, however, suggests that amphiboles were not in mutual equilibrium when they crystallised and that some are magmatic while others are subsolidus replacements after a primary crystallising phase.

Extensive experimental work on temperatures and pressures of crystallisation (Holloway and Burnham, 1972; Green and Ringwood, 1968) suggests that primary amphibole crystallisation in basaltic and andesitic liquids ceases as the temperature falls to 930-950°C under pressures of 5-15Kb. A breakdown of amphibole occurs at slightly below this temperature. Albuquerque (1974), examined the mineral chemistry of actinolitic hornblende from tonalitic rocks in Northern Portugal. He related the occurrence of actinolite to increased fH_2 and fH_2O during crystallisation of a partly crystalline, pyroxene bearing magma, a similar situation to that envisaged for the Glen Doll diorites. The primary amphiboles from the Glen Doll dioritic rocks occur as interstitial crystals or as jackets on pyroxene primocrysts (Chapter 4). They have therefore crystallised from an interstitial where a build up in water content would lead to the formation of a hydrous assemblage. Interstitial amphibole in the gabbroic rocks crystallised at a higher temperature than that in the diorites, suggesting that the intercumulus liquid became significantly hydrous at a higher Mg/Fe ratio than in the diorites. There was therefore no continual build up of H_2O in the bulk magma chamber (since the cumulus phases are generally anhy-

drous) but only in the interstitial (intercumulus) liquid.

5.3 Pyroxenes

Introduction

Both ortho and clino - pyroxenes occur in the basic and dioritic rocks in the Glen Doll Complex. Exsolution textures, commonly observed for example in the Skaergaard Intrusion (Wager and Brown, 1968) are absent from the Glen Doll pyroxenes. Pyroxenes do not occur in any of the intrusive facies of the Juan Jorge Complex. The pyroxenes have been classified according to the scheme of Deer et al. (1967) after Poldervaart and Hess (1951). The atomic formulae have been calculated on the basis of 6 oxygens per formula unit. In general the pyroxenes show a limited range of compositions. Orthopyroxenes range from En_{90-50} i.e. bronzite-hypersthene while the clinopyroxenes are of augite-salite composition, ranging from $Wo_{47}En_{43}Fs_{10}$ to $Wo_{43}En_{46}Fs_{11}$ (Figure 5.6).

5.3.1 Orthopyroxene

The olivine gabbro contains bronzite, with a typical composition of En_{80} . The gabbros however contain a more iron rich bronzite typically En_{73-77} , while the pyroxene diorites contain hypersthene, typically En_{68} . Representative pyroxene analyses are given in Table 5.4 for the range of rock types from the Glen Doll Complex. The calcium content of the orthopyroxenes varies from a maximum of 1.4% CaO in the gabbro, to 0.8% CaO in the olivine gabbro. These values for calcium are low compared to orthopyroxenes from, for example, the Skaergaard intrusion (Wager and Mitchell, 1951). The Glen Doll pyroxenes plot on the subsolidus trend for

the Skaergaard intrusion (Nwe, 1976) which may indicate that they crystallised at a lower temperature than those from the Skaergaard.

The ortho-pyroxenes are all more magnesium than those described from the Ben Nevis intrusion where a typical value of En_{63} is recorded for opx from a dioritic rock (Haslam, 1968). The Glen Doll opx are however of comparable composition with phenocrysts from the Sidlaw lava series (Gandy, 1975).

The amount of titanium in the Glen Doll opx is high compared with comparable pyroxenes from the Skaergaard intrusion for example (Wager and Mitchel, 1951), and varies from 0.07%–0.44% TiO_2 . Some examples show zoning with higher titanium and alumina cores than rims (Figure 5.7). A typical example, 88/PX/101 (Table 5.4), contains 0.21% TiO_2 and 1.31% Al_2O_3 in the core (Figure 5.7), decreasing to 0.07% TiO_2 and 0.98% Al_2O_3 at the rim. In addition, opx in the olivine gabbro contains more silica (55.14% SiO_2 $SD=0.46$) than opx in the gabbro (53.3% SiO_2 $SD=0.38$). Chromium levels are variable from 0.03–0.15% Cr_2O_3 . Chromium typically occurs in the 3+ form and commonly substitutes for Mg^{2+} (Mason, 1966).

5.3.2 Clinopyroxene

All of the cpx analyses fall within the field defined as augite or salite (Deer et al., 1983) with typically 21.5% CaO and an $Mg/Mg+Fe$ mol ratio of 0.8. Representative analyses are shown in Table 5.4. Zoned crystals are rare, these having higher alumina cores (2.23% Al_2O_3) than rims (1.59% Al_2O_3). Chromium contents are similar to those in the opx, typically 0.1% Cr_2O_3 .

Fig. 5.6
Pyroxenes and olivines plotted into the Wo-En-Fs triangle

Mineral	Rock type
I Olivine	Olivine gabbro
I Opx	Olivine gabbro
I Opx	Gabbro
0 Cpx	Gabbro
o Opx	Diorite

- - - Solidus trend for cpx from 14 layered igneous complexes
- - - Solidus trend from the Skaergaard intrusion (Nwe, 1976)
- - - Subsolidus trend from the Skaergaard intrusion (Nwe, 1976)

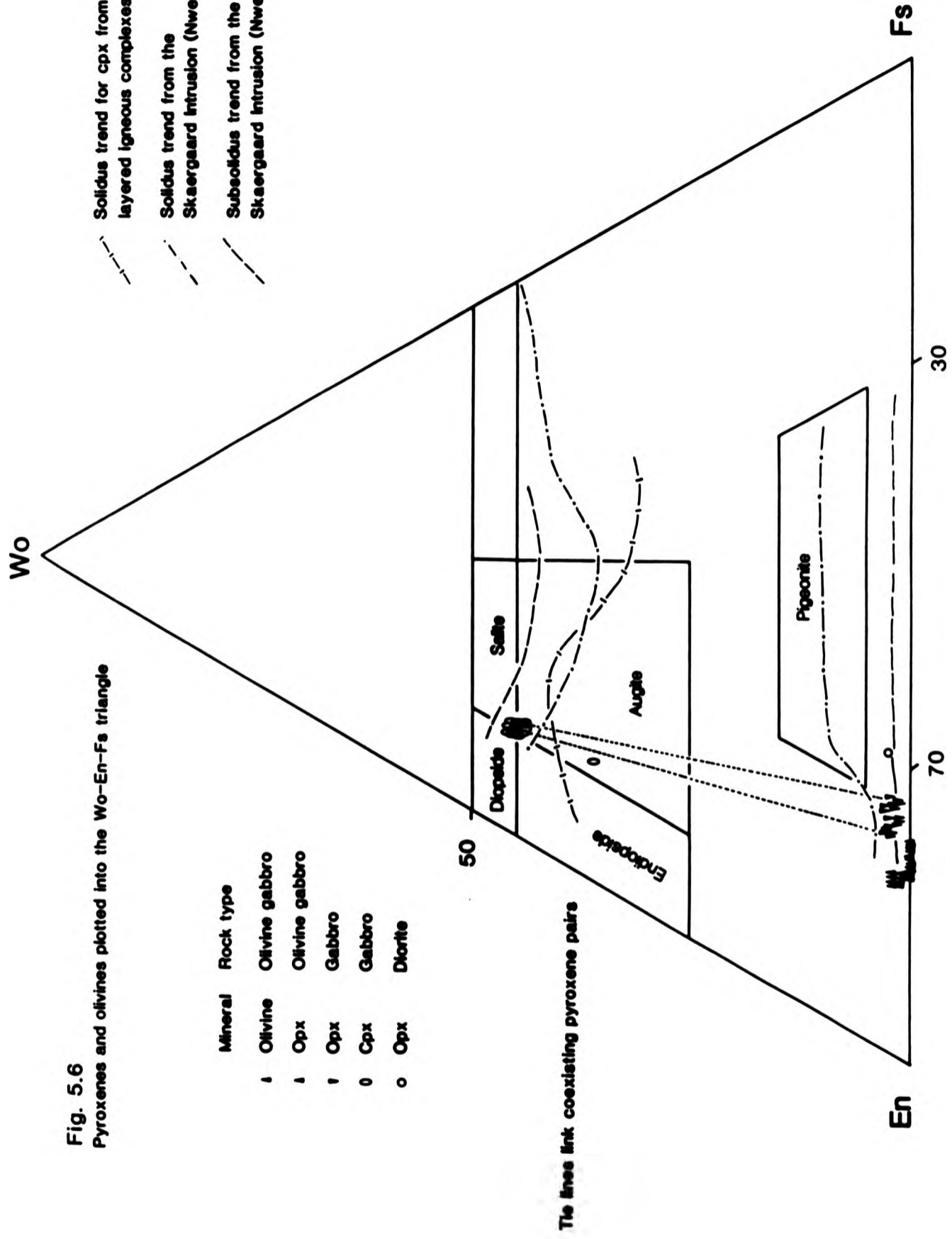


Fig. 5.7 A plot of Ti against Al(IV) in pyroxenes from the Glen Doll Complex

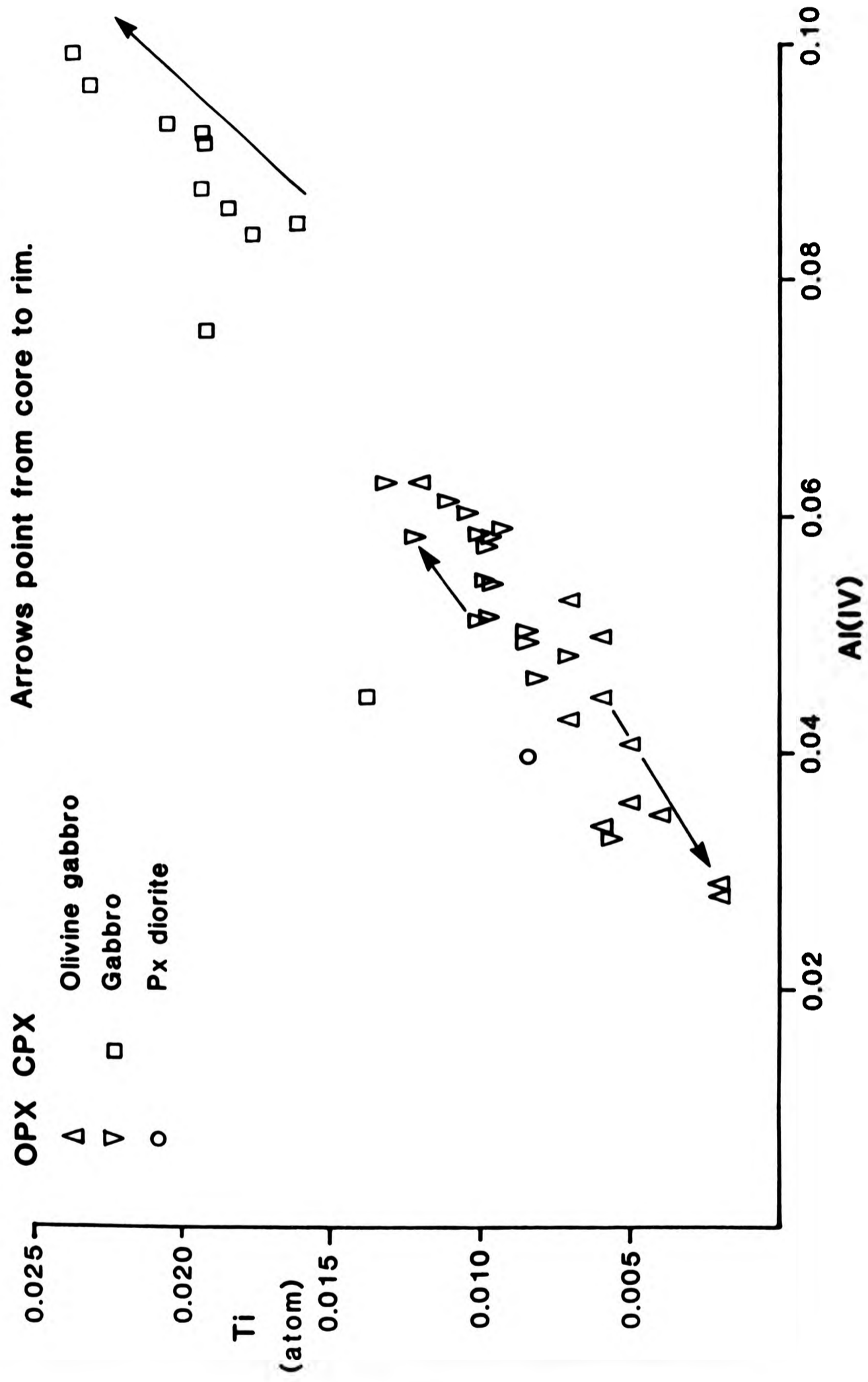
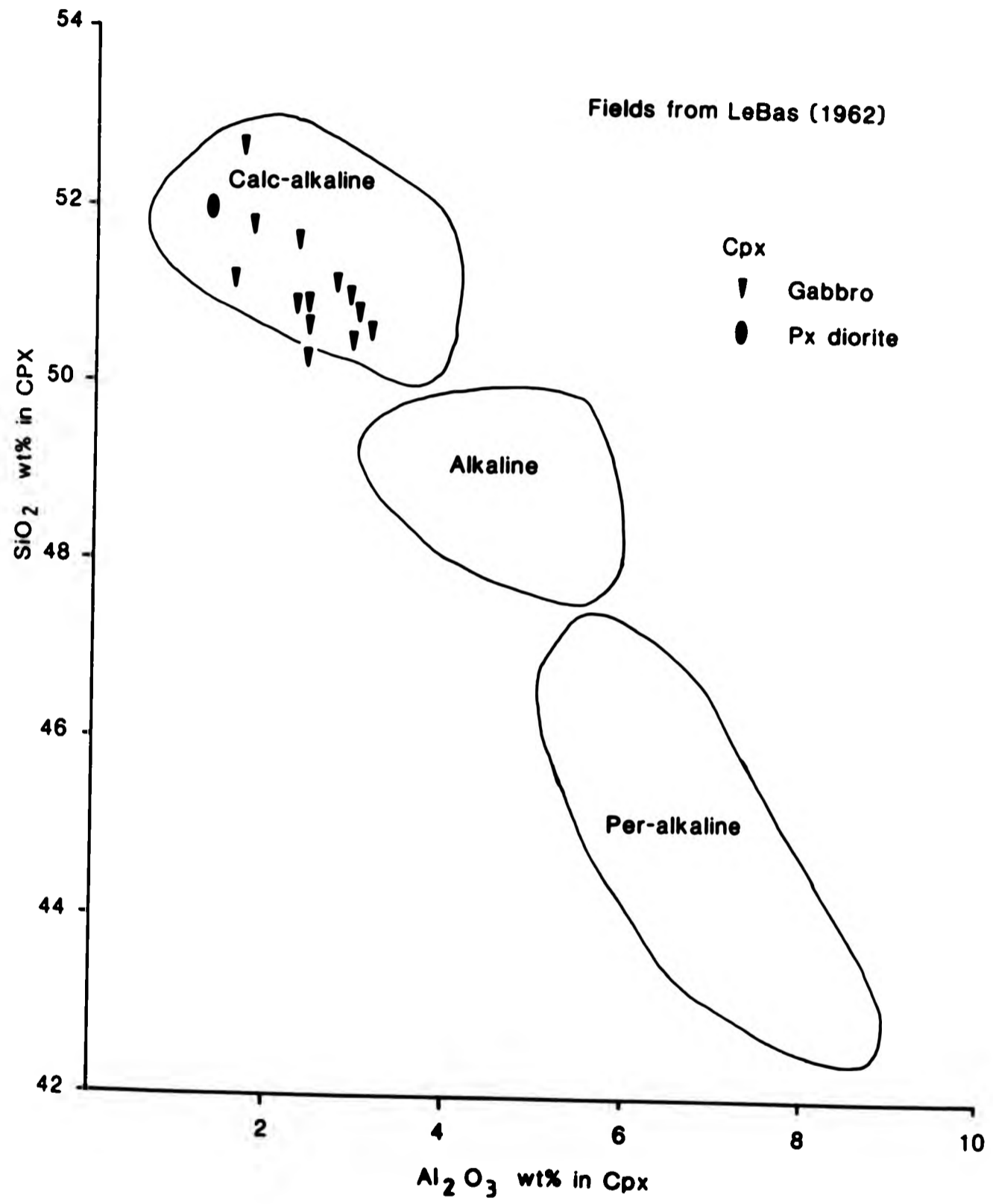


Fig. 5.8 Diagram to show compositions of clinopyroxenes from the Glen Doll Complex



A plot of SiO_2 vs Al_2O_3 has been used by Le Bas (1962) to discriminate clinopyroxenes from alkaline, peralkaline and calc-alkaline environments. The cpx data being consistent with other mineral data from the Glen Doll Complex, falls within the field of calc-alkaline compositions (Figure 5.8), with relatively high silica (50-53%) and low alumina (1-3%).

Discussion

The analysed data for the opx, cpx and olivine has been plotted into the system Ca:Mg:Fe calculated using molecular proportions (Figure 5.6). Tie lines are shown joining co-existing opx and cpx compositions. The tie lines show a similar pattern i.e. they do not cross, to those shown by basic igneous suites in general (e.g. Wager and Brown, 1968; Nwe, 1976; Gandy, 1975).

The gabbroic rocks from the Glen Doll Complex occur in a layered units at the S-W and N-E margins of the complex (Chapter 3). These layered rocks have been compared here with the layered basic sequences described for example from the Marginal Border series of the Skaergaard intrusion (Wager and Brown, 1968; Nwe, 1975, 1976). The crystallisation trends for the cpx and opx from the Skaergaard have been plotted on Figure 5.7 as an example of the path of crystallisation taken by a basic magma. The data for the Glen Doll Complex lie close to the initial composition of opx and cpx crystallising from a basic magma in terms of the Mg:Fe ratio, however calcium contents are comparable with the Skaergaard sub-solidus trend. This may indicate that since both the cpx and opx in Glen Doll are primary cumulus phases, that the liquidus temperature of the magma was depressed relative to that in the Skaergaard intrusion. This may be a result of the relatively high water content of

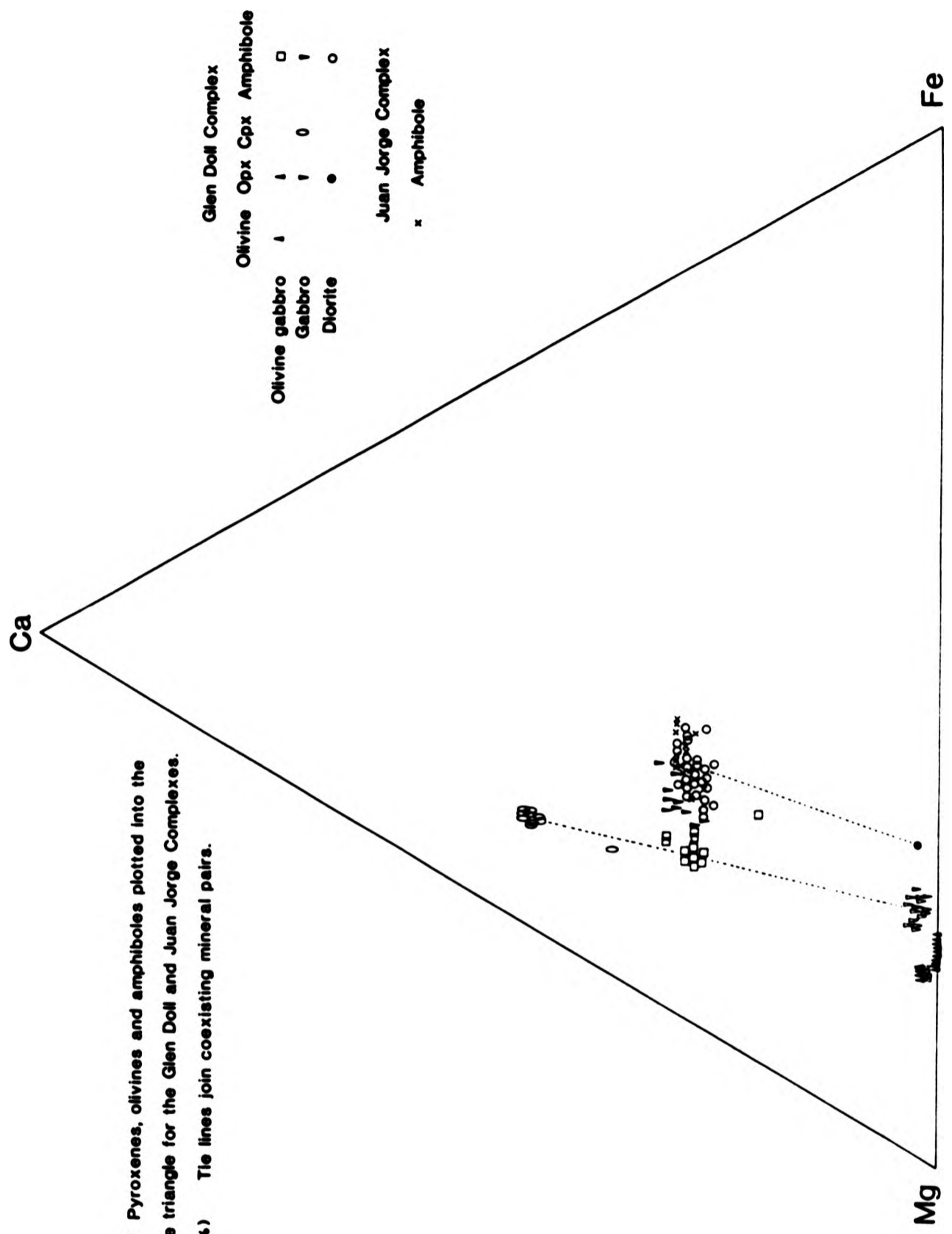


Fig. 5.9 Pyroxenes, olivines and amphiboles plotted into the Ca-Mg-Fe triangle for the Glen Doll and Juan Jorge Complexes. (atomic %) The lines join coexisting mineral pairs.

the magma (Section 1.2.7).

To display in more detail the variation in composition of the pyroxenes, an enlargement of the Mg corner of Figure 5.8 has been drawn (Figure 5.9). This shows clearly the progressive decrease in the Mg/Fe ratio of the opx from the olivine gabbros, to the gabbros to the pyroxene diorites. A slight increase in the proportion of calcium is also seen. Hess (1952) showed that the relatively large Ca^{2+} ion is unable to fit into the opx structure at low temperature. At higher temperatures, however, it can enter the structure, substituting for Mg^{2+} and Fe^{2+} .

Kushiro (1960), noted a positive correlation between Al_{iv} with Ti and of Al_{iv} with Al_{vi} and concluded that titanium substitution in the crystal lattice, increases with increasing temperature in opx. Figure 5.7 plots the relationship between Ti and Al_{iv} for all pyroxenes from the Glen Doll Complex. A positive linear correlation is seen between Ti and Al_{iv} , the trend for opx and cpx being collinear but with some overlap. The clinopyroxenes have the highest Ti and Al_{iv} contents, while the opx from the olivine gabbros have the lowest Ti and Al_{iv} contents. Corresponding core and rim compositions are shown for the opx.

5.4 Olivine

The occurrence of olivine is restricted to the olivine gabbro and olivine norite from the Kilbo Burn in the SW of the Glen Doll Complex. Representative analyses are given in Table 5.5. The olivines show a limited range of compositions from Fo_{78-81} , typical of magnesian olivines from gabbroic rocks. They are classified

according to Deer et al. (1983) as chrysolite since they contain between 10-30 atomic percent Fe^{2+} . The number of cations (Table 5.5) have been calculated on the basis of 4 oxygens per formula unit after Deer et al., (1983).

The chemistry of the olivines is relatively simple. The analysed samples typically contain less than 0.02% CaO. Nickel levels are variable and range from 0.04-0.20% NiO_2 . Titanium is typically absent. By comparison, olivine analysis from the Skaergaard intrusion (Nwe, 1976) typically contain 0.04-0.73% CaO and 0.01-0.07% TiO_2 . The calcium content of the Glen Doll samples lies within the range of calcium contents (<0.1% CaO) given by Simkin and Smith (1970) for plutonic rocks. Stormer (1973), suggested that a low level of calcium in olivine is indicative of low temperatures of crystallisation. The absence of, or very low level of, calcium in the Glen Doll olivine may indicate therefore a lower temperature of crystallisation than, for example, in the Skaergaard intrusion.

The data for the Glen Doll olivines has been plotted into the Ca:Mg:Fe triangle (Figures 5.7 and 5.9) to show its relationships with co-existing opx. The sequence of crystallisation of the minerals observed in the Glen Doll basic rocks is comparable to that described for the early stages of crystallisation of the Skaergaard intrusion (Wager and Brown, 1968; Nwe, 1976) as well as crystallisation of other calc-alkaline intrusive complexes such as Garabal Hill (Nockolds, 1940) and the Guadalupe Complex, California (Best and Mercy, 1967).

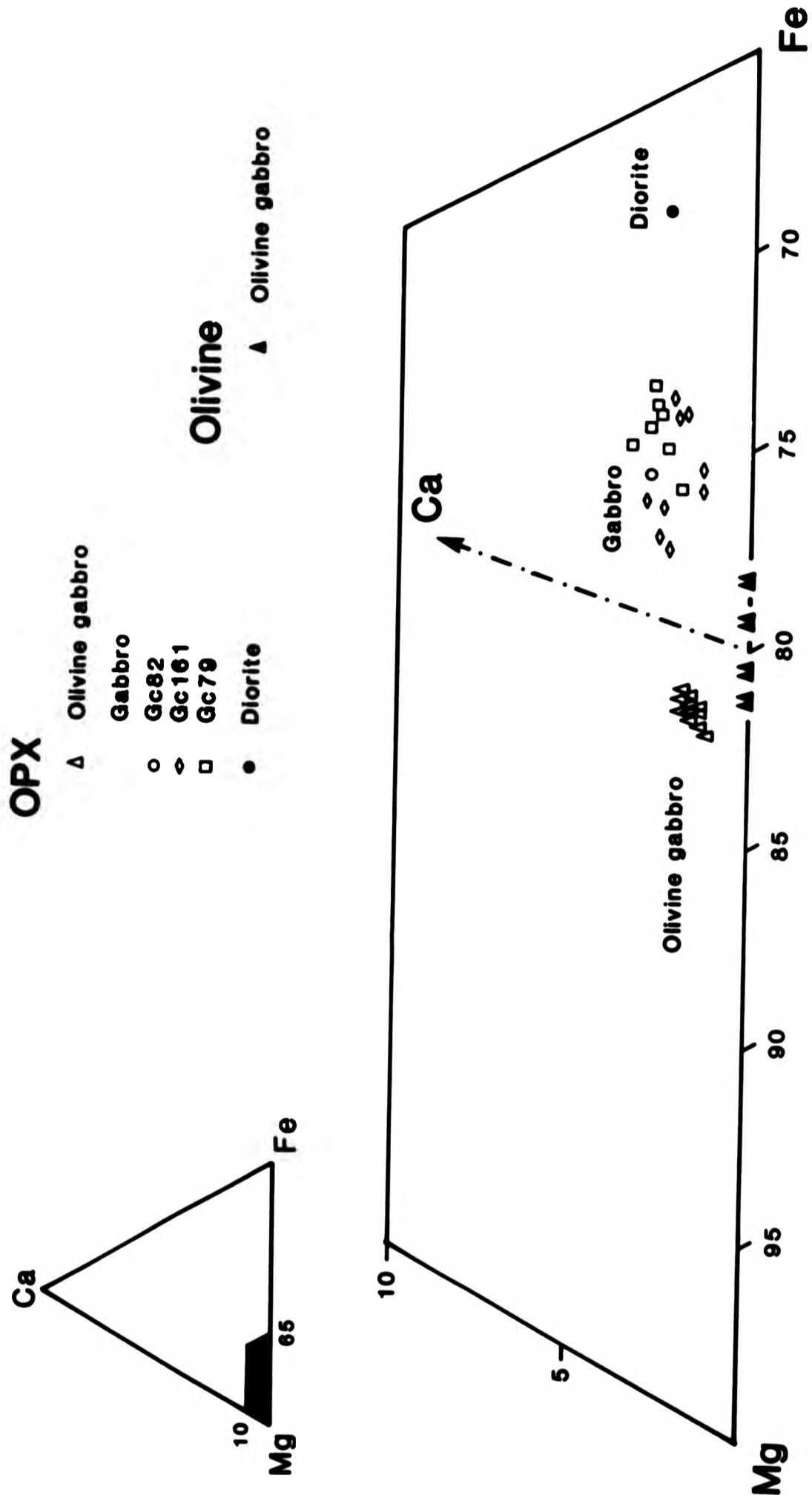


Fig. 5.10 Geochemical variation of orthopyroxenes and olivines from the Glen Doll Complex (atomic %)

5.5 Mica

Analysed micas are classified according to the scheme of Heinrich et al. (1953) on the basis of their Mg:Fe atomic ratio. Samples from the olivine gabbro have an Mg:Fe ratio $>2:1$ and are therefore classified as phlogopite. The micas from all other rock types have an Mg/Fe ratio of $<2:1$ and are therefore classified as biotite. In theory complete solid solution exists between phlogopite and biotite and the division at an Mg:Fe ratio of $2:1$, is therefore arbitrary.

Phlogopite and biotite are tri-octahedral micas with 6 Y site cations. The general formula being:-

	X	Y	Z
Phlogopite	K_2	$(Mg, Fe^{2+})_6$	Si_6Al_2
Biotite	K_2	$(Mg, Fe, Al)_6$	$Si_{6-5}Al_{2-3}$

Representative analyses for the phlogopites and biotites are given in Table 5.6.

5.5.1 Phlogonite

This phase occurs only in the olivine gabbros and olivine norites where it is poikilitic, typically enclosing tabular plagioclase. The crystals of phlogopite are commonly zoned with high titanium, low iron cores. A typical example contains 2.15% TiO_2 and 6.94% FeO (core) and 1.43% TiO_2 and 8.45% FeO (rim). The MgO/MgO+FeO (wt%) ratio decreases from core to rim (0.75-0.72). The titanium content is very variable from 0.76-4.37% TiO_2 and a negative correlation is noted between titania and magnesia,

reflecting the substitution of titanium for magnesium in the Y site of the mica structure (Table 5.6). Fluorine levels are consistently low, averaging 0.01-0.03% F.

5.5.2 Biotite

Biotite analyses from the gabbros are comparable with those from basic rocks from other calc-alkaline complexes e.g. Symes (1981), Deer (1937). Of the analysed samples, the biotites from the gabbro contain the highest titanium (<5.36% TiO₂) and a corresponding decrease in total iron, reflecting the substitution of Ti⁴⁺ for Fe³⁺. Biotites from the pyroxene diorites similarly display Ti-Fe substitution. The MgO/MgO+FeO (Wt%) ratio is high (0.57) in the gabbro biotites relative to the hornblende diorite biotites from both complexes (0.42-0.44). No distinction can be made between biotites from the Juan Jorge and Glen Doll diorites. Crystals from both complexes are typically zoned with higher TiO₂ rims (4.6%) than cores (3.6%). Data (Table 5.6) suggests that a combination of site substitutions occur, including Ti substitution for Fe³⁺ and Al_{vi}, and Na and Ca for K in the X site.

The granitic rocks contain biotite which is commonly zoned with respect to Ti and Fe. Typical cores contain 4.2% TiO₂ and 18.6% FeO while rims contain 3.3% TiO₂ and 19.6% FeO. The MgO/MgO+FeO (wt%) ratio is notably lower in biotites from the Juan Jorge granite (0.4-0.43) compared with those from the Glen Doll adamellite (0.46-0.48). The latter also contain 0.08-0.19% F, which substitutes for OH⁻ in the biotite lattice (Deer et al., 1983). In contrast with the Glen Doll diorites, the monzonite biotites typically have higher TiO₂ rims (4.4%) than rims (4.1%) and a lower MgO/MgO+FeO ratio.

The range of compositions for the biotites and phlogopites have been plotted into the (Na+K)-Mg-(Fe+Ti+Mn) triangle (Figure 5.10)(e.g. Symes, 1981). Those elements which commonly substitute (Mason, 1966), are included together e.g. Na+K. The phlogopites are clearly separated from the biotites, with the highest Mg and (Na+K) but there is an overlap between the biotite compositions for the range of rock types displayed. One example from each of the olivine gabbro, pyroxene diorite and Juan Jorge diorite plot with very low (Na+K). This is probably due to the volatilisation of (Na+K) by the electron beam, since low totals are recorded in these samples, either prior to or during analysis and thus represent an incomplete analysis.

Experimental data (Bowen and Tuttle, 1953) suggests that the breakdown of phlogopite occurs at $\sim 1120^{\circ}\text{C}$ (5Kb) and $\sim 1070^{\circ}\text{C}$ (2kb) in plutonic rocks. The experimental data places some constraints on the temperature of crystallisation of phlogopite in basic rocks.

Harry (1950), observed that micas formed at higher temperatures, tend to have higher Al_{IV} contents than those formed at lower temperatures. Phlogopite from the Glen Doll gabbros tend to contain lower Al_{IV} (typically 2.17) than the biotites (typically >2.4) from the dioritic rocks, indicating that the biotites may have crystallised at a higher temperature than the phlogopite micas.

5.6 Plagioclase

Introduction

Plagioclase compositions range from An_{21} , in the adamellite, to An_{78} in the gabbros. Both core and rim measurements have been

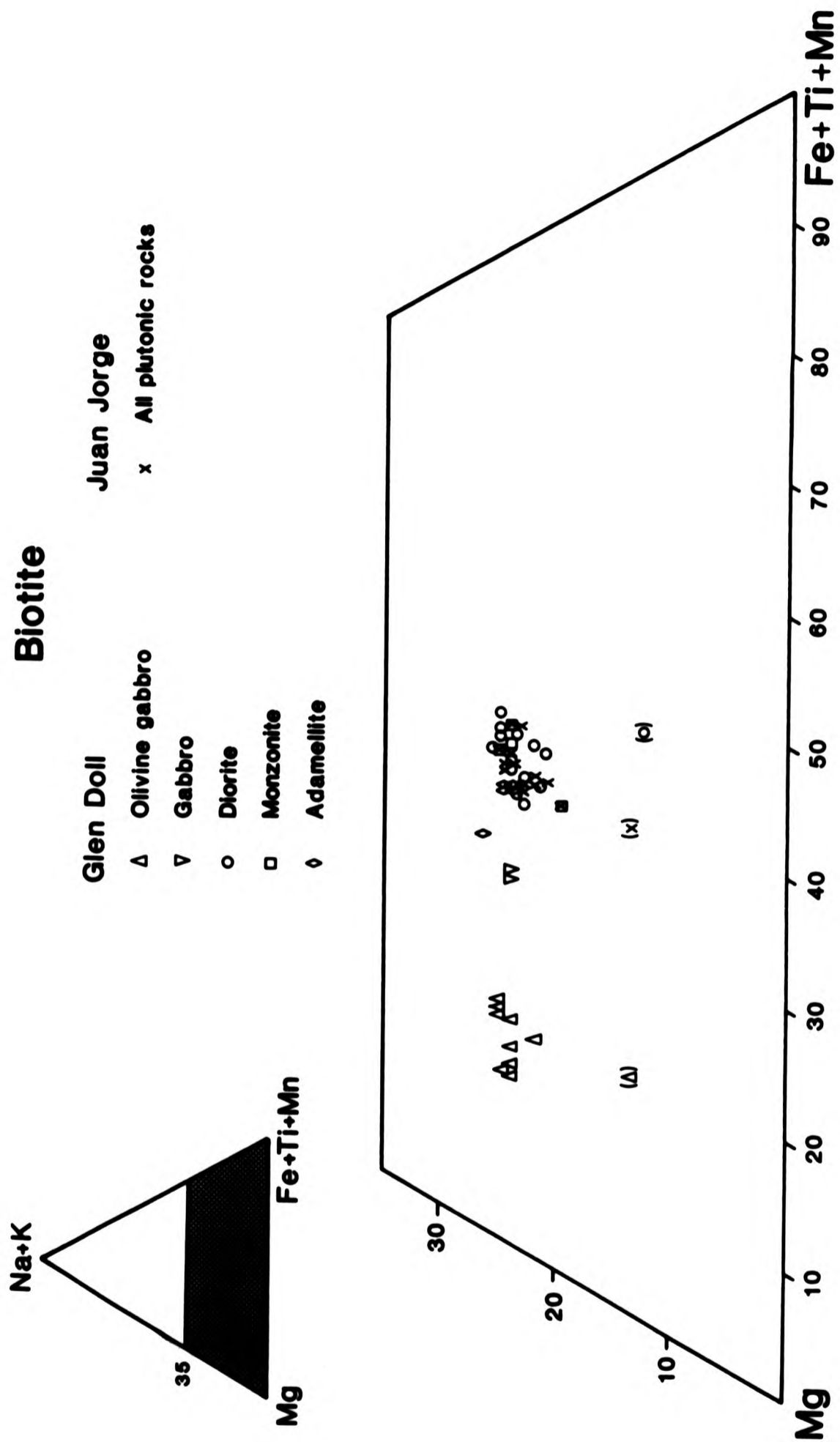


Fig. 5.11 Biotite compositions plotted into the Mg-Na+K-Fe+Ti+Mn triangle (atomic %)

made where possible to study the change in chemical composition of individual crystals. One feature should be noted concerning the anorthite content of the plagioclase determined using the electron microprobe compared with that obtained optically by the Michel-Levy method (Chapter 4). In general, the anorthite content is higher when determined by microprobe techniques compared to that determined optically. This difference is considered to be due to a combination of factors, including the difficulty in locating enough correctly orientated sections for optical determination of often large crystals.

The range of compositions determined by electron microprobe analysis have been plotted into the K-Na-Ca (atomic percent) triangle to display the gross variation in plagioclase chemistry (Figure 5.11). The diagram clearly shows the wide range of compositions. The orthoclase content is less than 5% in all samples, including the oligoclases where orthoclase content can vary widely..

5.6.1 Compositional variation

Representative analyses of plagioclase from the range of rock types are given in Table 5.7. Plagioclase from the dioritic rocks in the Glen Doll Complex display a range of compositions and compositional zoning. In general, the rocks containing higher bulk rock MgO (Appendix C) contain a more calcic plagioclase (labradorite) while those with lower MgO contain a lower calcium plagioclase (andesine)(Figure 5.11). However compositions vary widely. In a single sample many crystals display limited normal zoning, with typically broad cores of An₆₁ (11.74% CaO) and rims An₅₇ (10.88% CaO). A similar number of crystals have broad cores of labradorite (An₅₅) and narrow rims of andesine (An₃₇). Other large euhedral

crystals show oscillatory zoning from $An_{49}-An_{24}-An_{47}$. Both normal and oscillatory zoning occur in the same rock sample. Smaller interstitial crystals are typically unzoned and of andesine (An_{48}) composition. Reversely zoned crystals (An_{42-46}) are rare but can occur in a rock containing plagioclase which displays normal zoning. A complete overlap in composition and style of zoning is seen between the hornblende and pyroxene diorites from the Glen Doll Complex. Both normal and oscillatory types of zoning are commonly observed in basalt and basaltic andesite plagioclase phenocrysts from the Sidlaw lavas (Gandy, 1975). However reversely zoned crystals are rare in these lavas. The range of zoning styles observed in the Sidlaw lavas is attributed to variable water pressure during crystallisation of the magma (Gandy, 1975; Yoder, 1969)

The monzonitic rocks from Glen Doll have a low bulk rock magnesia content, typically around 2.8% MgO. They contain plagioclase which displays either normal or oscillatory zoning. The overall compositions are however less calcic than in the dioritic rocks, with cores typically of andesine (An_{49}) and rims of andesine (An_{23}). Oscillatory zoned crystals are typically $An_{27}-An_{34}-An_{27}$.

The adamellites tend to have a lower bulk rock magnesia content than the monzonites and they also contain a substantially less calcic plagioclase. Crystals are normally zoned, typically $An_{38}-An_{32}-An_{22}$. The potassium content of the plagioclase from the diorites, monzonites and adamellites, remains relatively constant at 0.22% K_2O throughout the range of compositions.

The gabbros contain the most calcic plagioclase seen in either complex. The rock samples from which the microprobe section were

prepared, cover a range of bulk rock compositions from 7.5-9.62% MgO. The lower magnesia sample contains the most calcic plagioclase and the higher magnesia, the least calcic plagioclase. Crystals commonly show normal zoning. In the low magnesia samples zoned crystals have cores of Bytownite (An₇₈) and rims of labradorite (An₆₀). Unzoned crystals are of bytownite composition (An₇₃). The higher MgO samples contain interstitial plagioclase which is most commonly unzoned with an average composition of labradorite (An₆₀).

The olivine gabbros contain plagioclase of labradorite or andesine composition. Large tabular crystals show reverse zoning with cores An₄₅ and rims An₅₂, compositions comparable with, for example, plagioclase from the norite of the Loch Doon Complex (Brown et al., 1979). The potassium content is very low at <0.07% K₂O, clearly separating these labradorite and andesine from the plagioclase in the dioritic rocks (Figure 5.11).

The dioritic rocks from the Juan Jorge Complex (bulk rock 3-3.86% MgO), by comparison with Glen Doll, contain plagioclase crystals which are always normally zoned. Core compositions range from An₃₈-An₄₅ (~7% CaO) and rims from An₂₆-An₃₇ (~5% CaO). The Juan Jorge granite (0.73% MgO) contains unzoned plagioclase typically An₂₅ (3.4% CaO). Potassium levels in the Juan Jorge granite plagioclase are consistently higher at 0.3% K₂O, than in the intermediate and acid rocks from Glen Doll.

The variation of the bulk rock MgO with anorthite content for the range of rock types is shown on Figure 5.12. There is a positive correlation between the two plotting parameters up to a bulk

Plagioclase

- Glen Doll
- ▲ Olivine gabbro
 - † Gabbro
 - Diorite
 - Monzonite
 - ◇ Adamellite
- Juan Jorge
- x All plutonic rocks

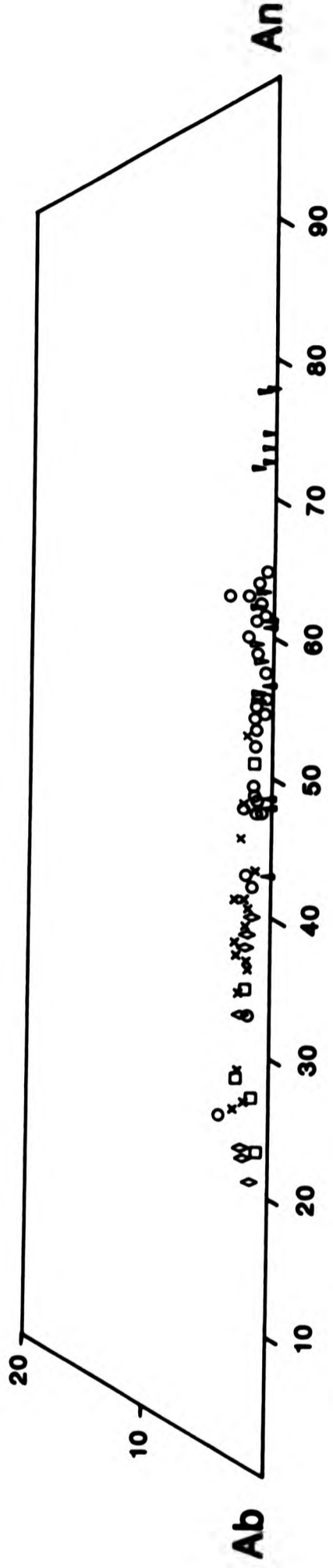
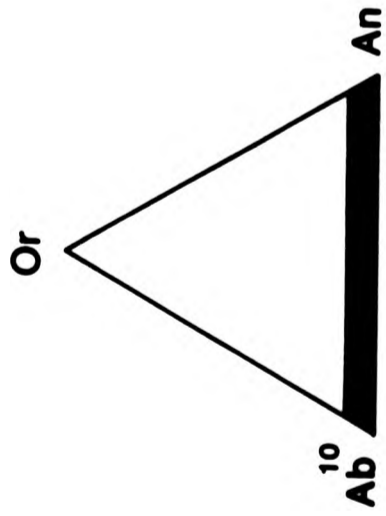


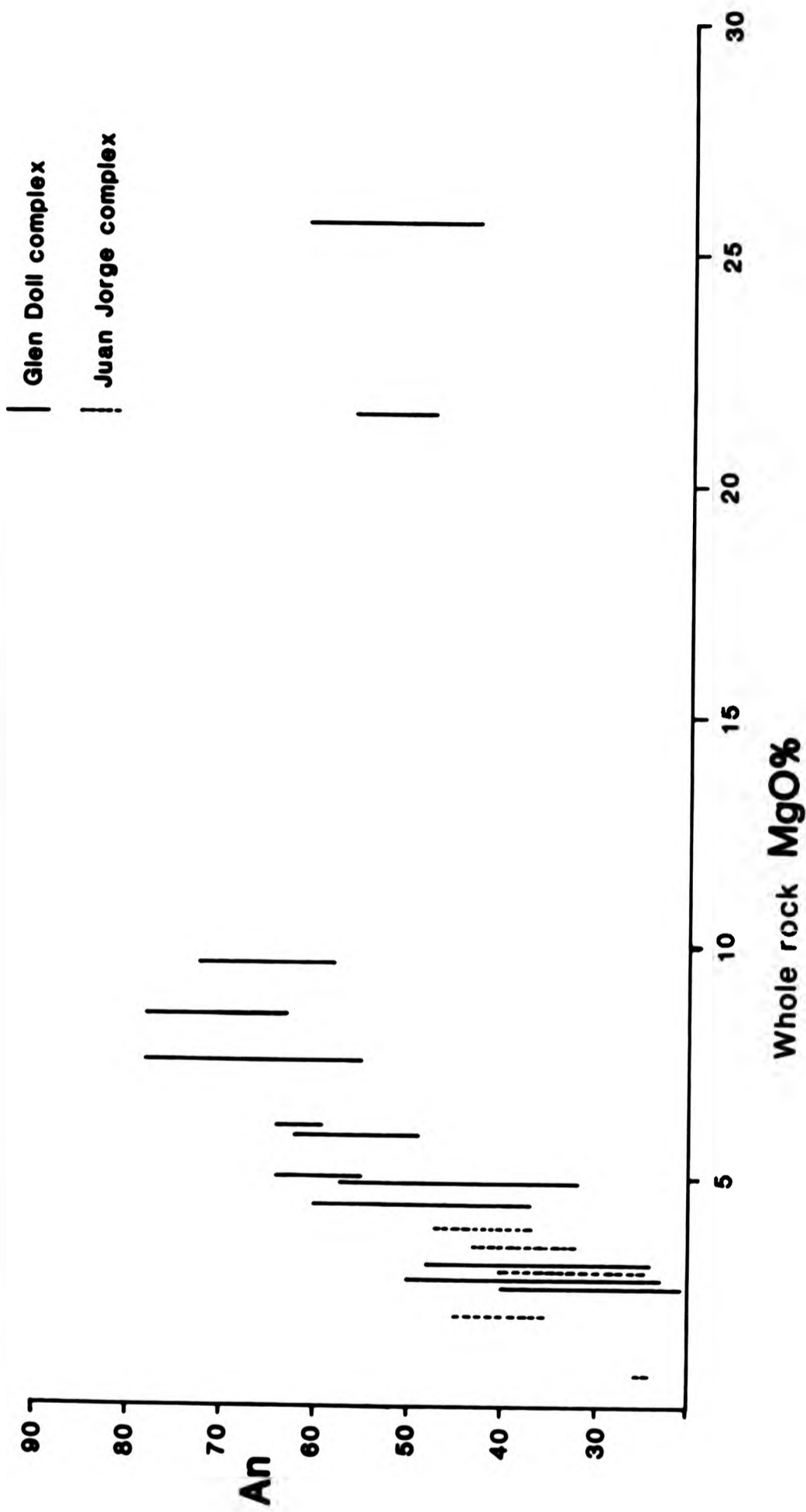
Fig. 5.12 Plagioclase compositions plotted into the system Or-Ab-An

rock value of ~9% MgO. Above this value there is apparently a decrease in anorthite content of the plagioclase with increasing MgO. In layered basic complexes such as the Skaergaard intrusion (Wager and Brown, 1968) a positive correlation between bulk rock MgO and plagioclase anorthite content occurs through the range of rock types. This may indicate that the most mafic liquid from which plagioclase was crystallising in the Glen Doll Complex, contained ~9% MgO.

5.6.2 Zoning in plagioclase

Several major studies have been undertaken concerning the origin of various types of zoning in plagioclase, both from real rock studies (Maaloe, 1976; Loomis and Welber, 1982; Wiebe, 1968) and using numerical modelling techniques (Loomis, 1982). In plagioclase from plutonic rocks, Noyes et al. (1983), suggested that normal zoning may be the result of not only decreasing temperature but also of decreasing H₂O pressure. Numerical modelling (Loomis, 1982) suggests that normal zoning should be promoted by rapid cooling (i.e. increased undercooling), contemporaneous crystallisation of other phases (i.e. a change in liquid composition) and the absence of volatiles. The gabbros, Juan Jorge diorites and some of the Glen Doll diorites display this type of zoning. Conversely, reverse zoning would be expected in crystals grown in slowly cooled melts or in melts where volatiles are concentrated (Loomis, 1982). A high concentration of volatiles are envisaged close to the sites of rafted xenoliths undergoing assimilation in the Glen Doll Complex (see Chapter 3). Thus the reverse zoning seen in many of the Glen Doll diorites may be related to high volatile contents (drusy cavities are seen in hand specimen) in the magma at the time of

Fig. 5.13
 Anorthite content of plagioclase feldspar plotted against whole
 rock MgO for the Glen Doll and Juan Jorge complexes



crystallisation of the plagioclase. The olivine gabbros, however, do not contain xenoliths and the reverse zoning seen in their plagioclase may be related to a combination of factors. Initially slow rates of cooling of the magma could lead to the formation of reversely zoned crystals. In addition crystallisation in an open system could allow for the formation of the low anorthite contents observed in the plagioclase in the olivine gabbros.

The third type of zoning seen in some of the Glen Doll diorites and monzonites, is oscillatory zoning. Early work by Harloff (1927) suggested that this type of zoning formed by the renucleation of a crystal followed by chemical diffusion. Maaloe (1976), considered that oscillatory zoned plagioclase from the Skaergaard Intrusion, formed under supercooled conditions (perhaps by only a few degrees). However Sibley et al., (1976) concluded that if oscillatory zoning is due to constitutional supercooling, then there should be no correlation of zoning between crystals, since the zoning is controlled by the diffusion gradient in the liquid at the individual crystal/liquid interface. Oscillatory zoning seen in some of the Glen Doll diorites and monzonites, is frequently observed in the same rock sample as other types of zoning and oscillatory zoning may therefore be a feature caused by a change in local conditions, similar to that proposed by Sibley et al., (1976).

5.7 Oxide minerals

Oxide minerals occur in both the Glen Doll and Juan Jorge Complexes. The analysed samples are from the dioritic rocks in both complexes and from a rafted metasedimentary xenolith. The oxides in the diorites include both ilmenite and spinel (magnetite) and in

the metasedimentary xenolith hercynitic spinel occurs. Since the mineral analyses have been undertaken using an electron microprobe, the oxidation state of the iron is not directly known. For the basis of this discussion, total iron in magnetite is calculated as Fe_2O_3 (* Fe_2O_3) and in ilmenite as FeO (* FeO). Representative analysis of ilmenite, magnetite and hercynite are given in Table 5.8.

Ilmenite and magnetite both occur in the dioritic rocks from the Glen Doll Complex. Ilmenite, typically contains 43-47% TiO_2 , though exceptionally 51% is recorded. Titanium substitutes for Fe^{2+} in the ilmenite lattice (Deer et al., 1967) and there is an inverse correlation between * FeO and TiO_2 due to this substitution in the analysed samples. The amount of manganese (an element which also substitutes for Fe) varies from 1.1-1.7% MnO . Titanium and manganese show a positive correlation. The ilmenites also typically contain ~0.03% Cr_2O_3 .

Magnetite occurs in two forms in the dioritic rocks. The first as interstitial anhedral crystals and the second as very small exolved crystals in secondary amphibole. The composition of the two forms is essentially similar with the latter having lower * Fe_2O_3 (96%) compared to the former (99%). These analyses also contain ~1.25% of SiO_2 which may reflect a problem with the analysis of a pure sample since the analyses were taken close to the margins of the crystal. The manganese content of the two forms is <0.10% MnO . The titanium content varies from 0.09-0.26% TiO_2 and shows a positive correlation with the bulk rock titanium content (Table 5.8 and appendix C). The magnetites also contain a low level of chromium, <0.03% Cr_2O_3 .

The oxide phase from the Juan Jorge diorites by comparison is dominantly magnetite, ilmenite being recorded only rarely. The former contain from 0.07-0.27% TiO_2 , titanium increasing with decreasing iron content (Table 5.8). Manganese remains constant at ~0.07% MnO . A characteristic feature of these magnetites is that they contain a variable and high level of chromium, from 0.24-1.4% Cr_2O_3 . Chromium can substitute extensively in the magnetite lattice for Fe^{3+} (Deer et al., 1974). Ilmenite occurs rarely but the few crystals characteristically contain a high level of manganese (7% MnO) compared with the Glen Doll ilmenite. High manganese ilmenite have been described from a granodiorite intrusion in Japan by Czamanske et al. (1981) where a positive correlation is noted between manganese content and bulk rock silica.

Heier (1956) demonstrated that the chemical composition of a magma, not its temperature, is the dominant factor in controlling the amount of titanium in magnetite. There is no apparent relationship between bulk rock TiO_2 and the titanium content of the magnetite in either the Glen Doll or the Juan Jorge Complexes. This may indicate three things, (a) that another crystallising phase is controlling the distribution of titanium, (b) that some of the magnetite is a secondary phase or (c) that the bulk composition plays little part in determining the composition of the oxide phase. Calcic amphibole may contain significant amounts of titanium (Leake, 1971) but a correlation between bulk rock and amphibole titanium content can not be demonstrated for the Glen Doll and Juan Jorge Complexes (Appendix B and C). A combination of the crystallisation of biotite and sphene (the only other titanium rich phases present in the complex), could control the distribution of titanium in the rock.

Ilmenite is thought to be a relatively early crystallising phase (Chapter 4). The crystallisation of ilmenite is partly controlled by the oxygen fugacity of the magma and therefore with evolution, and an increase in the oxygen fugacity, magnetite would be expected to replace ilmenite as the liquidus oxide phase.

5.7.1 Oxides from rafted metasedimentary xenoliths, Glen Doll Complex

Metasedimentary xenoliths are distributed throughout the dioritic rocks in the Glen Doll Complex and characteristically contain aggregates of anhedral, green hercynitic spinel. The crystals may be zoned, with alumina-rich and iron-poor cores (62.4% Al_2O_3 and 23.39% *FeO) and alumina-poor and iron-rich rims (59% Al_2O_3 and 28.2% *FeO). They also contain 11% MgO and minor amounts of MnO (0.2-0.3%). Titanium is not recorded.

Hercynitic spinel are commonly found in metamorphosed pelitic sediments due to the high alumina content. Unlike spinel s.s., hercynite is stable in the presence of free silica (Deer et al., 1974). Hercynites are also common in the pyroxene hornfels facies of the thermal aureole around the Glen Doll Complex (Schumacher, 1985) where they contain up to 14% ZnO. Hercynitic spinel also occur as isolated aggregates within the diorites and monzonites, where are thought to represent the remnants of an otherwise totally assimilated rafted xenolith.

5.8 Sphene and apatite

Sphene and apatite are two of the most important minor phases present in the wide range of rock types from both complexes. Apart

from the major constituents, the abundance of some of the light rare earth elements (LREE) (the only REE possible to determine at low concentrations by electron microprobe) have been determined. These are La and Ce in the sphene and La, Ce and Nd in the apatite. Representative analysis of sphene from a range of rock types are given in Table 5.9.

5.8.1 Sphene

This mineral typically occurs in the Glen Doll diorites as anhedral or interstitial crystals. Crystals are unzoned and of a uniform composition with respect to the major constituents, typically 39% TiO_2 , 29% SiO_2 and 28% CaO . Total iron (*FeO) varies from 0.61-1.5%. The abundance of the REE are generally low, La_2O_3 0.02%, Ce_2O_3 0.16-0.2%.

The Juan Jorge diorites by comparison contain sphene with typically 37% TiO_2 , 29% SiO_2 and 27% CaO . Iron content varies inversely with titanium content, indicating that there is extensive substitution of Ti for Fe. The REE abundances in the sphene are greater than in the Glen Doll Complex. Lanthanum varies from 0.21-0.45% La_2O_3 and cerium 0.42-1.87% Ce_2O_3 . The crystals of sphene are commonly zoned, with respect to the REE, with higher levels of REE in the cores than in the rims (Table 5.9). The sphene from the Juan Jorge granite contain a similar level of REE.

Analyses of sphene crystals from a micro diorite xenolith from the Juan Jorge Complex display comparable REE concentrations to sphenes from the Juan Jorge diorites.

5.8.2 Apatite

Apatite crystals from both complexes contain >2% fluorine and are classified as fluor-apatite (Deer et al., 1974). Those from the Glen Doll diorite contain 2.16-4.47% F (average 3.59%) and those from the Juan Jorge diorite contain 3.6-6.3% F (average 5.31%). Apatite from the Juan Jorge granite contain the highest levels with 5.59-6.47% F (Table 5.10).

The major element chemistry of the apatites varies between complexes, crystals from Glen Doll diorite typically containing lower levels of calcium (48% CaO) compared with 55% CaO in the Juan Jorge diorite. LREE abundances are comparable between complexes, and apatite crystals typically contain La_2O_3 0.1-0.2%, Ce_2O_3 0.1-0.3% and Nd_2O_3 0.08-0.15%.

5.8.3 Discussion of apatite and sphene chemistry

Henderson (1980), demonstrated that the LREE are preferentially incorporated in apatite relative to co-existing sphene through a range of bulk rock compositions. The REE, at terrestrial magmatic oxidation levels, are dominantly trivalent and are known to substitute for Ca^{2+} in apatite and sphene, and to a lesser extent in amphibole, plagioclase and biotite (Henderson, 1980; Alderton et al., 1980). It was suggested by Henderson (1980) that the difference in the partition coefficients of the REE in sphene and apatite are explicable in terms of the differences in the co-ordination of the REE in the two minerals.

Chondrite normalised patterns for co-existing sphene and apatite (Henderson, 1980) display the LREE enrichment of apatite relative to sphene and the relative heavy REE (HREE) depletion in both minerals. Recent experimental work (Green and Pearson, 1986)

has shown that the degree of LREE enrichment in sphene is related to (a) the increasing SiO_2 content of the bulk rock (b) increasing pressure and (c) decreasing temperature. Thus the REE content of the sphenes, crystallising in an evolving dioritic liquid at constant depth, for example would be expected to contain progressively higher levels of REE (particularly LREE) assuming that no other REE concentrating phase is crystallising.

The SiO_2 contents of the Juan Jorge diorites are higher than the Glen Doll diorites for the analysed samples. The REE contents of the sphenes are correspondingly higher. Sphene in the Glen Doll diorites is thought to have crystallised relatively late, at a time similar to apatite since both minerals occur as interstitial minerals. The sphene in the Juan Jorge rocks however is frequently euhedral and probably crystallised prior to apatite. The LREE data for apatite and sphene from the Glen Doll diorites supports this idea since the apatites contain higher levels of LREE than the co-existing sphene. Early crystallising sphene from the Juan Jorge diorites display high LREE levels.

CHAPTER 6

Geochemistry

6.1 Introduction

The major, trace and rare earth element (REE) geochemistry of the range of rock types from both the Glen Doll and Juan Jorge complexes have been determined. The major elements SiO_2 , Al_2O_3 , TiO_2 , $^*\text{FeO}$, MgO , MnO , CaO , Na_2O and K_2O were analysed in a lithium metaborate fusion solution using a Pye-Unicam SP1900 atomic absorption spectrophotometer. P_2O_5 was analysed in the same solution using a colorimetric technique. The trace elements Ba, Cr, Cu, Li, Ni, Rb, Sc, Sr, V and Zn were analysed after an open acid digestion, using a Philips PV8210 inductively coupled plasma atomic emission spectrometer (ICPAES). Zr was analysed by ICPAES and Rb by AA both using the lithium metaborate fusion solution. Zirconium is commonly located in the mineral zircon which is only partially attacked by acid digestion techniques. The REE were analysed by ICP following pre-concentration by a cation exchange procedure (Jarvis and Jarvis, 1986, modified after Walsh et al., 1981). Details of the analytical techniques, accuracy and precision of all methods are given in appendix D. The geochemistry has been plotted on a range of variation diagrams in order to display and aid interpretation of the data.

The geochemical data for all of the analysed samples are given in appendix C and representative analyses are also given in this chapter (Tables 6.1-6.5). Major and trace element variation diagrams have been plotted, initially using MgO as abscissa. Magnesium ranges from <0.2% MgO in the most evolved rocks to >25% MgO in the olivine gabbros. Magnesium shows a high correlation

Table 6.1 Representative analyses of the basic rocks and appinites from the Glen Doll Complex

	Olivine gabbro Gabbro					Appinite	
	GC200	GC88	GC70	GC79	GC76	GC30	GC206
SiO ₂	49.14	47.66	50.70	51.05	52.59	55.00	53.88
Al ₂ O ₃	6.33	6.49	15.14	18.49	18.59	9.40	11.89
TiO ₂	0.48	0.54	0.71	0.67	0.63	0.87	2.01
*FeO	9.07	9.30	6.54	5.50	5.44	7.28	9.13
MgO	20.66	21.55	10.79	8.53	6.58	11.60	11.22
MnO	0.15	0.15	0.10	0.10	0.10	0.16	0.17
CaO	8.93	8.55	11.84	12.47	9.79	8.10	7.50
Na ₂ O	1.15	1.31	1.98	1.93	2.99	2.28	1.80
K ₂ O	0.65	0.59	0.41	0.28	1.00	2.59	1.65
P ₂ O ₅	0.11	0.08	0.08	0.08	0.09	0.14	0.19
H ₂ O+	2.00	3.35	1.27	1.38	1.82	1.87	BD
CO ₂	0.15	0.26	0.25	BD	0.23	0.50	BD
Total	98.82	99.83	99.81	100.48	99.85	99.79	99.36
Ba	118	133	86	100	230	260	424
Cr	1368	820	285	205	389	398	572
Cu	49	35	60	44	20	51	19
La	ND	8	9	ND	ND	14	18
Li	13	15	12	11	18	21	ND
Ni	226	241	102	76	48	165	268
Rb	23	25	12	9	30	34	85
Sc	37	29	30	26	20	41	53
Sr	119	189	575	870	842	260	293
V	114	110	114	108	74	164	227
Y	13	9	13	15	24	16	50
Zn	100	89	59	57	61	89	94
Zr	71	62	66	27	68	120	199

Table 6.2 Representative analyses of the dioritic rocks
from the Glen Doll Complex

	Pyroxene diorite		Hornblende diorites					
	GC133	GC220	GC105	GC249	GC173	GC146	GC1	GC2
SiO ₂	48.60	54.07	52.29	48.41	52.25	56.30	50.02	48.93
Al ₂ O ₃	16.64	15.90	16.53	15.74	15.67	19.20	15.70	16.60
TiO ₂	3.20	1.56	1.68	3.35	3.09	1.60	2.75	2.62
*FeO	12.80	7.88	8.26	12.87	11.59	6.40	11.45	10.99
MgO	5.51	5.75	6.24	5.08	5.05	4.76	4.35	4.35
MnO	0.16	0.13	0.14	0.15	0.19	0.13	0.16	0.16
CaO	8.20	9.51	9.43	8.72	6.91	6.84	7.70	7.93
Na ₂ O	2.66	2.40	2.74	2.70	2.29	3.20	2.90	3.20
K ₂ O	0.51	1.35	0.79	1.23	1.11	0.85	1.86	1.51
P ₂ O ₅	0.11	0.16	0.15	0.25	0.14	0.14	0.43	1.14
H ₂ O+	1.45	BD	1.75	BD	2.02	0.57	1.73	1.37
CO ₂	BD	BD	BD	BD	BD	BD	0.40	0.10
Total	99.60	98.71	100.00	98.50	100.31	99.79	99.45	98.90
Ba	149	281	198	329	301	165	340	300
Cr	42	29	208	32	21	43	101	111
Cu	42	26	41	73	25	120	35	32
La	10	19	ND	ND	ND	ND	23	37
Li	14	ND	20	29	29	20	30	31
Ni	42	17	50	47	14	16	33	31
Rb	17	74	29	40	42	30	56	54
Sc	33	36	27	35	33	17	31	26
Sr	589	556	566	638	546	661	660	660
V	386	119	196	504	441	144	305	274
Y	13	18	23	22	13	8	22	32
Zn	128	77	75	117	137	76	99	89
Zr	214	135	113	96	84	120	157	127

Table 6.3 Representative analyses of monzonites and adamellites from the Glen Doll Complex

	Monzonite		Adamellite		
	GC21	GC19	GC117	GC116	GC276
SiO ₂	55.80	51.20	70.28	64.93	66.10
Al ₂ O ₃	16.80	17.10	14.12	15.92	15.57
TiO ₂	1.72	2.20	0.52	0.80	0.94
*FeO	7.36	9.68	2.36	4.33	4.51
MgO	2.85	3.90	0.85	1.46	2.71
MnO	0.11	0.15	0.05	0.12	0.09
CaO	5.49	6.55	0.85	1.84	3.07
Na ₂ O	3.87	3.30	3.51	3.73	3.56
K ₂ O	1.75	1.77	4.25	2.99	2.74
P ₂ O ₅	0.89	1.23	0.14	0.23	0.25
H ₂ O+	2.04	2.10	1.25	1.76	BD
CO ₂	0.10	0.10	0.04	0.07	BD
Total	98.82	99.28	98.52	98.18	99.20
Ba	450	440	815	759	775
Cr	86	102	32	93	53
Cu	20	25	8	17	13
La	35	40	ND	44	39
Li	36	30	21	35	ND
Ni	39	31	BD	29	33
Rb	55	56	117	107	141
Sc	11	21	6	10	13
Sr	600	600	236	311	511
V	181	234	39	68	85
Y	23	32	22	19	22
Zn	89	112	40	77	70
Zr	217	217	245	294	277

Table 6.4 Representative rock analyses from the Juan Jorge Complex and Bridge Outcrops

	Lochnagar Diorites Outcrops					Granite		Bridge	
	JJ1	JJ3	JJ4	JJ7	JJ23	JJ9	JJ17	JJ10	JJ12
SiO ₂	71.60	65.61	63.08	62.61	56.72	71.29	72.06	55.75	72.48
Al ₂ O ₃	14.12	16.22	15.70	16.05	17.27	15.78	15.44	17.09	14.60
TiO ₂	0.44	0.87	1.00	1.10	1.31	0.52	0.49	1.20	0.42
*FeO	2.00	4.23	5.32	5.92	6.41	2.53	2.36	6.96	1.82
MgO	0.65	2.03	3.01	3.49	3.66	0.81	0.73	5.33	0.64
MnO	0.04	0.07	0.09	0.10	0.10	0.06	0.05	0.13	0.04
CaO	1.28	3.39	4.60	5.36	6.72	1.59	1.56	6.31	1.22
Na ₂ O	3.11	3.78	3.57	3.65	3.93	4.23	4.07	3.77	3.39
K ₂ O	5.34	3.47	2.68	1.92	1.71	4.56	4.55	2.47	4.24
P ₂ O ₅	0.12	0.21	0.28	0.30	0.38	0.13	0.13	0.25	0.09
H ₂ O+	0.20	BD	BD	BD	0.80	BD	BD	BD	BD
CO ₂	BD	0.23	0.22	0.06	BD	BD	BD	BD	BD
Total	98.91	98.71	99.55	100.56	99.01	101.49	101.44	99.26	98.94
Ba	1269	1027	703	554	599	1355	1591	586	954
Cr	10	28	47	85	99	12	11	74	9
Cu	5	12	24	16	23	10	7	42	5
La	44	ND	ND	ND	36	ND	ND	ND	44
Li	ND	46	41	30	ND	17	16	35	ND
Ni	7	22	35	42	44	5	5	87	7
Rb	336	132	87	54	104	109	106	76	203
Sc	6	6	14	16	20	6	5	19	5
Sr	227	665	714	776	768	338	375	626	222
V	31	86	114	129	135	22	23	145	24
Y	12	18	28	28	26	16	18	29	12
Zn	41	83	87	87	89	49	48	103	30
Zr	223	463	276	202	255	322	325	204	241

Table 6.5 Representative analyses of intermediate and acid dykes from the Glen Doll Complex

	Microdiorite			QFP		Aplite	
	GC87	GC246	GC230	GC168	GC154	GC34	GC86
SiO ₂	61.99	58.72	68.13	75.82	75.00	79.91	75.58
Al ₂ O ₃	16.45	15.79	14.17	12.97	13.25	12.57	12.57
TiO ₂	1.22	1.40	0.84	0.13	0.05	BD	0.12
*FeO	5.65	6.16	3.94	0.55	1.05	0.60	1.01
MgO	3.63	4.49	2.08	0.19	0.51	0.05	0.15
MnO	0.09	0.11	0.07	0.03	0.03	BD	0.05
CaO	4.69	6.22	3.29	0.55	1.38	BD	0.72
Na ₂ O	3.68	3.85	4.24	3.34	3.69	3.59	4.44
K ₂ O	1.98	1.76	3.45	4.28	3.00	5.50	5.34
P ₂ O ₅	0.27	0.32	0.21	0.03	0.04	BD	0.05
H ₂ O+	1.22	BD	BD	BD	BD	0.74	0.75
CO ₂	0.11	BD	BD	BD	BD	BD	0.09
Total	110.98	98.82	101.12	98.77	99.04	99.13	100.82
Ba	506	633	753	524	267	BD	1152
Cr	110	38	40	BD	14	10	36
Cu	25	20	13	4	5	5	3
La	33	43	43	ND	ND	3	ND
Li	22	ND	ND	14	13	11	9
Ni	39	39	24	BD	BD	BD	BD
Rb	60	124	161	141	100	160	129
Sc	13	17	10	5	3	3	4
Sr	463	784	445	76	104	BD	155
V	107	141	83	BD	6	BD	BD
Y	21	20	20	19	20	7	18
Zn	66	75	55	29	121	41	31
Zr	247	239	260	94	230	77	102

Table 6.5A Representative analyses of microdiorite xenoliths
from the Glen Doll and Juan Jorge Complexes

	Glen Doll		Juan Jorge
	GC138	GC148	JJ19
SiO ₂	54.20	51.00	58.46
Al ₂ O ₃	12.60	16.25	17.60
TiO ₂	1.29	1.79	1.35
*FeO	10.35	13.10	5.85
MgO	8.07	7.88	3.02
MnO	0.24	0.22	0.17
CaO	10.50	6.58	5.62
Na ₂ O	1.60	2.53	5.21
K ₂ O	0.31	0.22	1.79
P ₂ O ₅	0.15	0.15	0.33
H ₂ O+	0.44	0.37	BD
CO ₂	BD	BD	BD
Total	99.75	100.09	99.40
Ba	109	115	243
Cr	230	268	22
Cu	60	30	41
La	ND	5	48
Li	14	13	ND
Ni	128	38	24
Rb	16	14	122
Sc	46	21	17
Sr	317	671	372
V	392	298	138
Y	26	9	21
Zn	126	147	105
Zr	117	95	290

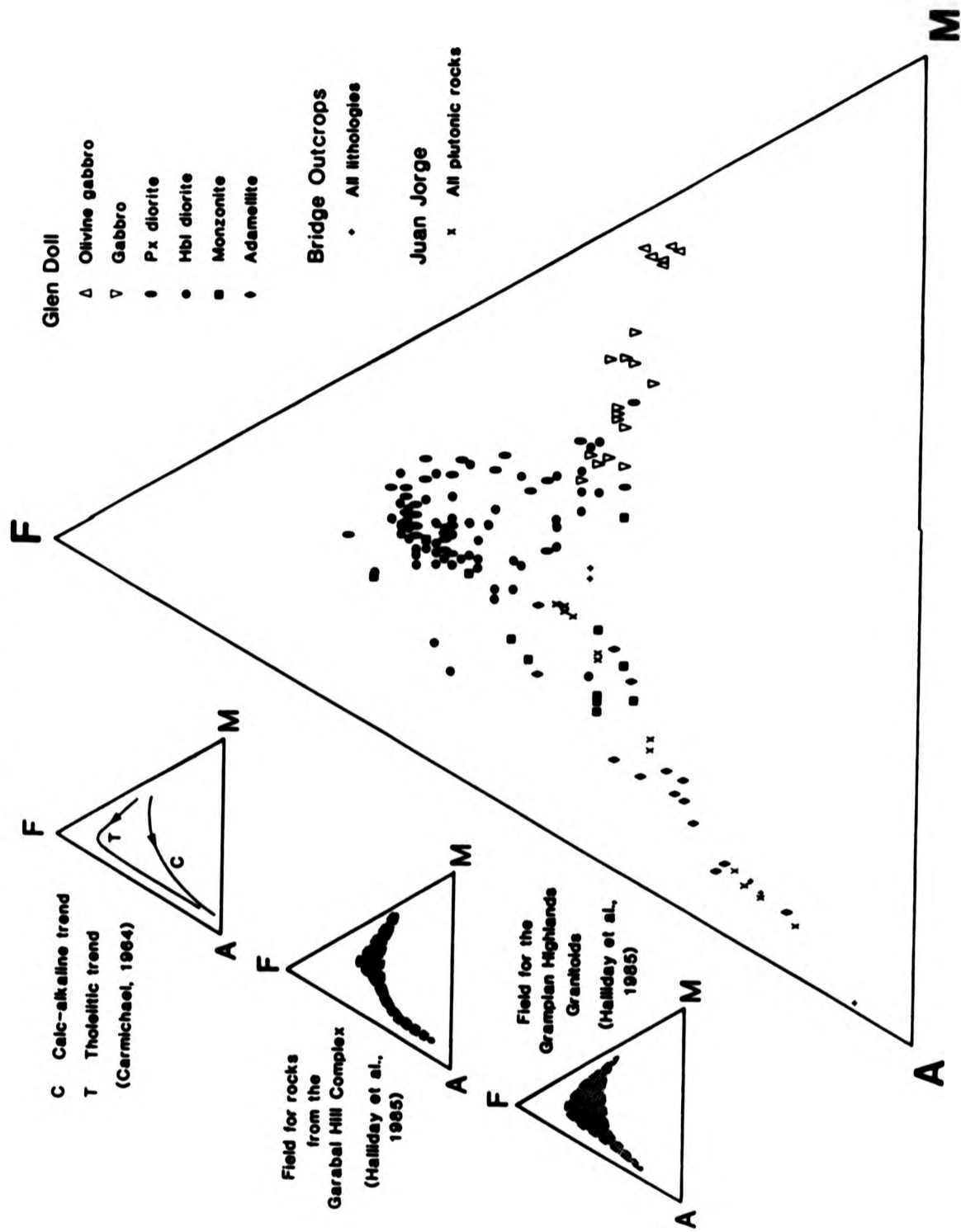
with many of the major elements and some of the trace elements through a range of rock types, and is therefore considered to be a good choice to demonstrate the chemical variation in the suite.

6.2 Major element chemistry

The Glen Doll and Juan Jorge complexes display chemical characteristics typical of many late Caledonian calc-alkaline intrusive complexes. Nockolds and Mitchell (1946), summarised the geochemistry of a range of rock types from some calc-alkaline intrusions in Scotland, including Garabal Hill, Strontian, Ben Nevis and Carn Chois. From this study these authors concluded that the major element data displayed a liquid line of descent in the acid to intermediate rock compositions, while the higher MgO compositions represented cumulate rocks. Modern data, mostly from granitic complexes, reinforces this interpretation (e.g. Halliday et al., 1985).

The iron, magnesium and alkali content of the Glen Doll and Juan Jorge rocks have been plotted on an AFM ($\text{Na}_2\text{O}+\text{K}_2\text{O}:\text{FeO}:\text{MgO}$) diagram to display the range of compositions (Figure 6.1.). A characteristic feature of the calc-alkaline lava suite, is that the magma compositions fall on an almost straight line trend from the Fe-Mg side of the triangle to the alkali apex (Green and Ringwood, 1968). There is often a little iron enrichment relative to magnesium with increasing total alkali content. The calc-alkaline trend contrasts with the typical tholeiitic fractionation trend, which shows marked iron enrichment in the early and middle stages of fractionation (Green and Ringwood, 1968; Wager, 1960) (Figure 6.1). A degree of iron enrichment in the calc-alkaline trend is thought by Green and Ringwood (1968) to be due to the crystallisa-

Fig. 6.1 AFM diagram for the Glen Doll and Juan Jorge Complexes and Bridge Outcrops. Comparative AFM diagrams show idealised liquid trends for calc-alkaline and tholeiitic lavas, and for other Late Caledonian calc-alkaline intrusive complexes



tion of hornblende, typically seen in rocks of this suite. A liquid line of descent plots as a smooth curve on this diagram, and the very small amount of scatter at the more mafic end of the trend, may be the result of crystal accumulation.

The AFM plot for the Glen Doll and Juan Jorge data (Figure 6.1) shows that the gabbroic rocks lie at the mafic end of the calc alkaline trend. The adamellites, Juan Jorge rocks and the Bridge rocks lie at the alkaline end of the same trend. However, the Glen Doll diorites and monzonites have variable amounts of iron and magnesium for a range of alkali values. They clearly do not lie on the simple liquid line of descent for the calc alkaline lava suite described by Green and Ringwood (1968).

The AFM diagram has been used by many authors (Brown et al., 1979; Groome and Hall, 1974; Fourcade and Allegre, 1981; Nockolds and Allen, 1953; Hall, 1967) to display the variation in the chemistry of series of calc-alkaline rocks from both volcanic and plutonic environments. The most Mg rich compositions are frequently accumulative rocks (Hutchison, 1964) which display patterns comparable with the gabbroic rocks from the Glen Doll complex. A comparison with published data from the Scottish Caledonides reveals that there are no examples of intermediate rock types from any single complex, which display the range of compositions seen in the Glen Doll diorites. The Garabal Hill complex contains a range of rock types comparable with the Glen Doll complex but the diorite compositions show little scatter from the calc-alkaline trend (Figure 6.1). Fourcade and Allegre (1981) investigated the chemical variation in a series of hornblende norites, gabbros, diorites and granites from the Querigut calc-alkaline complex from the French

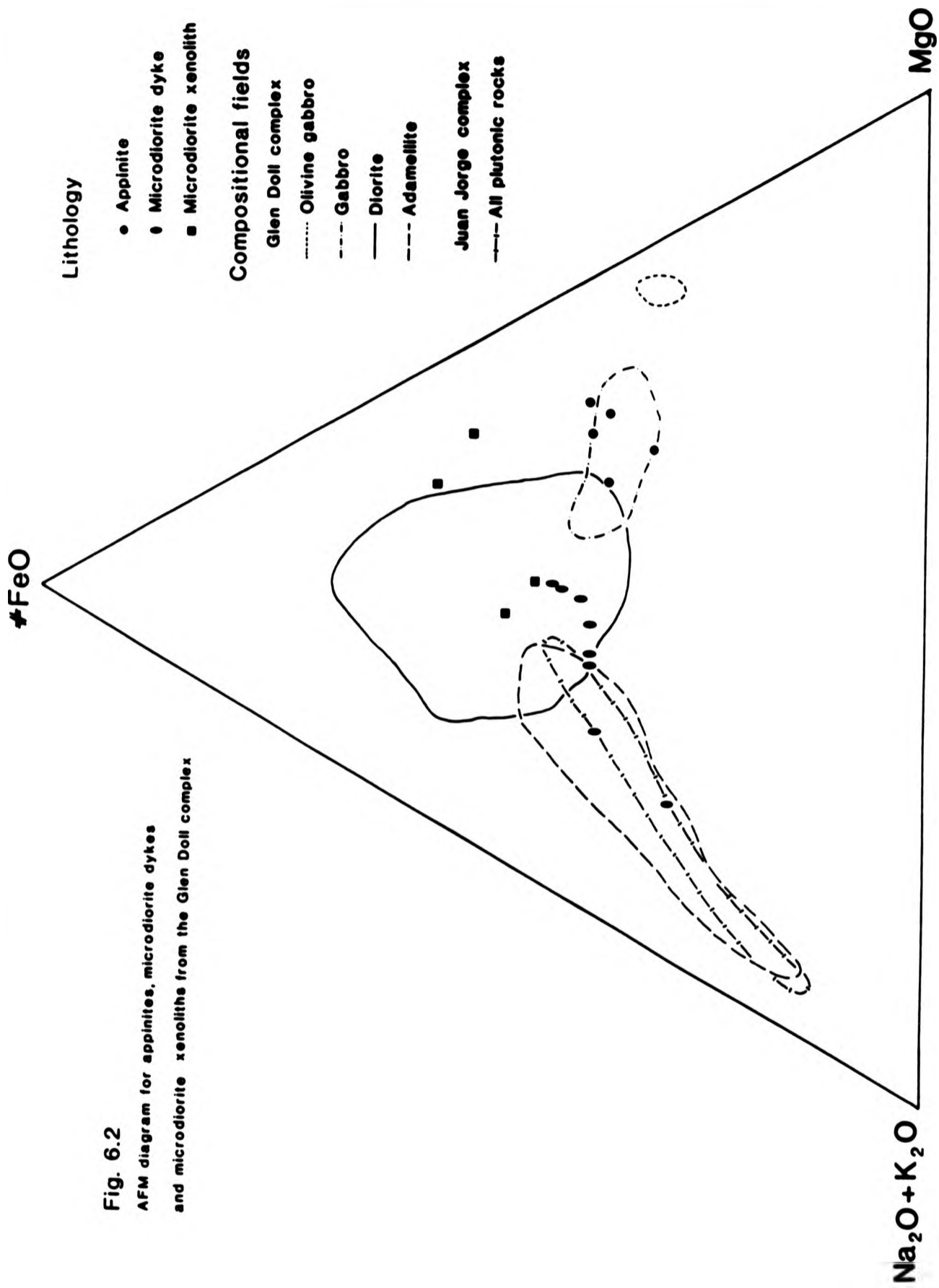


Fig. 6.2
 AFM diagram for appinites, microdiorite dykes
 and microdiorite xenoliths from the Glen Doll complex

Pyrenees. The intermediate compositions from that complex display a small amount of iron enrichment relative to the Glen Doll diorites. A study of the regional chemical variation of some Caledonian complexes in Scotland (Halliday et al., 1985; Stephens and Halliday, 1984) showed in general, that the compositions lie on the calc-alkaline trend. However, in the Grampian Highlands complexes, there is a scatter in the data towards the Fe apex, a similar pattern to that seen for the Glen Doll rocks (Figure 6.1).

The compositions of appinites, micro diorite xenoliths and dykes from the Glen Doll and Juan Jorge complexes, have also been plotted on an AFM diagram, (Figure 6.2). The appinites show a Mg enrichment relative to Fe, a feature comparable with the gabbroic rocks. The micro diorite xenoliths fall on a continuation of the trend defined by the Juan Jorge rocks, close to the calc-alkaline lava trend. The trend is similar to that defined by both the Cascades lava series (Carmichael, 1964) and the Lorne Lavas (Groome and Hall, 1974).

Figures 6.3-6.9 display the major element chemistry of the adamellites, diorites and basic rocks from Glen Doll, and of the diorites and granites from the Juan Jorge complex. Representative analyses are given in Tables 6.1-6.5. The olivine gabbros from the Glen Complex contain from 21-25% MgO and for reasons of scale their chemical variation and relationships with the diorites and adamellites is shown on separate diagrams (Figures 6.8 and 6.9). Representative chemical analyses of the olivine gabbros are given in Table 6.1. Simple linear patterns are shown by the Juan Jorge rocks whilst the Glen Doll diorites show variable chemistry and often display a scatter of data points. On each variation diagram

Key to Fig. 6.3 to Fig. 6.21

Glen Doll Complex

- △ Olivine gabbro
- △ Gabbro
- Pyroxene diorite
- Hornblende diorite
- ◇ Adamellite

Juan Jorge Complex

- + all rock types
- + Bridge Outcrops

Fig. 6.3

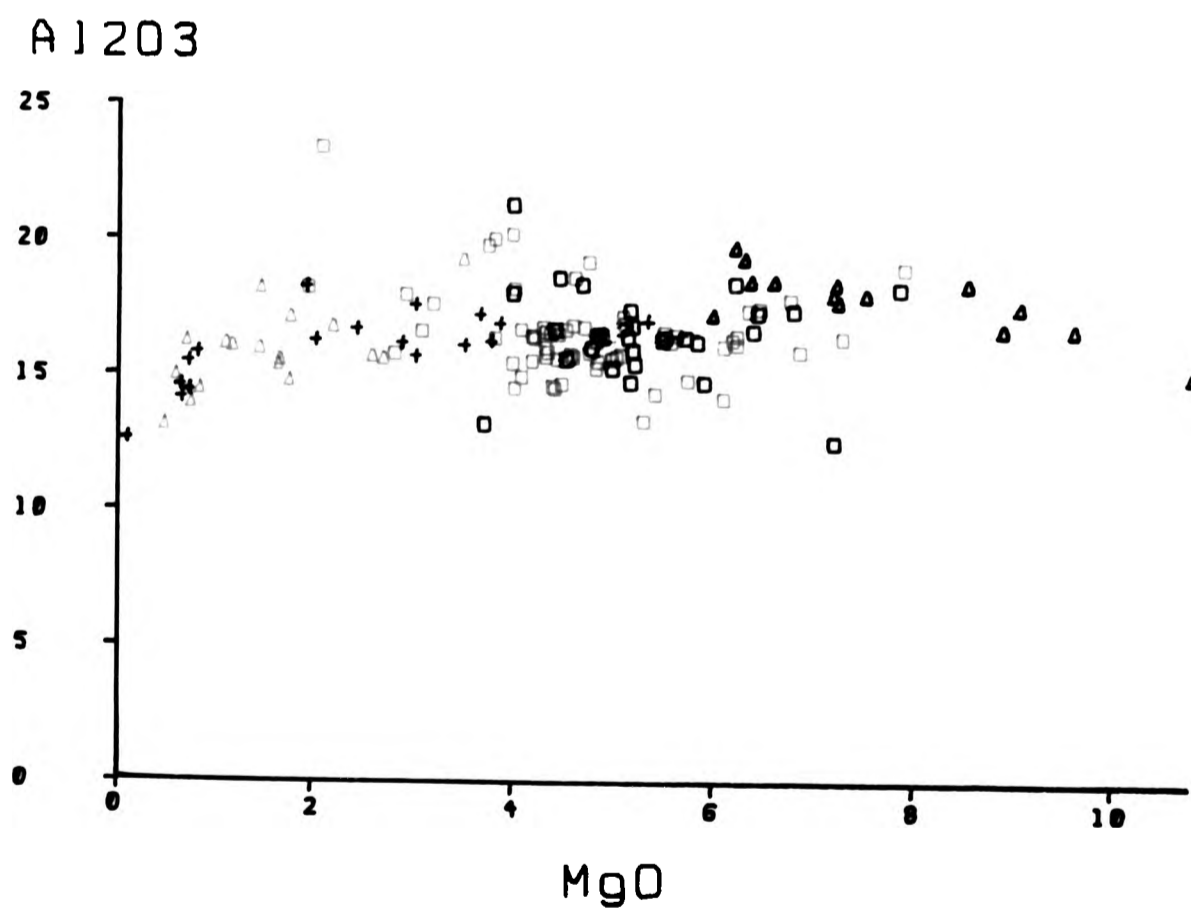
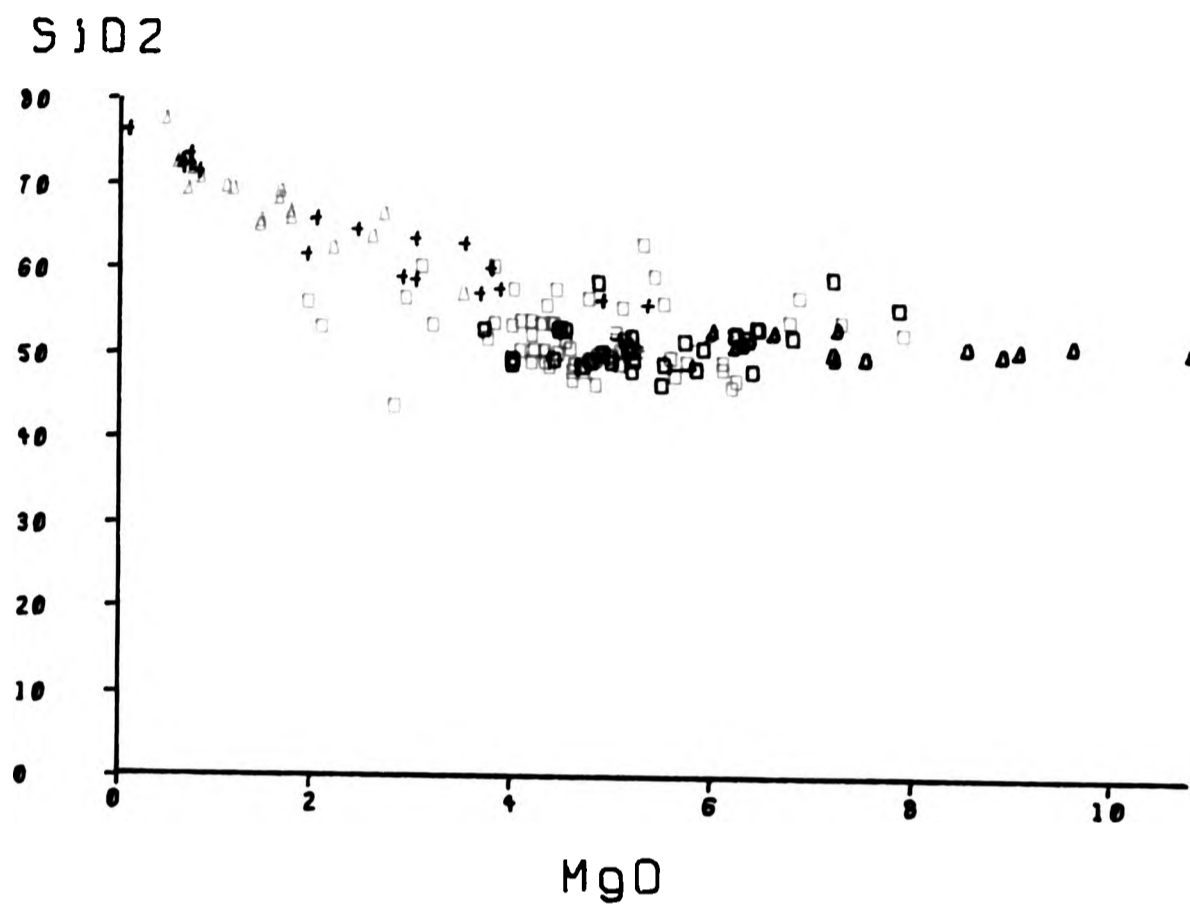


Fig. 6.4

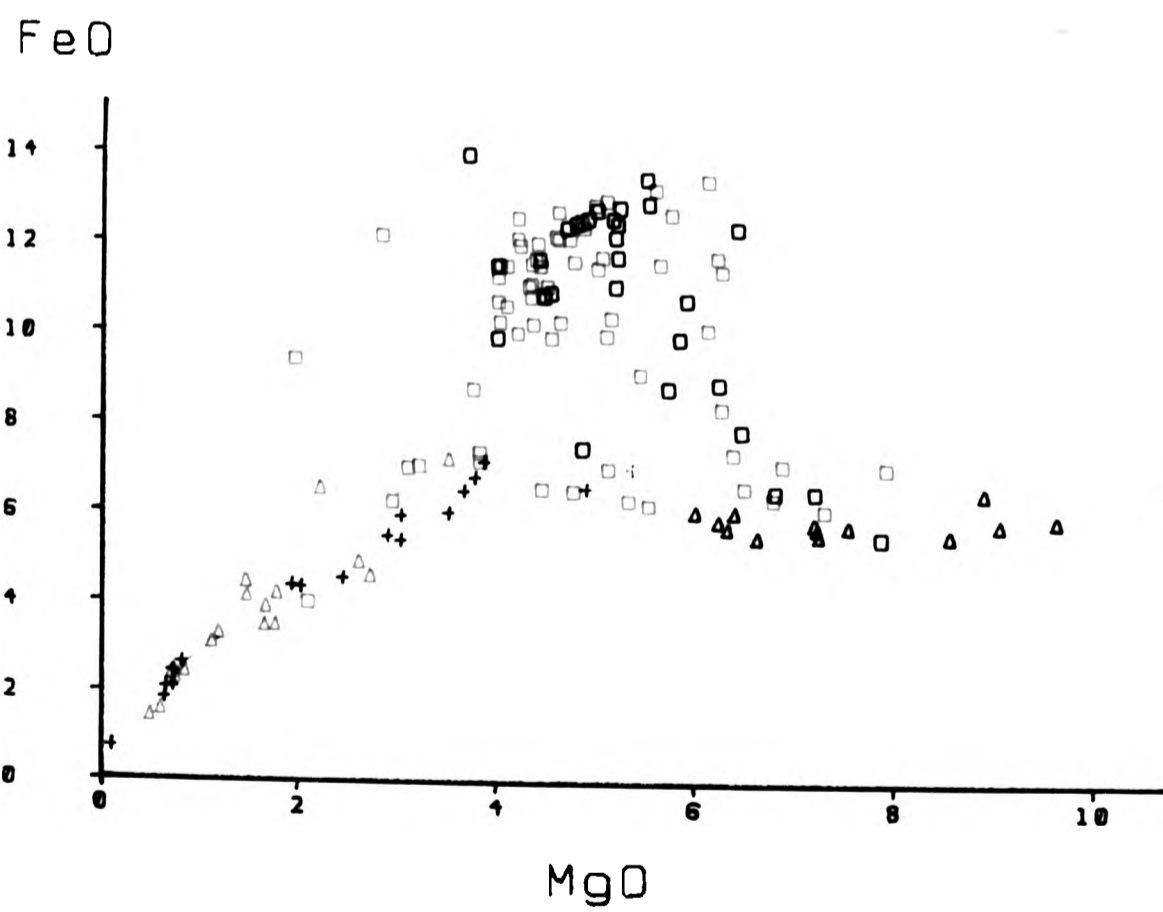
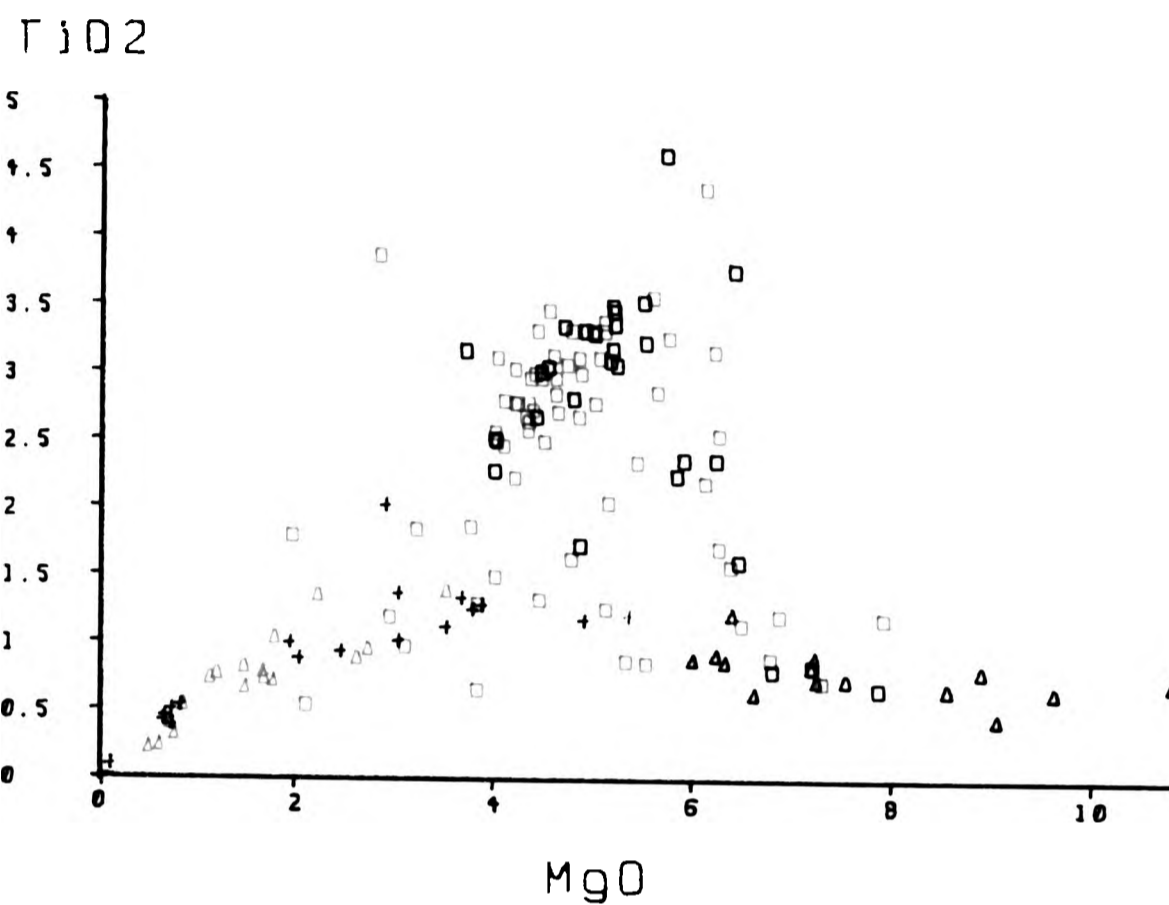


Fig. 6.5

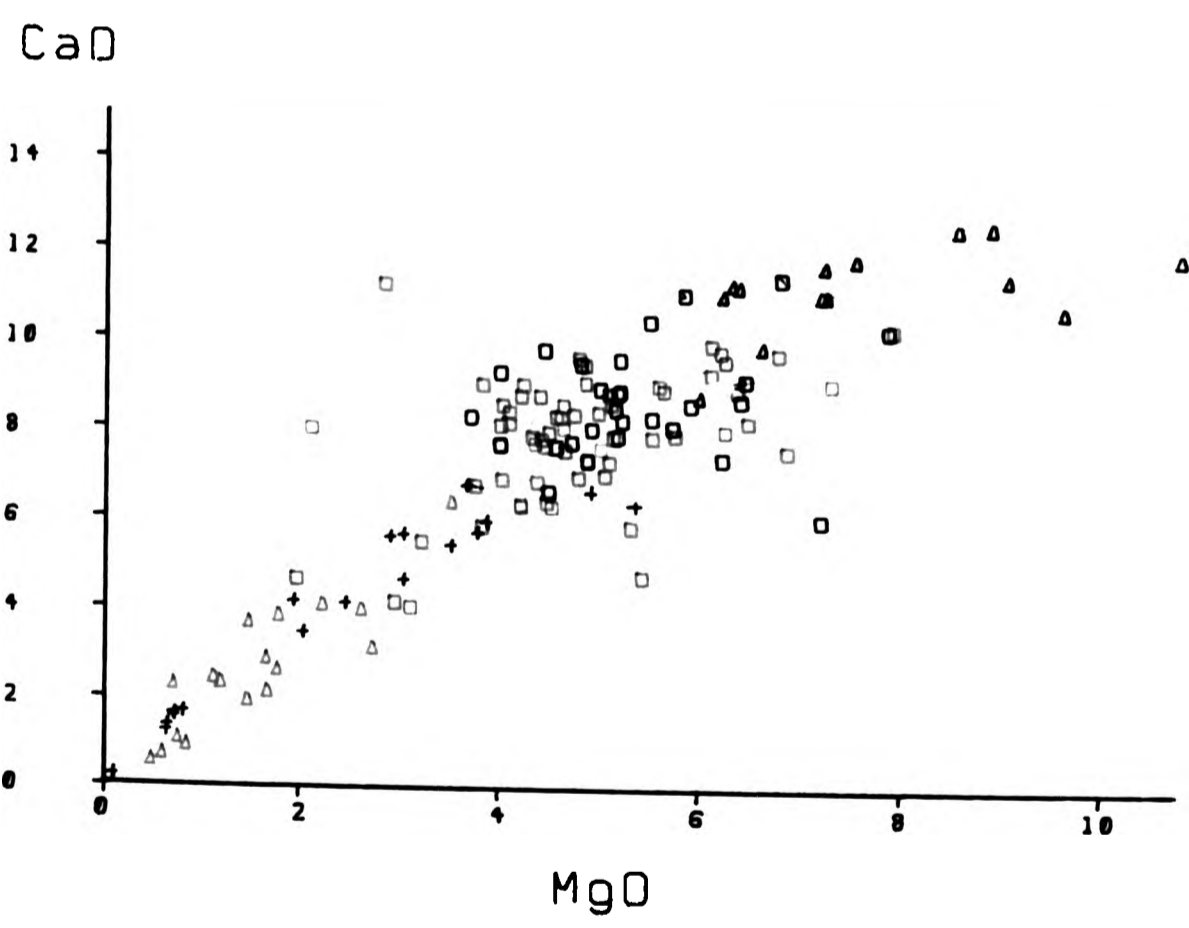
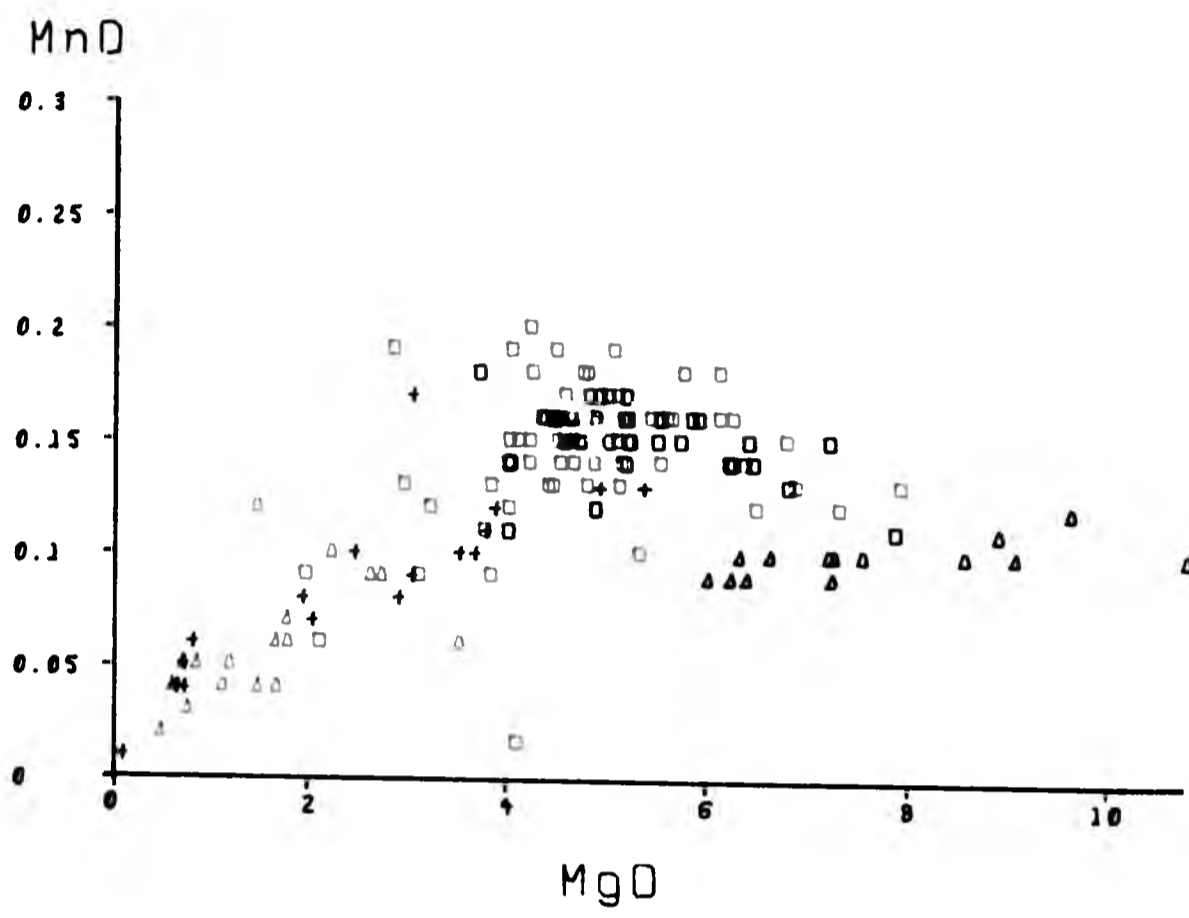


Fig. 6.6

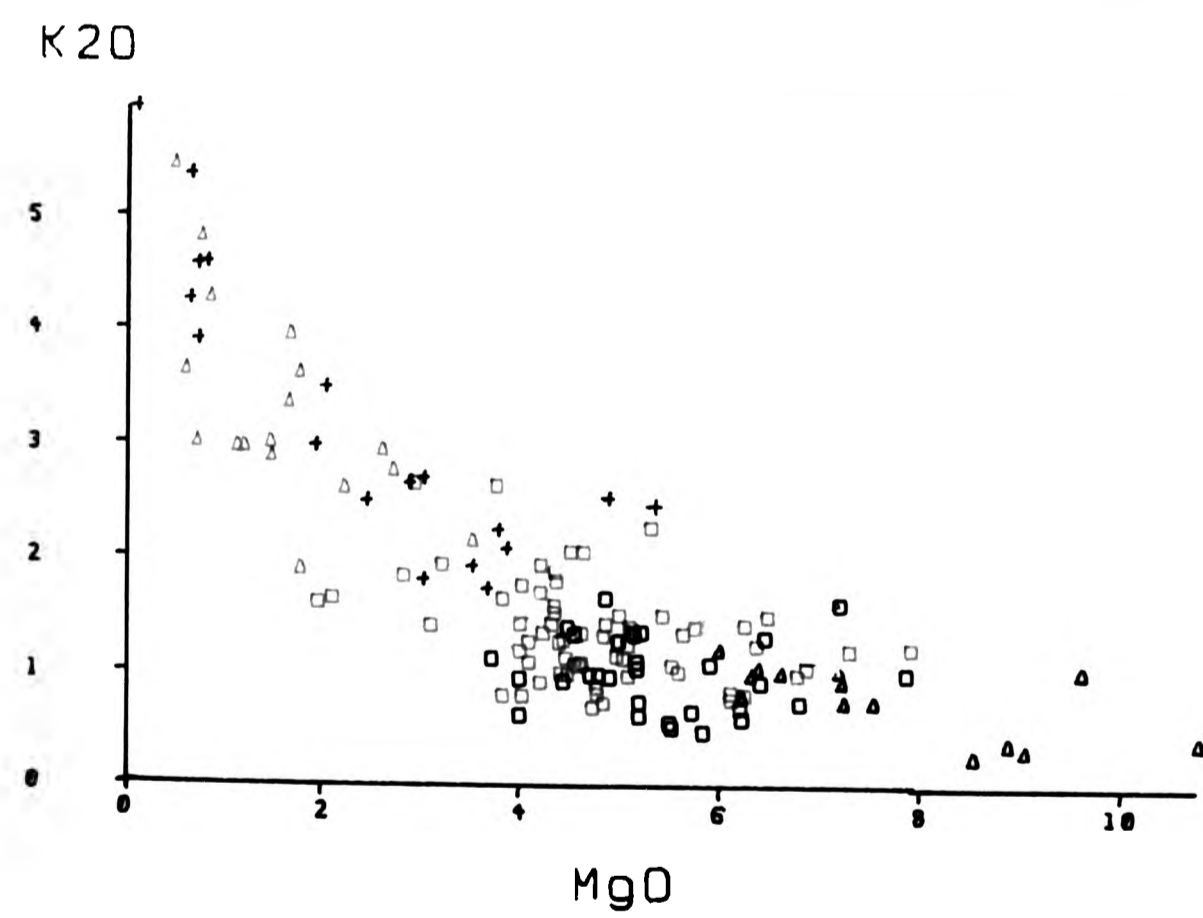
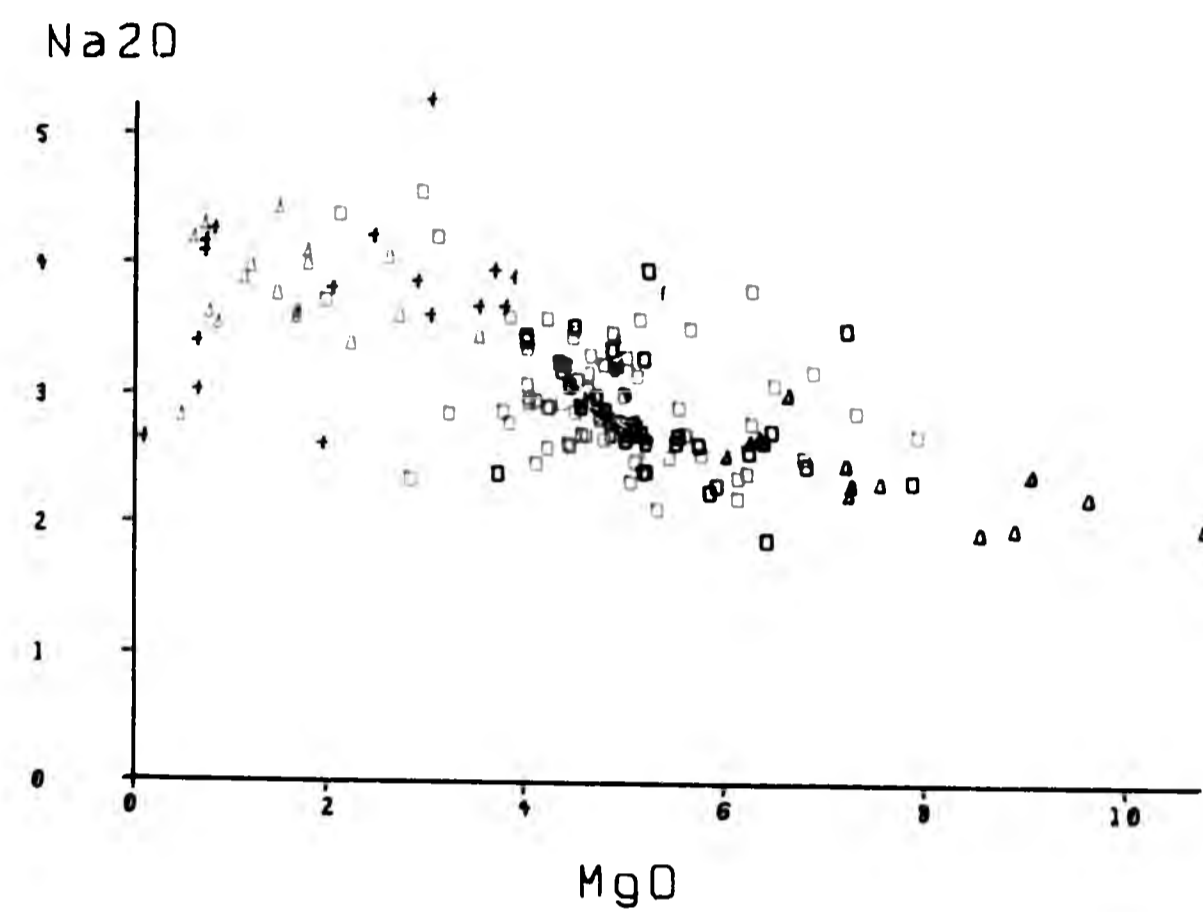


Fig. 6.7

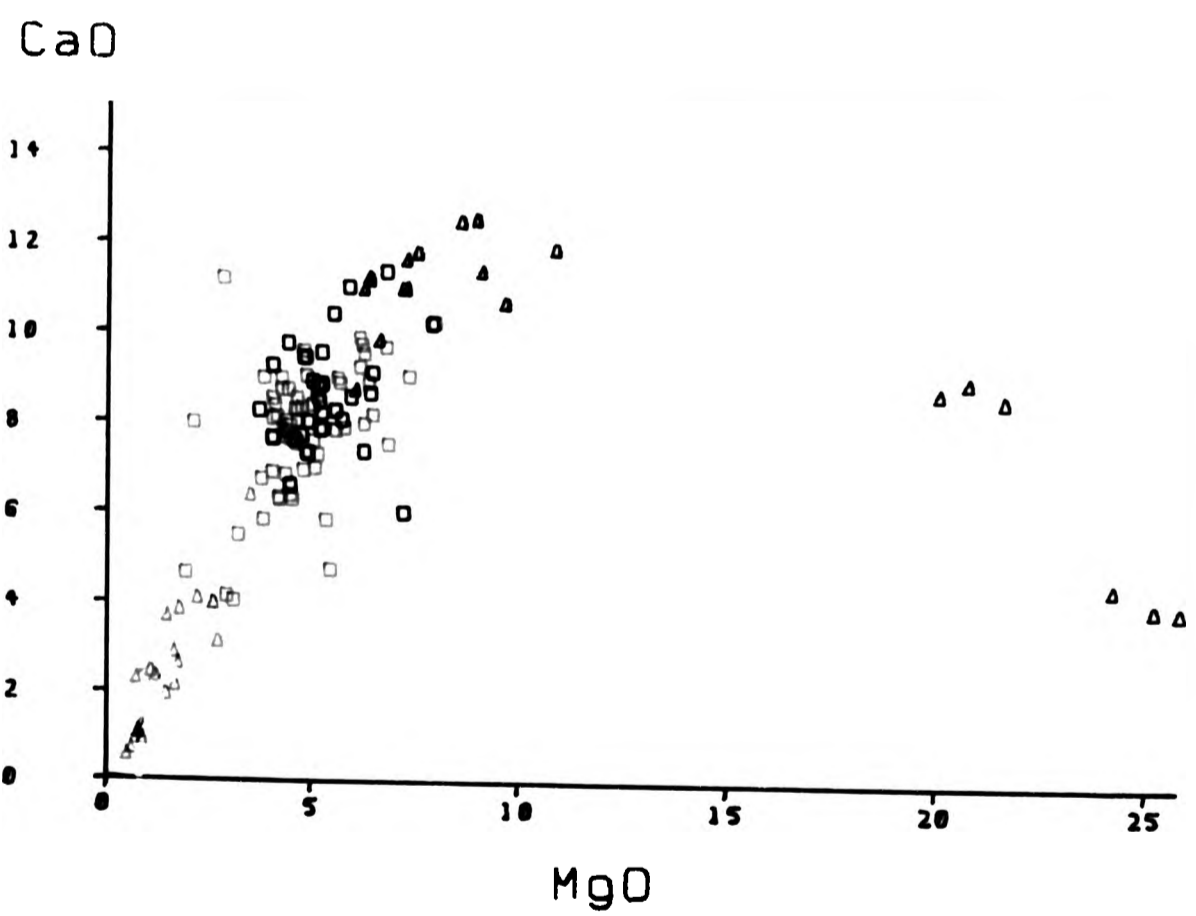
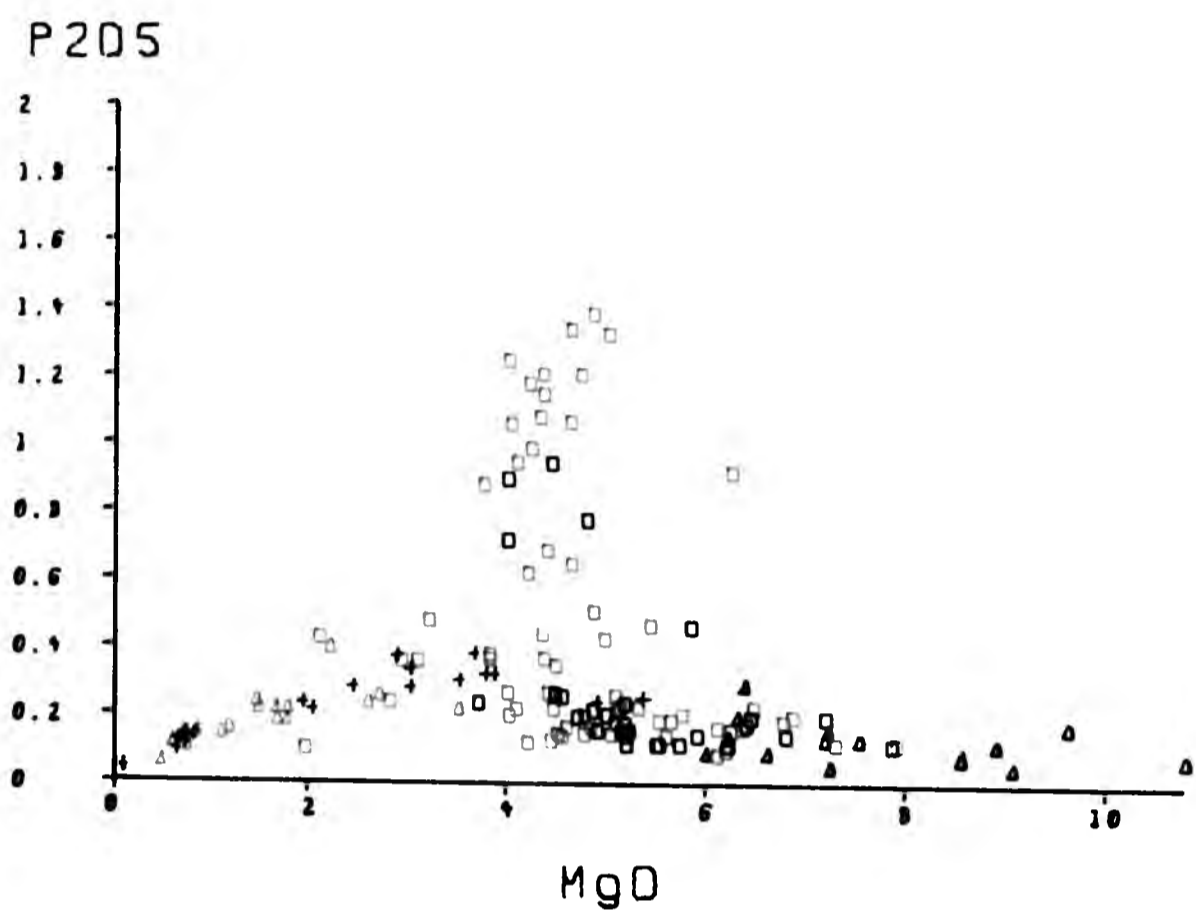


Fig. 6.8

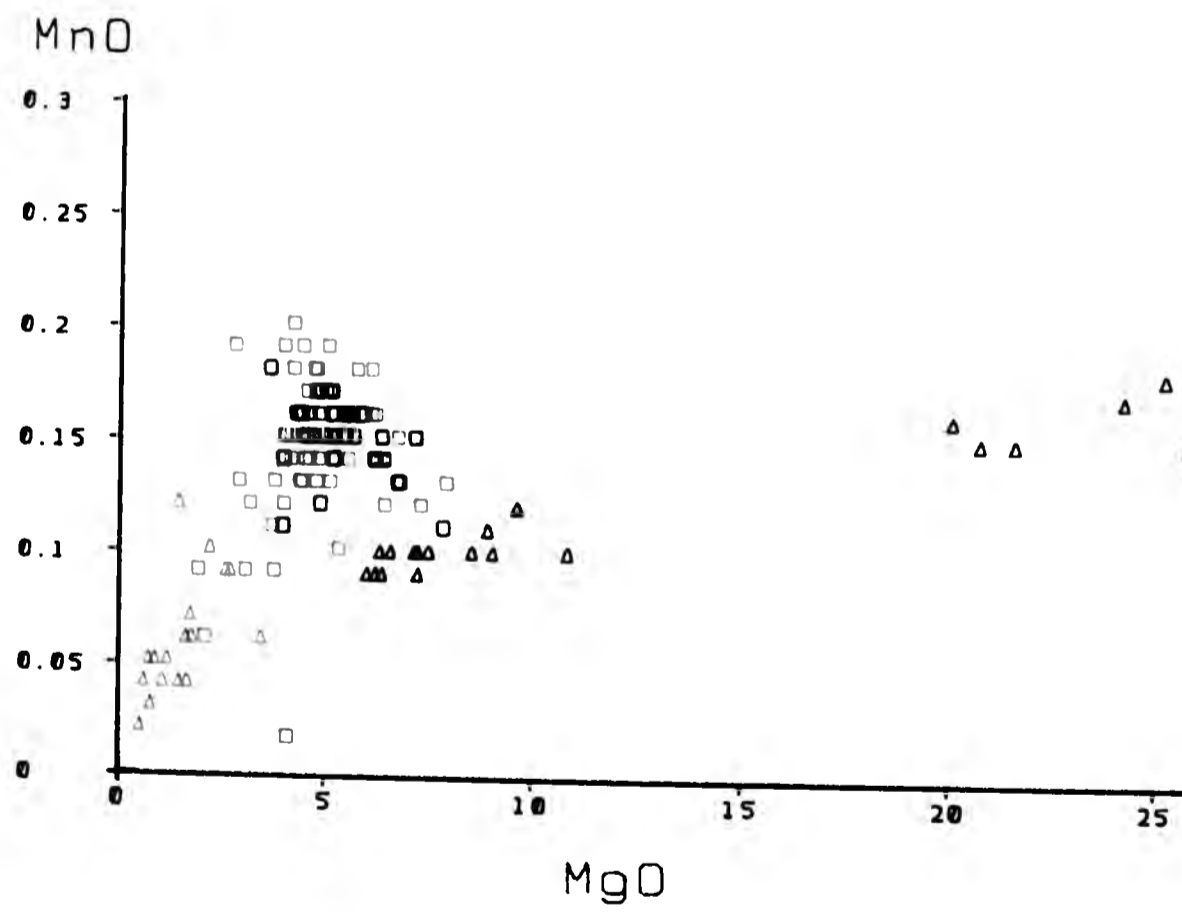
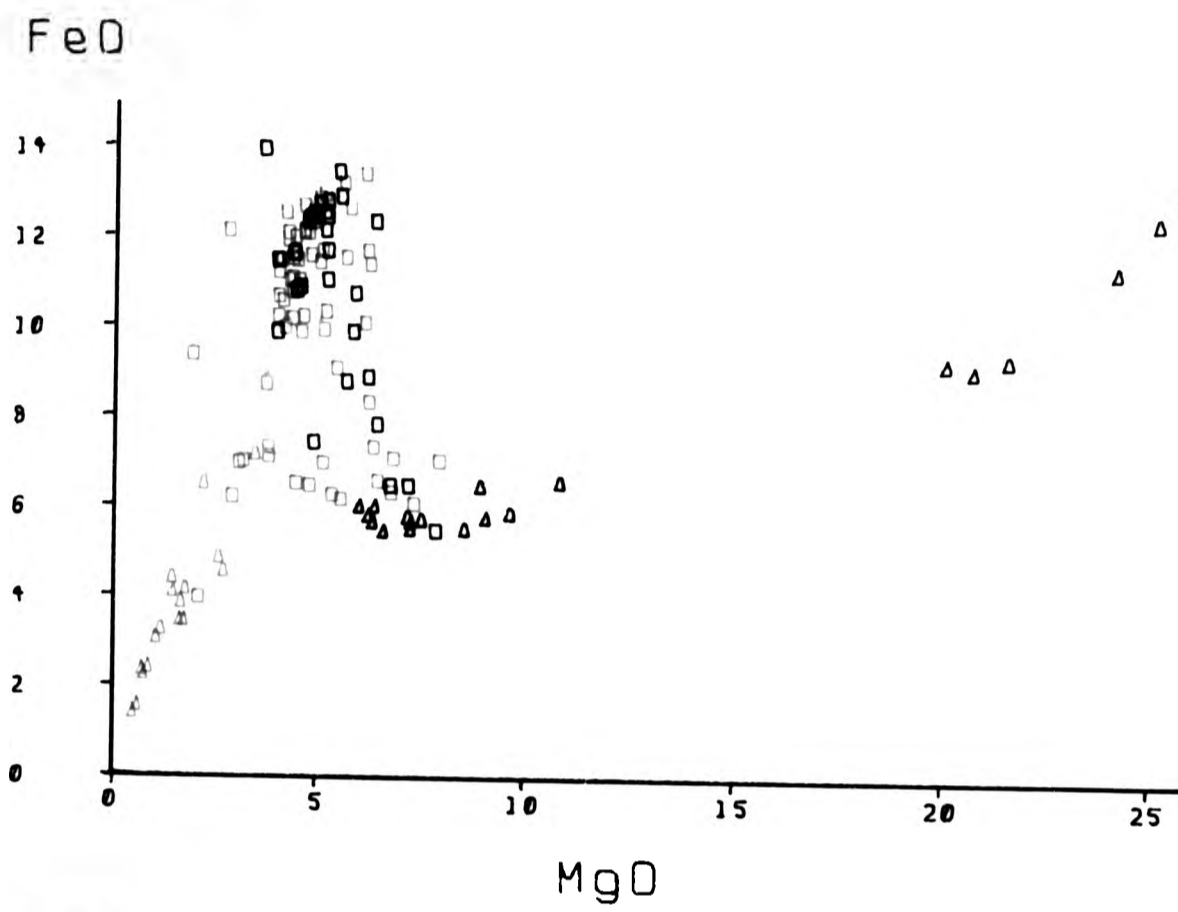


Fig. 6.9

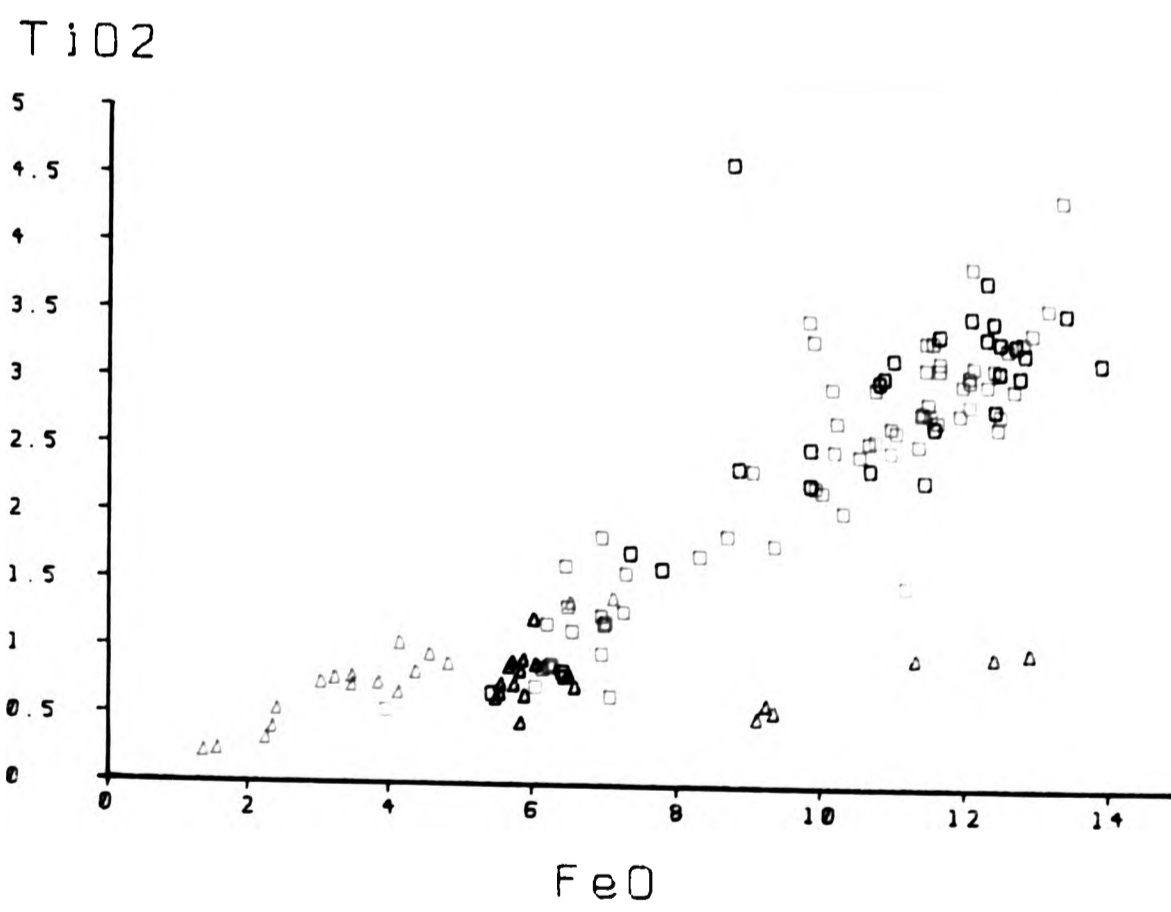
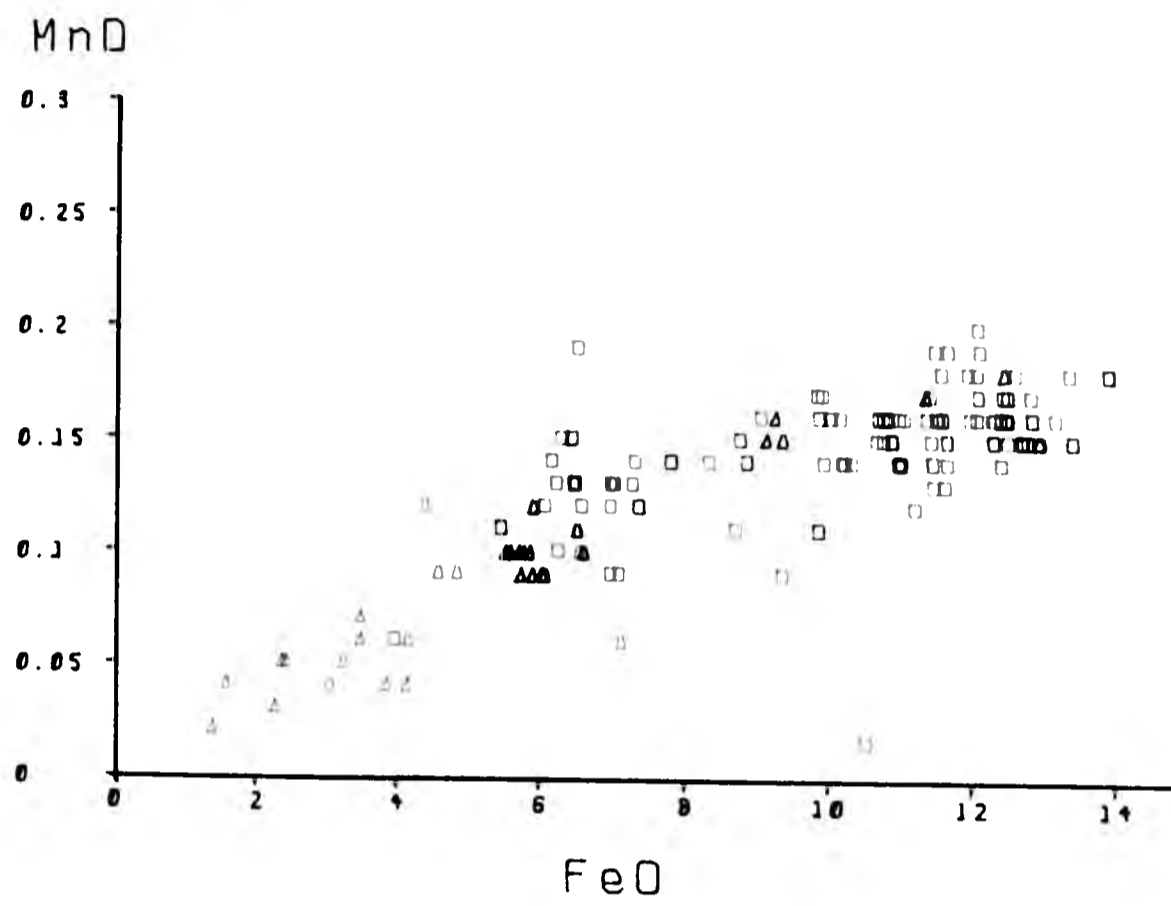


Fig. 6.10

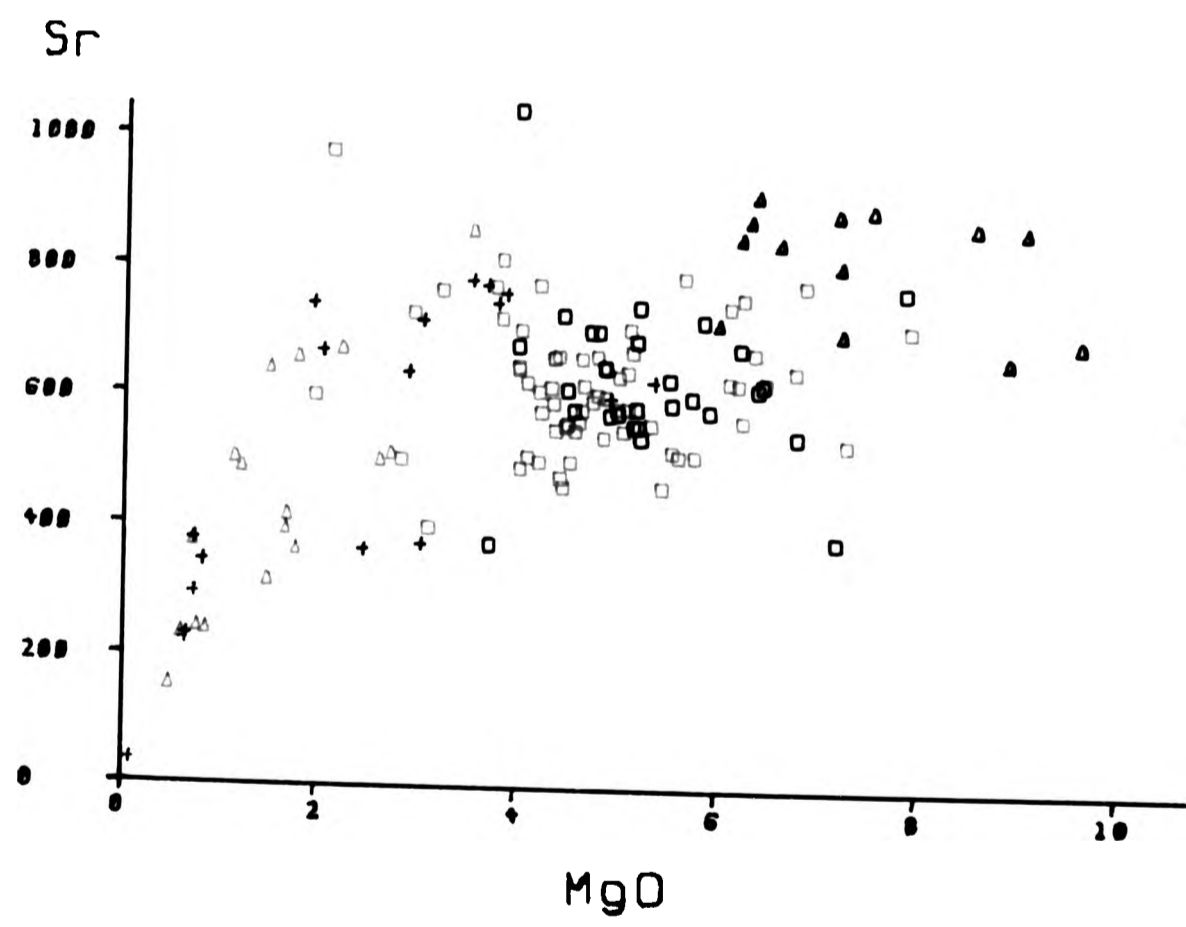
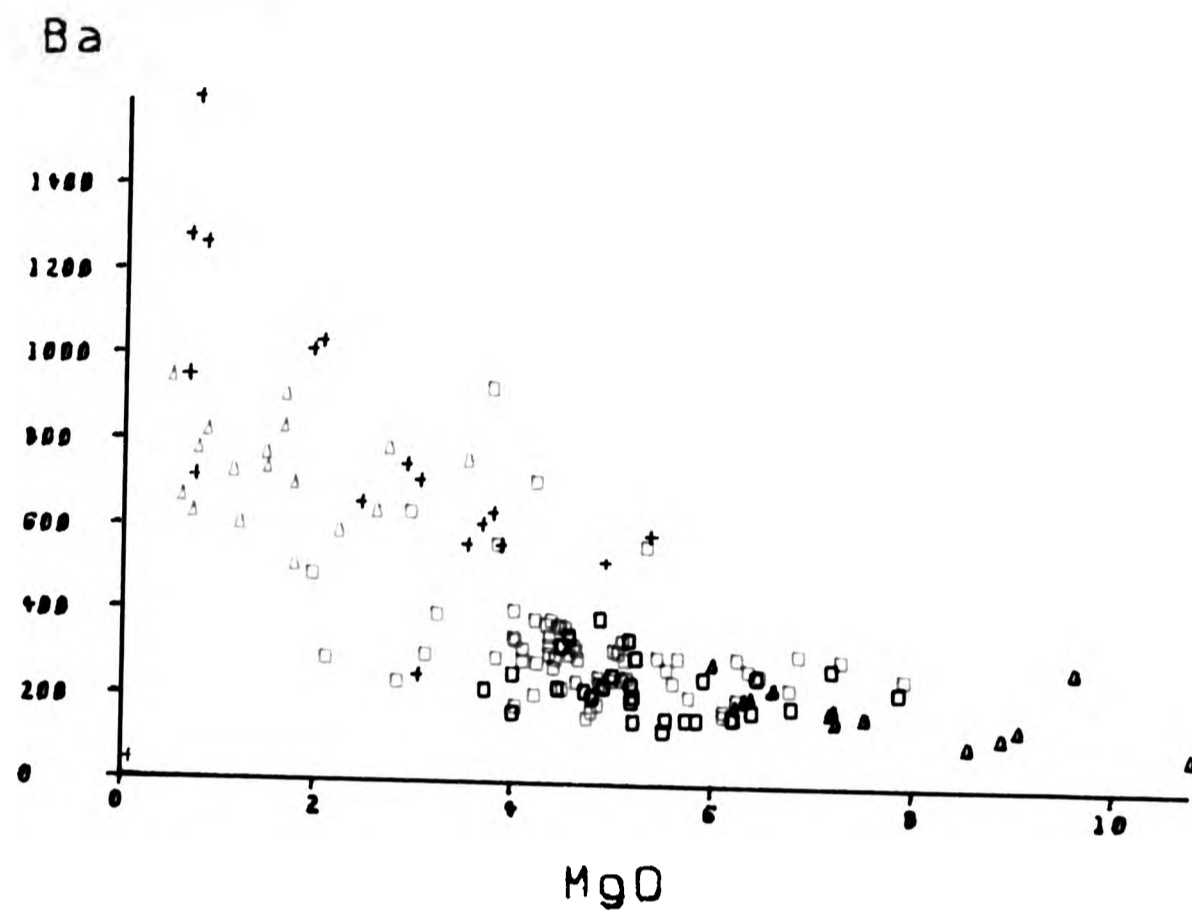


Fig. 6.11

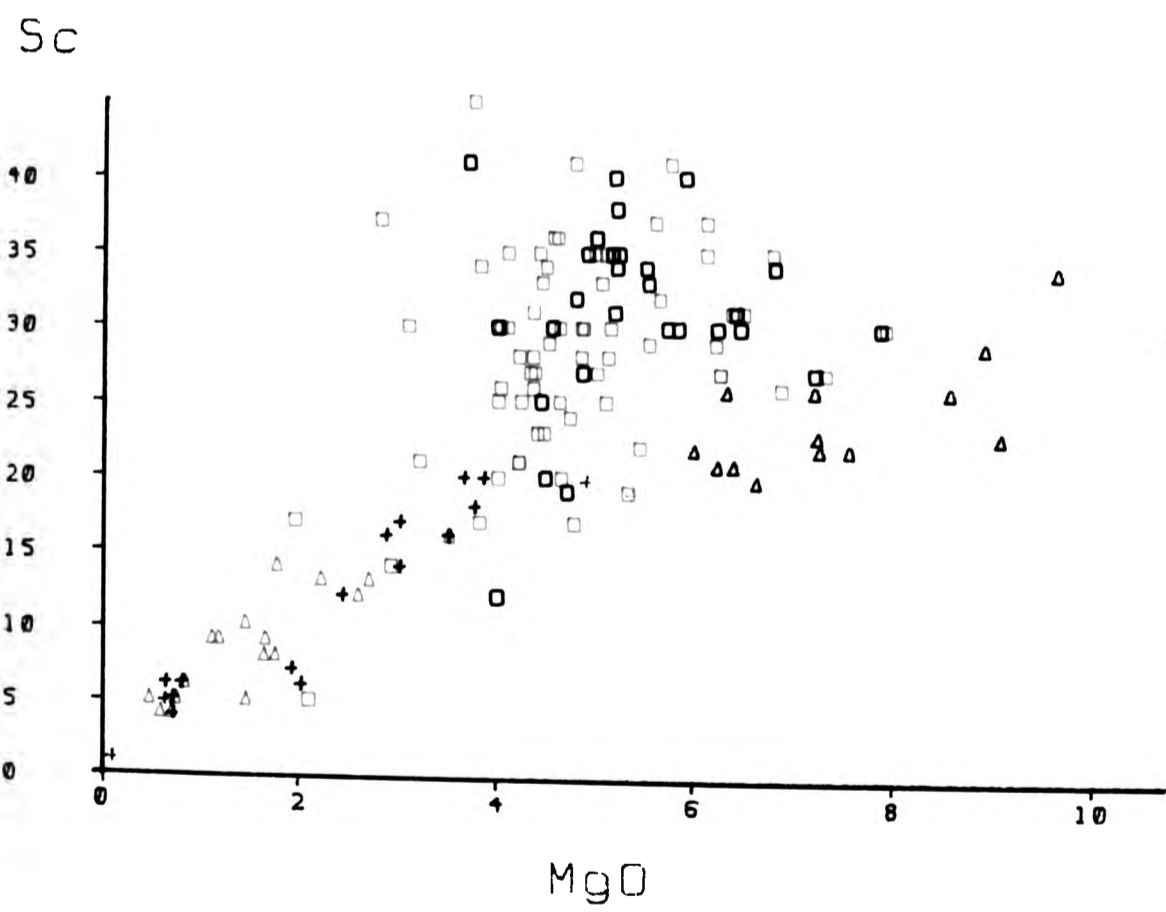
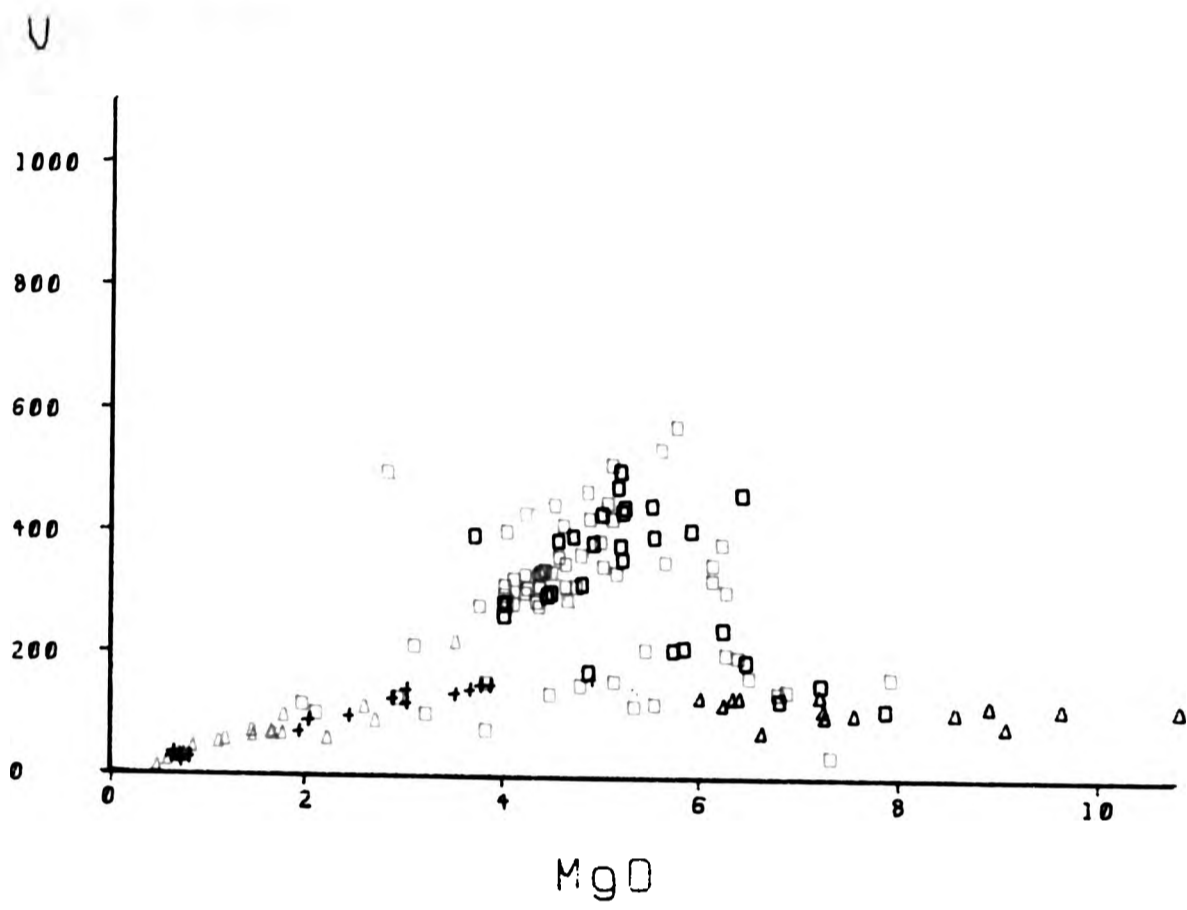


Fig. 6.12

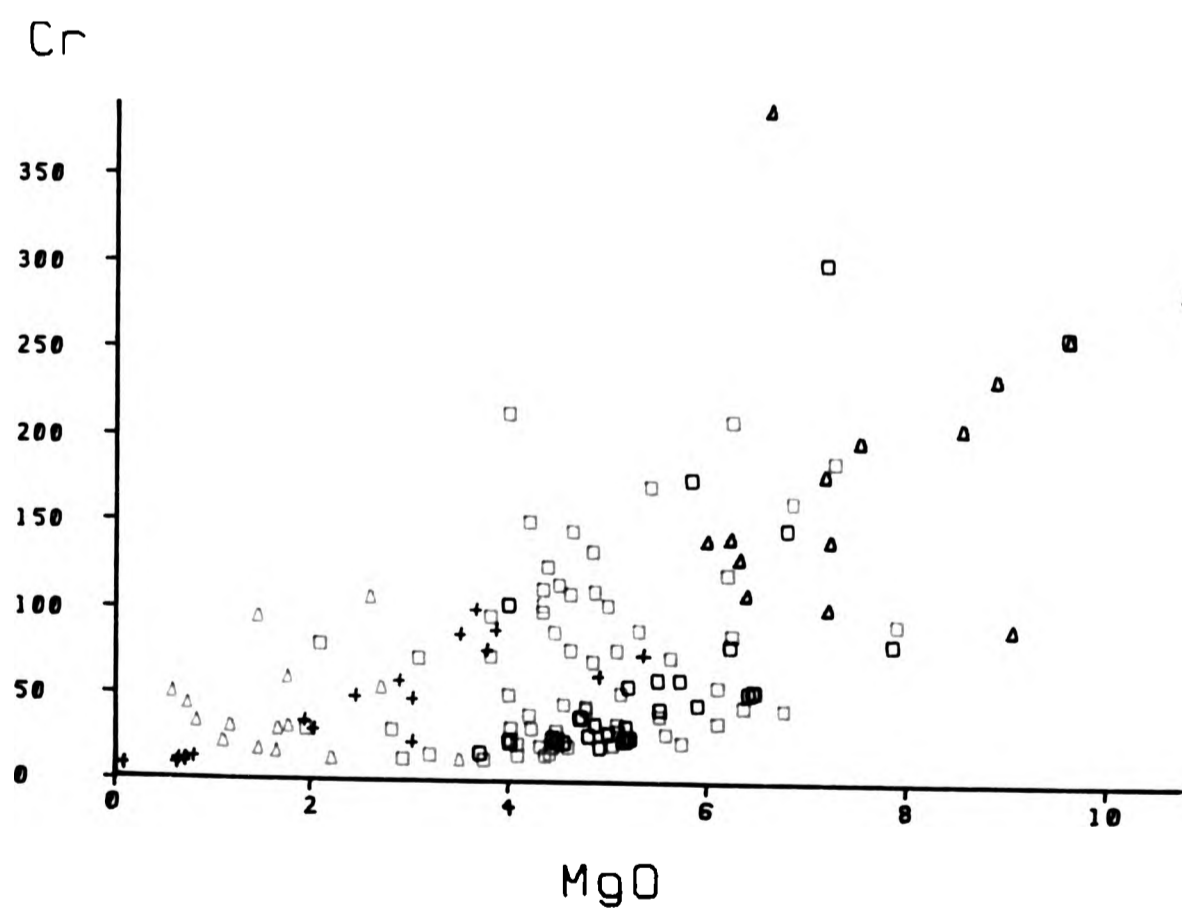
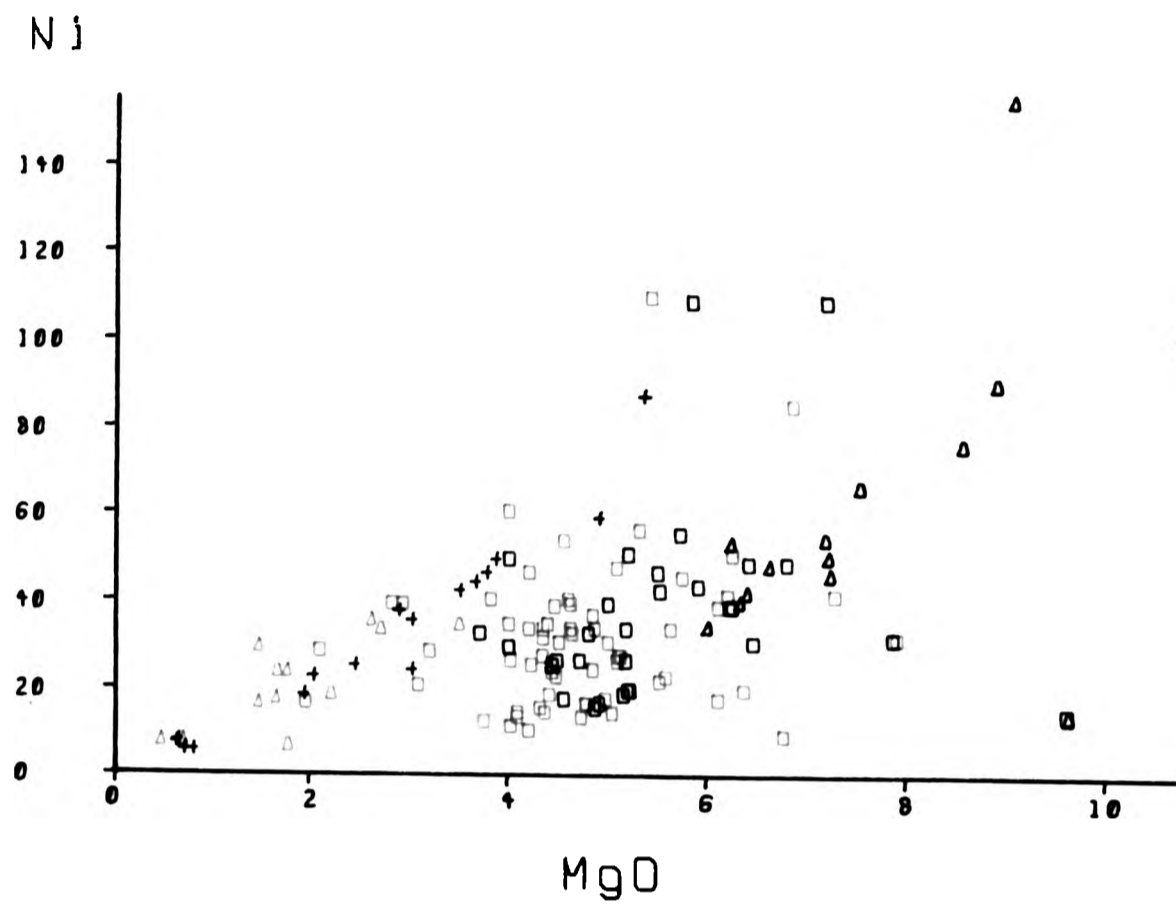
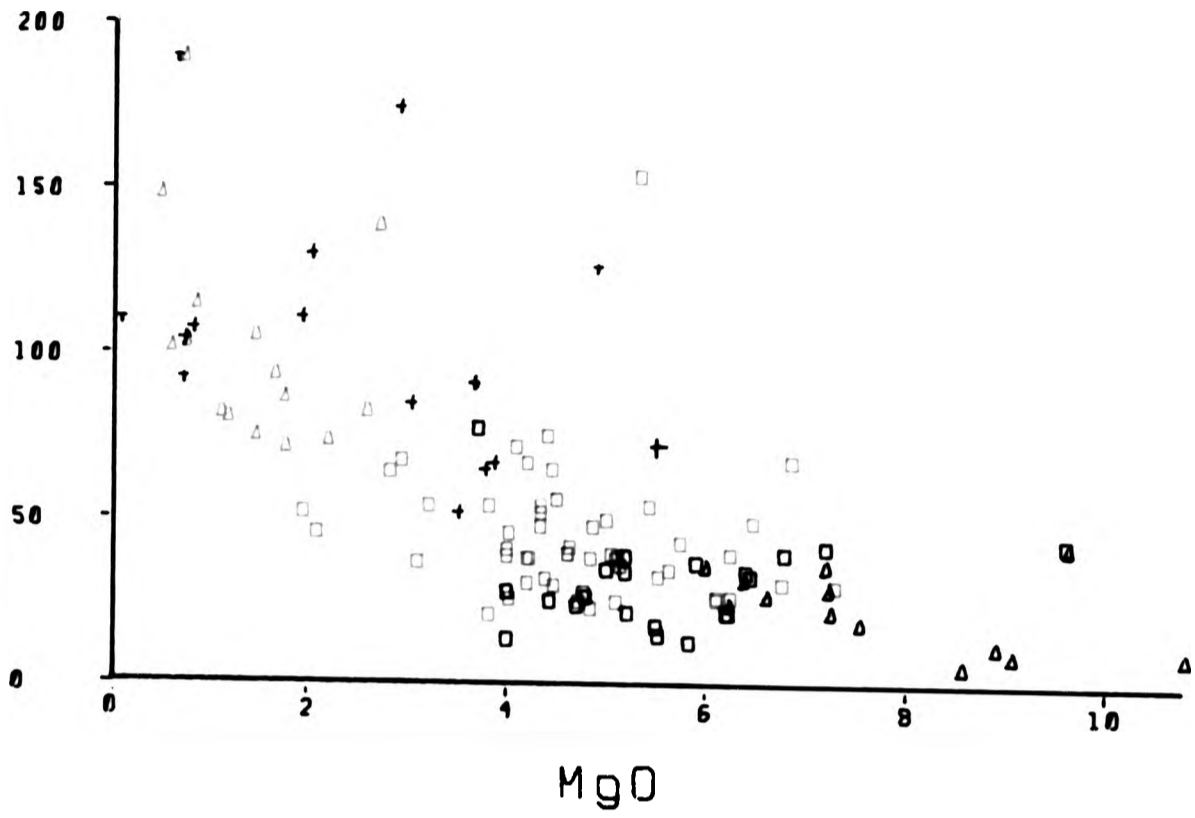


Fig. 6.13

Rb



Li

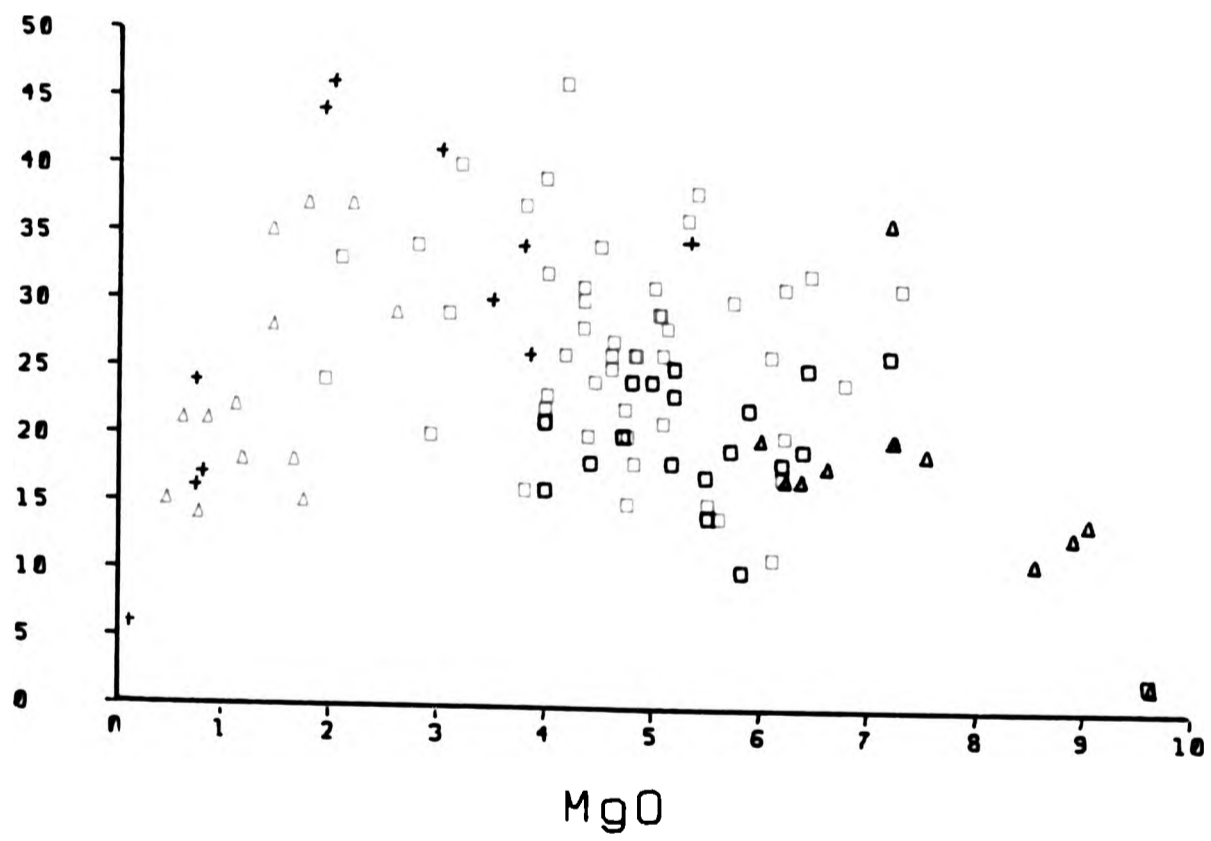


Fig. 6.14

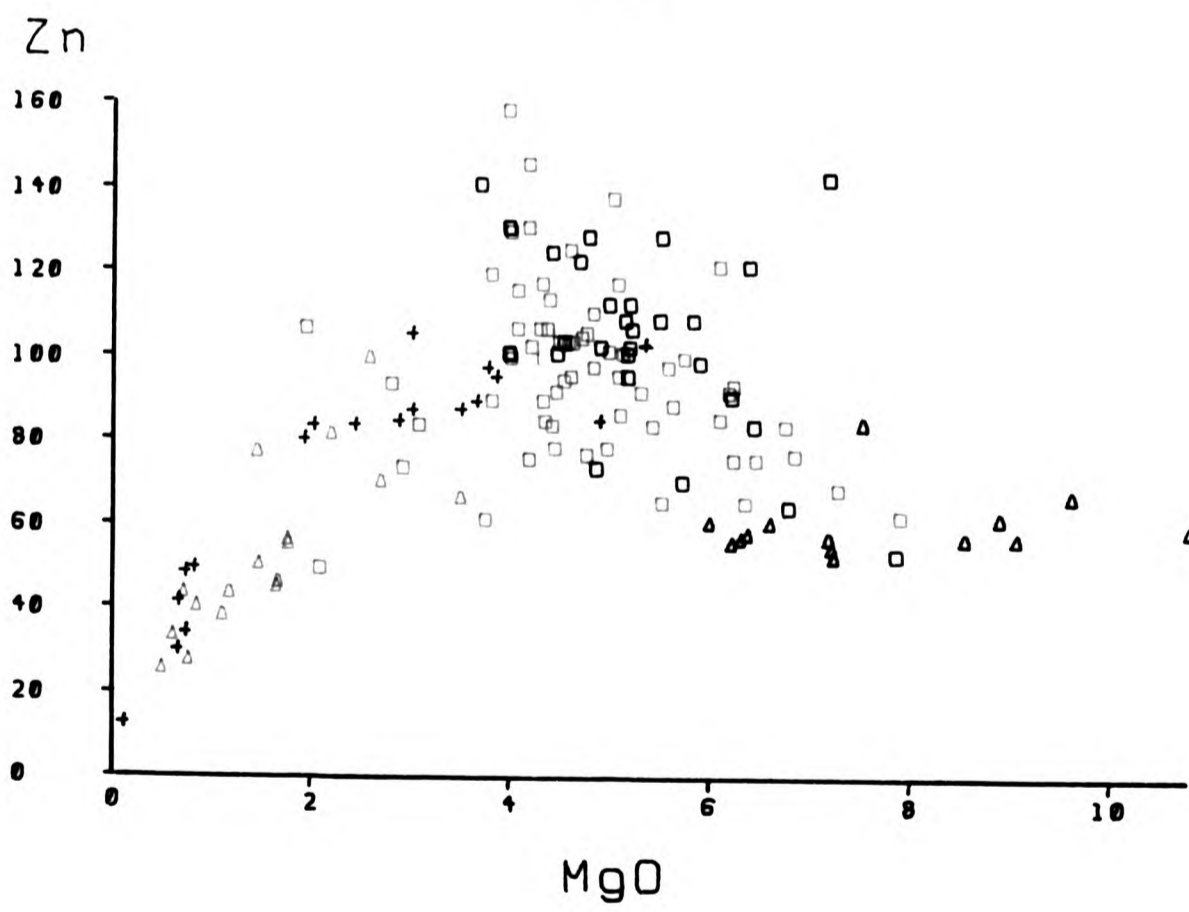
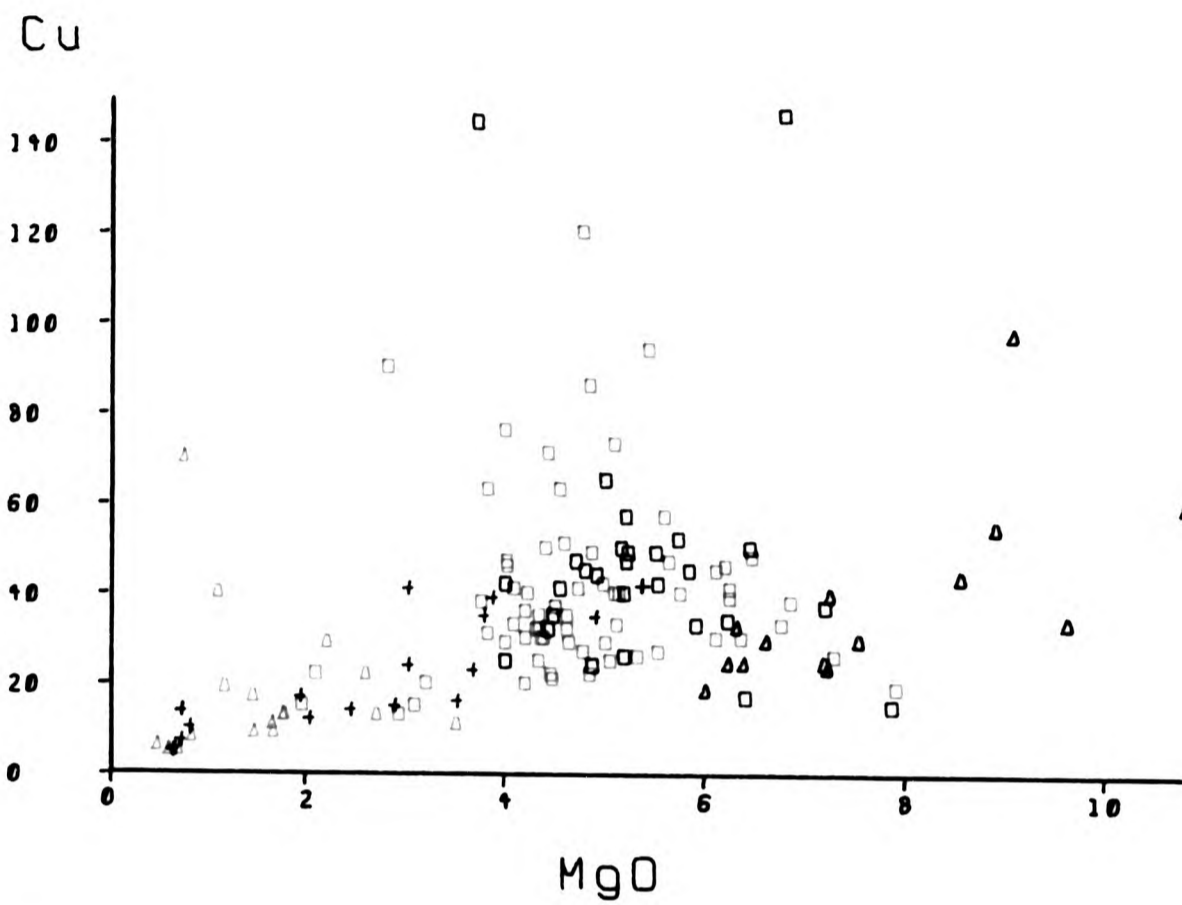


Fig. 6.15

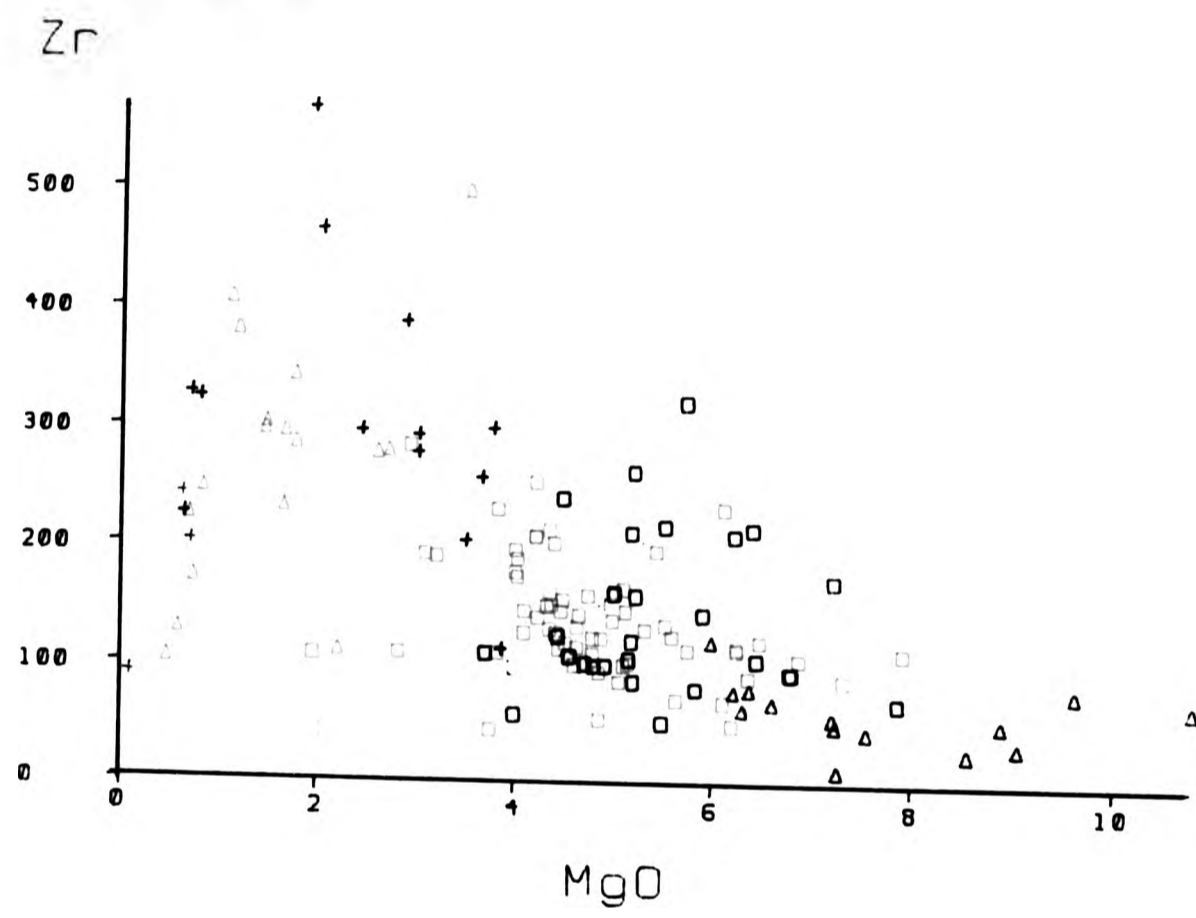


Fig. 6.15

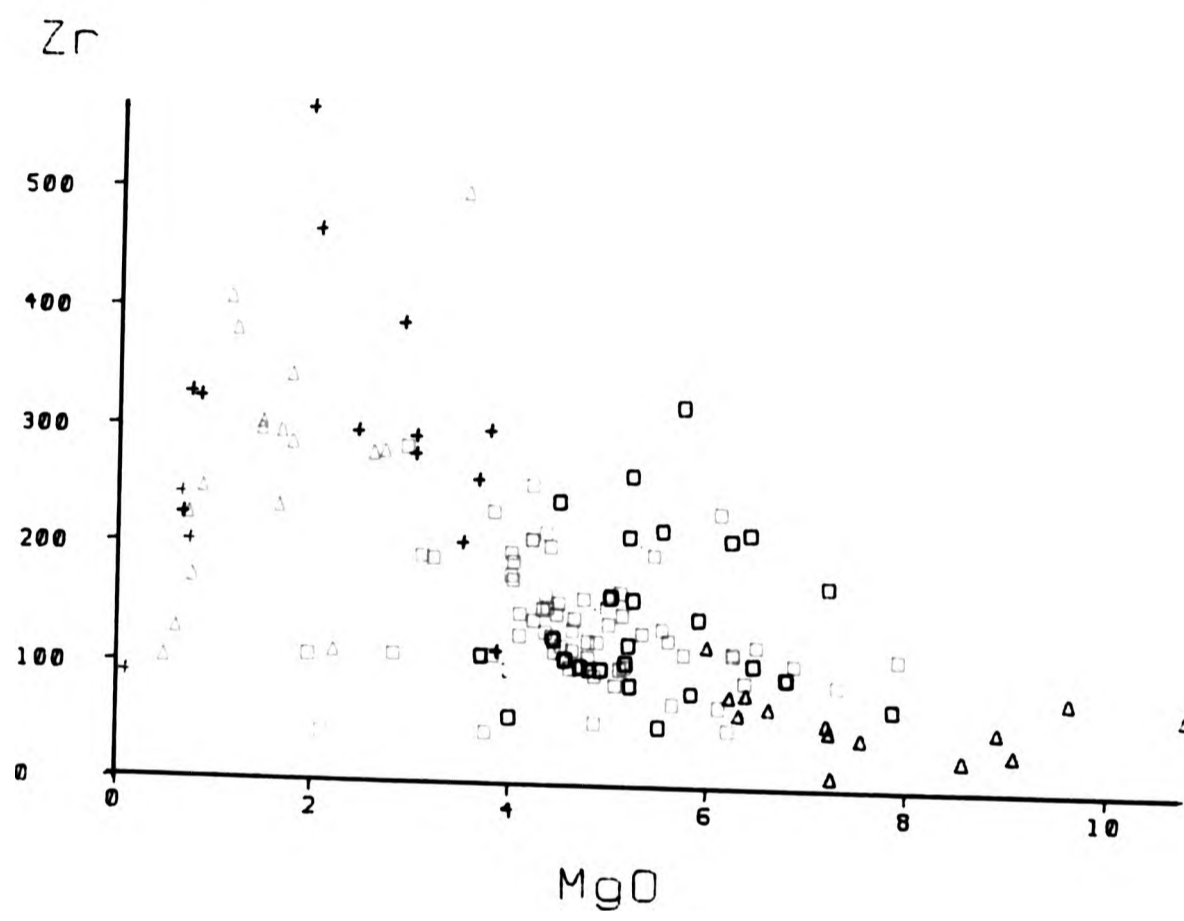


Fig. 6.16

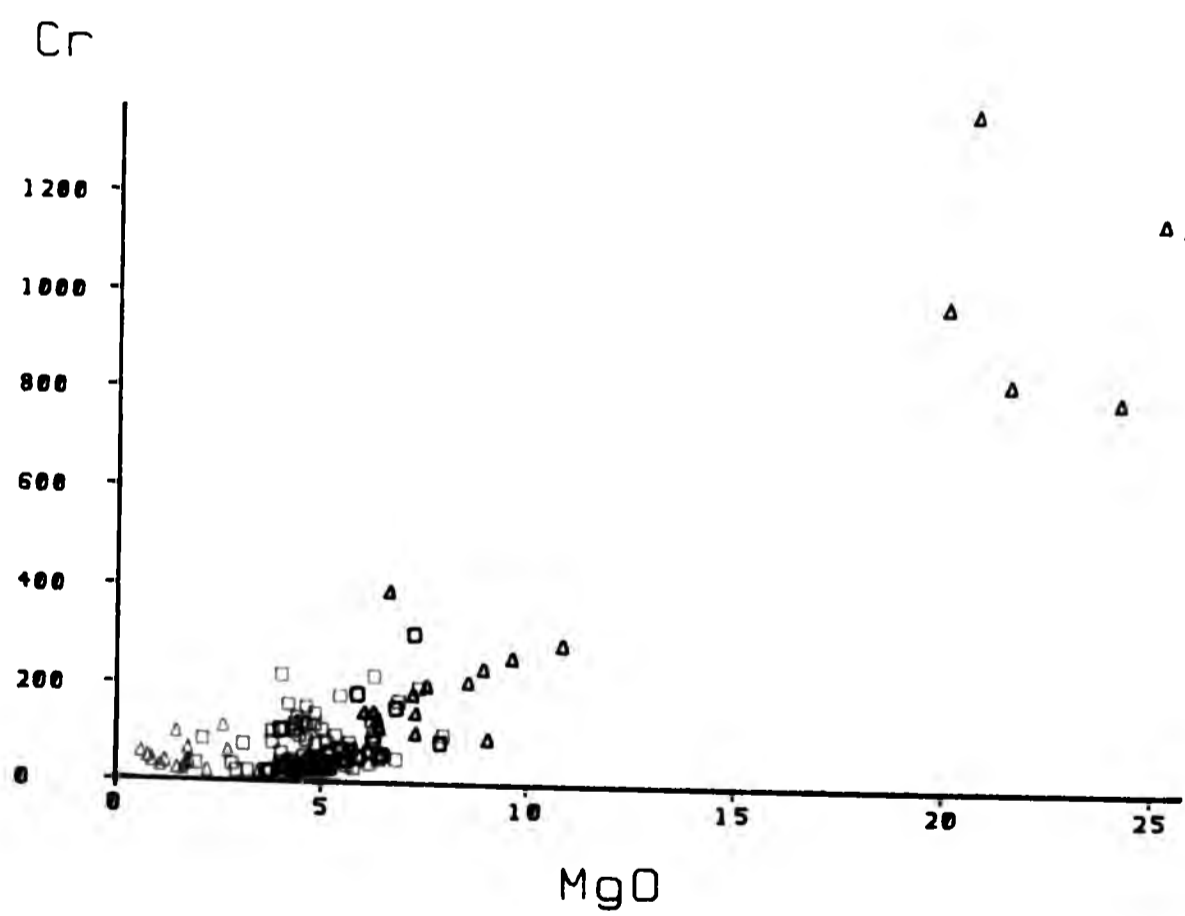
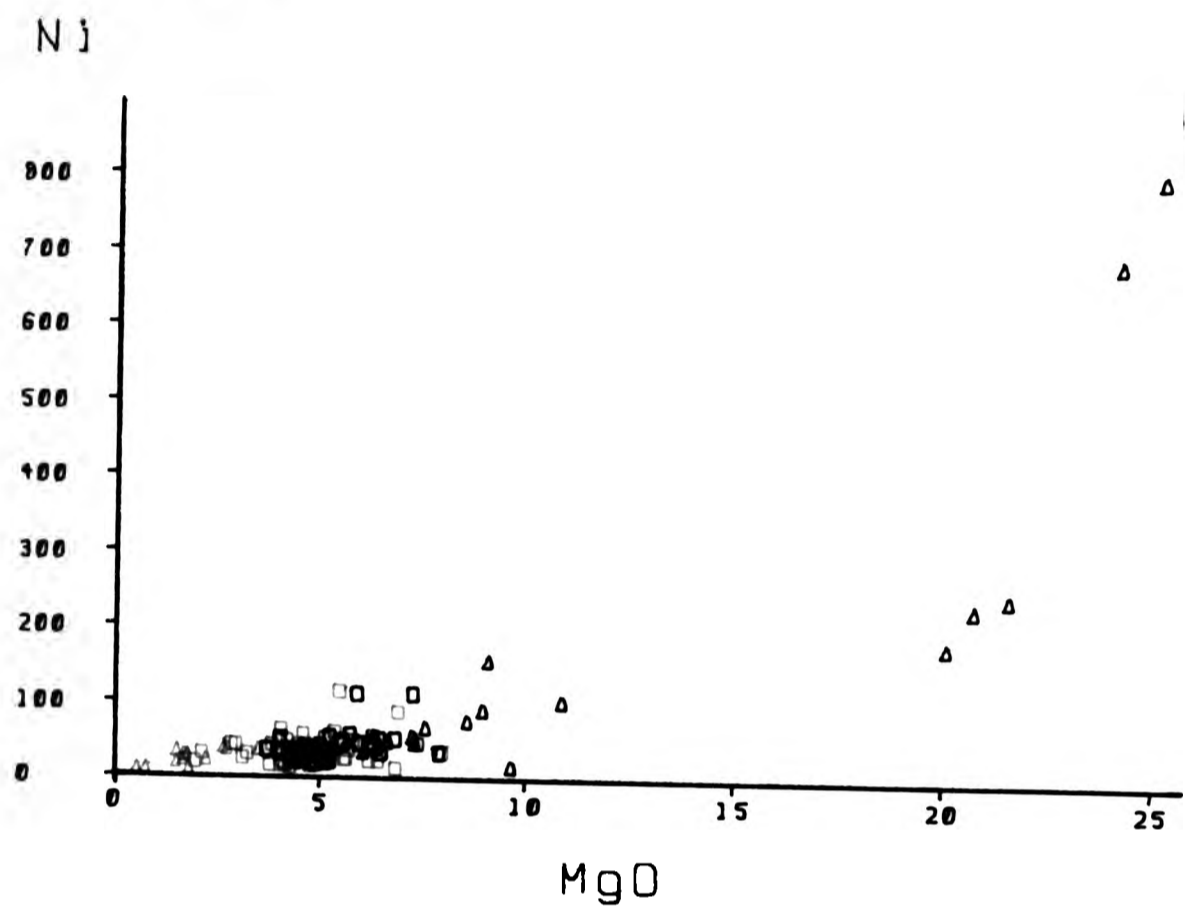


Fig. 6.17

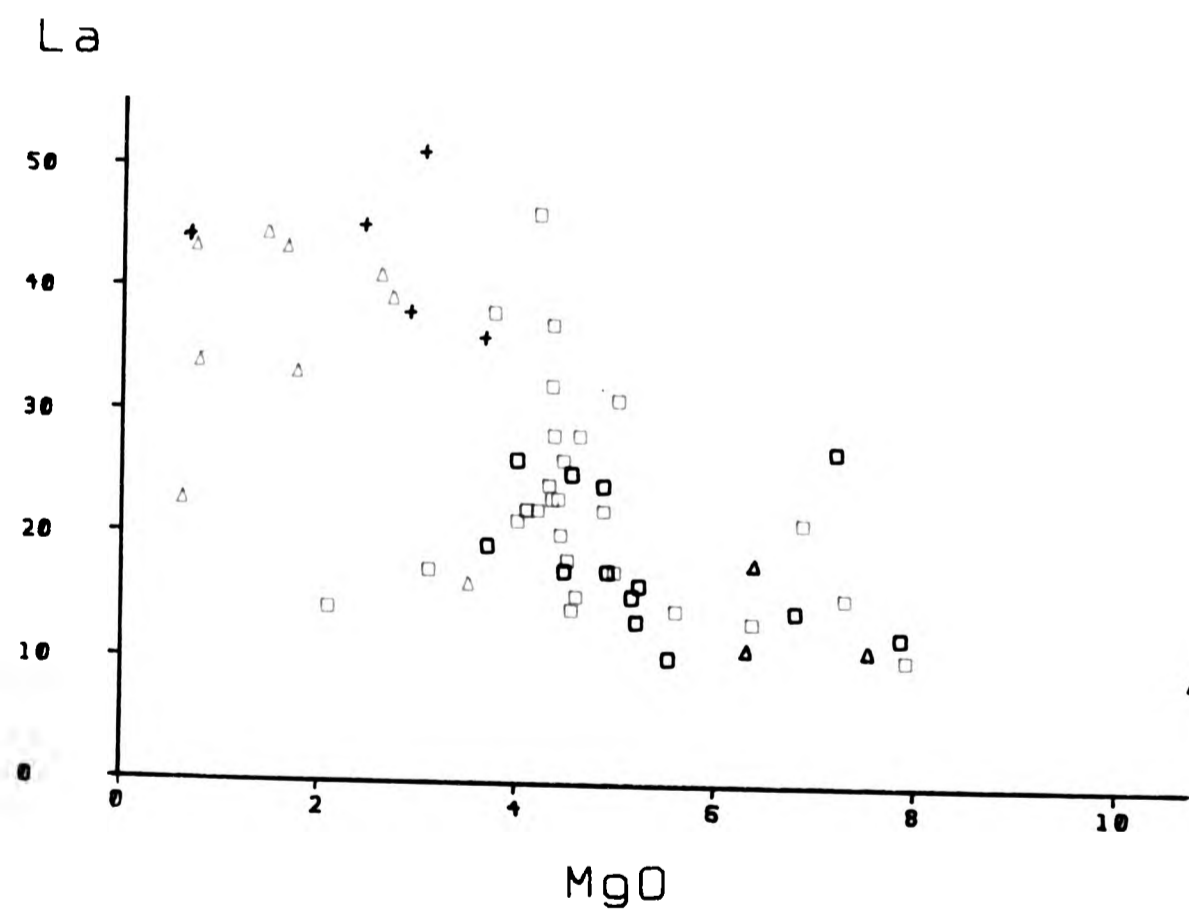
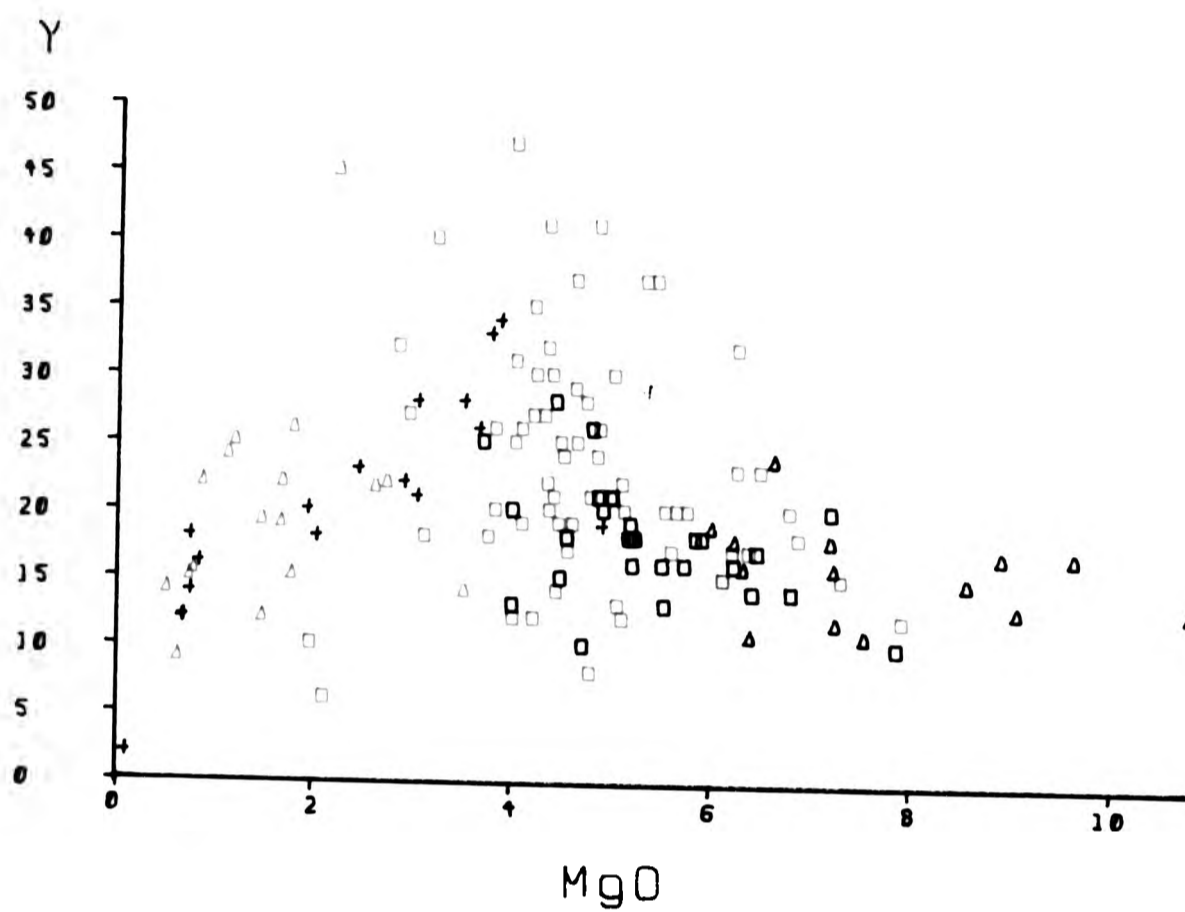


Fig. 6.18

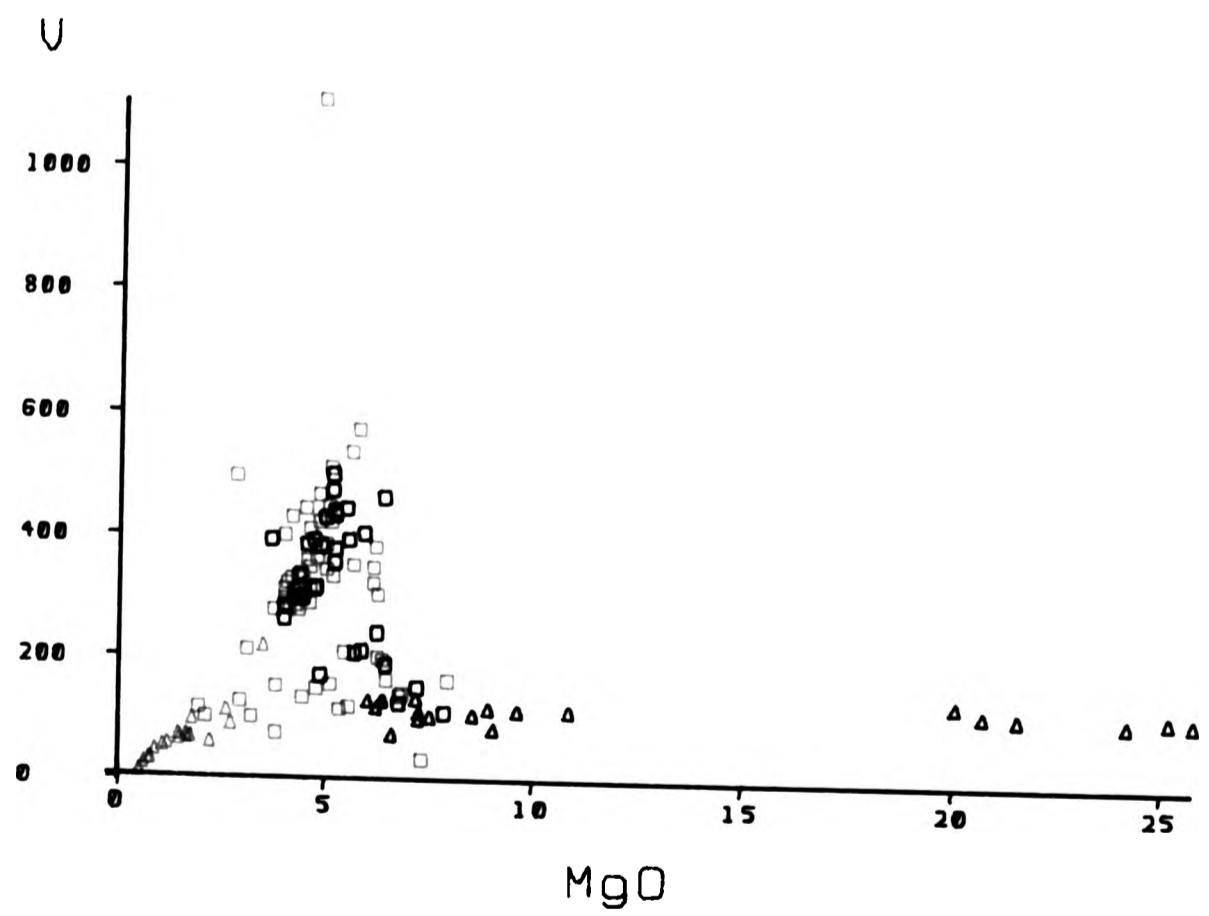
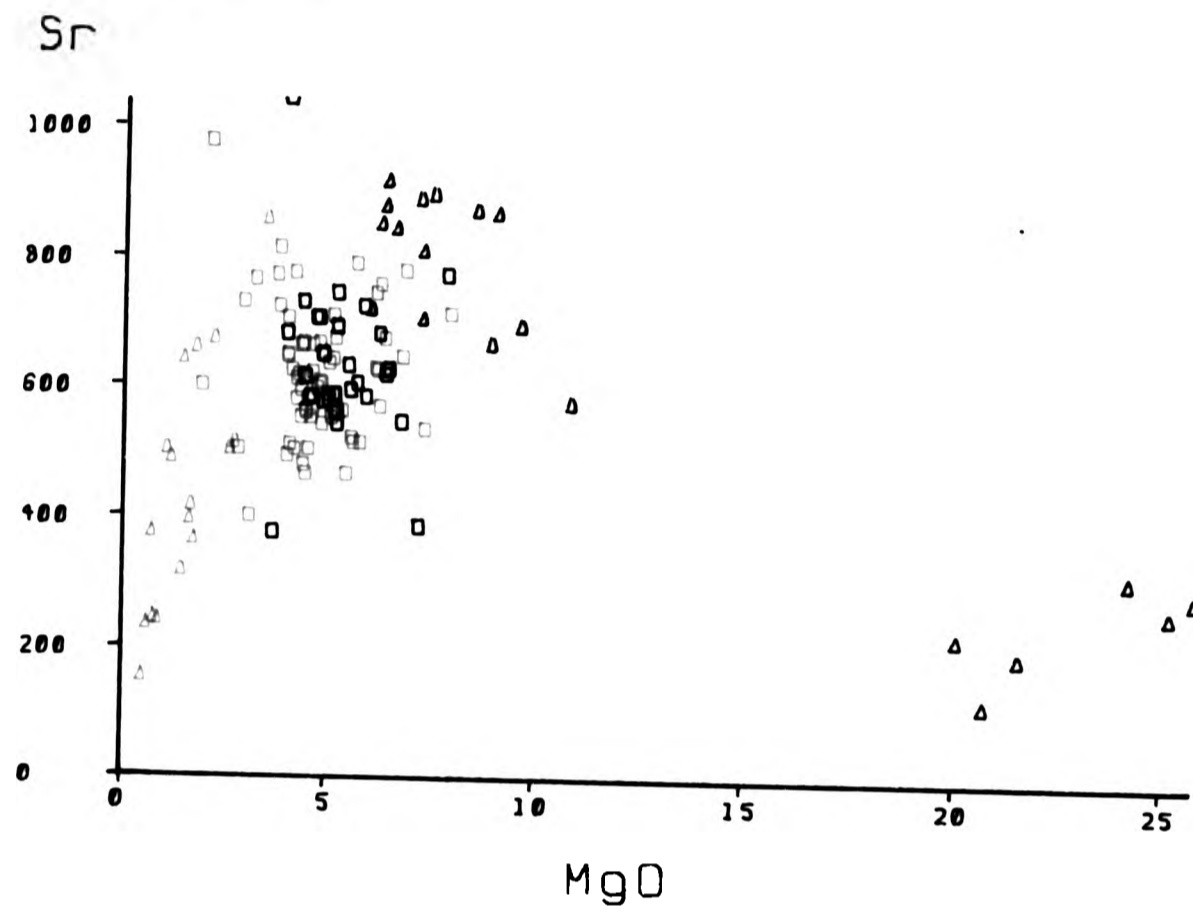


Fig. 6.19

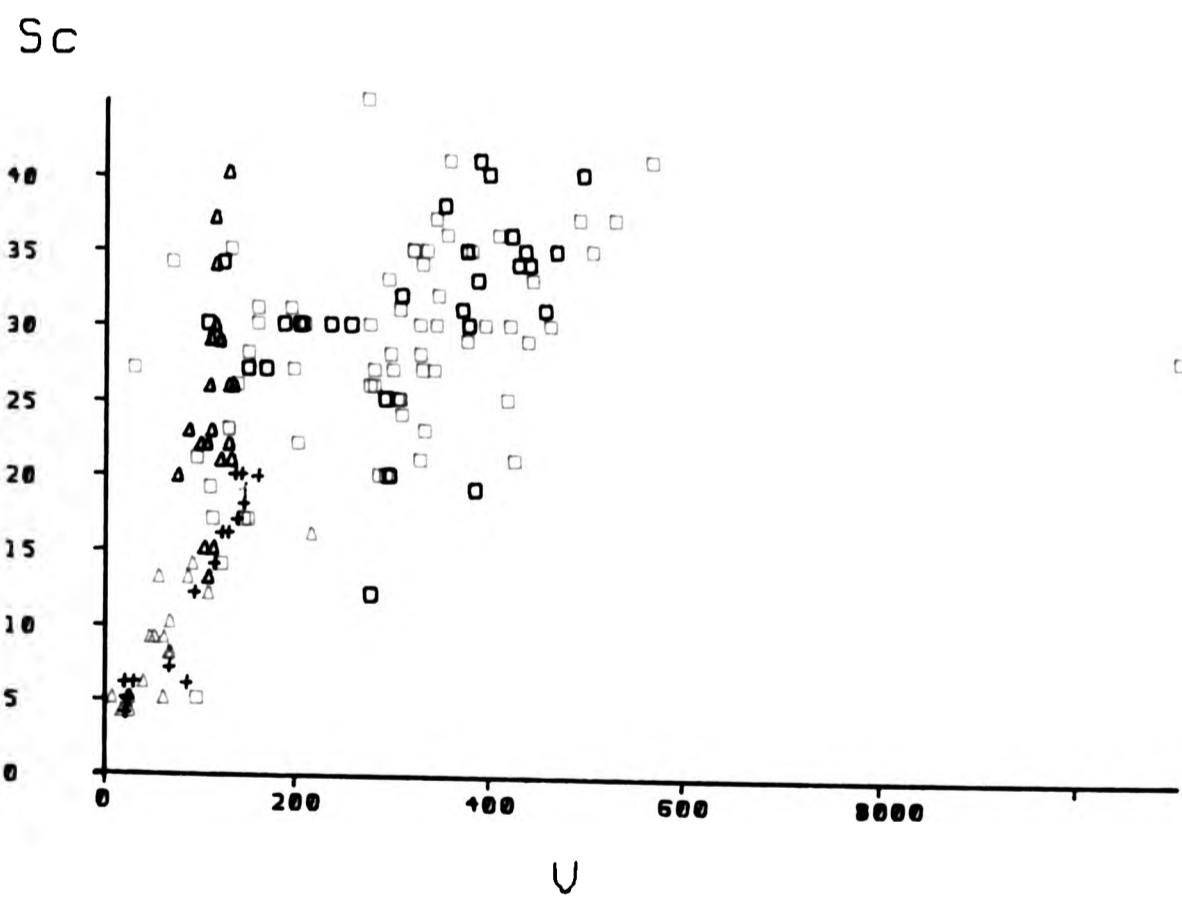
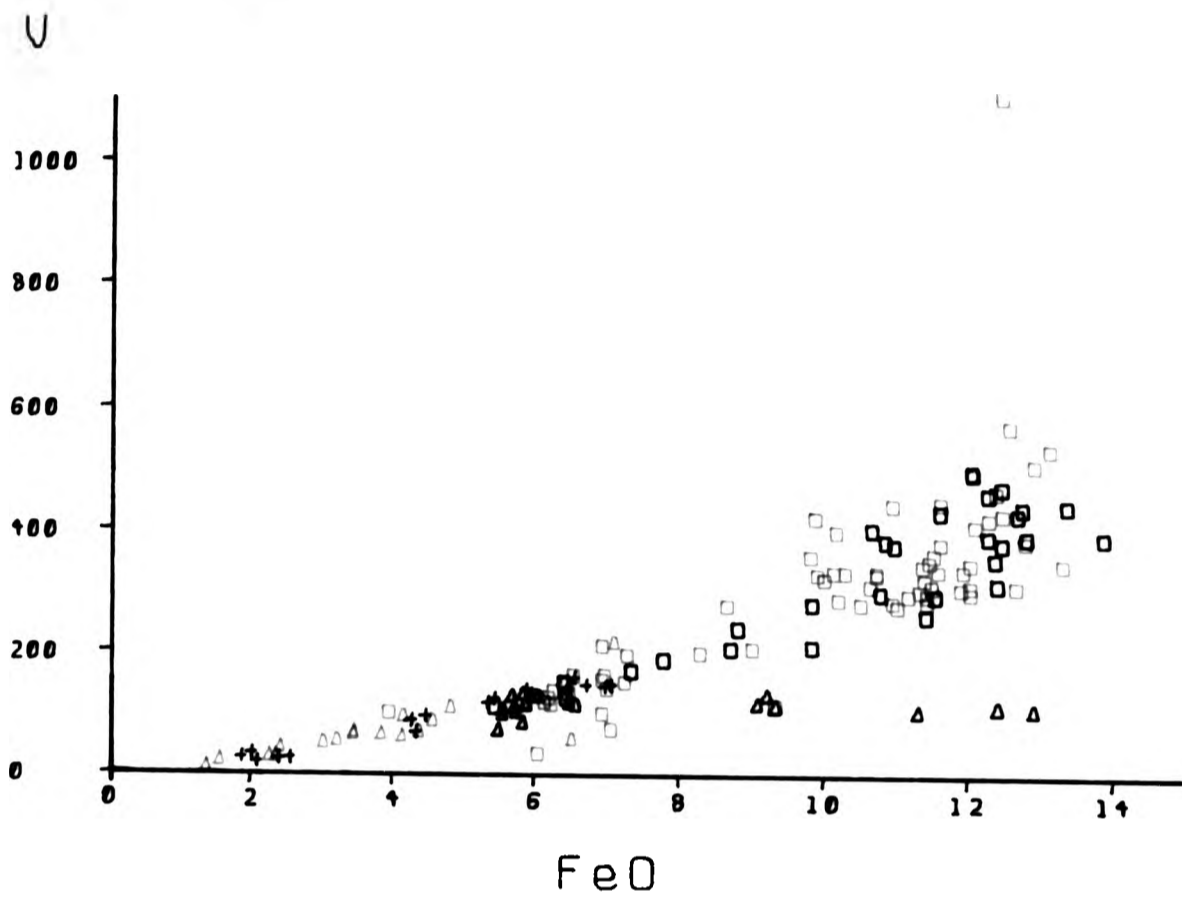


Fig. 6.20

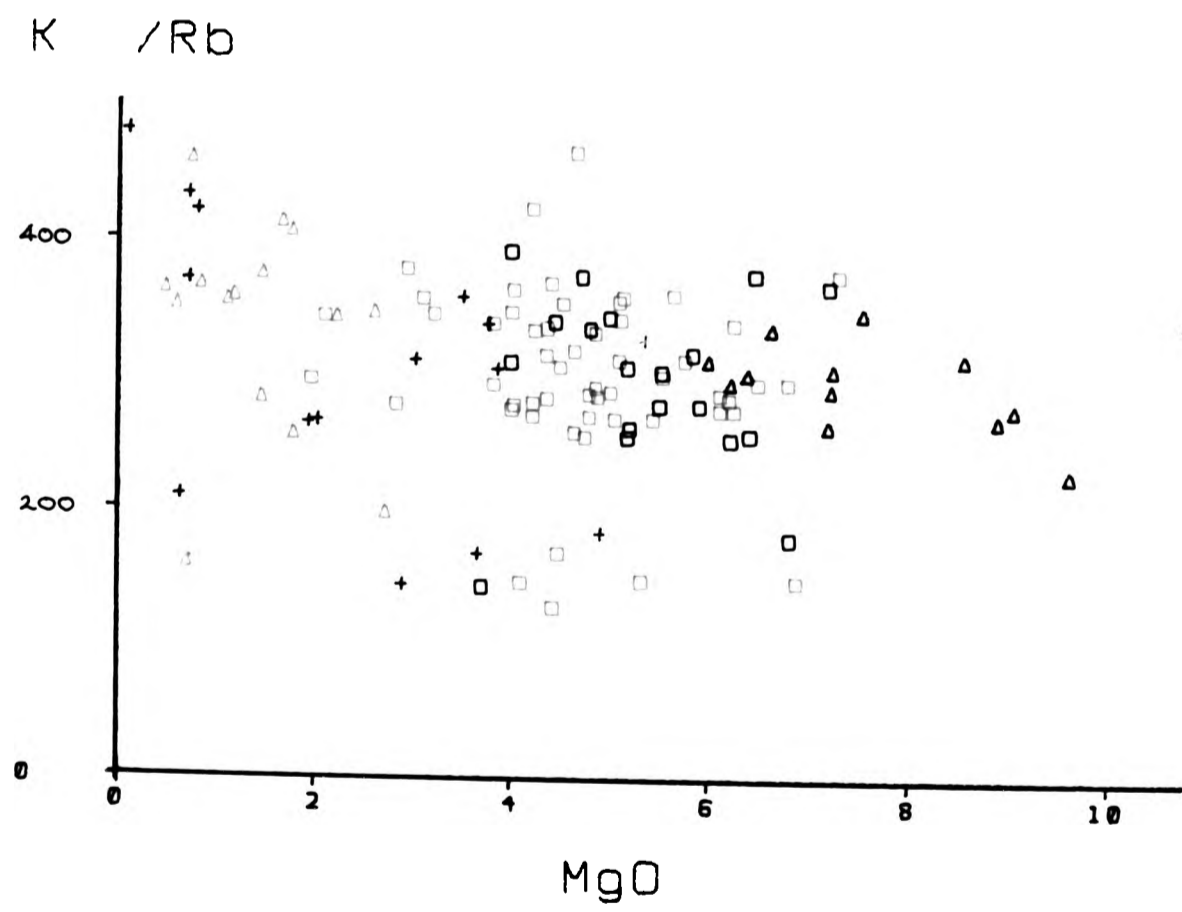
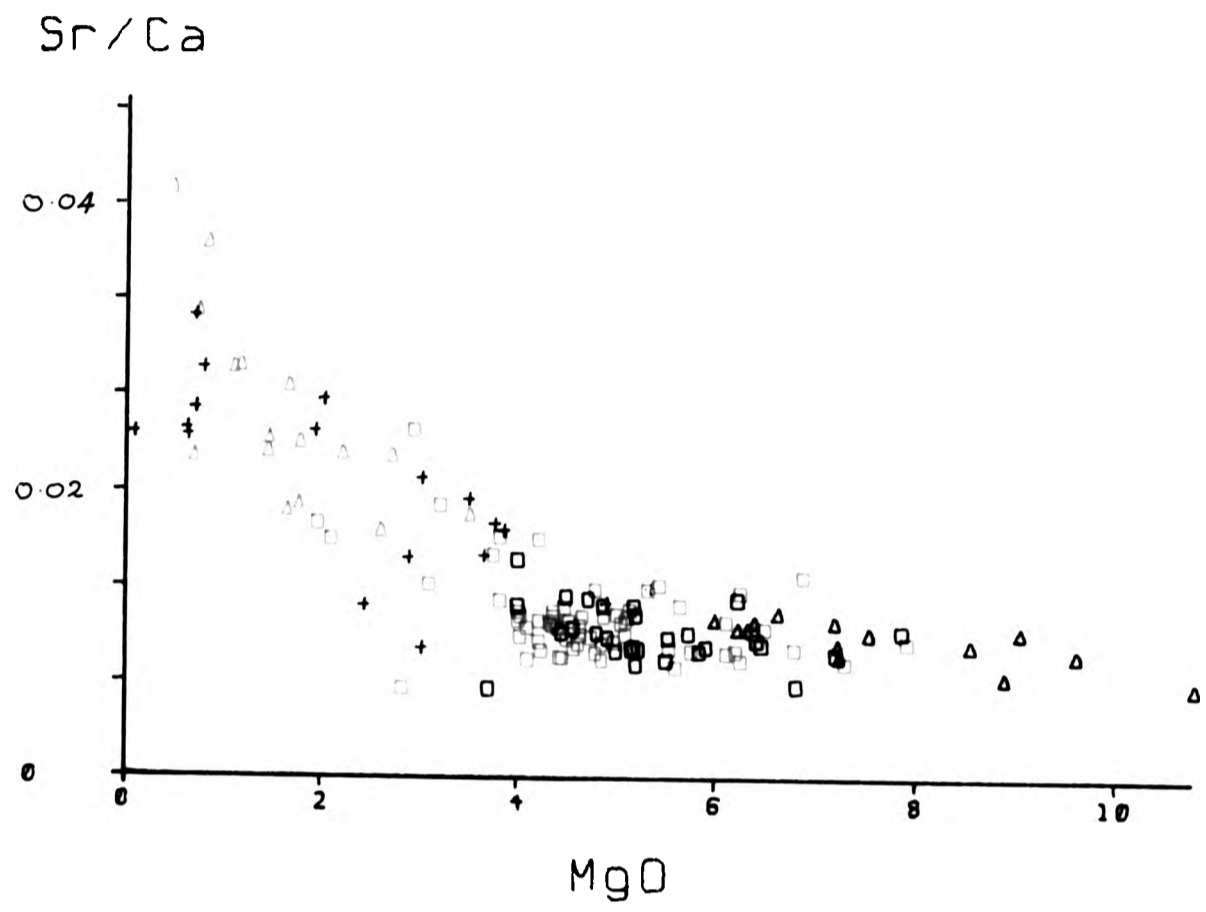
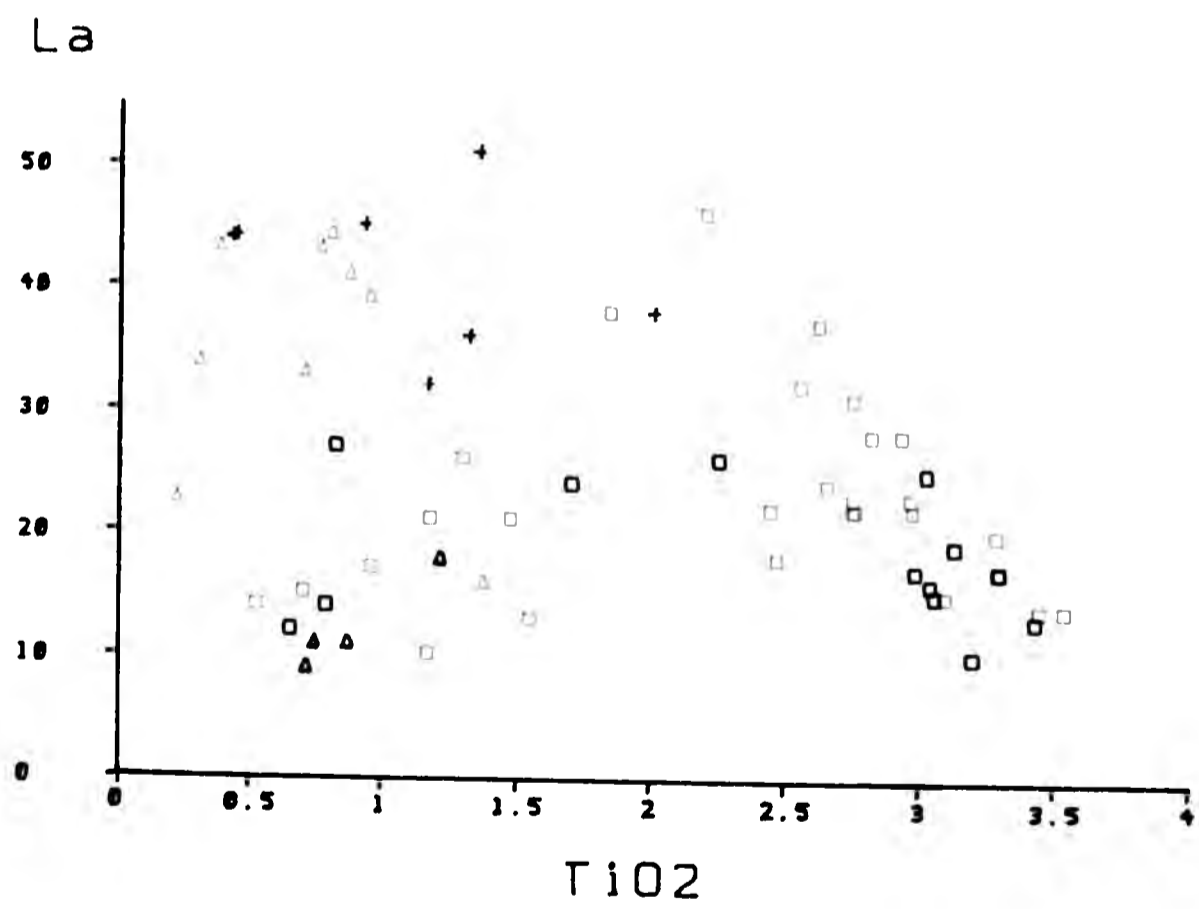
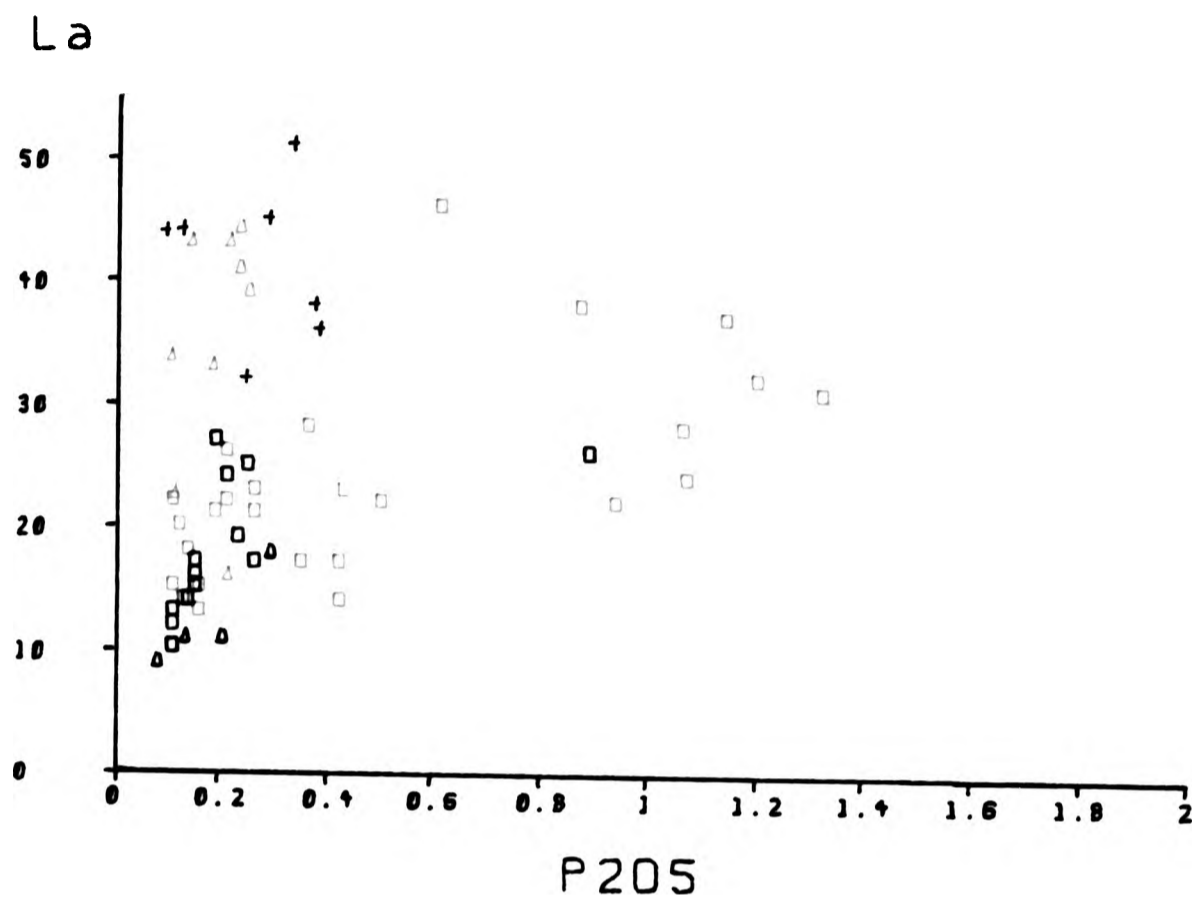


Fig. 6.21



different symbols are used to distinguish the Glen Doll complex pyroxene and hornblende diorites. However, no systematic variation can be established between the two rock types. The rocks from the Bridge Outcrops are also plotted on these diagrams and typically display a variation in chemistry similar to the Juan Jorge rocks.

6.2.1 Silicon and Aluminium

The variation in silica and alumina is shown in Figure 6.3. The basic rocks have the highest MgO contents and display a constant level of silica with increasing magnesia. The dioritic rocks from the Glen Doll complex display a wide range of silica values (48-60% SiO₂) for any given magnesium content. The Juan Jorge and Bridge samples by comparison are less magnesian (<5% MgO) and define a narrow linear trend of increasing silica with decreasing magnesia. The adamellites lie on essentially the same linear trend with maximum silica values of ~75% SiO₂.

Aluminium (Figure 6.3) varies from 12-19% Al₂O₃ in the Glen Doll dioritic rocks with the exception of two samples with >20% Al₂O₃. The basic rocks display a systematic increase in aluminium with decreasing magnesium but the diorites, in marked contrast display no correlation between aluminium and magnesium. Plagioclase feldspar varies considerably in modal abundance in both the diorites and gabbros (See Chapter 4). Microprobe analyses of plagioclase from both rock types show a variation from 23-30% Al₂O₃ (Chapter 5). The bulk rock aluminium content is therefore thought to reflect the abundance of modal plagioclase in the basic and intermediate rocks, the highest values reflecting plagioclase accumulation.

The Juan Jorge and Bridge samples show a little less scatter than the Glen Doll diorites and more scatter than the adamellites, but generally define a trend of decreasing alumina with decreasing magnesia.

6.2.2 Titanium, Iron and Manganese

The distribution of titanium, iron and manganese, is similar throughout the range of rock types (Figures 6.4 and 6.5). The basic rocks display low constant levels of these oxides with increasing MgO. They typically contain 0.5% TiO₂, 5.7% *FeO and 0.1% MnO (Table 6.1). These values are comparable with basic rocks from other Calc-alkaline complexes e.g. Garabal Hill (Nockolds, 1954).

The Glen Doll dioritic rocks by comparison, display a very wide range of *FeO, TiO₂ and MnO concentrations over a relatively narrow range of magnesia values, for example *FeO varies from 6-13%, TiO₂ from <0.1-4.5% and MnO from <0.1-0.17% at 5.5% MgO. In contrast, the Juan Jorge rocks, Bridge rocks and the Glen Doll adamellites all display coherent, linear trends of increasing oxide concentration with increasing magnesia. The most magnesium rich members of this group have higher titanium, iron and manganese contents than the basic rocks.

The distribution of these elements in the Glen Doll diorites probably reflects the variable modal abundance of the oxide minerals ilmenite and magnetite. Figure 6.9 displays a positive correlation between TiO₂ with *FeO and of MnO with *FeO in all rock types from both complexes except the Glen Doll gabbros. These relationships reflect the substitution of titanium and manganese

for iron in the oxide minerals (Chapter 5) in the acid and intermediate rocks from both the Glen Doll and Juan Jorge complexes. Ilmenite crystals from the latter complex contain ~7% MnO (Table 5.3) and would therefore strongly control the distribution of manganese, in the absence of any other manganese-bearing mineral phase. The chemical evidence suggests that the Glen Doll dioritic rocks have accumulated both ilmenite and magnetite.

The low levels of these elements in the gabbros, reflects the general absence of modal magnetite and ilmenite. The positive correlation seen between TiO_2 with *FeO and MnO with *FeO (Figure 6.9), suggests that crystallisation of cpx typically containing 0.68% TiO_2 , and opx typically containing 0.5% MnO (Table 5.4) may be important in controlling the distribution of these oxides in the absence of iron oxide minerals.

6.2.3 Calcium

Figure 6.5a shows the distribution of calcium relative to magnesia. In common with the behaviour described for the preceding major elements, the Glen Doll dioritic rocks display a wide range of calcium values (4-11% CaO) at a given value of magnesia (5.5% MgO). Two diorite samples contain ~8% and 11% CaO with only 2% and 3% MgO respectively. These samples lie away from the main data set. The former (8% CaO) also contains >23% Al_2O_3 and is a plagioclase cumulate. The latter (11% CaO) contains only 45% SiO_2 and contains extensively sericitised plagioclase. The data for the gabbros is a little scattered, but shows a general decrease in calcium (from 12-9.5% CaO) with decreasing magnesia. The adamellites, Juan Jorge samples and Bridge rocks, all lie on a common linear trend of decreasing CaO with decreasing MgO.

6.2.4 Sodium and Potassium

The alkali metals, sodium and potassium, by comparison with the above elements, display a scatter of data for the more evolved rocks (Figure 6.6). Sodium in particular, is very widely scattered for the Juan Jorge and Bridge rocks which contain 2.5-5.0% Na₂O. The adamellites display a similar scatter of data covering a range from 2.75-4.25% Na₂O. The basic rocks show an increase in sodium from 1.75%-2.75% Na₂O with decreasing MgO. The Glen Doll dioritic rocks display a characteristic spread of data with 1.75-4.25% Na₂O. The trends for potassium are a little more closely grouped although there is still considerable scatter (Figure 6.6). The basic rocks have the lowest levels of potassium with 0.25-1.0% K₂O, increasing slightly with decreasing magnesia. The more evolved rocks show a general increase in potassium with decreasing MgO. The Glen Doll diorites contain between 0.4 and 2.0% K₂O. It is notable that the least magnesian diorites from the Glen Doll complex, are poor in K₂O with respect to both the adamellites and the Juan Jorge diorites. All of the Glen Doll diorites contain less K₂O than the Bridge Outcrops. The low levels of K₂O in these diorites may reflect the small amount of intercumulus liquid. Biotite is the most important intercumulus mineral present which contains significant amounts of K₂O typically 9-9.25% (Table 5.6). Orthoclase is recorded only rarely in the diorites and is absent from the more mafic rocks. The main cumulus minerals, plagioclase, amphibole and pyroxene in the diorites and opx, cpx, olivine and plagioclase in the gabbros, contain only minor amounts of potassium.

6.2.5 Phosphorus

The distribution of phosphorus is shown in Figure 6.7. The basic rocks contain a low, constant level ($<0.2\% \text{P}_2\text{O}_5$). The Juan Jorge rocks, Bridge rocks and adamellites display an increase in phosphorus from 0.05 to 0.3% P_2O_5 with increasing magnesia (0.5-2.5% MgO). The Glen Doll dioritic rocks show a scatter of data points. At a constant value of 4.75% MgO , the phosphorus content of the rocks ranges from 0.1-1.4% P_2O_5 . The most common phosphorus bearing mineral in calc-alkaline rocks is apatite. This mineral is recorded in the Glen Doll diorites, adamellites, gabbros, Juan Jorge diorites and granites, although the modal proportion is variable, particularly within the Glen Doll diorites (Chapter 4). The wide range of P_2O_5 contents at any value of MgO reflects the occurrence of variable proportions of cumulus apatite in the Glen Doll diorites.

6.2.6 Olivine gabbros

Representative variation diagrams, show the relationship of the olivine gabbros to the other rock types (Figures 6.7, 6.8 and 6.9). There is a compositional break between the high MgO gabbros and the lowest MgO olivine gabbro i.e between 10% and 19% MgO . A linear trend (Figure 6.7) of increasing CaO with decreasing MgO is displayed by the olivine gabbros. Iron and manganese (Figure 6.8), display a linear decrease from the olivine gabbros (12.88% FeO and 0.18% MnO) to the gabbros (5.4% FeO and 0.10% MnO). The olivine gabbros are however totally separate from the iron-rich dioritic rocks from the Glen Doll complex which contain similar levels of FeO ($<14\%$) with only 4-6% MgO . Silica, titanium and aluminum contents remain low (Table 6.1) in the former. Silica varies from 41%-49% SiO_2 and tends to increase with decreasing alumina which varies from 6.3-8.2% Al_2O_3 . Titanium levels are low, and similar

to the gabbros, typically $<1.0\%$ TiO_2 . Sodium levels are lower than in the gabbros and show little variation (typically 1.2% Na_2O), while potassium shows a similar limited range of values to the gabbros from $0.5\text{--}0.9\%$ K_2O .

6.2.7 Discussion of the major element chemistry

The average chemical compositions of a range of rock types from the Calc-alkaline suite, including gabbro, diorite and andesite, was compiled by Nockolds (1954) (Table 6.6). The similarity between the volcanic-plutonic equivalents of andesite-diorite is clear. Comparison of these average values with the Glen Doll diorites and gabbros and Juan Jorge diorites, reveals some characteristic features. Although SiO_2 and Al_2O_3 in the Glen Doll and Juan Jorge diorites are similar to the published values, the other major elements show a contrast. TiO_2 , $^*\text{FeO}$ and P_2O_5 are typically higher in the Glen Doll diorites and lower in the Juan Jorge diorites than the average values. By contrast, MgO , MnO and CaO , are lower in both complexes than Nockolds average value. K_2O is characteristically low in the Glen Doll diorites and high in the Juan Jorge diorites. The Glen Doll gabbros display similar values to Nockolds average, except for SiO_2 and Al_2O_3 which are higher, and TiO_2 , $^*\text{FeO}$ and MnO which are lower. The characteristic differences in the Glen Doll data could result from crystal accumulation in the diorites and gabbros.

The most striking feature seen in the preceding variation diagrams (Figures 6.3-6.9), is the broad scatter of data shown by the dioritic rocks from the Glen Doll complex compared with the more restricted range of compositions and coherent linear variations displayed by the Juan Jorge rocks, Bridge rocks and the Glen

Table 6.6 Average chemical compositions of some igneous rocks.
(Data from Nockolds, 1954)

	Gabbro	Diorite	Andesite
SiO ₂	48.36	51.86	54.20
Al ₂ O ₃	16.84	16.40	17.17
TiO ₂	1.32	1.50	1.31
FeO	7.92	6.97	5.49
Fe ₂ O ₃	2.55	2.73	3.48
MgO	8.06	6.12	4.36
MnO	0.18	0.18	0.15
CaO	11.07	8.40	7.92
Na ₂ O	2.26	3.36	3.67
K ₂ O	0.56	1.33	1.11
P ₂ O ₅	0.24	0.35	0.28
H ₂ O ⁺	0.64	0.80	0.86

Table 6.7 Average trace element abundances from a range of Caledonian plutonic rocks (Data from Nockolds and Mitchell, 1946)

Rock type: Hypersthene gabbro, gabbro
Concentrations (ppm)

Ba 30-300
Cr 100-250
Li 25-60
Ni 200-300
Rb 50-500
Sc 10-40
Sr 800-1200
Zr 50-100

Rock type: Pyroxene diorite, appinitic diorite,
xenolithic diorite.
Concentrations (ppm)

Ba 150-300 (xenolithic diorite 800)
Cr 100-200
Cu 10-50
Li 25-40
Ni 50-150
Rb 100-500
Sc 10-30
Sr 1200-2000
V 80-200
Zr 50-300

Rock type: Granodiorite containing sedimentary material

Ba 1500
Li 60
Rb 600
Sr 3000

Doll adamellites.

The variation in the major element chemistry almost certainly reflects the progressive removal or accumulation of the various minerals crystallising from the magma. The distribution of aluminium and calcium, for example in the gabbros is consistent with the crystallisation and progressive accumulation of plagioclase and clinopyroxene. The low, constant levels of TiO_2 , $*FeO$ and MnO reflect the general absence of modal magnetite and ilmenite. The Glen Doll dioritic rocks by comparison, have variable amounts of $*FeO$, TiO_2 , MnO , CaO and Al_2O_3 reflecting the variable modal abundance of the oxide minerals and plagioclase feldspar. Cumulate textures have been described from both the gabbros and olivine gabbros (See Chapter 4). The very high level of MgO ($>21\%$) and high $*FeO$ ($>9\%$) in the olivine gabbros, is further evidence in support of a cumulate origin for this group of rocks.

The rocks from the Juan Jorge complex display very different chemical characteristics to the Glen Doll dioritic rocks and show features typical of a liquid line of descent resulting from fractional crystallisation of an intermediate magma similar to that described from other Caledonian complexes e.g. Loch Doon (Brown et al., 1979).

An important point brought out by the major element chemistry is that the Glen Doll basic rocks, Glen Doll diorites and Juan Jorge rocks are not linked by a single, simple liquid line of descent. The basic rocks are clearly, both in terms of chemistry and mineralogy, cumulates. They contain olivine, pyroxene and plagioclase as cumulate phases, and the major element chemistry of

the gabbros reflects the varying modes of these minerals. The Glen Doll diorites contain cumulate minerals which include pyroxene, plagioclase, Fe oxides and apatite. The Juan Jorge rocks and the Glen Doll adamellites lie on a common trend, which may be an indication that they are genetically related.

6.3 Trace element chemistry

Representative analyses of the range of rock types studied are given in Tables 6.1-6.5 and the variation in the trace element chemistry of the suite is shown on Figures 6.10-6.19. In general the behaviour of trace elements in igneous rocks can be divided into two types. Trace elements which typically substitute for major elements in a crystal lattice, due to their similar charge or ionic radius are termed compatible. There is a tendency for the distribution of these elements to mirror that of the major elements for which they substitute. Incompatible trace elements do not substitute directly for major elements and are more commonly incorporated in minor phases or locate loosely bound along crystal boundaries.

6.3.1 Barium

The olivine gabbros contain between 80-140ppm Ba and display no obvious correlation with MgO content. By contrast barium shows an increase in the gabbros, from 100ppm at 8.5% MgO to 285ppm at 6% MgO (Figure 6.10). Barium continues to increase from 150-500ppm with decreasing MgO content in the Glen Doll dioritic rocks, although the data is a little scattered. The adamellites show a broad distribution of data, generally of increasing barium with increasing magnesia.

The Juan Jorge rocks by contrast display a steep increase in barium from 500ppm at 4% MgO to >1600ppm at 0.75% MgO. These samples lie on a separate trend to that defined by the Glen Doll adamellites. The Bridge rocks display a progressive increase in concentration from the diorites (at 500ppm) to the granites. By contrast the granite chill contains only 45ppm Ba.

Ba^{2+} has an ionic radius of 1.34\AA and is therefore too large to easily replace either calcium or sodium in crystal lattices. It can replace potassium in biotite and K-feldspar. The latter mineral is recorded rarely in the Glen Doll diorites and is absent from the gabbros. The increase in barium concentration with decreasing magnesium, particularly in the basic rocks, suggests that barium is not significantly entering biotite but becomes progressively enriched throughout the early stages of crystallisation. The dioritic rocks from the Glen Doll Complex contain variable modal biotite, particularly the low MgO (<4.0%) diorites which also show a considerable scatter of barium data from 200-900ppm. The Glen Doll diorites with 4-7% MgO contain an average of 250ppm Ba. This value is low by comparison with other dioritic complexes for example with the Loch Doon complex where a range from 791-1184ppm Ba is recorded from the hypersthene diorite (Brown et al., 1979). The concentrations also contrast with data from the Midland Valley andesitic lavas (Thirlwall, 1986) which contain 668-837ppm Ba.

The Juan Jorge rocks by contrast display an increase from 500-1600ppm Ba and are therefore enriched in barium relative to the Glen Doll suite and relative to both the Loch Doon diorites and Midland Valley lavas. Halliday et al. (1985) pointed out that enrichment in barium is a provincial characteristic of many late

Caledonian Scottish granitoids and suggested that this feature may be inherited from an enriched mantle source.

6.3.2 Strontium

Strontium (Figure 6.10), is variable in the dioritic rocks from both complexes, ranging from 350-800ppm. The olivine gabbros display a broad decrease with increasing MgO, from 290 to 180ppm Sr (Figure 6.18). The gabbros by contrast display a broad increase in strontium to a maximum of 900ppm with decreasing MgO. The strontium data for the adamellites is scattered but shows a broad decrease with decreasing MgO from 600-150ppm Sr.

Sr^{2+} (1.12Å) can substitute for either Ca^{2+} (0.99Å) or K^+ (1.33Å) in crystal lattices due to their similar ionic radius. Strontium substitution for calcium in plagioclase is well documented (e.g. Berlin and Henderson, 1968; El Bouseily and El Sokkary, 1975). Published data suggests that the concentration of strontium in plagioclase, increases with differentiation (e.g. Wager and Mitchel, 1951). However in acid rocks Sr^{2+} can substitute for K^+ in alkali feldspar, which may result in an increase in the bulk rock Sr/Ca ratio. Figure 6.20 displays an increase in the Sr/Ca ratio from 0.005-0.006 in the Glen Doll gabbros with decreasing MgO, and a constant ratio of 0.02 in the Glen Doll dioritic rocks. The Glen Doll adamellites by contrast show a steep increase in Sr/Ca ratio from 0.02-0.04 with decreasing MgO. A positive correlation is observed between strontium and calcium in the intermediate and basic rocks. Unfortunately strontium was not determined in plagioclase from the Glen Doll Complex, so the exact location of the strontium is unknown. However, strontium substitution for calcium in both cpx and amphibole is thought to be very limited (Mason,

1966) and therefore plagioclase provides the most likely host for strontium in the Glen Doll diorite and gabbroic assemblages. In the more evolved rocks, there is an increase in Sr/Ca ratio with decreasing MgO, suggesting that strontium may substitute in K-feldspar in these rocks.

6.3.3 Vanadium and scandium

Vanadium and scandium (Figure 6.11), display a similar distribution of data to that shown by *FeO, TiO₂ and MnO. The abundance of vanadium in both the gabbros and olivine gabbros is consistently low (~100ppm) (Figure 6.18). There is a linear decrease in the adamellites from 100ppm V at 2.5% MgO to 17ppm V at 0.6% MgO. The Juan Jorge rocks lie on the same trend as the Glen Doll adamellites. The Glen Doll diorites by comparison show a scattered distribution and a wide range of concentrations from <100ppm-600ppm V. Scandium (Figure 6.12) similarly displays a wide range of concentrations from 11-41ppm Sc in the Glen Doll dioritic rocks. The distribution of scandium in the adamellites, Juan Jorge rocks and Bridge rocks, mirrors that of vanadium. In the olivine gabbros scandium content increases with decreasing MgO from 11ppm at >25% MgO to 40ppm at 21% MgO. By contrast the gabbros show a general decrease from 27ppm at 11% MgO to 20ppm at 6% MgO.

The distribution patterns shown by both vanadium and scandium mirror those of iron, titanium and manganese. Both scandium and vanadium commonly substitute for iron in ferromagnesian and oxide minerals (Mason, 1966). Sc²⁺ (0.732Å) has an ionic radius similar to that of ferrous iron (0.74Å) for which it commonly substitutes in pyroxene, amphibole and biotite. Vanadium (0.74Å) has an ionic radius greater than that of ferric iron (0.64Å) but lower electro-

negativity, and can substitute extensively for Fe^{2+} in magnetite. The substitution of both V^{3+} for Fe^{3+} in magnetite and Mn^{2+} for Fe^{2+} in ilmenite is well documented e.g. (Wager and Mitchell, 1951; Czamanske et al., 1981; Best and Mercy, 1967). The Glen Doll dioritic rocks contain variable amounts of modal ilmenite and magnetite and the distributional patterns for *FeO, MnO, TiO_2 and V reflect this modal variation, supporting the view that the opaque minerals are cumulus phases. A plot of V vs *FeO (Figure 6.19) displays a positive linear correlation in the intermediate and acid rocks. The gabbros form a small group of data points around 6% *FeO and 100ppm V, while the olivine gabbros show a decrease from 13-9% *FeO at a constant 100ppm V. This data is consistent with vanadium substitution for iron in the acid and intermediate rocks (in magnetite) but suggests that substitution in ferromagnesian phases such as opx, cpx or amphibole is controlling the distribution of vanadium in the olivine gabbros.

A plot of Sc vs V (Figure 6.19) shows no correlation between the two elements in the intermediate rocks suggesting that their distribution is controlled by different phases. Both the gabbros and olivine gabbros display a decrease in scandium from 40-15ppm at a constant 100ppm V. Scandium substitution for iron is recorded in opx from the Skaergaard intrusion (Wager and Mitchell, 1951; Mitchell, 1966). Amphiboles may also contain significant amounts of scandium (Dodge et al., 1968). Of particular relevance here is data for magmatic amphiboles from the Glen Tilt complex, Perthshire, which contain >100ppm Sc (C. Turner. pers. comm. 1987).

6.3.4 Nickel and chromium

The distribution of chromium and nickel are shown in Figures 6.12 and 6.16. A similar pattern is seen for both elements, and broadly shows falling chromium (from 260-100ppm) and nickel (from 100-30ppm) levels with decreasing MgO in the gabbros and a scatter of data in the intermediate rock types. The Glen Doll diorites display a scatter of data points and contain from 10-270ppm Cr and 10-100ppm Ni. The olivine gabbros contain the highest abundance of Cr and Ni in either complex. There is a steep increase in nickel from 150ppm at 20% MgO to >800ppm at 25% MgO. In contrast the data for chromium is scattered and varies from 650-1300ppm. The Glen Doll adamellites contain low levels of nickel varying from 30ppm at 3% MgO to only 5ppm at 0.5% MgO. The abundance of chromium is, by contrast, variable from less than 10 to greater than 100ppm. There is no observed correlation between chromium and magnesium in the adamellites. The Juan Jorge rocks display a smooth increase in both chromium and nickel content with increasing magnesia, a feature in contrast to the adamellites.

The Ni^{2+} ion (0.69\AA) has the same charge and essentially the same radius as Mg^{2+} and therefore substitution of Ni for Mg can occur. However the Ni:Mg ratio is highest in early-formed crystals in a magma (Mason, 1966) since the substitution takes place at higher temperatures. Forsteritic olivines from the Glen Doll Complex contain ~0.2% NiO (Table 5.5). Nickel was not determined in either opx or cpx, but typical levels recorded in these phases from other complexes are generally <200ppm (e.g. Wager and Mitchel, 1951; Groome and Hall, 1974) which is below the detection limit for the technique used. The Glen Doll olivine gabbros contain from 175-891ppm Ni. If all of the nickel is located in olivine, then the olivine gabbros should contain between 12% and 50% modal oli-

vine. These figures are consistent with measured modal abundances of olivine in the olivine gabbros. Thus early crystallisation of olivine, could have depleted the magma in nickel prior to the crystallisation of the gabbros which typically contain only 80ppm. Minor amounts (<100ppm) of nickel can substitute for magnesium in amphibole and pyroxene, for example in the dioritic rocks although the nickel content of these minerals has not been measured.

Chromium is commonly present in a magma as the trivalent ion. Cr^{3+} (0.63Å) has an ionic radius similar to that of Fe^{3+} (0.69Å) for which it commonly substitutes. Those minerals which most readily concentrate chromium in basic rocks are spinel and cpx. Chrome bearing spinels are not recorded in any of the rock types from either the Glen Doll or Juan Jorge Complexes. Both opx in the olivine gabbros and opx and cpx in the gabbros contain 0.05-0.16% Cr_2O_3 (Chapter 5). However, the large brown poikilitic pargasitic amphiboles also contain up to 0.16% Cr_2O_3 (Table 5.3) suggesting that the distribution of chromium in the basic rocks is controlled by the crystallisation of both pyroxene and amphibole. In the intermediate rocks, pyroxene is most frequently absent from the mode, and the secondary actinolitic amphiboles, which are considered to be replacement products of early pyroxene, contain 0.03% Cr_2O_3 (Table 5.4). The primary amphiboles from the dioritic rocks from both the Glen Doll and Juan Jorge Complexes contain from 0.02-0.06% Cr_2O_3 (Table 5.3). Thus either mineral phase may control the distribution of chromium in the dioritic rocks.

6.3.5 Rubidium

The distribution of rubidium, in part, reflects that of barium although a wider scatter of data is seen within each rock group.

The basic rocks contain low, relatively constant levels varying only from 10-40ppm Rb. There is a slight increase in rubidium with decreasing magnesium concentration. The Glen Doll dioritic rocks by contrast, contain a variable amount of rubidium, typically 30-60ppm and occasionally reaching 150ppm. The data is very scattered and no correlation is seen between Rb and MgO. The adamellites display an overlap with the Glen Doll diorites and broadly show an increase from 75ppm Rb at 2.5% MgO to 190ppm Rb at 5% MgO. A similar negative correlation is seen in the Juan Jorge rocks, which contain from 50-200ppm Rb.

Rubidium commonly replaces potassium in biotite and alkali feldspar in igneous rocks. Rb^{2+} is however considerably larger at 1.47\AA than that of K^+ (1.33\AA) and the K:Rb ratio therefore typically decreases with increasing differentiation. Various authors have suggested that low K:Rb ratios (e.g. <300) in calc-alkaline rocks can be attributed to fractional crystallisation of a magma and may be due to the crystallisation of amphibole which preferentially concentrates K^+ (e.g. Taylor, 1969). The K:Rb ratios from the Glen Doll and Juan Jorge Complexes (Figure 6.20) are variable throughout and vary considerably within each rock group. The ratios for both complexes plot as a broad band from a K:Rb ratio of 150-300, suggesting that simple crystal fractionation alone can not produce the range of observed ratios. Most of the rocks sampled, particularly the gabbros, are fresh and therefore alteration is not thought to cause the scatter seen in Figure 6.20.

6.3.6 Lithium

The distribution of lithium is displayed in Figure 6.10. The gabbros show a negative correlation, increasing from <5ppm at 11%

MgO to 20ppm at 6% MgO. One sample (GC73) lies away from this trend and contains >35ppm Li. The more mafic olivine gabbros display a spread of data (not shown on Figure 6.13) with an average content of 18ppm Li. The Glen Doll diorites by contrast are scattered, varying from 7-45ppm Li and display no correlation between Li and MgO. The lithium content of the adamellites is variable from 14-36ppm and shows no apparent correlation with MgO content. The Juan Jorge rocks, which for many other trace elements plot on one continuous trend, fall into two distinct groups. The first, samples with >1% MgO, are quartz-mica diorites which display an increase from 25-45ppm Li with decreasing MgO. The second, with >1% MgO, are granites which lie off the diorite trend and contain only 15ppm Li.

Little published data is available for lithium in basic and intermediate rocks. Lithium does not substitute for the other monovalent alkali metals such as potassium due to its small ionic radius (0.68Å). It is thought however, that limited substitution of lithium for magnesium can take place in pyroxenes, amphiboles and micas although it frequently remains in the magma until the last late stage of differentiation (Mason, 1966). The scatter of data shown by the Glen Doll diorites (Figure 6.13) may therefore be controlled by the modal abundance of the ferromagnesian minerals. The increase in the amount of lithium in the Juan Jorge diorites with decreasing magnesium, suggests that lithium is being preferentially excluded from the ferromagnesian minerals.

6.3.7 Copper and zinc

Both copper and zinc (Figure 6.14) show a broad scatter of data for the Glen Doll dioritic rocks. The abundance of copper

varies from 10-115ppm and of zinc from 50-160ppm. The data displays no coherent trend in these dioritic rocks. The Juan Jorge rocks, Bridge rocks and adamellites by contrast tend to show an increase in zinc and copper concentration with increasing MgO, although the copper data is very scattered. Zinc levels in the gabbros remain low and constant at ~60ppm, while copper is variable from 60ppm at 11% MgO to 20ppm at 6% MgO. The olivine gabbros contain a higher concentration of zinc than the gabbros, typically 100ppm, and tend to show a slight decrease with decreasing MgO. Copper levels are variable from 37-60ppm and show no correlation with MgO content.

Zn^{2+} has the same ionic radius (0.74Å) as, and similar electronegativity to, Fe^{2+} . The substitution of Zn for Fe^{2+} can therefore occur in ferromagnesian minerals such as pyroxene, amphibole and biotite, and in iron oxide minerals where iron is in the 2+ form (Mason, 1966). Zinc may also be incorporated in sulphide minerals. Copper typically occurs in igneous rocks as the 2+ ion and in common with zinc, can substitute for Fe^{2+} although the electronegativity for copper is greater than that for either zinc or iron.

Zinc and copper values for other calc-alkaline suites are generally lower than those recorded from the Glen Doll diorites. Typical values range from 10-50ppm Cu and 40-50ppm Zn (Halliday et al., 1985). The Glen Doll diorites rarely contain sulphide minerals and display no correlation between copper and zinc. There is similarly no observed correlation between modal levels of Fe and Ti oxides and zinc concentration. This data suggests that the distribution of these elements is controlled by substitution in silicate

minerals or by some minor phase.

The enhanced abundance of zinc (<160ppm) in the Glen Doll dioritic rocks, is considered to result from the assimilation of locally derived Dalradian metasedimentary xenoliths which are zinc rich. Partially assimilated pelitic and semi-pelitic xenoliths are recorded in the dioritic rocks in the Glen Doll Complex (Chapter 3). These xenoliths characteristically contain aggregates of hercynitic spinel. Detailed petrographic studies have revealed similar aggregates within the hornblende and pyroxene diorites, suggesting that due to their resistance to chemical and physical breakdown, these spinel are all that remain of otherwise totally assimilated xenoliths. The regionally metamorphosed Dalradian country rocks south of the Glen Doll complex contain zincian staurolite (Schumacher, 1985). Hercynitic zincian spinel, a breakdown product of these staurolite, are recorded in the thermal aureol of the Glen Doll Complex (Schumacher, 1985).

The origin of the zinc in the metasediments is unclear. It may be related to strata-bound sulphide mineralisation recorded in several areas of the Grampian Highlands e.g. Tyndrun, Aberfeldy (Fortey and Smith, 1986; Coats et al., 1980; Smith et al., 1984). The mineralisation, typically Zn-Cu-Pb-Ba, is confined to the Argyll Group (Middle Dalradian) and is thought to be synsedimentary in origin (Willan, 1980; Forty and Smith, 1986).

6.3.8 Zirconium

The Glen Doll dioritic rocks display a wide range of zirconium values, from 50 to over 300ppm, which display no correlation with MgO content (Figure 6.15). By contrast the gabbros display less

Table 6.8 Ranges of selected trace elements for the Glen Doll Complex. (Concentrations in ppm)

Rock type: Olivine gabbro	Gabbro
Ba 87-143	86-285
Cr 789-1368	90-389
Li 13-25	2-36
Ni 175-891	14-155
Rb 18-27	9-59
Sc 13-37	20-34
Sr 119-311	575-914
Zr 62-109	11-119
Rock type: Diorite	Adamellite
Ba 100-650	500-897
Cr 5-280	5-105
Cu 12-120	5-70
Li 10-46	14-37
Ni 5-100	5-35
Rb 23-156	74-191
Sc 4-41	4-16
Sr 400-1050	230-852
V 20-580	17-215
Zr 40-320	108-495

scatter and contain relatively low, constant levels of zirconium averaging 45ppm. Zr levels in the olivine gabbros are scattered and contain from 60-110ppm Zr. The adamellites and Juan Jorge rocks contain between 50 and ~500ppm Zr and these patterns display no correlation with MgO.

The combination of high charge (4+) and comparatively large ionic radius (0.79Å) sets Zr^{4+} apart from any of the major elements in igneous rocks. Consequently zirconium does not easily substitute in common rock forming minerals but occurs most commonly in the silicate mineral zircon. Zircons are recorded only rarely in the Glen Doll and Juan Jorge rocks. However, a typical zircon contains 51-67% ZrO_2 (Deer et al., 1983) and therefore a few grains may contain all of the zirconium content of the rock. Zircon is a common mineral in pelitic sediments and the distribution of zirconium may partly be controlled by traces of refractory residues left after assimilation of metasedimentary xenoliths. Zircons are less common in basic rocks than in acid ones and the low level of zirconium in the gabbros probably reflects the low modal abundance of zircon.

6.3.9 Discussion

Average values for several trace elements from a range of Caledonian plutonic complexes were compiled by Nockolds and Mitchell (1946) (Table 6.7). Several important features are noted when comparison of these data is made with trace element data from the Glen Doll Complex (Table 6.8). The ranges displayed for some elements from Glen Doll are similar to those from other complexes e.g. in the gabbros Ba, Sc, Li, Cr and Zr. However nickel ranges from 14-155ppm, Sr from 575-914ppm, and Rb from 9-59ppm in the Glen

Doll gabbros compared with 200-300ppm Ni, 800-1200ppm Sr and 50-500ppm Rb in average data from Nockolds and Mitchell (1946). The relatively low level of nickel in the Glen Doll gabbros could be due to the early crystallisation of the olivine cumulates which would have depleted the magma in nickel prior to crystallisation of the gabbros. The Glen Doll dioritic rocks contain a wide range of barium concentration (100-650ppm) with values close to that for a xenolithic diorite (Table 6.7) (Nockolds and Mitchell, 1946). Strontium is typically lower in all of the Glen Doll rocks than in Nockolds and Mitchell's average Caledonian diorite.

6.4 Geochemistry of the microdiorite dykes and microdiorite xenoliths

Representative analyses of microdiorite dykes, microdiorite xenoliths are given in Table 6.5A. The distribution of the microdiorite xenoliths is discussed in Chapter 3. They display a range of compositions from 5-8% MgO. The chemical data shows that the microdiorite xenoliths lie on a continuation of the trend defined by the microdiorite dykes, which passes between the areas defined by the diorites and gabbros from the Glen Doll Complex. The microdiorite xenoliths may be the remnants of an early formed chilled margin of the complex (Chapter 3). A micro diorite xenolith with a relatively primitive chemical composition is considered further in Chapter 8 as a possible parental composition from which the dioritic rocks may have crystallised.

6.5 Geochemistry of the appinites

Representative analyses (Table 6.1) show that some features of

the appinites are relatively primitive. They are relatively magnesium rich (8-12% MgO) and have high chromium and nickel levels compared to the gabbro. They contain abundant magmatic amphibole, reflected in the high MgO, FeO and SiO₂ values. They do however contain high levels of zirconium (>100ppm) and up to 2.6% K₂O and therefore exhibit a strange mixture of primitive and evolved characteristics.

6.6 Rare earth element geochemistry

The lanthanides or rare earth elements (REE) consist of the group of elements from La to Lu, which exhibit closely similar chemical properties. In terrestrial igneous rocks they are dominantly tri-valent and show a progressive decrease in ionic radii from 1.03Å for La to 0.861Å for Lu (Shannon, 1976). The REE can be split into two subgroups a) the light REE (LREE) La-Gd and b) the heavy REE (HREE) Dy-Lu. Although the group of elements as a whole exhibit similar behaviour, the LREE can be fractionated from the HREE particularly by minor mineral phases such as apatite, sphene, zircon, garnet, monazite and xenotime because of the reduced radius of the HREE. Europium commonly occurs in both the 2⁺ and 3⁺ forms, the ratio depending on the oxygen fugacity of the magma at the time of crystallisation (Drake, 1975). The divalent form can readily substitute for Ca²⁺ in plagioclase feldspar. Therefore europium can be fractionated relative to the other REE during plagioclase crystallisation.

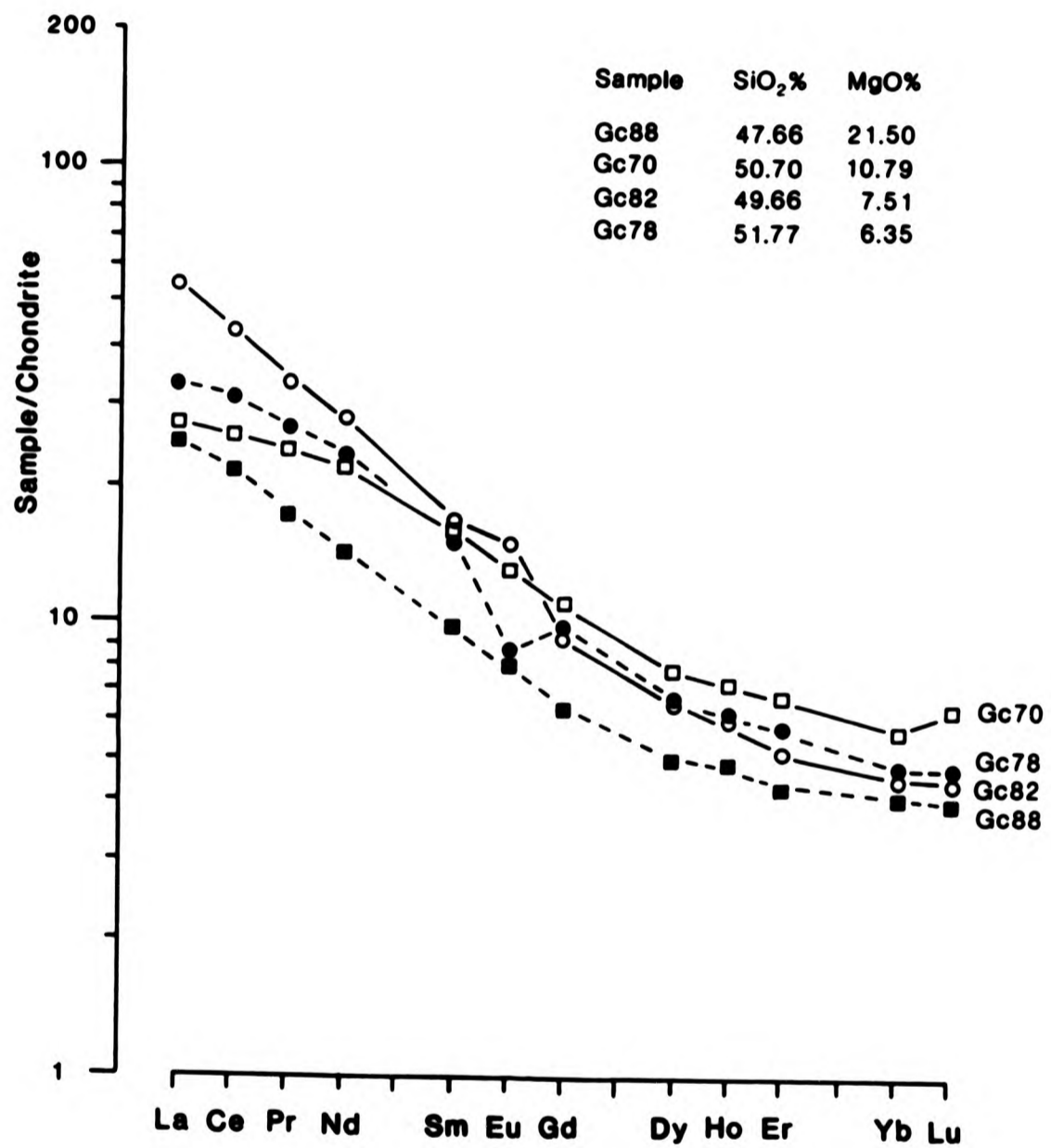
The distributional patterns of the REE in rocks corresponds to the Oddo-Harkins rule (Haskin et al, 1966); that is to say, a plot of concentration against atomic number shows striking differences

in abundance between neighbouring REE with odd and even atomic number. For comparative purposes, therefore, concentrations are usually divided by their abundance in average chondrite meteorites (Nakamura, 1974) which has the additional effect of emphasising any relative fractionation of the elements. A number of samples were selected for analysis which cover the chemical variability of the complexes.

Twelve of the fourteen naturally occurring REE (excluding Tb and Tm) have been analysed in the selected samples, using ICP following preconcentration by a cation exchange procedure (Jarvis and Jarvis, 1985, modified after Walsh et al. (1981)(Appendix D). The abundance of the REE have been normalised to average chondrite (Nakamura, 1974) and plotted on diagrams of chondrite normalised values vs element in order of increasing atomic number. In addition yttrium has been analysed. Although not strictly a member of the Lanthanide group, yttrium displays similar behaviour to the HREE (Mason, 1966). Both yttrium and lanthanum were also determined in the standard HF/HClO₄ open acid digestion, so data for these elements is available for most samples.

Lanthanum and yttrium have initially been plotted using MgO as abscissa (Figure 6.16). Yttrium data for the basic rocks is a little scattered, with a range from 10-24ppm Y at for example, 6.5% MgO. The Glen Doll diorites and adamellites display a wide scatter of data points, from 9-47ppm Y and neither rock type display any correlation with MgO. By comparison, the Juan Jorge rocks show a positive linear correlation between Y and MgO with an increase in yttrium from 16-33ppm.

Fig. 6.22 Chondrite normalised REE patterns of gabbros from the Glen Doll Complex. Gc88 is an olivine gabbro.



The distribution pattern of lanthanum data (Figure 6.16) from the Glen Doll Complex is similar to that seen for yttrium. The basic rocks display a slight scatter of data, averaging 10-12ppm La. Lanthanum in the Glen Doll diorites and adamellites is very scattered, displaying a wide range of values from <10-45ppm La. In contrast to yttrium, lanthanum displays an apparent increase with decreasing MgO in the Juan Jorge rocks.

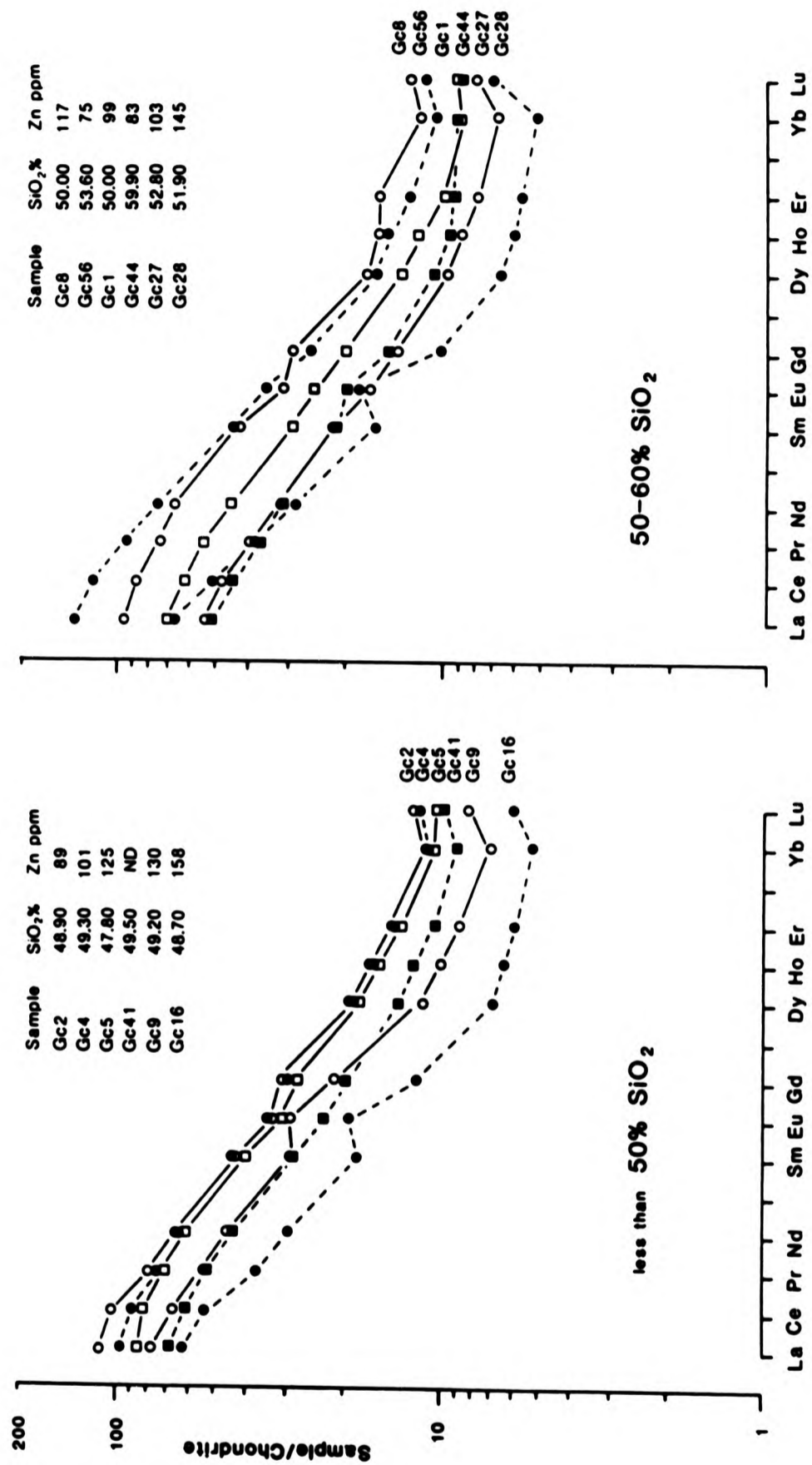
Due to the similarity of charge (2+) limited substitution of the REE and Y for Ca^{2+} can occur. Those minerals which preferentially concentrate the REE in granitoid rocks include amphibole, apatite, zircon and sphene. Analysis of both apatite and sphene from the Glen Doll and Juan Jorge Complexes, has shown these minerals to contain substantial amounts of the LREE (Table 5.11 and 5.12). A broad correlation is noted between La and P_2O_5 (Figure 6.21) in the Glen Doll diorites although the data is rather scattered. A similar distribution of data is seen for a plot of La vs TiO_2 (Figure 6.21) suggesting that apatite and sphene fractionation may account for some of the variation.

Chondrite normalised patterns

6.6.1 Basic rocks

The patterns displayed by the gabbroic rocks cover a range of LREE/HREE ratios (represented by La/Yb) from 7.11-17.23 with an average value of 11.82 (Figure 6.22). Chondrite normalised values for lanthanum (La_N) range from 26.0-54.0 and for lutetium from 4.4-6.5. The normalised profiles are either smooth, or show small negative ($\text{Eu}/\text{Eu}^*=0.71$) or positive ($\text{Eu}/\text{Eu}^*=1.25$) europium anomalies (Eu^* is interpolated from the adjacent REE). The olivine gabbro has a smooth profile and a La/Yb ratio of 8.6. An increase in the

Fig. 6.23 Chondrite normalised REE patterns of diorites from the Glen Doll Complex.
 All samples are hornblende diorites except Gc9, a pyroxene diorite.



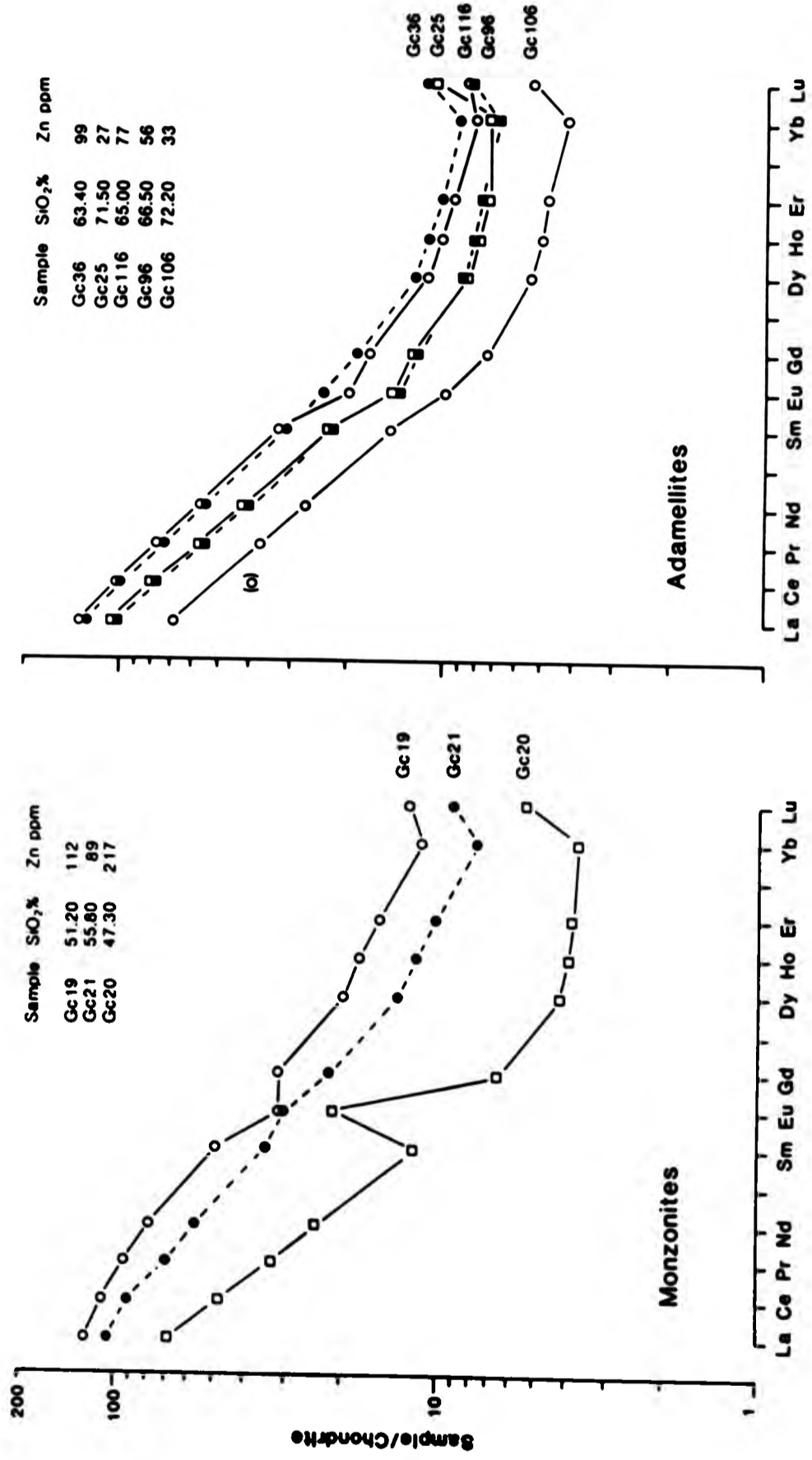
La/Yb ratio in the gabbros is correlated with decreasing bulk rock MgO. The gabbro sample displaying a positive Eu anomaly is a plagioclase orthocumulate (Chapter 4) and that with a negative anomaly, a pyroxene orthocumulate. The occurrence of a Eu anomaly, results from the differing oxidation states of europium. A magma which has undergone crystallisation and removal of plagioclase can display a negative anomaly due to the replacement of Ca^{2+} by Eu^{2+} . The major and trace element data coupled with petrographic observations, suggests that the gabbroic rocks are cumulates, which is compatible with the observed REE patterns.

6.6.2 Diorites

The diorites from the Glen Doll Complex display a range of chondrite normalised patterns (Figures 6.23). For convenience of plotting, the rocks have been subdivided into those with $<50\%$ SiO_2 and those with $50-60\%$ SiO_2 . Diorites with $<50\%$ SiO_2 display a range of La/Yb ratios, from 9.03-17.74, with an average of 13.65. There is no apparent correlation between the La/Yb ratio, the abundance of total REE and the whole rock silica content. The chondrite normalised profiles are either smooth or have small positive europium anomalies ($\text{Eu}/\text{Eu}^*=1.35$).

Diorites with between 50 and 60% SiO_2 display a similar range of patterns, with La/Yb ratios of 11.1-19.75, an average of 14.29. La_N varies from 54-135 and Lu_N 7.5-12.5. The profiles are typically smooth, although some display small positive europium anomalies ($\text{Eu}/\text{Eu}^*=1.11-1.38$). There is no correlation between either the La/Yb ratio or the total REE abundance, and the bulk rock silica content. The diorites display a complete overlap of patterns and there is clearly no simple correlation between absolute REE abun-

Fig. 6.24 Chondrite normalised REE patterns of monzonites & adamellites from the Glen Doll Complex.
 Sample Gc20 contains aggregates of hercynitic spinel.



dance and bulk rock silica content.

These patterns contrast with, for example, the Loch Doon Complex (Tindle and Pearce, 1981) where there is a positive correlation between REE abundance and bulk rock silica content from diorite through to granite compositions. The Glen Doll dioritic rocks do however display a broad correlation between La and P_2O_5 (Figure 6.21) indicating that apatite may in part control the distribution of the REE.

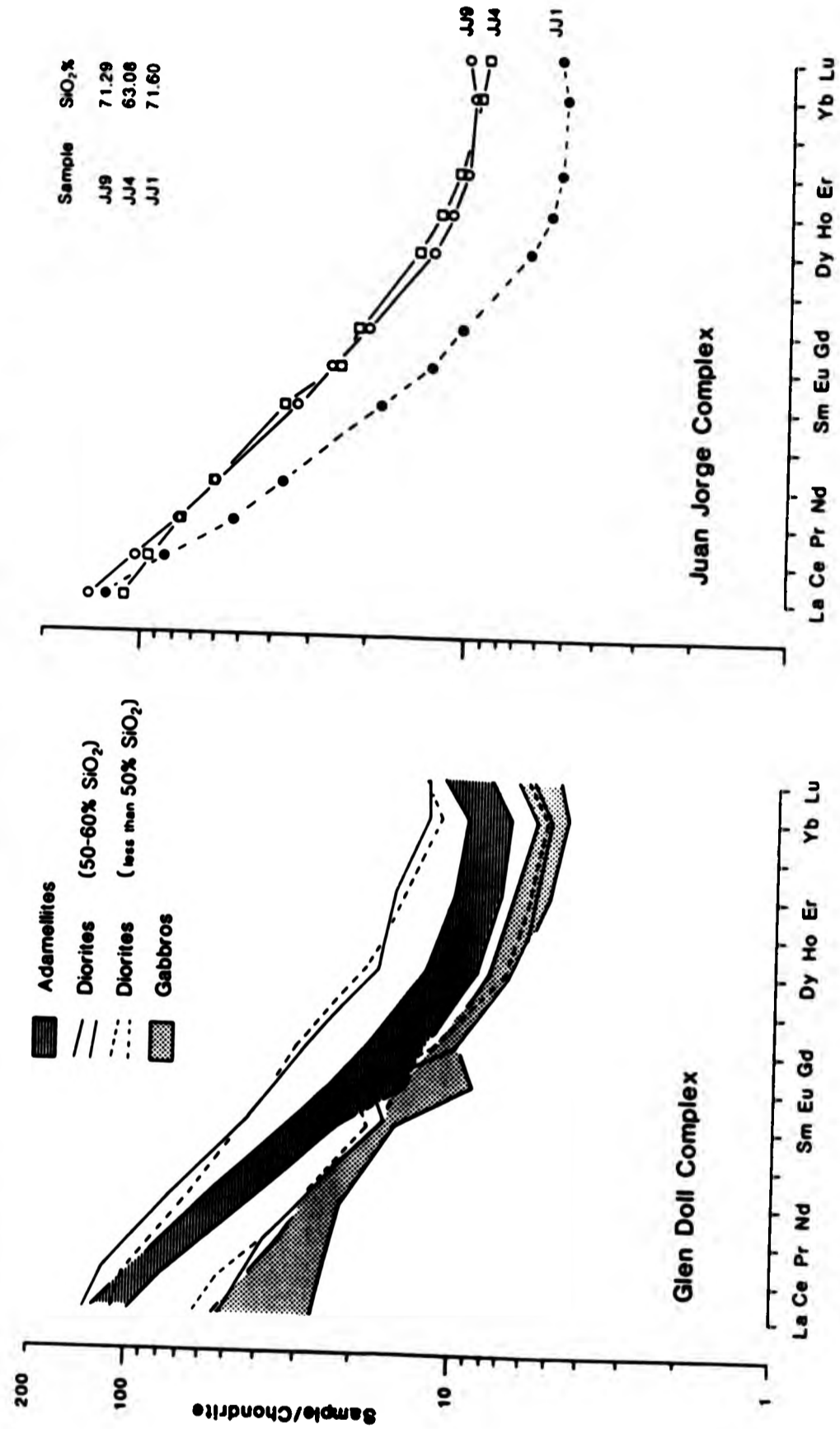
6.6.3 Monzonites

Three chondrite normalised patterns for these compositions are displayed in Figure 6.24. The two upper patterns (GC19 and GC21) have La/Yb ratios of 16.12 and 20.92. One pattern displays a small positive europium anomaly ($Eu/Eu^*=1.11$) while the other has a small negative anomaly ($Eu/Eu^*=0.79$). The third sample GC 20, has a steep pattern, with La/Yb=28.36 and a large positive europium anomaly ($Eu/Eu^*=2.47$). This sample contains aggregates of hercynitic spinel which are considered to be all that remains of otherwise totally assimilated metasedimentary xenoliths. The distribution of the REE in this sample may therefore partly be controlled by the distribution of the REE in the assimilated xenolithic material (See below).

6.6.4 Adamellites

The chondrite normalised patterns for this rock type are relatively steep, with La/Yb ratios from 20.75-25.34, with an average value of 22.75 (Figure 6.24). La_N varies from 68-120 and Lu_N from 5.2-11.5. The profiles are typically parallel and are either

Fig. 6.25 Summary diagram of the chondrite normalised REE patterns of the Glen Doll Complex showing compositional ranges and comparative patterns from the Juan Jorge Complex. Lochnagar Granite (JJ1) is also shown.



smooth or have small negative europium anomalies ($Eu/Eu^*=0.83$). The absolute abundance of the REE tends to decrease with increasing whole rock silica content.

6.6.5 Juan Jorge complex

Figure 6.27 displays the profiles for a quartz- mica diorite (JJ4), granite (JJ9) and the Lochnagar granite (JJ1). The granites have steep, smooth profiles ($La/Yb=24-32$) while the diorite displays the same pattern as granite JJ9, except for a very small negative europium anomaly. There is no correlation between REE abundance and either whole rock silica or magnesia content. The patterns displayed by the Juan Jorge rocks are comparable with those seen in the Glen Doll adamellites both in absolute abundance and LREE to HREE ratio.

6.6.6 Discussion of the REE data

A summary diagram for the Glen Doll Complex (Figure 6.25) displays the clear overlap between those Glen Doll diorites with $<50\%$ SiO_2 and those containing $50-60\%$ SiO_2 diorites. The field for the adamellites lies within that defined by the dioritic rocks. The gabbros have the lowest absolute REE abundances and are enriched in the HREE relative to the intermediate rocks.

In addition to the intrusive facies in the Glen Doll Complex, REE data have been determined for a sample of local Dalradian metasediment (meta-pelite), two gneissose xenoliths (thought to have been derived locally), and two rafted metasedimentary xenoliths (Figure 6.26). Trace element data, particularly zinc, suggests that the Glen Doll diorites are contaminated with Dalradi-

an metasediment. The rafted xenoliths, analysed here, contain zones of dioritic material between mafic and acidic layers (See Chapter 4) and have undergone varying amounts of partial melting. The analysis of these samples, therefore provides only an average value of a rather heterogenous sample.

The profile for the Dalradian country rock is very steep ($La/Yb=60.71$) and smooth. The two samples of gneiss xenolith (GC 15 and GC 46) have a greater absolute abundance of REE and shallower patterns than that of the country rock sample. One example has a small negative europium anomaly ($Eu/Eu^*=0.75$) while the other is smooth. The two gneiss samples show different levels of HREE enrichment while their lanthanum values are similar. Two examples of rafted metasedimentary xenoliths (GC3 and GC26) display widely different La/Yb ratios 33.54 and 6 respectively. The profile and absolute REE abundances displayed by GC26 are however identical to the monzonite GC20 (Figure 6.24).

REE data for other Caledonian suites in Scotland is limited. It is only in recent years that REE data has become relatively easily available. REE profiles from the Loch Doon Complex (Tindle and Pearce, 1981; 1983) for diorite and granodiorite compositions are typically shallow ($La/Yb=10.3$), broadly parallel and display negative europium anomalies. The sequence of rocks displayed in Loch Doon is thought to be the result of in-situ fractional crystallisation and the distribution of the REE, dominantly controlled by the crystallisation of minor phases such as apatite, zircon, sphene and allanite.

The primitive andesite lavas from the Lorne Plateau and the

Fig. 6.26 Chondrite normalised REE patterns for xenoliths from the Glen Doll Complex and a Dalradian country rock.

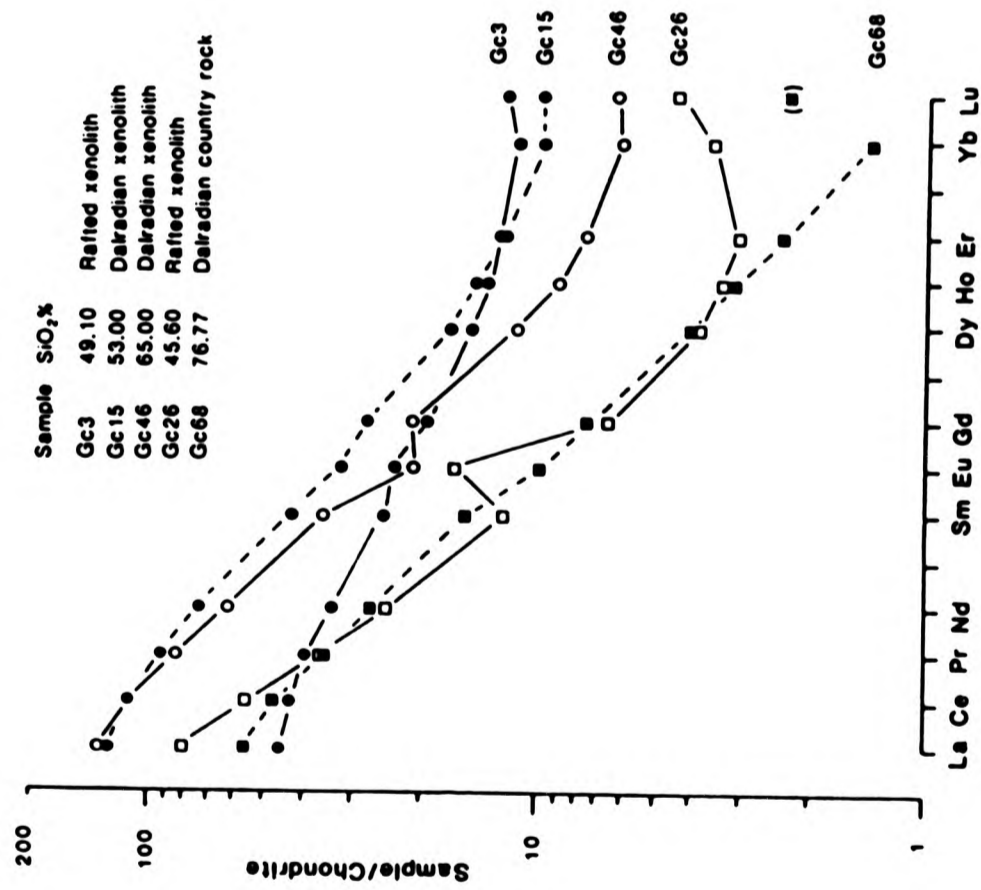
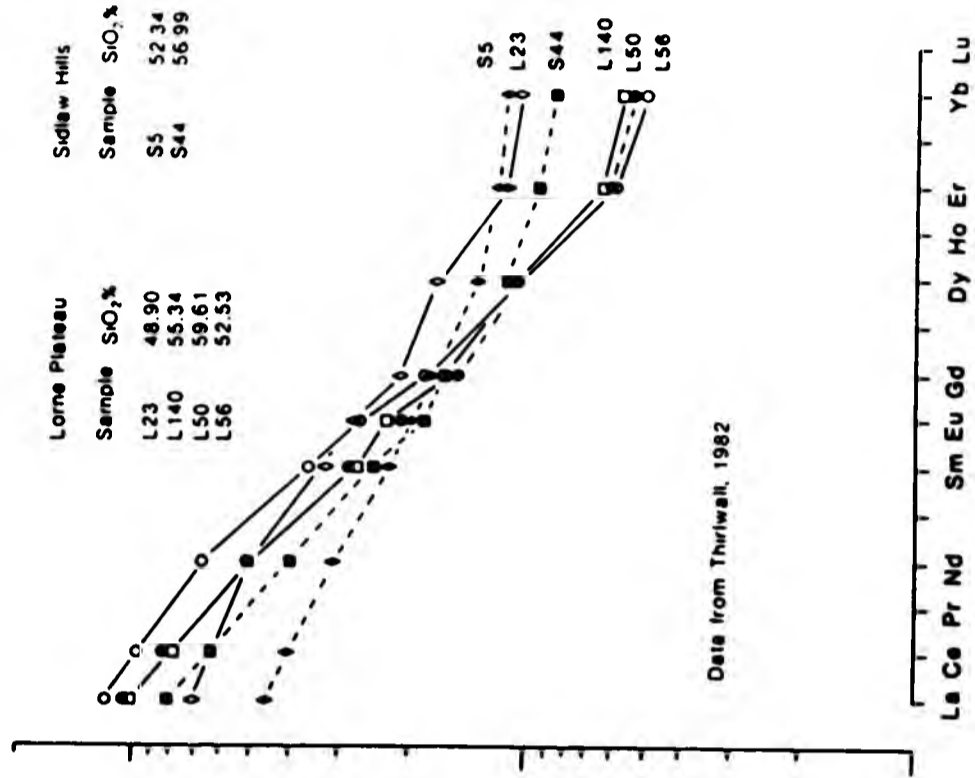


Fig. 6.27 Chondrite normalised REE patterns for andesitic lavas from the Lorne Plateau and the Sidlaw Hills.



Sidlaw Hills (Thirlwall, 1982) display relatively steep, smooth patterns (La/Yb=29). The Sidlaw lavas show an increase in the LREE/HREE ratio with increasing silica (Figure 6.27) a feature typical of a magma undergoing fractional crystallisation and a situation where the REE are behaving essentially as incompatible elements. It is notable that the lavas contain a higher abundance of REE than the Glen Doll gabbros and some of the Glen Doll diorites, reflecting the general exclusion of the REE in the cumulus mineral phases (olivine, pyroxene) in both rock types i.e. a dilution effect due to the presence of large proportions of cumulate minerals and relatively small proportions of intercumulus liquid.

CHAPTER 7

Isotope Geochemistry

7.1 Introduction

In recent years the use of stable and radiogenic isotopes has become increasingly important in the investigation of magma genesis. Radiogenic isotope systems which have been utilised include $^{87}\text{Rb}/^{86}\text{Sr}$ (e.g. Clayburn et al., 1983; Frost and O'Nions, 1985), $^{235}\text{U}/^{207}\text{Pb}$ (e.g. Thirlwall, 1985) and $^{147}\text{Sm}/^{143}\text{Nd}$ (e.g. Halliday, 1984; Halliday et al., 1986). The stable isotope system most commonly used in igneous petrology is that of $^{18}\text{O}/^{16}\text{O}$ (e.g. Clayburn et al., 1983). Used in combination, these isotope systems can sometimes identify and discriminate between magmas from different sources and permit assessment of magma contamination processes.

Facilities for isotope analysis were made available at the British Geological Survey (Dr. R. Pankhurst) for a limited number (15) of whole rock samples to be processed for Rb/Sr systematics. This data places some constraints on the extent of contamination and possible sources of contamination. The samples were analysed for Rb and Sr. The isotopes were separated from their matrix using ion-exchange techniques and analysed by thermal ionisation mass spectrometry. Details of the analytical techniques are given in appendix D.

7.2 Strontium isotopes

The isotope data were determined to establish two main points (a) the absolute age of the Glen Doll and Juan Jorge Complexes using measured $^{87}\text{Sr}/^{86}\text{Sr}$ and $^{87}\text{Rb}/^{86}\text{Sr}$ ratios and (b) the initial

$^{87}\text{Sr}/^{86}\text{Sr}$ ratios of the range of rock types seen in each complex. The data has subsequently been used in a numerical modelling procedure to establish the extent of crustal contamination.

Samples were chosen primarily to give a wide range of Rb/Sr ratios in order that the data could be used to fit an isochron. Consequently the sampling is biased towards the granitic members of both the Glen Doll (6 samples) and Juan Jorge Complexes (1 sample). In addition, a sample of the Lochnagar Granite (JJ1) was included in the study since it has a relatively high Rb/Sr ratio (0.85) and is closely related to the Juan Jorge Complex (Chapter 3). Seven samples of the intermediate and basic members of the Glen Doll suite including olivine gabbro, gabbro, hornblende diorite, pyroxene diorite and monzonite have also been included to study the effects of contamination and the relationships with the more evolved rocks. It was also thought likely that an isochron could be drawn from the uncontaminated rocks of this suite. All of the samples selected are fresh and unaltered.

Potential source materials for the late Caledonian granitoids and associated volcanics, including both mantle and crustal sources, have been extensively investigated using $^{87}\text{Sr}/^{86}\text{Sr}$ systematics (e.g. Dupre and Allegre, 1980; Hamilton et al., 1980; O'Nions et al., 1985; Frost and O'Nions, 1985; Halliday et al., 1980). Some authors have suggested that a depleted mantle with low $^{87}\text{Sr}/^{86}\text{Sr}$ ratios (<0.703) (e.g. Jacobson and Wasserburg, 1979) is an appropriate source, while others (Thirlwall, 1982, 1986) suggest that a vertically stratified, enriched (with respect to ^{87}Sr) mantle (0.7034-0.7069) is required to generate the range of isotope values observed in, for example, the primitive Lorne Lava series

Table 7.1 Strontium isotope data for the Glen Doll and Juan Jorge Complexes

Sample	Rock	$^{87}\text{Sr}/^{86}\text{Sr}(t)$	SD	Rb	Sr	$^{87}\text{Rb}/^{86}\text{Sr}$	K/Rb	Zn
GC78	Gabbro	0.70513	07	35	1040	0.0973	249	58
GC88	Ol gabbro	0.70556	08	25	213	0.2525	196	89
JJ1	Granite	. J558	36	184	217	2.4539	132	41
GC155	Px diorite	0.70632	07	19	695	0.0832	284	70
GC276	Granite	0.70638	09	141	524	0.4121	161	70
GC105	Diorite	0.70642	07	29	602	0.1263	226	75
GC36	Adamellite	0.70653	10	85	537	0.4399	285	99
GC281	Px diorite	0.70666	08	79	400	0.2958	116	140
JJ9	Granite	0.70687	17	108	301	1.0407	347	49
GC21	Monzonite	0.70688	08	55	647	0.2404	264	89
GC271	Adamellite	0.70789	12	191	342	0.6821	130	43
GC16	Diorite	0.70836	08	41	682	0.1697	285	158
GC25	Adamellite	0.70854	18	105	263	1.1451	379	27
GC117	Adamellite	0.70887	22	117	234	1.4313	301	40
GC116	Adamellite	0.71137	16	107	311	1.0139	232	77

NOTES: Initial strontium isotope ratios are calculated at time $t=400\pm 10\text{Ma}$. SD=1 sigma on the last two sig. figures. Rb, Sr and Zn concentrations in ppm. Ol=olivine, Px=pyroxene

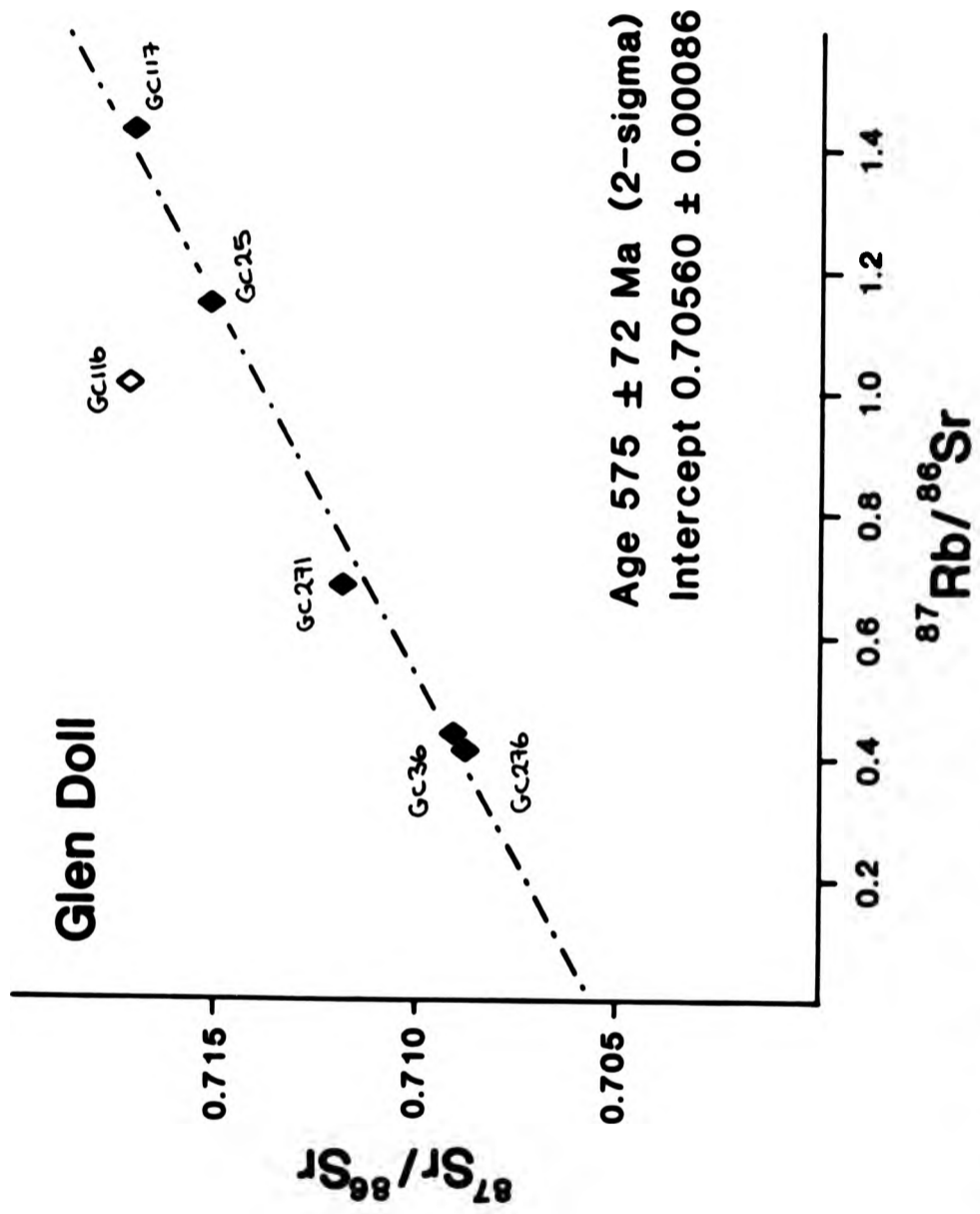


Fig.7.1 Pseudoisochron for the adamellites of the Glen Doll Complex.
Sample GC116 (unfilled diamond) excluded from the age calculation.
GC276 GRANITE

(Thirlwall, 1982). Investigations of other isotope systems suggests that some of the late Caledonian plutons owe their origin to a mantle derived magma subsequently modified isotopically with crustal material such as Dalradian, Lewisian, Moinian or Grenvillian (e.g. Frost and O'Nions, 1985; Clayburn et al., 1983; Harmon et al., 1984).

7.2.1 Age of the Glen Doll and Juan Jorge Complexes

The York-Williamson least squares fit routine (York, 1969) was applied to the measured ratios $^{87}\text{Sr}/^{86}\text{Sr}$ vs $^{87}\text{Rb}/^{86}\text{Sr}$ (Table 7.1) to determine the intercept value on the $^{87}\text{Sr}/^{86}\text{Sr}$ axis and the slope of the best fit line. The data were plotted by rock type and complex. Attempts were made to fit isochrons to each rock type in turn, and to the adamellites and Juan Jorge granite but these with one exception, failed. The Glen Doll ^{and granite GC276} adamellites, however, which have a range of Rb/Sr ratios from 0.1431-0.4957 (Figure 7.1) define a pseudo-isochron with an age of $575 \pm 72\text{Ma}$. This is clearly not the age of emplacement or of crystallisation of the intrusion since an age of 575Ma , predates the main period of regional metamorphism. The complexes are undeformed and display igneous mineralogy and textures. Since no isochron could be fitted to the data, the date of crystallisation, and hence emplacement, could not be obtained and initial $^{87}\text{Sr}/^{86}\text{Sr}$ ratio could not be directly measured.

The Lochnagar granite, which cuts the northwestern margin of the Juan Jorge Complex, has been dated at 415Ma (Harmon and Halliday, 1980). Isochrons have been obtained for other post tectonic Scottish Caledonian complexes using Rb/Sr techniques e.g. Garabal Hill 392 ± 4 - 406Ma (Summerhayes, 1966; Harmon and Halliday, 1980), Cairnsmore of Fleet $392 \pm 2\text{Ma}$, Crieffell-Dalbeattie $397 \pm 2\text{Ma}$ and Loch

Doon 408 ± 2 Ma (Halliday et al., 1980) and Glen Tilt 393 ± 5 Ma (granite member) (C. Turner pers. comm. 1987). Based on an average of the above data, a reasonable age for both the Glen Doll and Juan Jorge Complexes is thought to be 400 ± 10 Ma. (calculations using from 390-410 Ma do not produce significant differences in the initial Sr ratio)

7.2.2 Initial Strontium isotope ratios

The initial $^{87}\text{Sr}/^{86}\text{Sr}$ ratios were calculated for an assumed age of 400 ± 10 Ma for each sample (Table 7.1). As one might predict from the lack of an isochron, the rocks show a wide range of initial $^{87}\text{Sr}/^{86}\text{Sr}$ ratios, all of which are higher than an average mantle value (e.g. Frost and O'Nions, 1985) (Table 7.1). The initial ratios from the Glen Doll Complex range from 0.70513 in the gabbro to 0.71137 in an adamellite. The initial ratio from the Juan Jorge granite is 0.70687. The Lochnagar granite ratio is 0.70558, in contrast with data from Harmon and Halliday (1980) (0.7065).

To display the range of data, the $^{87}\text{Sr}/^{86}\text{Sr}_{400}$ (initial ratio) ratios have been plotted against the concentration of strontium, Rb/Sr ratio, K/Rb ratio and zinc (Figures 7.2-7.5).

7.2.2.1 Diorites and Basic rocks

The $^{87}\text{Sr}/^{86}\text{Sr}$ ratio is lowest in the basic rocks from the Glen Doll Complex with the olivine gabbro having a slightly higher ratio (0.70556) than that in the olivine free gabbro (0.70513). The diorites are very variable and display a range of ratios from 0.70632 to 0.70836. Four diorite samples were analysed, two of which are pyroxene diorites. Sample GC21 is a monzonite from the SE part of the complex. It has an initial ratio (0.70688) which is within the range covered by the diorites. It is notable that with-

- Olivine Gabbro
- Gabbro
- Diorite
- Monzonite
- ◇ Adamellite
- ✦ JJ & Lochnagar

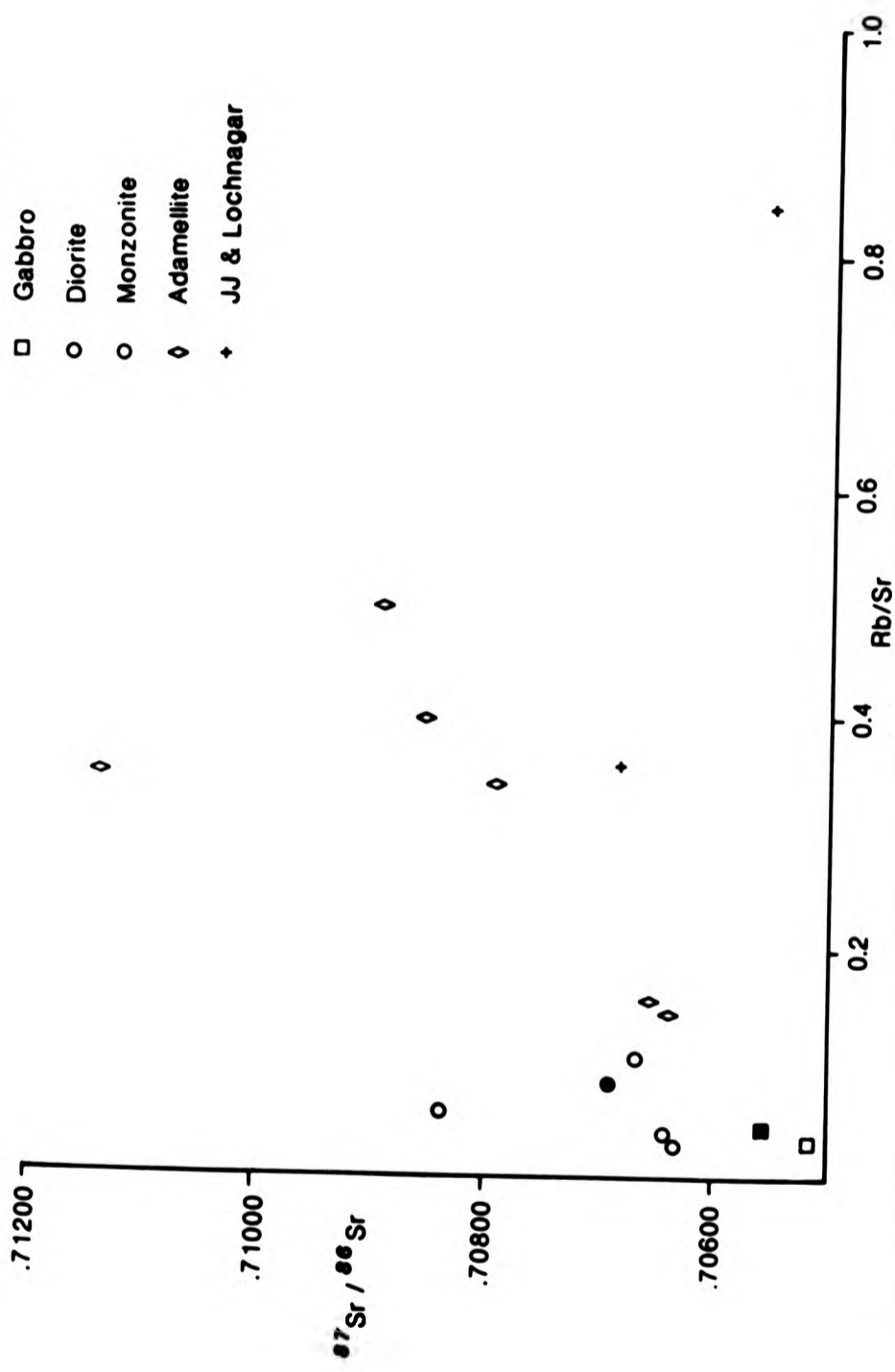


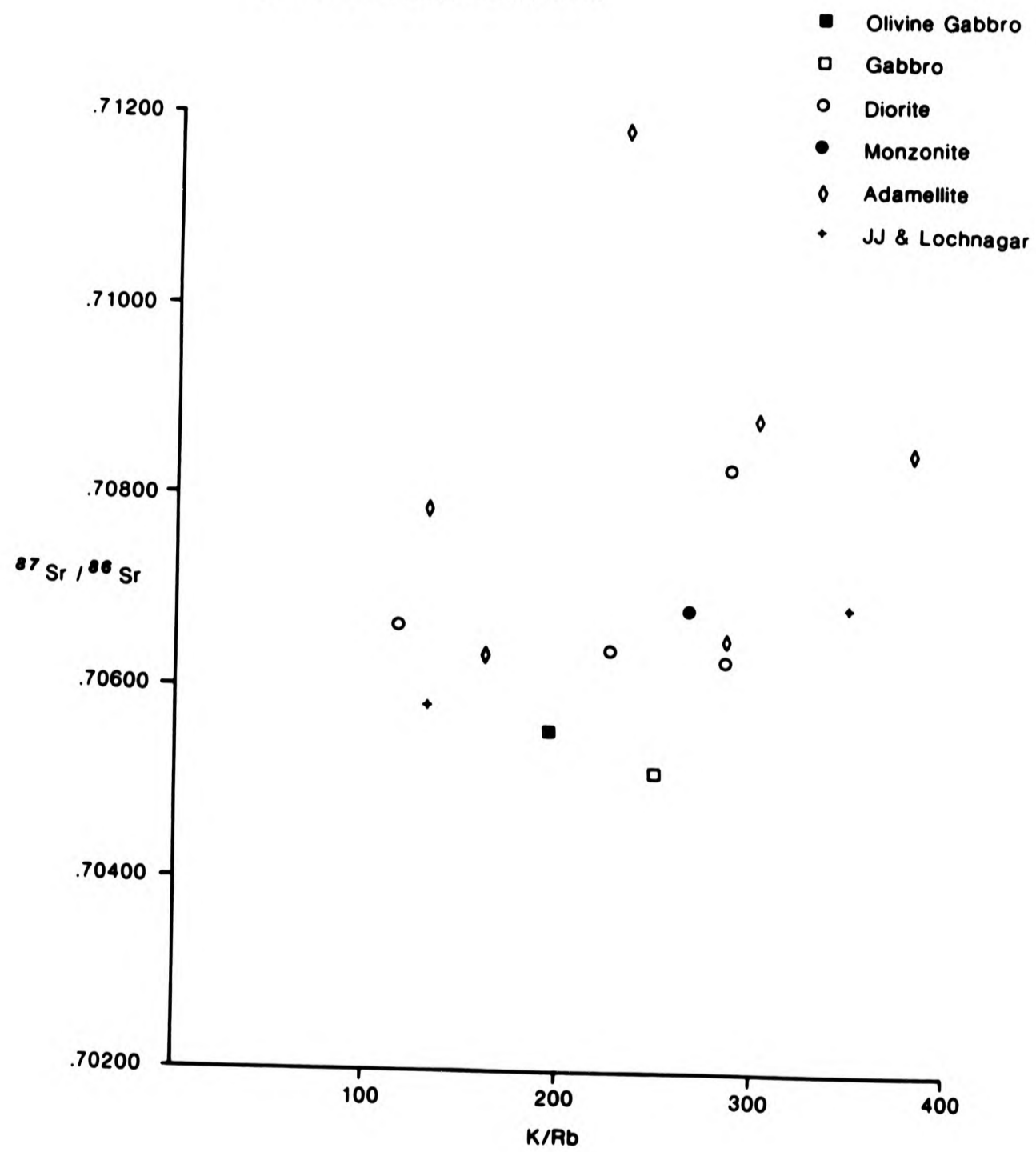
Fig. 7.2 Initial strontium isotope ratios plotted Rb/Sr for the Glen Doll & Juan Jorge Complexes.

in each pair of diorites (pyroxene bearing and pyroxene free), the sample with the highest initial ratio also contains the highest levels of zinc (Figure 7.5), as well as abundant rafted metasedimentary xenoliths. Trace element data, particularly for zinc (see chapter 6), suggests that the Glen Doll dioritic rocks have undergone some assimilation of local Dalradian metasediments. Figure 7.5 displays a positive relationship between the concentration of zinc and initial $^{87}\text{Sr}/^{86}\text{Sr}$ ratios in the Glen Doll intermediate and basic rocks. Typical $^{87}\text{Sr}/^{86}\text{Sr}$ ratios (calculated at 400ma) recorded from Dalradian metasediments around the Etive Complex vary from 0.71577 to 0.72602 (Frost and O'Nions, 1985). Interaction of magma in the Glen Doll Complex with Dalradian metasediment could therefore produce an increase in the $^{87}\text{Sr}/^{86}\text{Sr}$ ratio in parallel with increased zinc.

Data in figure 7.2 suggests that the diorites show an increase in Rb/Sr ratio from 0.0277 to 0.1025 with a small increase in $^{87}\text{Sr}/^{86}\text{Sr}$ ratio from 0.70632-0.70666. Conversely there is no correlation observed between K/Rb ratio and $^{87}\text{Sr}/^{86}\text{Sr}$ ratio in either the diorites or the gabbroic rocks (Figure 7.3). The basic and dioritic rocks display no correlation between $^{87}\text{Sr}/^{86}\text{Sr}$ ratio and the concentration of strontium.

The relationship between initial ratio and strontium is shown in Figure 7.4. The gabbro has >1000ppm Sr and a low $^{87}\text{Sr}/^{86}\text{Sr}$ ratio (0.70513). This gabbro is a cumulate rock and contains abundant plagioclase primocrysts, and the distribution of strontium is probably controlled by its substitution for calcium in the plagioclase feldspar lattice (Deer et al., 1983). Unfortunately, strontium was not determined during electron microprobe analysis of

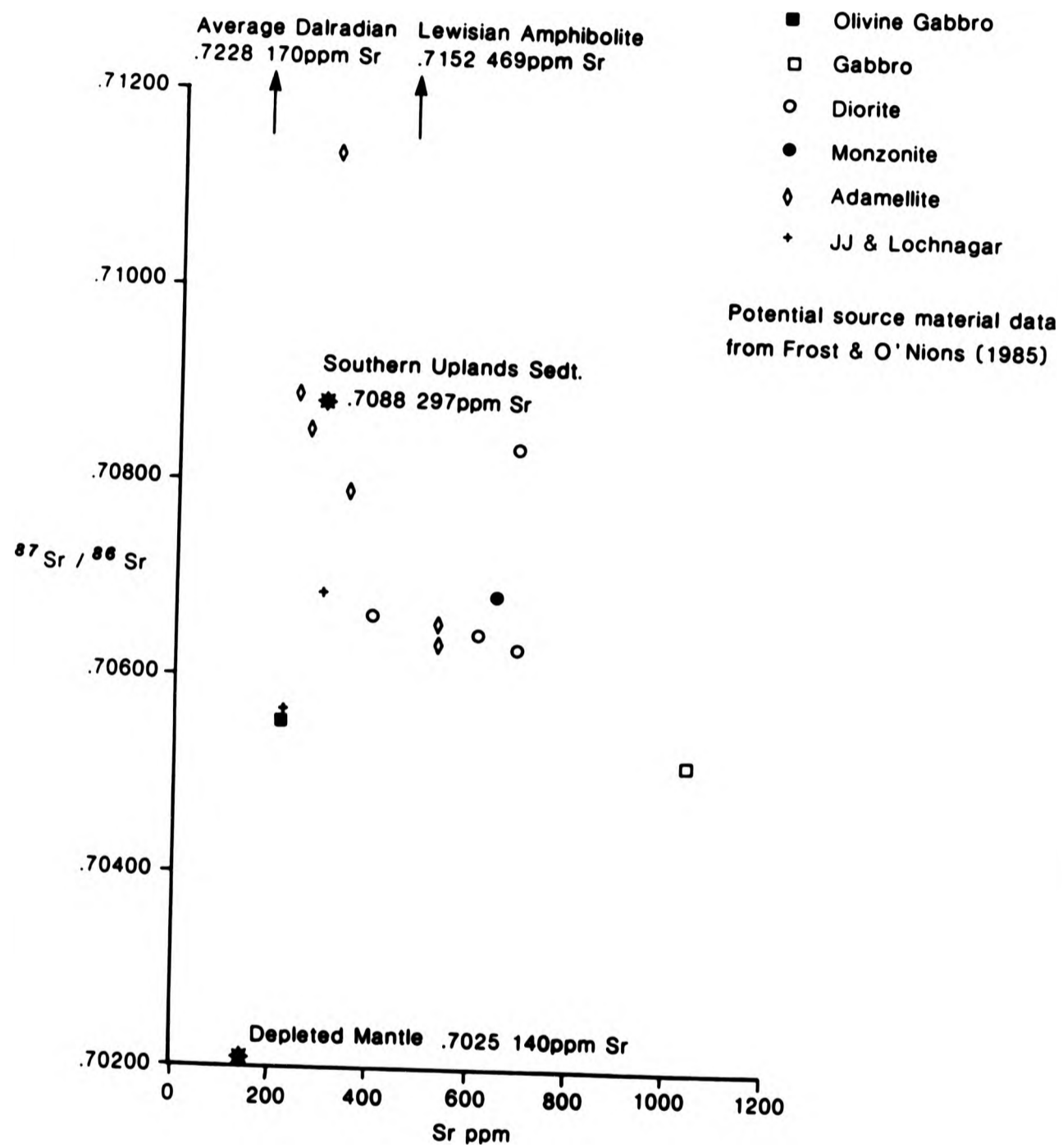
Fig. 7.3 Initial strontium isotope ratio plotted against K/Rb for the Glen Doll & Juan Jorge Complexes



these phases (Chapter 5) and therefore the exact location of the strontium is uncertain. The dioritic rocks similarly contain a high modal proportion of plagioclase and the distribution of strontium may again reflect the abundance of plagioclase. In addition to the analysed data (Figure 7.4) some potential source rocks and contaminants (Frost and O'Nions, 1985) are also plotted. Each is an average value which often represents a wide range of initial ratios e.g. Dalradian rocks range from 0.71577 to 0.72602 and contain 180-516ppm Sr. The effects of the accumulation of plagioclase may therefore mask the contamination with, for example, Dalradian metasediment.

The data show that the gabbros and diorites are isotopically heterogeneous. Therefore if these rocks crystallised from a single parent magma then there is a general increase in the amount of contamination between the crystallisation of the gabbros and the main diorite i.e. progressive contamination of the bulk magma. However the variation between the diorites is very large (Table 7.1) in spite of the four rocks all being derived from magmas at a similar stage of evolution. Visible heterogeneity in the diorites are observed close to partially assimilated Dalradian xenoliths (e.g. drusy cavities). Dalradian metasediments are characterised by relatively high levels of radiogenic strontium (Frost and O'Nions, 1985). It is thought that in the Glen Doll Complex, contamination occurred after the formation of the cumulates thus making interaction of intercumulus melt with fluids from partially assimilated xenoliths possible. It is suggested that an upward flow of fluids occurred through the crystal mush (Sparks et al., 1984) to produce plumes of contaminated fluid above the partially melted xenoliths.

Fig. 7.4 A plot of initial ratio against strontium concentration for the Glen Doll & Juan Jorge Complexes including data for potential source materials



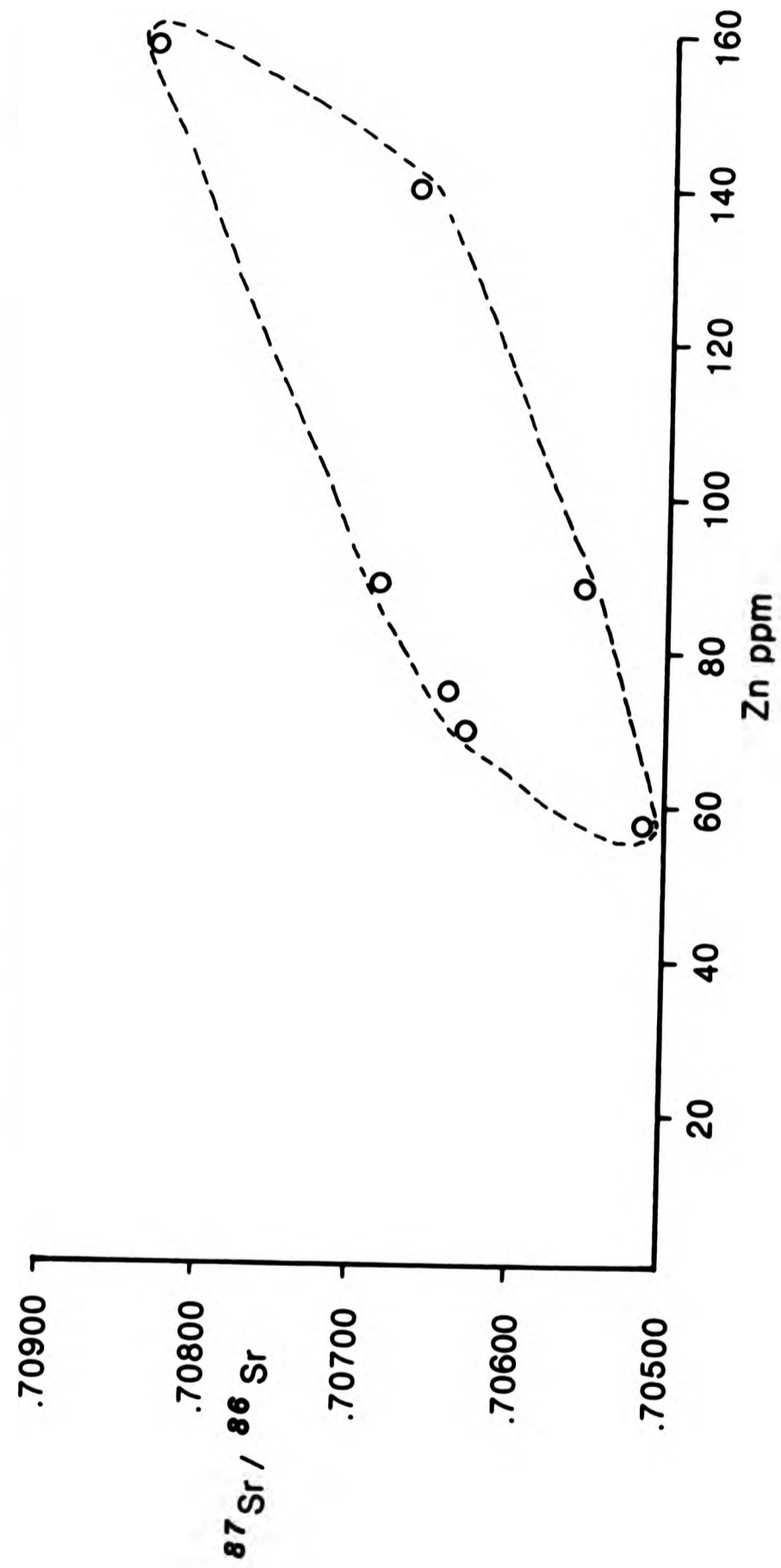
7.2.2.2 Glen Doll adamellites

The adamellites outcrop in an annular form around much of the complex and field evidence has shown that they post-date the intrusion of the dioritic rocks (see Chapter 3). The initial $^{87}\text{Sr}/^{86}\text{Sr}$ ratios are very variable, samples GC117 and GC36 were collected within 100m of each other (Appendix A) and display initial ratios of 0.70887 and 0.70653 respectively. Figures 7.2 and 7.4 display a clear correlation between the initial ratio and both Rb/Sr and Sr (ppm). There is a positive linear increase in Rb/Sr ratio from 0.1431-0.4957 and a decrease in Sr from 537-234ppm with increasing initial ratio.

The variation in initial ratio could indicate two possible modes of evolution for the adamellites. Firstly they may be derived by partial melting of a succession of country rocks with variable initial $^{87}\text{Sr}/^{86}\text{Sr}$ ratios. This process is likely to produce a pseudo-isochron (Figure 7.1). Secondly they may be derived from the lower crust/upper mantle but subsequently modified isotopically, by assimilation of either (a) varying amounts of relatively radiogenic upper crust, or (b) a series of metasediments containing different initial ratios.

Unlike the dioritic and basic rocks, the adamellites display no correlation between initial ratio and zinc concentration, suggesting that the source of contamination was different from the gabbros and diorites, in the more acid rocks in the Glen Doll Complex. A wide variation in initial $^{87}\text{Sr}/^{86}\text{Sr}$ ratios from 0.70887-0.70653 are observed in samples from around Red Craig in the southeastern part of the complex. Abundant metasedimentary

Fig. 7.5
Initial isotope ratio plotted against zinc for the Glen Doll adamellites.



xenoliths occur in the Red Craig area (Chapter 3) but these are sharply bounded and show no evidence of partial melting phenomena. The adamellites also contain rounded micro-granodiorite and micro-diorite inclusions. This suggests the possibility that the present adamellite body could result from partial mixing of diorite and granite magmas with low and high initial $^{87}\text{Sr}/^{86}\text{Sr}$ ratios respectively. Mixing between the two was followed immediately by quenching to prevent chemical and isotopic homogenisation. This evidence suggest that the isotopic heterogeneity is not of local origin, but originated at depth prior to emplacement of the intrusion at its present level. In contrast, the dioritic rocks contain partially digested metasedimentary xenoliths and aggregates of hercynitic spinel (Chapter 4). The xenoliths are thought to have been derived locally, possibly from the roof zone of the complex. The isotopic heterogeneity in the adamellites may therefore be inherited from a different source to that from the diorites and basic rocks.

7.2.2.3 Juan Jorge and Lochnagar samples

The Juan Jorge granite has an initial ratio of 0.70687 which is within the range displayed by the Glen Doll adamellites. The Lochnagar granite has a lower initial ratio of 0.70558 which is similar to that seen in the olivine gabbro in the Glen Doll Complex. Both the Lochnagar and Juan Jorge granites display low initial ratios which suggest a mantle derived parent magma, modified isotopically by interaction with crustal material.

7.3 Suggested further work on strontium isotope systematics

The data presented here has allowed an initial limited

interpretation to be put forward. Further work could firmly establish if the Juan Jorge diorites are isotopically homogenous as their bulk rock chemistry would suggest or if they are heterogenous like the Glen Doll diorites. It has been suggested that the bulk rock contamination with radiogenic strontium might arise from the movement of intercumulus fluid containing chemical components derived from partially assimilated xenoliths. In this case, the cumulate phases (e.g. cpx) may retain primitive Sr isotope ratios while the intercumulus minerals (e.g. hornblende) may reflect the higher contaminated isotope ratio. Thus an isotopic study of the cumulate mineral phases would establish if they are in equilibrium with the interstitial liquids or if isotopic contamination occurred by movement of interstitial fluids. Thirdly, determination of the isotopic systematics of the observed xenoliths (including micro diorite) and Dalradian country rocks, could allow more detailed modelling to be undertaken, particularly with respect to the intermediate and basic rocks.

7.4 Summary

Some general points can be brought out regarding the variation in the initial $^{87}\text{Sr}/^{86}\text{Sr}$ ratios. Firstly there is a very wide range of ratio values within each rock type indicating that the ratios may have been 'acquired' at different times during the evolution of the magma, certainly relatively late with respect to any process of homogenisation. Secondly none of the initial ratios are those of either depleted or of enriched mantle, suggesting that a significant component of the parent magma was derived from a crustal source. Thirdly, the isotopic data suggests (particularly well displayed in Figures 7.2 and 7.4) that the adamellites, diorites and gabbros are clearly separate intrusive phases, a feature which

supports the evidence of both major and trace element data. The adamellites and Juan Jorge rocks are also clearly distinguished on the basis of their initial $^{87}\text{Sr}/^{86}\text{Sr}$ ratios (Figure 7.2) although much of the trace element data suggests that they are closely related.

7.5 A Comparison of data with other late Caledonian complexes

A review of initial ratios and ages for seventeen igneous complexes south of the Great Glen Fault (dominantly granitic and granodioritic members) was presented by Stephens and Halliday (1984). Initial $^{87}\text{Sr}/^{86}\text{Sr}$ ratios range from 0.7035 (Kilmelford) to 0.7109 (Fleet) and ages range from 390Ma (Distinkhorn) to 415Ma (Lochnagar and Foyers).

It is generally accepted that an initial $^{87}\text{Sr}/^{86}\text{Sr}$ ratio (at 400Ma) of 0.7025-0.7045 (Frost and O'Nions, 1985; Thirlwall, 1982) is appropriate for the mantle under Scotland during the late Caledonian. Some of Caledonian granitoids are thought to have crystallised from essentially mantle derived parent magmas which have subsequently been modified (isotopically) by contamination with lower crust e.g. Etive complex (Clayburn et al., 1983).

Most of the strontium isotope data from the late Caledonian, is concentrated on the dominantly granitic complexes, while apart from Garabal Hill, little data is available for the more basic complexes. Early work on the Garabal Hill complex (Summerhayes, 1966) suggested an age of 392Ma, using an isochron based on only three samples from granodiorites and a pyroxene-mica diorite. A range of initial $^{87}\text{Sr}/^{86}\text{Sr}$ ratios were obtained varying from 0.7041-0.7109.

This range of values is similar to that observed in the Glen Doll Complex and covers a similar range of rock types. The highest initial ratios were recorded from a marginal facies of the complex thought to have been contaminated locally. The author concluded that individual members of the complex were derived from a common subcrustal source and that crustal contamination did not play a part in their evolution. More recent work (Halliday, 1984) suggests an age of 406Ma for the Garabal Hill granodiorite and an initial $^{87}\text{Sr}/^{86}\text{Sr}$ ratio of 0.70778 for the uncontaminated rocks.

The large granitic bodies give reasonable isochrons for individual intrusive units e.g. Meall Ohdar, Etive Complex (Clayburn et al., 1983). Isochrons from the Central Starav and Meall Ohdar granites from the Etive Complex, indicate an age of 396 ± 12 and 401 ± 6 Ma respectively and initial $^{87}\text{Sr}/^{86}\text{Sr}$ ratios of 0.7055 and 0.7058 (Clayburn et al., 1983). A combined isotope study (Pb, O and Sr) by Clayburn and co-workers (1983) suggests that the Etive magmas were derived from an homogeneous source but not solely from either the Archaean (Lewisian) or the Proterozoic (Dalradian) upper crust. The authors suggest that the origin of the Etive magmas is best explained in terms of contamination of a mantle derived melt by relatively unradiogenic (low $^{87}\text{Sr}/^{86}\text{Sr}$) middle proterozoic lower crust. By contrast the strontium isotope data from the Glen Doll Complex may best be explained by a mantle derived parent magma (with low initial ratio) contaminated by relatively radiogenic (high initial ratio) middle or upper crust (e.g. Dalradian).

Although locally xenolithic, most of the complexes are essentially homogenous at out crop level, petrographical changes occurring gradually over the whole pluton e.g. Loch Doon (Brown et

al., 1979). The isochrons show that the bodies are isotopically totally homogenous in spite of their petrographic variation. This shows that any contamination or mixing was complete, before crystallisation of the observed rocks occurred.

An initial ratio of 0.705 for the Glen Doll gabbros is comparable with the measured ratios from the Etive Complex (Frost and O'Nions, 1985) and the least radiogenic Garabal Hill data (Summerhayes, 1966) but more radiogenic than depleted mantle (Frost and O'Nions, 1985). Two possible origins exist therefore, for the origin of the gabbroic rocks. They may be the product of a magma derived from a radiogenic source or they may be derived from normal mantle and contaminated en-route to the present level.

Combined Nd-Sr isotope data from the Midland Valley lavas (Thirlwall, 1981) and more recent Pb isotope studies (Thirlwall, 1986) restricts any crustal involvement in the origin of the SW Highlands lavas and suggests that they were derived from the mantle. The primitive Cr and Ni rich basaltic andesites from the Lorne and Ochil series have an initial ratio of <0.706 (Thirlwall, 1986), a comparable value to that recorded from the Glen Doll gabbros and least contaminated diorites. The variation in $^{87}\text{Sr}/^{86}\text{Sr}$ ratio of the lavas from 0.70339-0.70691 is considered by Thirlwall (1982, 1986) to result from the presence of a vertically stratified mantle, formed by interaction of the mantle with subducted oceanic lithosphere.

The $^{87}\text{Sr}/^{86}\text{Sr}$ range of the Glen Doll gabbros and SW Highlands lavas overlap. So, it is possible that the gabbros were derived from magma that suffered very little crustal contamination.

However, the presence of some SW Highlands lavas with initial ratios of 0.704, indicate that liquids are available which would have to assimilate crust in order to achieve the initial ratio of the gabbros.

Some models of evolution of the late Caledonian granite bodies (e.g. Frost and O'Nions, 1985) invoke interaction with lower crust, so this must be considered a possibility for the magmas crystallising the gabbroic rocks from the Glen Doll Complex. A study of other isotope systems in the Glen Doll Complex e.g. Sm/Nd and Pb would test this hypothesis.

The Glen Doll gabbros may therefore have crystallised from a mantle derived magma which has not undergone isotopic contamination from a crustal source. The Glen Doll diorites by comparison, tend to have a higher initial ratio than most of the primitive lavas except for a few examples from the Ayreshire series. This may suggest that the diorites are cumulates of a more acid lava not represented by the bulk of the primitive Midland Valley lavas.

CHAPTER 8

Petrogenesis

8.1 Introduction

As demonstrated in the preceding chapters, the Glen Doll Complex comprises a diverse suite of lithologies from olivine gabbro to adamellite, a range of compositions seen in only a few other late Caledonian complexes in Scotland e.g. Garabal Hill (Nockolds, 1940). The Juan Jorge complex by comparison, has a narrower compositional range than the Glen Doll Complex, typically quartz-mica diorite and granite, a compositional range seen in many other late Caledonian complexes e.g. Ben Nevis (Haslam, 1968). The range of lithologies combined with the lack of any significant alteration, has provided the opportunity for a detailed geochemical study of two relatively small but well exposed complexes of contrasting character.

In this chapter the data and observations from mineral chemistry, bulk rock chemistry and isotope data are integrated with the aim of developing possible models for the evolution of the Glen Doll and Juan Jorge complexes.

The types of numerical modelling presented here fall broadly into three categories

- (a) trace element models involving fractional crystallisation and assimilation
- (b) major element modelling utilising a linear regression computer program
- (c) isotope contamination modelling.

(a) Trace element modelling

Trace element data has been widely used to model the evolution of many volcanic and plutonic complexes (e.g. McCarthy and Hasty, 1976; Allegre and Minster, 1978; Hanson, 1978; Pearce and Norrie, 1979; Tindle and Pearce, 1981). Crystallisation in plutonic complexes such as Glen Doll and Juan Jorge, probably lies between the two end members of equilibrium crystallisation (where the whole of each solid phase is in equilibrium with the host melt) and perfect or Rayleigh fractionation (where only the surface of the crystal is in equilibrium with the melt). A large body of magma cooling relatively slowly may provide sufficient time for equilibrium between a mineral and its host melt. However a processes such as convection may locally prevent a state of equilibrium being attained due to the continual replacement of magma locally. Shaw (1977,1978) showed that Rayleigh and equilibrium crystallisation produce similar trends for small amounts of crystallisation and that it is only for relatively large amounts of crystallisation that the trends produced become significantly different. Various authors (e.g. Tindle and Pearce, 1981) have suggested that surface equilibrium between crystal and melt, is likely to be a better assumption than total equilibrium particularly in cumulate rocks, since the composition of the intercumulus melt may change rapidly. Trace element models in this thesis therefore assume Rayleigh type fractionation.

Mineral analyses from the Glen Doll and Juan Jorge Complexes given in Chapter 5, were carried out using an electron microprobe. Trace element data is therefore not generally available for the phases analysed. Partition coefficients for a range of elements have therefore been compiled from the available literature (Table

TABLE 8.1 Partition coefficients used in trace element modelling

Glen Doll Complex

Basic and intermediate rocks

	Rb	Ba	Cr	Ni	Y	Ce	Yb
Plagioclase	0.03	0.15	0.001	0.04	0.03	0.24	0.077
Amphibole	0.30	0.40	12.000	3.00	-	0.30	0.050
Clinopyroxene	0.002	0.001	3.000	3.00	0.50	0.33	1.100
Orthopyroxene	0.0006	0.001	5.00	63.00	-	0.087	0.600
Olivine	-	-	1.00	14.00	-	0.007	0.014
Spinel	-	0.001	200.00	12.00	0.20	-	-
Biotite	3.1	5.6	-	-	1.30	-	-
Apatite	-	0.001	-	-	25.00	25.00	25.00
Sphene	-	-	-	-	-	80.00	60.00
Zircon	-	-	-	-	-	3.00	25.00

Adamellites

	Ba	Rb	Sr	Ce	Yb	Sc
Plagioclase	0.30	0.04	4.40	-	-	0.06
Biotite	10.00	2.00	0.08	-	-	5.00
K-feldspar	6.00	0.40	4.00	-	-	0.02
Amphibole	0.04	0.01	0.02	-	-	40.00
Apatite	-	-	-	25.00	25.00	-
Sphene	-	-	-	80.00	60.00	-
Zircon	-	-	-	3.00	250.00	-
Spinel	-	-	-	-	-	1.50

Juan Jorge Complex

All rock types

	Ba	La	Rb	Cr	Ni
Plagioclase	1.52	0.38	0.04	0.01	0.01
Biotite	5.60	1.28	3.10	7.00	3.50
Amphibole	0.04	1.50	0.30	12.00	3.00
Spinel	0.001	0.08	-	200.00	12.00
K-feldspar	6.00	0.04	0.40	-	-

Apatite, sphene and zircon as for adamellites

Sources: Baxter et al., 1985; Cox et al., 1979; Nash and Creecraft, 1985; All Ce and Yb data from Tindle and Pearce, 1981.

8.1). The data from Nash and Crecraft (1985) is derived from experimental studies of natural granitic rocks. Other partition coefficient data are taken from compilations for basic rocks (Baxter et al., 1985) and acid to basic rocks (Cox et al., 1979). The partition coefficients for La in amphibole, spinel and K-feldspar are assigned the same value as Ce (Data from Cox et al., 1979) since the two elements frequently exhibit similar behaviour.

Trace element modelling equations

Two equations describe the simplest extremes of trace element behaviour during crystallisation:-

(i) $C_1 = C_0 F^{(D-1)}$ Rayleigh fractionation

(ii) $C_1/C_0 = 1/F + D(1-F)$ Equilibrium crystallisation

Where C_0 = concentration of the element in the original liquid
 C_1 = concentration of the element in the residual liquid
 F = weight fraction of liquid remaining
 D = bulk distribution coefficient

A third equation which is particularly relevant to the Glen Doll Complex, describes the effects of assimilation coupled with fractional crystallisation (Depaolo, 1981):-

(iii) $C_m/C_m^0 = 1 + MaCa/MmC_m^0$

where C_m^0 = concentration of the element in the original liquid
 C_m = concentration of the element in the residual liquid
 Ma = mass of wall rock
 Mm = mass of magma
 Ca = concentration of the element in the wall rock

Equation 3, is the simplest proposed by De Paolo (1981), where the mass of wall rock assimilated is equivalent to the mass of crystals fractionated. The bulk distribution coefficient is arbitrarily set to be the same for both the assimilant and fractionated assemblage. In the models presented below, M_a is calculated as a continually variable percentage of the total mass of magma. M_m was arbitrarily calculated assuming a magma chamber of 1Km height across an area of 3x4km i.e. a mass of $3.09 \times 10^7 \text{ m}^3$.

Trace element pairs have been chosen, which as far as possible discriminate between the major and minor crystallising phases including olivine, orthopyroxene, clinopyroxene, amphibole, biotite, plagioclase, spinel, K-feldspar, apatite and sphene. The availability of appropriate partition coefficient data has further restricted the choice of trace elements used in the modelling program.

(b) Major element modelling

To constrain and complement trace element models, major element data has been empirically modelled using linear regression equations. This mathematical modelling technique has been included in a fortran computer program (Banks, 1979) to allow the rapid and easy handling of data. The programming techniques are given in full in Banks (1979). Linear regression equations can be used to model the change from composition A to B by the addition of C, for example. This technique can be applied to geological modelling of major element rock and mineral data where A=parent, B=daughter and C= composition of minerals added to, or removed from the parent to give the daughter composition. By the use of these linear regression equations in a computer program, the amount of each mineral

can be continually varied until the smallest difference between A and B+C is achieved. This difference is calculated for each oxide and the sum of the differences is termed a one-norm misfit. The degree of misfit can be used to assess the quality of the solution. Data from Wright and Doherty (1970) and Banks (1979) suggest that a one-norm misfit of less than twelve is likely to produce a statistically valid solution. It is particularly important to consider carefully the petrological constraints on the solutions given by this modelling technique since it is an empirical approach. Used in conjunction with observed mineralogy and other modelling techniques, the least squares program provides an additional tool with which to investigate the evolution of an igneous complex.

(c) Isotope modelling

Data presented in Chapter 7 suggests that a single source is inappropriate for the range of rock types displayed in the Glen Doll Complex. A modified Rayleigh type fractionation model (De Paolo, 1981) can be used to evaluate the extent of contamination of, for example, a mantle derived melt contaminated with crustal material. The equation used (section 8.5.1.4) allows isotope ratios rather than concentrations to be modelled, and the resultant vectors are therefore curved rather than linear. Combining this type of model with the Rayleigh fractionation model allows (section 8.1) the effect of assimilation to be assessed. Isotope modelling has been applied only to the Glen Doll Complex, since insufficient data is currently available for the Juan Jorge Complex.

8.2 Parental liquids and starting compositions

8.2.1 Glen Doll Complex

Two approaches to modelling, whether using major or trace elements, can be taken. The first is to model only the observed trend i.e. that displayed by the analysed samples. The data trend may be linear, such as that displayed by the Juan Jorge rocks and the Glen Doll adamellites for many trace and major elements. A model can then be proposed which allows the derivation, by some geological process such as crystal fractionation, of one observed composition from another.

The second approach is to choose a parental liquid composition, which may or may not lie directly on the observed trend, and to model the evolution of that composition towards the observed data. For example, the parent liquid composition of a series of cumulate rocks may not lie within the range of compositions represented by those rocks. In this case it is necessary to decide on an appropriate parent using available petrographic and geochemical data. The parental composition may not actually be represented by any of the analysed samples from the complex under study. Possible parental liquids may, for example, be represented in a coeval lava suite.

Any parent liquid chosen for the Glen Doll complex must be capable of generating the range of observed rock types. The most mafic rocks recorded are the olivine gabbros which contain 21-25% MgO. Clearly, therefore, evolved compositions occurring within the complex, such as adamellite are not possible candidates but andesitic or basaltic compositions may well be suitable.

Experimental work has shown that the molecular ratio of FeO to MgO in olivine is directly related to the molecular ratio of FeO to MgO in the liquid from which it crystallised (Roeder and Emslie, 1970). A number of experiments were carried out by the above authors over a range of temperatures (1150-1300e) and oxygen fugacities ($10^{-0.68}$ - 10^{-12} atmospheres) to study the equilibria between olivine and basaltic liquids to try and understand the conditions under which olivine can crystallise. The FeO to MgO molecular ratios were measured in liquids and co-existing olivines. A plot of the FeO to MgO ratio in the olivine versus the same ratio in the liquid, reveals a linear relationship between the two parameters, the slope of the line being equal to a distribution coefficient (K_D) of 0.3 (Roeder and Emslie, 1970). Therefore if the molecular FeO to MgO ratio of the olivine is known, the FeO to MgO ratio of the liquid from which it crystallised can be calculated.

The forsterite content of olivine from the Glen Doll olivine gabbros varies from Fo₇₈₋₈₁ (Molecular ratio FeO to MgO=0.273-0.226). Using data from Roeder and Emslie (1970, Figure 4) it has been calculated that these compositions would have crystallised from a liquid with a molecular FeO to MgO ratio between 0.91-0.75. Therefore a parent liquid (at least for the olivine bearing rocks) must have a molecular FeO to MgO ratio of between 0.91 and 0.75. If the diorites and gabbros are derived from the same parent, then the criteria used to select the composition of that parent must take into account the FeO to MgO ratio needed to crystallise olivine of the observed compositions.

The relative merits of various lithological compositions occurring within the Complex, as potential parental magmas, are

assessed below. The lithologies considered from the Glen Doll Complex are (a) olivine gabbro (b) gabbro (c) diorite (d) microdiorite: dyke (e) microdiorite: xenolith.

(a) Olivine gabbros

The olivine gabbros display petrographic features typical of cumulate rocks (see Chapter 4). They contain a high proportion of modal olivine (<45%) and pyroxene primocrysts which together form a cumulate framework. The olivine gabbros display relatively primitive chemistry, with MgO (>21%), Cr (>800ppm) and Ni (>200ppm), levels similar to those recorded from the Lorne Lavas (Thirlwall, 1982). High chromium and nickel levels are thought by some authors e.g. Thirlwall (1982) to characterise mantle derived liquids. However the bulk molecular FeO to MgO ratio of the Glen Doll olivine gabbros is typically 0.24. This low ratio coupled with cumulate textures in the olivine gabbros precludes their use as parental liquids.

(b) Gabbro

Petrographic data outlined in Chapter 4, suggests that many of the gabbros are either plagioclase or pyroxene orthocumulates and therefore unlikely to represent liquid compositions. They contain relatively high magnesia ranging from 6-10% MgO but low levels of *FeO, TiO₂, MnO, Cr and Ni (see Table 6.1). Consequently the gabbros have a low molecular FeO to MgO ratio of ca. 0.34. The gabbros are, therefore unlikely to represent liquid compositions and are not considered to be likely parental magmas.

Table 8.2 Parental compositions used to model the evolution of the Glen Doll and Juan Jorge Complexes.

	Diorites		Xenolith	Lorne Lavas ^a	
	GC120	GC169	GC138	L44	L73
SiO ₂	58.80	48.00	54.20	55.33	50.92
TiO ₂	2.31	2.22	1.29	1.43	1.59
Al ₂ O ₃	14.30	16.26	12.60	16.21	17.55
*FeO	9.00	9.82	10.35	8.64	8.54
MgO	5.42	5.84	8.07	5.63	4.77
MnO	0.16	0.16	0.24	0.08	0.11
CaO	4.66	10.95	10.50	5.74	10.35
Na ₂ O	2.48	2.23	1.60	3.43	3.56
K ₂ O	1.48	0.47	0.31	1.71	1.24
P ₂ O ₅	0.46	0.46	0.15	0.37	0.39
Ba	295	148	109	773	582
Cr	170	174	230	339	330
Cu	94	45	60	114	58
Li	38	10	14	ND	ND
Ni	109	108	128	181	153
Rb	56	15	16	33	18
Sc	22	30	46	24	35
Sr	461	718	317	727	888
V	201	205	392	176	201
Zn	83	108	126	77	82
Zr	193	78	117	205	203
La				25.90	26.80
Ce				60.10	59.40
Pr	No REE data available			ND	ND
Nd	for these samples			27.50	30.50
Sm				5.37	6.05
Eu				1.58	1.91
Gd				4.64	5.37
Dy				ND	4.52
Ho				ND	ND
Er				1.95	2.46
Yb				1.68	2.19
Lu				ND	ND
Y	37	18	26	20	26

Note;

^a Basaltic andesites from the Lorne Plateau, data from Thirlwall, 1982

(c) Diorites

This lithology displays a range of chemical compositions. Some features of the chemistry correlate with the abundance of plagioclase primocrysts (in some samples up to 60%) or Fe-oxide primocrysts (Chapter 6). Some of the diorites contain high zinc levels indicating that they may have undergone contamination by crustal material (Chapter 6).

Many of the diorites are therefore unlikely to represent liquid compositions. However, two samples of hornblende diorite and pyroxene diorite do display relatively primitive chemical features. The first, GC 120, contains 5.42% MgO with a molecular FeO to MgO ratio of 0.93 (Table 8.2). This sample also has high Cr (170ppm) and Ni (109ppm) levels with respect to the other diorites in the Glen Doll Complex. The second, GC 169, contains 5.84% MgO with a molecular FeO:MgO ratio of 0.94 and similarly contains high levels of Cr (174ppm) and Ni (108ppm). These two diorites from the Glen Doll Complex therefore display comparable chemical features to many of the primitive andesitic lavas described from the Lorne Plateau (Section 6.3.9 and 6.6.6). These lavas are thought to represent relatively undifferentiated mantle derived liquids (Thirlwall, 1982). The range of compositions displayed by the Lorne andesites are shown in Figure 8.1. The fields defined by the Glen Doll gabbros, diorites and adamellites are shown for comparison. The lavas lie on a liquid line of descent, the slight scatter of data being due to varying amounts (<20%) of plagioclase, pyroxene and olivine phenocrysts (Thirlwall, 1979). The two samples of Glen Doll diorite, GC120 and GC169, lie close to the lava trend. The Glen Doll gabbros are generally depleted in the elements shown

on Figure 8.1 when compared with the Lorne Lavas, since elements such as titanium, phosphorus and potassium are depleted in the cumulus minerals. In contrast the dioritic rocks are typically enriched in, for example, iron and titanium since they contain cumulate magnetite and ilmenite. Some of the dioritic rocks contain cumulus apatite (those with higher P_2O_5 levels than the lavas) while others contain a similar level to the gabbros and therefore lie below the lava trend. The petrography and lack of any cumulate texture combined with the above chemical data suggests that the two diorite samples may represent liquid compositions. The molecular FeO to MgO ratio of either sample would allow the crystallisation of olivine with a composition of Fo₇₈₋₈₁.

(d) Microdiorite: dyke

The microdiorite dykes are considered in this discussion of possible parental liquids since they are fine-grained and in some cases, aphyric. They could therefore represent liquid compositions. The microdiorite dykes display a range of chemical compositions but typically contain 4.5-5.5% MgO. One particular example, GC145, from the western part of the Glen Doll Complex is aphyric, contains 5.33% MgO and has an FeO to MgO molecular ratio of 0.78. A liquid of this composition could crystallise olivine within the range Fo₇₈₋₈₁. However all of the microdiorite dykes contain low levels of chromium (<70ppm) and nickel (<40ppm) and typically 2-3% K₂O, chemical features which indicate that they have undergone fractional crystallisation and are unlikely to represent unmodified liquids.

(e) Microdiorite: xenolith

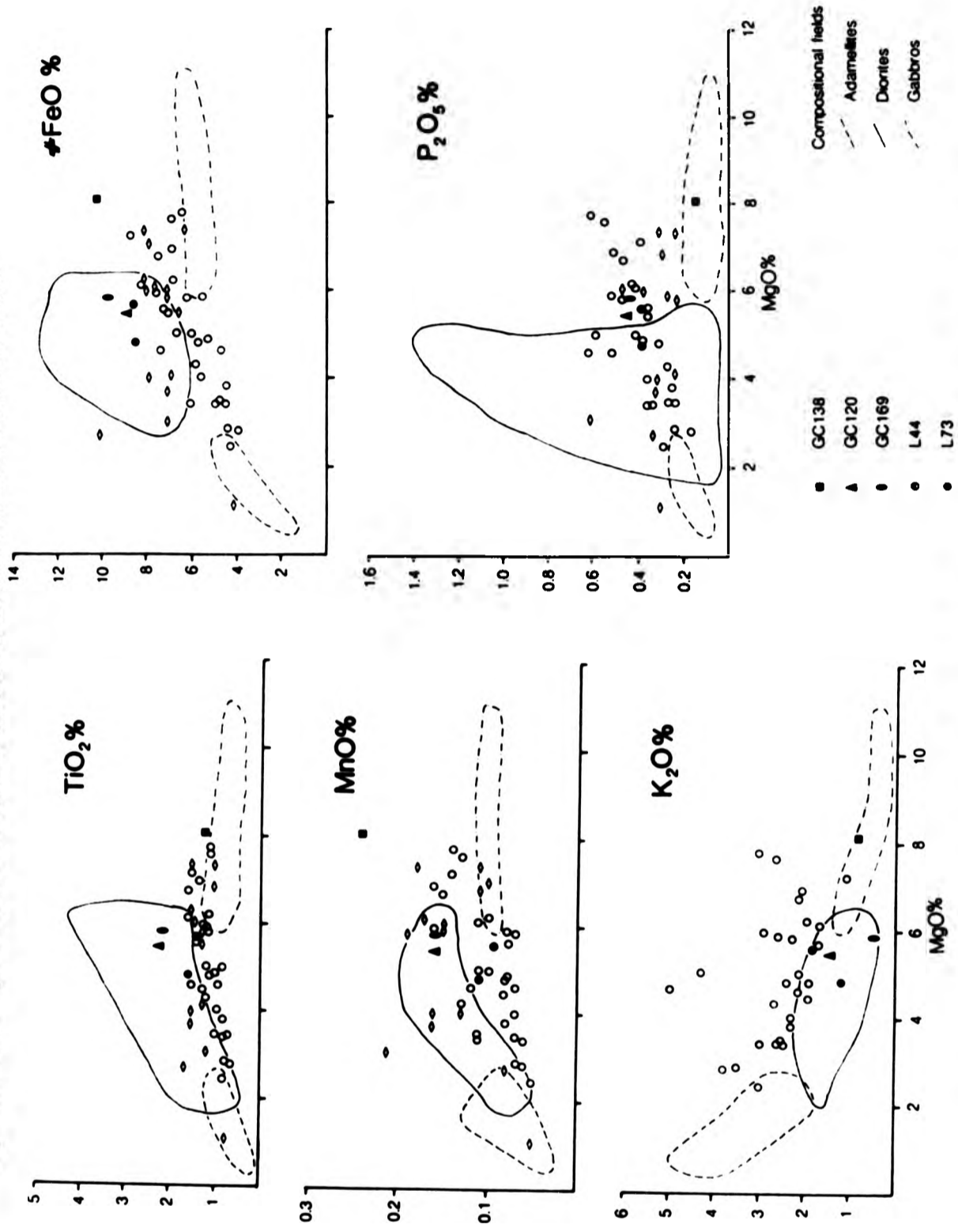
These xenoliths are found throughout the dioritic rocks of the complex, but occur most commonly in the River White Water (Figure 3.1). They are fine grained and may represent early chilled material, stoped from the margins of the complex. A typical example (GC 138) is relatively mafic (8.07% MgO) with a mol FeO:MgO ratio of 0.72 (Table 8.2). This particular sample has relatively primitive trace element chemistry and contains 128ppm Ni and 230ppm Cr. The other analysed samples however typically contain from 13-38ppm Ni and 30-260ppm Cr. The microdiorite dykes plot on the liquid line of descent, defined by the calc-alkaline lavas, on an AFM diagram (Figure 6.1). The composition of GC138 and may therefore represent a possible parent liquid from which the basic and intermediate rocks of the complex could be derived.

8.2.2 Juan Jorge Complex

The range of lithologies in the Juan Jorge Complex is more restricted than in the Glen Doll Complex, ranging from hornblende diorite and quartz mica diorite to granite. The most mafic diorite contains only 3.86% MgO and is unlikely, therefore, to represent a primitive liquid composition. None of the rock types within the Juan Jorge Complex contain either olivine or pyroxene.

Micro diorite xenoliths are common in the quartz mica diorite. They are fine grained, porphyritic and occasionally contain quartz xenocrysts (indicating that they may be of an hybrid origin). They typically contain only 3% MgO and have low Cr (22ppm) and Ni (24ppm) concentrations. This combined evidence suggests that the micro diorite xenoliths are unlikely to represent a single liquid composition.

Fig. 8.1 Geochemistry of the Lorne and Sidlaw lavas with fields for the plutonic rocks from the Glen Doll Complex.



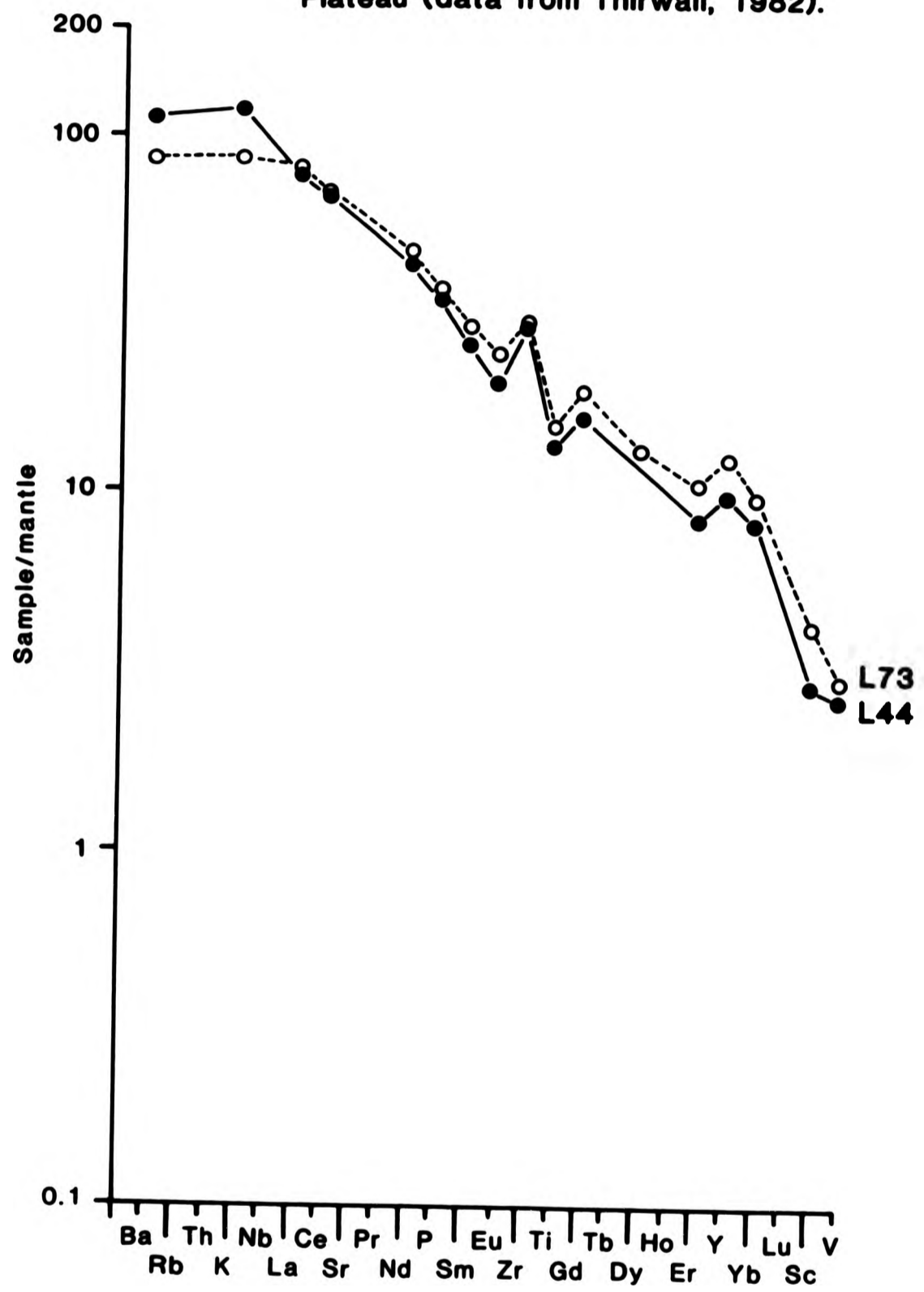
Since the Glen Doll and Juan Jorge Complexes are spatially related, the parental liquid compositions used to model the evolution of the former will also be used for the Juan Jorge Complex.

8.3 Other liquid compositions

With only a restricted choice of possible parental liquid compositions available from within the Glen Doll complex, it is necessary to consider 'external' candidates i.e. possible liquid compositions from other calc-alkaline volcanic or plutonic complexes. General geological and geochemical studies by Thirlwall (1979) suggest that the calc-alkaline Lorne lava series are closely related to the late Caledonian plutonic complexes. Many of the lavas, are basaltic andesites, which exhibit relatively primitive chemistry and are considered to represent mantle derived magmas, which have undergone <20% fractional crystallisation (Thirlwall, 1982, 1986). Some of the lavas contain pseudomorphed olivine phenocrysts of unknown composition (Thirlwall, 1981). However the molecular FeO to MgO ratio calculated for a number of the high Cr and Ni lavas from the Lorne suite, suggest that only a few would be capable of crystallising olivine with a composition Fo₇₈₋₈₁. Two lavas, for which chemical analyses are given in Thirlwall (1982) would be appropriate compositions to use as parental liquids for the Glen Doll and Juan Jorge Complexes. Samples L44 and L73 have molecular FeO to MgO ratios of 0.86 and 1.01 respectively and both contain >100ppm Ni and >150ppm Cr (Table 8.2).

A summary of some of the trace element characteristics of the Lorne Lava suite are presented in the form of an incompatible element mantle normalised diagram (Figure 8.1). In this, the abundance of each element is normalised against that of an estimat-

Fig. 8.2 Incompatible element mantle-normalised diagram for two basaltic andesites from the Lorne Plateau (data from Thirwall, 1982).



ed average mantle and the resulting values for each element are plotted in order of increasing field strength. The consequential patterns highlight elemental depletions and enrichment due to a variety of fractionation processes. A series of related rocks resulting from fractional crystallisation of a single liquid may display an increase in the slope of the profile with evolution.

Figure 8.2 displays the mantle normalised data for the two Lorne Lava samples considered above. The profiles are steep and generally smooth, with only minor anomalies for Zr, Ti and Y. A smooth profile may reflect the limited operation of a process such as crystal accumulation, while a jagged profile may result due to crystal accumulation for example. The two samples of basaltic andesite from the Lorne Lava series display features of primitive relatively undifferentiated liquids. These liquid compositions would be capable of crystallising olivine with a composition similar to that observed in the Glen Doll olivine gabbros.

Major and trace element models have been attempted using the parental compositions listed in Table 8.2.

8.4 Isotope modelling

The importance of isotopic variation in petrogenetic studies is that they are frequently insensitive to the chemical fractionation which accompanies the formation and evolution of magmas. They may therefore often be used as geochemical tracers of magma origins even where other trace element concentrations and ratios have been extensively modified. However, in the Glen Doll Complex, strontium isotope data places constraints on the origin of any parent liquid or liquids. The range of strontium isotope ratios recorded in the

Glen Doll complex suggests that extensive contamination of a mantle derived magma by crustal material may have taken place (Chapter 7).

The possible crustal sources of contamination within the Glen Doll Complex are Dalradian and Lewisian metasediment or Palaeozoic sediments. Each source of contamination is discussed below.

(a) Dalradian

The Glen Doll dioritic rocks contain abundant partially digested metasedimentary Dalradian xenoliths and these thus provide a identifiable source of possible contamination within the complex. However there is no strontium isotope data available for either the Dalradian xenoliths or the country rocks from the Glen Doll complex. In the Etive Complex, which is located in a similar tectonic setting to the Glen Doll Complex, binary mixing calculations indicate that up to 25% of the contaminated quartz diorite strontium, may be derived from Dalradian metasediments (Frost and O'Nions, 1985). The authors state that "it is reasonable to assume that marginal assimilation of country rocks occurred not only at shallow levels, where Dalradian rocks are present, but throughout the ascent of the Etive magma through the crust. However, only where the xenoliths of assimilate are preserved, as with the Dalradian, can this effect be quantified". Strontium isotope data from the Dalradian rocks of the Etive Complex has been used to model the evolution of the Glen Doll Complex.

(b) Lewisian

It has been suggested by various authors that much of northern Britain is underlain by Lewisian amphibolites and granulites with

inliers of Lewisian-like rock occurring as far south as Islay (Frost and O' Nions, 1985; Brown and Locke, 1979). Accordingly Lewisian amphibolite gneisses are considered as possible contributors to Caledonian granites lying both north and south of the Great Glen Fault (Frost and O' Nions, 1985). The effect on the $^{87}\text{Sr}/^{86}\text{Sr}$ ratio of a mantle-derived liquid by contamination with Lewisian amphibolite has been modelled for the Glen Doll Complex.

(c) Palaeozoic sediment

Southern Uplands type Palaeozoic sediment has figured prominently as a source component in some models of Caledonian granite provenance (Harmon and Halliday, 1980; Pidgeon and Aftalion, 1978). Ordovician and Silurian rocks of the Southern Uplands are considered to form a sedimentary prism accreted against the northwest margin of the Iapetus Ocean. As subducting crust, the Palaeozoic sediments may provide an important input of crustal material into the upper mantle reservoir.

Thus Dalradian metasediments, Lewisian amphibolite and conceivably, Palaeozoic sediments are all possible candidates for the basement rocks of the Glen Doll Complex. The average $^{87}\text{Sr}/^{86}\text{Sr}$ values for each of these potential 'reservoirs' are given in Table 8.3. These values have been used to evaluate the possible contribution of crustal material to a mantle derived parent magma required to give rise to the observed $^{87}\text{Sr}/^{86}\text{Sr}$ ratios in the Glen Doll complex.

8.5 Modelling

8.5.1 Glen Doll complex

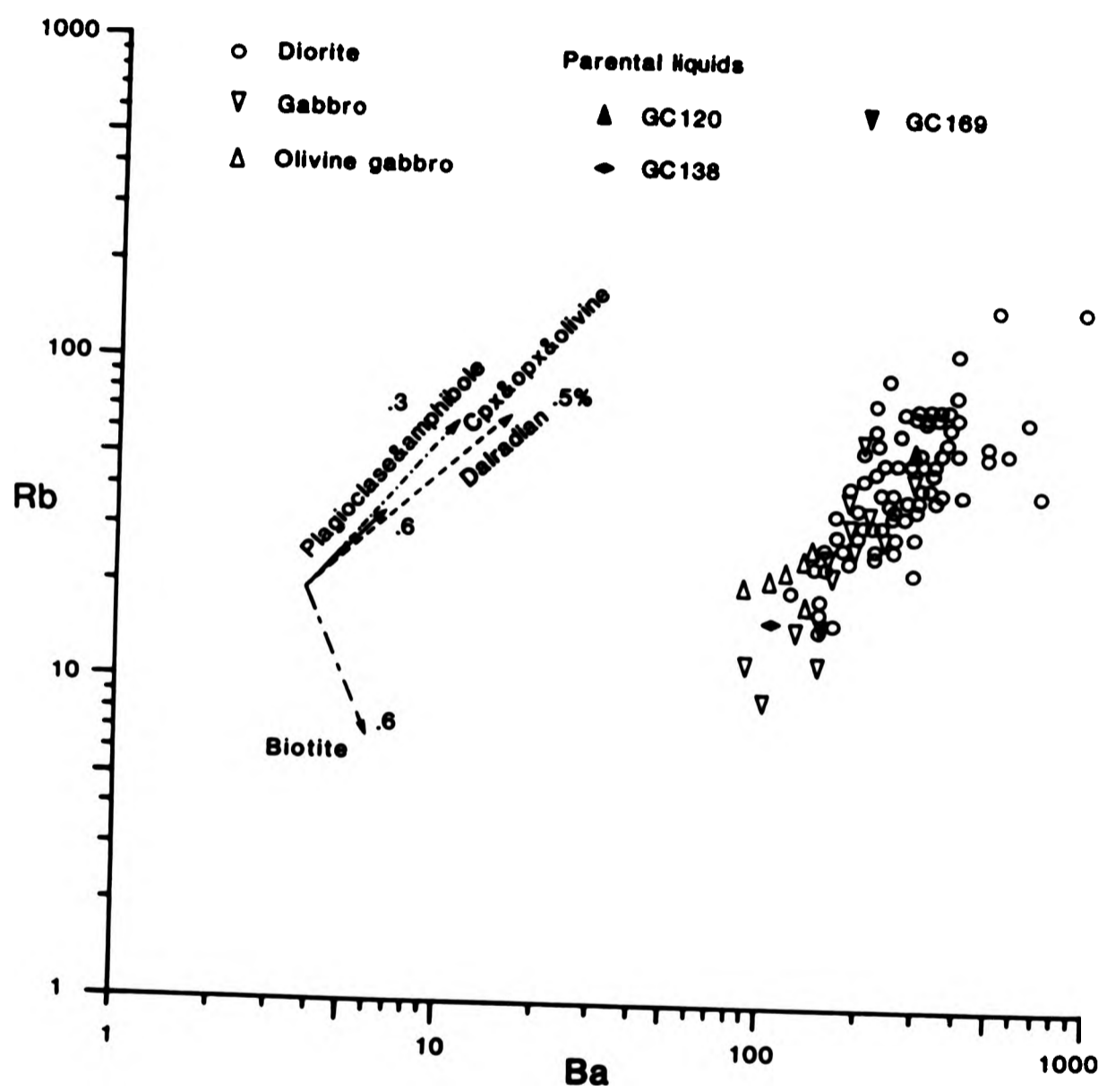
The objective of this section is to develop a petrogenetic model for the Glen Doll Complex. Any model for the crystallisation of the pluton must take into account several factors:-

- (a) the observed mineralogical and geochemical patterns
- (b) the general absence of any intrusive contact between the basic and intermediate rocks.
- (c) the presence of a sharp intrusive contact between the adamellite margin and the dioritic rocks.
- (d) the observed assimilation of country rocks.

The major, trace and isotope modelling programmes have been divided into sections. The first section attempts to model the evolution of the olivine gabbros, gabbros and dioritic rocks since on field, petrographic and chemical criteria these three lithologies appear to be closely related. The second section attempts to model the evolution of the adamellites, which form a separate intrusion around the margin of the complex. A range of trace element pairs have been used to determine the effects of major and minor phase crystallisation within each rock group and comparison is made with the observed mineralogy. The possible effects of contamination by Dalradian metasediments are also examined. Major elements have been used to constrain the crystallising proportions of each mineral phase and to further evaluate the process of contamination. Strontium isotopes are used to examine the early evolutionary history of the complex and to constrain the isotopic composition of the contaminant crust.

8.5.1.1 Trace element modelling for the olivine gabbros, gabbros and diorites

Fig. 8.3 Logarithmic, bivariate plot of Rb-Ba for the Glen Doll intermediate and basic rocks.



The major and trace element data presented in Chapter 6, shows that the diorites characteristically display little inter-element correlation, while the gabbroic rocks display more coherent trends. Figures 8.3-8.6 display geochemical data for a wide range of trace element pairs. The bivariate plots display some common characteristics, while other features are only shown by particular trace element pairs. In each figure the vectors give liquid compositions after specific amounts of fractional crystallisation or contamination. The percentage of Dalradian metasediment assumes a magma chamber of $3.096 \times 10^7 \text{ m}^3$ volume (see section 8.1). The mineral vectors are displayed on each diagram. Since the mineral trends are vectors, any change in starting composition simply translates their initial position, while the direction and length of the vectors remains constant. The range of possible starting compositions are indicated on each diagram.

(a) Bivariate plot of Rb and Ba (Figure 8.3)

The basic rocks display an increase in Rb with increasing Ba. The dioritic rocks, by contrast, are scattered and overlap the more basic compositions. Crystallisation of amphibole, plagioclase, opx, cpx and olivine could produce a series of liquids containing increasing amounts of rubidium and barium. This diagram can not adequately discriminate between opx, cpx and olivine crystallisation since the partition coefficients for rubidium and barium in these mineral phases are very similar (Table 8.1). If biotite also crystallised, the liquid composition would be progressively depleted in rubidium (due to preferential entry of Rb into K sites in biotite (Mason, 1966)) while barium becomes enriched. Crystallisation of biotite in the more evolved rocks could account for the scatter of data observed in those diorites containing the

highest levels of rubidium and barium.

The data therefore suggests the initial crystallisation of plagioclase, amphibole \pm cpx, opx and olivine accompanied during the later stages of crystallisation by biotite. However it is notable that more than 70% crystallisation is needed to generate those compositions with $<50\text{ppm}$ Rb and $<300\text{ppm}$ Ba. If a large amount of crystallisation were required to generate only a part of the data trend than the remaining, more evolved compositions should represent residual liquids which they clearly do not. If an open system is assumed, and continuous replenishment of magma with a similar composition takes place, then the amount of crystallisation required to generate the observed trends is reduced.

Contamination

The effect of contamination with two different Dalradian lithologies is considered. The first is a semipelite (Gc68) from the area south of the Glen Doll Complex which is representative of the lithology into which the complex is intruded. The second is an Appin slate taken from Hickman and Wright, (1983) which may represent an underlying lithology in the Glen Doll area. Although compositionally different, the direction of the calculated vectors in each case is similar and falls within the range of observed dioritic compositions (only GC68 is shown on Figure 8.3 for clarity). The levels of rubidium and barium are therefore relatively insensitive to the assimilation of these two different metasedimentary lithologies. Modelling of rubidium and barium data suggests that crystallisation of amphibole, plagioclase and biotite \pm olivine, opx and cpx could generate the range of dioritic compositions. The effects of contamination are not adequately separated from the effect of fractional crystallisation in this

Fig. 8.4
Logarithmic, bivariate plot of Cr-Ni for the Glen Doll intermediate and basic rocks.

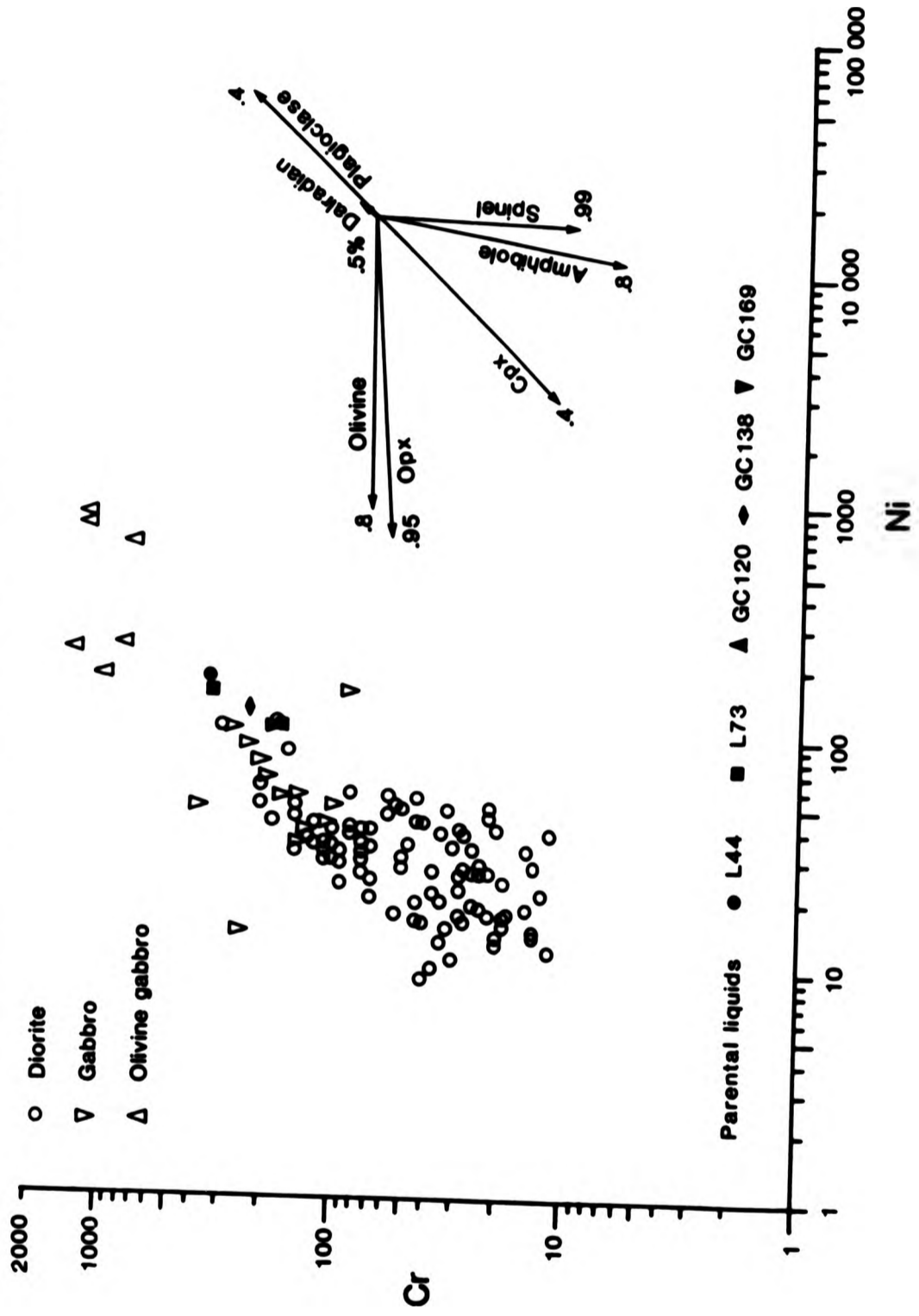


diagram.

(b) Bivariate plot of Cr and Ni (Figure 8.4)

The distribution of Cr and Ni displayed by the olivine gabbros in Figure 8.4, is thought to reflect the variable abundance of cumulate olivine and opx ± amphibole (see Chapter 6). The diorites and gabbros in contrast display a broad increase in Cr levels with increasing Ni content consistent with pyroxene fractionation. The calculated mineral vectors suggest that crystallisation of cpx, spinel, amphibole and opx would drive the liquid composition towards the low Cr and Ni diorites while crystallisation of plagioclase results in an opposing vector. Crystallisation and accumulation of relatively small amounts of olivine, opx and amphibole allows the broad scatter of data points for the olivine gabbros to develop.

Also displayed on this figure is the path of crystallisation for a liquid assimilating the locally present Dalradian metasediment (GC68). Even relatively large amounts of assimilation produce only a small movement in the liquid composition from the original starting point. The effects of assimilation are therefore masked by the effects of fractional crystallisation and accumulation on this diagram.

This diagram (Figure 8.4) allows discrimination to be made between accumulation of olivine, opx and amphibole in the olivine gabbros and suggests that accumulation of plagioclase is important in controlling the evolution of the dioritic rocks. The effects of assimilation of metasediment are masked because the metasediment

contains only low levels of chromium and nickel.

(c) Bivariate plot of Y and Ba (Figure 8.5)

Figure 8.5 displays a characteristic scatter of data for the diorites and rather less scatter for the basic rocks. The crystallisation of plagioclase, spinel, cpx and opx, generate a series of liquids which contain increasing levels of yttrium for only a small increase in barium concentration. Crystallisation of apatite (<1%) produces a range of liquid compositions with decreasing yttrium and constant barium levels. The vertical distribution of data can therefore be explained in terms of crystallisation and accumulation of the above modelled mineral phases. However many of the diorites contain a high concentration of barium (500-900ppm) with no corresponding increase for yttrium. The crystallisation of biotite produces a series of liquids with decreasing barium and yttrium concentrations while accumulation of biotite would produce a series of compositions enriched in barium. Some of the barium rich diorites (~500ppm Ba) are biotite cumulate enriched. However, assimilation by the dioritic rocks of Dalradian metasediment (GC68), which contains a relatively high level of barium (>500ppm), could partly control the horizontal scatter of data seen in Figure 8.5. Bulk rock trace element chemistry (Chapter 6), field and petrographic data suggest that the dioritic rocks have assimilated metasediment enriched in zinc. Zinc mineralisation in the Middle Dalradian commonly occurs in association with baryte deposits (Coats et al., 1980). The high levels of barium in some of the diorites may therefore reflect the assimilation of zinc and barium rich metasediments.

(d) Bivariate plot of Ce and Yb (Figure 8.6)

Fig. 8.5 Logarithmic, bivariate plot of Y-Ba for the Glen Doll intermediate and basic rocks.

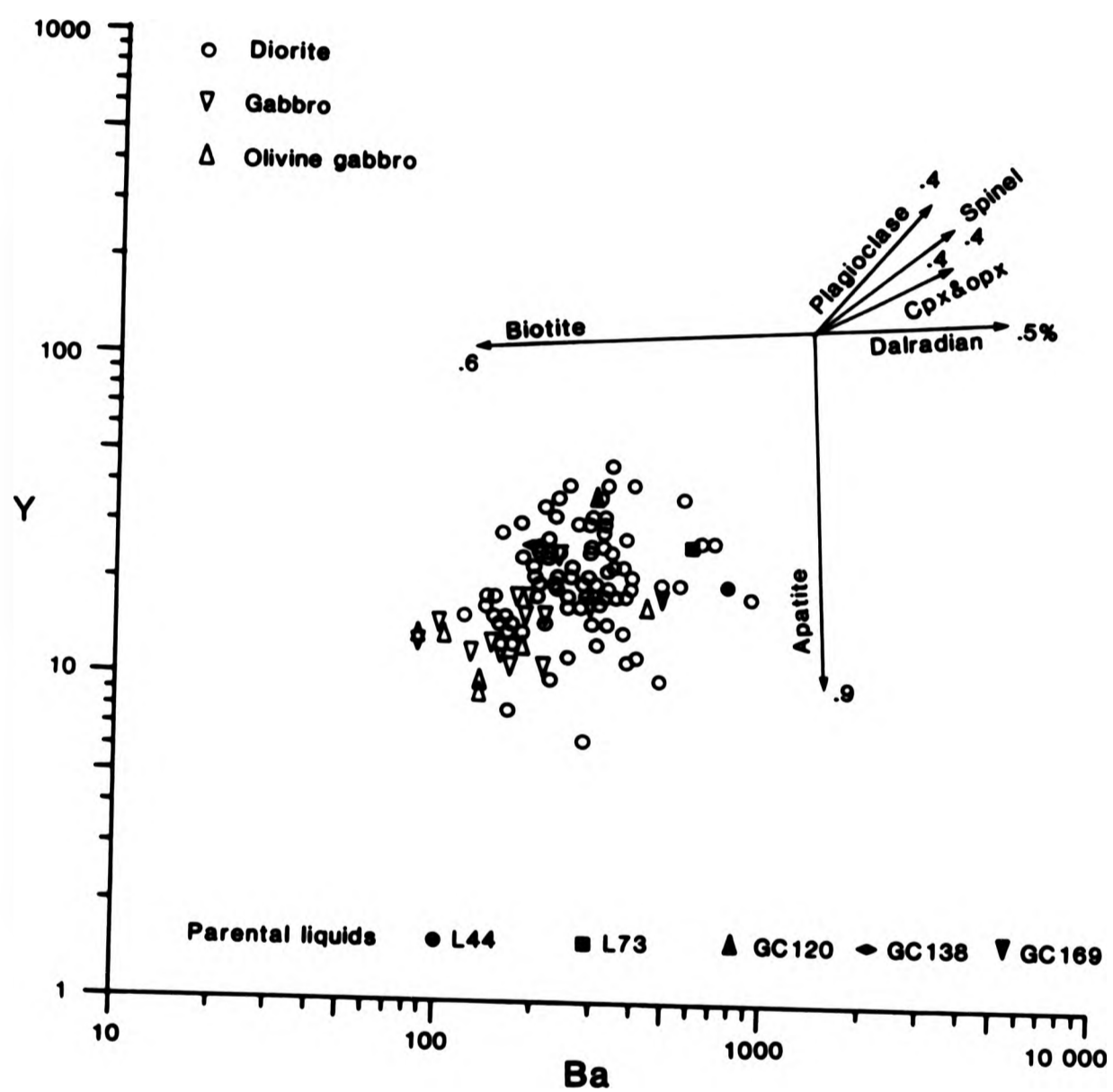
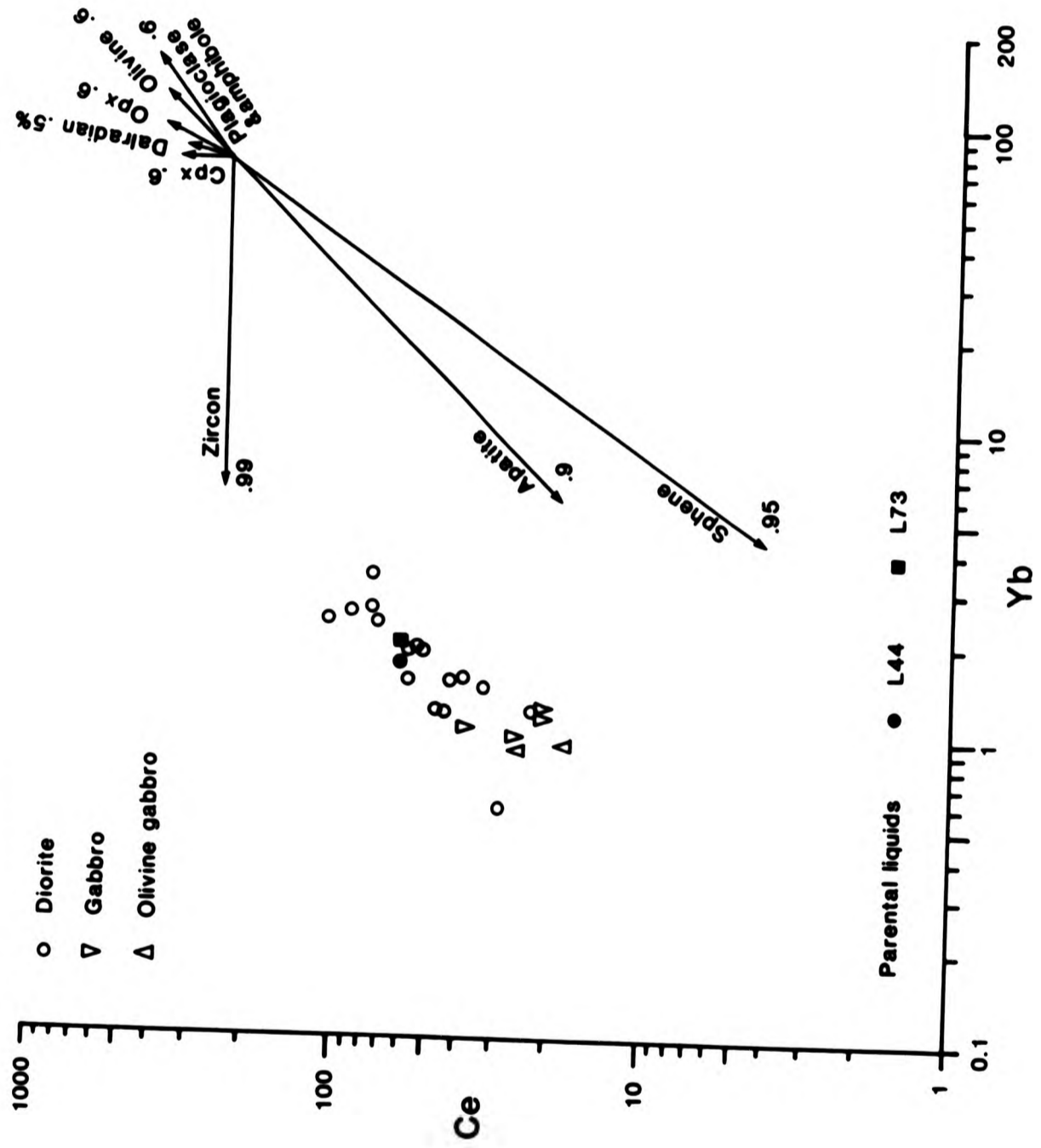


Fig. 8.6 Logarithmic, bivariate plot of Ce-Yb for the Glen Doll intermediate and basic rocks.



The REE are particularly useful in distinguishing between the effects of major and minor phase crystallisation. The minor phases in the Glen Doll diorites, sphene and apatite in particular, contain significant amounts (Chapter 5) of the LREE. The REE are used here to distinguish between the crystallisation of the major phases and zircon, apatite and sphene. Figure 8.6 displays a positive linear correlation between cerium and ytterbium in the dioritic rocks and an overlap of compositions between the gabbroic rocks and diorites is seen at 1.1ppm Yb and 25ppm Ce. The major mineral phases olivine, plagioclase, amphibole and opx, and minor phases apatite and sphene, could control the observed trends in the dioritic rocks. The effect of zircon crystallisation would be to deplete the magma in Yb while Ce remains constant. This feature is not observed in either the dioritic or gabbroic rocks.

The Dalradian metasediment (GC68) has a high $(Ce/Yb)_N$ ratio of 34 compared to the dioritic rocks which range from $(Ce/Yb)_N$ of 6 to 11. The effect of assimilation of Dalradian metasediment are therefore readily separated from the effects of fractional crystallisation. A small amount (<0.05%) of assimilation could account for the minor scatter of data points displayed by the dioritic rocks. Assimilation of Dalradian metasediment coupled with crystallisation of opx and cpx could cause the observed scatter of data for the gabbros and dioritic rocks.

(e) Summary

The modelled data constrains the number of crystallising phases and allows an evaluation of the role of assimilation in the evolution of the Glen Doll intermediate and basic rocks. The geo-

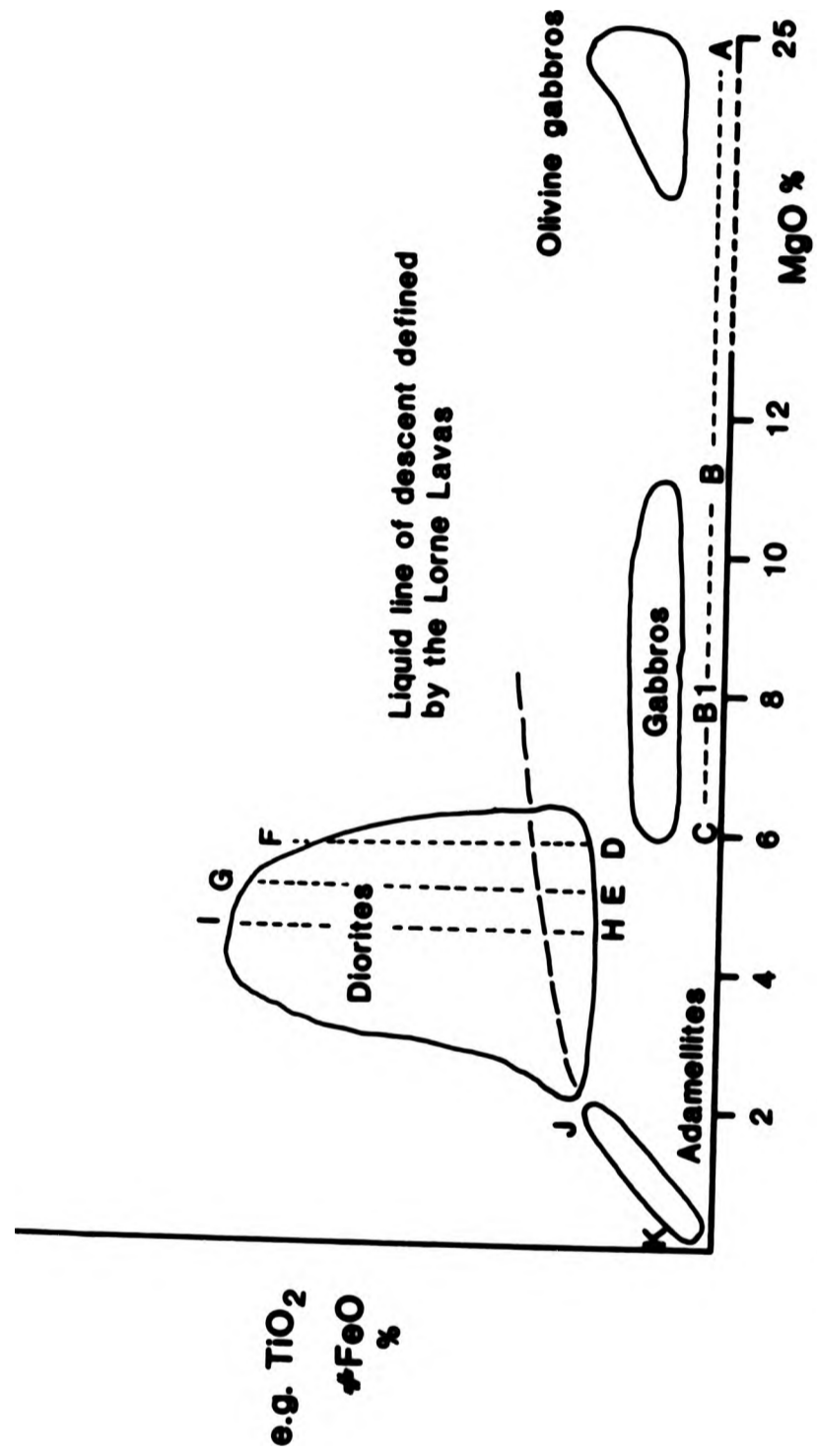


Fig. 8.7 Major-element modelling pathways for the Glen Doll Complex

Table 8.3 Average values for potential source materials
(Data from Frost and O'Nions, 1985)

<u>Reservoir</u>	<u>Sr ppm</u>	<u>$^{87}\text{Sr}/^{86}\text{Sr}$</u> <u>Average</u>	<u>$^{87}\text{Sr}/^{86}\text{Sr}$</u> <u>Range</u>	<u>Rb/Sr</u>
Depleted Mantle	140	0.7025	0.7021-0.7030	0.03 ^a
Lewisian Amphibolite	469	0.7152	0.7029-0.7571	0.05- 0.59 ^d
Lewisian Granulite	-	0.7026	0.7021-0.7031	-
Dalradian Metasediment	177	0.7228	0.7158-0.7440	0.4067 ^c
Southern Uplands Sediments	297	0.7088	0.7045-0.7109	0.65 ^b

Additional data from;

- a Baxter et al., 1985.
- b estimated
- c Glen Doll Complex sample GC68
- d Moorbath et al., 1975

chemical trends displayed by the gabbroic rocks can be modelled in terms of initial accumulation of opx and olivine in the olivine gabbros followed by opx ± amphibole (Figure 8.4) and plagioclase (Figure 8.5) in the gabbros. The gabbroic rocks typically contain low levels of Ce and Yb, however a few samples contain >30ppm Ce and >1.1ppm Yb indicating that they may have undergone contamination by metasediment (Figure 8.6). Trace element models for the dioritic rocks do not require the crystallisation of olivine, a feature consistent with observed mineralogy. The trace element data is best explained by crystallisation of plagioclase, amphibole, spinel, opx and cpx. In addition assimilation of up to 0.5% of Dalradian metasediment is consistent with the observed trends.

Trace element modelling has been carried out here assuming a closed system. The amount of fractionation required for some major mineral phases is large, typically >70% for each mineral. However, if the system is assumed to be at least partially open, with periodic replenishment of magma with a similar composition, then the amount of crystallisation required is reduced. A general lack of mineral zoning in some of the gabbros (Chapter 5) may support this hypothesis.

8.5.1.2 Major element modelling of the diorites and gabbroic rocks

The trace element modelling has provided a range of minerals which are consistent with observed mineral assemblages. Major element modelling has been undertaken using a computer program which uses linear regression equations to model mineral and bulk rock data (See section 8.1) (Banks, 1979). The modelled pathways for each rock type are shown in Figure 8.7. Pathway A-B (Figure 8.7)

TABLE 8.4 Modelled data for pathway A-B (22-11% MgO) from olivine gabbro to gabbro.

Oxide compositions of mineral phases used in modelled analysis

	OPX	CPX	OL	D1	PAR1
SiO ₂	54.15	52.10	39.00	51.58	49.53
Al ₂ O ₃	1.38	2.78	0.06	15.40	6.74
FeO	14.02	6.42	18.84	6.65	9.67
MgO	28.30	15.85	41.75	10.98	22.40
CaO	1.38	22.01	0.00	12.05	8.89
Na ₂ O	0.03	0.04	0.00	2.01	1.36
K ₂ O	0.00	0.00	0.00	0.42	0.61
TiO ₂	0.36	0.66	0.00	0.72	0.56
P ₂ O ₅	0.00	0.00	0.00	0.08	0.08
MnO	0.37	0.14	0.34	0.10	0.16

OPX=161/PX/72C, CPX=79/PX/39C, OL=88/OL/101C,
 Daughter (D1)=GC70, Parent (PAR1)=GC88

Modal composition which minimises one norm misfit

OPX	CPX	OLIVINE	GC70
22.05	17.92	21.53	38.50

Comparison of original and modelled rock composition

	Rock	Model	Misfit
SiO ₂	49.53	49.53	0.0
Al ₂ O ₃	6.74	6.74	0.0
FeO	9.67	10.86	-8.0
MgO	22.40	22.30	1.0
CaO	8.89	8.89	0.0
Na ₂ O	1.36	0.79	5.7
K ₂ O	0.61	0.16	9.1
TiO ₂	0.56	0.48	0.9
P ₂ O ₅	0.08	0.03	2.6
MnO	0.16	0.22	-6.5

one norm misfit = 33.7

has not been successfully modelled, but details of the best solution obtained (that with the lowest one-norm misfit) are given below. The poor misfit is thought to result because the essential difference between the gabbros and the olivine gabbros is the presence of olivine. However differences exist in the chemistry of the two lithologies for elements which are not present in olivine.

The mineral compositions given in each model are recalculated to 100%, CO₂ and H₂O free. Most of the mineral phases used in the modelling program have been analysed by electron microprobe (Appendix B). However, K-feldspar was not analysed and appropriate analyses are therefore taken from Deer et al. (1983, p300).

(a) Olivine gabbro

This rock type is characterised by the presence of modal olivine. In major and trace element variation diagrams (see Chapter 6), the olivine gabbros frequently lie on a continuation of the trend defined by the gabbros. If the gabbro part of the trend is assumed to represent a liquid, then the cumulate assemblage required to form the olivine gabbros, can be calculated (Pathway A-B). The best fit which could be achieved using the range of olivine, opx, cpx and plagioclase compositions observed in both the olivine gabbros and gabbros, is displayed on Table 8.4. The solution requires the accumulation of 61.5% crystals in the proportions 22.05% opx, 17.92% cpx, and 21.53% olivine plus 38.5% of the most mafic gabbro, to generate the change in composition from 11-25% MgO. However, the one norm mis-fit is large (33.66) and does not represent a reasonable fit of the data (Banks, 1979)(Section 8.1). The misfit is composed mainly of a poor fit for *FeO, Na₂O, K₂O.

P_2O_5 and MnO. It is concluded that the large misfit, particularly for Na_2O and K_2O , may reflect some alteration of the plagioclase feldspar. The proportion of mafic gabbro, would however be consistent with the likely volume of intercumulus liquid if the rock is a cumulate.

(b) Gabbros

The gabbros typically fall on a flat linear trend in both major and trace element variation diagrams. The trend defined by the gabbros (B-C, Figure 8.7) has been split into two parts to reflect the changing gabbroic mineralogy, from a pyroxene-dominated anhydrous assemblage to an amphibole-dominated hydrous assemblage. (Chapter 4). An attempt has been made to model compositions firstly from 11-8% MgO and secondly from 8-6% MgO. These values of magnesium respective limits of pyroxene and amphibole dominated assemblages.

In samples with >8% MgO, the composition of the plagioclase feldspar is typically labradorite-bytownite (An_{55-65}). In those with <8% MgO plagioclase is of labradorite composition (An_{50-55}). Olivine is not present in any of the gabbros but pseudomorphed crystals are sometimes seen in samples with >8% MgO. The low magnesia gabbros (6-8% MgO) commonly contain small amounts of primary hornblende, and amphibole is therefore considered to be a primary crystallising phase. Orthopyroxene and clinopyroxene occur as primary crystals throughout the range of gabbros. Tables 8.5 and 8.6 show the compositions of the mineral phases used in the model, together with the parent and daughter compositions. The model in Table 8.5, assumes that the most mafic gabbro (~11.0% MgO) is a liquid and

Table 8.5 Modelled data for pathway B-B1 (11-8% MgO)
for the high MgO gabbros.

Oxide compositions of mineral phases used in modelled analysis

	OPX	CPX	PLAG	OLIV	AP	D1	PAR1
SiO ₂	53.09	51.84	49.18	38.34	00.00	51.87	49.98
Al ₂ O ₃	1.61	3.08	32.22	0.01	00.00	18.14	17.02
FeO	14.79	6.22	0.24	20.10	0.16	5.98	6.15
MgO	28.26	15.94	0.20	41.25	0.03	8.11	11.28
CaO	1.41	21.78	15.42	0.00	57.89	11.85	12.51
Na ₂ O	0.05	0.36	2.58	0.00	0.00	2.33	1.95
K ₂ O	0.01	0.00	0.17	0.00	0.00	0.76	0.41
TiO ₂	0.44	0.66	0.00	0.00	0.00	0.76	0.51
P ₂ O ₅	0.00	0.00	0.00	0.00	41.92	0.10	0.08
MnO	0.34	0.13	0.00	0.30	0.00	0.10	0.11

OPX=82/PX/44C, CPX=88/PX/42C, PLAG=82/PL/46C, OLIV=88/OL/102C
AP=41/AP/113C, Daughter (D1)=average gabbro at 8% MgO,
Parent (PAR1)=average gabbro at 11% MgO.

Modal composition which minimises one norm misfit

OPX	CPX	PLAG	OLIVINE	APATITE	DAUGHTER
4.73	13.59	24.19	9.27	0.08	48.14

Comparison of original and modelled rock composition

	Rock	Model	Misfit
SiO ₂	49.98	49.98	0.0
Al ₂ O ₃	17.02	17.02	0.0
FeO	6.15	6.34	-1.3
MgO	11.28	11.28	0.0
CaO	12.51	12.51	0.0
Na ₂ O	1.95	1.80	1.5
K ₂ O	0.41	0.41	0.1
TiO ₂	0.51	0.48	0.4
P ₂ O ₅	0.08	0.08	0.0
MnO	0.11	0.11	0.2

one norm misfit = 3.5

Table 8.6 Modelled data for pathway B1-C (8-6% MgO) for the low MgO gabbros.

Oxide compositions of mineral phases used in modelled analysis

	OPX	CPX	PLAG	HBLD	AP	D1	PAR1
SiO ₂	53.09	51.84	54.01	44.34	00.00	53.45	51.87
Al ₂ O ₃	1.61	3.08	28.87	11.89	00.00	18.76	18.14
FeO	14.79	6.22	0.30	11.43	0.16	5.85	5.98
MgO	28.26	15.94	0.30	16.44	0.03	6.05	8.11
CaO	1.41	21.78	11.26	12.16	57.89	11.29	11.85
Na ₂ O	0.05	0.36	5.04	1.05	0.00	2.52	2.33
K ₂ O	0.01	0.00	0.19	0.92	0.00	1.01	0.76
TiO ₂	0.44	0.66	0.02	1.57	0.00	0.86	0.76
P ₂ O ₅	0.00	0.00	0.00	0.00	41.92	0.12	0.10
MnO	0.34	0.13	0.00	0.20	0.00	0.09	0.10

OPX=82/PX/44C, CPX=88/PX/42C, PLAG=108/PL/59R, HBLD=av. pargasitic amphibole, AP=41/AP/113C, Daughter (D1)=average gabbro at 6% MgO, Parent (PAR1)=average gabbro at 8% MgO.

Modal composition which minimises one norm misfit

OPX	CPX	PLAG	HBLD	APATITE	DAUGHTER
3.70	7.11	20.75	16.62	0.09	51.72

Comparison of original and modelled rock composition

	Rock	Model	Misfit
SiO ₂	51.87	51.87	0.0
Al ₂ O ₃	18.14	17.95	1.1
FeO	5.98	5.98	0.0
MgO	8.11	8.11	0.0
CaO	11.85	11.85	0.0
Na ₂ O	2.33	2.55	-2.2
K ₂ O	0.76	0.71	0.9
TiO ₂	0.76	0.77	-0.12
P ₂ O ₅	0.10	0.10	0.0
MnO	0.10	0.10	-0.1

one norm misfit = 4.3

Table 8.7 Modelled data for pathway D-F from a low to high titanium diorite.

Oxide compositions of mineral phases used in modelled analysis

	ILME	MT	CPX	GC105	GC132
SiO ₂	0.00	0.03	52.47	53.22	48.84
Al ₂ O ₃	0.06	0.23	2.27	16.82	14.45
FeO	48.26	99.64	6.39	8.41	13.53
MgO	0.08	0.00	15.77	6.35	6.22
CaO	0.00	0.00	21.90	9.60	9.31
Na ₂ O	0.00	0.00	0.04	2.79	2.21
K ₂ O	0.00	0.00	0.00	0.80	0.77
TiO ₂	49.93	0.09	0.66	1.71	4.42
P ₂ O ₅	0.00	0.00	0.00	0.15	0.08
MnO	1.67	0.01	0.00	0.14	0.18

CPX=79/PX/39C, ILME=179/OX/12C, MT=132/OX/33C,
Daughter=GC105, Parent=GC132

Modal composition which minimises one norm misfit

ILMENITE	MAGNETITE	CPX	GC105
5.82	3.18	4.67	86.33

Comparison of original and modelled rock composition

	Rock	Model	Misfit
SiO ₂	48.84	48.40	2.9
Al ₂ O ₃	14.45	14.66	-1.2
FeO	13.53	13.53	0.0
MgO	6.22	6.22	-0.1
CaO	9.31	9.31	0.0
Na ₂ O	2.21	2.41	-2.0
K ₂ O	0.77	0.69	1.6
TiO ₂	4.42	4.42	0.0
P ₂ O ₅	0.08	0.13	-2.5
MnO	0.18	0.22	-3.8

one norm misfit = 14.1 (excluding MnO and P₂O₅=8)

calculates the extract required to generate a liquid with 8% MgO, the most evolved gabbro with a pyroxene dominated assemblage. The calculated modal composition which best fits the observed data from 11 to 8% MgO requires 51.86% crystallisation of five mineral phases in the following percentages, 46.65% plagioclase (An₆₅), 26.21% cpx, 17.88% olivine, 9.12% opx and 0.15% apatite. The one norm mis-fit is 3.4 of which 0.2 is contributed by K₂O and MnO, a relatively small difference between rock and model resulting in a relatively large misfit for these elements. The calculated modal composition which best fits the trend from 8-6% MgO, requires 48.28% crystallisation of the five mineral phases in the proportions 42.99% plagioclase (An₅₅), 34.43% hornblende, 14.73% cpx, 7.66% opx and 0.19% apatite. The one norm mis-fit is 4.4. The high magnesia gabbros can be generated by crystallisation of a high calcium plagioclase, opx, cpx, olivine and a small amount of apatite, features consistent with observed mineralogy. The low magnesia varieties require the introduction of hornblende and the exclusion of olivine in order to generate the observed trends. This assemblage is consistent with the observed mineralogy.

(c) Diorites

The dioritic rocks define a more complex data pattern than the gabbroic rocks. The major element modelling processes has been divided into two parts, firstly to generate the observed variation using crystal fractionation and secondly to account for possible assimilation of metasedimentary material. The modelling pathways D-F (at 6.2% MgO) and E-G (at 5.0% MgO) (Figure 8.7) probably represent crystal fractionation pathways with cumulate ilmenite and magnetite occurring at 6.2% MgO and apatite at 5% MgO, while H-I

Table 8.8 Modelled data for pathway E-G from a low to high titanium-phosphorus diorite.

Oxide compositions of mineral phases used in modelled analysis

	ILME	MT	CPX	AP	PLAG	OPX	GC146	GC240
SiO ₂	0.00	0.03	52.47	0.19	54.24	53.34	56.63	49.73
Al ₂ O ₃	0.06	0.23	2.27	0.00	29.46	1.20	19.31	16.57
FeO	48.26	99.64	6.39	0.10	0.32	18.97	6.44	12.80
MgO	0.08	0.00	15.77	0.03	0.03	24.52	4.79	5.00
CaO	0.00	0.00	21.90	53.40	11.30	1.12	6.88	8.34
Na ₂ O	0.00	0.00	0.04	0.03	4.37	0.02	3.22	2.96
K ₂ O	0.00	0.00	0.00	0.00	0.27	0.00	0.85	0.70
TiO ₂	49.93	0.09	0.66	0.00	0.00	0.30	1.61	3.30
P ₂ O ₅	0.00	0.00	0.00	46.25	0.00	0.00	0.14	0.42
MnO	1.67	0.01	0.00	0.00	0.00	0.53	0.13	0.17

CPX=79/PX/39C, ILME=179/OX/12C, MT=132/OX/33C, OPX=108/PX/56C
 PLAG=179/PL/12C, AP=108/AP/9C, Daughter=GC146, Parent=GC240

Modal composition which minimises one norm misfit

ILMENITE	MAGNETITE	PLAG	CPX	OPX	AP	GC146
4.44	5.54	15.13	8.56	2.52	0.72	63.08

Comparison of original and modelled rock composition

	Rock	Model	Misfit
SiO ₂	49.73	49.77	-0.2
Al ₂ O ₃	16.57	16.92	-1.9
FeO	12.80	12.80	0.0
MgO	5.00	5.00	0.0
CaO	8.34	8.34	0.0
Na ₂ O	2.96	2.70	2.6
K ₂ O	0.70	0.58	2.4
TiO ₂	3.30	3.30	0.0
P ₂ O ₅	0.42	0.42	0.0
MnO	0.17	0.17	0.0

one norm misfit = 7.1

(Figure 8.7) has been used to demonstrate a combination of crystal fractionation and assimilation since the composition at I contains greater than 100ppm Zn (Chapter 6).

The models which give the lowest one-norm misfit are shown in Tables 8.7 (D-F) and 8.8 (E-G). Pathway E-G was chosen at a MgO content of ~5.0%. At this value an increase in the concentration of P_2O_5 is recorded (Figure 6.7) from 0.2-1.4%, a feature reflecting the variable modal proportion of apatite. Pathway D-F was chosen at ~6.2% MgO, a point where iron and titanium levels reach a maximum. Pathway H-I is modelled at ~4.8% MgO, a concentration at which the diorites contain both variable amounts of ilmenite and magnetite (Section 6.2.2), and also contain high zinc concentrations (Section 6.3.7). A model for pathway D-F (Table 8.7) requires only 13.67% crystallisation of ilmenite, magnetite and cpx (of which 9% is contributed by the cumulate iron oxide minerals) of GC132 parent to generate the high titanium parent from the low titanium daughter composition (GC105). The apparently high one norm mis-fit of 14, largely results from very small differences between the observed and modelled MnO and P_2O_5 contents. Without these the misfit is reduced to 8. This may indicate that the composition of the ilmenite used in the model is not representative of the actual composition with respect to manganese.

Table 8.8 displays the modelled data for trend E-G (Figure 8.7). The model requires a similar mineralogy to that needed for trend D-F with 4.4% ilmenite and 5.5% magnetite (Figure 8.7) with the addition of plagioclase (15.13%), opx (2.52%) and apatite (0.72%). The proportion of iron oxide minerals in trend E-G and D-F are consistent.

Table 8.9 Modelled data for pathway H-I from a low titanium uncontaminated diorite to a high titanium contaminated diorite.

Oxide compositions of mineral phases used in modelled analysis

	ILME	DAL	AL	AN	OPX	AP	GC104	PAR
SiO ₂	0.08	73.65	68.59	44.03	53.09	0.00	50.45	56.63
Al ₂ O ₃	0.05	15.17	19.87	36.30	1.61	0.00	15.79	19.31
FeO	45.92	4.20	0.02	0.02	14.79	0.10	12.68	6.44
MgO	0.05	1.75	0.04	0.00	28.26	0.00	4.96	4.79
CaO	0.00	0.71	0.00	19.43	1.41	57.89	9.19	6.88
Na ₂ O	0.00	1.24	11.19	0.22	0.05	0.00	2.72	3.22
K ₂ O	0.00	2.33	0.29	0.00	0.01	0.00	0.74	0.85
TiO ₂	51.34	0.83	0.00	0.00	0.44	0.00	3.16	1.61
P ₂ O ₅	0.00	0.07	0.00	0.00	0.00	41.92	0.16	0.41
MnO	2.56	0.05	0.00	0.00	0.34	0.00	0.14	0.13

ILME=108/OX/65C, OPX=82/PX/42C, Albite (AL) and Anorthite (AN)=Deer et al., 1983, AP=21/AP/81C, Average Dalradian (DAL)= from Glen Doll, Daughter=GC104, Parent=Average low titanium diorite.

Modal composition which minimises one norm misfit

ILME	AP	ALBITE	ANORTHITE	DAL	OPX	GC104
1.00	0.19	19.32	21.59	18.86	10.79	63.08

Comparison of original and modelled rock composition

	Rock	Model	Misfit
SiO ₂	56.63	56.63	0.0
Al ₂ O ₃	19.31	19.17	0.8
FeO	6.44	6.44	0.0
MgO	4.79	4.79	0.0
CaO	6.88	7.19	-2.1
Na ₂ O	3.22	3.22	0.0
K ₂ O	0.85	0.71	3.0
TiO ₂	1.61	1.61	0.0
P ₂ O ₅	0.41	0.14	0.0
MnO	0.13	0.11	1.8

one norm misfit = 7.7 (Excluding MnO=5.8)

The linear modelling technique was extended to include simultaneous fractional crystallisation and assimilation. The model is simplified, in that total assimilation is assumed and the assimilant (Dalradian metasediment GC68) is treated as an additional mineral phase. However it provides a first order constraint on major element modelling of crustal assimilation. The composition chosen for the country rock is an average of three analyses of the Dalradian metasediments (GC68, GC107 and GC129b) from around the Glen Doll Complex. The parent composition was interpolated from Figure 8.1. A best fit line was drawn through the lava compositions. The amount of each major element oxide was recorded at the intersection of 4.79% MgO with this line. GC104 was chosen as the daughter composition since it has a similar magnesia content to the parent but in addition contains 110ppm Zn indicating that it is probably contaminated with Dalradian metasediment (Section 6.3.7).

The minimum one norm mis-fit model (Table 8.9), allows a total of 52.89% crystallisation of apatite (0.19%), opx (10.79%), plagioclase (An₅₃) (40.91%) and ilmenite (1.0%) with 18.86% assimilation of average Dalradian metasediments to produce the most contaminated diorites. The amount of crystallisation is typically large, approximately that required to form the framework of a cumulate rock (Wager and Brown, 1968). An at least partially open system is required if this model is to be feasible. After 80% of crystallisation, the residual liquid would no longer crystallise rocks of dioritic composition and the rocks crystallising would become progressively more evolved.

(d) Rafted metasedimentary xenoliths

Table 8.10 A model for the production of a rafted xenolith from the Dalradian country rocks by partial melting.

Oxide compositions of mineral phases used in modelled analysis

	DILIQ	MUSC	QTZ	AL	BI	SILL	GC26	PAR
SiO ₂	56.63	49.50	100.00	68.59	36.42	37.03	47.26	73.65
Al ₂ O ₃	19.31	35.70	0.00	19.87	19.73	62.69	20.69	15.17
FeO	6.44	1.86	0.00	0.02	20.75	0.21	15.31	4.20
MgO	4.79	0.67	0.00	0.04	9.56	0.05	4.46	1.75
CaO	6.88	0.00	0.00	0.00	0.00	0.00	5.54	0.71
Na ₂ O	3.22	0.73	0.00	11.19	0.00	0.00	2.65	1.24
K ₂ O	0.85	10.54	0.00	0.29	10.14	0.00	1.63	2.33
TiO ₂	1.61	0.99	0.00	0.00	3.40	0.02	2.04	0.83
P ₂ O ₅	0.14	0.00	0.00	0.00	0.00	0.00	0.19	0.07
MnO	0.13	0.00	0.00	0.00	0.00	0.00	0.24	0.05

DILIQ=Diorite liquid composition., Muscovite (MUSC), Albite (AL) Deer et al., 1983, Biotite (BI) and Sillimanite (SILL) Schumacher, 1985., Daughter=GC26, Parent=Average Dalradian from Glen Doll.

Modal composition which minimises one norm misfit

DILIQ	MUSC	ALBITE	QUARTZ	BIOTITE	SILL	GC26
4.82	9.82	6.75	49.85	10.61	8.44	9.71

Comparison of original and modelled rock composition

	Rock	Model	Misfit
SiO ₂	73.65	73.65	0.0
Al ₂ O ₃	15.17	15.17	0.0
FeO	4.20	4.20	0.0
MgO	1.75	1.75	0.0
CaO	0.71	0.87	-1.1
Na ₂ O	1.24	1.24	0.0
K ₂ O	2.33	2.33	0.0
TiO ₂	0.83	0.74	0.9
P ₂ O ₅	0.07	0.02	2.3
MnO	0.05	0.03	2.1

one norm misfit = 6.4 (Excluding MnO AND P₂O₅=2)

This type of xenolith occur throughout the dioritic rocks of the Glen Doll Complex. From field and petrographic evidence it is clear that they have undergone partial melting, and therefore provide a potential source of contamination in the complex. They are also thought to be derived locally (Chapter 3). They are banded and contain zones of medium grained diorite. Major element modeling was used to assess whether an analysed rafted xenolith, such as GC26, could be derived from the local Dalradian country rocks. The bulk rock analysis of GC26, a rafted xenolith, contains only 45.60% SiO_2 compared with an average value for the local metasediment of 73.65% SiO_2 . The bulk analysis of GC26 is thought to represent a combination of dioritic material and layers of restite (Chapter 4). After the exclusion of P_2O_5 and MnO , a one norm mis-fit of 2.0 is recorded (Table 8.10). The model requires the addition of a total of ~85% crystals (muscovite, quartz, biotite, albite and sillimanite) and 4.82% of diorite liquid to 9.71% of rafted xenolith (GC26) to produce the composition of the Dalradian country rocks used. A partial melt of composition represented by 9.82% muscovite, 49.85% quartz, 10.61% biotite, 6.75% albite and 8.44% sillimanite, with the addition of 4.82% diorite liquid could give rise therefore to the analysed xenoliths. The large amount of quartz (49.85%) would preclude this assemblage as a cotectic granitic melt. However the percentage of quartz may reflect the original sediment composition.

(e) Summary

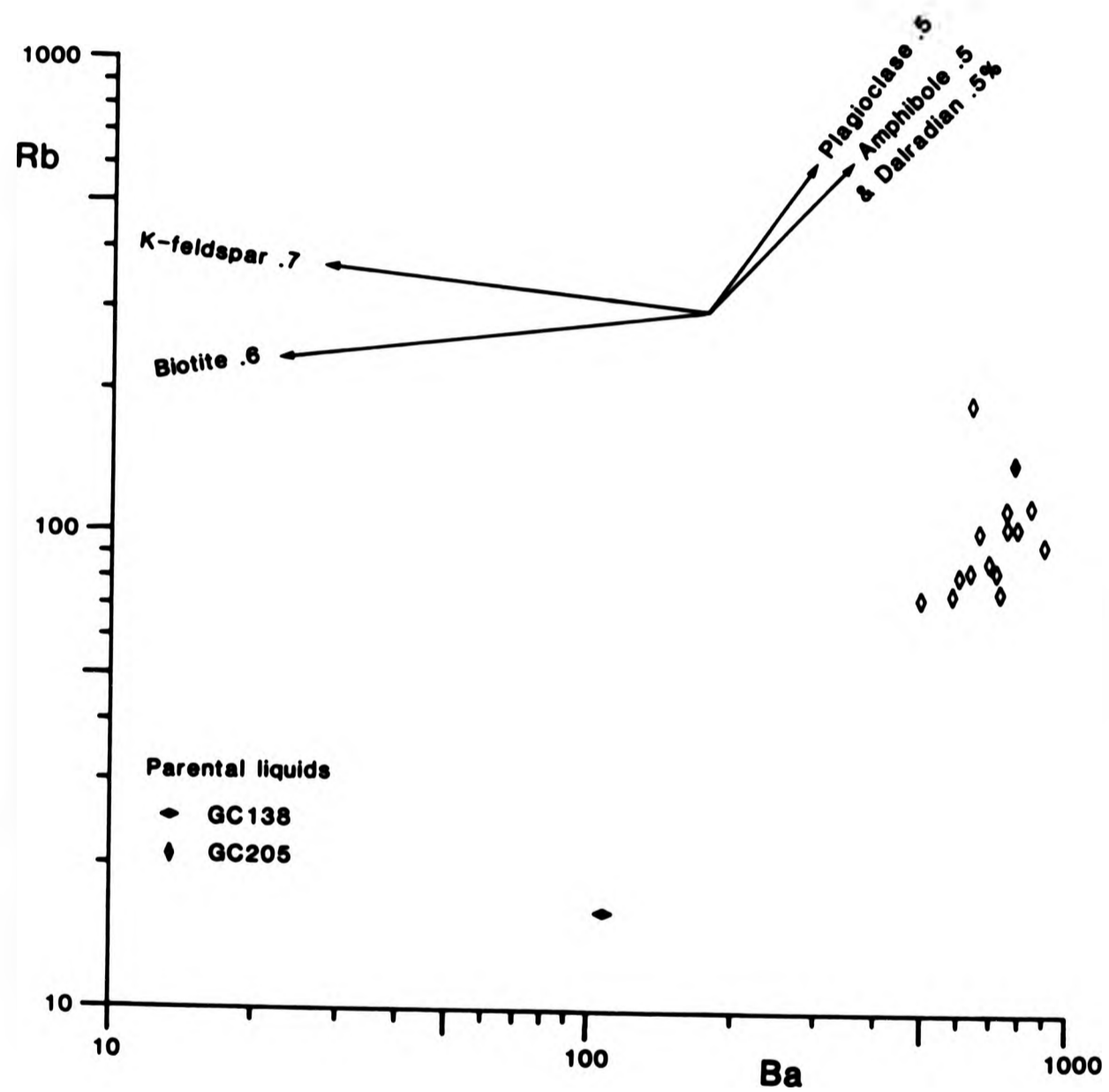
The major element models provide possible solutions which are consistent with the observed mineralogy. The link between the olivine gabbros and gabbros was not satisfactorily modelled. The

olivine gabbros and gabbros have a similar mineralogy with the exception that the former contain olivine primocrysts. The olivine gabbros therefore essentially represent a high MgO gabbro with additional olivine crystals. However the model with the lowest one-norm misfit (Table 8.4) requires the addition of opx, cpx and olivine to the gabbros to generate the olivine gabbro compositions. If the two rock types are cumulates as suggested by petrographic studies (Chapter 4), which have crystallised from a liquid of similar composition to GC138, for example, then linear regression models used here may be inappropriate.

The above models for the gabbroic rocks, provide solutions consistent with the observed mineralogy. The high magnesia part of the gabbro trend may be generated by the crystallisation of an anhydrous assemblage dominated by the crystallisation of calcic plagioclase. The high magnesia gabbros are commonly plagioclase orthocumulates (Chapter 4) and typically contain a more calcic plagioclase than the low magnesia gabbros. Those gabbros contain from 8-6% MgO, may be generated by crystallisation of an hydrous assemblage with 16% crystallisation of amphibole. The transition from a pyroxene-dominated anhydrous to an amphibole-dominated hydrous assemblage is observed in the gabbroic rocks (Chapter 4).

The models for the evolution of the diorite rocks support a cumulate origin for those samples containing a large proportion of modal ilmenite and magnetite. The models also require the crystallisation of both opx and cpx to generate the observed trends. Remnant pyroxene crystals are observed in some of the diorites, frequently jacketed by primary amphibole. Secondary, subsolidus amphiboles occur, which are thought to be replacement products

Fig. 8.8 Logarithmic, bivariate plot of Rb-Ba for the Glen Doll adamellites.



after pyroxene (See Chapters 4 and 5). The required large amount of crystallisation (Table 8.8) of the primocryst phases is consistent with a cumulate origin for the iron and titanium-rich diorites.

8.5.1.3 Semi-quantitative trace element modelling of the adamellites

The adamellite margin of the Glen Doll complex clearly post-dates the emplacement of the main part of the complex. Therefore, the relationship between the adamellites and the dioritic rocks is unlikely to be a direct one. However, the adamellites frequently contain rounded inclusions of a more mafic granodiorite indicating that they may be of a hybrid origin.

Unlike the diorites, the adamellites frequently display linear trends for many of the major and trace elements (Chapter 6). These could result from fractional crystallisation of a single magma or alternatively from the mixing of two magmas. The observed trend is however similar to that for the calc-alkaline Lorne lava suite (Figure 6.1).

The major and trace element trends for the adamellites are frequently collinear with the liquid line of descent defined by the calc-alkaline lava suite. One starting composition used in the following models is that of the least evolved adamellite taken as that with the lowest SiO_2 content (GC205).

(a) Bivariate plot of Rb and Ba (Figure 8.8)

after pyroxene (See Chapters 4 and 5). The required large amount of crystallisation (Table 8.8) of the primocryst phases is consistent with a cumulate origin for the iron and titanium-rich diorites.

8.5.1.3 Semi-quantitative trace element modelling of the adamellites

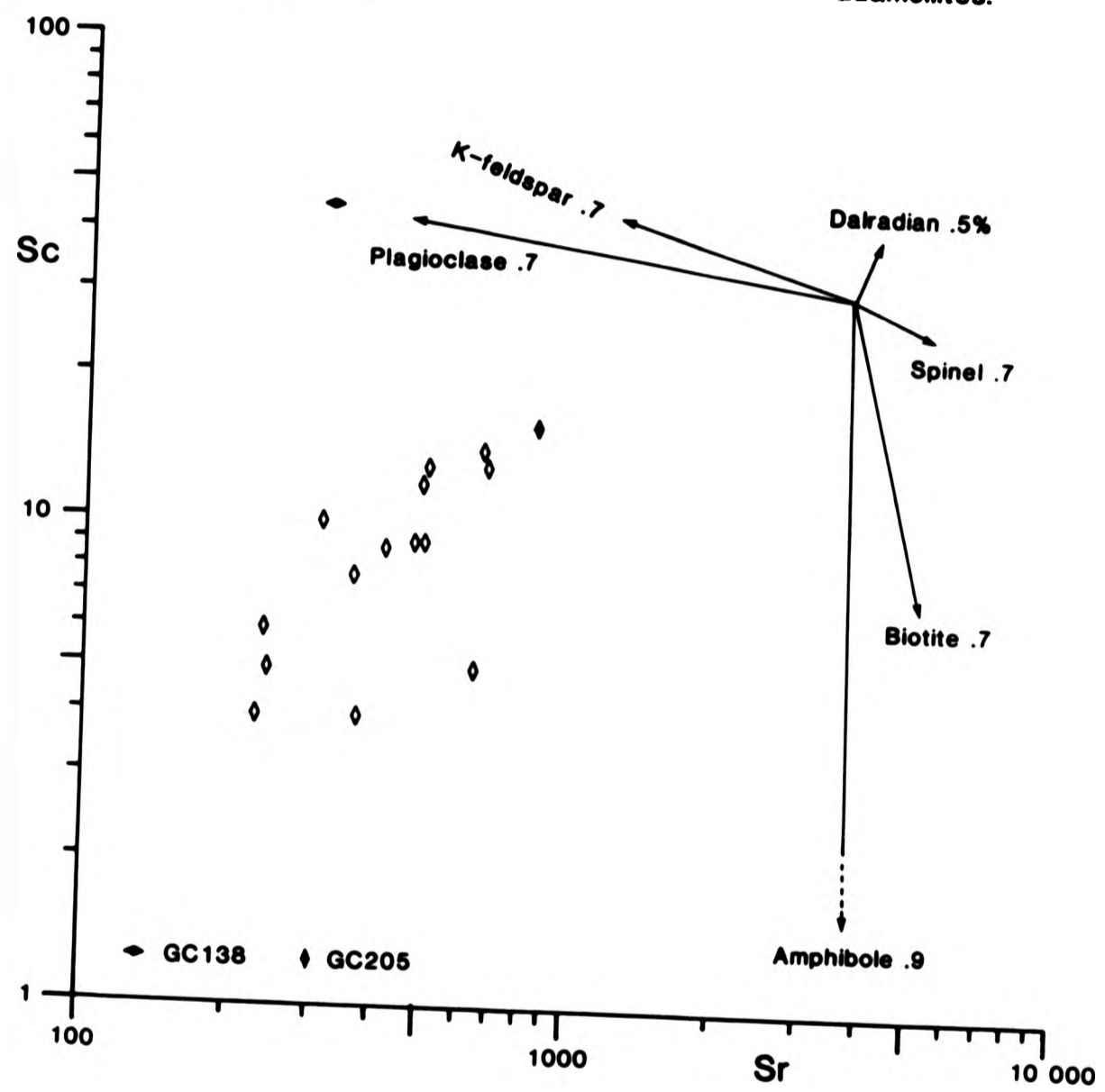
The adamellite margin of the Glen Doll complex clearly post-dates the emplacement of the main part of the complex. Therefore, the relationship between the adamellites and the dioritic rocks is unlikely to be a direct one. However, the adamellites frequently contain rounded inclusions of a more mafic granodiorite indicating that they may be of a hybrid origin.

Unlike the diorites, the adamellites frequently display linear trends for many of the major and trace elements (Chapter 6). These could result from fractional crystallisation of a single magma or alternatively from the mixing of two magmas. The observed trend is however similar to that for the calc-alkaline Lorne lava suite (Figure 6.1).

The major and trace element trends for the adamellites are frequently collinear with the liquid line of descent defined by the calc-alkaline lava suite. One starting composition used in the following models is that of the least evolved adamellite taken as that with the lowest SiO_2 content (GC205).

(a) Bivariate plot of Rb and Ba (Figure 8.8)

Fig. 8.9 Logarithmic, bivariate plot of Sc-Sr for the Glen Doll adamellites.



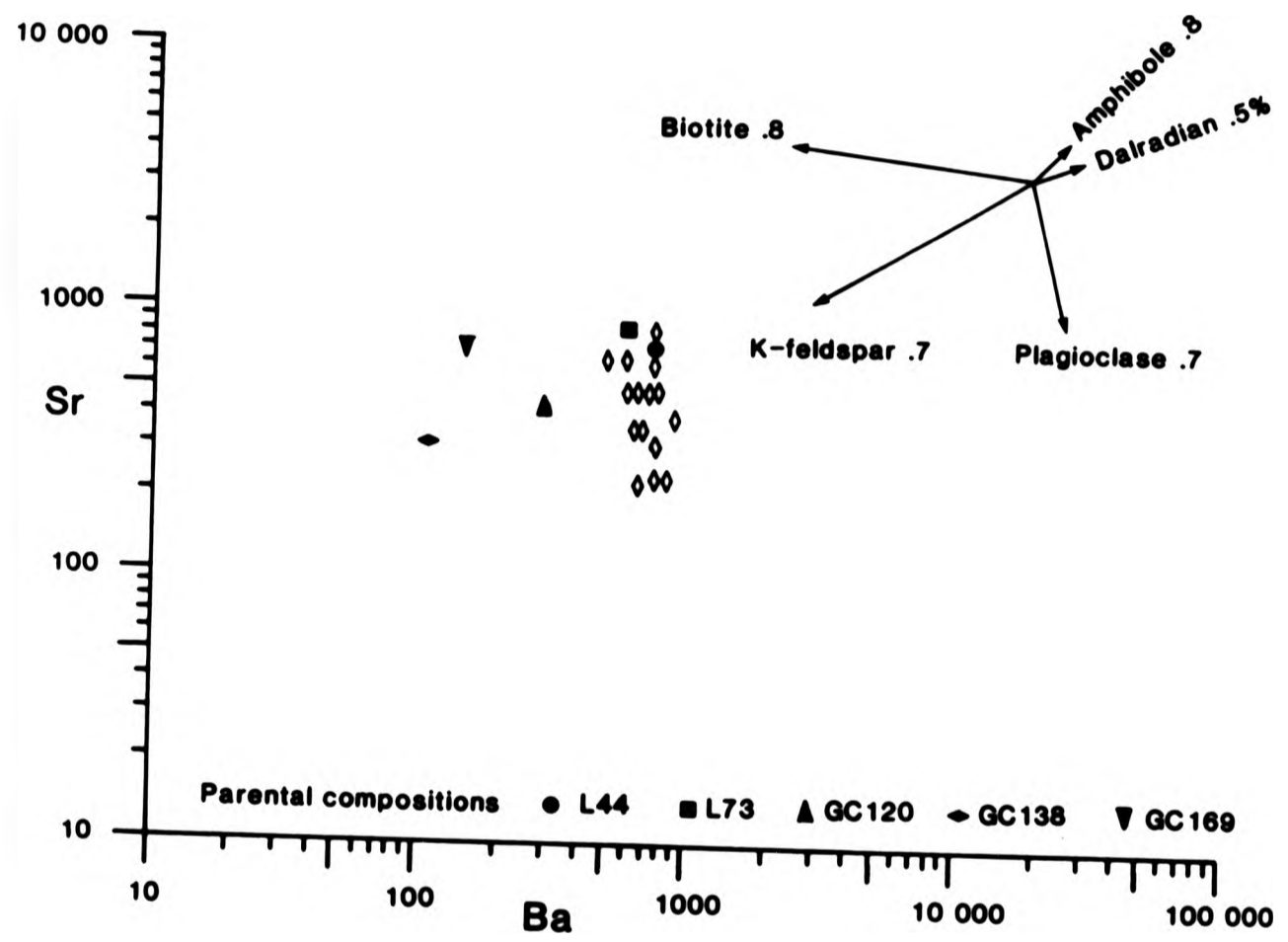
A broadly linear relationship between Rb and Ba is displayed by the adamellites on Figure 8.8. Using a starting composition at the least evolved end of the trend (low Ba and Rb) the model requires ~50% crystallisation of plagioclase and amphibole to generate the observed trend. On this diagram no separation can be made between the effects of assimilation of average Dalradian metasediment and the fractional crystallisation of amphibole.

Using the most mafic adamellite (Gc205) as a starting composition, crystallisation of K-Feldspar and biotite are required in addition to amphibole and plagioclase in order to generate the observed compositions. The composition of GC138 (microdiorite xenolith) is also shown on this figure. It is notable that very large amounts of crystallisation, would be required to generate a series of liquids of adamellite composition from this parent. This may indicate that if the diorites and adamellites are derived from a common parent, then either a very large reservoir of parent material existed or the magma chamber was periodically refilled with magma of a similar composition.

(b) Bivariate plots of Sc and Sr, Sr and Ba (Figures 8.9 and 8.10)

A strontium-barium diagram was used by Tindle and Pearce (1981) to model the evolution of the Loch Doon granitic complex. In that intrusion the two elements display coherent behaviour a pattern commonly seen in such rock suites (e.g. Perkins, 1986). The Glen Doll adamellites, by contrast, display an increase in Sr levels at relatively constant values of Ba (600-800ppm). Figure 8.10 (Sr and Ba) was constructed to distinguish between the crystallisation of amphibole (which has a similar K_D for Sr and Ba) and

Fig. 8.10 Logarithmic, bivariate plot of Sr - Ba for the Glen Doll adamellites.



the other major phases. A Sc and Sr diagram (Figure 8.9) allows an evaluation of the effect of spinel crystallisation since since K_D for spinel is much larger for Sc than for Sr (Table 8.1).

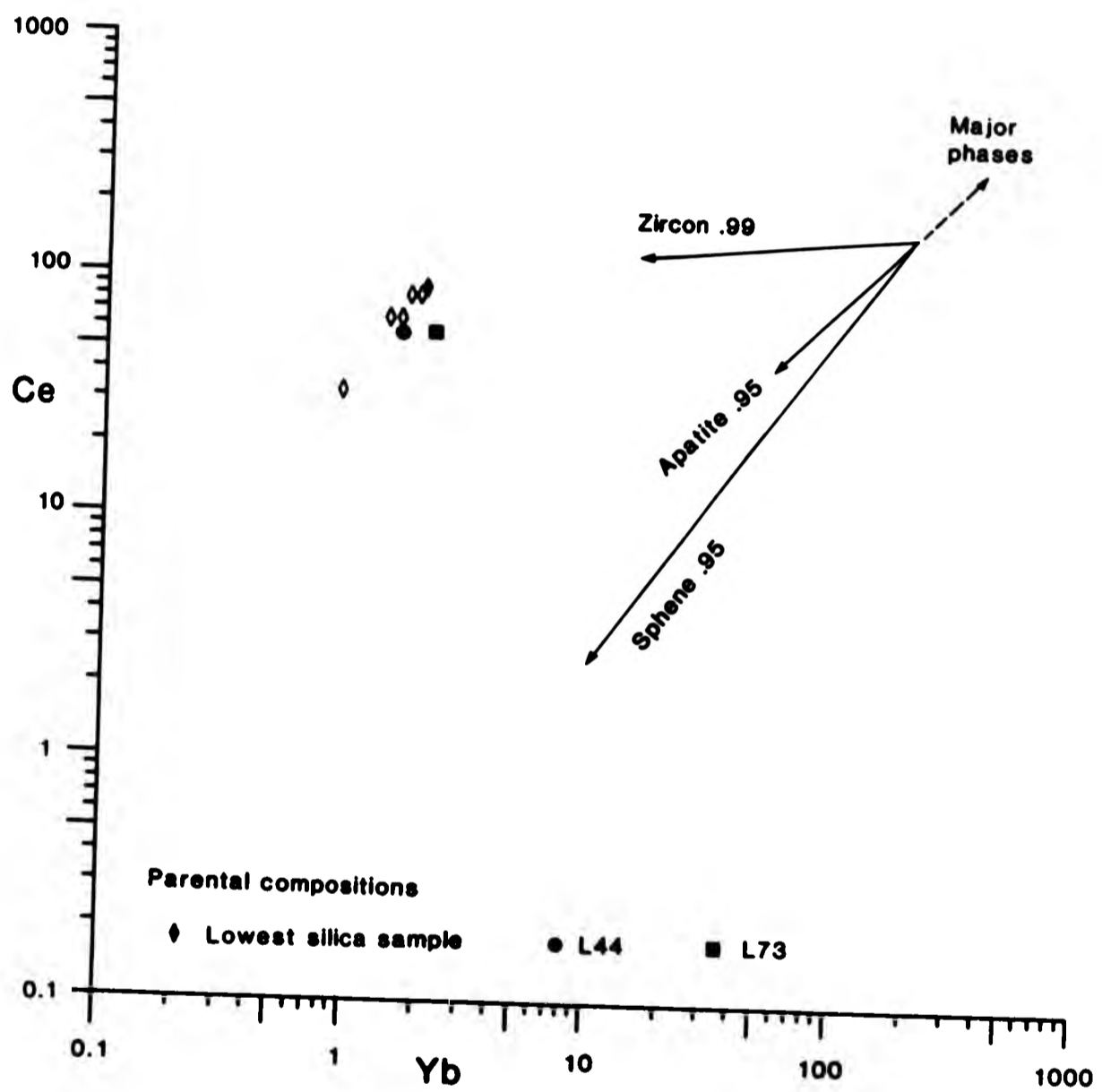
The mineral vectors on Figure 8.8 suggest that the crystallisation of amphibole, plagioclase and K-feldspar could control the observed trends since the mineral vectors lie close to the observed data. Figure 8.9 supports a model involving K-feldspar and plagioclase crystallisation. However the crystallisation of small amounts of amphibole and biotite could account for the scatter of data away from the main trend.

The effects of the assimilation of Dalradian country rock is not clearly separated from the crystallisation of amphibole on the Sr/Ba plot or from major phase crystallisation on the Sc/Sr plot.

(c) Bivariate plot of Ce and Yb (Figure 8.11)

The effect of crystallisation of minor phases such as apatite, zircon and sphene in an evolving intermediate liquid, has been assessed by various authors (e.g. Tindle and Pearce, 1981) using a Ce/Yb bivariate diagram. These minor phases commonly partition the REE (e.g. Henderson, 1983). Indeed apatite and sphene from the Glen Doll and Juan Jorge Complexes contain up to 1.8% total LREE oxides (Appendix B). These elements therefore help to distinguish between the crystallisation of major and minor phases. In addition the HREE may be partitioned more strongly than the LREE e.g. in zircon and therefore a Ce/Yb diagram allows a distinction to be made between the effects of crystallisation of LREE and HREE enriched minerals. The vectors for sphene and apatite lie directly on the data points, which display a linear pattern for the adamel-

Fig. 8.11 Logarithmic, bivariate plot of Ce-Yb for the Glen Doll adamellites.



lites (Figure 8.11). This diagram suggests that zircon is not an important crystallising phase but that the evolutionary trend of the adamellites is dominated by the crystallisation of very small amounts (0.1-0.5%) of apatite and sphene.

8.5.1.4 Strontium isotope modelling of the Glen Doll complex

The strontium isotope data discussed in Chapter 7, suggests that the rocks in the Glen Doll complex may be the products of a mantle derived magma, subsequently modified isotopically by interaction with crustal material, a process also described for other late Caledonian igneous complexes (e.g. Frost and O'Nions, 1986; Halliday et al., 1985). A number of possible contamination sources for Scottish Caledonian granites (discussed in section 8.4) have been suggested by various authors e.g. Lewisian, Dalradian (Frost and O'Nions, 1985; Pankhurst and Pidgeon, 1976; Bamford et al., 1977).

A modified Rayleigh type fractionation model (DePaolo, 1981) has been applied to the calculated $^{87}\text{Sr}/^{86}\text{Sr}$ initial ratios for the olivine gabbro, gabbros, diorites and adamellites from the Glen Doll complex. The equation which describes the evolution of a liquid during simultaneous fractional crystallisation and contamination is:-

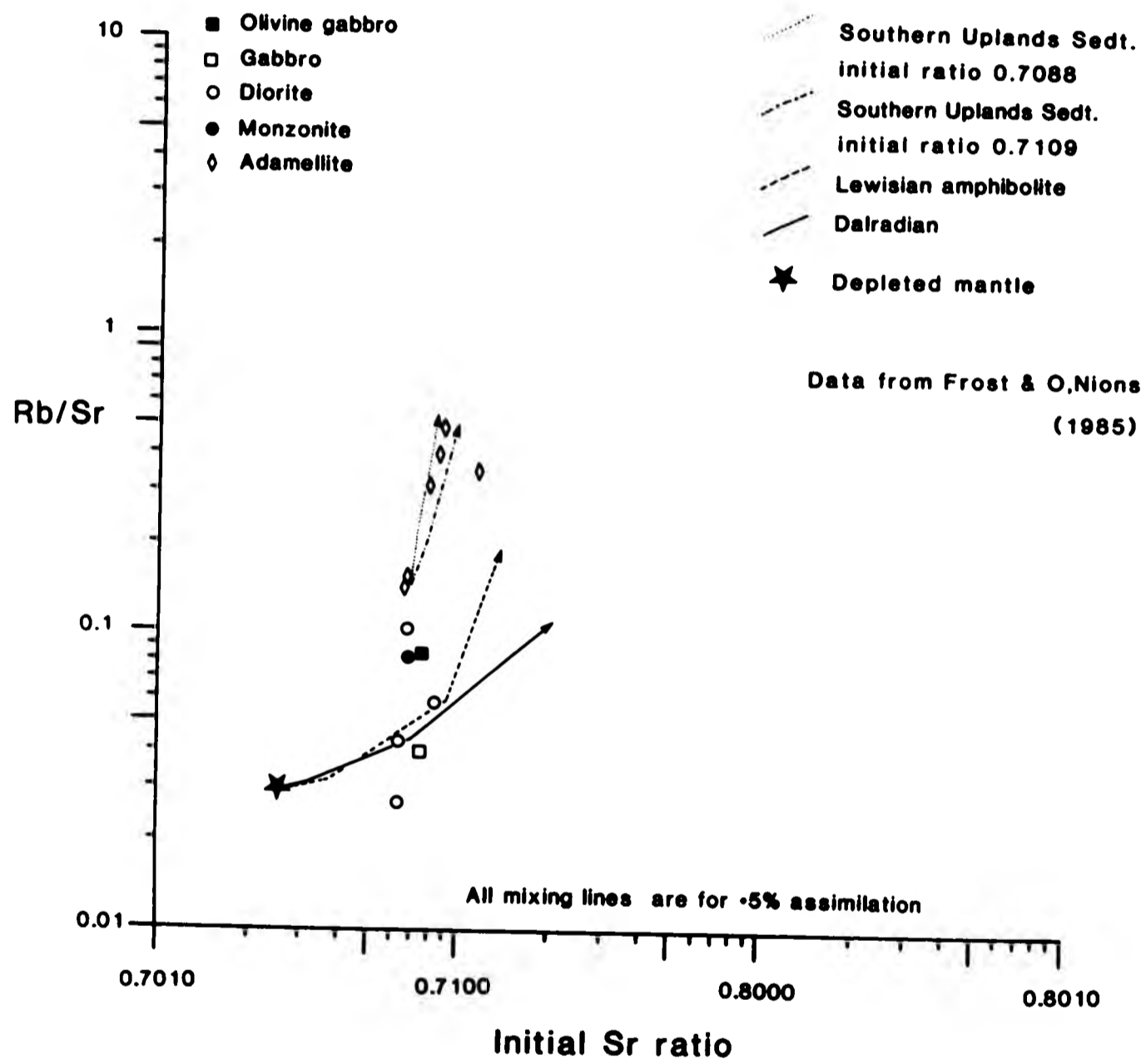
$$E_m - E_m^0 / E_a - E_m^0 = (1 + C_m^0 M_m / C_a M_a)^{-1}$$

where E_m = isotope ratio in the magma

E_a = isotope ratio of the contaminant

E_m^0 = initial isotope ratio

Fig. 8.12 A diagram to show the effect of assimilation of potential crustal contaminants, Glen Doll Complex



C_m^0 = initial concentration of trace element T

M_m = mass of magma

C_a = concentration of trace element T in contaminant

M_a = mass of contaminant

The initial isotope ratio E_m^0 (depleted mantle), values for E_a and C_a and initial concentrations were taken from Frost and O'Nions (1985) since these values are considered appropriate for modelling the evolution of the Glen Doll Complex. The initial concentration for Rb i.e. the concentration of Rb in the mantle was taken from Sun (1980). The mass of magma, M_m , was calculated as detailed in section 8.1. The mass of contaminant, M_a , was continually varied from 0.01-0.5% of M_m to assess the effect of assimilation of a range of crustal materials.

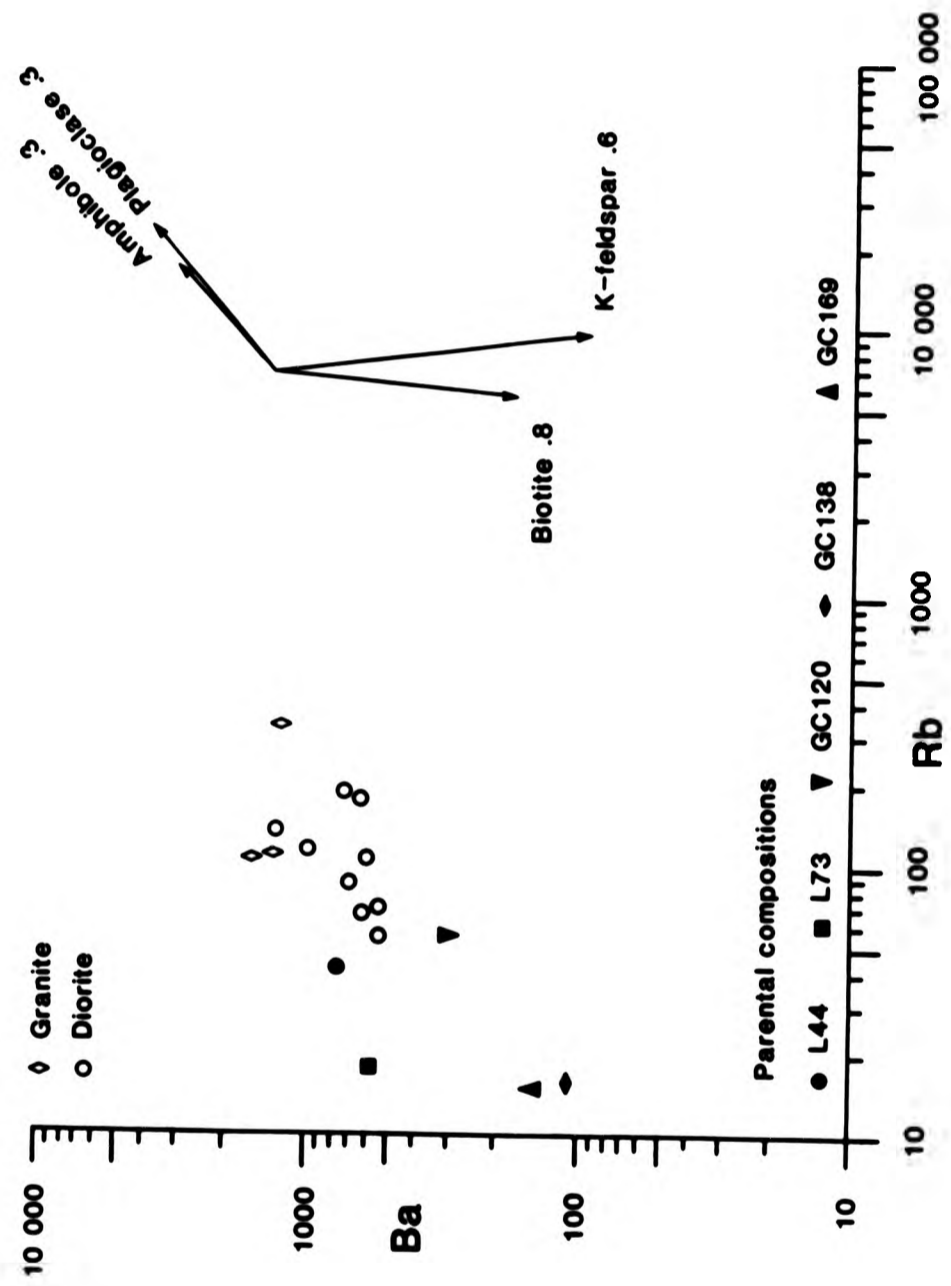
The evolutionary pathways calculated for a range of potential crustal contaminants are shown in figures 8.12. In addition to using depleted mantle as a starting composition, the evolutionary path of each rock type was calculated using the least radiogenic diorite (GC155) as E_m^0 for the diorites and the least radiogenic adamellite (GC276) as E_m^0 for the adamellites since the relationship between the diorites and adamellites has not been clearly established.

The basic and intermediate rocks form a scatter of data points on figure 8.12. The gabbro has the lowest initial $^{87}\text{Sr}/^{86}\text{Sr}$ ratio although this is still higher than the value for depleted mantle. Figure 8.12 suggests that the initial strontium ratios in the gabbros could result from small amounts of contamination of depleted mantle with Dalradian metasediments, Lewisian amphibolite or South-

ern Uplands sediments (SUP). The initial strontium ratios in the dioritic rocks could result from relatively small amounts of assimilation of the same materials. The modelled trends do not however allow the derivation of the range of values seen in the adamellites if a depleted mantle is taken as the parent material. The assimilation vectors can not produce the high initial strontium ratios observed in the adamellites.

The adamellites display a linear trend of increasing initial ratio with increasing Rb/Sr ratio. Using the adamellite with the lowest initial $^{87}\text{Sr}/^{86}\text{Sr}$ ratio, the other adamellites could be derived by assimilation of small amounts of SUP type sediments. The assimilation vectors for the Dalradian and Lewisian metasediments suggests that assimilation of these crustal types is unlikely to produce the observed variation in the acid rocks. Assimilation of Dalradian metasediments with low Rb/Sr (<0.2) ratios coupled with a high (0.715 initial $^{87}\text{Sr}/^{86}\text{Sr}$ ratio could not produce the range of observed data. However a combination of contaminants provides a possible model which relates the intermediate and basic rocks to the adamellites. The vectors suggest that the basic and intermediate rocks could be crystallised from a mantle derived magma subsequently contaminated with either Dalradian or Lewisian metasediment i.e. relatively low Rb/Sr ratio and high initial strontium ratio. Only 0.05% assimilation of either Dalradian or Lewisian type metasediment are required to generate initial strontium isotope ratios of 0.707 from a mantle parent. A portion of this magma may then be further contaminated ($\sim 0.5\%$ assimilation) with material showing a SUP type initial ratio to produce the range of ratios observed in the adamellites. SUP sediments are not recorded north of the Highland Boundary Fault. However subduction

Fig. 8.13 Logarithmic, bivariate plot of Ba-Rb for the Juan Jorge Complex.



of SUP sediments during the late stages of the closing of the Iapetus Ocean, would provide a mechanism for the introduction of SUP type initial ratios into the lower crust. The above model is however only based on one isotope system and could be further constrained by neodymium, lead and oxygen isotope data.

8.5.2 Juan Jorge Complex

Both petrographic and chemical data suggest that the range of compositions seen in the Juan Jorge complex may be related by fractional crystallisation processes. The chemical variation frequently displays linear relationships for major and trace elements with respect to bulk rock MgO. There is no field evidence to suggest that contamination of the diorites or granites with country rock metasediments has occurred although quartz xenocrysts in micro diorite xenoliths (Chapter 4) may indicate a hybrid origin, at least for the xenoliths. The lack of any clear cumulate textures in the diorites and granites also suggests that these rocks may represent magma compositions. The bulk geochemical data for the intermediate rocks is also comparable with data from the more andesitic lavas from the Sidlaw Hills (Groome and Hall, 1974) which lie to the southeast of the Glen Doll Complex.

8.5.2.1 Trace element modelling

Four trace element pairs have been chosen to demonstrate the range of crystallising mineral phases which could generate the observed trends. Crystallisation of amphibole, biotite, plagioclase and spinel could produce the range of compositions (Figures 8.13 and 8.14). However small amounts of crystallisation

Fig. 8.14 Logarithmic, bivariate plot of Cr-Ni for the Juan Jorge Complex.

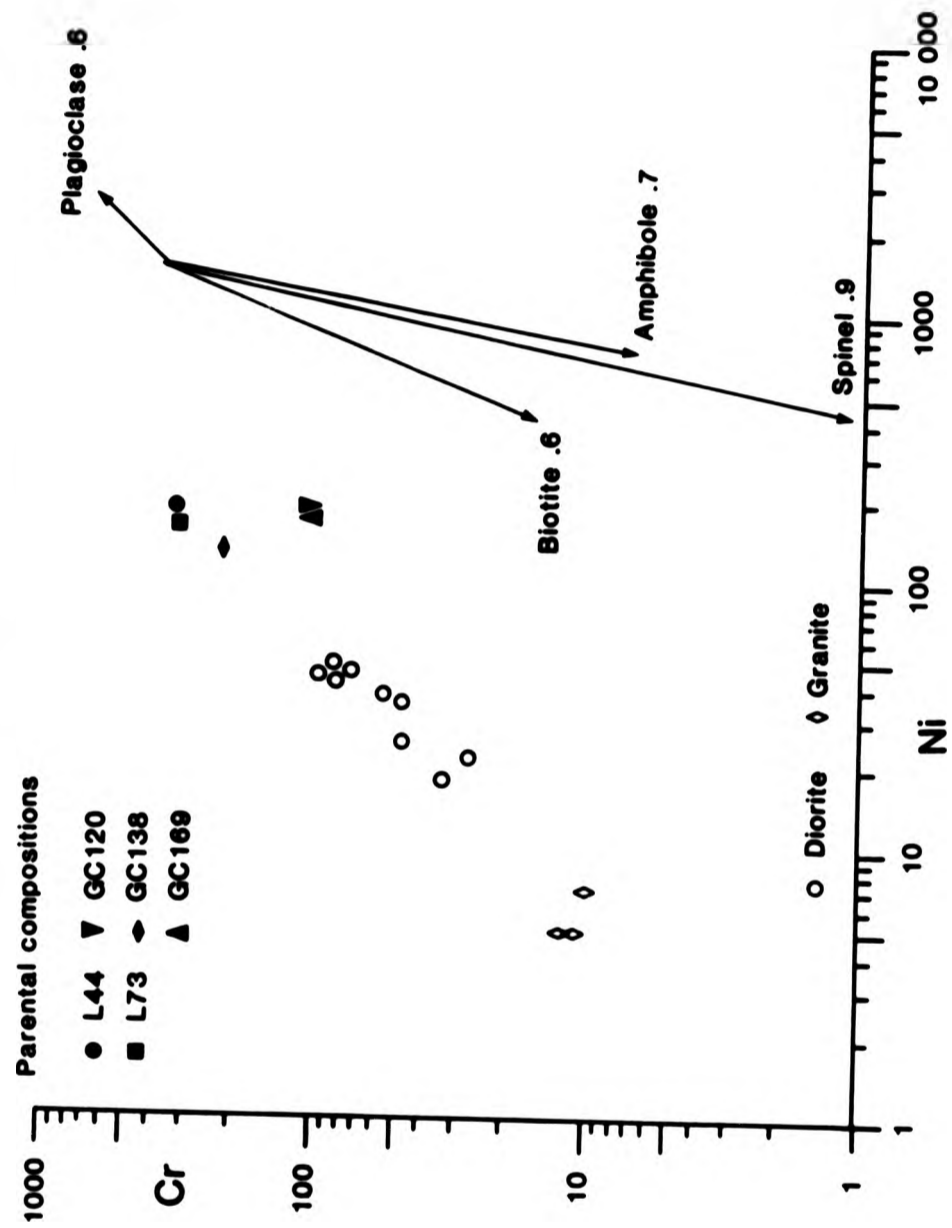
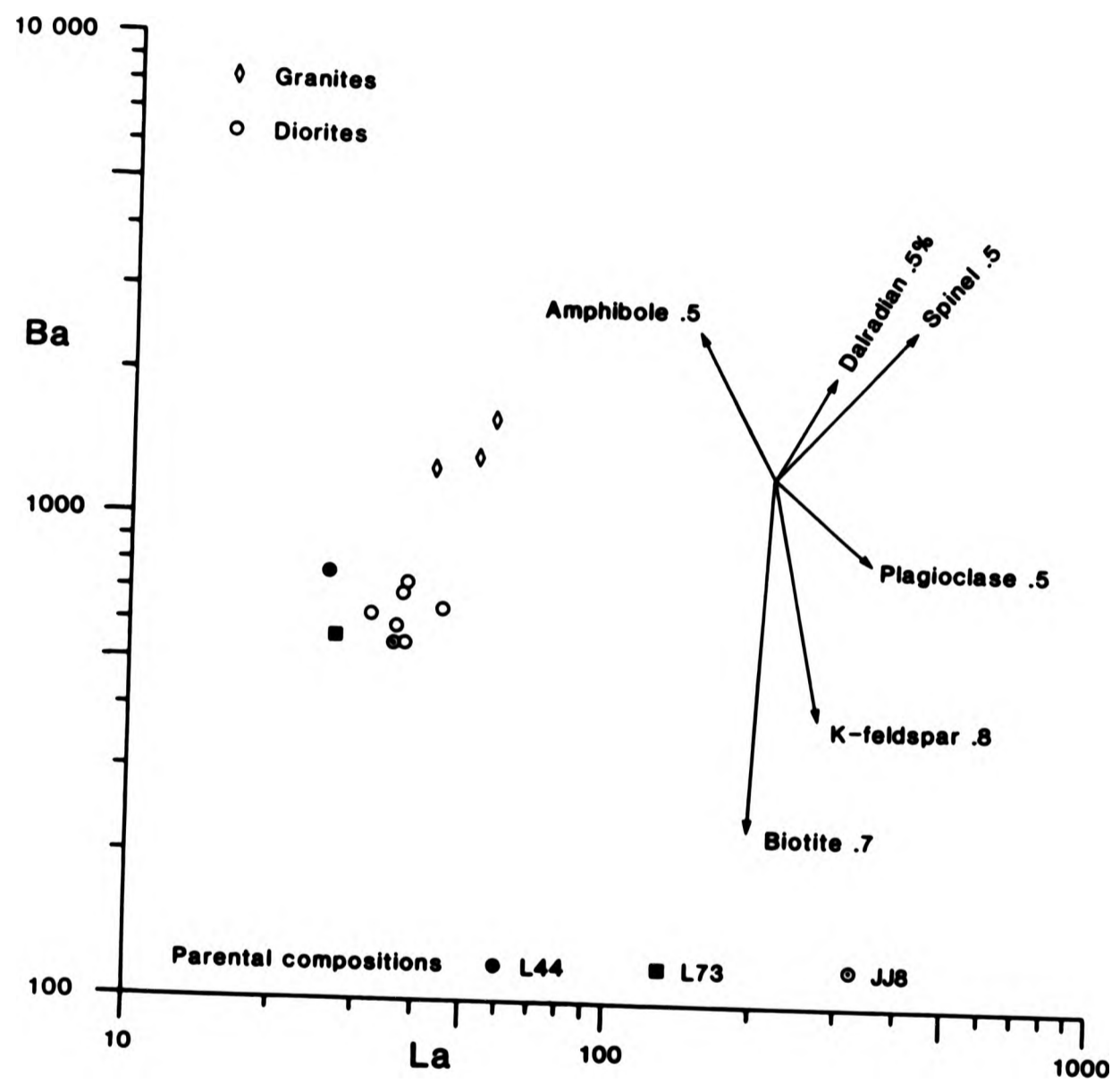


Fig. 8.15 Logarithmic, bivariate plot of Ba-La, Juan Jorge Complex

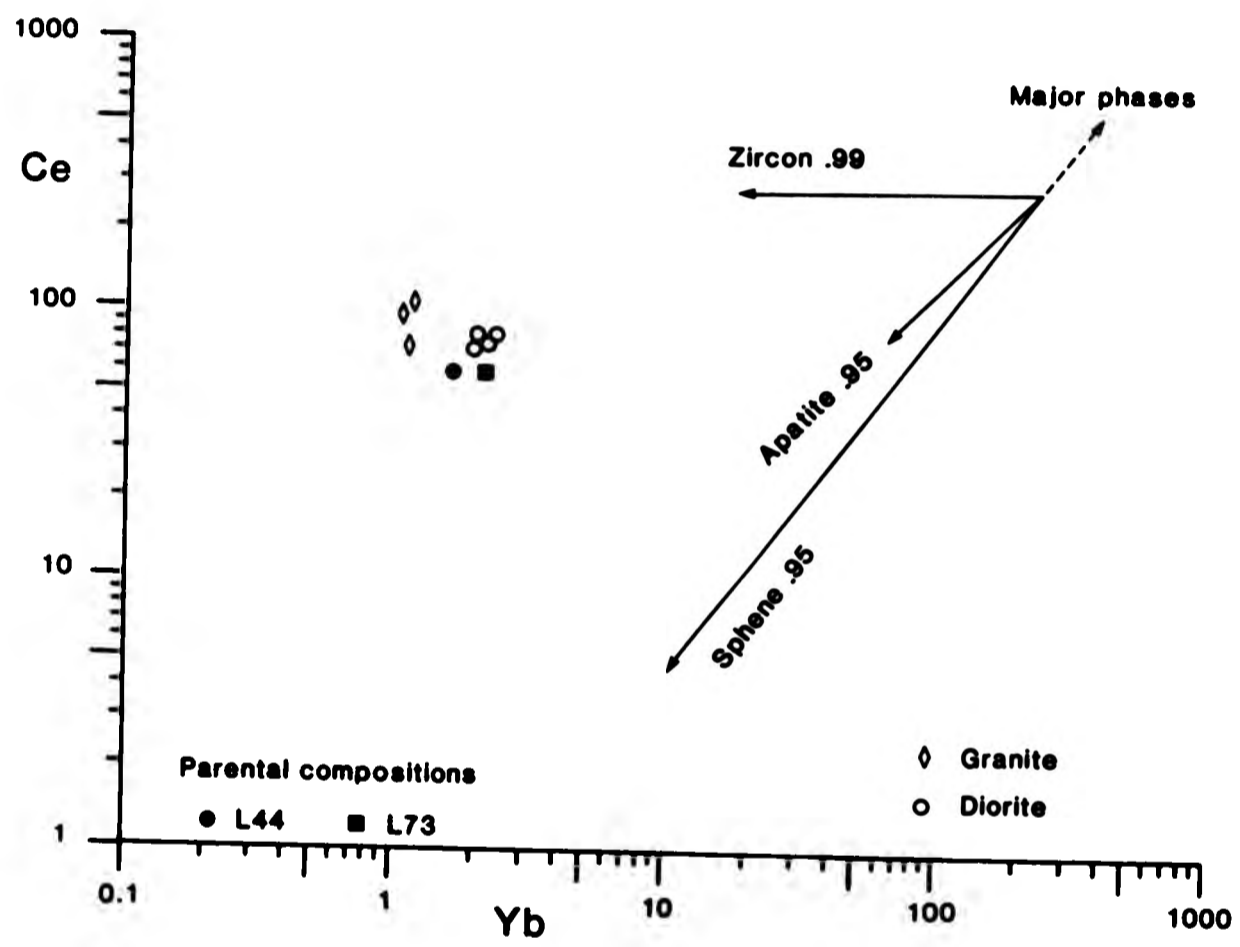


of biotite and K-Feldspar are required to generate the horizontal scatter of data seen in Figure 8.13. An increased modal abundance of biotite accompanied by a decrease in amphibole is observed towards the contact of the Juan Jorge diorite with the Lochnagar Granite. The bulk rock compositions also become more evolved towards this contact (See Chapter 3). The mineral vectors on the plot of Ba and La (Figure 8.15) similarly suggest that the crystallisation of amphibole, spinel and plagioclase could generate the observed chemical trends, with about 70% crystallisation required to generate granitic compositions i.e. high Ba samples.

The evolutionary path of a liquid, which would be generated by the assimilation of Dalradian metasediments, is also shown (Figure 8.15) for comparison with the Glen Doll Complex. Contamination is not thought to be an important process in the evolution of the complex. However, the vectors shown could explain the trend of the data, although the amount of assimilation is large and exceeds 1.5%.

To examine the effect of minor phase crystallisation, cerium and ytterbium data has been plotted (Figure 8.16). The mineral vectors indicate that very small amounts of crystallisation (<0.01%) of apatite ± sphene could produce the trend observed for the dioritic rocks. However, assuming a common parent for the granites and diorites, generation of the granitic compositions requires the initial crystallisation of a minor phase enriched in the HREE, such as zircon. To generate the data pattern displayed by the granitic rocks would then require the crystallisation of a mineral phase which would allow the level of ytterbium to remain constant while enriching successive liquids in cerium. A mineral

Fig. 8.16 Logarithmic, bivariate plot of Ce-Yb, Juan Jorge Complex



with these characteristics is not recorded in the complex. The separation of the diorites and granites on this diagram may indicate that the two rock types are derived from separate parental compositions. Further Ce and Yb data for more samples may separate the data into clearly distinctive trends which can then be more rigorously modelled.

8.5.2.2 Major element modelling

Most major and trace element variation in the Juan Jorge Complex could be explained by either of two processes (a) fractional crystallisation or (b) simple mixing of two end member compositions. However the bivariate plots display a broad scatter of data which precludes simple mixing to give the range of observed compositions. Fractional crystallisation of a single parent is thought to be the dominant fractionation process in the Juan Jorge Complex since no evidence exists suggesting that the rocks are formed from mixed magmas.

Using mineral data from the Juan Jorge complex itself, major element modelling can provide a fractional crystallisation model for the evolution of the complex. The parent composition chosen is that of the most mafic diorite, with 3.86% MgO and 57.21% SiO₂ while the daughter is the most evolved granite JJ9 which contains 0.81% MgO and 71.29% SiO₂. The resulting model (Table 8.11) suggests that 73.98% crystallisation of plagioclase (42.8%), amphibole (18.6%), magnetite (2.32%), apatite (0.68%) and sphene (1.96%) (Table 8.11) could evolve granite JJ9 from diorite JJ8. The amount of crystallisation is large (>70%) but is consistent with the results from trace element models. The one norm mis-fit (excluding

Table 8.11 Modelled data for the Juan Jorge Complex.

Oxide compositions of mineral phases used in modelled analysis

	PLAG	AMPH	IMT	AP	BI	SPH	JJ9	JJ8
SiO ₂	62.93	50.29	0.04	0.19	38.41	30.73	70.24	58.10
Al ₂ O ₃	25.76	5.98	0.11	0.00	14.41	1.08	15.55	17.16
FeO	0.27	14.09	96.69	0.05	18.74	1.44	2.49	7.15
MgO	0.01	14.50	0.03	0.00	13.31	0.00	0.80	3.92
CaO	5.58	12.26	0.00	56.61	0.00	28.11	1.57	6.01
Na ₂ O	5.20	0.89	0.00	0.03	0.13	0.00	4.17	3.66
K ₂ O	0.24	0.54	0.00	0.00	9.76	0.00	4.49	2.11
TiO ₂	0.00	1.05	0.07	0.00	4.71	38.50	0.51	1.42
P ₂ O ₅	0.00	0.00	0.00	43.11	0.00	0.00	0.13	0.33
MnO	0.00	0.40	0.06	0.00	0.53	0.14	0.06	0.13

PLAG=JJ7/PL/57C, AMPH=JJ8/AM/35R, MT=JJ8/OX/77C, AP=JJ4/AP/22C, BI=JJ17/BI/52C, SPH=JJ17/SH/87C, Daughter=JJ9, Parent=JJ8

Modal composition which minimises one norm misfit

PLAG	AMPH	BIOTITE	MAGNETITE	APATITE	SPHENE	JJ9
42.83	18.60	7.59	2.32	0.68	1.96	26.02

Comparison of original and modelled rock composition

	Rock	Model	Misfit
SiO ₂	58.10	58.10	0.0
Al ₂ O ₃	17.16	17.31	-0.8
FeO	7.15	7.15	0.0
MgO	3.92	3.92	0.0
CaO	6.01	6.01	0.0
Na ₂ O	3.66	3.49	1.7
K ₂ O	2.11	2.11	0.0
TiO ₂	1.42	1.44	-0.2
P ₂ O ₅	0.33	0.33	0.0
MnO	0.13	0.13	-0.3

one norm misfit = 3 (Excluding MnO = 2.7)

MnO) is low at 2.7.

This crystallising assemblage is consistent with observed mineralogy. Large euhedral crystals of sphene are particularly common in some of the Juan Jorge diorites. It is notable that the mineral extract is of dioritic composition. If this extract is recast to 100% the proportion of each mineral would be; 50% plagioclase, 25% amphibole, 10% biotite, 3.1% magnetite, 0.9% apatite and 2.6% sphene. This modal mineralogy (with the exception of a large percentage of sphene) compares closely with the diorite cumulates from the Glen Doll Complex.

8.6 Conclusions

8.6.1 Glen Doll Complex

8.6.1.1 Intermediate and basic rocks

Major and trace element models suggest that crystal fractionation combined with assimilation are important factors in the evolution of the intermediate and basic rocks in the complex at the level of observation. Trace element mineral vectors are consistent with the accumulation of olivine in some of the gabbros, while major element models support accumulation of iron oxides in the high iron/titanium diorites.

Mantle-normalised diagrams can be used to summarise data for a number of elements (Figure 8.17). These diagrams display patterns consistent with the major and trace element models. The olivine gabbros (e.g. GC88) display a relatively smooth profile with small troughs for Sr, Eu, P, and Ti while the gabbros (e.g. GC82) typically have a large positive peak for strontium (Figure 8.17)

Fig. 8.17 Incompatible element mantle-normalised diagram for the basic rocks of the Glen Doll Complex.

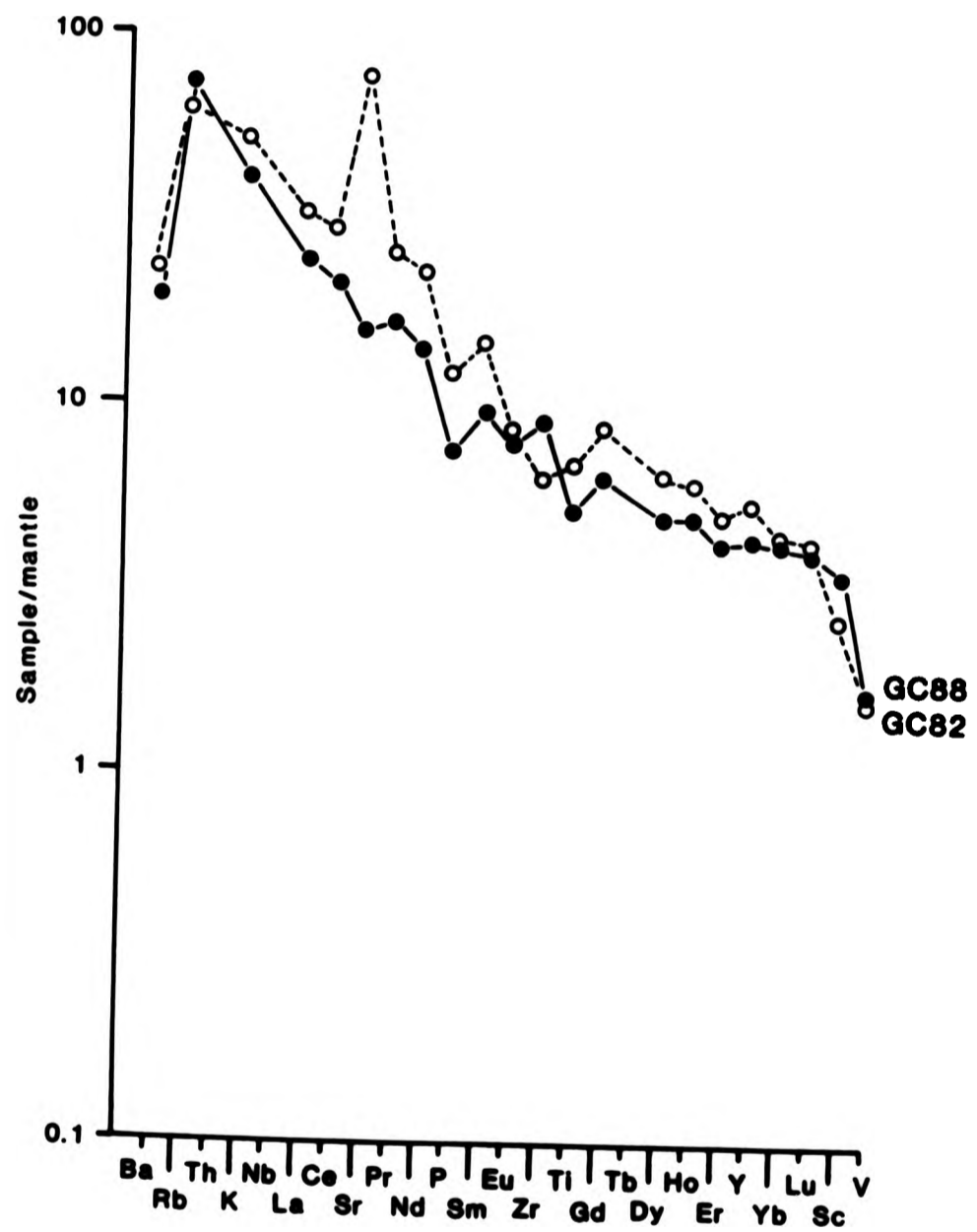
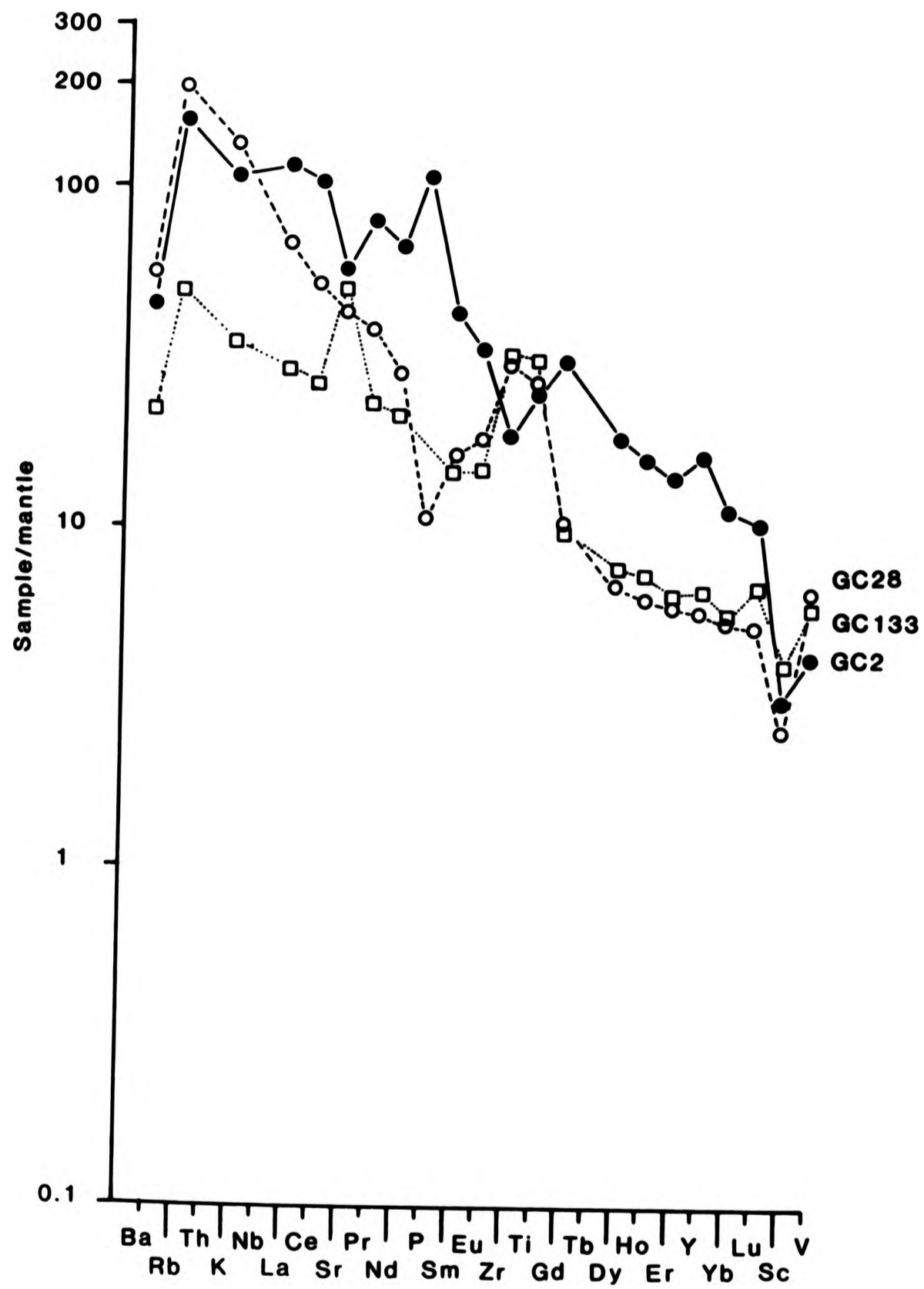


Fig. 8.18 Incompatible-element mantle-normalised diagram for some diorites from the Glen Doll Complex



suggesting that accumulation of plagioclase has occurred (Chapter 4). The high iron-titanium diorites (Figure 8.18) display a range of features including large positive or negative peaks for Sr, Ti, and P suggesting that the fractionation of mineral phases such as plagioclase, ilmenite, and apatite has occurred mineralogical features which are consistent with major and trace element models. The diorites generally contain a greater abundance of the elements represented on these diagrams than the gabbros, and commonly display steeper profiles. The removal of olivine, cpx and opx from a basic liquid, to form the cumulate rocks, could cause an increase in the abundance of titanium, iron, phosphorus and potassium in the liquid. This would in turn promote the crystallisation of magnetite, ilmenite and apatite from the evolving liquid.

The isotopic modelling suggests that the basic and intermediate rocks may result from a mantle derived parent magma subsequently contaminated by relatively small amounts (<1%) of lower or upper crustal material. Strontium isotope data alone, allows initial modelling to be attempted, but it is clear that other isotope systems would further characterise the source of contamination of the intermediate and basic rocks. Strontium isotope data suggests that a contaminant with a low Rb/Sr ratio coupled with a high $^{87}\text{Sr}/^{86}\text{Sr}$ ratio is required to generate the observed compositions.

8.6.1.2 Adamellites

The adamellite margin of the Glen Doll complex has been modelled as a separate intrusive unit since field evidence suggests that the emplacement of the adamellite post-dates that of the dior-

ites. Trace element models suggest that that much of the observed variation could result from crystal fractionation of a single magma with the crystallisation of amphibole, plagioclase \pm biotite, K-feldspar, sphene and apatite. The amount of crystallisation required to generate the adamellite compositions is large if a diorite parental composition is used. Therefore a large reservoir of source material is required to generate the adamellites from a parent such as GC138. The data suggests that the adamellites may not have crystallised in a closed system.

The chemical consequences of contamination of the magma by assimilation of Dalradian metasediments are not readily separable from those produced by fractional crystallisation of, for example, amphibole (Figure 8.8). In general the trace element models suggest that assimilation of Dalradian metasediments is not required to generate the observed chemical trends. However, strontium isotopes display a wide range of initial ratios and preliminary modelling supports the assimilation of SUP type sediment. Contamination must have occurred therefore in the lower crust. The isotope heterogenities in the adamellites suggest that a single magma chamber source is unlikely. Subduction of SUP type sediments could provide a possible source for contamination.

8.6.2 Juan Jorge Complex

Geochemical distribution patterns displayed by rocks from the Juan Jorge complex contrast with those from the Glen Doll complex. Both major and trace element models indicate that fractional crystallisation of a single parent magma could produce the observed geochemical trends. The modelled data requires up to 60% crystallisation of amphibole, plagioclase, spinel \pm biotite and K-feldspar

ites. Trace element models suggest that that much of the observed variation could result from crystal fractionation of a single magma with the crystallisation of amphibole, plagioclase \pm biotite, K-feldspar, sphene and apatite. The amount of crystallisation required to generate the adamellite compositions is large if a diorite parental composition is used. Therefore a large reservoir of source material is required to generate the adamellites from a parent such as GC138. The data suggests that the adamellites may not have crystallised in a closed system.

The chemical consequences of contamination of the magma by assimilation of Dalradian metasediments are not readily separable from those produced by fractional crystallisation of, for example, amphibole (Figure 8.8). In general the trace element models suggest that assimilation of Dalradian metasediments is not required to generate the observed chemical trends. However, strontium isotopes display a wide range of initial ratios and preliminary modelling supports the assimilation of SUP type sediment. Contamination must have occurred therefore in the lower crust. The isotope heterogeneities in the adamellites suggest that a single magma chamber source is unlikely. Subduction of SUP type sediments could provide a possible source for contamination.

8.6.2 Juan Jorge Complex

Geochemical distribution patterns displayed by rocks from the Juan Jorge complex contrast with those from the Glen Doll complex. Both major and trace element models indicate that fractional crystallisation of a single parent magma could produce the observed geochemical trends. The modelled data requires up to 60% crystallisation of amphibole, plagioclase, spinel \pm biotite and K-feldspar

to generate observed trends. The large amounts of crystallisation required to generate the granitic members of the complex (e.g. Figure 8.13) would require a relatively large magma source since the exposed granites comprise 10% of the complex. This may indicate that the Juan Jorge rocks are the result of a mixed magma source. However the linear variation displayed by the major and trace elements prevent any resolution of these sources. Minor mineral phase crystallisation (Figure 8.16) is best explained by a separate magma for the diorites and granites since the granitic compositions cannot be generated from the dioritic ones by crystallisation of either apatite, zircon or sphene.

Chapter 9

Conclusions

9.1 Introduction

This work examines the petrogenesis and geochemistry of some late Caledonian calc-alkaline plutonic complexes in Scotland. The Glen Doll and Juan Jorge Complexes were chosen for study, because the level of exposure was thought to be good, and a wide range of fresh rock types was expected. These expectations have been fulfilled although, the low valley sides are commonly covered with till which obscures the solid geology. The range of lithologies, particularly within the Glen Doll Complex, is extensive and includes olivine gabbro, gabbro, pyroxene diorite, hornblende diorite, monzonite, quartz-mica diorite, adamellite and granite. Both complexes have been intruded by a series of later intermediate and acid dykes.

The study for this thesis has shown that the Glen Doll and Juan Jorge Complexes are of contrasting character both petrologically and geochemically, and exemplify a wide range of petrological processes. The Glen Doll Complex contains a wide range of rock types including relatively primitive compositions, and is similar to the Garabal Hill Complex (Nockolds, 1940). Petrography and geochemistry suggest that cumulate processes have operated, but the dioritic rocks in particular, have also suffered contamination by partial assimilation of Dalradian metasediments. In contrast, the Juan Jorge Complex displays features comparable with many other late Caledonian plutonic complexes. The range of lithologies is similar to that seen for example in the Cruachan Granite in the Etive Complex (Perkins, 1986). The geochemical trends in the Juan

Jorge Complex dominantly reflect processes of fractional crystallisation and there is no evidence of contamination with crustal material.

9.2 Glen Doll Complex

The Glen Doll Complex is dominated by heterogenous (both texturally and chemically), xenolith hornblende- and pyroxene-diorites which together form 80% of the complex. There is an area of gabbro in the southwest, around the Kilbo Burn, which includes an olivine-bearing facies, and gabbros outcrop in the NE in the valley of the Moulzie Burn (Figure 3.1). Field evidence and petrographic data suggest that the diorites and gabbros are closely related (Chapter 4). A later separate unit of adamellite occurs as a discontinuous ring around the perimeter of the complex. The external contacts of the complex are near vertical in the south, north and east, but in the SW the contact is inferred to be sub-horizontal (Durig, 1981).

9.2.1 The cumulate rocks

The gabbros, which occur in the SW and NE part of the complex, display near-vertical wall-parallel layering. In contrast, the diorites contain horizontally layered units in the SW part of the complex and a typically horizontal igneous fabric occurs through much of the diorite. The diorites therefore display floor-parallel layering.

The observed textural data in both the pyroxene and hornblende diorites suggests the early crystallisation of unzoned calcic plagioclase and magnesian ortho- and clino- pyroxenes as cumulus

phases. These minerals are followed in the hornblende diorites by the crystallisation of zoned plagioclase, brown amphibole, ilmenite and magnetite. In the pyroxene diorites however, ophitic textures indicate the crystallisation of additional cpx; primary hornblende and zoned plagioclase then crystallised accompanied by ilmenite and magnetite. The interstitial minerals are the last minerals to crystallise in both rock types (Chapter 4). These minerals include green amphibole, sphene, quartz, K-feldspar, and the rims of zoned plagioclase feldspars.

The intercumulus crystallisation of the two types of diorite initially follows two paths, one dominated by crystallisation under wet conditions (indicated by hornblende) while the other crystallised under dry conditions (indicated by cpx). Both the pyroxene-bearing and pyroxene-free diorites show the late stage alteration of pyroxene to subsolidus actinolitic amphibole (Plate 4.4).

The textures displayed by the Glen Doll gabbros are plagioclase and pyroxene orthocumulates. The textural information suggests the early crystallisation of plagioclase, cpx and possibly olivine (now altered to serpentine). These minerals are followed in some gabbros by the crystallisation of opx and plagioclase with late-stage intercumulus phlogopite, apatite and rare magnetite. In other gabbros, the initial stages of crystallisation of interstitial opx and brown pargasitic amphibole are followed by biotite, magnetite and apatite. The interstitial amphibole in these gabbros is thought to have crystallised at a higher temperature than interstitial amphibole in the diorites, suggesting that the intercumulus liquid in the gabbros became significantly hydrous at a higher

Mg/Fe ratio than in the dioritic rocks. There was therefore no continual build up of H_2O in the magma chamber but only in the interstitial (intercumulus) liquid (Chapter 4). This may therefore indicate a periodic venting of H_2O from the magma chamber.

In addition to the above gabbros, some examples of olivine gabbros are recorded. These typically have an anhydrous assemblage and contain up to 40% cumulus olivine in addition to plagioclase, opx and cpx. Most plagioclase feldspar primocrysts (typically An_{50}) in the olivine gabbros are unzoned. This general lack of zoning is thought to result from insitu crystallisation and convective fractionation (Sparks et al., 1984). The latter process causes a change in the composition of the intercumulus fluid locally. Convection is driven by local changes in magma composition as crystallisation proceeds. The occurrence of relatively sodic plagioclase in the olivine gabbros suggests that the intercumulus liquid was part of an open system. In addition, an abrupt change is observed in the Kilbo Burn section between olivine-bearing and olivine-free facies (Figure 3.7). This may indicate that the magma was only intermittently in the olivine stability field. The incoming of olivine is best explained by a periodic recharging of magma locally.

Local convective fractionation could lead to the formation of layering, such as that observed in the gabbroic rocks, without the necessity to invoke a mechanism such as large-scale convection for which there is little evidence.

When compared with the near contemporaneous calc-alkaline lavas of the Lorne Lava Suite, whose geochemistry and magmatic evo-

lution is well described (Thirlwall, 1982) and which probably represent a liquid line of descent, the gabbros and diorites typically lie off these trends (Figure 8.1). The gabbros are characteristically depleted in elements such as titanium, potassium and phosphorus, which occur only in the intercumulus minerals. In contrast the diorites contain a greater abundance of iron, titanium and phosphorus than, for example, the Lorne Lavas, supporting a cumulate origin for this rock type.

Initial $^{87}\text{Sr}/^{86}\text{Sr}$ ratios (Table 7.1) in the basic and intermediate rocks suggest that a mantle-derived parent magma, subsequently contaminated with more radiogenic upper crustal material could give rise to the observed compositions.

9.2.2 Contamination

Partially assimilated rafted metasedimentary xenoliths occur throughout the dioritic rocks in the complex. These xenoliths provide an observable source of contamination within the complex. Geochemical features such as enhanced levels of zinc in some of the diorites cannot be readily explained in terms of fractional crystallisation. These features are, however, consistent with contamination of a parent magma with crustally derived material enriched in zinc. Metasediments containing strata-bound zinc mineralisation are recorded in Middle Dalradian rocks of the Aberfeldy area, SW of the Glen Doll Complex (Smith et al., 1984). Strontium isotope data provide further evidence of crustal contamination within the complex. The high and variable initial Sr-isotope ratios recorded in the diorites (and adamellites) could not be inherited solely from a mantle source. Strontium isotope and zinc heterogeneities in the diorites suggest that contamination did not

affect the bulk magma as this would probably lead to a uniform $^{87}\text{Sr}/^{86}\text{Sr}$ ratio throughout the rocks.

Initial $^{87}\text{Sr}/^{86}\text{Sr}$ ratios (Table 7.1), suggest that the gabbros crystallised from a mantle-derived magma. Whether the liquids had been subsequently modified by interaction with lower crust, is unclear since the range of values falls within the suggested possible range of mantle heterogeneity. Data from other isotope systems would help to establish if the magmas are derived from an 'enriched' mantle source or from a crustally contaminated 'normal' mantle.

The rafted metasedimentary xenoliths provide a local source of contamination within the cumulate pile in the dioritic rocks. Small xenoliths of restite material also occur within samples, providing evidence for contamination. Studies by Sparks et al., (1984) suggest that local changes in the chemistry of the interstitial fluids, due to crystallisation due to changes in H_2O and O_2 fugacity, can lead to local convection within the intercumulus fluid. In the Glen Doll Complex, coarse-grained appinitic bodies provide evidence of the migration of interstitial fluids enriched in volatiles. The timing of this event was relatively late. The igneous fabric in the coarse grained facies is frequently disturbed or destroyed by the upward movement of interstitial fluids. These facies are commonly located vertically above the sites of partially melted rafted xenoliths, providing a source for the high volatile content of the interstitial liquids and therefore a mode of contamination (Chapter 3). The release of partial melts from the xenoliths may also act as a trigger to local convection.

9.2.3 History of the rafted xenoliths

These xenoliths are thought to be derived from the now eroded Middle-Upper Dalradian above the magma chamber. Incorporation in an essentially fluid magma, would lead to rapid sinking of the relatively dense xenoliths. Partial probably occurred close to the floor of the magma chamber under a limited cover of cumulates. With increased loading from above, as the cumulate pile increased in thickness, partial melts from the xenoliths would be expelled, leading to contamination of the intercumulus fluid.

9.2.4 Relative importance of cumulate processes and contamination

The cumulate processes provide a mechanism whereby, (1) the gross structures within the rocks are established i.e. wall and floor parallel layering, (2) the chemistry of the major silicate mineral phases is controlled, and (3) the bulk geochemistry is controlled.

Contamination provides a mechanism for the development of isotopic and trace element heterogeneities which cannot be easily explained by crystal fractionation processes alone.

9.2.5 Adamellites

The adamellites are variable in grain size and colour index. They are typically medium to coarse grained and pink in colour. However, fine-grained more mafic granodioritic patches occur locally within the adamellite. Field data shows that the adamellites were intruded after the crystallisation of the intermediate and

basic rocks within the Glen Doll Complex (Plate 3.9).

The adamellites are composed of variable modal proportions of biotite, amphibole, K-feldspar, plagioclase and quartz. Bulk-rock major and trace element data shows linear trends and are consistent with either mixing of two granitic-end members or fractional crystallisation of a single parent magma. The REE data displays a clear overlap with the intermediate rock compositions of the Glen Doll Complex (Figure 6.27) but trace element models suggest that the adamellites are not derived from a dioritic parent magma.

Initial $^{87}\text{Sr}/^{86}\text{Sr}$ ratios provide additional evidence for a mixed or hybrid history for the adamellites. The wide range of initial ratios coupled with high ratio values, points to crustal assimilation as a possible mechanism of contamination. Assimilation would allow for the development of heterogeneous initial ratios within a small body of magma. Marginal melting of the country rocks at depth during the emplacement of the adamellites could allow the development of heterogeneity in initial $^{87}\text{Sr}/^{86}\text{Sr}$ ratios and prevent a single homogenous ratio developing throughout the body.

9.3 Juan Jorge Complex

The Juan Jorge Complex contrasts sharply with the Glen Doll Complex which is intruded only 1km to the south. The character of the dioritic facies in the Juan Jorge Complex is substantially different to that described from Glen Doll. The former is dominantly composed of a medium to coarse-grained leucocratic quartz-mica diorite. An igneous lamination, is recorded in many of the diorites. The orientation of the fabric is variable but, unlike Glen

Doll, tends to be vertical in the central part of the complex. The diorites are homogeneous over large distances (>1km), changes in mineralogy (e.g. an increase in modal biotite accompanied by a decrease in modal amphibole) are subtle and essentially associated with closeness of the contact with the Lochnagar granite.

Two areas of granite occur within the complex, the Juan Jorge and Gourock Granite (Oldershaw, 1958). Both are composed of homogeneous pink porphyritic granite commonly containing abundant xenoliths of fine-grained metasediment and microdiorite. The intrusion of the granites postdates the crystallisation of the dioritic rocks.

A characteristic feature of the Juan Jorge rocks, is the absence of any trace of pyroxenes and consequently of subsolidus amphibole. This contrasts strongly with the Glen Doll Complex where pyroxenes are common. The modal mineralogy of the dioritic rocks in the Juan Jorge Complex is dominated by primary green amphibole, plagioclase and biotite, while amphibole is absent from the granitic rocks (Chapter 4).

The distribution of the major and trace elements is frequently similar to the Glen Doll adamellites, although the two display contrasting REE profiles. The distribution of the REE in the Juan Jorge rocks is thought to be controlled by the crystallisation of minor phases, particularly sphene and apatite in the diorites, and zircon, apatite and sphene in the granitic rocks (Chapter 7). The bulk rock compositions fall on the liquid line of descent shown by the coeval calc-alkaline lavas, and probably represent magma compositions. Major and trace-element models show that fractional

crystallisation of a single magma could derive both the intermediate and acid rocks although the linear variation trends could conceivably be the result of mixed magmas.

9.4 Dykes

A series of acid and intermediate dykes cut both the Glen Doll and Juan Jorge Complexes. The dykes are typically vertical and display a common strike, varying from 020-030° (Figure 3.1). This trend is broadly consistent with the regional trend of Caledonian dykes in Scotland. The acid dykes are either quartz-feldspar, porphyries or aplites. The latter, probably crystallised from residual liquids and are the final rocks to crystallise in both complexes. The intermediate dykes are composed of microdiorite. Field evidence at the Bridge Outcrops suggests that, locally, the intrusion of acid and some of the intermediate magma is broadly synchronous. The Bridge Outcrops are composed of dyke-like bodies of coarse-grained porphyritic granite containing broken blocks of banded and unbanded gneiss, foliated microdiorite and fine-grained microdiorite. Microdiorite is seen chilled against the granite but is also cut by it. The observed textures are thought to result from contemporaneous intrusion of acid and intermediate magmas. Other evidence from xenoliths of gneiss, themselves intruded by microdiorite dykes prior to incorporation in the magma, suggest that at least locally some of the microdiorite dykes predate the crystallisation of the intrusive rocks.

9.5 Development of future work

Three main areas of work are envisaged:

- (a) Field work- detailed studies of additional outcrops would allow

a more complete study of contamination processes.

(b) Mineral chemistry- further electron microprobe analysis of cumulus and intercumulus mineral phases would allow a better evaluation of the relationships between the mineral phases. In addition, trace element analysis by ion probe of the mineral phases, would allow more accurate partition coefficient data to be used in modelling schemes and enable a better evaluation of a parental liquid composition to be made.

(c) Isotopes- strontium isotope measurements of separated mineral phases may provide an isochron and age for the complex. In addition strontium isotope measurements of cumulus and intercumulus minerals may indicate if the two have crystallised from different liquids. Nd, Pb and O isotope data would allow a better evaluation of potential sources for crustal contamination.

9.6 Comparison of the study areas with other Scottish late Caledonian calc-alkaline plutonic complexes.

A review of the available literature on the late Caledonian granitoids (Chapter 2), reveals that most are composed of relatively large, homogeneous granitic bodies (e.g. Nockolds and Mitchell, 1946; Halliday et al., 1985; Perkins, 1986). The range of lithologies within any one complex is commonly restricted to the intermediate to acid members of the calc-alkaline suite (e.g. Strontian Complex; MacGregor and Kennedy, 1932). The Juan Jorge Complex is perhaps comparable, in terms of lithology and chemistry, with these more evolved complexes.

Relatively few of the late Caledonian complexes contain a wider range of lithologies although examples include Garabal Hill

(ultra-basic to acid; Nockolds, 1940) and Loch Doon (intermediate to acid; Brown et al., 1979). The Glen Doll Complex compares most closely with the former. The range of lithologies from the Garabal Hill Complex, including the ultra-basic rocks, was considered by Nockolds (1940) to result from fractionation of a single parent magma, represented by the pyroxene-mica diorites exposed in the complex. Strontium-isotope data from Garabal Hill supports a single, mantle-derived parent magma for that range of lithologies (Summerhayes, 1966). Large scale contamination is not thought to be an important processes in the evolution of the Garabal Hill Complex, although marginal contamination with Dalradian metasediments does occur (Summerhayes, 1966). It is concluded that, although both complexes are broadly dominated by fractional crystallisation and accumulation, the Glen Doll Complex differs in that no Rb/Sr isochron can be drawn because individual members of the complex display different strontium isotope characteristics.

The most mafic facies recorded in the Loch Doon Complex is a hypersthene diorite (Brown et al., 1979), similar to some of the pyroxene diorites in the Glen Doll Complex. Field, geochemical, petrographic and strontium-isotope data suggest, however, that the range of lithologies and zonal structure displayed in the Loch Doon complex are consistent with in-situ fractional crystallisation (Tindle and Pearce, 1981; 1983). The complex is comparable, therefore with the Juan Jorge Complex, since the rocks probably represent magma compositions.

The Glen Tilt complex, Perthshire, is composed dominantly of granite and a rather basic diorite (Deer, 1938; 1950; 1953). A recent study (C. Turner pers. comm. 1987) of the complex has

shown that the dioritic rocks display variable initial strontium isotope ratios from 0.70602 to 0.71631 (similar to the Glen Doll Complex) while the granitic members of the complex define a good isochron dating the complex at 393 ± 5 Ma with an initial $^{87}\text{Sr}/^{86}\text{Sr}$ ratio of 0.71243 (C. Turner pers. comm. 1987).

9.7 Summary

The Glen Doll Complex contrasts petrographically and geochemically with most other late Caledonian calc-alkaline plutonic complexes. The study of the complex has revealed clear cumulate characteristics within the intermediate rocks as well as in the basic rocks. The cumulate assemblages are, however, significantly different. The geochemical data, in particular, has been used to discriminate between liquid and cumulate compositions in the range of rock types. Contamination of the magmas with crustal material plays an important role and allows local heterogeneities in texture, bulk chemistry and Sr isotopes to be developed.

In contrast, the rocks of the Juan Jorge Complex appear to represent liquid compositions and therefore do not display cumulate textures. Fractional crystallization is thought to be the dominant process although without further isotop data, magma mixing cannot be ruled out in the evolution of the complex.

References

- Akaad, M.K. 1956. The northern aureole of the Ardara pluton, County Donegal. Geol. Mag. 93, 377-392
- Akaad, M.K. 1956. The Ardara granitic diapir of County Donegal. Q. J. Geol. Soc. Lond. 112, 263-288
- de Albuquerque, C.A.R. 1971. Petrochemistry of a series of granitic rocks from Northern Portugal. Bull. Geol. Soc. Am. 82, 2783-2798.
- de Albuquerque, C.A.R. 1973. The origin of enclaves in granitic rocks from Northern Portugal. Spec. Publ. Geol. Soc. S. Africa 3, 479-493.
- Alderton, D.H.M., Pearce, J.A. and Potts, P.J. 1980. Rare earth element mobility during granite alteration: evidence from S.W. England. Earth Planet. Sci. Lett. 49, 149-165.
- Allegre, C.J. and Minster, J.F. 1978. Quantitative models of trace element behaviour in magmatic processes. Earth Planet. Sci. Lett. 38, 1-25
- Anderson, A.T. 1976. Magma mixing: Petrological process and volcanological tool. J. Volcan. Geotherm. Res. 1, 3-33
- Anderson, J.G.C. 1935. The Arrochar intrusive complex. Geol. Mag. 72, 263-282
- Anderson, J.G.C. 1935. The marginal intrusions of Ben Nevis. Trans. Geol. Soc. Glasgow 19, 225-269.
- Anderson, J.G.C. 1937. The Etive complex. Q. J. Geol. Soc. Lond. 93, 487-533

- Arth, J.G. and Hanson, G.A. 1972. Quartz diorites derived by partial melting of eclogite or amphibolite at mantle depths. Contrib. Mineral. Petrol. 37, 161-174
- Bailey, E.B. 1960. The geology of Ben Nevis and Glen Coe. Memoir of the Geol. Surv. UK
- Bamford, D., Nunn, K., Prodehl, C. and Jacob, B. 1977. LISPB-111 Upper crustal structure of northern Britain. J. Geol. Soc. Lond. 133, 481-488.
- Banks, R. 1979. The use of linear programming in the analysis of petrological mixing problems. Contrib. Mineral. Petrol. 70, 237-244
- Barrow, G. 1893. On the intrusion of muscovite-biotite gneiss in the south-eastern highlands of Scotland and its accompanying metamorphism. Q. J. Geol. Soc. Lond 49, 330-358
- Barrow, G. and Cunningham-Craig, E.H. 1912. The geology of the districts of Braemar, Ballater and Glen Clova. Memoir Geol. Survey Scotland.
- Baxter, A.N., Upton, B.G.J. and White, W.M. 1985. Petrology and geochemistry of Rodrigues Island, Indian Ocean. Contrib. Mineral. Petrol. 89, 90-101.
- Bell, K. 1968. The age relations and provenance of the Dalradian series of Scotland. Bull. Geol. Soc. Am. 79, 1167-1194
- Berlin, R. and Henderson, C.M.B. 1968. A re-interpretation of Sr and Ca fractionation trends in plagioclase from basic rocks. Earth Planet. Sci. Lett. 4, 79-83

- Rest, M.G. 1963 Petrology of the Guadalupe Igneous Complex, SW Sierra Nevada foothills, California. J. Pet. 4, 223-259
- Best, M.G. and Mercy, E.L.P. 1967. Composition and crystallisation of mafic minerals in the Guadalupe Igneous Complex, California. Am. Mineral. 52, 436-474.
- Binns, R. 1965. The mineralogy of metamorphosed basic rocks from the Willyana Complex, Broken Hill district, New South Wales. Pt. 1, Hornblendes. Min. Mag. 35, 306-326.
- Bishop, A.C. 1964. The petrogenesis of hornblende, mica-lamprophyre dykes at South Hill, Jersey, C.I. Geol. Mag. 101, 302-313.
- Bishop, A.C. and French, W.J. 1982. Nature and origin of meladiorite layers in northern Guernsey, Channel Islands. Min. Mag. 46, 301-321
- Bowen, N.L. and Tuttle, O.F. 1953. Beginning of melting of some natural granites. Carnegie Inst. Washington. Ann. Rep. Dir. Geophys. Lab. 52, 1952-1953.
- Bowes, D. 1962. Kentallanite - lamprophyre - granite age relationships at Kentallan, Argyll. Geol. Mag. 99, 118-122.
- Bowes, D.R. and McArthur, A.C. 1976. Nature and genesis of the appinite suite. Krystalinikum 12, 31-46
- Bradbury, H.J. 1979. Migmatization, deformation and porphyroblasts growth in the dalradian of Tayside, Scotland. In The Caledonides of the British Isles- reviewed ed. A.L. Harris, C.H. Holland and B.E. Leake. Geol. Soc. Spec. Pub. 8
- Bradshaw, R., Plant, A.C., Burke, K.C. and Leake, B.E. 1969. The Oughterard granite, Connemara, Co. Galway. Proc. R. Irish.

Acad. 68B, 39-65

- Van Breemen, O. and Bluck, B.J. 1981. Episodic granite plutonism in the Scottish Caledonides. Nature 291, 113-117.
- Brindley, J.C. 1970. Appinitic intrusions associated with the Leinster granite, Ireland. Proc. R. Irish Acad. 70B, 93-104
- Briqueu, L. and Lancelot, J.R. 1979. Rb-Sr systematics and crustal contamination models for calc-alkaline igneous rocks. Earth Planet. Sci. Lett. 43, 385-396
- Brown, G.C., Cassidy, J., Tindle, A.G. and Hughes, D.J. 1979. The Loch Doon granite: an example of granite petrogenesis in the British Caledonides. J. Geol. Soc. Lond. 136, 745-753
- Brown, G.C. and Locke, C.A. 1979. Space-time variation in British Caledonian granites: some geophysical correlations. Earth Planet. Sci. Lett. 45, 69-79.
- Brown, M., Topley, C.G. and Power, G.M. 1980. The origin of the dioritic and associated rocks of Chouet, N.W. Guernsey, Channel Islands. Min. Mag. 43, 919-930.
- Coats, J.S., Smith, C.G., Fortey, N.J., Gallagher, M.J., May, F. and McCourt, W.J. 1980. Strata-bound barium-zinc mineralisation in Dalradian schist near Aberfeldy, Scotland. Trans. Inst. Min. Met. 89B, B110-B122.
- Chinner, G.A. 1960. Pelitic gneisses with varying ferrous/ferric ratios from Glen Clova, Angus, Scotland. J. Pet. 11, 178-217
- Clayburn, J.A.P., Harmon, R.S., Pankhurst, R.J. and Brown, J.F. 1983. Sr, O and Pb isotope evidence and evolution of Etive igneous Complex, Scotland. Nature 303, 492-497

- Cox, K.G., Bell, J.D. and Pankhurst, R.J. 1979. The interpretation of the igneous rocks. George Allen and Unwin.
- Czamanske, G.K., Ishihara, S. and Atkin, S.A. 1981. Chemistry of rock forming minerals of the Cretaceous-Palaeocene batholith in southwestern Japan and implications for magma genesis. J. Geophys. Res. 86, 10431-10469.
- Dakyns, J.R. and Teall, J.J.H. 1892. The plutonic rocks of Garabal Hill and Meall Breac. Q. J. Geol. Soc. Lond. 17, 104-121
- Darbyshire, D.P.F. and Shepherd, T.J. 1985. Chronology of granite magmatism and associated mineralisation, S.W. England. J. Geol. Soc. 142, 1159-1177.
- Deer, W.A. 1935. The Cairnsmore of Carsphairn Igneous Complex Q. J. Geol. Soc. Lond. 91, 47-76
- Deer, W.A. 1937. The marginal rocks of the Cairnsmore of Carsphairn Complex. Geol. Mag. 74, 361-376
- Deer, W.A. 1937. The composition and paragenesis of the biotites of the Carsphairn Igneous Complex. Min. Mag. 24, 495-502
- Deer, W.A. 1938. The composition and paragenesis of the hornblendes of the Glen Tilt Complex, Perthshire. Min. Mag. 25, 56-74
- Deer, W.A. 1950. The diorites and associated rocks of the Glen Tilt Complex, Perthshire pt 2. Geol. Mag. 87, 181-195
- Deer, W.A. 1953. The diorites and associated rocks of the Glen Tilt complex, Perthshire pt 3. Geol. Mag. 90, 27-35
- Deer, W.A., Howie, R.A. and Zussman, J. 1967. Rock forming minerals: vol 2 chain silicates. Longmans.

- Deer, W.A., Howie, R.A. and Zussman, J. 1967. Rock forming minerals: vol 5 non-silicates. Longmans.
- Deer, W.A., Howie, R.A. and Zussman, J. 1983. An introduction to the rock-forming minerals Longman, 528pp
- DePaolo, D.J. 1981. Trace element and isotopic effects of combined wallrock assimilation and fractional crystallisation. Earth Planet. Sci. Lett. 53, 189-202.
- Didier, J. 1973. Granites and their enclaves. The bearing of enclaves on the origin of granites. Developments in petrology 3. Elsevier, 393pp.
- Dodge, F.C.W., Moore, J.G., Papike, J.J. and May, R.E. 1968. Hornblendes from granitic rocks of the Central Sierra Nevada Batholith, California. J. Pet. 9, 378-410.
- Drake, M.J. 1975. The oxidation state of europium as an indicator of oxygen fugacity. Geochim. Cosmochim. Acta. 39, 55-64.
- Eichelberger, J.C. 1978. Andesitic volcanism and crustal evolution. Nature 275, 21-27
- ElBouseily, A.M. and ElSokkary, A.A. 1975. The relation between Rb, Ba and Sr in granitic rocks. Chem. Geol. 16, 207-219.
- Exley, R.A. 1980. Microprobe studies of REE-rich accessory minerals: implications for Skye granite petrogenesis and REE mobility in hydrothermal systems. Earth Planet. Sci. Lett. 48, 97-110
- Fortey, N.J. and Smith, C.G. 1986. Strata-bound mineralisation in Dalradian rocks near Tyndrum, Perthshire. Scot. J. Geol. 22, xxx-xxx.

- Fourcade, S. and Allegre, C.J. 1981. Trace elements behaviour in granite genesis: A case study. The calc-alkaline plutonic association from the Querigut Complex (Pyrenees, France). Contrib. Mineral. Petrol. 76, 177-195.
- French, W.J. 1966. Appinitic intrusions clustered around the Ardara pluton, County Donegal. Proc. R. Irish Acad. 64B, 303-322
- French, W.J. 1976. The origin of leuco diorites associated with the appinitic intrusions of County Donegal Proc. York. Geol. Soc. 41, 107-125
- Frost, C.D. and O'Nions, R.K. 1985. Caledonian magma genesis and crustal recycling J. Pet. 26, 515-544
- Gandy, M.K. 1975. The petrology of the lower Old Red Sandstone lavas of the Eastern Sidlaw Hills, Perthshire, Scotland. J. Pet. 16, 189-211
- Gardiner, C.I. and Reynolds, S.H. 1932. The Loch Doon 'granite' area, Galloway Quart. J. Geol. Soc. Lond. 88, 1-34
- Gardiner, C.I. and Reynolds, S.H. 1937. Cairnsmore of Fleet granite and metamorphic aureole Geol. Mag. 74, 289-301
- Green, D.H. and Ringwood, A.E. 1968. Genesis of the calc-alkaline igneous rock suite. Contrib. Mineral. Petrol. 18, 105-162
- Green, T.H. and Pearson, N.J. 1986. REE partitioning between sphene and coexisting silicate liquid at high pressure and temperature. Chem. Geol. 55, 105-119.
- Groome, D.R. and Hall, A. 1974. The geochemistry of the Devonian lavas of the northern Lorne Plateau, Scotland. Min. Mag. 39,

621-640

- Hall, A. 1966. The Ardara pluton: a study of the chemistry and crystallisation of a contaminated granite intrusion. Proc. R. Irish Acad. 65B, 203-235
- Hall, A. 1966. A petrogenetic study of the Rosses Granite Complex, Donegal. J. Pet. 7, 202-220
- Hall, A. 1967. The chemistry of appinitic rocks associated with the Ardara Pluton, Donegal. Contrib. Mineral. Petrol. 16, 156-171
- Hall, A. 1967. The variation of some trace elements in the Rosses Granite Complex, Donegal. Geol. Mag. 104, 99-109
- Hall, J. and Al-Haddad, F.M. 1976. Seismic velocities in the Lewisian metamorphic complex, north-west Britain—*in situ* measurements. Scot. J. Geol. 12, 305-314
- Hall, J. and Simmons, G. 1979. Seismic velocities of Lewisian metamorphic rocks at pressures to 8Kbar: relationships to crustal layering in northern Britain. Geophys. J. R. Astronom. Soc. 58, 337-347
- Halliday, A.N. 1984. Coupled Sm-Nd and U-Pb systematics in Late Caledonian granites and the basement under northern Britain. Nature 307, 229-233
- Halliday, A.N., Stephens, W.E. and Harmon, R.S. 1980. Rb-Sr isotopic relationships in three zoned Caledonian granitic plutons, Southern Uplands, Scotland: evidence for varied sources and hybridisation of magmas. J. Geol. Soc. Lond. 137, 329-348
- Halliday, A.N., Stephens, W.E., Hunter, R.H., Menzies, M.A., Dickin, A.P. and Hamilton, P.J. 1985. Isotopic and chemical constraints

on the building of the deep Scottish lithosphere. Scot. J. Geol.
21, 465-491

Halliday, A.N., Aftalion, M., Van Breeman, O. and Jocelyn, J. 1979.
Petrogenetic significance of Rb-Sr and U-Pb isotopic systems in the
400Ma old British Isles granitoids and their hosts. In: The
Caledonides of the British Isles - reviewed. ed. A.L. Harris.
C.H. Holland and B.E. Leake Geol. Soc. Lond. Spec. Pub. 8.

Hamilton, P.J., O'Nions, R.K. and Pankhurst, R.J. 1980. Isotopic evi-
dence for the provenance of some Caledonian granites Nature 287,
279-284

Hanson, G.N. 1978. The application of trace elements to the petro-
genesis of igneous rocks of granitic composition. Earth Planet.
Sci. Lett. 38, 26-43

Hardy, M. 1985. Juan Jorge Kingston Polytechnic project.

Harloff, C. 1927. Zonal structure in plagioclase. Leids. Geol.
Meded. 2, 99-114.

Harmon, R.S. and Halliday, A.N. 1980. Oxygen and strontium isotope
relationships in the British late Caledonian granites. Nature 283,
21-25

Harmon, R.S., Halliday, A.N., Clayburn, J.A.P and Stephens, W.E. 1984
Chemical and isotopic systematics of the Caledonian intrusions of
Scotland and northern England: a guide to magma source region and
magma-crust interaction. Phil. Trans. R. Soc. Lond. A310,
709-742

Harris, A.L., Baldwin, C.T., Bradbury, H.J., Johnson, H.D. and Smith,
R.A. 1978. Ensialic basin sedimentation: the Dalradian Supergro-

- up. In: The crustal evolution in northwestern Britain and adjacent regions, ed. D.R. Bowes and B.E. Leake Geol. J. Spec. issue 10, Liverpool. pp115-138
- Harry, W.T. 1950. Aluminium replacing silicon in some silicate lattices. Min. Mag. 29, 142-149.
- Harry, W.T. 1965. The form of the Cairngorm Granite pluton Scot. J. Geol. 1, 1-8
- Harte, B. 1979. The Tarfside succession and the structure and stratigraphy of the eastern Scottish Dalradian rocks. In: The Caledonides of the British Isles - reviewed, ed. A.L. Harris, C.H. Holland and B.E. Leake, pub. Geol. Soc. Lond. p221-228.
- Haskin, L.A., Frey, F.A., Schmitt, R.A. and Smith, R.H. 1966. Meteoric, solar and terrestrial rare earth distributions. In L.H. Ahrens, F.Press, S.K. Runcorn and H.C. Urey (editors), Physics and chemistry of the earth vol. 7. Pergamon, Oxford. pp167-321.
- Haslam, H.W. 1968. The crystallisation of intermediate and acid magmas at Ben Nevis, Scotland. J. Pet. 9, 84-104
- Haslam, H.W. 1970. Appinitic xenoliths and associated rocks from the Ben Nevis igneous Complex. Geol. Mag. 107, 341-356
- Heier, K. 1956. Thermometric and petrogenetic significance of titaniferous magnetite- discussion. Am. J. Sci. 254, 506-510.
- Heinrich, E.W., Levinson, A.A., Levandowski, D.W. and Hewitt, C.H. 1953. Studies in the natural history of micas. Univ. Michigan Engineering Res. Inst. Project M978 Final report.
- Henderson, C.M.B. 1966. Chemistry of Hastingsitic amphiboles from the

- up. In: The crustal evolution in northwestern Britain and adjacent regions. ed. D.R. Bowes and B.E. Leake Geol. J. Spec. issue 10, Liverpool. pp115-138
- Harry, W.T. 1950. Aluminium replacing silicon in some silicate lattices. Min. Mag. 29, 142-149.
- Harry, W.T. 1965. The form of the Cairngorm Granite pluton Scot. J. Geol. 1, 1-8
- Harte, B. 1979. The Tarfside succession and the structure and stratigraphy of the eastern Scottish Dalradian rocks. In: The Caledonides of the British Isles - reviewed. ed. A.L. Harris, C.H. Holland and B.E. Leake. pub. Geol. Soc. Lond. p221-228.
- Haskin, L.A., Frey, F.A., Schmitt, R.A. and Smith, R.H. 1966. Meteoric, solar and terrestrial rare earth distributions. In L.H. Ahrens, F.Press, S.K. Runcorn and H.C. Urey (editors), Physics and chemistry of the earth vol. 7. Pergamon, Oxford. pp167-321.
- Haslam, H.W. 1968. The crystallisation of intermediate and acid magmas at Ben Nevis, Scotland. J. Pet. 9, 84-104
- Haslam, H.W. 1970. Appinitic xenoliths and associated rocks from the Ben Nevis igneous Complex. Geol. Mag. 107, 341-356
- Heier, K. 1956. Thermometric and petrogenetic significance of titaniumiferous magnetite- discussion. Am. J. Sci. 254, 506-510.
- Heinrich, E.W., Levinson, A.A., Levandowski, D.W. and Hewitt, C.H. 1953. Studies in the natural history of micas. Univ. Michigan Engineering Res. Inst. Project M978 Final report.
- Henderson, C.M.B. 1966. Chemistry of Hastingsitic amphiboles from the

- Marangudzi Igneous Complex, Southern Rhodesia. Proc. 5th Int. Min. Assoc. 291-304.
- Henderson, P. 1980. Rare earth element partition between sphene, apatite and other co-existing minerals of the Kangerdlugssuaq Intrusion, E. Greenland. Contrib. Mineral. Petrol. 72, 81-85
- Henderson, P. 1983. Rare earth element geochemistry: developments in geochemistry 2. Elsevier. 510pp.
- Hess, H.H. 1952. Orthopyroxenes of the Bushveld type, ion substitutions and changes in unit cell dimensions. Am. J. Sci. Bowen Volume, 173-187.
- Hickman, A.H. and Wright, A.E. 1983. Geochemistry and chemostratigraphy correlation of slates, marbles and quartzites of the Appin Group, Argyll, Scotland. Trans. R. Soc. Edin. Earth Sci. 73, 251-278.
- Holgate, N. 1951. The Glen Banvie Igneous Complex. Q. J. Geol. Soc. Lond. 106, 433-460
- Holloway, J.R. and Burnham, C.W. 1972. Melting relations of basalts with equilibrium water pressure less than total pressure. J. Pet. 13, 1-29.
- Hutchison, C.S. 1964. A gabbro-granodiorite association in Singapore Island. Q. J. Geol. Soc. Lond. 120, 283-298
- Jacobson, S.B. and Wasserburg, G.J. 1979. Interpretation of Nd, Sr and Pb isotope data from Archean migmatites in Lofoten-Vesteralen, Norway. Earth Planet. Sci. Lett. 41, 245-253.
- Jarvis, I. and Jarvis, K.E. 1985. Rare earth element geochemistry of standard sediments: a study using inductively coupled plasma spec-

- trometry. Chem. Geol. 53, 335-344.
- Jarvis, K.E. and Jarvis, I. 1987. Determination of the rare earth elements in standard reference materials by ICP-AES. Geostand. Newslett. in press
- Johnstone, G.S., Plant, J. and Watson, J.V. 1979. Caledonian granites in relation to regional geochemistry in northern Scotland. In: The Caledonides of the British Isles reviewed. Ed. A.L.Harris, C.H. Holland and B.E. Leake. Geol. Soc. Spec. Pub. 8.
- Kennan, P.S. 1979. Plutonic rocks in the Irish Caledonides. In The Caledonides of the British Isles reviewed. Ed. A.L. Harris, C.H. Holland and B.E. Leake. Geol. Soc. Spec. Pub. 8.
- Key, C.H. 1974. The layered diorites of Jersey, Channel Islands. unpub. Ph.D. thesis Univ. of London.
- Kushiro, I. 1960. Si-Al relations in clinopyroxenes from igneous rocks. Am. J. Sci. 258, 548-554.
- Larsen, E.S. 1938. Some new variation diagrams for groups of igneous rocks. J. Geol. 46, 505-520
- Leake, B.E. 1965. The relationship between composition of calciferous amphiboles and grade of metamorphism. In: Controls of metamorphism eds. Pitcher, W.S. and Flinn, G.W. pp299-318.
- Leake, B.E. 1971. On aluminous and edenitic hornblendes. Min. Mag. 38, 389-407
- Leake, B.E. 1978. Nomenclature of amphiboles. Min. Mag. 42, 533-563
- Leake, B.E. 1978. Granite emplacement: the granites of Ireland and their origin. In: Crustal evolution of northwestern Britain and

- adjacent regions. (eds D.R. Bowes and B.E. Leake) Geol. J. special issue 10 pp221-248.
- LeBas, M.J. 1962. The role of aluminium in igneous clinopyroxenes with relation to their parentage. Am. J. Sci. 260, 267-288.
- Loomis, T.P. 1982. Numerical simulations of crystallisation processes of plagioclase in complex melts: the origin of major and oscillatory zoning in plagioclase. Contrib. Mineral. Petrol. 81, 230-239.
- Loomis, T.P. and Welber, P.W. 1982. Crystallisation processes in the Rocky Hill Granodiorite Pluton, California: an interpretation based on compositional zoning of plagioclase. Contrib. Mineral. Petrol. 82, 230-239.
- Maaloe, S. 1976. The zoned plagioclase of the Skaergaard Intrusion, East Greenland. J. Pet. 17, 398-419.
- MacGregor, A.G. and Kennedy, W.Q. 1932. The Movern-Strontian granite. Geol. Surv. summary of progress report for 1931 105-109.
- McBirney, A.R. 1975. Differentiation of the Skaergaard Intrusion. Nature 253, 691-694.
- McCarthy, T.S. and Hasty, R.A. 1976. Trace element distribution patterns and their relationship to the crystallisation of granitic melts. Geochim. Cosmochim. Acta. 40, 1351-1358
- Macdonald, G.A. and Katsura, T. 1965. Eruption of Lassen Peak, Cascade Range, California, in 1915: example of mixed magmas. Geol. Soc. Am. Bull. 76, 475-482
- Mackenzie, W.S., Donaldson, C.H. and Guilford, C. 1982. Atlas of igneous rocks and their textures. Longman.

- Mason, B. 1966. Principles of geochemistry Wiley and sons, 329pp.
- McKerrow, W.S., Leggett, J.K. and Eales, M.H. 1977. Inbricate thrust model of the Southern Uplands of Scotland. Nature 267, 237-239
- Nakamura, N. 1974. Distribution of REE, Ba, Fe, Mg, Na and K in carbonaceous and ordinary chondrites. Geochim. Cosmochim. Acta. 38, 757-775
- Nash, W.P. and Crecraft, H.R. 1985. Partition coefficients for trace elements in silicic magmas. Geochim. Cosmochim. Acta. 49, 2309-2322.
- Nicholls, G.D. 1950. The Glenelg-Ratagain igneous complex. Q. J. Geol. Soc. Lond. 106, 309-344
- Nockolds, S.R. 1932. The contaminated granite of Bibette Head, Alderney. Geol. Mag. 69, 433-451
- Nockolds, S.R. 1933. Some theoretical aspects of contamination in acid magmas. J. Geol. 41, 561-590
- Nockolds, S.R. 1940. The Garabal Hill - Glen Fyne igneous complex. Q. J. Geol. Soc. Lond. 384, 451-510
- Nockolds, S.R. 1954. Average chemical compositions of igneous rocks. Bull. Geol. Soc. Am. 65, 1007-1032.
- Nockolds, S.R. and Allen, R. 1953. The geochemistry of some igneous rock series. Geochim. Cosmochim. Acta. 4, 105-142
- Nockolds, S.R. and Mitchell, R.L. 1946. The geochemistry of some Caledonian plutonic rocks. Trans. Roy. Soc. Edin. 61, 533-
- Noyes, H.J., Wones, D.R. and Frey, F.A. 1983. A tale of two plutons:

- petrographic and mineralogic constraints on the petrogenesis of the Red Lake and Eagle Peak Plutons, Central Sierra Nevada, California. J. Pet. 4, 353-379.
- Nwe, Y.Y. 1975. Two different pyroxene crystallisation trends in the trough bands of the Skaergaard Intrusion, East Greenland. Contrib. Mineral. Petrol. 49, 285-300.
- Nwe, Y.Y. 1976. Electron-probe studies of the earlier pyroxenes and olivines from the Skaergaard Intrusion, East Greenland. Contrib. Mineral. Petrol. 55, 105-126.
- Oldershaw, W. 1958. A study of the Lochnagar granitic ring complex, Aberdeenshire. unpub. Ph.D. thesis Univ. Lond.
- Oldershaw, W. 1974. The Lochnagar granitic ring complex, Aberdeenshire. Scot. J. Geol. 10, 297-309
- Osborne, E.F. 1962. Reaction series for sub-alkaline igneous rocks based on different oxygen pressure conditions. Am. Min. 47, 211-226.
- Pankhurst, R.J. and O'Nions, R.K. 1973. Determination of Rb/Sr and $^{87}\text{Sr}/^{86}\text{Sr}$ ratios of some standard rocks and evaluation of X-Ray fluorescence spectrometry in Rb-Sr geochemistry. Chem. Geol. 12, 127-136.
- Pankhurst, R.J. and Pidgeon, R.T. 1976. Inherited isotope systems and the source region pre-history of early Caledonian granites in the Dalradian Series of Scotland. Earth Planet. Sci. Lett. 31, 55-68.
- Pattison, D and Harte, B. 1985. A petrogenetic grid for pelites in the Ballachulish and other Scottish thermal aureoles. J. Geol. Soc.

- petrographic and mineralogic constraints on the petrogenesis of the Red Lake and Eagle Peak Plutons, Central Sierra Nevada, California. J. Pet. 4, 353-379.
- Nwe, Y.Y. 1975. Two different pyroxene crystallisation trends in the trough bands of the Skaergaard Intrusion, East Greenland. Contrib. Mineral. Petrol. 49, 285-300.
- Nwe, Y.Y. 1976. Electron-probe studies of the earlier pyroxenes and olivines from the Skaergaard Intrusion, East Greenland. Contrib. Mineral. Petrol. 55, 105-126.
- Oldershaw, W. 1958. A study of the Lochnagar granitic ring complex, Aberdeenshire. unpub. Ph.D. thesis Univ. Lond.
- Oldershaw, W. 1974. The Lochnagar granitic ring complex, Aberdeenshire. Scot. J. Geol. 10, 297-309
- Osborne, E.F. 1962. Reaction series for sub-alkaline igneous rocks based on different oxygen pressure conditions. Am. Min. 47, 211-226.
- Pankhurst, R.J. and O'Nions, R.K. 1973. Determination of Rb/Sr and $^{87}\text{Sr}/^{86}\text{Sr}$ ratios of some standard rocks and evaluation of X-Ray fluorescence spectrometry in Rb-Sr geochemistry. Chem. Geol. 12, 127-136.
- Pankhurst, R.J. and Pidgeon, R.T. 1976. Inherited isotope systems and the source region pre-history of early Caledonian granites in the Dalradian Series of Scotland. Earth Planet. Sci. Lett. 31, 55-68.
- Pattison, D and Harte, B. 1985. A petrogenetic grid for pelites in the Ballachulish and other Scottish thermal aureoles. J. Geol. Soc.

- Lond. 142, 7-28.
- Pearce, J.A. and Norry, N.J. 1979. Petrogenetic implications of Ti, Zr, Y, and Nb, V variations in volcanic rocks. Contrib. Mineral. Petrol. 69, 33-47
- Perkins, S.G. The Cruachan unit of the Etive Complex. PhD thesis CNA.
- Philips, W.J. 1956. The minor intrusive suite associated with the Criffell-Dalbeattie Granodiorite Complex. Proc. Geol. Assoc. 67, 103-121.
- Phillips, W., Stillman, C.J. and Murphy, T. 1976. A Caledonian plate tectonic model. J. Geol. Soc. Lond. 132, 579-609
- Phillips, W.E.A. 1978. The Caledonian orogen in Ireland. Geol. Surv. Canada Paper 78-13. 97-103.
- Pidgeon, R.J. and Aftalion, M. 1978. Crustal evolution in NW Britain and adjacent regions. Eds D.R. Bowes and B.E. Leake. Geol. J. Special issue 10.
- Pitcher, W.S. 1953. The Rosses Granite Ring Complex, County Donegal, Eire. Proc. Geol. Assoc. 64, 153-182.
- Pitcher, W.S. and Berger, A.R. 1972. The geology of Donegal- a study of granite emplacement and unroofing. ed. L.U. DeSitter. Wiley.
- Poldervaart, A. and Hess, H.H. 1951. Pyroxenes in the crystallisation of basaltic magma. J. Geol. 59, 472-489.
- Potts, P.J. 1987. A handbook of silicate rock analysis Blackie, Glasgow, pp
- Read, H.H. 1961. Aspects of Caledonian magmatism. Liv. and Man. Geol. J. 2, 653-683

- Reid, J.B., Evans, O.C. and Fates, D.G. 1983. Magma mixing in granitic rocks of the Central Sierra Nevada, California. Earth Planet. Sci. Lett. 66, 243-261.
- Roaldset, E. 1975. Rare earth element distributions in some Precambrian rocks and their phyllosilicates, Numedal, Norway. Geochim. Cosmochim. Acta. 39, 455-469.
- Schumacher, R. 1985. Zincian staurolite in Glen Doll, Scotland. Min. Mag. 49, 561-571
- Scott, G.B. and Vogel, T.A. 1980. The origin of the acidic and basic rocks of the Tichka Massif, Morocco, based on rare earth elements. Contrib. Mineral. Petrol. 75, 89-95.
- Shannon, R.D. 1976. Revised effective ionic radii and systematic studies of interatomic distances in halides and chalcogenides. Acta. Crystallogr. A32, 751-767.
- Shaw, D.M. 1977. Trace element behaviour during anatexis. In: Magma Genesis Bull. 96.
- Shaw, D.M. 1978. Trace element behaviour during anatexis in the presence of a fluid phase. Geochim. Cosmochim. Acta. 42, 933-943.
- Sibley, D.F., Vogel, T.A., Walker, B.M. and Byerly, G. 1976. The origin of oscillatory zoning in plagioclase: a diffusion and growth controlled model. Am. J. Sci. 276, 273-284.
- Simkin, T. and Smith, J.V. 1970. Minor-element distribution in olivine. J. Geol. 78, 304-325.
- Smith, C.G., Gallagher, M.J., Coats, J.S. and Parker, M.E. 1984.

- Detection and general characteristics of strata-bound mineralisation in the Dalradian of Scotland. Trans. Inst. Min. Met. 93, B125-B133.
- Sparks, R.S.J., Huppert, H.E. and Turner, J.S. 1984. The fluid dynamics of evolving magma chambers. Phil. Trans. Roy. Soc. Lond. Ser.A. 310, 511-534
- Stephens, W.E. and Halliday, A.N. 1984. Geochemical contrasts between late Caledonian granitoid plutons of northern, central and southern Scotland. Trans. R. Soc. Edin. Earth Sci. 75, 259-273.
- Stormer, J.C. 1973. Calcium zoning in olivine and its relationship to silica activity and pressure. Geochim. Cosmochim. Acta. 37, 1815-1821.
- Streckeisen, A. 1975. To each plutonic rock its proper name. Earth Sci. Rev. 12, 1-33
- Strelow, F. and Jackson, P. 1974. A determination of trace and ultra-trace quantities of rare earth elements by ion exchange chromatography-mass spectrometry. Anal. Chem. 46, 1481-1487
- Summerhayes, C.P. 1966. A geochronological and strontium isotope study on the Garabal Hill - Glen Fyne complex, Scotland. Geol. Mag. 103, 153-165
- Sweatman, T.R. and Long, J.V.P. 1969. Quantitative electron-probe microanalysis of rock forming minerals. J. Pet. 10, 332-379.
- Symes, R.F. 1981. The central diorite of Alderney, Channel Islands and associated orbicular rocks. Unpub. PhD. thesis Univ. of London.
- Tait, S.R., Huppert, H.E. and Sparks, R.S.J. 1984. The role of compositional convection in the formation of adcumulate rocks. Lithos.

17, 139-146

- Taylor, S.R. 1969. Trace element chemistry of andesites and associated calc-alkaline rocks. Proc. Andesite conf. (ed A.R. McBirnev). Bull. Dept. Geol. Min. Ind. Oregon. 65, 43-63
- Thirlwall, M.T. 1979. The petrochemistry of the British Old Red Sandstone volcanic province. Unpub PhD thesis Univ. of Edinburgh.
- Thirlwall, M.F. 1981. Implications for Caledonian plate tectonic models of chemical data from volcanic rocks of the British Old Red sandstone. J. Geol. Soc. Lond. 138, 123-138
- Thirlwall, M.F. 1982. Systematic variation in chemistry and Nd-Sr isotopes across a Caledonian calc-alkaline volcanic arc: implications for source materials. Earth Planet. Sci. Lett. 58, 27-50
- Thirlwall, M.F. 1986. Lead isotope evidence for the nature of the mantle beneath Caledonian Scotland. Earth Planet. Sci. Lett. 80, 55-70.
- Thompson, M. and Walsh, J.N. 1983. A handbook of inductively coupled plasma spectrometry. Blackie, Glasgow, 273pp.
- Thompson, R.N. 1982. Magmatism of the British Tertiary volcanic province. Scot. J. Geol. 18, 49-107
- Tindle, A.G. and Pearce, J.A. 1981. Petrogenetic modelling of in situ fractional crystallisation in the zoned Loch Doon pluton, Scotland. Contrib. Mineral. Pet. 78, 196-207
- Tindle, A.G. and Pearce, J.A. 1983. Assimilation and partial melting of continental crust: evidence from the mineralogy and geochemistry of autoliths and xenoliths. Lithos 16, 185-202.

- Topley, C.G., Brown, M. and Power, G.M. 1982. Interpretation of field relationships of diorites and associated rocks with particular reference to N.W. Guernsey, Channel Islands. Geol. J. 17, 323-343.
- Vejnar, Z. 1975. Hornblendes and problems of recrystallisation of gabbroic rocks. Lithos 8, 59-68.
- Vogel, T.A. 1982. Magma mixing in the acidic-basic complex of Ardnamurchan: implications on the evolution of shallow magma chambers. Contrib. Mineral. Petrol. 79, 411-423.
- Wager, L.R. 1960. The major element variation of the Skaergaard Layered series of the Skaergaard Intrusion and a re-estimation of the average composition of the hidden Layered Series of the successive residual magmas. J. Pet. 1, 364-398.
- Wager, L.R. and Brown, G.M. 1968. Layered igneous rocks pub. Oliver and Boyd, Edinburgh. 588pp.
- Wager, L.R. and Mitchell, R.L. 1951. The distribution of trace elements during strong fractionation of basic magma—a further study of the Skaergaard Intrusion, East Greenland. Geochim. Cosmochim. Acta. 1, 129-208.
- Walsh, J.N., Buckley, F. and Barker, J. 1981. The simultaneous determination of the rare earth elements in rocks using inductively coupled plasma source spectrometry. Chem. Geol. 33, 141-153.
- Walsh, N.J. and Clarke, E. 1982. The role of fractional crystallisation in the formation of granitic and intermediate rocks of the Beinn Chaisgidle Centre, Mull, Scotland. Min. Mag. 45, 247-255.
- Watson, J.V. 1984. The ending of the Caledonian orogeny in Scotland.

- J. Geol. Soc. Lond. 141, 193-214
- Wiebe, R.A. 1968. Plagioclase stratigraphy: a record of magmatic conditions and events in a granitic stock. Am. J. Sci 266, 690-703.
- Wiebe, R.A. and Wild, T. 1983. Fractional crystallisation and magma mixing in the Tigalak layered intrusion, the Nain anorthosite complex, Labrador. Contrib. Mineral. Petrol. 84, 327-344.
- Wilkinson, J.F.G., Vernon, R.H. and Shaw, S.E. 1964. The petrology of an adamellite-porphyrite from the New England Batholith (New South Wales). J. Petrol. 5, 461-488
- Willan, R.C.R. 1980. Stratabound sulphide mineralisation in the Dalradian Supergroup of the Grampian Highlands, Scotland. Norges Geol. Unders. 300, 241-258.
- Williamson, W.O. 1933. The composite gneiss and contaminated granodiorite of Glen Shee, Perthshire. Q. J. Geol. Soc. Lond. 91, 382-419.
- Wright, A.E. and Bowes, D.R. 1979. Geochemistry of the appinite suite. In: The Caledonides of the British Isles- reviewed. ed. A.L. Harris, C.H. Holland and B.E. Leake. Geol. Soc. Lond. Spec. Pub. no 8.
- Wright, T.L. and Doherty, P.C. 1970. A linear and least squares computer method for solving petrologic mixing problems. Geol. Soc. Amer. Bull. 81, 1995-2008
- Yoder, H.S. 1969. Calc-alkaline andesites: experimental data bearing on the origin of their assumed characteristics. Oregon Dept. Geol. Min. Ind. Bull. 65, 77-89.

York, D. 1969. Least squares fitting of a straight line with correlated errors. Earth planet. Sci. Lett. 5, 320-324.

Appendix A
Sample localities and rock types

Glen Doll Complex

Sample	Grid ref.	Rock type
GC1	2866 7595	Hornblende diorite
GC2	2864 7605	Hornblende diorite (xenolithic)
GC3	2864 7605	Rafted xenolith
GC4	2863 7624	Hornblende diorite
GC5	2858 7629	Hornblende diorite
GC6	2860 7628	QFP Dyke
GC7	2855 7640	Leuco-diorite
GC8	2871 7611	Hornblende diorite
GC9	2865 7644	Pyroxene diorite
GC13	2887 7629	QFP Dyke
GC15	2897 7612	Dalradian xenolith
GC16	2888 7620	Qtz monzonite (xenolithic)
GC17	2925 7638	Hornblende diorite
GC19	2898 7616	Qtz monzonite
GC20	2899 7596	Qtz monzonite (xenolithic)
GC21	2899 7596	Qtz monzonite
GC25	2894 7593	Adamellite
GC26	2895 7591	Rafted xenolith
GC27	2895 7591	Hornblende diorite
GC28	2896 7591	Hornblende diorite
GC30	2917 7596	Appinite
GC31	2930 7562	Hornblende diorite
GC33	2934 7566	QFP Dyke
GC34	2947 7563	Aplite Dyke
GC36	2946 7559	Adamellite
GC41	2860 7621	Hornblende diorite
GC44	2873 7602	Hornblende diorite
GC46	2867 7657	Dalradian xenolith
GC56	2858 7688	Hornblende diorite
GC68	2985 7490	Dalradian schist
GC70	2845 7795	Gabbro
GC71	2845 7795	Norite
GC72	2857 7819	Pyroxene diorite
GC73	2855 7814	Gabbro
GC75	2870 7835	Appinite
GC76	2870 7835	Gabbro
GC78	2872 7840	Gabbro
GC79	2848 7803	Norite
GC80	2851 7811	Gabbro
GC81	2858 7823	Norite
GC82	2859 7829	Gabbro
GC83	2867 7832	Gabbro
GC86	2882 7868	Aplite Dyke
GC87	2882 7868	Porphyritic microdiorite dyke
GC88	2690 7498	Olivine Gabbro
GC89	2700 7521	QFP dyke
GC90	2845 7718	Gabbro
GC91	2843 7720	Olivine Gabbro
GC92	2846 7723	Aplite dyke
GC93	2860 7756	Hornblende diorite
GC96	2770 7800	Porphyritic micro adamellite sheet
GC98	2865 7724	Pyroxene diorite

Appendix A (cont.)

GC99 2867 7721 QFP dyke
 GC100 2868 7722 Hornblende diorite
 GC101 2884 7724 Rafted xenolith
 GC102 2883 7776 Hornblende diorite
 GC104 2894 7780 Hornblende diorite
 GC105 2911 7794 Hornblende diorite
 GC106 2929 7808 Adammelite
 GC107 2929 7808 Dalradian metasediment
 GC108 2894 7723 Hornblende diorite
 GC109 2868 7690 Hornblende diorite
 GC111 2878 7778 Hornblende diorite
 GC112 2887 7619 Rafted xenolith
 GC113 2891 7615 Rafted xenolith
 GC114 2911 7678 Hornblende diorite
 GC115 2936 7677 Appinite
 GC116 2942 7552 Adamellite
 GC117 2955 7555 Adamellite
 GC118 2955 7555 Aplite dyke
 GC119 2851 7606 Hornblende diorite
 GC120 2884 7856 Hornblende diorite
 GC122 2783 7538 Hornblende diorite
 GC124 2783 7538 Rafted xenolith
 GC125 2763 7577 Hornblende diorite
 GC126 2825 7488 Aplite dyke
 GC127 2793 7517 Adamellite
 GC128 2793 7517 Qtz monzanite
 GC129B 2793 7517 Dalradian gneiss containing green spinel
 GC130 2787 7522 Adamellite
 GC131 2787 7522 Adamellite
 GC132 2788 7528 Hornblende diorite
 GC133 2825 7626 Pyroxene diorite
 GC134 2817 7627 Pyroxene diorite
 GC136 2815 7652 Pyroxene diorite
 GC137 2795 7665 Rafted xenolith
 GC138 2777 7685 Fine-grained metasedimentary xenolith
 GC139 2807 7642 Pyroxene diorite
 GC140 2803 7629 Pyroxene diorite
 GC143 2752 7616 Hornblende diorite
 GC144 2715 7603 QFP dyke
 GC145 2709 7603 Microdiorite dyke
 GC146 2709 7603 Leuco diorite
 GC148 2685 7590 Microdiorite xenolith
 GC149 2796 7603 Microdiorite dyke porphyritic
 GC150 2793 7604 Hornblende diorite
 GC151 2784 7604 Hornblende diorite
 GC152 2784 7604 QFP dyke phase 1
 GC154 2784 7604 QFP dyke phase 2
 GC155 2643 7587 Pyroxene diorite
 GC160 2687 7505 Olivine Gabbro
 GC161 2687 7505 Gabbro
 GC162 2687 7514 Olivine Norite
 GC163 2606 7515 Olivine Gabbro
 GC164 2606 7515 Porphyritic microdiorite dyke
 GC165 2685 7531 Pyroxene diorite
 GC166 2685 7531 QFP dyke
 GC167 2684 7538 Fine-grained diorite
 GC168 2685 7551 QFP dyke

Appendix A (cont.)

GC169 2683 7551 Pyroxene diorite (xenolithic)
 GC170 2680 7561 Monzonite
 GC171 2769 7610 Hornblende diorite
 GC172 2769 7610 Microdiorite xenolith
 GC173 2747 7566 Qtz diorite
 GC174 2770 7587 Hornblende diorite
 GC175 2788 7572 Hornblende diorite
 GC176 2598 7550 Hornblende diorite
 GC177 2609 7533 Hornblende diorite
 GC178 2618 7560 Pyroxene diorite
 GC179 2627 7569 Pyroxene diorite
 GC180 2612 7558 Hornblende diorite
 GC181 2591 7546 Hornblende diorite
 GC182 2648 7529 Hornblende diorite xenolithic
 GC183 2625 7451 Qtz monzonite
 GC184 2616 7461 Qtz monzonite
 GC185 2614 7473 Appinite
 GC187 2623 7472 Qtz monzonite
 GC188 2623 7472 Porphyritic microgranite
 GC190 2632 7474 Qtz monzonite
 GC191 2633 7481 Hornblende diorite
 GC192 2643 7486 Hornblende diorite xenolithic
 GC193 2645 7596 Qtz-mica diorite
 GC194 2646 7500 Rafted xenolith
 GC195 2633 7502 Hornblende diorite xenolithic
 GC196 2627 7497 Microdiorite
 GC197 2606 7492 Rafted xenolith
 GC198d 2606 7492 Adamellite
 GC199 2591 7486 Qtz-mica diorite xenolithic
 GC200 2679 7494 Olivine Gabbro
 GC203 2870 7835 Gabbro
 GC205 2870 7835 Adamellite pegmatite
 GC206 2870 7835 Appinite
 GC207 2763 7695 Hornblende diorite
 GC208 2758 7698 Pyroxene diorite
 GC211 2746 7713 Diorite
 GC212 2759 7732 Pyroxene diorite
 GC213 2746 7739 Diorite pegmatite
 GC215 2735 7747 Pyroxene diorite
 GC217 2769 7726 QFP white dyke
 GC219 2746 7739 Epidiorite xenolith
 GC220 2750 7737 Pyroxene diorite
 GC222 2757 7734 Pyroxene diorite
 GC223 2768 7739 Pyroxene diorite
 GC224 2768 7739 Pyroxene diorite
 GC228 2692 7667 Qtz-mica diorite
 GC229 2685 7660 Diorite
 GC230 2651 7648 Porphyritic micro diorite dyke
 GC231 2645 7641 Qtz monzonite
 GC232 2640 7632 Hornblende diorite
 GC233 2638 7627 Hornblende diorite
 GC234 2687 7592 Pyroxene diorite
 GC236 2707 7675 Hornblende diorite
 GC237 2710 7672 Hornblende diorite
 GC238 2714 7670 Rafted xenolith
 GC239 2717 7670 Hornblende diorite
 GC240 2720 7665 Hornblende diorite

Appendix A (cont.)

GC241 2722 7660 Pyroxene diorite
GC242 2725 7651 Pyroxene diorite
GC243 2732 7630 Pyroxene diorite
GC244 2666 7622 Hornblende diorite
GC245 2663 7623 Pyroxene diorite
GC246 2663 7623 Microdiorite dyke
GC247 2672 7629 Granite dyke
GC248 2672 7629 Porphyritic microdiorite dyke
GC249 2672 7629 Hornblende diorite
GC251 2676 7638 Hornblende diorite
GC252 2678 7638 Granite
GC253 2665 7637 Pyroxene diorite
GC254 2669 7645 Pyroxene diorite
GC256 2783 7744 Granite
GC257 2783 7744 Diorite
GC258 2782 7751 Pyroxene diorite
GC259 2782 7751 QFP dyke
GC260 2777 7764 Micro-monzonite dyke
GC261 2774 7765 Pyroxene diorite
GC263 2769 7784 Hornblende diorite
GC264 2881 7568 Hornblende diorite
GC265 2885 7572 Hornblende diorite
GC270 2914 7837 Hornblende diorite
GC271 2914 7837 Adamellite
GC272 2958 7927 QFP dyke
GC273 2915 7964 Diorite
GC274 2925 7958 Hornblende diorite
GC276 2913 7909 Xenolithic granite
GC279 2904 7844 Hornblende diorite
GC281 2894 7834 Pyroxene diorite

Juan Jorge Complex and Bridge Outcrops

JJ1 2500 8000 Lochnagar granite
JJ3 2510 7993 Qtz-mica diorite
JJ4 2522 7984 Qtz-mica diorite
JJ6 2555 7952 Xenolithic Qtz-mica diorite
JJ7 2602 7931 Qtz-mica diorite
JJ8 2622 7923 Hornblende diorite
JJ9 2640 7916 Xenolithic granite
JJ10 2777 7877 Microdiorite
JJ11 2776 7882 Hornblende diorite
JJ12 2775 7885 Granite dyke
JJ15 2774 7893 Granite
JJ16 2774 7893 Porphyritic granite
JJ17 2667 7919 Granite
JJ18 2694 7920 Qtz-mica diorite
JJ19 2714 7925 Microdiorite xenolith
JJ20 2714 7925 Qtz-mica diorite
JJ21 2565 7968 Qtz-mica diorite
JJ23 2661 7948 Qtz-mica diorite

Key to Tables B.1-B.9 inclusive

The atomic formula were calculated on the basis of x oxygens as follows:

Mineral	Number of oxygens
Amphiboles	23
Pyroxenes	6
Olivines	4
Biotites	23

*FeO= total iron calculated as FeO

*Fe₂O₃= total iron calculated as Fe₂O₃

BD= below detection

ND= not determined

Sample numbering is composed of three parts:

e.g. 88/PL/27C or JJ3/PX/4R

88 = rock number, no prefix for Glen Doll Samples, JJ prefix for Juan Jorge samples

PL = mineral phase, Am=amphibole, PX=pyroxene, OL=olivine, BI=biotite, PL=plagioclase, OX=oxide, AP=apatite, SP=sphene

27C = analysis number, C=core, R=rim, M=margin

Table B.1 Amphibole microprobe analyses

Element (Z)	Sample	Olivine gabbros											
		88 AM 95C	88 AM 95R	88 AM 96C	88 AM 96R	91 AM 85C	91 AM 85R	91 AM 86C	91 AM 86R	91 AM 87R	91 AM 126C		
SiO ₂	41.07	41.60	43.19	43.40	41.87	42.38	43.21	38.75	42.54	42.15			
TiO ₂	3.91	3.97	1.14	1.18	3.43	2.62	3.56	2.42	2.85	3.70			
Al ₂ O ₃	11.19	11.35	10.74	11.23	11.61	12.32	10.54	13.16	11.74	11.52			
*FeO	8.13	8.06	8.17	7.94	8.59	8.46	8.26	11.87	8.03	8.73			
MgO	15.37	15.29	17.38	16.68	15.68	15.89	16.04	15.95	16.07	15.27			
MnO	0.11	0.10	0.08	0.09	0.12	0.14	0.13	0.48	0.13	0.12			
CaO	11.52	11.53	11.00	11.37	10.38	10.22	10.52	7.95	11.04	10.76			
Na ₂ O	3.06	3.06	2.68	2.88	2.99	2.93	2.84	2.30	3.01	3.06			
K ₂ O	0.64	0.63	0.65	0.61	0.54	0.29	0.49	0.31	0.34	0.51			
TOTAL	95.00	95.58	95.03	95.36	95.21	95.26	95.59	93.18	95.71	95.81			
Si	6.161	6.190	6.422	6.426	6.235	6.275	6.385	5.964	6.278	6.247			
Al(IV)	1.839	1.810	1.578	1.574	1.765	1.725	1.615	2.036	1.722	1.753			
Al(VI)	0.140	0.182	0.305	0.386	0.274	0.426	0.221	0.352	0.352	0.259			
Ti	0.442	0.445	0.128	0.132	0.384	0.292	0.396	0.280	0.317	0.413			
*Fe ²⁺	1.021	1.003	1.017	0.983	1.070	1.049	1.022	1.528	0.991	1.803			
Mn	0.014	0.012	0.010	0.012	0.016	0.018	0.016	0.063	0.017	0.016			
Mg	3.437	3.391	3.851	3.680	3.481	3.507	3.533	3.659	3.535	3.372			
Ca	1.852	1.839	1.754	1.804	1.657	1.622	1.667	1.311	1.746	1.709			
Na	0.890	0.882	0.773	0.827	0.863	0.843	0.813	0.687	0.861	0.879			
K	0.123	0.121	0.124	0.115	0.103	0.056	0.093	0.061	0.064	0.096			

COO

Table B.1 Amphibole microprobe analyses (cont.)

Element (Z)	Sample	Olivine gabbros											
	91 AM 126R	79 AM 41C	79 AM 41R	82 AM 41C	82 AM 41R	82 AM 42C	82 AM 42R	82 AM 43C	82 AM 43R	161 AM 44C			
SiO ₂	41.44	42.76	42.53	41.17	43.79	41.36	40.67	48.25	50.00	41.62			
TiO ₂	3.69	3.68	3.47	3.76	2.54	4.33	4.41	0.89	0.70	4.18			
Al ₂ O ₃	11.56	11.00	11.34	11.18	9.77	11.36	11.62	6.16	5.45	11.56			
*FeO	8.82	10.52	10.83	11.59	11.49	10.92	11.44	10.72	10.58	9.88			
MgO	15.17	14.45	13.95	13.04	14.41	13.71	13.39	16.57	16.93	14.32			
MnO	0.13	0.14	0.14	0.15	0.15	0.16	0.20	0.19	0.19	0.15			
CaO	10.48	11.34	11.72	11.87	11.35	11.62	11.40	11.47	11.67	11.05			
Na ₂ O	2.98	1.83	1.74	1.68	1.29	2.00	1.89	0.94	0.82	1.84			
K ₂ O	0.53	0.96	1.04	1.03	0.94	0.88	0.87	0.52	0.42	0.60			
TOTAL	94.80	96.75	96.87	95.49	94.74	96.33	95.89	95.71	96.75	95.54			
Si	6.212	6.319	6.297	6.228	6.544	6.179	6.122	7.110	7.256	6.220			
Al(IV)	1.788	1.681	1.703	1.772	1.456	1.821	1.878	0.890	0.744	1.780			
Al(VI)	0.256	0.236	0.276	0.223	0.266	0.181	0.184	0.181	0.189	0.256			
Ti	0.417	0.409	0.386	0.428	0.286	0.487	0.500	0.099	0.077	0.470			
*Fe ²⁺	1.106	1.300	1.341	1.466	1.437	1.365	1.441	1.321	1.284	1.235			
Mn	0.017	0.018	0.018	0.020	0.019	0.020	0.025	0.024	0.024	0.019			
Mg	3.390	3.183	3.076	2.940	3.210	3.052	3.005	3.640	3.661	3.190			
Ca	1.684	1.796	1.860	1.925	1.818	1.859	1.839	1.812	1.815	1.770			
Na	0.865	0.524	0.500	0.495	0.375	0.578	0.553	0.269	0.231	0.533			
K	0.102	0.181	0.197	0.200	0.179	0.168	0.167	0.098	0.078	0.114			

Table B.1. Amphibole microprobe analyses (cont.)

Element (Z)	Sample		Pyroxene diorites											
	Gabbros		179 AM 2R	179 AM 10C	179 AM 10R	179 AM 11C	179 AM 11M	179 AM 11R	161 AM 73C	161 AM 73R	161 AM 45C	161 AM 44R	161 AM 45C	161 AM 44R
SiO ₂	41.98	41.98	49.30	44.50	43.75	47.75	43.69	43.28	41.96	41.75	44.46	41.98	44.46	41.98
TiO ₂	3.69	3.69	0.66	2.46	2.75	1.47	2.79	2.75	3.66	3.95	4.11	3.69	4.11	3.69
Al ₂ O ₃	11.75	11.75	5.34	9.05	9.84	6.52	9.64	9.78	11.51	11.71	11.56	11.75	11.56	11.75
*FeO	10.02	10.02	13.67	13.68	13.51	12.99	13.54	13.64	9.83	9.93	10.01	10.02	10.01	10.02
MgO	14.42	14.42	14.50	13.04	12.85	14.41	13.03	12.71	14.68	14.34	14.03	14.42	14.03	14.42
MnO	0.15	0.15	0.17	0.19	0.18	0.24	0.19	0.21	0.13	0.12	0.13	0.15	0.13	0.15
CaO	11.58	11.58	12.05	11.67	11.34	11.58	11.32	11.22	11.74	11.57	11.63	11.58	11.63	11.58
Na ₂ O	2.21	2.21	0.85	1.62	1.87	1.22	1.85	1.87	2.22	2.05	2.10	2.21	2.10	2.21
K ₂ O	0.80	0.80	0.39	0.91	0.91	0.57	0.90	0.92	0.70	0.68	0.70	0.80	0.70	0.80
TOTAL	96.84	96.84	96.77	96.97	97.03	96.88	96.97	96.37	96.40	96.40	96.02	96.84	96.02	96.84
Si	6.208	6.208	7.257	6.627	6.526	7.050	6.524	6.509	6.214	6.200	6.386	6.208	6.386	6.208
Al(IV)	1.792	1.792	0.743	1.374	1.474	0.950	1.476	1.491	1.786	1.802	1.615	1.792	1.615	1.792
Al(VI)	0.257	0.257	0.184	0.215	0.256	0.185	0.221	0.243	0.224	0.250	0.343	0.257	0.343	0.257
Ti	0.411	0.411	0.073	0.276	0.309	0.163	0.313	0.311	0.408	0.441	0.444	0.411	0.444	0.411
*Fe ²⁺	1.240	1.240	0.683	0.704	1.686	1.604	1.691	1.715	1.218	1.233	1.203	1.240	1.203	1.240
Mn	0.019	0.019	0.021	0.024	0.023	0.030	0.024	0.027	0.016	0.015	0.016	0.019	0.016	0.019
Mg	3.179	3.179	3.181	2.894	2.857	3.174	2.900	2.849	3.241	3.174	3.004	3.179	3.004	3.179
Ca	1.835	1.835	1.901	1.862	1.813	1.832	1.811	1.808	1.863	1.841	1.790	1.835	1.790	1.835
Na	0.634	0.634	0.243	0.482	0.541	0.349	0.536	0.545	0.638	0.950	0.585	0.634	0.585	0.634
K	0.151	0.151	0.073	0.173	0.173	0.107	0.172	0.177	0.132	0.114	0.128	0.151	0.128	0.151

Table B.1 Amphibole microprobe analyses (cont.)

Element (%)	Sample		Diorites												
	Pyroxene diorites		41 AM 49C		41 AM 49R		41 AM 50C		41 AM 50R		41 AM 51C		41 AM 51R		41 AM 115C
SiO ₂	179 AM 73C	46.99	179 AM 73R	46.91	49.10	47.82	44.23	47.80	48.04	48.51	49.36	47.80	48.04	48.51	49.36
TiO ₂	179 AM 73C	1.78	179 AM 73R	1.58	1.17	1.40	2.62	1.44	1.53	1.41	1.18	1.44	1.53	1.41	1.18
Al ₂ O ₃	179 AM 73C	7.01	179 AM 73R	6.45	5.37	6.12	9.11	6.09	6.33	5.79	5.07	6.09	6.33	5.79	5.07
*FeO	179 AM 73C	13.18	179 AM 73R	13.25	11.42	11.93	11.71	12.20	11.52	11.86	12.13	12.20	11.52	11.86	12.13
MgO	179 AM 73C	14.17	179 AM 73R	13.88	15.94	15.18	14.54	15.19	15.35	15.73	15.54	15.19	15.35	15.73	15.54
MnO	179 AM 73C	0.21	179 AM 73R	0.22	0.33	0.30	0.22	0.31	0.30	0.30	0.34	0.31	0.30	0.30	0.34
CaO	179 AM 73C	11.55	179 AM 73R	11.49	11.12	11.37	11.17	11.40	11.47	11.41	11.50	11.40	11.47	11.41	11.50
Na ₂ O	179 AM 73C	1.35	179 AM 73R	1.09	1.19	1.26	1.09	1.31	1.15	1.28	1.02	1.31	1.15	1.28	1.02
K ₂ O	179 AM 73C	0.63	179 AM 73R	0.60	0.42	0.53	0.79	0.55	0.50	0.49	0.45	0.55	0.50	0.49	0.45
TOTAL	179 AM 73C	96.89	179 AM 73R	95.48	96.06	95.92	96.41	96.28	96.20	96.78	96.60	96.28	96.20	96.78	96.60
Si	6.951	7.037	6.993	7.222	7.088	7.072	6.586	7.072	7.080	7.117	7.247	7.072	7.080	7.117	7.247
Al(IV)	1.049	0.963	1.007	0.778	0.912	0.928	1.414	0.928	0.920	0.883	0.753	0.928	0.920	0.883	0.753
Al(VI)	0.173	0.178	0.153	0.154	0.159	0.134	0.165	0.134	0.180	0.119	0.125	0.134	0.180	0.119	0.125
Ti	0.198	0.178	0.180	0.130	0.156	0.161	0.193	0.161	0.170	0.156	0.130	0.161	0.170	0.156	0.130
*Fe ²⁺	1.631	1.663	1.631	1.405	1.479	1.510	1.457	1.510	1.420	1.456	1.490	1.510	1.420	1.456	1.490
Mn	0.026	0.028	0.026	0.042	0.038	0.039	0.028	0.039	0.038	0.038	0.042	0.039	0.038	0.038	0.042
Mg	3.124	3.104	3.167	3.495	3.354	3.350	3.224	3.350	3.374	3.440	3.401	3.350	3.374	3.440	3.401
Ca	1.831	1.847	1.776	1.753	1.807	1.807	1.781	1.807	1.812	1.795	1.810	1.807	1.812	1.795	1.810
Na	0.387	0.317	0.420	0.339	0.363	0.375	0.374	0.375	0.330	0.363	0.291	0.375	0.330	0.363	0.291
K	0.119	0.115	0.112	0.080	0.101	0.105	0.149	0.105	0.095	0.093	0.085	0.105	0.095	0.093	0.085

Table B.1 Amphibole microprobe analyses (cont.)

Element (%)	Sample		Diorites											
	41 AM 115R	44 AM 38C	44 AM 38R	108 AM 54C	108 AM 54R	108 AM 57C	108 AM 57R	177 AM 14C	177 AM 14R	132 AM 18C				
SiO ₂	48.81	50.30	49.57	43.68	43.68	53.62	43.68	45.04	45.85	52.67				
TiO ₂	1.38	0.68	0.79	2.76	2.73	0.14	1.15	2.43	1.85	0.32				
Al ₂ O ₃	5.75	4.50	5.01	9.57	9.43	1.59	5.90	8.98	7.76	2.21				
*FeO	11.65	11.95	11.90	12.25	12.60	9.41	13.08	11.99	12.59	12.64				
MgO	15.74	16.47	15.94	14.01	13.85	19.51	15.15	14.61	14.36	15.60				
MnO	0.30	0.42	0.41	0.16	0.21	0.29	0.32	0.15	0.18	0.23				
CaO	11.40	10.39	10.99	11.13	11.09	11.48	11.03	11.22	11.34	12.67				
Na ₂ O	1.25	1.11	1.17	1.94	1.93	0.21	0.99	1.56	1.19	0.20				
K ₂ O	0.50	0.31	0.38	0.85	0.95	0.11	0.44	0.83	0.70	0.05				
TOTAL	96.77	96.61	96.15	96.42	96.54	95.37	96.76	96.80	95.94	96.59				
Si	7.149	7.351	7.291	6.520	6.544	7.778	7.159	6.657	6.846	7.689				
Al(IV)	0.851	0.649	0.709	1.480	1.457	0.222	0.841	1.343	1.155	0.271				
Al(VI)	0.142	0.126	0.159	1.205	0.202	0.050	0.182	0.222	0.212	0.069				
Ti	0.152	0.075	0.088	0.310	0.306	0.015	0.127	0.270	0.208	0.035				
*Fe ²⁺	1.427	1.460	1.464	1.530	1.572	1.142	1.609	1.482	1.572	1.543				
Mn	0.037	0.053	0.051	0.020	0.027	0.036	0.040	0.019	0.023	0.028				
Mg	3.435	3.587	3.494	3.117	3.080	4.002	3.321	3.218	3.196	3.395				
Ca	1.799	1.705	1.733	1.781	1.773	1.785	1.738	1.777	1.815	1.982				
Na	0.094	0.314	0.335	0.562	0.558	0.059	0.282	0.447	0.345	0.057				
K	0.094	0.057	0.071	0.162	0.162	0.020	0.083	0.157	0.133	0.009				

Table B.1 Amphibole microprobe analyses (cont.)

Element (X)	Sample		Monzonites											
	Diorites		132 AM 18R	132 AM 19C	132 AM 19R	251 AM 4C	251 AM 4R	251 AM 5C	251 AM 5R	251 AM 6C	251 AM 6R	21 AM 121C		
SiO ₂	52.97	52.05	50.73	49.51	50.82	50.98	48.77	47.64	47.71	51.95				
TiO ₂	0.33	0.28	1.06	0.82	0.46	0.36	0.73	1.67	1.61	0.38				
Al ₂ O ₃	2.16	3.07	4.27	5.23	3.79	3.94	5.88	6.46	6.43	3.25				
*FeO	13.77	12.29	12.24	13.39	13.71	12.62	13.76	12.43	12.84	13.76				
MgO	15.11	15.82	15.64	14.65	14.41	15.30	14.20	15.03	14.65	15.24				
MnO	0.24	0.17	0.17	0.23	0.30	0.26	0.19	0.17	0.22	0.56				
CaO	11.99	12.32	12.08	12.27	12.60	12.51	12.09	11.32	11.33	11.08				
Na ₂ O	0.30	0.35	0.56	0.68	0.39	0.49	0.80	1.35	1.24	0.66				
K ₂ O	0.10	0.15	0.23	0.40	0.22	0.22	0.46	0.63	0.59	0.22				
TOTAL	96.96	96.49	96.99	97.15	96.72	96.69	96.91	96.73	96.81	97.09				
Si	7.725	7.597	7.387	7.262	7.480	7.465	7.193	7.024	7.048	7.584				
Al(IV)	0.275	0.403	0.613	0.738	0.520	0.535	0.807	0.976	0.952	0.416				
Al(VI)	0.097	0.126	0.120	0.167	0.138	0.145	0.216	0.147	0.168	0.143				
Ti	0.036	0.031	0.116	0.091	0.051	0.040	0.081	0.185	0.179	0.042				
*Fe ²⁺	1.680	1.498	1.491	1.643	1.688	1.546	1.698	1.533	1.587	1.680				
Mn	0.030	0.021	0.021	0.029	0.037	0.032	0.024	0.021	0.028	0.069				
Mg	3.285	3.442	3.394	3.203	3.162	3.339	3.122	3.303	3.226	3.317				
Ca	1.874	1.927	1.885	1.929	1.988	1.963	1.911	1.789	1.794	1.733				
Na	0.085	0.099	0.158	0.193	0.111	0.139	0.229	0.286	0.355	0.187				
K	0.019	0.028	0.043	0.075	0.042	0.041	0.087	0.119	0.111	0.042				

Table B-1 Amphibole microprobe analyses (cont.)

Element (%)	Sample		Monzonites Appinites											
	21 AH 121R	30 AH IC	30 AH 2R	30 AH 3C	30 AH 3R	30 AH 9C	30 AH 9R	75 AH 58C	75 AH 58R	75 AH 59C	TOTAL	TOTAL		
SiO ₂	50.33	43.06	43.46	42.24	51.66	44.00	51.97	48.12	49.74	42.83	97.43	96.18		
TiO ₂	0.85	3.29	2.80	3.79	0.48	2.53	0.30	1.22	1.07	3.13	0.29	0.26		
Al ₂ O ₃	4.79	10.00	9.77	10.72	3.84	9.95	3.36	7.00	5.57	10.71	0.59	0.53		
*FeO	14.07	11.00	10.76	11.07	10.04	10.68	9.15	11.51	10.70	13.17	0.29	0.26		
MgO	14.78	14.00	14.80	14.13	17.63	15.04	18.38	15.47	16.52	12.75	95.84	96.68		
MnO	0.59	0.17	0.18	0.14	0.27	0.16	0.27	0.25	0.28	0.26	0.59	0.53		
CaO	10.73	11.42	11.16	11.14	11.36	11.17	11.22	11.44	11.41	11.52	0.29	0.26		
Na ₂ O	1.00	2.30	2.35	2.48	0.89	2.10	0.84	1.31	1.01	1.80	0.29	0.26		
K ₂ O	0.29	0.59	0.53	0.57	0.20	0.56	0.20	0.53	0.39	0.76	0.29	0.26		
TOTAL	97.43	95.84	95.80	96.27	96.37	96.18	95.67	96.86	96.68	96.92	97.43	96.18		
Si	7.357	6.441	6.483	6.298	7.478	6.518	7.539	7.040	7.232	6.393	7.357	7.040		
Al(IV)	0.643	1.559	1.517	1.702	0.522	1.482	0.461	0.960	0.768	1.607	0.643	0.960		
Al(VI)	0.182	0.205	0.201	0.182	0.134	0.256	0.114	0.247	0.188	0.277	0.182	0.247		
Ti	0.094	0.371	0.215	0.425	0.053	0.283	0.033	0.135	0.118	0.351	0.094	0.135		
*Fe ²⁺	1.721	1.374	1.343	1.380	1.216	1.323	1.110	1.408	1.301	1.644	1.721	1.408		
Mn	0.074	0.022	0.023	0.018	0.034	0.020	0.033	0.032	0.034	0.034	0.074	0.032		
Mg	3.221	3.119	3.290	3.141	3.803	3.322	3.973	3.374	3.580	2.836	3.221	3.374		
Ca	1.681	1.830	1.784	1.780	1.762	1.774	1.744	1.794	1.778	1.843	1.681	1.794		
Na	0.284	0.666	0.680	0.718	0.251	0.603	0.236	0.372	0.285	0.520	0.284	0.372		
K	0.055	0.113	0.102	0.109	0.038	0.107	0.038	0.100	0.073	0.146	0.055	0.100		

Table B.1 Amphibole microprobe analyses (cont.)

Element (%)	Sample	Diorites (Juan Jorge Complex)																					
		Appinites			75 AM 65C			75 AM 65R			JJ3 AM 28C			JJ3 AM 28R			JJ4 AM 65C			JJ4 AM 65R			JJ4 AM 66C
SiO ₂	42.60	75 AM 59R	75 AM 64C	75 AM 64R	75 AM 65C	75 AM 65R	75 AM 65C	75 AM 65R	JJ3 AM 28C	JJ3 AM 28R	JJ4 AM 65C	JJ4 AM 65R	JJ4 AM 66C	47.08	46.58	48.10	47.52	47.51					
TiO ₂	2.99								1.20	1.33	1.10	1.14	1.15	6.63	6.57	5.90	6.32	6.09					
Al ₂ O ₃	10.69							10.13	10.04	13.79	13.23	12.97	13.15	13.79	13.23	12.93	12.97	13.15					
*FeO	13.27							15.35	12.94	13.74	14.15	14.38	14.29	13.79	14.15	14.49	14.38	14.29					
MgO	12.88							13.57	13.22	0.47	0.48	0.41	0.44	13.74	0.44	0.48	0.41	0.44					
MnO	0.24							0.22	0.23	11.60	11.43	11.71	11.51	0.47	0.44	0.48	0.41	0.44					
CaO	11.29							10.86	11.33	1.28	1.47	1.24	1.17	11.60	11.43	11.61	11.71	11.51					
Na ₂ O	1.82							1.83	1.73	1.28	1.47	1.24	1.17	1.28	1.47	1.21	1.24	1.17					
K ₂ O	0.82							0.56	0.62	0.68	0.62	0.57	0.49	0.68	0.62	0.42	0.57	0.49					
TOTAL	96.58							97.25	95.62	96.72	96.17	96.34	96.01	96.72	96.17	96.34	96.27	96.01					
Si	6.386							6.318	6.440	7.020	6.983	7.137	7.095	7.020	6.983	7.137	7.065	7.095					
Al(IV)	1.614							1.682	1.560	0.980	1.017	0.863	0.905	0.980	1.017	0.863	0.933	0.905					
Al(VI)	0.272							0.113	0.229	0.186	0.144	0.169	0.167	0.186	0.144	0.169	0.171	0.167					
Ti	0.338							0.304	0.327	0.135	0.150	0.123	0.129	0.135	0.150	0.123	0.128	0.129					
*Fe ²⁺	1.663							1.930	1.635	1.720	1.659	1.613	1.643	1.720	1.659	1.605	1.613	1.643					
Mn	0.031							0.028	0.030	0.059	0.056	0.060	0.056	0.059	0.056	0.060	0.052	0.056					
Mg	2.878							3.039	2.975	3.054	3.162	3.205	3.181	3.054	3.162	3.205	3.197	3.181					
Ca	1.813							1.750	1.833	1.854	1.836	1.846	1.842	1.854	1.836	1.846	1.866	1.842					
Na	0.530							0.534	0.507	0.370	0.427	0.358	0.339	0.370	0.427	0.348	0.358	0.339					
K	0.157							0.108	0.120	0.129	0.119	0.080	0.093	0.129	0.119	0.080	0.108	0.093					

100
100
100

Table B.1 Amphibole microprobe analyses (cont.)

Element (Z)	Sample		Diorites (Juan Jorge Complex)											
	JJ4 AM 66R	JJ7 AM 24C	JJ7 AM 24R	JJ7 AM 25C	JJ7 AM 25R	JJ8 AM 30C	JJ8 AM 30R	JJ8 AM 31C	JJ8 AM 31R	JJ8 AM 35C				
SiO ₂	47.02	44.61	45.74	50.54	46.31	43.18	47.90	46.61	47.49	45.95				
TiO ₂	1.21	2.27	1.55	0.49	1.43	2.83	1.20	1.66	1.27	1.76				
Al ₂ O ₃	6.26	8.69	7.99	4.67	7.65	9.97	6.28	7.34	6.54	7.45				
*FeO	12.91	14.50	14.32	11.96	14.10	13.85	12.72	13.74	13.93	13.37				
MgO	14.08	12.32	13.00	15.67	13.08	12.03	14.44	13.36	13.57	13.13				
MnO	0.40	0.39	0.36	0.42	0.41	0.33	0.39	0.44	0.43	0.48				
CaO	11.73	11.52	11.73	11.97	11.41	11.54	11.73	11.30	11.58	11.17				
Na ₂ O	1.21	1.58	1.19	0.73	1.33	1.96	1.24	1.45	1.24	1.46				
K ₂ O	0.58	0.77	0.70	0.30	0.77	0.74	0.53	0.54	0.51	0.50				
TOTAL	95.48	96.82	96.62	97.13	96.53	96.67	96.62	96.70	96.95	96.50				
Si	7.058	6.695	6.840	7.380	6.917	6.496	7.093	6.944	7.062	6.885				
Al(IV)	0.942	1.305	1.160	0.621	1.083	1.504	0.907	1.056	0.938	1.118				
Al(VI)	0.166	0.233	0.249	0.183	0.264	0.264	0.190	0.234	0.208	0.198				
Ti	0.137	0.256	0.174	0.054	0.161	0.320	0.134	0.186	0.142	0.198				
*Fe ²⁺	1.621	1.820	1.791	1.461	1.762	1.743	1.576	1.712	1.733	1.801				
Mn	0.051	0.050	0.046	0.052	0.052	0.042	0.049	0.056	0.054	0.061				
Mg	3.150	2.856	1.898	3.410	1.912	2.698	3.187	2.967	3.008	2.933				
Ca	1.887	1.853	1.880	1.873	1.826	1.860	1.862	1.804	1.845	1.794				
Na	0.352	0.460	0.345	0.207	0.385	0.572	0.356	0.419	0.358	0.424				
K	0.111	0.148	0.134	0.056	0.147	0.142	0.100	0.103	0.097	0.096				

116

Table B.1 Amphibole microprobe analyses (cont.)

Element (Z)	Sample	Microdiorite Xenolith (Juan Jorge Complex)									
		JJ8 AM 35R	JJ19 AM 10C	JJ19 AM 11C	JJ19 AM 12C	JJ19 AM 13C	JJ19 AM 14C	JJ19 AM 15C	JJ19 AM 16C	JJ19 AM 17C	JJ19 AM 17C
SiO ₂	48.52	47.59	47.25	48.89	45.15	47.30	48.50	43.69	47.45	47.45	
TiO ₂	1.01	0.90	1.04	0.95	1.47	1.05	0.85	1.56	1.14	1.14	
Al ₂ O ₃	5.77	5.33	6.04	5.07	7.55	5.82	4.94	8.59	5.64	5.64	
*FeO	13.60	13.96	14.57	13.78	15.70	14.37	13.74	16.41	14.23	14.23	
MgO	13.99	13.55	13.10	13.96	11.89	13.35	13.84	10.86	13.32	13.32	
MnO	0.39	0.65	0.66	0.66	0.62	0.72	0.65	0.64	0.63	0.63	
CaO	11.83	11.74	11.47	11.61	11.44	11.72	11.67	11.62	11.59	11.59	
Na ₂ O	0.86	1.07	1.39	1.16	1.43	1.22	1.15	1.62	1.38	1.38	
K ₂ O	0.52	0.49	0.61	0.48	0.82	0.57	0.47	0.95	0.58	0.58	
TOTAL	96.65	95.58	96.66	97.10	96.38	96.54	96.47	96.23	96.22	96.22	
Si	7.190	7.183	7.100	7.254	6.854	7.103	7.260	6.699	7.133	7.133	
Al(IV)	0.819	0.817	0.901	0.746	1.146	0.877	0.740	1.301	0.868	0.868	
Al(VI)	0.198	0.131	0.170	0.141	0.205	0.134	0.131	0.252	0.132	0.132	
Ti	0.113	0.102	0.118	0.106	0.168	0.119	0.096	0.180	0.129	0.129	
*Fe ²⁺	1.686	1.762	1.831	1.710	1.994	1.805	1.720	2.105	1.789	1.789	
Mn	0.049	0.083	0.084	0.083	0.080	0.092	0.083	0.083	0.080	0.080	
Mg	3.090	3.048	2.934	3.067	2.690	2.988	3.088	2.482	2.985	2.985	
Ca	1.879	1.899	1.867	1.846	1.861	1.886	1.872	1.909	1.867	1.867	
Na	0.247	0.313	0.405	0.334	0.421	0.355	0.334	0.482	0.402	0.402	
K	0.098	0.094	0.117	0.091	0.159	0.109	0.090	0.186	0.111	0.111	

Table B.2 Amphibole mineralogy

GLEN DOLL COMPLEX

OLIVINE GABBRO

88/AM/95C	Pargasite
88/AM/95R	Pargasite
88/AM/96C	Pargasitic hornblende
88/AM/96R	Pargasite
91/AM/85C	Pargasite
91/AM/85R	Pargasitic hornblende
91/AM/86C	Pargasitic hornblende
91/AM/86R	Pargasite
91/AM/87R	Pargasitic hornblende
91/AM/126C	Pargasite
91/AM/126R	Pargasite

GABBRO

79/AM/41C	Pargasitic hornblende
79/AM/41R	Pargasitic hornblende
82/AM/41C	Ferroan pargasite
82/AM/41R	Edenitic hornblende
82/AM/42C	Ferroan pargasite
82/AM/42R	Kaersutite
82/AM/43C	Magnesio-hornblende
82/AM/43R	Actinolitic hornblende
161/AM/44C	Pargasite
161/AM/44R	Pargasite
161/AM/45C	Pargasitic hornblende
161/AM/73C	Pargasite
161/AM/73R	Pargasite

Table B.2 Amphibole mineralogy (cont.)

PYROXENE DIORITE

179/AM/2R	Actinolitic hornblende
179/AM/10C	Edenitic hornblende
179/AM/10R	Edenitic hornblende
179/AM/11C	Magnesio-hornblende
179/AM/11R	Edenitic hornblende
179/AM/11M	Edenitic hornblende
179/AM/73C	Magnesio-hornblende
179/AM/73R	Magnesio-hornblende
179/AM/73M	Magnesio-hornblende

HORNBLLENDE DIORITE

41/AM/49C	Magnesio-hornblende
41/AM/49R	Magnesio-hornblende
41/AM/50C	Edenitic hornblende
41/AM/50R	Magnesio-hornblende
41/AM/51C	Edenite
41/AM/51R	Magnesio-hornblende
41/AM/115C	Magnesio-hornblende
41/AM/115R	Magnesio-hornblende
44/AM/38C	Actinolitic hornblende
44/AM/38R	Actinolitic hornblende
108/AM/54C	Edenitic hornblende
108/AM/54R	Edenitic hornblende
108/AM/57C	Actinolite
108/AM/57R	Magnesio-hornblende
132/AM/18C	Actinolite
132/AM/18R	Actinolite
132/AM/19C	Actinolite
132/AM/19R	Actinolitic hornblende
177/AM/14C	Edenitic hornblende
177/AM/14R	Magnesio-hornblende
251/AM/4C	Actinolitic hornblende
251/AM/4R	Actinolitic hornblende
251/AM/5C	Actinolitic hornblende

Table B.2 Amphibole mineralogy (cont.)

HORNBLENDE DIORITE (cont.)

251/AM/5R	Magnesio-hornblende
251/AM/6C	Magnesio-hornblende
251/AM/6R	Magnesio-hornblende

MONZONITE

21/AM/121C	Actinolite
21/AM/121R	Magnesio-hornblende

APPINITE

30/AM/1C	Ferroan pargasitic hornblende
30/AM/2R	Edenite
30/AM/3C	Tschermakitic hornblende
30/AM/3R	Actinolitic hornblende
30/AM/9C	Edenitic hornblende
30/AM/9R	Actinolite
75/AM/58C	Magnesio-hornblende
75/AM/58R	Magnesio-hornblende
75/AM/59C	Ferroan pargasitic hornblende
75/AM/59R	Ferroan pargasitic hornblende
75/AM/64C	Ferroan pargasitic hornblende
75/AM/64R	Ferroan pargasitic hornblende
75/AM/65C	Ferroan pargasitic hornblende
75/AM/65R	Ferroan pargasitic hornblende

Table B.2 Amphibole mineralogy (cont.)

JUAN JORGE COMPLEX

QUARTZ MICA DIORITE

JJ3/AM/28C	Magnesio-hornblende
JJ3/AM/28R	Edenite
JJ4/AM/65C	Magnesio-hornblende
JJ4/AM/65R	Magnesio-hornblende
JJ4/AM/66C	Magnesio-hornblende
JJ4/AM/66R	Magnesio-hornblende
JJ7/AM/24C	Edenitic hornblende
JJ7/AM/24R	Edenite
JJ7/AM/25C	Actinolitic hornblende
JJ7/AM/25R	Magnesio-hornblende
JJ8/AM/31C	Magnesio-hornblende
JJ8/AM/31R	Magnesio-hornblende
JJ8/AM/35C	Magnesio-hornblende
JJ8/AM/35R	Magnesio-hornblende
JJ8/AM/30C	Ferroan pargasitic hornblende
JJ8/AM/30R	Magnesio-hornblende

MICRODIORITE XENOLITH

JJ19/AM/10C	Magnesio-hornblende
JJ19/AM/11C	Edenite
JJ19/AM/12C	Actinolitic hornblende
JJ19/AM/13C	Edenite
JJ19/AM/14C	Magnesio-hornblende
JJ19/AM/15C	Actinolitic hornblende
JJ19/AM/16C	Edenitic hornblende
JJ19/AM/17C	Magnesio-hornblende

Table B.3 Biotite microprobe analyses

Element (%)	Sample		Olivine gabbros											
	88 BI 97C	88 BI 97R	88 BI 98C	91 BI 88C	91 BI 88R	91 BI 91C	91 BI 92C	91 BI 92R	91 BI 93C	91 BI 125C				
SiO ₂	37.61	38.48	37.65	36.79	37.04	36.47	37.11	34.66	36.66	37.25				
TiO ₂	0.76	0.84	1.41	4.23	4.13	4.06	2.15	1.43	4.41	4.23				
Al ₂ O ₃	14.72	15.01	14.55	15.03	15.57	14.43	16.64	16.96	15.58	15.52				
*FeO	7.34	7.16	7.17	6.77	7.20	6.76	6.94	8.45	6.61	7.05				
MgO	22.56	22.17	22.07	20.78	20.06	21.25	21.03	20.90	20.25	19.82				
MnO	0.02	0.05	0.02	0.02	0.01	0.03	0.08	0.13	0.01	BD				
CaO	0.01	0.01	0.01	0.02	0.02	0.03	0.09	2.85	0.03	BD				
N ₂ O	1.34	1.27	1.93	1.76	1.87	1.70	2.17	1.46	1.92	1.86				
K ₂ O	7.69	8.04	7.01	7.24	7.33	6.45	6.23	2.64	7.15	7.43				
F	BD	0.03	BD	0.01	BD	BD	BD	BD	BD	0.07				
TOTAL	92.04	93.05	91.81	92.64	93.23	91.18	92.44	89.49	96.61	93.66				
Si	5.830	5.893	5.836	5.660	5.670	5.680	5.680	5.462	5.634	5.727				
Al(IV)	2.170	2.107	2.164	2.340	2.330	2.310	2.320	2.538	2.366	2.267				
Al(VI)	0.521	0.603	0.495	0.387	0.479	0.329	0.683	0.613	0.456	0.518				
Ti	0.089	0.097	0.165	0.49	0.476	0.476	0.248	0.170	0.51	0.484				
Fe ²⁺	0.952	0.918	0.929	0.871	0.921	0.881	0.889	1.114	0.85	0.898				
Mn	0.003	0.007	0.003	0.003	0.002	0.004	0.011	0.018	0.001	-				
Mg	5.212	5.060	5.097	4.764	4.577	4.932	4.798	4.909	4.639	4.496				
Ca	0.002	0.001	0.002	0.003	0.004	0.005	0.015	0.482	0.005	-				
Na	0.402	0.378	0.581	0.524	0.556	0.512	0.644	0.448	0.573	0.550				
K	1.521	1.571	1.386	1.422	1.432	1.282	1.218	0.532	1.402	1.444				

Table B.3 Biotite microprobe analyses (cont.)

Element (X)	Sample		Gabbro			Pyroxene diorite			Diorites		
SiO ₂	91 BI 125R	37.25	161 BI 56C	179 BI 36R	179 BI 71C	179 BI 71R	44 BI 36C	44 BI 36R	44 BI 37C		
TiO ₂		4.37	36.96	36.81	35.77	32.77	35.07	36.44	35.84		
Al ₂ O ₃		15.36	5.25	5.06	4.88	5.96	3.67	4.66	4.30		
*FeO		6.97	14.68	14.02	14.14	13.95	13.38	13.61	13.01		
MgO		19.50	11.90	18.40	18.16	19.31	18.82	16.03	16.22		
MnO		BD	16.27	12.21	12.06	13.25	12.96	13.81	14.32		
CaO		BD	0.11	0.13	0.11	0.09	0.16	0.17	0.19		
Na ₂ O		BD	BD	BD	BD	1.76	0.06	0.03	0.03		
K ₂ O		1.98	0.12	0.13	0.14	0.07	0.07	0.07	0.08		
F		7.11	9.23	9.38	9.10	4.38	7.87	9.09	8.77		
TOTAL		0.03	0.25	BD	BD	BD	BD	0.01	0.02		
		92.59	94.93	96.57	94.36	91.53	92.05	93.93	92.75		
Si		5.727	5.722	5.467	5.500	5.154	5.776	5.821	5.809		
Al(IV)		2.273	2.278	2.533	2.500	2.846	2.224	2.179	2.191		
Al(VI)		0.512	0.400	0.039	0.063	0.261	0.374	0.387	0.295		
Ti		0.506	0.611	0.602	0.564	0.705	0.455	0.561	0.524		
Fe ²⁺		0.897	1.541	2.316	2.335	2.539	2.592	2.141	2.200		
Mn		-	0.015	0.017	0.014	0.011	0.022	0.024	0.026		
Mg		4.469	3.755	2.746	2.763	3.106	3.181	3.288	3.459		
Ca		-	-	-	-	0.297	0.011	0.006	0.006		
Na		0.592	0.035	0.037	0.043	0.023	0.024	0.023	0.025		
K		1.395	1.823	1.764	1.784	0.879	1.653	1.852	1.813		

23
24

Table B.3 Biotite microprobe analyses (cont.)

Element (%)	Sample		Monzonite																
	Diorites		251 BI 8C	251 BI 8R	251 BI 9C	251 BI 9R	251 BI 23C	21 BI 82C	132 BI 35C	108 BI 60R	108 BI 60C	108 BI 60R	132 BI 35C	251 BI 8C	251 BI 8R	251 BI 9C	251 BI 9R	251 BI 23C	21 BI 82C
SiO ₂	35.30	37.22	36.61	36.24	36.13	37.03	35.53	35.82	36.28	37.25	37.22	36.28	36.61	36.24	36.13	37.03	35.53	35.82	36.28
TiO ₂	4.66	4.37	4.69	4.38	4.64	4.53	4.55	4.18	4.99	4.47	4.37	4.99	4.69	4.38	4.64	4.53	4.55	4.18	4.99
Al ₂ O ₃	13.33	14.36	14.20	14.07	13.81	15.52	13.84	13.36	14.32	14.35	14.36	14.32	14.20	14.07	13.81	15.52	13.84	13.36	14.32
*FeO	17.93	17.07	18.14	18.36	18.49	17.05	18.54	18.60	16.53	17.17	17.07	16.53	18.14	18.36	18.49	17.05	18.54	18.60	16.53
MgO	12.52	13.28	11.95	11.79	12.12	12.23	12.26	12.45	14.01	13.38	13.28	14.01	11.95	11.79	12.12	12.23	12.26	12.45	14.01
MnO	0.23	0.13	0.18	0.17	0.15	0.14	0.16	0.23	0.09	0.12	0.13	0.09	0.18	0.17	0.15	0.14	0.16	0.23	0.09
CaO	0.09	BD	BD	BD	BD	BD	BD	0.02	BD	BD	BD	BD	BD	BD	BD	BD	BD	0.02	BD
Na ₂ O	0.09	0.16	0.16	0.17	0.19	0.18	0.14	0.10	0.13	0.14	0.14	0.13	0.16	0.17	0.19	0.18	0.14	0.10	0.13
K ₂ O	8.33	8.66	9.29	9.35	8.60	9.42	9.16	9.16	8.13	9.04	8.66	8.13	9.29	9.35	8.60	9.42	9.29	9.16	8.13
F	BD	BD	BD	BD	BD	BD	BD	0.05	BD	BD	BD	BD	BD	BD	BD	BD	BD	0.05	BD
TOTAL	92.47	95.23	95.21	94.52	94.14	96.10	94.30	93.95	94.52	95.94	95.23	94.52	95.21	94.52	94.14	96.10	94.30	93.95	94.52
Si	5.778	5.599	5.570	5.570	5.590	5.538	5.491	5.811	5.734	5.578	5.599	5.734	5.570	5.570	5.590	5.538	5.491	5.811	5.734
Al(IV)	2.222	2.401	2.430	2.430	2.441	2.462	2.509	2.189	2.267	2.422	2.401	2.267	2.430	2.430	2.441	2.462	2.509	2.189	2.267
Al(VI)	0.351	0.145	0.116	0.117	0.063	0.274	0.012	0.367	0.401	0.111	0.145	0.401	0.116	0.117	0.063	0.274	0.012	0.367	0.401
Ti	0.574	0.494	0.537	0.506	0.537	0.509	0.529	0.510	0.593	0.503	0.494	0.593	0.537	0.506	0.537	0.509	0.529	0.510	0.593
Fe ²⁺	2.454	2.147	2.309	2.360	2.379	2.132	2.396	2.523	2.185	2.152	2.147	2.185	2.309	2.360	2.379	2.132	2.396	2.523	2.185
Mn	0.032	0.016	0.023	0.022	0.019	0.017	0.029	0.032	0.012	0.016	0.016	0.012	0.023	0.022	0.019	0.017	0.029	0.032	0.012
Mg	3.054	2.977	2.709	2.700	2.780	2.727	2.825	3.009	2.185	2.986	2.977	2.185	2.709	2.700	2.780	2.727	2.825	3.009	2.185
Ca	0.017	-	-	-	-	-	-	0.003	-	-	-	-	-	-	-	-	-	0.003	-
Na	0.028	0.046	0.048	0.049	0.058	0.052	0.041	0.032	0.041	0.041	0.041	0.041	0.048	0.049	0.058	0.052	0.041	0.032	0.041
K	1.740	1.662	1.803	1.843	1.688	1.798	1.831	1.896	1.640	1.727	1.662	1.640	1.803	1.843	1.688	1.798	1.831	1.896	1.640

424

Table B.3 Biotite microprobe analyses (cont.)

Element (%)	Monzonite				Adameellite					
	21 BI 82K	21 BI 119C	21 BI 119R	21 BI 120C	21 BI 120R	36 BI 25C	36 BI 25R	36 BI 26C	36 BI 27C	36 BI 27R
SiO ₂	35.89	37.64	35.89	36.66	37.30	36.34	36.90	36.49	36.33	36.61
TiO ₂	4.43	4.04	1.28	4.20	4.39	4.91	4.73	4.70	4.73	4.57
Al ₂ O ₃	13.75	13.41	14.73	13.41	13.26	13.00	12.90	13.12	13.02	13.02
*FeO	18.35	18.50	18.79	19.38	19.13	15.94	15.42	16.14	15.99	15.87
MgO	12.44	12.59	14.26	12.10	12.37	14.00	14.40	14.05	13.80	14.04
MnO	0.18	0.13	0.13	0.18	0.17	0.29	0.28	0.30	0.28	0.29
CaO	0.02	0.01	0.13	BD	BD	0.03	0.03	0.03	0.04	0.03
Na ₂ O	0.10	0.12	0.11	0.10	0.12	0.07	0.08	0.08	0.06	0.07
K ₂ O	9.21	9.44	6.88	9.19	9.39	9.26	9.10	9.12	9.14	9.30
F	0.04	0.05	0.08	0.14	0.06	0.14	0.08	0.17	0.19	0.11
TOTAL	94.41	95.93	92.28	95.47	96.18	93.98	93.91	94.19	93.59	93.91
Si	5.782	5.948	5.836	5.862	5.904	5.825	5.886	5.834	5.847	5.864
Al(IV)	2.218	2.052	2.164	2.138	2.096	2.175	2.114	2.166	2.153	2.136
Al(VI)	0.394	0.446	0.660	0.389	0.378	0.282	0.310	0.308	0.318	0.323
Ti	0.537	0.481	0.157	0.505	0.523	0.593	0.568	0.565	0.573	0.551
Fe ²⁺	2.472	2.445	2.555	2.592	2.533	2.137	2.057	2.158	2.153	2.126
Mn	0.024	0.018	0.018	0.025	0.023	0.04	0.038	0.040	0.039	0.040
Mg	2.986	2.966	3.456	2.908	2.918	3.344	3.424	3.349	3.311	3.353
Ca	0.003	0.002	0.024	-	-	0.005	0.005	0.005	0.007	0.005
Na	0.033	0.037	0.034	0.030	0.038	0.023	0.024	0.026	0.020	0.022
K	1.894	1.904	1.428	1.876	1.896	1.895	1.852	1.861	1.877	1.901

Table B.3 Biotite microprobe analyses (cont.)

Element (X)	Sample		Diorites (Juan Jorge Complex)											
	JJ3 BI 27C	JJ3 BI 27R	JJ3 BI 29C	JJ3 BI 29R	JJ4 BI 61C	JJ4 BI 61R	JJ7 BI 23C	JJ7 BI 23R	JJ7 BI 48C	JJ8 BI 34C				
SiO ₂	37.32	36.64	36.71	37.01	35.07	36.82	37.12	36.79	34.16	36.34				
TiO ₂	3.88	3.76	4.14	3.88	3.96	3.98	3.79	4.54	3.07	3.16				
Al ₂ O ₃	14.20	14.19	14.02	14.03	13.74	14.23	14.37	14.36	14.83	13.43				
*FeO	17.31	17.07	17.18	17.57	16.99	16.74	16.98	16.90	18.05	17.41				
MgO	13.72	13.94	13.05	12.98	13.52	13.69	13.40	12.73	16.13	13.19				
MnO	0.32	0.33	0.28	0.35	0.31	0.30	0.25	0.24	0.23	0.21				
CaO	BD	BD	BD	BD	BD	BD	BD	BD	BD	BD				
Na ₂ O	0.07	0.08	0.10	0.08	0.09	0.09	0.11	0.11	0.07	0.09				
K ₂ O	7.99	8.61	9.13	8.95	8.87	8.88	8.22	8.54	9.98	7.93				
F	0.96	BD	BD	BD	BD	BD	BD	BD	BD	BD				
TOTAL	95.77	94.61	94.61	94.84	92.54	94.72	94.81	94.21	91.52	91.75				
Si	5.838	5.563	5.592	5.623	5.481	5.579	5.859	5.595	5.03	5.682				
Al(IV)	2.162	2.437	2.408	2.377	2.519	2.421	2.141	2.405	2.698	2.318				
Al(VI)	0.457	0.100	0.110	0.136	0.012	0.120	0.533	0.168	0.015	0.156				
Ti	0.456	0.429	0.474	0.443	0.466	0.453	0.451	0.519	0.358	0.371				
Fe ²⁺	2.264	2.167	2.188	2.233	2.221	2.121	2.242	2.149	2.343	2.277				
Mn	0.042	0.042	0.036	0.045	0.041	0.039	0.034	0.031	0.030	0.028				
Mg	3.198	3.154	2.964	2.940	3.150	3.092	3.151	2.886	3.732	3.073				
Ca	-	-	-	-	-	-	-	-	-	-				
Na	0.022	0.023	0.03	0.024	0.026	0.028	0.033	0.034	0.021	0.028				
K	1.594	1.667	1.774	1.734	1.768	1.716	1.654	1.656	0.987	1.582				

Table B.3 Biotite microprobe analyses (cont.)

Element (Z)	Sample	Granites (Juan Jorge Complex)																	
		JJ8 BI 34R	JJ17 BI 51C	JJ17 BI 52C	JJ17 BI 52R	JJ17 BI 53C	JJ17 BI 53R	JJ17 BI 53M	TOTAL	Si	Al(IV)	Al(VI)	Ti	Fe ²⁺	Mn	Mg	Ca	Na	K
SiO ₂	36.93	34.93	36.30	37.22	36.53	37.00	36.56	95.39	5.474	5.570	5.643	5.557	5.627	5.572	5.572	5.572	5.572	5.572	5.572
TiO ₂	4.28	4.29	4.45	4.02	4.26	4.41	4.09	2.414	2.526	2.430	2.358	2.443	2.373	2.428	2.428	2.428	2.428	2.428	2.428
Al ₂ O ₃	14.32	13.78	13.62	13.49	13.96	13.48	13.86	0.140	0.019	0.0329	0.053	0.060	0.044	0.063	0.063	0.063	0.063	0.063	0.063
*FeO	17.79	18.62	17.71	17.40	17.78	17.03	17.79	0.487	0.506	0.514	0.458	0.488	0.505	0.469	0.469	0.469	0.469	0.469	0.469
MgO	12.61	12.19	12.58	13.24	12.82	13.02	12.79	2.251	2.440	2.274	2.206	2.262	2.166	2.267	2.267	2.267	2.267	2.267	2.267
MnO	0.24	0.51	0.50	0.47	0.58	0.52	0.58	0.030	0.068	0.064	0.060	0.074	0.067	0.075	0.075	0.075	0.075	0.075	0.075
CaO	BD	BD	BD	BD	BD	BD	BD	2.844	2.846	2.878	2.992	2.907	2.952	2.907	2.907	2.907	2.907	2.907	2.907
Na ₂ O	0.12	0.11	0.12	0.07	0.08	0.08	0.09	-	-	-	-	-	-	-	-	-	-	-	-
K ₂ O	9.12	8.52	9.22	9.44	9.28	9.40	9.44	0.034	0.033	0.035	0.020	0.024	0.025	0.025	0.025	0.025	0.025	0.025	0.025
F	BD	BD	BD	BD	BD	BD	BD	1.760	1.704	1.806	1.826	1.801	1.824	1.835	1.835	1.835	1.835	1.835	1.835
TOTAL	95.39	92.95	94.50	95.35	95.29	94.95	95.21												

Table B.4 Olivine microprobe analyses

Element (Z)	Sample		Olivine gabbros													
	88 OL 101C	88 OL 102C	88 OL 104C	88 OL 106C	91 OL 107C	91 OL 108C	91 OL 109C	91 OL 110C	88 OL 101C	88 OL 102C	88 OL 104C	88 OL 106C	91 OL 107C	91 OL 108C	91 OL 109C	91 OL 110C
SiO ₂	38.61	38.15	38.62	38.09	38.38	38.66	39.28	38.68	38.61	38.15	38.62	38.09	38.38	38.66	39.28	38.68
Al ₂ O ₃	0.06	0.03	0.02	0.01	0.02	0.01	0.02	0.02	0.06	0.03	0.02	0.01	0.02	0.01	0.02	0.02
*FeO	18.65	19.98	19.25	19.97	17.32	18.06	17.21	17.86	18.65	19.98	19.25	19.97	17.32	18.06	17.21	17.86
MgO	41.33	41.07	41.60	40.98	42.95	42.24	42.77	42.38	41.33	41.07	41.60	40.98	42.95	42.24	42.77	42.38
MnO	0.34	0.29	0.25	0.30	0.23	0.27	0.25	0.27	0.34	0.29	0.25	0.30	0.23	0.27	0.25	0.27
CaO	BD	0.02	BD	BD	BD	BD	BD	0.02	BD	0.02	BD	BD	BD	BD	BD	0.02
H ₂ O	BD	0.05	0.04	0.04	0.19	0.18	0.20	0.20	BD	0.05	0.04	0.04	0.19	0.18	0.20	0.20
TOTAL	98.99	99.58	99.78	99.39	99.10	99.43	99.71	99.42	98.99	99.58	99.78	99.39	99.10	99.43	99.71	99.42
Si	0.998	0.988	0.993	0.988	0.987	0.993	1.001	0.993	0.998	0.988	0.993	0.988	0.987	0.993	1.001	0.993
Al	0.002	0.001	0.001	-	0.001	-	0.001	0.001	0.002	0.001	0.001	-	0.001	-	0.001	0.001
Mg	-	0.001	0.001	0.001	0.004	0.004	0.005	0.005	-	0.001	0.001	0.001	0.004	0.004	0.005	0.005
*Fe ²⁺	0.404	0.433	0.414	0.434	0.373	0.388	0.367	0.384	0.404	0.433	0.414	0.434	0.373	0.388	0.367	0.384
Mn	0.008	0.007	0.006	0.007	0.006	0.006	0.006	0.006	0.008	0.007	0.006	0.007	0.006	0.006	0.006	0.006
Mg	1.592	1.585	1.594	1.584	1.645	1.617	1.624	1.621	1.592	1.585	1.594	1.584	1.645	1.617	1.624	1.621
Ca	-	0.001	-	-	-	-	-	0.001	-	0.001	-	-	-	-	-	0.001
Wo	-	-	-	-	-	-	-	-	-	-	-	-	-	-	-	-
En	79.44	78.23	79.15	78.22	81.27	80.41	81.32	80.57	79.44	78.23	79.15	78.22	81.27	80.41	81.32	80.57
Fe	20.56	21.77	20.85	21.78	18.73	19.59	18.68	19.43	20.56	21.77	20.85	21.78	18.73	19.59	18.68	19.43
Fo	69	67	68	67	71	70	71	70	69	67	68	67	71	70	71	70

Table 8.5 Pyroxene microprobe analyses
Element
(Z)

Element (Z)	88 PX 100C	88 PX 100R	88 PX 101C	88 PX 101R	91 PX 122C	91 PX 122R	91 PX 123C	91 PX 123R	91 PX 124C	91 PX 124R
SiO ₂	54.14	55.49	54.96	55.84	55.32	55.23	54.61	55.45	55.61	55.08
TiO ₂	0.41	0.16	0.21	0.06	0.19	0.17	0.23	0.24	0.24	0.13
Al ₂ O ₃	1.51	1.31	1.31	1.05	1.32	1.24	1.29	1.26	1.16	1.33
*FeO	11.56	11.71	11.88	11.67	11.59	11.72	11.40	11.46	11.60	11.74
MgO	30.22	30.15	30.16	30.34	30.11	30.47	30.66	30.68	30.73	30.73
MnO	0.20	0.22	0.21	0.20	0.24	0.25	0.26	0.27	0.24	0.28
CaO	1.06	1.02	1.00	0.91	0.67	0.68	0.79	0.83	0.56	0.66
Na ₂ O	BD	BD	BD	BD	0.03	0.03	0.05	0.03	0.04	0.03
Cr ₂ O ₃	0.14	0.06	0.06	BD	0.09	0.09	0.08	0.09	0.07	0.06
TOTAL	99.25	100.10	99.78	100.17	99.57	99.86	99.38	100.31	100.12	100.12
Si	1.937	9.964	1.955	1.972	1.966	1.959	1.947	1.957	1.965	1.950
Al(IV)	0.063	0.036	0.045	0.028	0.034	0.041	0.053	0.043	0.035	0.05
Al(VI)	0.001	0.019	0.010	0.016	0.022	0.011	0.002	0.001	0.014	0.006
Ti	0.012	0.005	0.006	0.002	0.006	0.005	0.007	0.007	0.004	0.006
Cr	0.005	0.002	0.002	-	0.003	0.003	0.003	0.003	0.002	0.002
*Fe ²⁺	0.346	0.347	0.354	0.345	0.345	0.348	0.340	0.339	0.343	0.348
Mn	0.006	0.007	0.007	0.007	0.008	0.008	0.008	0.008	0.008	0.009
Mg	1.611	1.590	1.599	1.603	1.595	1.611	1.629	1.614	1.618	1.622
Ca	0.041	0.039	0.038	0.035	0.026	0.026	0.031	0.032	0.022	0.025
Na	-	-	-	-	0.003	0.002	0.004	0.002	0.003	0.003
Vo	2.00	1.97	1.90	1.76	1.32	1.30	1.50	1.60	1.10	1.25
En	80.39	80.18	80.00	80.55	80.80	80.83	81.13	80.98	81.47	80.94
Fs	17.61	17.85	18.10	17.69	18.68	17.87	17.37	17.42	17.43	17.81

Table B.5 Pyroxene microprobe analyses (cont.)
 Element Sample Gabbros
 (Z)

Element (Z)	79 PX 36C	79 PX 36R	79 PX 37C	79 PX 37R	79 PX 38C	79 PX 38R	79 PX 39C	79 PX 39R	79 PX 40C	79 PX 40R
SiO ₂	52.66	53.36	53.42	53.36	53.53	53.43	51.18	50.71	53.27	53.41
TiO ₂	0.49	0.36	0.35	0.35	0.37	0.37	0.65	0.68	0.25	0.38
Al ₂ O ₃	1.71	1.41	1.58	1.32	1.54	1.46	2.73	2.42	1.31	1.33
*FeO	7.42	16.06	14.88	15.85	14.82	15.33	6.31	6.55	14.22	15.86
MgO	18.09	26.33	26.71	26.60	27.68	27.29	15.57	15.37	26.74	17.07
MnO	0.20	0.38	0.34	0.40	0.34	0.36	0.14	0.22	0.33	0.41
CaO	17.57	1.35	1.79	1.35	0.98	1.19	21.62	21.81	1.46	1.36
Na ₂ O	0.34	0.02	0.05	0.04	0.03	0.02	0.04	0.40	0.02	0.01
Cr ₂ O ₃	0.03	0.05	0.05	0.04	0.05	0.03	0.16	0.08	0.07	0.05
TOTAL	98.52	99.33	99.15	99.30	99.32	99.45	98.75	98.24	98.67	99.88
Si	1.955	1.949	1.946	1.948	1.942	1.942	1.913	1.912	1.952	1.939
Al(IV)	0.045	0.051	0.054	0.052	0.058	0.058	0.087	0.088	0.048	0.061
Al(VI)	0.030	0.010	0.014	0.005	0.008	0.004	0.033	0.019	0.008	0.004
Ti	0.014	0.010	0.010	0.010	0.010	0.010	0.018	0.019	0.007	0.010
Cr	0.001	0.001	0.001	0.001	0.001	0.001	0.005	0.002	0.002	0.002
*Fe ²⁺	0.230	0.490	0.453	0.484	0.450	0.466	0.197	0.207	0.466	0.482
Mn	0.006	0.012	0.011	0.012	0.011	0.011	0.004	0.007	0.010	0.013
Mg	1.001	1.433	1.450	1.447	1.496	1.478	0.868	0.864	1.460	1.465
Ca	0.699	0.052	0.070	0.053	0.038	0.046	0.966	0.881	0.057	0.053
Na	0.024	0.002	0.003	0.003	0.002	0.001	0.029	0.030	0.002	0.001
Wo	36.08	2.66	3.51	2.65	1.90	2.30	44.75	44.99	2.87	2.62
En	51.69	72.08	73.11	72.49	75.03	73.85	44.84	44.11	73.23	71.81
Fs	12.23	25.26	23.38	24.86	23.07	23.84	10.42	10.90	23.90	24.56

Table B.5 Pyroxene microprobe analyses (cont.)
 Element
 (X)

	79 PX 42C	79 PX 42R	82 PX 42C	82 PX 42R	82 PX 44R	161 PX 26C	161 PX 29C	161 PX 46C	161 PX 46R	161 PX 47C
SiO ₂	51.59	50.88	50.61	52.84	53.70	53.67	50.97	50.31	53.71	53.47
TiO ₂	0.58	0.67	0.65	0.80	0.44	0.34	0.29	0.72	0.83	0.39
Al ₂ O ₃	2.41	2.30	3.02	3.07	1.55	1.47	1.08	2.87	2.96	1.60
*FeO	6.44	6.73	6.10	6.48	14.73	15.01	15.35	6.20	6.46	13.76
MgO	15.78	15.29	15.64	14.86	27.23	28.05	27.62	15.15	15.24	28.28
MnO	0.20	0.20	0.13	0.16	0.30	0.38	0.37	0.18	0.17	0.35
CaO	21.52	21.98	31.37	21.93	1.42	0.73	0.72	22.19	21.55	1.18
Na ₂ O	0.37	0.39	0.35	0.37	BD	BD	0.03	0.43	0.42	0.03
Cr ₂ O ₃	0.12	0.09	0.18	0.16	BD	0.04	0.02	0.17	0.17	0.11
TOTAL	98.44	99.23	98.31	98.43	98.50	99.71	99.16	98.87	98.31	99.42
Si	1.915	1.924	1.908	1.903	1.937	1.941	1.953	1.907	1.900	1.939
Al(IV)	0.085	0.076	0.092	0.097	0.063	0.059	0.047	0.093	0.100	0.061
Al(VI)	0.022	0.025	0.042	0.039	0.004	0.003	0.001	0.033	0.032	0.007
Ti	0.016	0.019	0.019	0.023	0.013	0.009	0.008	0.020	0.024	0.011
Cr	0.004	0.003	0.006	0.005	-	0.001	0.001	0.005	0.005	0.003
*Fe ²⁺	0.202	0.210	0.192	0.204	0.452	0.454	0.467	0.194	0.203	0.415
Mn	0.007	0.006	0.005	0.005	0.010	0.012	0.012	0.006	0.005	0.011
Mg	0.883	0.850	0.874	0.833	1.487	1.511	1.498	0.845	0.855	1.521
Ca	0.866	0.879	0.859	0.884	0.056	0.028	0.028	0.889	0.869	0.046
Na	0.027	0.028	0.026	0.028	-	-	0.002	0.031	0.031	0.002
Wo	44.23	45.18	44.51	45.90	2.79	1.40	1.41	45.99	44.96	2.29
En	45.11	43.71	45.28	43.25	74.17	75.38	74.72	43.70	44.24	76.33
Fs	10.67	11.19	10.21	10.85	23.04	23.22	23.88	10.32	10.80	21.38

Table B.5 Pyroxene microprobe analyses (cont.)

Element (%)	Gabbros				Diorite				
	161 PX 47R	161 PX 51C	161 PX 52C	161 PX 53C	161 PX 55C	161 PX 72C	161 PX 72R	161 PX 470C	108 PX 56C
SiO ₂	53.47	50.27	51.78	50.87	52.21	53.81	52.86	53.22	52.65
TiO ₂	0.44	0.67	0.40	0.61	0.30	0.36	0.20	0.31	0.30
Al ₂ O ₃	1.50	2.34	1.81	2.23	1.29	1.37	0.77	1.32	1.18
*FeO	14.29	6.04	6.37	6.67	15.80	13.93	15.70	13.84	18.72
MgO	27.55	15.40	15.99	15.89	26.14	28.12	26.37	26.69	24.20
MnO	0.31	0.18	0.19	0.21	0.37	0.37	0.40	0.35	0.52
CaO	1.54	22.12	21.77	21.23	1.11	1.37	0.95	1.09	1.11
Mn ₂ O	0.03	0.41	0.39	0.41	0.30	0.03	0.03	0.03	0.02
Cr ₂ O ₃	0.04	0.14	0.10	0.11	0.05	0.03	0.04	0.03	BD
TOTAL	99.17	97.58	98.79	98.23	97.59	99.39	97.30	98.86	98.69
Si	1.941	1.907	1.936	1.916	1.951	1.945	1.967	1.950	1.960
Al(IV)	0.059	0.093	0.064	0.084	0.045	0.055	0.033	0.050	0.040
Al(VI)	0.006	0.012	0.015	0.015	0.007	0.003	0.001	0.007	0.011
Ti	0.012	0.019	0.011	0.017	0.008	0.058	0.006	0.008	0.008
Cr	0.001	0.004	0.003	0.003	0.001	0.001	0.001	0.001	-
*Fe ²⁺	0.434	0.192	0.199	0.210	0.491	0.421	0.489	0.485	0.583
Mn	0.009	0.006	0.006	0.007	0.012	0.112	0.013	0.011	0.016
Mg	1.491	0.871	0.891	0.892	1.447	1.515	1.463	1.457	1.342
Ca	0.060	0.899	0.872	0.857	0.044	0.053	0.038	0.043	0.044
Na	0.002	0.030	0.028	0.030	0.002	0.002	0.002	0.002	0.002
Wo	3.00	45.69	44.30	43.59	2.22	2.66	1.88	2.15	2.23
En	74.76	46.26	45.27	45.39	72.58	75.73	73.08	73.00	67.61
Fs	22.24	10.05	10.43	11.02	25.20	21.62	24.05	24.85	30.16

100
20

Table B.6 Plagioclase microprobe analyses

Element (%)	Sample		Gabbros											
	Olivine gabbros		91				79				82			
	PL	FL	PL	FL	PL	FL	PL	FL	PL	FL	PL	FL	PL	FL
SiO ₂	54.40	53.35	52.20	50.57	56.46	56.68	46.57	52.10	53.19	48.88				
TiO ₂	0.01	0.05	0.08	0.09	0.05	0.03	BD	BD	0.01	0.04				
Al ₂ O ₃	27.01	28.89	30.11	29.09	27.14	27.83	32.64	29.94	28.77	31.50				
*FeO	1.01	0.20	0.15	1.92	0.19	0.24	0.44	0.34	0.25	0.36				
MgO	1.50	0.03	0.02	1.12	0.05	0.05	0.03	0.04	0.03	0.03				
CaO	9.36	11.71	12.53	11.62	8.93	9.85	15.53	12.39	11.24	14.68				
Na ₂ O	5.59	4.95	4.43	4.05	6.46	5.91	2.41	3.86	4.96	3.04				
K ₂ O	0.04	0.07	0.02	0.03	0.06	0.02	0.10	0.20	0.18	0.08				
TOTAL	98.92	99.22	99.56	98.48	99.34	99.62	97.73	98.86	98.74	98.62				
Ab	51.8	43.2	39.0	38.6	56.5	52.0	21.8	35.6	43.9	27.2				
Or	0.3	0.4	0.0	0.2	0.3	0.1	0.6	1.2	1.1	0.5				
An	47.9	56.4	61.0	61.2	43.2	47.9	78.0	63.2	55.0	72.3				

Table B.6 Plagioclase microprobe analyses (cont.)

Element (%)	Sample										
	Gabbros										
	82 PL 46R	82 PL 47R	82 PL 47C	82 PL 48M	82 PL 47C	82 PL 48C	161 PL 48R	161 PL 49C	161 PL 49R	161 PL 71C	161 PL 71R
SiO ₂	48.29	48.02	47.90	48.02	47.90	51.91	51.92	51.94	53.20	42.24	50.98
TiO ₂	0.06	0.06	0.05	0.06	0.05	BD	BD	BD	BD	BD	BD
Al ₂ O ₃	31.79	31.89	31.98	31.89	31.98	29.96	29.92	29.36	29.42	31.81	29.27
*FeO	0.39	0.48	0.38	0.48	0.38	0.41	0.38	0.42	0.37	0.40	0.34
MgO	0.04	0.03	0.03	0.03	0.03	0.03	0.03	0.03	0.04	0.03	0.04
CaO	14.89	15.03	15.65	15.03	15.65	12.43	12.29	11.74	11.49	14.60	12.16
Na ₂ O	2.94	2.81	2.46	2.81	2.46	3.98	4.05	4.45	4.49	3.05	4.58
K ₂ O	0.07	0.08	0.07	0.08	0.07	0.23	0.27	0.22	0.18	0.14	0.23
TOTAL	98.46	98.38	98.51	98.38	98.51	98.94	98.86	98.15	99.17	99.27	97.61
Ab	26.2	25.1	22.0	25.1	22.0	36.2	36.8	40.2	41.0	27.2	40.0
Or	0.4	0.5	0.4	0.5	0.4	1.4	1.6	1.3	1.0	0.8	1.3
An	73.4	74.4	77.6	74.4	77.6	62.4	61.6	58.6	58.0	72.0	58.7

Table B.6 Plagioclase microprobe analyses

Element (Z)	Sample		Gabbros		Pyroxene diorite		Diorites		Diorites		Diorites		Diorites	
	161 PL 71H	179 PL 12C	179 PL 12R	179 PL 12R	179 PL 12C	179 PL 13C	179 PL 13R	41 PL 52R	41 PL 53C	41 PL 53R	41 PL 54C	41 PL 54C	41 PL 54C	41 PL 111C
SiO ₂	51.96	53.51	55.21	52.08	51.98	53.71	52.81	59.57	54.12	57.06	54.12	57.06	57.06	57.06
TiO ₂	BD	BD	BD	BD	BD	BD	BD	0.01	0.06	0.02	0.06	0.02	0.02	0.02
Al ₂ O ₃	29.71	29.07	27.66	29.73	29.90	28.34	28.76	24.82	27.85	26.16	27.85	26.16	26.16	26.16
*FeO	0.36	0.32	0.27	0.38	0.38	0.35	0.29	0.19	0.44	0.25	0.44	0.25	0.25	0.25
MgO	0.03	0.03	0.02	0.03	0.02	0.03	0.02	0.02	0.04	0.03	0.04	0.03	0.03	0.03
CaO	12.21	11.15	9.43	12.12	12.17	10.85	11.36	6.76	10.57	8.69	10.57	8.69	8.69	8.69
Na ₂ O	4.60	4.31	4.92	4.00	3.93	5.24	4.93	7.69	5.33	6.48	5.33	6.48	6.48	6.48
K ₂ O	0.24	0.27	0.78	0.22	0.20	0.20	0.21	0.25	0.33	0.37	0.33	0.37	0.37	0.37
TOTAL	99.10	98.66	98.29	98.57	98.58	98.78	98.44	99.29	98.71	99.04	98.71	99.04	99.04	99.04
Ab	40.0	40.5	46.2	36.9	36.4	46.1	43.5	66.3	46.9	56.2	46.9	56.2	56.2	56.2
Or	1.4	1.7	4.8	1.3	1.2	1.2	1.2	1.5	1.7	2.1	1.7	2.1	2.1	2.1
An	58.6	57.8	49.0	61.8	62.4	52.7	55.3	32.2	51.4	41.7	51.4	41.7	41.7	41.7

109
51

Table B.6 Plagioclase microprobe analyses (cont.)

Element (Z)	Sample	Diorites									
	41 PL 111R	41 PL 112C	44 PL 33C	44 PL 33R	44 PL 33H	44 PL 34C	44 PL 34R	44 PL 34H	108 PL 58C	108 PL 58R	
SiO ₂	55.82	52.66	54.52	60.58	55.18	54.63	53.34	54.58	52.18	59.40	
TiO ₂	0.05	0.07	0.06	0.02	0.05	0.05	0.08	0.08	BD	BD	
Al ₂ O ₃	26.73	28.75	27.82	24.34	27.41	27.58	27.51	27.57	29.42	25.29	
*FeO	0.28	0.39	0.29	0.16	0.25	0.29	0.30	0.30	0.37	0.25	
MgO	0.03	0.03	0.02	0.03	0.02	0.02	0.02	0.03	0.02	0.02	
CaO	9.65	11.86	10.14	4.95	9.65	9.85	9.89	9.97	11.74	6.64	
Na ₂ O	6.08	4.72	5.68	8.20	6.02	5.84	5.83	5.86	4.08	6.01	
K ₂ O	0.33	0.28	0.26	0.68	0.19	0.26	0.26	0.25	0.22	0.37	
TOTAL	98.96	98.75	98.79	98.95	98.78	98.52	98.22	98.65	98.02	97.97	
Ab	52.3	41.2	49.6	72.0	52.4	51	50.8	50.8	38.1	60.6	
Or	1.9	1.6	1.5	4.0	1.1	1.5	1.5	1.4	1.4	2.5	
An	45.8	57.2	48.9	24.0	46.5	47.5	47.7	47.8	60.6	37.0	

60

Table B.6 Plagioclase microprobe analyses (cont.)

Element (Z)	Sample																			
	Diorites																			
	108	108	132	132	132	132	132	132	132	132	132	132	132	132	132	132	132	132	132	132
	PL	PL	PL	PL	PL	PL	PL	PL	PL	PL	PL	PL	PL	PL	PL	PL	PL	PL	PL	PL
	59C	59R	20C	20R	21C	21R	16C	16R	17C	17R	16C	16R	17C	17R	16C	16R	17C	17R	16C	16R
SiO ₂	54.20	53.74	51.81	53.43	52.04	51.60	51.55	52.23	52.13	53.77										
TiO ₂	BD	BD	BD	BD	BD	BD	BD	BD	BD	BD										
Al ₂ O ₃	27.84	28.86	29.76	28.94	29.52	29.26	30.40	29.97	30.03	28.88										
*FeO	0.30	0.29	0.67	0.56	0.66	0.60	0.39	0.32	0.60	0.34										
MgO	0.04	0.01	0.06	0.03	0.09	0.07	0.02	0.01	0.02	0.02										
CaO	9.91	10.88	12.33	11.10	12.13	11.49	12.73	12.17	12.35	10.93										
Na ₂ O	5.07	4.43	3.82	4.12	4.04	3.63	3.84	4.17	4.01	4.89										
K ₂ O	0.27	0.14	0.20	0.32	0.25	0.60	0.13	0.09	0.21	0.12										
TOTAL	97.62	98.34	98.65	98.51	98.73	97.32	99.06	98.97	99.35	98.95										
Ab	47.3	42.0	35.5	39.4	37.0	35.0	35.0	38.0	36.5	44.4										
Or	1.6	0.9	1.2	2.0	1.5	3.8	0.8	0.6	1.2	0.7										
An	51.1	57.1	63.3	58.6	61.5	61.2	64.2	61.4	62.2	54.9										

Table B.6 Plagioclase microprobe analyses (cont.)

Element (%)	Sample		Monzonite																	
	Diorites		251 PL 2R		251 PL 2M		251 PL 3C		251 PL 3R		21 PL 78C		21 PL 78R		21 PL 78M		21 PL 79C		21 PL 79R	
SiO ₂	53.65	56.25	53.39	56.44	57.48	60.06	57.87	60.14	54.96	61.55										
TiO ₂	BD	BD	BD	BD	BD	BD	BD	BD	BD	BD	BD	BD	BD	BD	BD	BD	BD	BD	BD	BD
Al ₂ O ₃	28.84	26.68	28.94	26.62	26.15	24.07	25.70	24.11	28.10	23.42										
*FeO	3.13	0.28	0.36	0.30	0.26	0.23	0.19	0.13	0.25	0.18										
MgO	0.03	0.08	0.01	0.02	BD	BD	BD	BD	BD	BD	BD	BD	BD	BD	BD	BD	BD	BD	BD	BD
CaO	11.17	7.82	11.19	8.58	7.93	5.59	6.91	5.51	10.35	4.94										
Na ₂ O	5.24	4.70	5.19	6.46	6.77	8.06	7.24	8.33	5.50	8.80										
K ₂ O	0.24	0.31	0.16	0.27	0.30	0.47	0.35	0.29	0.29	0.17										
TOTAL	99.47	98.11	99.24	98.69	98.90	98.48	98.30	98.53	99.49	99.09										
Ab	45.3	50.9	45.2	56.8	60.0	70.3	64.1	72.0	48.2	75.6										
Or	1.4	2.2	0.9	1.5	1.7	2.7	2.1	1.7	1.7	1.0										
An	53.3	46.9	53.9	41.7	38.3	27.0	33.8	26.3	50.1	23.4										

Table B.6 Plagioclase microprobe analyses (cont.)

Element (%)	Sample		Diorites (Juan Jorge Complex)																												
	Adameillite		36 PL 28C			36 PL 28M			36 PL 28R			36 PL 29C			36 PL 29R			36 PL 30C			36 PL 31C			JJ3 PL 63C			JJ3 PL 64C			JJ4 PL 1C	
SiO ₂	58.05	59.46	61.94	57.85	61.91	57.17	61.8	56.66	60.46	59.93	60.46	59.93	60.46	59.93	60.46	59.93	60.46	59.93	60.46	59.93	60.46	59.93	60.46	59.93	60.46	59.93	60.46	59.93	60.46	59.93	
TiO ₂	0.05	0.03	0.01	0.04	0.01	0.02	0.02	0.01	0.02	0.01	0.02	0.02	0.01	0.02	0.01	0.02	0.01	0.02	0.01	0.02	0.01	0.02	0.01	0.02	0.01	0.02	0.01	0.02	0.01		
Al ₂ O ₃	25.38	24.43	23.07	25.86	22.99	26.22	23.16	26.62	24.90	24.78	26.62	24.90	24.78	26.62	24.90	24.78	26.62	24.90	24.78	26.62	24.90	24.78	26.62	24.90	24.78	26.62	24.90	24.78	26.62	24.90	
*FeO	0.36	0.33	0.22	0.40	0.12	0.37	0.19	0.31	0.19	0.20	0.37	0.19	0.20	0.37	0.19	0.20	0.37	0.19	0.20	0.37	0.19	0.20	0.37	0.19	0.20	0.37	0.19	0.20	0.37		
MgO	0.02	0.01	0.01	0.02	0.01	0.01	0.01	0.01	0.01	0.01	0.01	0.01	0.01	0.01	0.01	0.01	0.01	0.01	0.01	0.01	0.01	0.01	0.01	0.01	0.01	0.01	0.01	0.01	0.01		
CaO	7.74	6.54	4.59	7.76	4.29	8.20	4.57	8.29	5.71	5.93	8.20	4.57	5.93	8.20	4.57	5.93	8.20	4.57	5.93	8.20	4.57	5.93	8.20	4.57	5.93	8.20	4.57	5.93	8.20		
Na ₂ O	6.87	7.49	8.68	6.97	8.89	6.64	8.71	8.29	5.46	5.20	6.64	8.71	5.46	5.20	6.64	8.71	5.46	5.20	6.64	8.71	5.46	5.20	6.64	8.71	5.46	5.20	6.64	8.71	5.46		
K ₂ O	0.33	0.39	0.37	0.33	0.24	0.28	0.35	0.28	0.28	0.38	0.28	0.35	0.28	0.38	0.28	0.38	0.28	0.38	0.28	0.38	0.28	0.38	0.28	0.38	0.28	0.38	0.28	0.38	0.28		
TOTAL	98.80	98.69	98.88	99.22	98.45	98.91	98.84	97.69	97.02	96.43	98.91	98.84	97.69	97.02	96.43	98.91	98.84	97.69	97.02	96.43	98.91	98.84	97.69	97.02	96.43	98.91	98.84	97.69	97.02	96.43	
Ab	60.4	65.9	75.7	60.7	77.9	58.5	75.9	52.9	62.0	60.0	58.5	75.9	52.9	62.0	60.0	58.5	75.9	52.9	62.0	60.0	58.5	75.9	52.9	62.0	60.0	58.5	75.9	52.9	62.0		
Or	1.9	2.3	2.2	1.9	1.3	1.6	2.1	2.4	2.1	2.9	1.6	2.1	2.4	2.1	2.9	1.6	2.1	2.4	2.1	2.9	1.6	2.1	2.4	2.1	2.9	1.6	2.1	2.4	2.1		
An	37.7	31.8	22.1	37.4	20.8	39.9	22.0	44.7	35.9	37.1	39.9	22.0	44.7	35.9	37.1	39.9	22.0	44.7	35.9	37.1	39.9	22.0	44.7	35.9	37.1	39.9	22.0	44.7	35.9		

Table B.6 Plagioclase microprobe analyses (cont.)

Element (Z)	Sample	Diorites (Juan Jorge Complex)																		
	JJ4	JJ4	JJ4	JJ4	JJ4	JJ4	JJ4	JJ4	JJ4	JJ4	JJ7	JJ7	JJ7	JJ7	JJ7	JJ7	JJ8	JJ8	JJ8	JJ8
	PL	PL	PL	PL	PL	PL	PL	PL	PL	PL	PL	PL	PL	PL	PL	PL	PL	PL	PL	PL
	62C	62R	63C	63R	57.17	61.70	60.44	59.43	59.28	60.34	57.61	56.89	57.61	56.89	57.61	56.89	57.61	56.89	57.61	56.89
SiO ₂	58.05	61.79	57.17	61.70	60.44	59.43	59.28	60.34	57.61	56.89	57.61	56.89	57.61	56.89	57.61	56.89	57.61	56.89	57.61	56.89
TiO ₂	BD	BD	BD	BD	BD	BD	BD	BD	BD	BD	BD	BD	BD	BD	BD	BD	BD	BD	BD	BD
Al ₂ O ₃	25.49	22.85	26.23	23.33	24.50	25.33	25.66	24.70	25.66	24.70	26.63	26.92	25.66	24.70	26.63	26.92	25.66	24.70	26.63	26.92
*FeO	0.18	0.16	0.27	0.20	0.25	0.23	0.22	0.26	0.22	0.26	0.23	0.23	0.22	0.26	0.23	0.23	0.22	0.26	0.23	0.23
MgO	0.01	0.02	0.02	BD	0.01	0.02	BD	0.01	BD	0.01	0.02	0.02	BD	0.01	0.02	0.02	BD	0.01	0.02	0.02
CaO	7.05	3.93	7.80	4.36	5.48	6.45	6.78	5.35	6.78	5.35	7.98	8.44	6.78	5.35	7.98	8.44	6.78	5.35	7.98	8.44
Mn ₂ O	6.23	6.04	6.15	5.98	5.73	5.08	4.88	4.99	4.88	4.99	4.84	5.34	4.88	4.99	4.84	5.34	4.88	4.99	4.84	5.34
K ₂ O	0.32	0.27	0.34	0.42	0.34	0.38	0.21	0.23	0.21	0.23	0.31	0.30	0.21	0.23	0.31	0.30	0.21	0.23	0.31	0.30
TOTAL	97.33	95.06	97.97	95.98	96.74	96.92	97.02	95.89	97.02	95.89	97.63	98.15	97.02	95.89	97.63	98.15	97.02	95.89	97.63	98.15
Ab	60.3	72.0	57.6	69.0	63.8	57.1	55.7	61.6	55.7	61.6	51.2	52.3	55.7	61.6	51.2	52.3	55.7	61.6	51.2	52.3
Or	2.0	2.1	2.1	3.2	2.5	2.9	1.6	1.9	1.6	1.9	2.2	2.0	1.6	1.9	2.2	2.0	1.6	1.9	2.2	2.0
An	37.7	25.9	40.3	27.8	33.7	40.0	42.7	36.5	42.7	36.5	46.7	45.7	42.7	36.5	46.7	45.7	42.7	36.5	46.7	45.7

Table B.6 Plagioclase microprobe analyses (cont.)

Element (%)	Sample		Diorites (Juan Jorge Complex)		Granite	
	JJ8 PL 33R	JJ8 PL 87C	JJ8 PL 89C	JJ17 PL 43C		
SiO ₂	57.70	56.07	56.96	63.92		
TiO ₂	BD	BD	BD	BD		
Al ₂ O ₃	24.93	25.70	26.97	23.49		
*FeO	0.26	0.24	0.27	0.23		
MgO	0.03	0.01	BD	BD		
CaO	6.44	6.92	8.45	3.41		
Na ₂ O	5.88	5.53	5.25	5.39		
K ₂ O	0.33	0.31	0.23	0.37		
TOTAL	95.48	97.78	98.03	96.82		
Ab	60.6	57.8	52.1	71.7		
Or	2.3	2.2	1.5	3.3		
An	37.1	40.0	46.4	25.0		

Table B.7 Apatite microprobe analyses

Element (%)	Sample		Monsonite															
	Diorites		108			108			108			177			21			
	41	108	AP	AP	AP	AP	AP	AP	AP	AP	AP	AP	AP	AP	AP	AP	AP	AP
	113C	6C	6R	8C	9C	10C	12C	81C	116C	117C								
SiO ₂	ND	0.11	0.22	0.21	0.17	0.21	0.30	ND	ND	0.21	0.21	0.21	0.21	0.21	0.21	0.21	0.21	0.21
*FeO	0.14	0.04	0.05	0.27	0.09	0.15	0.16	0.05	0.03	0.16	0.16	0.16	0.05	0.03	0.03	0.03	0.03	0.03
MgO	0.03	BD	BD	BD	0.03	0.03	0.08	0.03	0.01	0.08	0.08	0.08	0.03	0.01	0.01	0.01	0.01	0.01
CaO	51.40	50.11	48.77	47.78	48.68	46.91	46.23	53.24	53.44	46.91	46.91	46.23	53.24	53.44	53.44	53.44	53.44	53.44
Na ₂ O	BD	BD	0.05	0.07	0.03	0.09	0.04	BD	BD	0.09	0.09	0.04	BD	BD	BD	BD	BD	BD
P ₂ O ₅	37.22	42.28	42.12	41.58	42.16	41.73	40.97	39.88	39.48	41.73	41.73	40.97	39.88	39.48	39.48	39.48	39.48	39.48
La ₂ O ₃	ND	0.09	0.09	0.10	0.11	0.14	0.20	ND	ND	0.14	0.14	0.20	ND	ND	ND	ND	ND	ND
Ce ₂ O ₃	ND	0.12	0.16	0.14	0.19	0.21	0.29	ND	ND	0.21	0.21	0.29	ND	ND	ND	ND	ND	ND
Md ₂ O ₃	ND	0.14	0.08	0.10	0.13	0.13	0.13	ND	ND	0.13	0.13	0.13	ND	ND	ND	ND	ND	ND
Cl	0.25	ND	ND	ND	ND	ND	ND	0.33	0.31	ND	ND	ND	0.33	0.31	0.31	0.31	0.31	0.31
F	2.16	3.87	4.47	3.48	3.17	4.07	3.92	2.11	2.58	4.07	4.07	3.92	2.11	2.58	2.58	2.58	2.58	2.58
TOTAL	91.18	96.76	96.02	93.73	94.75	93.66	92.30	95.65	95.91	93.66	93.66	92.30	95.65	95.91	95.91	95.91	95.91	95.91

Table B.7 Apatite microprobe analyses (cont.)

Element (%)	Sample		Monzonite Diorites (Juan Jorge Complex)											
	21 AP 118C	ND	JJ4 AP 22C	JJ4 AP 23C	JJ4 AP 24C	JJ7 AP 13C	JJ7 AP 14C	JJ7 AP 17C	JJ8 AP 18C	JJ8 AP 19C	JJ8 AP 20C	TOTAL		
SiO ₂	53.73	ND	55.94	55.48	55.73	51.25	49.38	55.20	55.83	55.38	54.95			
*FeO	0.09	0.19	0.05	0.19	0.11	0.63	0.10	0.13	0.31	0.16	0.38			
MgO	0.01	0.01	BD	BD	0.01	BD	BD	BD	BD	BD	BD			
CaO	39.65	42.60	42.60	42.36	42.57	42.18	42.38	42.28	42.12	42.14	42.24			
Na ₂ O	ND	0.23	0.23	0.24	0.10	0.14	0.15	0.22	0.21	0.17	0.18			
P ₂ O ₅	ND	0.23	0.23	0.23	0.08	0.10	0.21	0.31	0.27	0.16	0.17			
La ₂ O ₃	ND	0.05	0.05	0.07	0.06	0.06	0.12	0.15	0.07	0.06	0.06			
Ce ₂ O ₃	0.29	ND	ND	ND	ND	ND	ND	ND	ND	ND	ND			
Md ₂ O ₃	2.60	5.92	5.92	5.44	5.84	3.68	4.10	4.80	6.34	5.19	5.85			
Cl	96.42	105.23	105.23	104.32	104.62	98.27	96.70	103.42	105.41	103.69	103.96			
F														
TOTAL														

Table B.7 Apatite microprobe analyses (cont.)

Element (%)	Sample	Granite (Juan Jorge Complex)																							
		Diorites (Juan Jorge Complex)			JJ17 AP 1C			JJ17 AP 2C			JJ17 AP 3C			JJ17 AP 4C			JJ17 AP 5C								
SiO ₂	1.06	1.70	0.27	0.35	0.85	0.59	0.81	0.07	0.04	0.09	0.11	0.07	0.85	0.59	0.07	0.81	0.07	0.04	0.09	0.11	0.07	0.85	0.59	0.07	
*FeO	0.81	0.07	0.04	0.09	0.11	0.07	0.81	0.07	0.04	0.09	0.11	0.07	0.81	0.07	0.04	0.09	0.11	0.07	0.04	0.09	0.11	0.07	0.81	0.07	0.04
MgO	0.53	BD	BD	BD	BD	BD	0.53	BD	BD	BD	BD	BD	0.53	BD	BD	BD	0.53	BD	BD	BD	BD	BD	0.53	BD	BD
CaO	53.67	52.87	55.46	55.43	52.59	55.22	53.67	52.87	55.46	55.43	52.59	55.22	53.67	52.87	55.46	55.43	52.59	55.22	55.46	55.43	52.59	55.22	53.67	52.87	55.46
Na ₂ O	0.06	0.18	0.06	0.06	0.02	0.02	0.06	0.18	0.06	0.06	0.02	0.02	0.06	0.18	0.06	0.06	0.02	0.02	0.06	0.06	0.02	0.02	0.06	0.18	0.06
P ₂ O ₃	40.77	39.57	42.36	42.51	42.23	42.11	40.77	39.57	42.36	42.51	42.23	42.11	40.77	39.57	42.36	42.51	42.23	42.11	42.36	42.51	42.23	42.11	40.77	39.57	42.36
La ₂ O ₃	0.17	1.21	0.22	0.24	0.53	0.33	0.17	1.21	0.22	0.24	0.53	0.33	0.17	1.21	0.22	0.24	0.53	0.33	0.22	0.24	0.53	0.33	0.17	1.21	0.22
Ce ₂ O ₃	0.16	1.58	0.26	0.27	0.58	0.35	0.16	1.58	0.26	0.27	0.58	0.35	0.16	1.58	0.26	0.27	0.58	0.35	0.26	0.27	0.58	0.35	0.16	1.58	0.26
Nd ₂ O ₃	0.12	0.43	0.07	0.08	0.12	0.07	0.12	0.43	0.07	0.08	0.12	0.07	0.12	0.43	0.07	0.08	0.12	0.07	0.07	0.08	0.12	0.07	0.12	0.43	0.07
Cl	ND	ND	ND	ND	ND	ND	ND	ND	ND	ND	ND	ND	ND	ND	ND	ND	ND	ND	ND	ND	ND	ND	ND	ND	ND
F	6.00	6.43	5.59	5.82	6.47	5.96	6.00	6.43	5.59	5.82	6.47	5.96	6.00	6.43	5.59	5.82	6.47	5.96	5.59	5.82	6.47	5.96	6.00	6.43	5.59
TOTAL	103.35	104.05	104.35	104.87	103.51	104.7	103.35	104.05	104.35	104.87	103.51	104.7	103.35	104.05	104.35	104.87	103.51	104.7	104.35	104.87	103.51	104.7	103.35	104.05	104.35

Table B.8 Sphene microprobe analyses

Element (%)	Sample		Diorites									
	44 SH 39C	44 SH 39R	132 SH 26C	132 SH 30C	132 SH 34C	132 SH 84C	132 SH 84R	132 SH 85C	132 SH 85R	132 SH 85H	TOTAL	
SiO ₂	29.28	29.92	29.26	28.44	29.83	29.70	29.65	29.86	29.69	29.83	29.83	
TiO ₂	37.10	36.85	36.77	39.19	39.37	38.19	38.46	39.47	39.28	39.87	39.87	
Al ₂ O ₃	1.27	1.33	1.58	0.41	0.64	0.87	0.76	0.63	0.56	0.50	0.50	
*FeO	0.80	1.12	1.52	0.55	0.61	1.05	1.01	0.68	0.69	0.53	0.53	
MgO	BD	0.02	BD	BD	BD	BD	BD	BD	BD	BD	BD	
MnO	0.07	0.02	0.03	0.04	0.04	0.05	0.06	0.05	0.03	0.01	0.01	
CaO	27.93	28.12	28.33	28.03	28.37	28.24	28.21	28.73	28.60	28.57	28.57	
Na ₂ O	0.04	BD	BD	BD	BD	BD	BD	BD	BD	BD	BD	
K ₂ O	0.02	BD	BD	BD	BD	BD	BD	BD	BD	BD	BD	
La ₂ O ₃	ND	ND	BD	0.02	ND	0.09	BD	BD	BD	0.03	0.03	
Ce ₂ O ₃	ND	ND	0.17	0.20	ND	0.20	0.13	0.19	0.21	0.18	0.18	
TOTAL	96.49	97.38	97.66	96.88	98.87	98.39	98.28	99.61	99.06	99.52	99.52	

Table B.8 Sphene microprobe analyses (cont.)

Element (%)	Sample		Diorites (Juan Jorge Complex)																												
	Diorites		251 SH 35C			251 SH 36C			251 SH 37C			251 SH 38C			251 SH 39C			JJ3 SH 17R			JJ3 SH 78C			JJ3 SH 78R			JJ3 SH 79C			JJ3 SH 79R	
SiO ₂	30.01		29.46		30.01		29.80		29.95		29.79		29.50		30.05		29.73		29.38		29.79		29.50		30.05		29.73		29.38		
TiO ₂	37.54		36.92		38.72		38.31		38.95		36.93		36.60		37.46		37.51		37.04		36.93		36.60		37.46		37.51		37.04		
Al ₂ O ₃	1.11		1.41		0.73		1.07		0.82		1.23		1.17		1.15		0.99		1.14		1.23		1.17		1.15		0.99		1.14		
*FeO	1.10		1.52		0.68		1.05		0.94		1.60		1.66		1.26		1.25		1.56		1.60		1.66		1.26		1.25		1.56		
MgO	BD		BD		BD		BD		BD		BD		BD		BD		BD		BD		BD		BD		BD		BD		BD		
MnO	0.06		0.04		0.05		0.07		0.06		0.10		0.09		0.13		0.10		0.10		0.10		0.09		0.13		0.10		0.10		
CaO	28.23		28.29		28.38		28.83		28.61		27.93		26.83		27.65		27.29		27.65		27.93		26.83		27.65		27.29		27.65		
Na ₂ O	BD		BD		BD		BD		BD		BD		BD		BD		BD		BD		BD		BD		BD		BD		BD		
K ₂ O	BD		BD		BD		BD		BD		BD		BD		BD		BD		BD		BD		BD		BD		BD		BD		
La ₂ O ₃	BD		BD		BD		0.01		0.02		0.22		0.45		0.30		0.28		0.17		0.22		0.45		0.30		0.28		0.17		
Ce ₂ O ₃	0.16		0.17		0.19		0.20		0.18		0.42		1.62		0.74		0.78		0.44		0.42		1.62		0.74		0.78		0.44		
TOTAL	98.21		97.81		98.75		99.34		99.52		98.22		97.92		98.74		97.93		97.48		98.22		97.92		98.74		97.93		97.48		

Table B.8 Sphene microprobe analyses (cont.)

Element (%)	Sample	Diorites (Juan Jorge Complex)									
	JJ3 SH 80C	JJ3 SH 80R	JJ4 SH 1C	JJ4 SH 2C	JJ4 SH 3C	JJ4 SH 64C	JJ4 SH 64R	JJ4 SH 76C	JJ4 SH 76R	JJ4 SH 76M	
SiO ₂	28.30	30.27	29.71	29.47	29.31	28.15	29.55	28.92	28.85	29.49	
TiO ₂	35.00	34.50	37.53	37.97	37.88	34.38	36.15	37.35	37.37	37.37	
Al ₂ O ₃	1.33	1.75	0.79	0.84	0.88	1.11	1.21	0.89	0.92	1.04	
*FeO	1.89	1.58	1.04	0.97	1.08	1.57	0.53	1.14	1.14	1.32	
MgO	BD	BD	BD	BD	BD	0.03	0.01	BD	BD	BD	
MnO	0.09	0.11	0.07	BD	0.11	0.09	0.11	0.09	0.09	0.11	
CaO	27.02	25.01	27.32	27.49	27.39	25.79	27.38	26.83	26.90	27.57	
Na ₂ O	BD	BD	BD	BD	BD	0.04	BD	BD	BD	BD	
K ₂ O	BD	BD	BD	BD	BD	BD	BD	BD	BD	BD	
La ₂ O ₃	0.44	0.40	0.23	0.25	0.30	ND	ND	0.42	0.36	0.22	
Ce ₂ O ₃	1.87	1.54	0.70	0.86	0.33	ND	ND	1.26	1.28	0.59	
TOTAL	95.94	95.16	97.40	97.85	97.77	91.15	95.99	96.89	96.90	97.70	

Table B.8 Sphene microprobe analyses (cont.)

Element (%)	Sample	Granite (Juan Jorge Complex)								
		Diorites (Juan Jorge Complex)		Granite (Juan Jorge Complex)		Granite (Juan Jorge Complex)				
		JJ4 SH 77C	JJ4 SH 78C	JJ17 SH 40C	JJ17 SH 42C	JJ17 SH 45C	JJ17 SH 86C	JJ17 SH 86R	JJ17 SH 87C	JJ17 SH 87R
SiO ₂		29.04	29.24	29.35	29.20	29.40	29.45	29.25	29.58	29.29
TiO ₂		37.70	37.30	35.59	36.83	36.92	37.30	36.94	37.06	36.90
Al ₂ O ₃		0.89	1.13	1.23	1.08	1.04	0.97	0.12	1.04	1.23
*FeO		1.18	1.37	1.70	1.53	1.46	1.30	1.54	1.39	1.81
MgO		BD	BD	0.03	BD	BD	BD	BD	BD	BD
MnO		0.10	0.12	0.15	0.14	0.15	0.14	0.19	0.13	0.17
CaO		27.16	27.80	27.43	26.72	27.08	27.08	27.39	27.06	27.48
Na ₂ O		BD	BD	0.01	BD	BD	BD	BD	BD	BD
K ₂ O		BD	BD	BD	BD	BD	BD	BD	BD	BD
La ₂ O ₃		0.37	0.21	ND	0.43	0.46	0.40	0.37	0.48	0.37
Ce ₂ O ₃		1.25	0.60	ND	1.60	1.34	1.24	0.98	1.41	0.97
TOTAL		97.69	97.76	95.52	97.52	97.84	97.86	97.90	98.14	98.22

3

Table B.8 Sphene microprobe analyses (cont.)

Element (%)	Sample										
	Microdiorite xenolith (Juan Jorge Complex)										
	JJ19 SH 25C	JJ19 SH 67C	JJ19 SH 67R	JJ19 SH 69C	JJ19 SH 69R	JJ19 SH 70C	JJ19 SH 70R	JJ19 SH 81C	JJ19 SH 81R	JJ19 SH 83C	
SiO ₂	29.66	28.82	29.50	28.90	28.85	28.91	29.55	29.69	29.46	29.64	
TiO ₂	36.79	35.34	36.08	35.48	36.52	35.78	36.86	36.09	36.57	36.45	
Al ₂ O ₃	1.19	1.12	1.20	1.17	0.99	1.30	1.13	1.15	1.11	1.25	
*FeO	1.55	1.65	1.58	1.65	1.37	1.71	1.39	1.62	1.51	1.92	
MgO	BD	BD	0.02	0.02	BD	BD	BD	BD	BD	BD	
MnO	0.16	0.13	0.18	0.12	0.10	0.15	0.16	0.13	0.15	0.15	
CaO	28.30	27.02	27.82	26.82	27.45	27.29	29.97	26.87	26.65	27.46	
Na ₂ O	BD	0.03	0.02	0.07	0.05	0.02	0.04	BD	BD	BD	
K ₂ O	BD	BD	BD	BD	0.01	BD	0.01	BD	BD	BD	
La ₂ O ₃	ND	ND	ND	ND	ND	ND	ND	0.53	0.39	0.27	
Ce ₂ O ₃	ND	ND	ND	ND	ND	ND	ND	1.50	1.11	0.88	
TOTAL	97.82	94.13	96.41	94.24	97.37	95.28	97.15	97.58	96.95	98.02	

Table B.8 Sphene microprobe analyses (cont.)

Element (%)	Sample
	Microdiorite xenolith (Juan Jorge Complex)
	JJ19
	SH
	83R
SiO ₂	29.46
TiO ₂	37.70
Al ₂ O ₃	1.04
*FeO	1.17
MgO	BD
MnO	0.13
CaO	27.32
Na ₂ O	BD
K ₂ O	BD
La ₂ O ₃	0.40
Ce ₂ O ₃	1.21
TOTAL	98.43

Table B.9 Oxide microprobe analyses

Element (%)	Sample		Diorites																	
	Pyroxene diorite		179		179		179		108		108		108		108					
	OX	11C	OX	12C	OX	13C	OX	114C	OX	59C	OX	60C	OX	61C	OX	62C	OX	65C	OX	66C
SiO ₂	0.05		0.04		0.02		0.01		0.02		0.02		0.04		0.03		0.08		1.25	
TiO ₂	0.22		47.95		45.31		43.29		44.89		0.26		0.26		0.11		49.19		0.09	
Al ₂ O ₃	0.22		0.05		0.04		0.02		0.03		0.29		0.29		0.26		0.05		0.07	
*FeO	-		46.97		50.15		50.69		50.65		-		-		-		43.24		-	
*Fe ₂ O ₃	99.98		-		-		-		-		101.62		98.94		99.00		-		99.09	
MgO	0.05		0.02		0.11		0.09		0.20		0.02		0.02		0.03		0.05		0.21	
MnO	0.04		1.20		1.35		1.26		1.20		0.03		0.03		0.04		2.45		0.10	
Cr ₂ O ₃	0.03		BD		BD		0.01		0.02		BD		BD		0.03		BD		0.03	
TOTAL	100.59		96.23		96.98		95.37		97.01		99.58		99.50		99.50		95.06		100.84	

10-1
CZ
H

Table B.9 Oxide microprobe analyses (cont.)

Element (Z)	Sample											
	Diorites											
	132	177	177	177	177	251	251	251	251	251	251	251
	OX	OX	OX	OX	OX	OX	OX	OX	OX	OX	OX	OX
	32C	28C	29C	30C	31C	7C	7R	14C	18C			
SiO ₂	BD	BD	BD	BD	BD	BD	BD	BD	BD	BD	BD	BD
TiO ₂	48.77	43.70	0.10	43.16	45.20	49.26	47.96	47.20	51.19			
Al ₂ O ₃	0.03	0.04	0.31	0.04	0.05	0.06	0.03	0.02	0.04			
*FeO	47.63	51.28	-	51.63	48.95	47.61	48.91	49.65	45.28			
*Fe ₂ O ₃	-	-	99.16	-	-	-	-	-	-			
MgO	0.14	0.11	0.03	0.10	0.12	0.08	0.10	0.12	0.05			
MnO	1.53	1.30	0.05	1.16	1.39	1.65	1.57	1.53	1.71			
Cr ₂ O ₃	0.03	0.02	0.25	0.04	0.04	0.02	BD	0.01	0.02			
TOTAL	98.13	96.45	99.90	96.13	95.75	98.68	98.57	98.53	98.34			

Table B.9 Oxide microprobe analyses (cont.)

Element (Z)	Sample	Diorites (Juan Jorge Complex)													
		Rafted xenolith				26			JJ3			JJ4		JJ4	
SiO ₂	26 OX 68C	26 OX 68R	26 OX 70C	26 OX 71C	26 OX 71R	26 OX 72C	JJ3 OX 65C	JJ3 OX 72C	JJ4 OX 9C	JJ4 OX 67C					
TiO ₂	BD	1.31	BD	BD	BD	0.65	0.09	0.03	0.21	0.02					
Al ₂ O ₃	BD	0.04	BD	47.27	44.11	BD	0.27	0.13	49.97	0.07					
*FeO	59.08	58.68	59.13	0.01	0.03	62.41	0.14	0.10	0.20	0.11					
*Fe ₂ O ₃	27.93	25.28	28.22	50.32	52.09	23.39	-	-	34.11	-					
MgO	-	-	-	-	-	-	94.65	99.29	-	97.55					
MnO	11.92	12.21	11.76	0.10	0.08	10.45	0.04	0.04	0.11	0.03					
Cr ₂ O ₃	0.33	0.30	0.28	1.77	1.65	0.20	0.07	0.08	7.04	0.07					
TOTAL	BD	BD	BD	0.04	0.09	BD	0.24	0.20	BD	0.29					
	99.26	97.83	99.39	99.51	98.05	97.11	95.50	99.87	91.64	98.14					

67
68

Table B.9 Oxide microprobe analyses (cont.)

Element (%)	Sample		Diorites (Juan Jorge Complex)									
			J17		J17		J17		J18			
	OX	69C	OX	54C	OX	55C	OX	56C	OX	58C	OX	77C
SiO ₂	0.07		0.04		0.04		0.04		0.04	0.18		0.06
TiO ₂	0.10		0.08		0.15		0.10		0.10	0.14		0.07
Al ₂ O ₃	0.26		0.09		0.09		0.15		0.15	0.17		0.11
*FeO												
*Fe ₂ O ₃	98.08		99.65		98.56		100.52		97.36			99.17
MgO	0.05		BD		0.03		0.04		0.06			0.03
MnO	0.09		0.06		0.08		0.08		0.11			0.06
Cr ₂ O ₃	0.76		0.26		0.40		0.37		1.38			0.33
TOTAL	99.61		100.18		99.35		101.30		99.60			99.81

Table C.1 Whole rock geochemical analyses
Olivine gabbros

Sample	Gabbros									
	GC88	GC91	GC160	GC162	GC163	GC200	GC70	GC71	GC72	GC73
Major elements (%)										
SiO ₂	47.66	41.25	48.92	42.02	43.37	49.14	50.70	50.72	59.93	50.15
TiO ₂	0.54	0.98	0.59	0.95	0.93	0.48	0.71	0.45	0.88	0.83
Al ₂ O ₃	6.49	7.19	7.03	6.70	8.23	6.33	15.14	17.65	17.34	18.06
*FeO	9.30	12.88	9.20	12.38	11.28	9.07	6.54	5.77	6.01	5.77
MgO	21.55	25.78	20.02	25.20	24.16	20.66	10.79	9.03	5.97	7.18
MnO	0.15	0.15	0.16	0.18	0.17	0.15	0.10	0.10	0.09	0.10
CaO	8.55	3.91	8.69	3.93	4.38	8.93	11.84	11.34	8.71	10.95
Na ₂ O	1.31	1.21	1.28	1.07	1.31	1.15	1.98	2.38	2.52	2.45
K ₂ O	0.59	0.50	0.64	0.95	0.93	0.65	0.41	0.33	1.21	1.02
P ₂ O ₅	0.08	0.21	0.13	0.22	0.22	0.11	0.08	0.05	0.09	0.13
H ₂ O	3.35	5.11	1.95	6.05	6.81	2.00	1.27	1.50	2.19	2.42
CO ₂	0.26	0.22	0.62	0.17	<0.10	0.15	0.25	0.36	0.70	0.47
TOTAL	99.83	99.39	99.24	99.82	101.79	98.82	99.81	99.68	98.64	99.54
Trace elements (ppm)										
Ba	133	135	143	102	87	118	86	146	285	177
Cr	820	1146	979	1156	789	1368	285	90	141	178
Cu	35	46	37	61	36	49	60	98	19	25
La	8	11	ND	ND	ND	ND	9	ND	ND	ND
Li	15	13	25	16	24	13	12	14	20	36
Ni	241	891	175	801	686	226	102	155	34	54
Rb	25	18	27	22	22	23	12	12	39	39
Sc	29	13	40	15	15	37	30	23	22	26
Sr	189	285	219	261	311	119	575	866	718	888
V	110	107	128	112	103	114	114	86	129	132
Y	9	10	17	14	14	13	13	13	19	18
Zn	89	107	109	126	121	100	5	57	61	57
Zr	62	75	83	109	106	71	66	33	119	56

Table C.1 Whole rock geochemical analyses (cont.)
Sample Gabbros

	GC76	GC78	GC79	GC80	GC81	GC82	GC83	GC90	GC161	GC203
Major elements (%)										
SiO ₂	52.29	51.77	51.05	50.09	51.01	49.66	49.59	53.10	51.14	51.18
TiO ₂	0.63	1.21	0.67	0.80	0.92	0.73	0.90	0.74	0.65	0.86
Al ₂ O ₃	18.59	18.56	18.49	16.84	19.87	18.10	18.51	17.86	16.80	19.40
*FeO	5.44	5.98	5.50	6.45	5.81	5.69	5.64	5.49	5.85	5.63
MgO	6.58	6.35	8.53	8.89	6.20	7.51	7.20	7.22	9.62	6.30
MnO	0.10	0.09	0.10	0.11	0.09	0.10	0.09	0.10	0.12	0.10
CaO	9.79	11.15	12.47	12.50	10.93	11.76	11.58	10.96	10.65	11.19
Na ₂ O	2.99	1.63	1.93	1.97	2.62	2.31	2.23	2.29	2.21	2.66
K ₂ O	1.00	1.05	0.28	0.40	0.79	0.76	0.92	0.76	1.02	0.98
P ₂ O ₅	0.09	0.29	0.08	0.12	0.14	0.13	0.16	0.05	0.17	0.20
H ₂ O	1.82	1.51	1.38	1.14	1.58	1.25	1.85	1.64	1.28	<0.10
CO ₂	0.23	0.27	<0.10	0.15	<0.10	0.15	0.39	0.15	<0.10	<0.10
TOTAL	99.85	100.86	100.48	99.46	99.97	98.15	99.06	100.36	99.51	98.52
Trace elements (ppm)										
Ba	230	207	100	123	185	163	181	153	283	204
Cr	389	109	205	324	142	198	102	141	258	130
Cu	30	25	44	55	25	30	24	40	34	33
La	ND	18	ND	9	ND	11	ND	ND	ND	11
Li	18	17	11	13	17	19	20	20	2	ND
Ni	48	42	76	90	53	66	50	46	14	40
Rb	30	35	9	15	27	22	32	25	45	59
Sc	20	21	26	29	21	22	23	22	34	26
Sr	842	914	870	667	851	993	807	704	695	878
V	74	130	108	119	119	104	110	98	114	129
Y	24	11	15	12	18	11	16	12	17	16
Zn	61	58	57	62	56	84	55	53	67	57
Zr	68	79	27	52	78	44	49	11	77	62

GC76
GC78
GC79

Table C.1 Whole rock geochemical analyses (cont.)
Sample Pyroxene diorites

Major elements (Z)	GC9	GC31	GC98	GC133	GC134	GC136	GC139	GC140	GC155	GC165
SiO ₂	49.17	58.77	46.12	48.60	50.20	52.00	47.70	51.70	51.20	48.62
TiO ₂	2.25	0.82	3.50	3.20	3.15	2.34	3.74	3.34	4.58	2.49
Al ₂ O ₃	18.00	12.60	16.35	16.40	17.45	18.40	16.70	15.59	16.45	21.22
*FeO	11.40	6.39	13.37	12.80	10.95	8.80	12.25	11.60	8.70	9.81
MgO	4.00	7.20	5.50	5.51	5.19	6.22	6.41	5.20	5.72	4.00
MnO	0.14	0.15	0.15	0.16	0.14	0.14	0.15	0.15	0.15	0.11
CaO	7.58	5.96	10.34	8.20	7.80	7.30	8.60	8.80	8.00	9.20
Na ₂ O	3.38	3.47	2.61	2.66	3.25	2.54	1.86	2.38	2.58	3.42
K ₂ O	0.92	1.60	0.55	0.51	1.09	0.60	0.91	0.62	0.65	0.62
F ₂ O ₃	0.89	0.19	0.11	0.11	0.23	0.11	0.17	0.14	0.11	0.71
H ₂ O	1.58	2.08	1.55	1.45	0.86	1.73	1.91	0.71	1.75	<0.10
CO ₂	<0.10	0.70	0.35	<0.10	<0.10	<0.10	<0.10	<0.10	<0.10	<0.10
TOTAL	99.31	99.93	100.50	99.60	100.31	100.18	100.40	100.59	99.89	100.20
Trace elements (ppm)										
Ba	250	270	120	149	192	152	168	141	148	161
Cr	102	299	59	42	31	78	51	55	58	22
Cu	25	37	49	42	26	34	17	47	52	42
La	26	26	ND	10	ND	ND	ND	ND	ND	ND
Li	21	26	17	14	23	18	19	25	19	16
Ni	29	108	46	42	33	38	48	50	55	49
Rb	30	44	20	17	36	24	36	24	ND	16
Sc	30	27	34	33	31	30	31	34	30	12
Sr	675	380	629	589	688	677	612	738	601	1038
V	257	149	439	386	371	236	456	427	202	277
Y	20	20	16	13	18	16	14	18	16	13
Zn	130	142	108	128	95	90	121	112	70	100
Zr	95	170	49	214	209	208	212	260	320	55

Table C.1 Whole rock geochemical analyses (cont.)
 Sample Pyroxene diorites

	GC169	GC178	GC179	GC208	GC212	GC215	GC220	GC222	GC223	GC234
Major elements (%)										
SiO ₂	48.00	50.18	50.33	52.59	49.19	58.08	54.07	50.70	49.85	49.17
TiO ₂	2.22	3.46	2.34	2.98	3.04	1.70	1.56	3.06	3.29	2.65
Al ₂ O ₃	16.26	14.76	14.71	18.62	15.42	16.49	15.90	16.44	16.38	16.66
*FeO	9.82	12.03	10.63	10.77	12.72	7.33	7.88	12.45	12.44	11.53
MgO	5.84	5.18	5.90	4.47	5.23	4.87	5.75	5.15	4.90	4.42
MnO	0.16	0.17	0.16	0.16	0.15	0.12	0.13	0.16	0.17	0.16
CaO	10.95	8.73	8.50	6.55	8.13	7.24	9.51	8.40	7.95	9.69
Na ₂ O	2.23	2.38	2.28	3.49	3.93	3.32	2.40	2.68	3.17	3.04
K ₂ O	0.47	1.03	1.07	1.38	1.35	1.64	1.35	1.33	0.95	0.91
P ₂ O ₅	0.46	0.17	0.14	0.26	0.15	0.21	0.16	0.15	0.15	0.94
H ₂ O	1.73	2.29	2.55	<0.10	<0.10	<0.10	<0.10	<0.10	<0.10	0.30
CO ₂	0.64	0.34	<0.10	<0.10	<0.10	<0.10	<0.10	<0.10	<0.10	0.17
TOTAL	98.78	101.38	98.95	101.27	99.31	101.00	98.71	100.52	99.25	99.64
Trace elements (ppm)										
Ba	148	228	245	319	291	385	281	335	224	218
Cr	174	23	44	23	25	33	29	23	19	25
Cu	45	40	33	35	49	24	26	50	44	32
La	ND	ND	ND	17	16	24	19	15	17	ND
Li	10	18	22	ND	ND	ND	ND	ND	ND	18
Ni	108	26	43	26	19	15	17	18	16	25
Rb	15	41	39	74	76	84	74	70	47	27
Sc	30	40	40	20	35	27	36	35	35	25
Sr	718	584	578	611	537	644	556	554	571	723
V	205	495	397	295	434	167	199	468	375	290
Y	18	19	18	15	18	21	18	18	20	28
Zn	108	100	98	100	106	73	77	108	102	124
Zr	78	118	149	238	155	ND	135	192	96	121

23

Table C.1 Whole rock geochemical analyses (cont.)
 Pyroxene diorites

Sample	GC241	GC242	GC243	GC245	GC253	GC254	GC258	GC261	GC281	GC1
Major elements (%)										
SiO ₂	47.82	48.33	48.72	48.85	52.61	55.10	52.86	51.86	52.25	50.02
TiO ₂	3.43	3.31	2.79	3.26	3.02	0.65	1.59	0.78	3.13	2.75
Al ₂ O ₃	16.86	18.13	16.04	15.26	15.58	18.26	17.37	17.39	13.15	15.70
*FeO	12.35	12.25	12.37	12.65	10.82	5.39	7.77	6.41	13.85	11.45
MgO	5.20	4.71	4.80	4.99	4.55	7.86	6.44	6.79	3.71	4.35
MnO	0.16	0.15	0.17	0.15	0.15	0.11	0.14	0.13	0.18	0.16
CaO	9.52	7.64	9.42	8.86	7.54	10.13	9.04	11.32	8.19	7.70
Na ₂ O	2.61	2.95	2.84	2.62	2.89	2.31	2.70	2.44	2.37	2.90
K ₂ O	0.73	0.96	0.96	1.26	1.32	0.98	1.30	0.74	1.10	1.86
P ₂ O ₅	0.11	0.19	0.77	0.20	0.25	0.11	0.19	0.14	0.23	0.43
H ₂ O	<0.10	<0.10	<0.10	<0.10	<0.10	<0.10	<0.10	0.60	1.00	1.73
CO ₂	<0.10	<0.10	<0.10	<0.10	<0.10	<0.10	<0.10	<0.10	<0.10	0.40
TOTAL	98.79	98.62	99.06	98.06	98.73	100.90	99.40	98.60	99.43	99.45
Trace elements (ppm)										
Ba	202	214	200	252	339	218	248	180	213	340
Cr	25	37	26	27	22	79	52	146	15	101
Cu	57	47	45	65	41	15	50	61	144	35
La	13	ND	ND	ND	25	12	ND	14	19	23
Li	ND	20	24	24	ND	ND	25	ND	ND	30
Ni	19	26	32	39	17	31	30	48	32	33
Rb	55	26	29	37	75	59	35	42	79	56
Sc	38	19	32	36	30	30	30	34	41	31
Sr	556	701	699	574	578	766	621	541	370	660
V	351	385	308	422	378	107	186	123	388	305
Y	16	10	26	21	18	10	17	14	25	22
Zn	102	122	128	112	103	53	83	64	140	99
Zr	83	99	97	158	105	66	103	91	107	157

Table C.1 Whole rock geochemical analyses (cont.)
 Sample Diorites

	GC2	GC4	GC5	GC7	GC8	GC16	GC17	GC27	GC28	GC41
Major elements (wt %)										
SiO ₂	48.93	49.32	47.79	52.76	50.04	48.65	53.60	52.84	51.89	49.51
TiO ₂	2.62	2.75	2.82	0.52	2.55	1.47	0.70	2.47	2.75	2.97
Al ₂ O ₃	16.60	15.55	15.70	23.37	15.98	20.20	16.40	14.70	16.40	15.50
*FeO	10.99	11.33	12.00	3.90	10.69	11.15	6.00	10.94	12.43	12.25
MgO	4.35	5.00	4.60	2.10	4.35	4.00	7.30	4.50	4.20	4.85
MnO	0.16	0.17	0.16	0.06	0.16	0.12	0.12	0.14	0.15	0.16
CaO	7.93	7.48	7.95	7.88	7.60	7.53	8.93	6.18	6.18	7.25
Na ₂ O	3.20	3.25	3.13	4.34	3.15	3.31	2.83	3.08	2.87	3.44
K ₂ O	1.51	1.48	1.32	1.63	1.56	1.41	1.19	2.03	1.91	1.41
P ₂ O ₅	1.14	1.32	1.06	0.42	1.20	0.26	0.11	0.14	0.11	0.50
H ₂ O ⁺	1.37	1.84	1.91	1.87	1.67	1.72	2.09	2.04	1.84	2.07
CO ₂	0.10	0.15	0.40	0.15	<0.10	0.40	0.35	0.40	0.10	<0.10
TOTAL	98.90	99.64	98.84	99.00	98.96	100.22	99.64	99.46	100.83	99.91
Trace elements (ppm)										
Ba	300	310	310	280	320	400	290	360	380	230
Cr	111	102	108	78	98	212	185	113	149	109
Cu	32	29	32	22	25	76	26	37	30	49
La	37	31	28	14	32	21	15	18	22	22
Li	31	31	26	33	28	39	31	34	46	26
Ni	31	30	39	28	27	60	41	30	46	33
Rb	54	52	42	48	50	41	32	58	69	50
Sc	26	27	30	5	28	20	27	29	21	30
Sr	660	630	580	970	590	640	530	500	500	600
V	274	339	342	96	325	291	30	438	424	418
Y	32	30	29	6	41	12	15	24	12	26
Zn	89	101	125	49	117	158	68	103	145	ND
Zr	127	160	130	40	210	175	85	115	205	120

Table G.1 Whole rock geochemical analyses (cont.)
Diorites

Sample	GC44	GC56	GC93	GC100	GC102	GC104	GC105	GC108	GC109	GC111
Major elements (wt %)										
SiO ₂	59.90	53.60	46.75	45.93	46.55	49.16	52.29	48.27	47.25	46.03
TiO ₂	0.95	2.20	2.522	3.14	2.93	3.08	1.68	2.70	2.84	2.65
Al ₂ O ₃	16.60	15.50	16.18	16.31	16.80	15.29	16.53	16.52	16.53	16.25
*Fe	6.91	9.89	11.30	11.59	12.62	12.36	8.26	11.56	11.44	12.42
MgO	3.10	4.20	6.24	6.20	4.60	4.83	6.24	4.39	5.63	4.83
MnO	0.09	0.14	0.16	0.14	0.15	0.14	0.14	0.13	0.16	0.16
CaO	3.97	6.27	7.88	9.63	8.46	8.95	9.43	8.63	8.79	9.34
Na ₂ O	4.16	3.54	3.77	2.37	3.01	2.65	2.74	3.19	3.48	2.74
K ₂ O	1.38	1.68	1.41	0.67	1.07	0.72	0.79	1.24	1.32	1.31
P ₂ O ₅	0.35	0.61	0.91	0.09	1.33	0.16	0.15	0.68	0.18	1.38
H ₂ O	2.49	1.75	2.03	1.63	2.09	1.65	1.75	1.55	2.17	1.75
CO ₂	<0.10	0.75	0.41	0.37	0.26	0.33	<0.10	0.35	0.15	0.28
TOTAL	99.90	100.13	99.56	98.07	99.87	99.32	100.00	99.21	99.94	99.13
Trace elements (ppm)										
Ba	290	700	295	154	233	179	198	265	291	245
Cr	70	ND	85	120	76	132	208	124	71	69
Cu	15	20	39	46	35	86	41	30	47	22
La	17	46	ND	ND	ND	ND	ND	ND	ND	ND
Li	29	26	31	17	25	18	20	20	14	26
Ni	20	33	38	41	33	36	50	34	33	24
Rb	39	40	42	24	42	25	29	34	37	40
Sc	30	21	27	29	25	30	27	23	32	28
Sr	395	770	753	622	657	537	566	661	785	644
V	206	325	297	374	305	461	196	330	345	ND
Y	18	17	32	17	37	24	23	30	20	41
Zn	83	75	93	91	95	110	75	106	88	97
Zr	190	250	110	48	112	92	113	199	68	52

Table C-1 Whole rock geochemical analyses (cont.)
Sample Diorites

	GC114	GC119	GC120	GC122	GC125	GC132	GC143	GC146	GC150	GC151
Major elements (%)										
SiO ₂	53.00	48.50	58.80	55.80	49.80	48.00	48.80	56.30	49.10	56.23
TiO ₂	2.54	2.69	2.31	1.75	2.93	4.34	3.00	1.60	3.03	3.08
Al ₂ O ₃	15.43	18.56	14.30	18.20	16.50	14.20	16.45	19.20	16.75	18.15
*FeO	10.61	10.16	9.00	9.30	10.70	13.30	12.00	6.40	12.00	11.40
MgO	3.99	4.63	5.42	1.96	4.47	6.11	4.21	4.76	4.73	4.03
MnO	0.15	0.14	0.16	0.09	0.15	0.18	0.21	0.13	0.18	0.19
CaO	7.98	7.47	4.66	4.55	7.85	9.15	8.65	6.84	8.25	8.45
Na ₂ O	3.04	3.26	2.48	3.68	2.83	2.17	2.55	3.20	2.78	2.94
K ₂ O	1.17	2.03	1.48	1.58	0.97	0.76	0.88	0.85	0.68	0.77
P ₂ O ₅	1.24	0.64	0.46	0.09	0.34	0.08	1.17	0.14	1.20	1.05
H ₂ O	1.61	1.51	0.70	1.63	1.61	1.80	2.05	0.57	1.77	1.00
CO ₂	0.15	0.37	<0.10	<0.10	<0.10	<0.10	<0.10	<0.10	<0.10	<0.10
TOTAL	100.88	99.96	99.77	98.64	98.17	100.09	99.96	99.99	98.97	100.16
Trace elements (ppm)										
Ba	337	286	295	479	216	158	202	165	151	177
Cr	49	144	170	28	29	34	38	43	36	30
Cu	29	29	94	15	21	45	36	120	41	46
La	ND	ND	ND	ND	ND	ND	ND	ND	ND	ND
Li	22	27	38	24	24	26	ND	20	22	32
Ni	34	32	109	16	22	38	10	16	13	11
Rb	43	44	56	54	32	28	33	30	27	28
Sc	25	20	22	217	34	37	28	17	24	26
Sr	645	616	461	596	558	740	608	661	592	700
V	305	283	201	111	327	343	296	144	307	280
Y	47	25	37	10	25	15	35	8	28	31
Zn	100	103	83	106	91	121	130	76	104	129
Zr	193	138	193	105	152	230	206	120	155	187

Table C.1 Whole rock geochemical analyses (cont.)
Diorites

Sample	GCI167	GCI171	GCI173	GCI174	GCI175	GCI176	GCI177	GCI180	GCI181	GCI182
Major elements (%)										
SiO ₂	56.23	48.69	52.25	48.97	53.55	55.64	50.10	48.70	52.92	53.38
TiO ₂	1.17	2.17	3.09	3.29	0.87	0.84	3.28	3.23	1.11	0.64
Al ₂ O ₃	17.94	16.06	15.67	15.83	17.83	16.56	16.71	14.85	17.53	19.97
*FeO	6.16	9.99	11.59	11.50	6.23	6.10	9.84	12.53	6.50	7.03
MgO	2.92	6.12	5.05	4.76	6.77	5.51	5.09	5.74	6.47	3.81
MnO	0.13	0.16	0.19	0.18	0.15	0.14	0.17	0.18	0.12	0.09
CaO	4.03	9.78	6.91	9.48	9.59	7.75	7.20	7.80	8.09	8.88
Na ₂ O	4.52	2.32	2.29	2.62	2.48	2.86	2.45	2.50	3.04	3.56
K ₂ O	2.62	0.82	1.11	0.80	0.96	1.04	0.95	1.39	1.49	0.77
P ₂ O ₅	0.35	0.16	0.14	0.19	0.18	0.18	0.17	0.20	0.22	0.36
H ₂ O	1.98	1.53	2.02	1.52	<0.10	1.66	3.02	2.43	2.24	<0.10
CO ₂	<0.10	0.60	<0.10	<0.10	<0.10	0.23	0.38	<0.10	<0.10	<0.10
TOTAL	98.05	98.40	100.31	99.14	98.61	98.51	99.36	99.55	99.73	98.49
Trace elements (ppm)										
Ba	628	168	301	195	225	267	241	200	253	187
Cr	12	55	21	42	41	38	75	22	52	95
Cu	13	30	25	27	33	27	40	40	48	63
La	ND	ND	ND	ND	ND	ND	ND	ND	ND	ND
Li	20	11	29	15	24	15	21	30	32	16
Ni	39	17	14	16	9	21	26	45	ND	ND
Rb	70	29	42	30	33	35	27	45	51	23
Sc	14	35	33	41	35	29	25	41	31	34
Sr	726	624	546	603	640	517	583	510	625	809
V	120	318	441	357	131	114	417	566	158	70
Y	27	15	13	21	20	20	12	20	23	26
Zn	73	85	137	105	83	65	95	99	75	89
Zr	282	66	84	106	91	131	162	110	117	107

Table C.1 Whole rock geochemical analyses (cont.)
Diorites

Sample	GC191	GC192	GC193	GC195	GC207	GC211	GC228	GC232	GC233	GC236
Major elements (%)										
SiO ₂	62.75	59.97	58.72	53.03	50.13	53.31	52.38	55.28	51.85	51.29
TiO ₂	0.85	1.26	1.74	1.82	2.44	2.65	1.17	1.23	1.55	3.44
Al ₂ O ₃	13.36	16.35	17.84	127.61	16.70	16.72	18.97	17.13	17.39	16.64
FeO	6.20	7.24	6.77	6.93	10.49	10.93	6.95	6.92	7.26	9.80
MgO	5.32	3.72	2.71	3.20	4.10	4.31	7.90	5.10	6.36	4.54
MnO	0.10	0.13	0.11	0.12	0.16	0.16	0.13	0.13	0.14	0.17
CaO	5.75	5.77	5.89	5.41	8.04	7.74	10.13	8.51	8.78	8.21
Na ₂ O	2.08	2.75	2.64	2.81	2.92	3.22	2.66	3.10	2.61	2.66
K ₂ O	2.26	1.62	1.80	1.91	1.24	1.40	1.21	1.39	1.22	1.05
P ₂ O ₅	0.22	0.37	0.38	0.47	0.94	1.07	0.11	0.21	0.16	0.13
H ₂ O ⁺	<0.10	0.50	0.10	<0.10	1.05	<0.10	<0.10	<0.10	1.00	1.01
CO ₂	<0.10	0.11	0.47	<0.10	0.50	<0.10	<0.10	<0.10	0.50	<0.10
TOTAL	98.89	99.89	99.17	101.00	98.73	101.51	101.61	99.00	98.82	98.94
Trace elements (ppm)										
Ba	553	555	473	386	309	366	251	287	267	299
Cr	87	71	13	14	21	19	91	28	43	44
Cu	26	31	26	20	33	32	19	33	30	63
La	ND	ND	ND	ND	21	24	10	ND	13	14
Li	36	37	33	40	ND	ND	ND	26	ND	ND
Ni	56	40	21	28	13	15	31	27	19	53
Rb	156	56	59	56	74	75	63	41	74	72
Sc	19	17	17	21	30	27	30	28	31	36
Sr	558	719	853	760	620	613	708	705	668	548
V	110	148	96	95	275	280	1158	150	193	354
Y	37	20	20	40	26	27	12	20	17	17
Zn	91	119	76	ND	106	106	62	86	65	94
Zr	127	228	133	188	123	146	109	143	87	105

Table C.1 Whole rock geochemical analyses (cont.)
Diorites

Sample	GC237	GC239	GC240	GC244	GC249	GC251	GC257	GC263	GC264	GC265
Major elements (%)										
SiO ₂	50.36	50.02	49.57	51.47	48.41	53.33	43.46	51.57	57.26	55.34
TiO ₂	3.10	2.75	3.29	2.02	3.35	3.28	3.84	1.84	2.46	2.93
Al ₂ O ₃	15.72	16.32	16.52	16.89	15.74	14.50	15.72	19.74	14.51	15.87
*FeO	12.07	11.87	12.76	10.25	12.87	11.41	12.03	8.64	10.15	10.11
MgO	4.59	4.22	4.98	5.14	5.08	4.43	2.81	3.75	4.02	4.36
MnO	0.16	0.18	0.17	0.14	0.15	0.13	0.19	0.11	0.14	0.16
CaO	8.18	8.98	8.31	7.75	8.72	7.53	11.09	6.64	6.81	6.77
Na ₂ O	2.66	2.87	2.95	3.55	2.70	2.57	2.31	2.83	2.90	3.15
K ₂ O	1.05	1.32	1.12	1.35	1.23	1.27	1.82	2.60	1.73	1.78
P ₂ O ₅	0.16	0.98	0.42	0.22	0.25	0.12	0.23	0.87	0.19	0.36
H ₂ O	0.80	<0.10	<0.10	<0.10	<0.10	<0.10	2.00	<0.10	<0.10	<0.10
CO ₂	<0.10	<0.10	<0.10	<0.10	<0.10	<0.10	4.68	<0.10	0.64	<0.10
TOTAL	98.85	99.44	100.08	98.78	98.50	98.58	100.08	98.59	100.81	100.83
Trace elements (ppm)										
Ba	321	277	238	243	329	361	226	918	328	380
Cr	20	30	18	51	32	19	29	12	24	14
Cu	51	40	42	40	73	71	90	38	47	30
La	15	ND	17	ND	ND	20	ND	38	ND	28
Li	ND	ND	ND	28	29	ND	34	ND	23	ND
Ni	40	25	17	27	47	23	39	12	26	14
Rb	63	40	93	38	40	74	66	155	48	113
Sc	36	25	35	30	35	33	37	45	30	27
Sr	562	575	584	669	638	462	498	766	488	546
V	406	302	380	326	504	292	490	272	393	329
Y	19	30	21	ND	22	14	32	18	25	20
Zn	103	102	78	100	117	83	93	61	99	84
Zr	97	137	134	98	96	110	196	41	171	149

Table C.1 Whole rock geochemical analyses (cont.)
Diorites

Sample	Monzonites									
	GC270	GC273	GC274	GC279	GC19	GC20	GC21	GC131	GC183	GC184
Major elements (wt %)										
SiO ₂	53.41	56.51	57.28	53.49	51.20	47.29	55.80	63.00	58.54	63.69
TiO ₂	2.96	1.18	1.30	2.76	2.20	1.90	1.72	1.11	0.80	0.85
Al ₂ O ₃	14.55	15.95	15.57	14.88	17.10	18.36	16.80	18.20	14.03	15.60
*FeO	11.89	6.98	6.44	11.38	9.68	14.13	7.36	4.65	5.89	5.03
MgO	4.40	6.86	4.46	4.08	3.90	3.30	2.85	2.01	6.25	3.13
MnO	0.16	0.13	0.19	0.15	0.15	0.15	0.11	0.06	0.11	0.10
CaO	7.68	7.44	6.31	8.30	6.55	5.10	5.49	4.22	5.00	3.57
Na ₂ O	2.58	3.14	3.40	2.43	3.30	2.93	3.87	3.59	3.26	3.64
K ₂ O	0.96	1.02	1.11	1.06	1.77	2.12	1.75	2.30	2.06	3.02
P ₂ O ₅	0.26	0.19	0.21	0.21	1.23	0.09	0.89	0.24	0.18	0.19
H ₂ O	<0.10	<0.10	1.88	1.00	2.10	2.31	2.04	0.36	2.74	<0.10
CO ₂	<0.10	<0.10	0.50	<0.10	0.10	0.25	0.10	<0.10	<0.10	<0.10
TOTAL	98.85	99.40	98.65	98.74	99.28	97.93	98.83	99.74	98.86	99.00
Trace elements (ppm)										
Ba	289	301	367	284	440	520	450	450	471	590
Cr	15	161	86	14	102	218	86	32	199	44
Cu	50	38	22	41	25	21	20	19	43	15
La	23	21	26	22	40	23	35	ND	ND	ND
Li	ND	ND	ND	ND	30	52	36	38	31	34
Ni	18	84	38	14	31	59	39	10	73	12
Rb	77	70	67	74	56	72	55	72	67	79
Sc	35	26	23	35	21	12	11	16	25	16
Sr	474	772	555	505	600	580	600	680	467	454
V	332	138	128	318	234	375	181	99	122	104
Y	21	18	19	19	32	7	23	26	24	36
Zn	113	76	78	115	112	217	89	59	90	78
Zr	123	103	142	142	217	232	217	344	149	307

Table C.1 Whole rock geochemical analyses (cont.)
 Sample Monzonites

	GC187	GC190	GC199	GC213	GC229	GC231	GC25	GC36	GC96	GC106
Adameillites										
Major elements (Z)										
SiO ₂	62.60	63.90	59.63	65.18	61.14	52.79	71.50	63.40	66.50	72.20
TiO ₂	1.20	0.83	1.52	0.76	0.67	3.21	0.30	0.87	0.70	0.22
Al ₂ O ₃	13.90	15.29	17.40	16.51	19.75	16.99	13.90	15.70	14.77	14.90
*FeO	9.63	5.30	6.55	5.26	4.44	11.61	2.20	4.78	3.41	1.50
MgO	3.78	3.27	2.39	2.32	1.82	4.96	0.75	2.60	1.74	0.60
MnO	0.13	0.08	0.13	0.05	0.07	0.17	0.03	0.09	0.07	0.04
CaO	4.55	3.27	5.00	2.83	5.77	6.79	0.99	3.92	2.55	0.65
Na ₂ O	2.56	3.35	3.47	3.66	4.04	3.33	3.60	4.02	4.07	4.16
K ₂ O	0.93	2.30	2.28	2.84	1.79	1.24	4.79	2.92	3.59	3.62
P ₂ O ₅	0.17	0.21	0.34	0.32	0.25	0.32	0.10	0.23	0.18	0.11
H ₂ O	<0.10	1.20	1.00	<0.10	<0.10	<0.10	1.36	1.00	1.53	1.45
CO ₂	<0.10	1.13	0.21	0.19	<0.10	<0.10	<0.10	<0.10	0.33	0.09
TOTAL	99.47	99.41	99.92	99.92	99.80	101.41	100.90	99.63	99.45	99.54
Trace elements (ppm)										
Ba	394	583	476	655	493	312	770	630	691	660
Cr	116	58	13	11	26	20	43	105	59	50
Cu	20	13	22	13	41	37	70	22	13	5
La	ND	ND	ND	ND	ND	17	34	41	33	23
Li	24	32	38	39	35	ND	14	29	15	21
Ni	86	30	17	10	17	18	<5	35	23	<5
Rb	44	75	73	84	60	67	105	85	89	104
Sc	30	16	15	7	9	30	5	12	8	4
Sr	188	510	707	617	516	592	240	500	361	230
V	243	118	73	131	62	400	25	107	64	17
Y	28	26	18	20	12	19	16	22	15	9
Zn	99	77	85	61	66	86	27	99	56	33
Zr	203	156	135	174	157	117	170	275	340	125

Table C.1 Whole rock geochemical analyses (cont.)
Adameillites

Sample	GC116	GC117	GC127	GC128	GC130	GC198	GC205	GC252	GC256	GC271
Major elements (wt %)										
SiO ₂	64.93	70.28	69.20	69.00	65.60	62.03	56.88	65.29	68.77	69.14
TiO ₂	0.80	0.52	0.71	0.75	1.01	1.34	1.37	0.65	0.71	0.38
Al ₂ O ₃	15.92	14.42	16.10	16.00	17.10	16.72	19.26	18.17	15.50	16.18
*FeO	4.33	2.36	3.00	3.20	4.10	6.46	7.08	4.07	3.80	2.32
MgO	1.46	0.85	1.11	1.17	1.78	2.20	3.49	1.45	1.66	0.71
MnO	0.12	0.05	0.04	0.05	0.06	0.10	0.06	0.04	0.4	0.05
CaO	1.84	0.85	2.35	2.26	3.76	3.99	6.28	3.61	2.03	2.21
Na ₂ O	3.73	3.51	3.86	3.94	3.96	3.35	3.41	4.39	3.60	4.27
K ₂ O	2.99	4.25	2.95	1.95	1.88	2.59	2.14	2.86	3.93	2.98
P ₂ O ₅	0.23	0.14	0.14	0.15	0.21	0.39	0.21	0.21	0.18	0.14
H ₂ O	1.76	1.25	0.38	0.34	0.48	<0.10	<0.10	<0.10	<0.10	0.50
CO ₂	0.07	0.04	<0.10	<0.10	<0.10	<0.10	<0.10	<0.10	<0.10	<0.10
TOTAL	98.18	98.52	99.84	99.81	99.94	99.17	100.18	100.74	100.22	98.88
Trace elements (ppm)										
Ba	759	815	719	596	500	578	747	730	897	624
Cr	93	32	21	30	30	12	12	17	28	<5
Cu	17	8	40	19	13	29	11	9	9	5
La	44	ND	ND	ND	ND	ND	16	ND	ND	43
Li	35	21	22	18	37	37	ND	28	18	ND
Ni	29	<5	<5	<5	6	18	34	16	23	7
Rb	107	117	84	83	74	76	114	77	96	191
Sc	10	6	9	9	14	13	16	5	9	4
Sr	311	236	500	485	655	669	852	637	414	370
V	19	22	24	25	26	56	215	60	61	26
Y	77	40	38	43	55	45	14	12	22	16
Zn	77	40	38	43	55	81	66	50	46	43
Zr	294	245	405	378	284	108	495	300	293	223

CC
CC

Table C.1 Whole rock geochemical analyses (cont.)
 Sample Adameillites Aplite dykes

Major elements (%)	Quartz feldspar porphyry dykes									
	GC276	GC34	GC86	GC92	GC118	GC126	GC6	GC13	GC33	GC89
SiO ₂	66.10	75.91	75.58	76.81	75.28	75.90	71.16	72.99	75.18	68.08
TiO ₂	0.94	BD	0.12	0.07	0.24	0.10	0.15	0.12	0.05	0.10
Al ₂ O ₃	15.57	12.57	12.57	14.25	12.89	13.80	16.00	14.50	12.50	13.47
*FeO	4.51	0.60	1.01	0.73	1.43	0.70	1.14	1.10	0.64	1.07
MgO	2.71	0.05	0.15	0.16	0.36	0.10	0.70	0.45	0.30	0.92
MnO	0.09	BD	0.05	0.02	0.02	0.01	BD	BD	0.03	0.01
CaO	3.07	BD	0.72	0.40	0.28	0.62	0.53	0.63	0.67	0.41
Na ₂ O	3.56	3.59	4.44	3.93	2.16	3.22	4.68	4.25	3.23	4.27
K ₂ O	2.74	5.50	5.34	4.55	6.11	5.10	2.80	4.24	5.39	2.97
P ₂ O ₅	0.25	BD	0.45	0.03	0.05	0.01	0.09	0.07	0.03	0.05
H ₂ O _f	<0.10	0.74	0.75	0.87	1.09	1.11	1.72	1.08	1.09	0.72
CO ₂	<0.10	BD	BD	BD	BD	BD	0.25	BD	0.25	BD
TOTAL	99.20	99.13	100.82	100.95	99.93	101.37	99.24	99.45	99.36	100.63

Trace elements (ppm)	Quartz feldspar porphyry dykes									
	GC276	GC34	GC86	GC92	GC118	GC126	GC6	GC13	GC33	GC89
Ba	775	BD	1152	491	298	615	210	630	210	534
Cr	53	10	36	45	108	19	20	22	19	35
Cu	13	5	3	BD	13	6	4	4	4	16
La	39	3	ND	ND	14	ND	26	26	14	ND
Li	ND	11	9	15	9	12	10	13	5	BD
Ni	33	BD	BD	BD	BD	BD	9	8	BD	BD
Rb	141	160	129	143	148	149	100	123	177	70
Sc	13	3	4	4	4	4	3	3	2	3
Sr	511	BD	155	86	91	84	110	180	40	153
V	85	BD	BD	BD	17	BD	12	9	BD	7
Y	22	7	18	20	10	23	8	13	9	10
Zn	70	41	31	29	21	14	ND	23	15	11
Zr	277	77	102	39	123	344	120	107	52	59

Table C.1 Whole rock geochemical analyses (cont.)
 Quartz feldspar porphyry dykes

Sample	GC99	GC144	GC152	GC154	GC166	GC168	GC188	GC217	GC224	GC247
Major elements (%)										
SiO ₂	72.74	75.60	75.80	75.00	75.07	75.82	77.24	75.93	75.60	67.97
TiO ₂	0.07	0.11	0.08	0.05	0.14	0.13	0.20	0.13	0.09	0.76
Al ₂ O ₃	13.95	13.60	13.70	13.25	14.08	12.97	13.07	13.90	13.75	15.33
*FeO	0.96	0.75	0.90	1.05	1.26	0.55	1.34	0.97	0.86	3.41
MgO	1.66	0.14	0.28	0.51	0.38	0.19	0.47	0.30	0.26	1.64
MnO	0.06	0.03	0.02	0.03	0.01	0.03	0.02	0.01	0.03	0.06
CaO	1.91	0.61	0.83	1.38	1.06	0.55	0.49	1.19	0.65	2.81
Na ₂ O	0.55	3.82	3.90	3.69	4.07	3.34	2.79	3.44	4.07	3.56
K ₂ O	2.13	4.50	3.70	3.00	4.23	4.28	5.41	4.45	4.64	3.35
P ₂ O ₅	0.03	0.03	0.04	0.04	0.06	0.03	0.05	0.10	0.07	0.21
H ₂ O	3.74	0.86	0.70	1.04	BD	BD	BD	BD	BD	BD
CO ₂	1.67	BD	BD	BD	BD	BD	BD	BD	BD	BD
TOTAL	99.47	100.05	99.95	99.04	100.36	98.77	101.08	100.42	100.02	99.10
Trace elements (ppm)										
Ba	116	431	478	267	634	524	941	387	675	826
Cr	18	14	30	14	5	BD	BD	9	5	16
Cu	4	3	3	5	11	4	6	BD	BD	11
La	ND	ND	13	ND	ND	ND	ND	ND	ND	ND
Li	69	17	9	13	10	14	15	7	11	ND
Ni	BD	BD	BD	BD	BD	BD	7	BD	BD	ND
Rb	98	140	120	100	85	141	150	132	141	17
Sc	4	3	3	3	4	5	5	4	3	158
Sr	36	90	144	104	176	76	150	136	181	8
V	BD	3	7	6	BD	BD	7	BD	BD	390
Y	22	20	13	20	15	19	14	10	16	68
Zn	35	29	12	121	17	29	25	17	22	19
Zr	42	253	200	230	107	94	101	50	64	45

Table C.1 Whole rock geochemical analyses (cont.)
 Quartz feldspar
 porphyry dykes

Sample	GC259	GC272	GC87	GC145	GC149	GC164	GC230	GC246	GC248	GC260
Major elements (wt %)										
SiO ₂	75.51	74.21	61.99	54.90	54.90	56.13	68.13	58.72	58.61	60.10
TiO ₂	0.17	0.15	0.22	1.91	1.80	1.17	0.84	1.40	1.22	1.10
Al ₂ O ₃	13.40	14.42	16.45	16.85	16.85	17.00	14.87	15.79	16.13	17.35
*FeO	1.06	1.29	5.65	7.45	7.60	6.38	3.94	6.16	6.34	5.31
MgO	0.28	0.37	3.63	5.33	5.49	4.87	2.08	4.49	4.11	2.59
MnO	0.04	0.03	0.09	0.13	0.12	0.11	0.07	0.11	0.11	0.06
CaO	0.65	0.64	4.69	6.00	6.73	6.71	3.29	6.22	5.70	4.94
Na ₂ O	3.71	2.74	3.68	3.57	3.86	3.16	4.24	3.85	3.88	3.97
K ₂ O	4.84	5.28	1.98	1.63	1.19	1.89	3.45	1.76	2.44	2.52
P ₂ O ₅	0.08	0.04	0.27	0.35	0.35	0.26	0.21	0.32	0.34	0.31
H ₂ O	BD	BD	1.22	2.43	1.01	1.46	BD	BD	BD	0.90
CO ₂	BD	BD	0.11	BD	BD	BD	BD	BD	0.40	BD
TOTAL	99.74	99.17	100.98	100.55	99.90	99.14	101.12	98.82	99.28	99.15
Trace elements (ppm)										
Ba	967	2063	506	350	221	496	753	633	606	990
Cr	10	BD	110	47	68	65	40	38	30	71
Cu	BD	7	25	30	28	28	13	20	27	27
La	ND	20	33	21	ND	ND	43	43	ND	43
Li	15	ND	22	37	29	25	ND	ND	29	ND
Ni	5	7	39	33	45	57	24	39	42	32
Rb	134	191	60	55	36	609	161	124	66	151
Sc	3	4	13	19	17	23	10	17	16	15
Sr	138	368	463	685	595	556	445	784	785	557
V	BD	12	107	175	163	160	83	141	132	110
Y	17	5	21	18	26	27	20	20	23	21
Zn	36	26	66	95	88	86	55	75	78	67
Zr	126	95	247	827	697	197	260	2239	256	134

Table C.1 Whole rock geochemical analyses (cont.)
 Sample Appinites

Sample	Major elements (wt %)		Rafted xenoliths							
	GC30	GC75	GC115	GC185	GC206	GC3	GC26	GC101	GC112	GC113
SiO ₂	55.00	51.20	59.00	57.29	53.80	49.12	45.60	48.91	41.54	48.00
TiO ₂	0.87	1.57	0.83	1.11	2.01	1.52	1.97	0.92	1.68	1.83
Al ₂ O ₃	9.40	11.36	9.96	13.22	11.89	13.95	19.96	15.06	25.55	20.16
*FeO	7.28	9.24	7.38	7.23	9.13	12.60	14.77	8.21	13.36	12.32
MgO	11.60	12.26	10.20	8.54	11.22	7.55	4.30	7.15	3.52	4.33
MnO	0.16	0.18	0.15	0.15	0.17	0.23	0.13	0.13	0.13	0.11
CaO	8.10	7.51	7.74	8.23	7.50	9.45	5.35	14.01	6.75	7.58
Na ₂ O	2.28	1.91	1.96	2.65	1.80	2.63	2.56	2.16	2.79	2.29
K ₂ O	2.59	1.13	1.02	1.54	1.65	0.94	1.57	0.54	1.32	0.63
P ₂ O ₅	0.14	0.21	0.07	0.20	0.19	0.16	0.08	0.07	0.13	0.08
H ₂ O	1.87	2.33	1.75	BD	BD	0.79	1.84	1.93	1.70	2.12
Co ₂	0.50	0.40	0.43	BD	BD	BD	0.40	1.22	0.35	BD
TOTAL	99.79	99.30	100.49	100.16	99.36	98.94	98.53	100.31	98.82	99.49
Trace elements (ppm)										
Ba	260	264	235	268	424	210	350	71	585	185
Cr	398	630	335	329	572	349	296	119	151	461
Cu	51	32	98	16	19	30	61	41	111	67
La	14	18	ND	ND	18	15	27	ND	ND	ND
Li	21	20	21	22	ND	19	52	20	47	18
Ni	165	353	201	90	268	89	87	61	122	125
Rb	34	32	43	49	85	32	51	19	49	29
Sc	41	32	35	36	53	48	15	46	19	20
Sr	260	358	340	372	293	510	480	534	642	587
V	164	167	126	145	227	308	422	182	212	274
Y	16	32	40	29	50	26	6	25	19	8
Zn	89	104	88	1067	94	145	236	78	257	141
Zr	120	146	85	133	199	120	570	41	151	66

Table C.1 Whole rock geochemical analyses (cont.)
Sample Rafted xenoliths

Major elements (%)	Microdiorite xenoliths										Dalradia xenoliths	
	GC124	GC137	GC194	GC197	GC238	GC138	GC148	GC172	GC196	GC15		
SiO ₂	53.90	49.80	52.80	60.19	44.31	54.20	51.00	53.34	54.22	53.47		
TiO ₂	1.71	1.81	1.22	0.95	2.34	1.29	1.79	1.86	1.73	0.92		
Al ₂ O ₃	17.60	23.10	17.64	17.58	22.26	12.60	16.25	14.85	17.48	19.70		
*FeO	10.85	7.70	19.86	6.43	14.46	10.35	13.10	8.05	7.78	5.99		
MgO	2.53	4.17	5.84	3.42	4.30	8.07	7.88	4.15	5.11	2.85		
MnO	0.18	0.10	0.16	0.10	0.14	0.24	0.22	0.14	0.12	0.10		
CaO	3.37	5.61	6.69	3.04	5.74	10.50	6.58	6.66	7.57	9.52		
Na ₂ O	2.78	2.80	2.23	2.92	2.33	1.60	2.53	3.26	3.13	4.10		
K ₂ O	1.95	1.69	0.87	1.98	2.42	0.31	0.22	1.55	1.70	0.88		
P ₂ O ₅	0.18	0.09	0.34	0.12	0.40	0.15	0.15	0.42	0.32	1.13		
H ₂ O	2.38	2.73	BD	2.80	BD	0.44	0.37	2.66	0.40	1.26		
CO ₂	BD	BD	BD	BD	BD	BD	BD	1.85	0.21	BD		
TOTAL	97.42	99.60	98.65	99.59	98.70	99.75	100.09	98.79	99.77	99.92		
Trace elements (ppm)												
Ba	525	399	269	576	733	109	115	410	340	240		
Cr	126	118	227	111	125	230	268	47	30	111		
Cu	15	151	131	22	28	60	30	26	31	15		
La	38	ND	ND	ND	24	ND	5	ND	ND	43		
Li	55	56	22	68	ND	14	13	18	30	14		
Ni	83	138	80	60	40	128	38	13	47	35		
Rb	80	55	31	64	162	16	14	37	42	23		
Sc	17	161	33	19	18	46	21	26	20	18		
Sr	408	624	358	435	519	317	671	603	721	740		
V	179	1322	268	130	410	392	298	195	177	183		
Y	11	9	ND	10	21	26	9	35	25	28		
Zn	215	223	126	122	148	126	147	103	96	61		
Zr	195	160	93	222	124	117	95	298	244	145		

Sample	Whole rock geochemical analyses (cont.)										Juan Jorge Diorites											
	Dalradian xenoliths					Dalradian meta sediments					JJ3		JJ4		JJ6		JJ7		JJ8		JJ18	
	GC46	GC68	GC107	GC129B		GC68	GC107	GC129B			JJ3	JJ4	JJ6	JJ7	JJ8	JJ18						
Major elements (%)																						
SiO ₂	65.00	76.77	72.60	72.80		76.77	72.60	72.80			65.61	63.08	59.76	62.61	57.21	61.26						
TiO ₂	0.90	0.75	0.47	0.82		0.75	0.47	0.82			0.87	1.00	1.24	1.10	1.26	0.98						
Al ₂ O ₃	16.70	10.40	12.61	13.00		10.40	12.61	13.00			16.22	15.70	16.26	16.05	16.90	18.24						
*FeO	6.53	4.56	3.53	4.15		4.56	3.53	4.15			4.23	5.32	6.68	5.92	7.04	4.28						
MgO	1.75	1.20	0.99	1.73		1.20	0.99	1.73			2.03	3.01	3.78	3.49	3.86	1.94						
MnO	0.08	0.05	0.03	0.05		0.05	0.03	0.05			0.07	0.09	0.11	0.10	0.13	0.08						
CaO	1.27	0.98	1.64	0.70		0.98	1.64	0.70			3.39	4.60	5.66	5.36	5.92	4.11						
Na ₂ O	1.88	2.19	2.21	3.23		2.19	2.21	3.23			3.78	3.57	3.64	3.65	3.88	4.59						
K ₂ O	3.76	1.94	2.31	2.30		1.94	2.31	2.30			3.47	2.68	2.24	1.92	2.08	2.96						
P ₂ O ₅	0.27	0.04	0.03	0.07		0.04	0.03	0.07			0.21	0.28	0.32	0.30	0.32	0.23						
H ₂ O _f	0.22	0.68	1.89	1.83		0.68	1.89	1.83			BD	BD	BD	BD	BD	BD						
CO ₂	BD	BD	BD	BD		BD	BD	BD			0.23	0.22	0.34	BD	BD	BD						
TOTAL	98.46	100.02	98.40	100.68		100.02	98.40	100.68			100.11	99.55	100.03	100.56	98.59	98.67						
Trace elements (ppm)																						
Ba	660	500	747	692		500	747	692			1027	703	629	554	554	1004						
Cr	147	75	77	53		75	77	53			28	47	76	85	87	34						
Cu	31	23	29	25		23	29	25			12	24	35	16	39	17						
La	45	19	ND	22		19	ND	22			ND	37	32	36	36	ND						
Li	72	33	34	43		33	34	43			46	41	34	30	26	44						
NI	57	31	27	30		31	27	30			22	35	46	42	49	18						
Rb	122	61	83	84		61	83	84			132	87	67	54	69	113						
Sc	16	8	8	10		8	8	10			6	14	18	16	20	7						
Sr	95	150	182	148		150	182	148			665	714	742	776	754	738						
V	112	76	38	79		76	38	79			86	114	145	129	142	68						
Y	19	8	5	7		8	5	7			18	28	23	24	27	20						
Zn	88	59	54	69		59	54	69			83	87	97	87	95	80						
Zr	230	297	203	181		297	203	181			463	276	297	202	110	567						

Table C.1 Whole rock geochemical analyses (cont.)

Sample	Diorites		Granites		Xenolith		Bridge outcrops All lithologies			
	JJ20	JJ21	JJ23	JJ1	JJ9	JJ17	JJ19	JJ10	JJ11	JJ12
Major elements (%)										
SiO ₂	64.32	58.60	56.72	71.61	71.29	72.06	58.46	55.75	56.33	72.48
TiO ₂	0.92	2.00	1.31	0.44	0.52	0.49	1.35	1.20	1.16	0.42
Al ₂ O ₃	16.63	16.18	17.27	14.12	15.78	15.44	17.60	17.09	16.56	14.60
*FeO	4.43	5.41	6.41	2.00	2.53	2.36	5.85	6.96	6.52	1.82
MgO	2.43	2.88	3.66	0.65	0.81	0.73	3.02	5.33	4.89	0.64
MnO	1.10	0.08	0.10	0.04	0.06	0.05	0.17	0.13	0.13	6.04
CaO	4.06	5.56	6.72	1.28	1.59	1.56	5.62	6.31	6.60	1.22
Na ₂ O	4.18	3.83	3.93	3.11	4.23	4.07	5.21	3.77	3.39	3.39
K ₂ O	2.50	2.65	1.71	5.34	4.56	4.55	1.79	2.47	2.54	4.24
P ₂ O ₅	0.28	0.37	0.38	0.12	0.13	0.13	0.33	0.25	0.24	0.09
H ₂ O	BD	1.00	0.80	0.20	BD	BD	BD	BD	BD	BD
CO ₂	BD	BD	BD	BD	BD	BD	BD	BD	BD	BD
TOTAL	99.35	98.56	99.01	98.91	101.49	101.44	99.40	99.26	98.36	99.94
Trace elements (ppm)										
Ba	649	740	599	1269	1355	1591	243	586	519	954
Cr	48	57	99	10	12	11	22	74	61	9
Cu	14	15	23	5	10	7	41	42	35	5
La	45	38	36	43	53	57	48	ND	30	44
Li	ND	ND	ND	ND	17	16	ND	35	ND	ND
NI	25	37	44	7	5	5	24	87	59	7
Rb	175	186	104	336	109	106	122	76	140	203
Sc	12	16	20	6	6	5	17	19	20	5
Sr	538	633	768	227	338	375	372	626	601	222
V	93	120	135	31	22	23	138	145	158	24
Y	23	22	26	12	11	12	22	29	19	12
Zn	83	84	89	41	49	48	105	103	85	30
Zr	295	386	255	223	322	325	290	204	150	241

Table C.1 Whole rock geochemical analyses (cont.)

Sample	Bridge outcrops	All lithologies
	JJ15	JJ16
Major elements (%)		
SiO ₂	76.31	73.22
TiO ₂	0.08	0.38
Al ₂ O ₃	12.60	14.45
*FeO	0.68	2.04
MgO	0.10	0.72
MnO	0.01	0.04
CaO	0.20	1.53
Na ₂ O	2.64	4.15
K ₂ O	5.93	3.90
P ₂ O ₅	0.04	0.11
H ₂ O	BD	BD
CO ₂	BD	BD
TOTAL	98.59	100.54
Trace elements (ppm)		
Ba	43	710
Cr	8	10
Cu	BD	14
La	BD	14
Li	ND	ND
Ni	6	24
Rb	BD	BD
Sc	124	106
Sc	1	4
Sr	36	296
V	BD	20
Y	2	14
Zn	12	34
Zr	89	202

Table C.3 REE concentrations for the Glen Doll Complex
Element sample (ppm)

Element	Olivine gabbros		Gabbros		Pyroxene diorites			Hornblende diorites		
	GC88	GC91	GC70	GC78	GC80	GC82	GC9	GC31	GC133	GC1
La	8.07	10.75	8.75	17.75	8.99	11.13	25.60	26.48	9.51	22.85
Ce	18.13	14.66	21.80	37.16	21.50	26.21	57.99	56.93	22.72	53.99
Pr	2.05	3.10	2.84	4.09	2.63	3.19	6.30	6.30	2.81	6.57
Nd	8.88	13.78	13.74	17.53	11.98	14.45	27.50	25.22	12.95	28.21
Sm	1.98	2.77	3.09	3.37	3.01	3.04	5.79	5.01	2.93	5.90
Eu	0.62	0.91	1.00	1.15	1.01	0.67	2.29	1.44	1.11	1.90
Gd	1.77	2.31	3.00	2.55	2.68	2.73	5.69	4.32	2.72	5.51
Dy	1.73	2.07	2.68	2.34	2.39	2.28	3.99	3.79	2.62	4.61
Ho	0.38	0.44	0.55	0.48	0.46	0.47	0.76	0.76	0.55	0.92
Er	0.96	1.11	1.50	1.35	1.26	1.24	2.02	2.03	1.45	2.23
Yb	0.94	0.89	1.23	1.03	1.11	1.00	1.56	1.85	1.21	1.94
Lu	0.14	0.21	0.22	0.16	0.17	0.15	0.28	0.31	0.23	0.31
Y	9.03	9.99	13.25	11.32	11.55	10.99	19.58	19.74	13.14	22.28

Table C.3 REE concentrations for the Glen Doll Complex (cont.)
 Element sample (ppm)

	Hornblende diorites										
	GC2	GC4	GC5	GC7	GC8	GC16	GC27	GC28	GC41	GC44	
La	37.20	31.43	28.15	13.67	31.81	20.75	17.76	22.08	22.39	17.31	
Ce	88.20	76.37	71.75	29.10	75.90	46.84	41.33	44.32	52.16	38.52	
Pr	9.69	8.95	8.52	3.13	9.10	4.58	4.84	4.64	6.37	4.58	
Nd	41.75	39.96	38.25	12.12	42.76	18.88	20.42	17.80	27.37	19.65	
Sm	8.79	8.48	8.02	2.18	8.78	3.69	4.20	3.28	5.67	4.35	
Eu	2.60	2.51	2.34	1.48	2.40	1.52	1.30	1.41	1.77	1.53	
Gd	8.51	8.04	7.56	1.86	8.02	3.32	3.92	2.79	5.31	4.11	
Dy	6.27	6.18	5.94	1.29	6.59	2.42	3.37	2.31	4.59	3.67	
Ho	1.22	1.23	1.16	0.26	1.31	0.49	0.68	0.47	0.91	0.73	
Er	3.17	3.25	2.98	0.67	3.56	1.48	1.75	1.31	2.36	1.86	
Yb	2.48	3.48	2.32	0.56	2.59	1.17	1.53	1.15	1.96	1.56	
Lu	0.42	0.41	0.35	0.10	0.43	0.21	0.28	0.25	0.34	0.30	
Y	32.43	30.45	29.32	6.45	41.00	11.74	24.00	11.51	26.00	18.21	

Table C.3 REE concentrations for the Glen Doll Complex (cont.)

Element	REE concentrations (ppm)									
	Hornblende diorites		Monzonites		Adamellites				Aplite dykes	
	GC56	GC19	GC20	GC21	GC25	GC36	GC96	GC106	GC116	GC34
La	45.82	40.13	22.69	34.51	33.72	40.89	33.06	22.54	44.10	3.25
Ce	103.77	93.84	40.97	77.74	68.46	84.66	67.42	33.96	87.70	10.39
Pr	11.58	11.03	4.00	8.32	6.74	8.79	7.09	4.51	9.25	0.74
Nd	47.80	49.27	14.86	35.04	24.98	34.55	26.67	16.73	35.54	2.31
Sm	8.74	9.75	2.38	6.80	4.59	6.25	4.60	2.98	6.41	0.82
Eu	2.66	2.38	1.62	2.33	1.07	1.82	1.11	0.76	1.51	0.12
Gd	7.12	8.48	1.80	5.98	3.38	5.14	3.45	2.05	4.71	1.09
Dy	5.55	6.70	1.42	4.46	2.91	4.22	2.97	1.82	3.93	1.34
Ho	1.12	1.31	0.30	0.89	0.60	0.85	0.62	0.37	0.78	0.26
Er	2.87	3.72	0.85	2.25	1.65	2.27	1.71	1.17	2.09	0.62
Yb	2.32	2.49	0.80	1.65	1.60	1.97	1.48	0.93	1.74	0.72
Lu	0.39	0.42	0.19	0.31	0.37	0.36	0.28	0.18	0.29	0.12
Y	27.32	32.27	7.17	22.59	15.52	21.62	15.11	8.98	19.17	6.96

Table C.3 REE concentrations for the Glen Doll Complex (cont.)

Element	Aplite dykes		Quartz feldspar porphyry dykes		Microdiorite dykes		Appinites		Rafted xenoliths	
	GC118	GC6	GC13	GC33	GC152	GC87	GC145	GC30	GC75	GC3
La	13.79	25.93	25.84	13.70	13.22	32.69	20.99	14.41	17.78	15.04
Ce	33.38	53.51	53.88	25.27	28.21	69.12	49.34	30.22	49.13	37.50
Pr	3.22	5.40	5.33	2.45	3.07	7.46	5.65	3.74	6.62	4.88
Nd	11.99	19.96	18.98	7.74	11.86	30.05	24.58	16.52	33.26	21.14
Sm	2.54	3.51	3.59	1.71	2.41	5.61	4.95	3.62	7.44	5.11
Eu	0.52	1.07	0.85	0.36	0.63	1.57	1.13	2.00	1.81	1.30
Gd	2.18	2.54	2.78	1.48	2.25	4.45	4.29	3.87	6.69	5.32
Dy	2.26	1.80	1.91	1.62	2.24	4.07	3.56	3.10	6.45	5.06
Ho	0.47	0.34	0.40	0.36	0.45	0.85	0.72	0.67	1.32	1.03
Er	1.24	1.02	1.15	1.00	1.23	2.42	1.91	2.10	3.33	2.74
Yb	1.35	0.98	1.21	1.38	1.48	2.05	1.56	1.48	2.85	2.49
Lu	0.21	0.18	0.27	0.25	0.23	0.32	0.24	0.35	0.42	0.42
Y	10.40	8.422	13.00	9.32	12.67	21.33	19.80	16.22	31.79	25.94

Table C.3 REE concentrations for the Glen Doll Complex (cont.)

Element	Sample (ppm)		Microdiorite xenoliths		Dalradian xenoliths		Dalradian metasediments	
	Rafted xenoliths		GC148	GC15	GC46	GC68	GC129B	
La	37.61		5.42	42.60	45.03	18.81	21.82	
Ce	74.05		11.87	98.82	96.23	41.40	49.36	
Pr	7.98		1.41	11.19	10.36	4.33	5.10	
Nd	30.19		6.18	47.06	39.94	17.05	20.22	
Sm	5.07		1.29	8.80	7.31	3.10	3.57	
Eu	2.00		0.98	2.47	1.62	0.76	0.99	
Gd	3.74		1.29	7.65	5.68	2.08	2.67	
Dy	2.55		1.18	5.79	3.86	1.40	1.64	
Ho	0.48		0.26	1.14	0.68	0.24	0.30	
Er	1.27		0.68	2.64	1.77	0.54	0.74	
Yb	0.88		0.72	2.18	1.33	0.31	0.47	
Lu	0.13		0.12	0.34	0.22	0.08	0.08	
Y	10.70		9.00	27.97	18.71	8.00	6.50	

Table C.4 REE concentrations for the Juan Jorge Complex
Element Sample (ppm)

Element	Diorites				Granites				Microdiorite xenolith	
	JJ4	JJ6	JJ7	JJ8	JJ1	JJ9	JJ17	JJ19		
La	37.06	32.34	36.12	36.04	422.50	53.10	57.43	48.40		
Ce	80.40	76.64	78.46	83.69	75.60	96.70	109.10	91.50		
Pr	9.24	8.33	10.29	9.98	6.35	8.96	11.13	9.70		
Nd	37.90	35.33	37.91	41.59	23.40	32.50	35.75	37.50		
Sm	7.49	7.29	7.80	8.64	3.77	4.92	5.67	7.04		
Eu	1.88	1.75	2.00	2.08	0.98	1.29	1.27	1.26		
Gd	5.92	5.86	6.23	7.49	2.85	3.74	3.55	5.59		
Dy	4.89	4.69	4.98	5.62	2.16	2.47	2.45	4.41		
Ho	0.92	0.91	0.94	1.11	0.42	0.46	ND	0.85		
Er	2.44	2.29	2.47	2.81	1.16	1.23	ND	2.27		
Yb	2.05	1.99	2.15	2.34	1.11	1.04	1.17	2.17		
Lu	0.30	0.30	0.32	0.39	0.18	0.17	0.20	0.35		
Y	23.90	22.65	24.17	27.28	11.91	11.20	12.28	21.50		

Appendix D

Analytical techniques

D.1 Bulk rock major and trace element analysis

Approximately 1kg samples were collected for geochemical analysis. Samples were split using a geological hammer or a conventional rock splitter composed of two hardened steel plates forced together by a hydraulic mechanism. A piece of each sample was retained for hand specimen description from which a 30 μ thin section was cut. The remaining sample was cleaned to remove any organic material from the surface and washed in distilled water. Each sample was broken into small (<0.5cm) using a Sturtevant hardened-steel jaw crusher. A split of each sample was retained at this stage, while the remaining sample was ground to a fine powder (<30 μ) using a tungsten carbide "Tema" disc mill. The resultant powders were stored in glass jars.

These initial stages of preparation lead to contamination of the samples with tungsten and cobalt (an impurity in the tungsten carbide). These elements were therefore not analysed.

The sample powders were then dried in an oven at 105 $^{\circ}$ for 24hrs prior to use. Two methods of sample preparation were used to allow a wide range of major and trace elements to be determined. The two techniques are detailed below and are evaluated in Potts (1987) and Thompson and Walsh (1983).

D.1.1 Preparation of solutions for trace element determination using an open acid digestion

1. Dry powder at 105°C for 24hrs.
2. Place 0.5g of accurately weighed powder in a PTFE beaker.
3. Moisten with 2ml of cold deionised water.
4. Add 10ml of 48% Hydrofluoric acid followed by 8ml of 60% Perchloric acid (HClO_4).
5. Slowly decompose on a hot plate at 230°C. Take to near dryness but do not allow to dry. ++
6. Allow to cool. Add 5ml Perchloric acid.
7. Evaporate slowly on a hot plate to near dryness but do not dry.
8. Add 10ml of 5N Nitric acid and digest slowly on a hot plate for about 10mins.
9. Allow to cool. Transfer to a 50ml volumetric flask and make to volume with deionised water. Store in a plastic bottle.

++Stages 4 and 5 were repeated if an incomplete digestion occurred at this stage.

This open acid digestion was used for the analysis of Ba, Cr, Cu, La, Li, Ni, Sc, Sr, V, Y and Zn by ICPAES. Facilities were made available at Dept. of Geology, Kings College London using a Philips PV8120 1.5m path length simultaneous ICPAES. Details of the Philips system are given elsewhere (Walsh et al., 1981). A summary of the operating parameters, spectral wavelengths and detection limits are given in Table D.2. Calibrations were made using standard reference materials (SRM) prepared at the same time

as the samples. SRM's were also used to assess the analytical accuracy and precision. The limits of detection, based on real rock samples are given in Table D.2.

A lithium metaborate fusion solution was used for the analysis of SiO_2 , Al_2O_3 , TiO_2 , $^*\text{FeO}$, MgO , MnO , CaO , Na_2O , K_2O and Rb by atomic absorption spectrometry (AAS). A 1000x dilution factor (0.25g of sample in 250ml) allows the direct measurement of the major elements without further dilution. Rb, an alkali metal, is very sensitive by AAS but is easily ionised, therefore CsCl was added to all solutions as an ionisation suppressent. Details of the operating conditions are given in Table D.1. Calibrations were made using a number of standard reference materials (SRM) containing a similar matrix to the samples. SRM's were also included in each run to assess the analytical accuracy of the method. Zirconium commonly occurs in the mineral zircon which is not completely attacked during an open acid digestion. Zr was therefore measured in the fusion solution using inductively coupled plasma atomic emission spectrometry (ICPAES)(See below). In addition to the major elements listed above, P_2O_5 was also determined using a fusion solution. Phosphorus is relatively insensitive by AAS therefore the concentration was determined by colorimetry. The technique is outlined below.

D.1.2 Preparation of solutions for major element analysis using a Lithium Metaborate fusion.

1. Dry powders at 105°C for 24hrs.
2. Accurately weigh 0.25g of sample powder. Add to this approximately

1.25g of Lithium Metaborate (Spectroflux*) and mix carefully. Transfer into a clean graphite crucible. Twelve samples are fused in each batch.

3. Fuse the samples at 1050°C for 20mins.
4. Whilst the samples are fusing, measure 150ml of approximately 3.5% HNO₃** into some wide neck plastic bottles and place a clean magnetic stirring bar in each.
5. Transfer the samples from the crucibles to the bottles immediately after removing each one from the furnace.
6. Stir until dissolved
7. Add 5ml of 10% Caesium chloride (Spec Pure*) solution.
8. Filter the solutions into a 250ml plastic volumetric flask using
Whatman No 54 papers. Make to volume.
9. Store in a plastic bottle.

All chemicals used are analytical reagent grade

* Trade mark of Johnson Matthey Chemicals Ltd.

** 1 litre of 3.5% HNO₃ is made by adding 50ml of concentrated acid to a few hundred mls of deionised H₂O. Make to 1000ml in a volumetric flask.

D.1.3 Determination of phosphorus by colorimetry

Preparation of 1000ppm standard solution.

Dissolve 0.4264g of Di-Ammonium Hydrogen Orthophosphate in 100ml of deionised water. Store in a plastic bottle.

D.1.3.1 Preparation of standards

Standard reference material NIM-G which contains only 0.02% P₂O₅.

10ml aliquots of NIM-G were transferred to a series of plastic bottles. 25, 50 and 100 micro litres of 1000ppm standard solution were added to each bottle to give a set of standards containing 0.57%, 1.14% and 2.26% P_2O_5 respectively.

D.1.3.2 Preparation of reagent for colorimetric determination of phosphorous

Prepare just before use. Dissolve 1.25g of Ammonium Molybdate (AR) in 56ml of 25% vol/vol Sulphuric acid (H_2SO_4) in a 250ml beaker. Partially dissolve 20g of Ascorbic acid (AR) in 40 ml of deionised water and add to the acidified molybdate solution. Then dissolve 0.10g of Antimony Potassium Tartrate in 10ml of deionised water and add this to the mixture and stir well. Dissolve 25.0g of Hydroxylammonium Chloride in 80ml of water. Thoroughly mix and add this to the 250ml beaker. when the solution is clear, transfer to a 250ml volumetric flask and make to volume. Transfer solutions in the order and proportions shown directly into 1cm light path cuvettes.

200 micro litres sample

2500 micro litres deionised water

500 micro litres reagent

Allow the cuvettes to stand for 1 hour. Measure the absorbance of each solution at 880nm using the Pye Unicam SP6-550 UV/VIS Spectrophotometer.

D.2 Rare earth element analysis

After major and trace element determinations were made a number of samples were chosen for REE analysis. The samples were

initially prepared using an open acid digestion (Section D.1.1) with the exception that the final solution was made up in 10% v/v HCl. Separation of the REE was carried out by the cation exchange procedure described in Jarvis and Jarvis (1985), a method modified after Strelow and Jackson (1974) and evaluated by Walsh et al (1981). This technique involves the progressive elution of samples with increasing concentrations of hydrochloric acid, the final dried residues being taken up in 1N nitric acid prior to being sprayed into the ICPAES.

Twelve of the fourteen naturally occurring REE (excluding Tb and Tm) and Y were determined simultaneously using the Philips PV8210 ICPAES. Operating parameters and spectral lines are given in Table D.2. Analysis were undertaken using compromise instrumental conditions (discussed in detail by Walsh et al., 1981) as all of the REE were determined simultaneously. Experimentally evaluated determination limits (Table D.2) indicate that the chosen wavelengths are capable of resolving the REE distributions of all the analysed samples.

In addition to the REE, five other elements (Ba, Sr, Ca, Ti and Zr) were determined in order to correct for interferences on the REE caused by the small and variable amounts of the former elements which by-pass the cation exchange procedure. Details of the correction procedure are given in Jarvis and Jarvis (in press). Calibrations were made using synthetic multielement mixtures (made from Aldrich 1000ppm standard solutions) prepared in 1N nitric acid. SRM's were included in each run to assess analytical accuracy.

D.3 Strontium isotope analysis

Fifteen samples were selected for strontium isotope analysis. All sample preparation and subsequent measurements were undertaken at the BGS, Gray's Inn Road, London and the provision of these facilities is gratefully acknowledged. The sample preparation is outlined below.

- 1) Dry samples at 105° for 24hrs.
- 2) Weigh 200mg of sample into clean PTFE beakers.
- 3) Add 2ml of 16N nitric acid and 8ml of hydrofluoric acid and evaporate to dryness in a heating block.
- 4) Add 2ml of 16N nitric acid and evaporate to dryness.
- 5) Add 10ml of 6N hydrochloric acid and evaporate to dryness.
- 6) Add 3ml of 2.5N hydrochloric acid and centrifuge
- 7) Decant the clear solution.

D.3.1 Ion exchange procedure

- 1) Load glass columns with a 10cm height resin bed (Dowex AG50W-x12, 200-400 mesh).
- 2) Rinse columns with 50ml of deionised water.
- 3) To clean columns, elute with 50ml of 6N HCl.
- 4) Prime columns with 15ml of 2.5N HCL.
- 5) Load sample onto columns
- 6) Elute with 1ml of 2.5N HCl
- 7) Elute with 28ml of 2.5N HCl and discard all washings.
- 8) Elute with 12ml of 2.5N HCl and collect the resultant solution.
- 9) Evaporate to dryness in a heating block.

After this chemical separation, strontium was loaded on single

tantalum filaments prepared with phosphoric acid. Isotopic measurements were made on an automated VG Micromass 354, 30cm radius, 90° magnetic field sector mass spectrometer, operated at 7.2Kv acceleration voltage. Details of the analytical errors are given in Darbyshire and Shepherd (1985).

Rb and Sr concentrations (initially measured by AAS and ICPAES) were re-determined by X-Ray fluorescence spectrometry on 20g pellets pressed to 15tonnes. Each batch of samples included international SRM's and appropriate corrections were made for instrumental dead time, background and line interferences (Pankhurst and O'Nions, 1973).

D.4 Electron microprobe analysis

Twenty one representative samples were chosen for microprobe analysis. Facilities were made available at the Dept. of Geology, Experimental petrology unit, University of Edinburgh, using two wavelength dispersive electron microprobes. The first is a Cambridge Instruments Microscan 5 and the second, a Cameca Camebax Microbeam. Correction techniques (after Sweatman and Long, 1969) were applied to both machines.

Polished sections were prepared from thin sections initially cut to 3mm and subsequently ground to ~80 μ using a Logitech rotary grinder. The sections were then polished on a rotary polisher using 14 μ , 6 μ , 1 μ and 0.25 μ diamond paste to attain a relief free surface. Prior to microprobe analysis, samples were coated with a carbon film to increase the conductivity of the surface.

Table D.1

Machine: Pye Unicam SP1900 Atomic Absorption Spectrometer
 Elements analysed: Si, Ti, Al, Fe, Mg, Mn, Ca, Na, K, Rb

Element	Wavelength	Current ma	Bandpass	Fuel
Al	309.27	10	200	N ₂ O 5.0, C ₂ H ₂ 4.5
Ca	422.7	10	100	N ₂ O 5.0, C ₂ H ₂ 4.0
Fe	248.8	15	100	N ₂ O 5.0, C ₂ H ₂ 3.1
Mg	285.2	4	200	N ₂ O 5.0, C ₂ H ₂ 3.5
Mn	279.5	12	100	Air 5.0, C ₂ H ₂ 1.1
K	766.5	8	200	Air 5.0, C ₂ H ₂ 1.0
Rb	780.0	emission	300	Air 5.0, C ₂ H ₂ 1.2
Si	251.6	15	100	N ₂ O 5.0, C ₂ H ₂ 4.6
Na	589.0	8	200	Air 5.0, C ₂ H ₂ 1.0
Ti	365.4	15	100	N ₂ O 5.0, C ₂ H ₂ 4.5

Precision is better than 5% for all elements

Machine: Philips PV 8210 1.5m ICP atomic emission spectrometer
 Elements analysed: Ba, Cr, Cu, Li, Ni, Sc, Sr, V, Y, Zn, Zr and REE

Element	Wavelength nm	Practical detection limit* $\mu\text{g g}^{-1}$	Chondrite**
Ba	455.40	1	0.329
Cr	267.72	5***	0.865
Cu	324.75	2	0.122
Li	670.78	2	0.630
Ni	231.60	5	0.203
Sc	361.38	1	0.077
Sr	407.77	1	0.276
V	290.88	2	0.343
Y	371.03	1	0.076
Zn	213.86	5	0.226
Zr	339.20	10***	0.220
REE			
La	398.85	0.75	0.034
Ce	418.66	0.86	
Pr	422.29	0.16	
Nd	430.36	0.67	
Sm	359.26	0.11	
Eu	389.17	0.02	
Gd	335.05	0.14	
Dy	353.17	0.05	
Ho	345.60	0.02	
Er	390.63	0.08	
Yb	328.94	0.04	
Lu	261.54	0.01	

* Thompson and Walsh, 1983

** Nakamura, 1974

*** This work

Table D.1 (cont.)

Operating parameters for REE and trace element determination by ICPAES.

Coolant gas flow	15.0lmin ⁻¹
Auxiliary gas flow	0lmin ⁻¹
Injector gas flow	1.2lmin ⁻¹
Sample uptake rate	2.0mlmin ⁻¹
Observation zone above coil	15-19mm
Power input	1.0Kw (50MHz)

RARE-EARTH ELEMENT GEOCHEMISTRY OF STANDARD SEDIMENTS: A STUDY USING INDUCTIVELY COUPLED PLASMA SPECTROMETRY

I. JARVIS and K.E. JARVIS

School of Geological Sciences, Kingston Polytechnic, Kingston-upon-Thames, Surrey KT1 2EE (Great Britain)
Department of Geology, City of London Polytechnic, London E1 2NG (Great Britain)

(Received September 21, 1984; accepted for publication March 6, 1985)

Abstract

Jarvis, I. and Jarvis, K.E., 1985. Rare-earth element geochemistry of standard sediments: a study using inductively coupled plasma spectrometry. *Chem. Geol.*, 53: 335–344.

The rare-earth elements (REE) and Y have been determined in 15 international standard sediments from France, German Democratic Republic, Canada and the U.S.A. Samples were prepared using conventional rock-dissolution techniques and the REE and Y were separated from other constituents using cation-exchange chromatography. The REE (La, Ce, Pr, Nd, Sm, Eu, Gd, Dy, Ho, Er, Yb, Lu) and Y were analysed simultaneously by inductively coupled plasma atomic-emission spectrometry. Results indicate that U.S.G.S. standard shale SCo-1 (Cody Shale) is a good reference material to use for the normalisation of the REE distributions of sediments. Data normalised to SCo-1 are more readily interpreted than those normalised to existing estimates of "average" shale. The REE patterns of standard sediments vary considerably in shape, span an order of magnitude in absolute concentration, and provide valuable reference values for the REE analysis of other sedimentary materials.

1. Introduction

A large number of internationally circulated rock standards is available for the inter-laboratory standardisation of major- and trace-element data (Flanagan, 1973; Abbey, 1980, 1982). Few of these standards are, however, of sedimentary origin, and many of these are certificated for only a few elements. Concentrations of the rare-earth elements (REE) are particularly poorly characterised.

The REE have short residence times in the oceans of ~500 yr. (Goldberg et al., 1963; Elderfield and Greaves, 1982). They are dominantly trivalent and have closely similar chem-

ical properties, showing a progressive decrease in ionic radii (Shannon, 1976) from 1.03 Å for La^{3+} (atomic number 57) to 0.861 Å for Lu^{3+} (atomic number 71). This leads to the preferential uptake by some minerals of the heavy REE (HREE) relative to the light REE (LREE), or vice-versa. In addition, Ce occurs as a tetravalent form under oxidising conditions, while Eu^{3+} may be reduced to Eu^{2+} . Potentially, therefore, the REE provide a valuable guide to the mineralogy, provenance and diagenetic history of sedimentary rocks.

Early workers (Goldberg et al., 1963; Schofield and Haskin, 1964; Wildeman and Haskin, 1965; M.A. Haskin and Haskin, 1966;

L.A. Haskin et al., 1966a, b, 1968) emphasised the similarities in the REE distributions of different lithologies and between samples from different areas and of different age. Subsequently, studies of the REE in Precambrian sediments, for example, have demonstrated that they display small but significant stratigraphical trends (Wildeman and Haskin, 1973; Nance and Taylor, 1976; McLennan et al., 1979a, b, 1980), which have been used to elucidate the chemical evolution of the Earth's crust.

Analyses of modern marine sediments in general (Goldberg et al., 1963; Piper, 1974b), and authigenic/diagenetic phases in particular (Piper, 1972, 1974a; Piper and Graef, 1974; Piper et al., 1975; Addy, 1979; Fleet et al., 1980; Elderfield and Greaves, 1981; Elderfield et al., 1981; Fleet, 1983; Murphy and Dymond, 1984) have indicated that fractionation of the REE occurs in the oceans. Partitioning of the REE by ferromanganese phases, for instance, has been advanced as a major mechanism for producing the characteristic REE distribution of modern seawater (Piper, 1972, 1974b; Klinkhammer et al., 1983), which generally exhibits a large negative Ce anomaly (relative to La, Pr) and is strongly enriched in the HREE relative to the LREE (Høgdahl et al., 1968). Most deep-ocean ferromanganese nodules, for example, have positive Ce anomalies and are HREE depleted.

Recently, the REE distributions of pelagic sediments have been shown to be composites, with components of different grain size and mineralogy having widely different REE patterns (Tlig, 1982; Tlig and Steinberg, 1982). It has also been demonstrated that the REE are fractionated during estuarine mixing (Martin et al., 1976; Keasler and Loveland, 1982; Hoyle et al., 1984) and have depth-related distributions in the deep ocean (Elderfield and Greaves, 1982, 1983; De Baar et al., 1983; Klinkhammer et al., 1983).

Few data are available, however, concerning the REE distributions of most sedimen-

tary rocks. In this paper, we present results of analyses of 15 international sedimentary standards for 12 REE and Y.

2. Experimental

Sample preparation and analytical procedures were modified from Jarvis (1980), Walsh et al. (1981), and Thompson and Walsh (1983). Samples were digested initially by HF-HClO₄ attack and finally dissolved in HCl. The REE were separated from the other constituents by a simple cation-exchange procedure (Strelow and Jackson, 1974; Jones and Dixon, 1978), and the final concentrated REE solutions were analysed simultaneously using inductively-coupled plasma (ICP) atomic-emission spectrometry. Similar techniques have been utilised recently by Bolton et al. (1982), Crock and Lichte (1982), Crock et al. (1984) and Brenner et al. (1984) for a variety of rock types.

2.1. Dissolution procedure

All sediments were dried overnight at 105°C before weighing. 0.500-g subsamples were transferred to 60-ml PTFE beakers and the powders moistened with a few milliliters of deionised water. 10 ml HF and then 8 ml HClO₄ were added slowly and the solutions evaporated to incipient dryness (until they formed a crystalline paste). The HF-HClO₄ digestion was repeated, and then 5 ml HClO₄ followed by 4 ml saturated H₃BO₃ were added and the solutions again evaporated until nearly dry. 10 ml of 6 N HCl was added to the warm beakers, the solutions diluted to ~50 ml, and the samples allowed to dissolve slowly on a hot-plate. Any residues remaining at this stage (estuarine sediment N.B.S. 1646 only) were removed by filtration and digested using the "mini-fusion" method (Walsh et al., 1981; Thompson and Walsh, 1983). Solutions were allowed to cool before starting the cation-exchange procedure.

2.2. REE separation

Separation of the REE was achieved using columns packed with Dowex[®] AG 50W-X8 (200–400 mesh) ion-exchange resin. 25-cm long glass columns with 2 cm ID, glass sinter discs and PTFE burette taps at the bottom were used. New resin was soaked in 4 N HCl before use, and then rinsed and stored in 1 N HCl. Separations were organised into individual runs utilising ten identical columns. Each run consisted of nine sediment solutions and one blank through which only successive normalities of HCl were passed. Between runs, columns were emptied and the resin homogenised before being reloaded and rinsed with 200 ml of 1 N HCl. Columns were loaded to give settled resin heights of 12 cm (when equilibrated with 1 N HCl).

Solutions were further diluted with 50 ml deionised water, loaded onto the columns and washed with 450 ml of 1.70 N HCl. The normality of the acid at this stage was found to be critical to ensure optimum separation of the REE from other elements without the loss of the HREE. Accuracy was ensured by determining the normality of each batch of concentrated HCl before diluting to 1.70 N. The 1.70 N HCl eluted fractions contained all of the major constituents and most of the trace elements, and were discarded. The REE (together with Ba, Sc, Y and some Hf, Sr, Zr) are held quantitatively on the resin (Walsh et al., 1981; Thompson and Walsh, 1983; Crock et al., 1984), and were eluted with 500 ml of 4 N HCl. Solutions were filtered through Whatman[®] No. 42 filter papers to remove particles of resin, then evaporated to dryness, being stored as dried residues in 60-ml glass beakers.

The REE were redissolved in 5 ml of 1.6 N (10% v/v) HNO₃ immediately prior to being sprayed into the ICP.

2.3. ICP analysis

Twelve (La, Ce, Pr, Nd, Sm, Eu, Gd, Dy, Ho, Er, Yb, Lu) of the fourteen naturally oc-

curing REE (excluding only Tb, Tm) and Y were determined simultaneously using a Philips[®] PV 8210 1.5-m ICP atomic-emission spectrometer in the Department of Geology, King's College London. Further details of the Philips[®] ICP system are available elsewhere (Boumans, 1978; Walsh and Howie, 1980). Operating parameters (gas flow rates, sample uptake rate, observation height and generator power) were necessarily compromise conditions (Table I) because all REE were determined simultaneously.

TABLE I

Operation parameters for REE determination by ICP

Coolant gas flow	15 l min. ⁻¹
Auxiliary gas flow	0 l min. ⁻¹
Injector gas flow	1.2 l min. ⁻¹
Sample uptake rate	2 ml min. ⁻¹
Observation zone above coil	15–19 mm
Power input	1.0 kW (50 MHz)

The spectral wavelengths used are listed in Table II. The choice of spectral lines had to take into account their analytical sensitivities in relation to the expected abundance of each element in geological samples, the relative importance of spectral interferences caused by overlap from adjacent REE and other element lines, and finally the practicalities of mounting all of the lines on the Rowland circle of the simultaneous spectrometer. The lines used here optimised these considerations (see Walsh et al., 1981 for discussion). A comparison between experimentally determined detection limits of these lines (Table II) and the abundance of individual REE in chondritic meteorites (regarded as representing the lowest levels to be expected in most geological samples) indicates that the chosen wavelengths are capable of easily resolving the REE distributions of sediments. In addition to the REE and Y, five other elements (Ba 455.40 nm, Ca 315.89 nm, Sr 407.77 nm, Ti 337.28 nm, Zr 339.20 nm) were analysed to determine the amounts which had passed through or had been incompletely removed

TABLE II

Wavelengths and detection limits of ICP lines used for REE analysis

Element	Wavelength (nm)	Detection limit* ¹ ($\mu\text{g g}^{-1}$)	Chondrite* ² ($\mu\text{g g}^{-1}$)
La	398.85	0.75	0.329
Ce	418.66	0.86	0.865
Pr	422.29	0.16	0.122
Nd	430.36	0.67	0.630
Sm	359.26	0.11	0.203
Eu	381.97	0.02	0.077
Gd	335.05	0.14	0.276
Dy	353.17	0.05	0.343
Ho	345.60	0.02	0.076
Er	390.63	0.08	0.226
Yb	328.94	0.04	0.220
Lu	261.54	0.01	0.034

*¹ Walsh et al. (1981) and Thompson and Walsh (1983).

*² Nakamura (1974)

during the cation-exchange procedure.

Multi-element REE calibration standards were prepared from Aldrich® 1000 $\mu\text{g/ml}^{-1}$ standard solutions for atomic absorption. Calibrations were performed using five standards having REE contents ranging from 0.1 X to 5 X that of average shale (M.A. Haskin and Haskin, 1966; Piper, 1974b). A further set of five single-element interference standards (1000 $\mu\text{g ml}^{-1}$ Ba, 500 $\mu\text{g ml}^{-1}$ Ca, 100 $\mu\text{g ml}^{-1}$ Sr, 50 $\mu\text{g ml}^{-1}$ Ti, 50 $\mu\text{g ml}^{-1}$ Zr) were used to calculate spectral overlaps on the REE by other elements present in the sample solutions.

Data were obtained on punch tape as unprocessed intensities (arbitrarily scaled current readings from individual photomultipliers) and processed subsequently using a FORTRAN IV computer program written by the senior author for a DEC PDP® 11-34 minicomputer in the Department of Geology, City of London Polytechnic. The program, which incorporates background and drift correction provides calibration curves and regression statistics, deducts spectral overlaps, and subtracts individual run blanks from the cor-

responding samples. Final concentrations are reported as $\mu\text{g g}^{-1}$ in the sediment and as values normalised to average chondrite (Nakamura, 1974) and average shale (M.A. Haskin and Haskin, 1966; Piper, 1974b).

3. Results and discussion

The REE were determined in triplicate for 15 international sedimentary standards (Table III) from France, German Democratic Republic, Canada and the U.S.A. The precision of the analyses was generally better than $\pm 3\%$ (Tables IV and V) over a wide range of concentrations. The relative accuracy of the analyses is more difficult to assess. The conventional comparison between the new measure-

TABLE III

Description of standard sediments with their distributors analysed for the REE by ICP

Designation	Sediment type
<i>A.N.R.T. (Association Nationale de la Recherche Technique), France:</i>	
GL-0	glauconite
<i>N.B.S. (National Bureau of Standards), U.S.A.:</i>	
1b	argillaceous limestone
1c	argillaceous limestone
88a	dolomitic limestone
120b	phosphate rock
1646	estuarine sediment
<i>N.R.C.C. (National Research Council of Canada), Canada:</i>	
BCSS-1	marine sediment
MESS-1	marine sediment
<i>U.S.G.S. (United States Geological Survey), U.S.A.:</i>	
MAG-1	marine mud
SGR-1	Green River Shale
SCo-1	Cody Shale
<i>Z.G.I. (Zentrales Geologisches Institut), German Democratic Republic:</i>	
FK	feldspar sand
KH	limestone
TB	slate
TS	black shale

ments and accepted values is not possible for the REE in sedimentary standards because none are sufficiently well characterised (see Abbey, 1980). Our results for U.S.G.S. standard basalt BCR-1 (Table VI), however, correspond well with the usable values of Abbey

(1980) and independent data obtained by isotope-dilution mass spectrometry (Potts et al., 1981), a technique generally regarded as being the most accurate for REE analysis (Thirlwall, 1981). These data indicate an accuracy of $\sim \pm 5\%$ for our analyses. An additional assess-

TABLE IV

Concentrations (in $\mu\text{g g}^{-1}$) of the REE in A.N.R.T., N.B.S. and N.R.C.C. sedimentary standards as determined by ICP

Element	Standard							
	A.N.R.T.		N.B.S.			N.R.C.C.		
	GL-0	1b	1c	88a	120b	1646	BCSS-1	MESS-1
La	19.50±0.30	6.86±0.35	4.26±0.10	1.44±0.16	92.80±1.60	35.70±0.50	29.40±0.30	36.80±0.40
Ce	52.60±0.80	7.81±0.48	6.87±0.14	2.46±0.27	128.00±3.00	76.00±0.90	58.40±0.40	75.90±0.80
Pr	6.21±0.15	1.18±0.03	0.90±0.02	0.31±0.02	17.90±0.20	8.56±0.19	6.97±0.03	8.74±0.08
Nd	27.00±0.70	4.88±0.09	3.73±0.05	1.26±0.11	79.50±0.90	34.70±0.60	28.60±0.09	36.00±0.36
Sm	5.42±0.11	0.89±0.04	0.73±0.02	0.28±0.01	15.80±0.20	6.21±0.13	5.21±0.03	6.90±0.12
Eu	1.27±0.03	0.24±0.01	0.16±0.00	0.07±0.01	3.89±0.07	1.36±0.00	1.19±0.01	1.31±0.02
Gd	4.36±0.05	0.97±0.05	0.65±0.01	0.32±0.02	17.80±0.30	5.09±0.13	4.35±0.05	5.45±0.09
Dy	2.71±0.05	0.90±0.03	0.64±0.01	0.27±0.01	17.30±0.20	4.04±0.07	3.59±0.03	4.43±0.11
Ho	0.50±0.02	0.20±0.01	0.14±0.01	0.06±0.01	4.03±0.04	0.84±0.03	0.74±0.01	0.91±0.02
Er	1.27±0.03	0.57±0.02	0.41±0.02	0.18±0.01	11.40±0.10	2.41±0.04	2.03±0.02	2.52±0.02
Yb	0.64±0.02	0.55±0.02	0.39±0.01	0.17±0.01	10.80±0.20	2.12±0.02	1.94±0.01	2.42±0.06
Lu	0.08±0.01	0.08±0.01	0.06±0.00	0.03±0.01	1.71±0.05	0.32±0.00	0.29±0.01	0.37±0.01
Y	12.50±0.20	7.00±0.34	5.05±0.02	2.16±0.06	172.00±5.00	19.90±0.40	18.00±0.20	22.60±0.50

Values and standard deviations are based on three separate determinations.

TABLE V

Concentrations (in $\mu\text{g g}^{-1}$) of the REE in U.S.G.S. and Z.G.I. sedimentary standards as determined by ICP

Element	Standard						
	U.S.G.S.			Z.G.I.			
	MAG-1	SCo-1	SGR-1	FK	KH	TB	TS
La	41.80±0.60	29.60±1.20	18.60±0.60	7.49±0.70	11.90±0.10	50.60±1.90	51.30±0.20
Ce	88.90±0.90	60.00±2.00	35.80±1.20	14.90±1.40	17.90±0.20	104.00±2.30	126.00±1.00
Pr	9.24±0.10	6.22±0.06	3.49±0.05	1.69±0.02	2.40±0.03	11.30±0.50	12.30±0.10
Nd	36.10±0.60	24.70±0.06	13.20±0.20	6.49±0.06	9.88±0.21	43.70±2.00	51.80±0.30
Sm	6.64±0.10	4.71±0.04	2.35±0.03	1.33±0.05	1.88±0.01	7.57±0.06	10.10±0.00
Eu	1.50±0.02	1.16±0.01	0.52±0.02	0.58±0.03	0.46±0.00	1.60±0.02	2.33±0.00
Gd	5.45±0.09	3.97±0.05	1.92±0.09	1.18±0.09	1.78±0.01	5.21±0.15	8.85±0.02
Dy	4.29±0.08	3.27±0.06	1.57±0.02	0.87±0.02	1.50±0.01	3.35±0.09	6.90±0.10
Ho	0.83±0.02	0.66±0.01	0.32±0.01	0.17±0.01	0.30±0.01	0.63±0.02	1.48±0.02
Er	2.27±0.05	1.90±0.02	0.95±0.01	0.48±0.02	0.89±0.01	1.92±0.06	4.54±0.07
Yb	2.13±0.04	1.88±0.04	0.90±0.02	0.47±0.03	0.79±0.01	1.87±0.08	5.31±0.06
Lu	0.32±0.01	0.29±0.01	0.13±0.00	0.07±0.01	0.13±0.01	0.29±0.02	0.94±0.01
Y	22.20±0.05	20.30±0.50	9.92±0.34	5.09±0.59	9.73±0.00	14.80±1.30	51.10±1.30

Values and standard deviations are based on three separate determinations.

TABLE VI

Concentrations (in $\mu\text{g g}^{-1}$) of the REE in U.S.G.S. standard basalt BCR-1, standard shale SCo-1 and "average shale"

Element	Basalt BCR-1			Shale average**	Shale SCo-1 ICP**
	usable value*1	IDMS**	ICP**		
La	27	24.60	23.60	41.00	29.60
Ce	53	53.40	52.50	83.00	60.00
Pr	7	6.42	6.26	10.10	6.22
Nd	26	28.90	27.50	38.00	24.70
Sm	6.5	6.73	6.04	7.50	4.71
Eu	2.0	1.97	1.96	1.61	1.16
Gd	6.6	6.71	6.23	6.35	3.97
Dy	7	6.31	5.99	5.50	3.27
Ho	1.2	1.34	1.25	1.34	0.66
Er	3.5	3.63	3.33	3.75	1.90
Yb	3.4	3.40	3.19	3.53	1.88
Lu	0.5	0.52	0.51	0.61	0.29

*1 Abbey (1980).

** Potts et al. (1981); IDMS = isotope dilution mass spectrometry.

** This study.

** Piper (1974b).

ment of analytical accuracy may be obtained by normalising the REE to chondrite and plotting the results against atomic number (Coryell et al., 1963; Masuda, 1965; L.A. Haskin et al., 1966b). The coherence of the REE group should result in a smooth curve for all elements, except Ce and Eu which may show anomalies due to their different oxidation states. The smoothness of our chondrite-normalised data (Fig. 1) supports the acceptable accuracy indicated by our determinations of basalt BCR-1, which also produce a smooth curve (Fig. 2).

The interpretation of the REE distributions of sediments is aided by normalisation to average shale (Table VI) rather than chondrite (M.A. Haskin and Haskin, 1966; Piper, 1974b) because the relative concentrations of REE in sediments are very different from those in chondrite. Normalisation to chondrite, therefore, stresses these differences rather than displaying the smaller but more significant differences between sediment samples. Analytical techniques for REE deter-

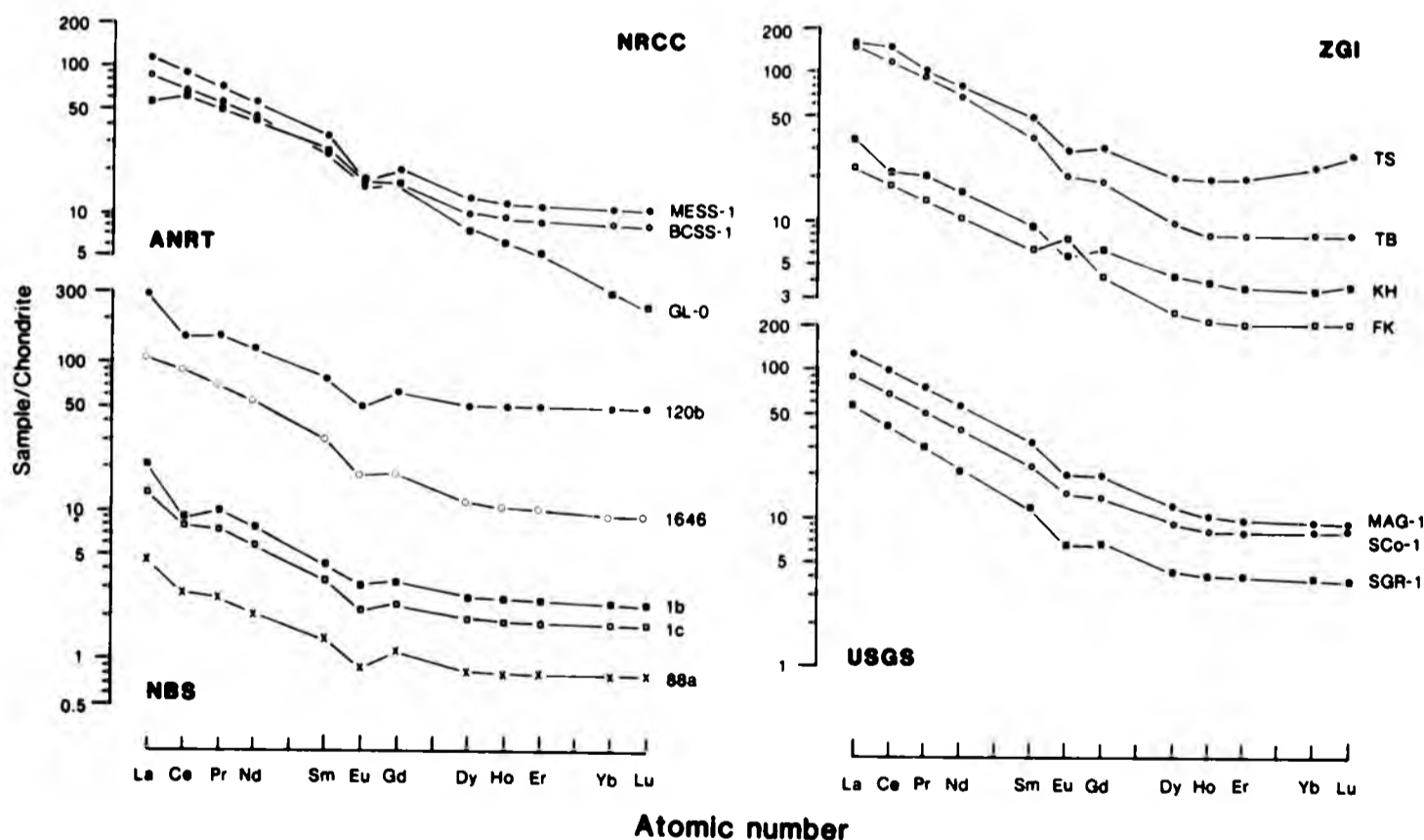


Fig. 1. Chondrite-normalised REE patterns of standard sediments.

mination have improved greatly since the analyses of M.A. Haskin and Haskin (1966) used to estimate the value of "average" shale (Piper, 1974b) and utilised subsequently by most REE geochemists. When plotted against chondrite (Fig. 2), it is clear that the coherence of the REE distribution of "average" shale (Table VI) is poor. Consequently, irregu-

larities in REE distributions normalised to "average" shale may be partly attributed to the inadequacy of the normalisation data.

A recent study by McLennan and Taylor (1980), has demonstrated that the major- and trace-element distribution of U.S.G.S. standard shale SCo-1 (Cody Shale) corresponds closely to estimates of average shale (Krauskopf, 1967) for 45 elements, including the REE. We suggest, therefore, that SCo-1 is a better reference for REE normalisation than Piper's (1974b) "average" shale. Our determinations of SCo-1 (Table VI) produce a smooth chondrite-normalised curve with a small negative Eu anomaly (Fig. 2), and a shape that is broadly similar to "average" shale. When normalised to SCo-1, our results for other sedimentary standards (Fig. 3) display smooth curves which indicate subtle differences in the REE distributions. "Average" shale has a lumpy, weakly HREE-enriched pattern. The use of "in-house" determinations of SCo-1 as a normalisation standard has the

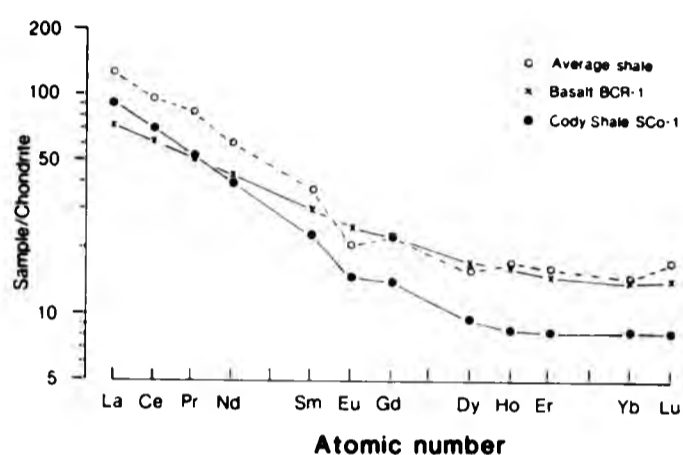


Fig. 2. Chondrite-normalised REE patterns of U.S.G.S. standard basalt BCR-1, standard shale SCo-1 and "average shale".

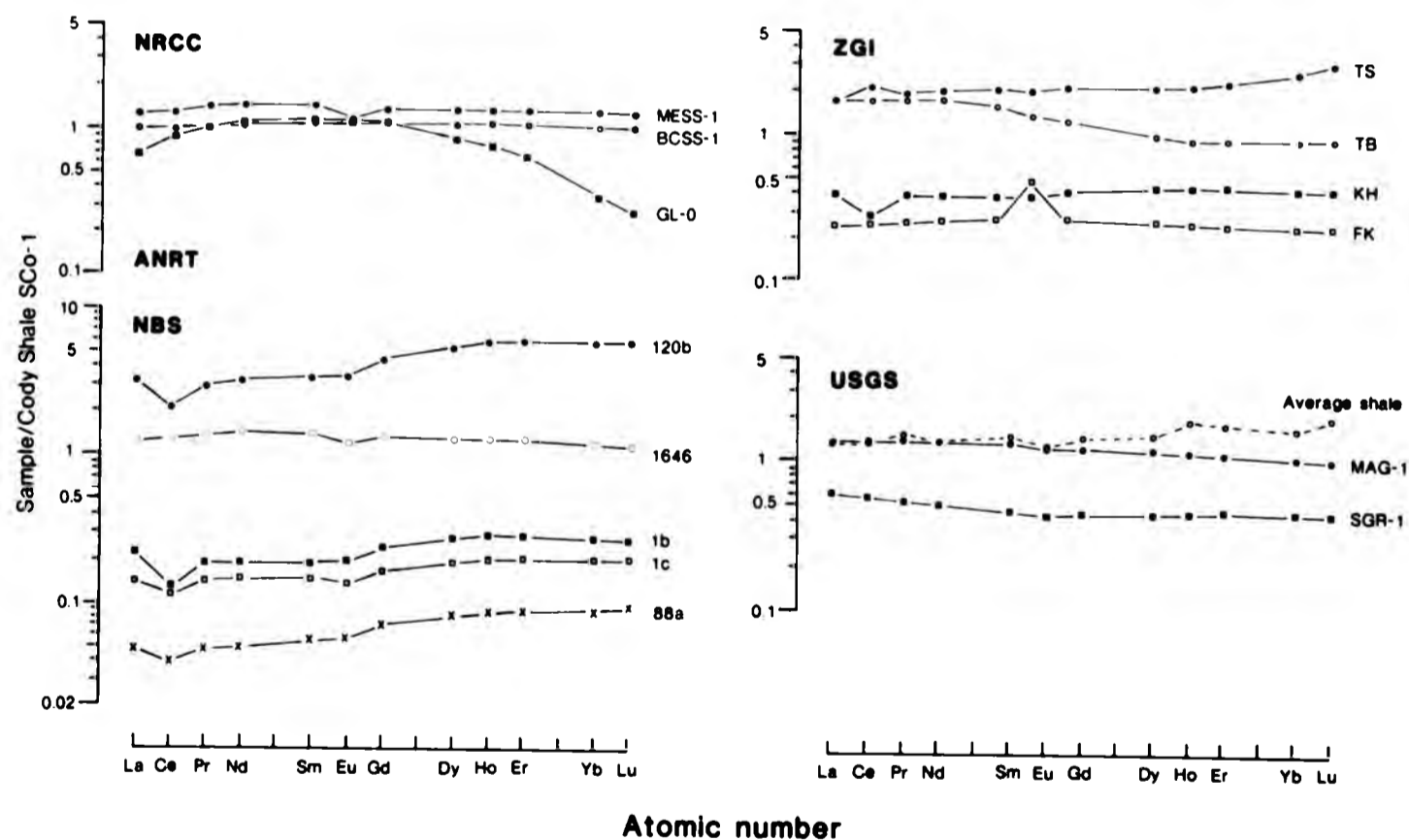


Fig. 3. REE distribution of standard sediments and "average shale" normalised to U.S.G.S. standard shale SCo-1.

additional advantage that analytical accuracy (which is difficult to determine) becomes subordinate to precision (which is easily measured) for the construction and interpretation of REE patterns. Absolute differences in concentrations of different elements as determined by different laboratories or methods would not, therefore, effect the comparison of the REE distributions which they produce.

An examination of the normalised data (Fig. 3) indicates a number of significant groups. Limestones (1b, 1c, 88a, KH) and the phosphate rock (120b) have negative Ce anomalies and are slightly enriched in the HREE, a pattern typical of carbonate rocks (Piper, 1974a, b; Parekh et al., 1977; Jarvis, 1984). Most shales and marine muds (MESS-1, BCSS-1, SGR-1, MAG-1, 1646) have relatively flat patterns with only weak HREE or LREE enrichment. Marine mud BCSS-1, in particular, has a flat pattern with very similar REE concentrations to SCo-1, and may provide a useful alternative normalisation reference should supplies of SCo-1 become exhausted. Marine mud MESS-1, on the other hand, has a small negative Eu anomaly and a higher REE content. Standard glauconite GL-0 is depleted in the LREE and strongly depleted in the HREE relative to the intermediate REE. This pattern varies considerably from previously published analyses of other pelletal glauconites (Fleet et al., 1980). Slate TB is depleted in the HREE, while black shale TS has a small positive Ce anomaly and is enriched in the HREE. Feldspar sand FK has a flat pattern with a strong positive Eu anomaly which is typical of feldspar minerals (Schnetzler and Philpotts, 1970; Arth, 1976).

An interpretation of these patterns is outside the scope of this paper and would require considerable geological data concerning the nature and origin of the various samples. The quality of our results, however, demonstrates that our cation-exchange and ICP methods are capable of accurately and precisely determining the REE distributions of a great variety of sedimentary rocks and minerals. Existing standard sediments display a wide range of REE

patterns and have REE contents from 0.05X to 5X those of "average" shale. It must be concluded, however, that more determinations are necessary before these standards can act as unequivocal reference materials for the REE.

Acknowledgements

ICP facilities and advice concerning analytical techniques were generously provided by Dr. J.N. Walsh. The ICP could not have been operated without the jovial assistance of Simon Chenery. Analytical data were obtained during the tenure of an I.L.E.A. Research Fellowship to the senior author while at the Department of Geology, City of London Polytechnic.

References

- Abbey, S., 1980. Studies in "standard samples" for use in the general analysis of silicate rocks and minerals. *Geostand. Newsl.*, 4: 163-190.
- Abbey, S., 1982. An evaluation of USGS III. *Geostand. Newsl.*, 6: 47-70.
- Addy, S.K., 1979. Rare earth element patterns in manganese nodules and micronodules from the northwest Atlantic. *Geochim. Cosmochim. Acta*, 43: 1105-1115.
- Arth, J.G., 1976. Behaviour of trace elements during magmatic processes - A summary of theoretical models and their applications. *J. Res. U.S. Geol. Surv.*, 4: 41-47.
- Bolton, A., Hwang, J. and Vander Voet, A., 1982. The determination of rare-earth elements in geological materials by ICP emission spectrometry. *ICP Info. Newsl.*, 7: 498-500.
- Boumans, P.W.J.M., 1978. ICP atomic emission spectrometry - a multielement analysis method for liquid and dissolved solids. *Sci. Ind. (Philips Gloeilampenfabrieken, Eindhoven)*, 12: 1.
- Brenner, I.B., Jones, E.A., Watson, A.E. and Steele, T.W., 1984. The application of a N₂-Ar medium-power ICP and cation-exchange chromatography for the spectrometric determination of the rare-earth elements in geological matrices. *Chem. Geol.*, 45: 135-148.
- Coryell, C.D., Chase, J.W. and Winchester, J.W., 1963. A procedure for geochemical interpretation of terrestrial rare-earth abundance patterns. *J. Geophys. Res.*, 68: 559-566.

- Crock, J.G. and Lichte, F.E., 1982. Determination of rare-earth elements in geological materials by inductively coupled argon plasma-atomic emission spectrometry. *Anal. Chem.*, 54: 1329-1332.
- Crock, J.G., Lichte, F.E. and Wildeman, T.R., 1984. The group separation of the rare-earth elements and yttrium from geologic materials by cation-exchange chromatography. *Chem. Geol.*, 45: 149-163.
- De Baar, H.J.W., Bacon, M.P. and Brewer, P.G., 1983. Rare-earth distributions with a positive Ce anomaly in the western North Atlantic Ocean. *Nature (London)*, 301: 324-327.
- Elderfield, H. and Greaves, M.J., 1981. Negative cerium anomalies in the rare earth element patterns of oceanic ferromanganese nodules. *Earth Planet. Sci. Lett.*, 55: 163-170.
- Elderfield, H. and Greaves, M.J., 1982. The rare earth elements in seawater. *Nature (London)*, 296: 214-219.
- Elderfield, H. and Greaves, M.J., 1983. Determination of the rare earth elements in sea water. In: C.S. Wong, E. Boyle, K.W. Bruland, J.D. Burton and E.D. Goldberg (Editors), *Trace Elements in Seawater*. Plenum, New York, N.Y., pp. 427-445.
- Elderfield, H., Hawkesworth, C.J. and Greaves, M.J., 1981. Rare earth element geochemistry of oceanic ferromanganese nodules and associated sediments. *Geochim. Cosmochim. Acta*, 45: 513-528.
- Flanagan, F.J., 1973. 1972 values for international geochemical reference samples. *Geochim. Cosmochim. Acta*, 37: 1189-1200.
- Fleet, A.J., 1983. Hydrothermal and hydrogenous ferromanganese deposits: do they form a continuum? The rare earth element evidence. In: P.A. Rona, K. Boström, L. Laubier and K.L. Smith (Editors), *Hydrothermal Processes at Seafloor Spreading Centers*. Plenum, New York, N.Y., pp. 535-555.
- Fleet, A.J., Buckley, H.A. and Johnson, L.R., 1980. The rare earth element geochemistry of glauconites and celadonites. *J. Geol. Soc. London*, 137: 683-688.
- Goldberg, E.D., Koide, M., Schmitt, R.A. and Smith, R.H., 1963. Rare earth distributions in the marine environment. *J. Geophys. Res.*, 68: 4209-4217.
- Haskin, L.A., Wildeman, T.R., Frey, F.A., Collins, K.A., Keedy, C.R. and Haskin, M.A., 1966a. Rare earths in sediments. *J. Geophys. Res.*, 71: 6091-6105.
- Haskin, L.A., Frey, F.A., Schmitt, R.A. and Smith, R.H., 1966b. Meteoric, solar and terrestrial rare-earth distributions. In: L.H. Ahrens, F. Press, S.K. Runcorn and H.C. Urey (Editors), *Physics and Chemistry of the Earth*, Vol. 7. Pergamon, Oxford, pp. 167-321.
- Haskin, L.A., Haskin, M.A., Frey, F.A. and Wildeman, T.R., 1968. Relative and absolute terrestrial abundances of the rare earths. In: L.H. Ahrens (Editor), *Origin and Distribution of the Elements*. Pergamon, Oxford, pp. 889-912.
- Haskin, M.A. and Haskin, L.A., 1966. Rare earths in European shales: a redetermination. *Science*, 154: 507-509.
- Høgdahl, O.T., Melsom, S. and Bowen, V.T., 1968. Neutron activation of lanthanide elements in seawater. *Adv. Chem. Ser.*, 73: 308-325.
- Hoyle, J., Elderfield, H., Gledhill, A. and Greaves, M., 1984. The behaviour of the rare earth elements during mixing of river and sea waters. *Geochim. Cosmochim. Acta*, 48: 143-149.
- Jarvis, I., 1980. Genesis and diagenesis of Santonian to early Campanian (Cretaceous) phosphatic chalks of the Anglo-Paris Basin. D. Phil. Thesis, Oxford University, Oxford, (unpublished).
- Jarvis, I., 1984. Rare-earth element geochemistry of late Cretaceous chalks and phosphorites from northern France. *Proc. 4th Int. Seminar on Phosphorite*, Udaipur, Nov. 1981. *Spec. Publ. Geol. Surv. India*, 17: 179-180.
- Jones, E.A. and Dixon, K., 1978. A review of the literature on the separation and determination of rare earth elements. *Natl. Inst. Metall., Randburg, Rep. No.* 1945.
- Keasler, K.M. and Loveland, W.D., 1982. Rare earth elemental concentrations in some Pacific Northwest rivers. *Earth Planet. Sci. Lett.*, 61: 68-72.
- Klinkhammer, G.P., Elderfield, H. and Hudson, A., 1983. Rare earth elements in sea water near hydrothermal vents. *Nature (London)*, 305: 185-188.
- Krauskopf, K.B., 1967. *Introduction to Geochemistry*. McGraw-Hill, New York, N.Y., 721 pp.
- Martin, J.-M., Høgdahl, O. and Philippot, J.C., 1976. Rare earth element supply to the Ocean. *J. Geophys. Res.*, 81: 3119-3124.
- Masuda, A., 1965. The abundance ratios between the average basic rock and chondrites as a function of reciprocal ionic radii. *Tectonophysics*, 2: 299-317.
- McLennan, S.M. and Taylor, S.R., 1980. Geochemical standards for sedimentary rocks: trace-element data for U.S.G.S. standards SCo-1, MAG-1 and SGR-1. *Chem. Geol.*, 29: 333-343.
- McLennan, S.M., Fryer, B.J. and Young, G.M., 1979a. Rare earth elements in Huronian (Lower Proterozoic) sedimentary rocks: composition and evolution of the post-Kenoran upper crust. *Geochim. Cosmochim. Acta*, 43: 375-388.
- McLennan, S.M., Fryer, B.J. and Young, G.M., 1979b. The geochemistry of the carbonate-rich Espanola Formation (Huronian) with emphasis on the rare earth elements. *Can. J. Earth Sci.*, 16: 230-239.
- McLennan, S.M., Nance, W.B. and Taylor, S.R., 1980. Rare earth element-thorium correlations in sedimentary rocks, and the composition of the conti-

- mental crust. *Geochim. Cosmochim. Acta*, 44: 1833-1839.
- Murphy, K. and Dymond, J., 1984. Rare earth element fluxes and geochemical budget in the eastern equatorial Pacific. *Nature (London)*, 307: 444-447.
- Nakamura, N., 1974. Determination of REE, Ba, Fe, Mg, Na and K in carbonaceous and ordinary chondrites. *Geochim. Cosmochim. Acta*, 38: 575-775.
- Nance, W.B. and Taylor, S.R., 1976. Rare earth element patterns and crustal evolution, I. Australian post-Archean sedimentary rocks. *Geochim. Cosmochim. Acta*, 40: 1539-1551.
- Parekh, P.P., Moller, P., Dulski, P. and Bausch, W.M., 1977. Distribution of trace elements between carbonates and non-carbonate phases of limestone. *Earth Planet. Sci. Lett.*, 34: 39-50.
- Piper, D.Z., 1972. Rare-earth elements in manganese nodules from the Pacific Ocean. In: D.R. Horn (Editor), *Ferromanganese Deposits on the Ocean Floor*. U.S. Government Printing Office, Washington, D.C., pp. 123-130.
- Piper, D.Z., 1974a. Rare-earth elements in ferromanganese nodules and other marine phases. *Geochim. Cosmochim. Acta*, 38: 1007-1022.
- Piper, D.Z., 1974b. Rare-earth elements in the sedimentary cycle: a summary. *Chem. Geol.*, 14: 285-304.
- Piper, D.Z. and Graef, P.A., 1974. Gold and the rare-earth elements in sediments from the East Pacific Rise. *Mar. Geol.*, 17: 287-297.
- Piper, D.Z., Veeh, H.H., Bertrand, W.G. and Chase, R.L., 1975. An iron-rich deposit from the north-west Pacific. *Earth Planet. Sci. Lett.*, 26: 114-120.
- Potts, P.J., Thorpe, O.W. and Watson, J.S., 1981. Determination of the rare-earth element abundances of 29 international rock standards by instrumental neutron activation analysis: a critical appraisal of calibration errors. *Chem. Geol.*, 34: 331-352.
- Schnetzler, C.C. and Philpotts, J.A., 1970. Partition coefficients of rare-earth minerals between igneous matrix material and rock-forming phenocrysts. *Geochim. Cosmochim. Acta*, 34: 331-340.
- Schofield, A. and Haskin, L.A., 1964. Rare-earth distribution patterns in eight terrestrial materials. *Geochim. Cosmochim. Acta*, 28: 437-446.
- Shannon, R.D., 1976. Revised effective ionic radii and systematic studies of interatomic distances in halides and chalcogenides. *Acta Crystallogr.*, A32: 751-767.
- Strelow, F.W.E. and Jackson, P.F.S., 1974. Determination of trace and ultra-trace quantities of rare-earth elements by ion exchange chromatography-mass spectrography. *Anal. Chem.*, 46: 1481-1486.
- Thirlwall, M., 1981. A triple-filament method for rapid and precise analysis of rare-earth elements by isotope dilution. *Chem. Geol.*, 35: 155-166.
- Thompson, M. and Walsh, J.N., 1983. *A Handbook of Inductively Coupled Plasma Spectrometry*. Blackie, Glasgow, 273 pp.
- Tlig, S., 1982. Distribution des terres rares dans les fractions de sédiments et nodules de Fe et Mn associés en l'Océan Indien. *Mar. Geol.*, 50: 257-274.
- Tlig, S. and Steinberg, M., 1982. Distribution of rare-earth elements (REE) in size fractions of recent sediments of the Indian Ocean. *Chem. Geol.*, 37: 317-333.
- Walsh, J.N. and Howie, R.A., 1980. An evaluation of the performance of an inductively coupled plasma source spectrometer for the determination of the major and trace constituents of silicate rocks and minerals. *Mineral. Mag.*, 43: 967-974.
- Walsh, J.N., Buckley, F. and Barker, J., 1981. The simultaneous determination of the rare-earth elements in rocks using inductively coupled plasma source spectrometry. *Chem. Geol.*, 33: 141-153.
- Wildeman, T.R. and Haskin, L.A., 1965. Rare-earth elements in ocean sediments. *J. Geophys. Res.*, 70: 2905-2910.
- Wildeman, T.R. and Haskin, L.A., 1973. Rare earths in Precambrian sediments. *Geochim. Cosmochim. Acta*, 37: 419-438.

Attention is drawn to the fact that the copyright of this thesis rests with its author.

This copy of the thesis has been supplied on condition that anyone who consults it is understood to recognise that its copyright rests with its author and that no quotation from the thesis and no information derived from it may be published without the author's prior written consent.

III

D

D74933'87

END